The Impact of Alkyl- and Alkoxy-functionalization on the Responsive Behaviour of Metal-Organic Frameworks: From Conventional to Frustrated Flexibility

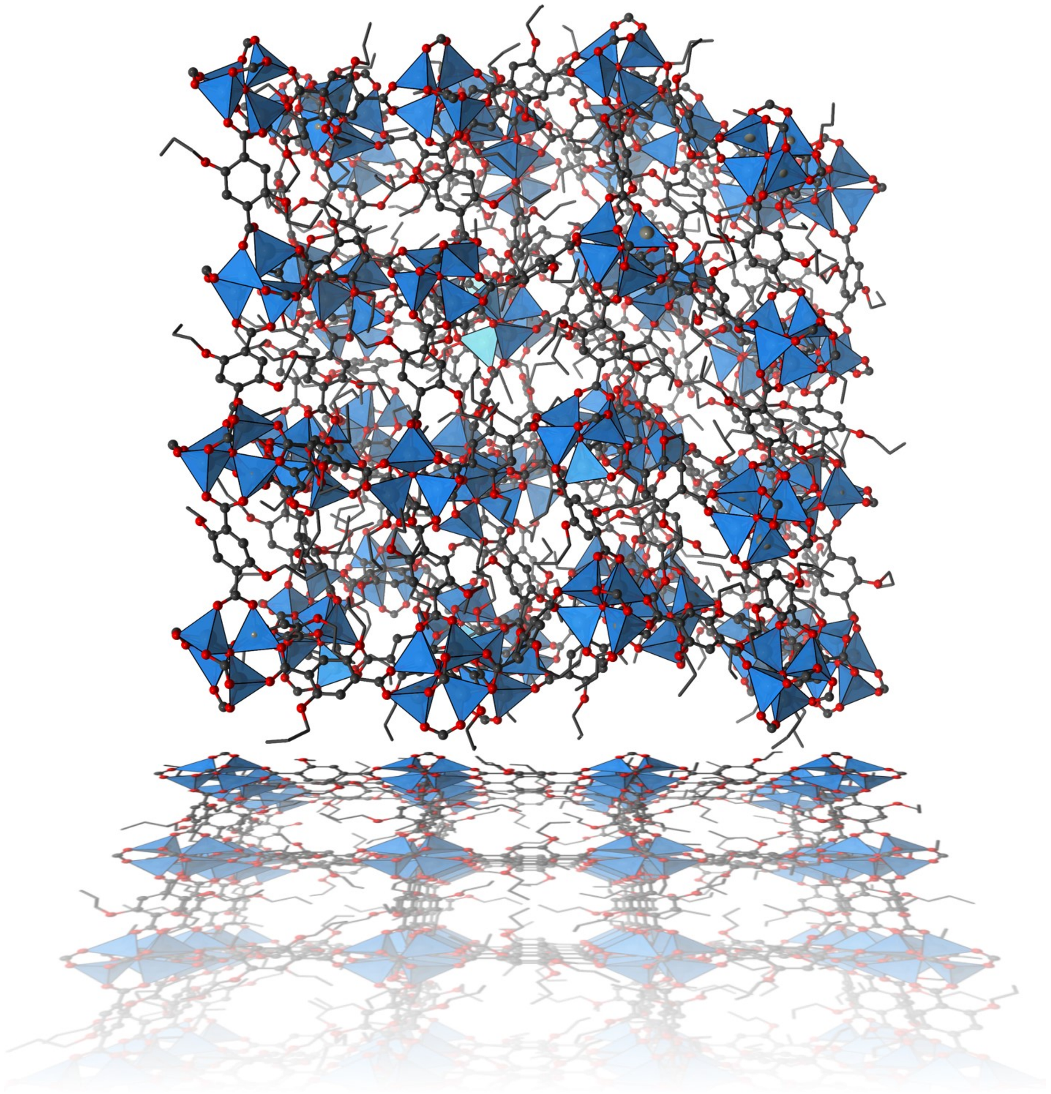

Dissertation

Roman Pallach

August 2022

The Impact of Alkyl- and Alkoxy-functionalization on the Responsive Behaviour of Metal-Organic Frameworks: From Conventional to Frustrated Flexibility

Faculty of Chemistry and Chemical Biology

Technische Universität Dortmund

Dissertation

Submitted by

Roman Pallach

August 2022

This work has been performed in the time between March 2017 and August 2022 in the Inorganic Chemistry Department of the Faculty of Chemistry and Chemical Biology of the Technische Universität Dortmund.

1st referee: Prof. Dr. Sebastian Henke

2nd referee: Prof. Dr. Rochus Schmid

Date of Submission: 19.08.2022

Date of Examination: 17.10.2022

You can know the name of a bird in all the languages of the world, but when you're finished, you'll know absolutely nothing whatever about the bird...

So let's look at the bird and see what it's doing – that's what counts.

- *Richard P. Feynman (1918-1988)*

I am deeply indebted to my supervisor

Prof. Dr. Sebastian Henke

for giving me the opportunity to work on this stimulating topic and the invaluable support, teaching, and motivation throughout the work on this dissertation.

I also thank Prof. Dr. Rochus Schmid for accepting to be the second referee of this dissertation.

Furthermore, I am thankful to the dedicated beamline scientists without whom it would not have been possible to realize this work:

Dr. Phil Chater for the collection and the support during the processing of X-ray total scattering data at DLS (Diamond Light Source, UK).

Dr. Michael Wharmby for his great support during beamtimes at DESY (Deutsches Elektronen Synchrotron, Hamburg, Germany).

Dr. Christian Sternemann and Dr. Michael Paulus for their straightforward support at our friendly neighbourhood synchrotron, DELTA (Dortmunder Elektronen Speicherring-Anlage, Dortmund, Germany).

I am also thankful to Dr. Julian Keupp and Prof. Dr. Rochus Schmid for running MD simulations and the fruitful discussions on computational and experimental data.

Further, Julia Kotschy, Dr. Suresh Vasa and Prof. Dr. Rasmus Linser are acknowledged for the collection and discussion of MAS NMR data.

I would also like to thank Erik Svensson Grape and Dr. Andrew Kentaro Inge for the collection and interpretation of 3D electron diffraction data.

Besides, I would also like to thank the staff of the NMR department for measuring a number of NMR spectra over the years and Dr. Katarina Peikert of Micromeritics for collecting high-resolution gas sorption isotherms.

I would like to acknowledge the inorganic chemistry secretaries, Helga Schulte, Peggy Sieg, Birgit Thormann and Michaela Markert for the enormous help with paperwork and all sorts of things.

Furthermore, I am thankful to the students and trainees who have partially contributed to this thesis: Kai Terlinden, Nicholas Jankowski, Julia Kuhnt, Veronika Leier, Lennart Eisel, Christian Nelle, Thomas Halmanseder, Kevin Schäfer, Adrian Podlesny, Sven Golenia, Julian Dyrda and Jannik Engel.

In particular, I would like to thank the bachelor and master students I had the pleasure to work with during the course of this dissertation: Timo Schüppen, Andrea Machalica, and Lars Lobert.

I wish to thank all the past and present members of the Henke group who created a very pleasant and enjoyable working climate: Louis Frentzel-Beyme, Marvin Kloss, Stefan Koop, Julia Kuhnt, Pascal Kolodzeiski, Kai Terlinden, Andrea Machalica, Jianbo Song, Xue Wenlong, Jan-Benedikt Weiß, Dr. Athanasios Koutsianos, Dr. Collins Erinmwingbovo, Christian Nelle, Michael Strobl, Dr. Chinmoy Das, Lennard Richter, Elizaveta Stoliarova, Denise Zickler, Lena Hafner, and Jannik Engel.

Special thanks go to Louis Frentzel-Beyme for being a very good colleague to share the lab and office with, the fun times abroad at conferences or workshops and all the conversations about chemistry and non-chemistry throughout the last years.

I would also like to thank my friends, especially Phil and Andre, for the great time we spend together and keeping the right work-life balance while studying chemistry.

Last but not least, I am grateful to my family for the unconditional and unequivocal support and, finally, Britta for her constant patience, understanding and support.

Abstract

The investigation of functional materials, which can change their physical properties depending on external triggers is of ongoing interest for various fields of materials research. Metal-organic frameworks (MOFs) are porous coordination polymers constructed of inorganic building units (e.g., metal-ions, metal-oxo-clusters) joined by organic building units (e.g., multidentate carboxylates), also called linkers. A particular subclass of MOFs are flexible MOFs, which undergo structural changes as a function of external stimuli. This behaviour arises from a delicate balance between enthalpic (e.g., dispersion interactions) and entropic (e.g., vibrational motions) contributions, which can be modified and controlled by the introduction of additional functional groups at the organic building unit of the framework.

In this work, alkyl-, alkoxy-, and methoxy-alkoxy group functionalization of the organic building unit was utilized to modulate and study the influence of sidechain length and polarity on the structural responsivity of two fundamentally different MOF platforms. Of these, one is intrinsically flexible (DMOF-1), while the other one is structurally rigid (MOF-5).

For the DMOF-1-based materials, it has been shown in the past that the implementation of alkoxy groups induces a guest- and temperature-depending switching between contracted and expanded phases. In this work, a series of purely alkyl-functionalized DMOF-1 derivatives was studied and structurally characterized in great detail by means of single crystal and powder X-ray diffraction. Furthermore, their sorption behaviour towards N_2, CO_2 and C_3 and C_4 hydrocarbons was investigated and subsequently compared to their alkoxy counterparts, which revealed significant differences that strongly relate to the different polarities of the functional groups. Particular highlights are path-depending multi-step CO_2 sorption behaviours and an interesting propane/propylene gating behaviour with potential for an application in the separation of the gases, both phenomena were studied by *in-situ* X-ray diffraction techniques. Upon thermal treatment, the new alkyl functionalized DMOF-1 derivatives exhibit a significantly softer behaviour than their alkoxy counterparts indicating a much flatter free energy landscape for these materials in connection with weaker intra-framework interactions of the less polar alkyl groups.

In the second part of this thesis, the concept of *frustrated flexibility* of MOFs is introduced. Due to the incompatibility of a rigid, non-responsive MOF structure type (here MOF-5) with intra-framework dispersion forces demanding a densification of the structure a new type of responsive behaviour evolves. Controlled by chemical functionalization of the organic linkers with dispersion energy donating (DED) alkoxy groups, a series of materials is obtained, which reversibly switch between a cubic crystalline and either a non-crystalline or a rhombohedral phase. These transitions are either driven enthalpically through guest adsorption/desorption or by vibrational entropy at elevated temperatures. Importantly, frustratedly flexible behaviour is shown to be tuneable by adjusting the length and polarity of the DED groups.

Overall, the results presented herein demonstrate that linker functionalization is a powerful tool to modulate the free energy landscape of MOF materials. For intrinsically flexible MOFs this approach allows targeted fine-tuning of their flexible behaviour, while for rigid MOFs it allows for the generation of completely new and exotic responsive behaviour.

Kurzfassung

Funktionelle Materialien, die ihre physikalischen Eigenschaften in Reaktion auf einen äußeren Reiz verändern können, verbleiben im Fokus verschiedenster Teildisziplinen der Materialwissenschaften. Bei Metallorganischen Gerüstverbindungen (MOFs) handelt es sich um poröse Koordinationspolymere, bestehend aus anorganischen Baueinheiten (z.B. Metallkationen, Metall-oxo-Cluster), welche durch organische Baueinheiten (z.B. multidentate Carboxylate), auch als Linker bezeichnet, miteinander verknüpft werden. Eine spezielle Teilklasse sind hierbei die sogenannten flexiblen MOFs, welche induziert durch einen externen Stimulus strukturelle Transformationen unternehmen können. Dieses Verhalten resultiert aus einem empfindlichen Zusammenspiel enthalpischer (z.B. Dispersionswechselwirkungen) und entropischer (z.B. angeregte Schwingungszustände) Beiträge, das leicht durch zusätzliche funktionelle Gruppen an der organischen Baueinheit beeinflusst werden kann.

Im Rahmen dieser Arbeit wurde das flexible Verhalten zweier MOF Systeme durch das gezielte Einbringen von Alkyl-, Alkoxy- und Methoxy-alkoxygruppen an der organischen Baueinheit systematisch moduliert. Hierbei unterscheiden sich die untersuchten MOF Systeme grundlegend: Das eine zeigt intrinsisch flexibles Verhalten (DMOF-1), das andere besitzt eine starre Gerüstarchitektur (MOF-5).

Im Falle der DMOF-1 basierten Materialien konnte in der Vergangenheit bereits gezeigt werden, dass eine Funktionalisierung der organischen Linker mit Alkoxygruppen zu Gast- oder Temperatur-schaltbaren Phasenumwandlungen zwischen einer kontrahierten und einer expandierten Phase führt. In dieser Arbeit wurde das Phasenverhalten von neuen rein alkyl-funktionalisierten DMOF-1-Derivaten untersucht. Diese Materialien erlauben eine detaillierte strukturelle Charakterisierung sowohl der expandierten als auch der kontrahierten Phasen durch Pulver- und Einkristallröntgenstrukturanalyse. Ein Vergleich des Sorptionsverhaltens gegenüber den Gasen N$_2$, CO$_2$, sowie C$_3$ und C$_4$ Kohlenwasserstoffen zeigt deutliche Unterschiede zu den verwandten alkoxy-Derivaten auf, welche sich auf die geringeren Polaritäten der alkyl-Seitenketten zurückführen lassen. Besonders ins Auge stechen hier ein mehrstufiges, richtungsabhäniges CO$_2$-Sorptionsverhalten, sowie ein hochinteressantes Schaltverhalten (gating) bei der Sorption von Propan und Propylen, das Anwendungspotential für die Trennung dieser Gase birgt. Diese beiden Phänomene wurden mittels *in-situ* Röntgenpulverbeugung im Detail untersucht. Durch die thermische Behandlung der alkyl-DMOF-1-Derivate wird außerdem klar, dass diese bedingt durch schwächere Wechselwirkungen der Alkylgruppen untereinander und mit dem Netzwerkrückgrat ein deutlich weicheres Verhalten zeigen als ihre Alkoxy-Pendants. Dies deutet somit auf eine flachere Energielandschaft dieser Materialien hin.

Im zweiten Teil der Arbeit wird das Prinzip der Frustrierten Flexibilität von MOFs vorgestellt. Dieses basiert auf der Inkompatibilität eines starren MOF Strukturtyps (hier MOF-5) mit der Präsenz von Dispersionswechselwirkungen innerhalb des Netzwerks, welche jedoch eine Kontraktion des Materials begünstigen. Dies führt zu einem bisher unbeschriebenen Typ responsiven Verhaltens. Erreicht wird dies durch chemische Funktionalisierung der organischen Baueinheit mit Dispersionsenergie-donierenden (DED) Alkoxygruppen variabler Länge. Auf diesem Wege wird ein Phasenverhalten zwischen kubisch-kristallinen und nichtkristallinen bzw.

kubisch-kristallinen und rhomboedrischen Phasen erzeugt. Diese Phasenumwandlungen sind entweder durch Adsorption von Gastmolekülen Enthalpie getrieben oder durch Vibrationsentropie bei erhöhter Temperatur. Hervorzuheben ist, dass überdies gezeigt werden konnte, dass die Polarität der Seitenketten das frustriert-flexible Verhalten der vorgestellten MOF-5-Derivate entscheidend beeinflusst.

Anhand der vorliegenden Ergebnisse zeigt sich die chemische Funktionalisierung der organischen Baueinheiten von MOFs als effektives Mittel zur gezielten Manipulation der Energielandschaft von MOF-Materialien. Auf diese Weise kann sowohl das Verhalten intrinsisch flexibler MOFs gezielt beeinflusst werden als auch grundlegend neues und ungewöhnliches responsives Verhalten in vormals starren MOFs hervorgerufen werden.

Contents

List of Abbreviations

bp	boiling point
V_{pore}	pore volume
V_{ads}	adsorbed volume
p_{trans}	critical phase transition pressure
Q_{FSP}	Q-value of the maximum of the FSP
S_{BET}	specific BET surface area
3DED	3D electron diffraction
Ac	acetyl
bdc^{2-}	benzene dicarboxylate
BET	Brunauer-Emmett-Teller
bpdc^{2-}	biphenyl dicarboxylate
btb^{3-}	1,3,5-benzene-tris(4'-benzoate)
btc^{3-}	1,3,5-benzenetricarboxylate
CCDC	Cambridge crystallographic data centre
DLS	Diamond Light Source
CP	cross-polarization
CSEV	Connolly solvent-excluded volume
CTE	coefficient of thermal expansion
Dabco	1,4-diazabicyclo[2.2.2]octane
DBAD	di-*tert*-butyl azodiformate
DCM	dichloromethane
DDED	dipolar and dispersion energy donor
DED	dispersion energy donator
DEF	*N*,*N*-diethylformamide
DELTA	Dortmunder Elektronenspeicherring Anlage

DESY	Deutsches Elektronen Synchrotron
DMF	*N*,*N*-dimethylformamide
DMOF	dabco-MOF
DMSO	dimethyl sulfoxide
dhcb^{2-}	1,2-dihydrocyclobutabenzene-3,6-dicarboxylate
dppf	1,1′- bis(diphenylphosphino) ferrocene
DSC	differential scanning calorimetry
Et	Ethyl
FT-IR spectroscopy	Fourier Transform Infrared spectroscopy
FSP	first scattering peak
FWHM	full width at half maximum
HKUST	Hong Kong University of Science and Technology
ip	intermediate pore
iPr	iso-propyl
IRMOF	Isoreticular MOF
IUPAC	International Union of Pure and Applied Chemistry
lp	large pore
MAS	magic angle spinning
MD	molecular dynamics
Me	methyl
MIL	Material of Institute Lavoisier
MOF	Metal-organic Framework
ndc^{2-}	2,6-naphthalene dicarboxylate
NMP	*N*-methyl-2-pyrrolidone
NMR spectroscopy	Nuclear Magnetic Resonance spectroscopy
np	narrow pore
pbc	periodic boundary conditions

PXRD	Powder X-ray Diffraction
RH	relative humidity
RT	room temperature
SBU	secondary building unit
SCXRD	Single Crystal X-ray Diffraction
SPC	soft porous crystal
TG	thermogravimetry
THF	tetrahydrofuran
tpdc^{2-}	terphenyl dicarboxylate
VT	variable temperature
XPDF	X-ray pair distribution function

1 Motivation & Aims

The discovery and exploration of stimuli-responsive materials, which change their physical properties depending on an external stimulus continues to draw attention from different fields of materials science due to its high relevance for the development of future technology. One class of functional materials are Metal-organic Frameworks (MOFs), which are constructed of inorganic building units interconnected by organic building units yielding a framework with permanent porosity. A particular subclass of MOFs are the so-called flexible MOFs, which are characterized by the ability to undergo structural transformations in response to an external stimulus. This property renders these materials interesting candidates for applications in various fields such as gas storage, separations, chemical sensing, controlled drug release or as shock absorbers.

The stimuli-dependent behaviour of flexible MOFs is governed by a delicate balance of enthalpic (e.g., covalent, and coordinative bonds, dispersion and dipolar interactions) and entropic contributions (e.g., vibrational and configurational degrees of freedom). It has been demonstrated that this balance is highly affected by the implementation of functional groups at the organic building unit of the framework due to additional dispersion interactions between the functional groups and the framework backbone.

As a general basis for this work, the means of choice for a tuning of the flexible behaviour of a MOF are 2,5-di-R-bdc^{2-} (R = alkyl (CX), alkoxy (OCX), or methoxy-alkoxy (OCXOC1)) linkers, where the length of the R-group can be varied. This type of organic linker has been demonstrated to be applicable to a wide range of MOF materials. In this work, it will be applied to two fundamentally different MOF platforms, (i) the intrinsically flexible DMOF-1, and (ii) the structurally rigid MOF-5.

In the case of alkoxy-functionalized DMOF-1 derivatives previous works have shown that their free energy landscape is changed to the effect that reversible transitions between a guest-filled expanded large pore phase and a guest-free contracted narrow pore phase occur. Here, the latter phase is stabilized by dispersion and dipolar interactions of the alkoxy groups with themselves and the framework backbone. However, detailed structural information on these materials, which would be crucial for a comprehensive understanding and the development of design principles for this kind of compounds, could not be obtained to date.

In the first part of this work, the library of functionalized DMOF-1 materials is extended towards three new purely alkyl functionalized derivatives. For the first time for this material class, sought-after high-detail structural data on both large and narrow pore phases are available and will be precisely analysed. Furthermore, the sorption and thermal properties of these new materials will be studied compared to their alkoxy relatives in order to pinpoint the differences in their behaviours arising from the less polar nature of the alkyl substituents. Importantly, over the course of this study, both the alkyl- and alkoxy functionalized DMOF-1 derivatives will be evaluated in terms of their sorption behaviour towards industrially relevant C4 and C3 hydrocarbons. In particular, the separation of propane and propylene is a major separation problem in petrochemical industry with huge energy and monetary saving potential.

The second part will move away from the generally well-investigated crystalline-to-crystalline type of MOF flexibility and gain insights into a fundamentally new type of flexible behaviour. Here, the concept of frustrated flexibility will be introduced, which is based on the incompatibility between the geometrical constraints of the rigid MOF-5 structure type and dispersion energy donating alkoxy groups, which demand a densification of the structure in its guest-free state. Thus, the minimization of enthalpy should only occur upon entering a frustrated state upon loss of crystalline order giving rise to materials featuring reversible crystalline-to-non-crystalline phase transitions.

In order to evaluate this concept, a series of MOF-5 derivatives bearing alkoxy groups of variable length will be investigated regarding their structural behaviour as a function of guest content and temperature. Furthermore, the tunability of frustrated flexibility will be assessed via adjustment of the polarity of the functional groups. Finally, it will be discussed, which other MOF platforms could also exhibit frustrated flexibility when suitably functionalized.

2 General Introduction

2.1 Metal-Organic Frameworks (MOFs)

Since their advent in the late 1990s,[1–4] Metal-Organic Frameworks, abbreviated MOFs, have gained considerable attention due to their unique combination of properties, such as high porosity with high internal surface areas (up to 9140 m^{2}g^{-1})[5] and high thermal stability (up to 600 °C)[6] teamed with a chemically modular nature. These render this class of solid-state materials promising candidates for applications in the fields of gas storage and separation, catalysis, and sensing.[7]

In 2013, the IUPAC recommended a definition of the term Metal-Organic Framework, abbreviated MOF, according to which a MOF can be considered a "coordination network with organic ligands containing potential voids".[8] Most conveniently, the construction of MOFs can be understood in terms of inorganic building units or nodes (e.g., metal-ions, metal-oxo-clusters), which are interconnected by organic building units (e.g., multidentate carboxylates, imidazolates), also called linkers, forming a permanently porous framework (Figure 2.1).

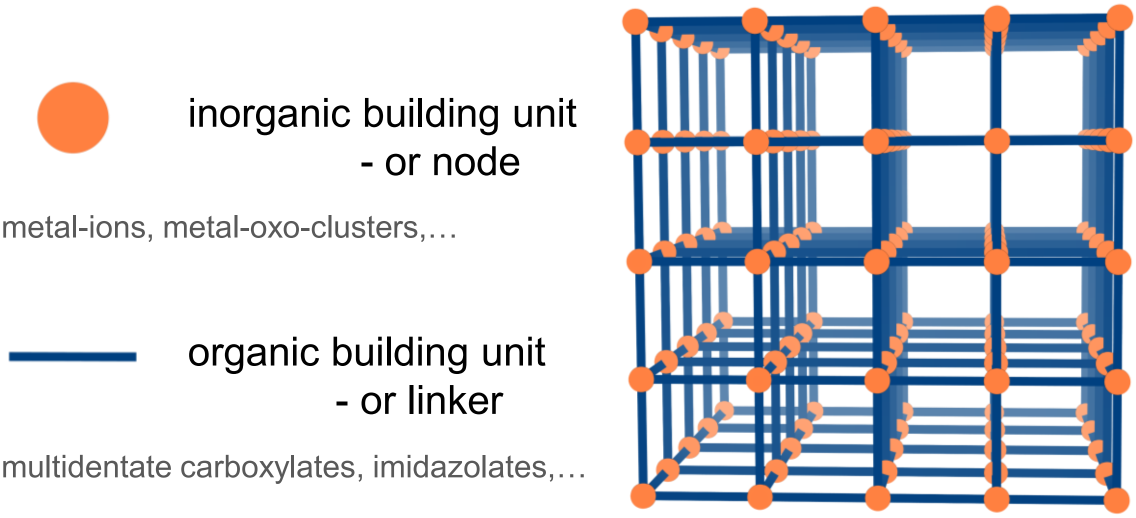

Figure 2.1: Schematic structure of a Metal-Organic Framework (MOF).

In many cases MOFs are denoted by a 2 – 5 letter code according to the institute or university at which they were discovered followed by a serial number (e.g., HKUST-1 (Hong Kong University of Science and Technology),[3] MIL-53 (Materials of Institute Lavoisier)[9]). However, there are naming schemes deviating from this rule, e.g., MOF materials prepared in the YAGHI group are simply called MOF-n (n = serial number).[2]

MOFs are prepared most frequently via solvothermal synthesis from a metal salt and linker precursor (e.g., carboxylic acids, imidazoles) containing solution.[10] But also, other methods have been established such as microwave-assisted,[11] electrochemical,[12] sonochemical,[13] and mechanochemical[14] approaches. Importantly, the reaction conditions have to be chosen in such a way, that specific inorganic building units of distinct geometries are generated *in-situ*.[15]

At the heart of MOF chemistry lies the concept of *reticular synthesis*, which was introduced by Yaghi and O'Keefe in the early 2000s, as it aims at the targeted design of the underlying connectivity, i.e., the topology of a MOF structure.[15,16] In this approach, inorganic and organic building units are reduced to defined geometrical shapes according to their basic connectivity. These shapes are called secondary building units (SBUs).[17,18] A list of selected examples taken from the domain of carboxylate-based MOFs is given in Figure 2.2.[15] Thus, a desired topology can be realized by the utilization of the corresponding set of SBUs and furthermore, potential topologies resulting from a given set of SBUs can be identified. In practice, the reticular synthesis concept has not only helped to understand and generate a wide range of new MOF structures over the years,[19–23] but also to evermore yield record porosities and specific surface areas, for example.[5,24–26] This is because limitations in porosity often arise from framework interpenetration (i.e., the intergrowth of two or more frameworks in a structure without a chemical linking)[15], a problem, which was overcome by the selection of a topology, which by itself cannot interpenetrate, followed by *isoreticular* expansion of the framework.

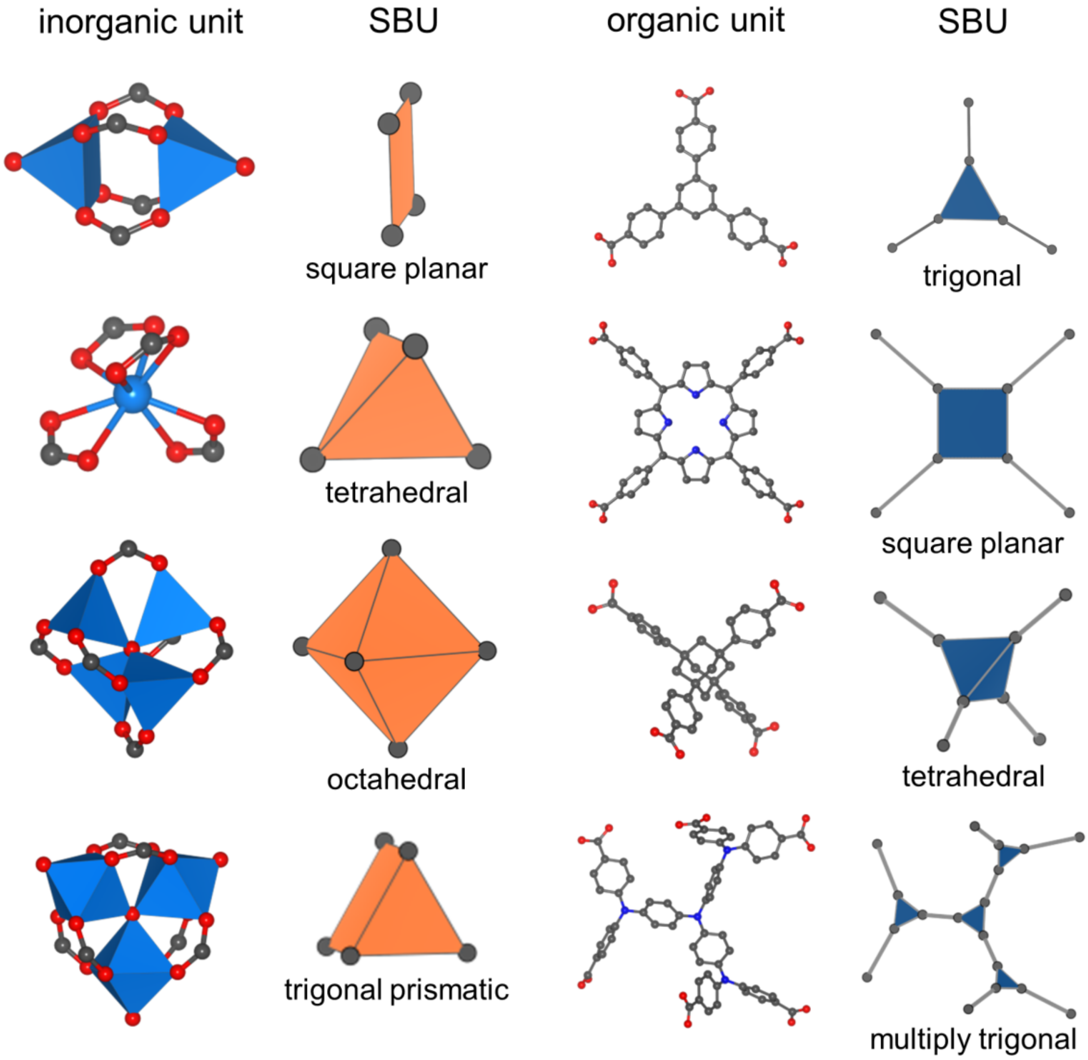

Figure 2.2: Compilation of various inorganic and organic units and their corresponding SBUs according to the literature.[15] Atoms are coloured in standard colouring (Carbon: dark grey, Nitrogen: blue, Oxygen: red), while metal cations and coordination polyhedrons are coloured in light blue.

This further connects to the invaluable branch of reticular chemistry, which is the discipline of *isoreticular chemistry*. Here, the underlying topology of the MOF structure is retained, while the implemented organic linkers are elongated or decorated, resulting either in an expansion of the framework structure or a chemical functionalization of the material.[15] Furthermore, the inorganic unit may be altered, for example by the usage of different metal ions.[27] Importantly, upon modification of the organic or inorganic unit, its chemical connectivity needs to remain unchanged to retain its exact topological function.

The term isoreticular was coined in 2002 with the introduction of the IRMOF-n (Isoreticular MOF; n = consecutive integer) series of isoreticular MOFs.[28] This series is based on the framework architecture of the archetypical MOF-5, also called IRMOF-1, which is constructed of the octahedrally connecting $Zn_4O(CO_2)_6$ units linked by 1,4-benzenedicarboxylate (bdc^{2-}) giving a framework of primitive cubic (**pcu**) topology (Figure 2.3).[2]

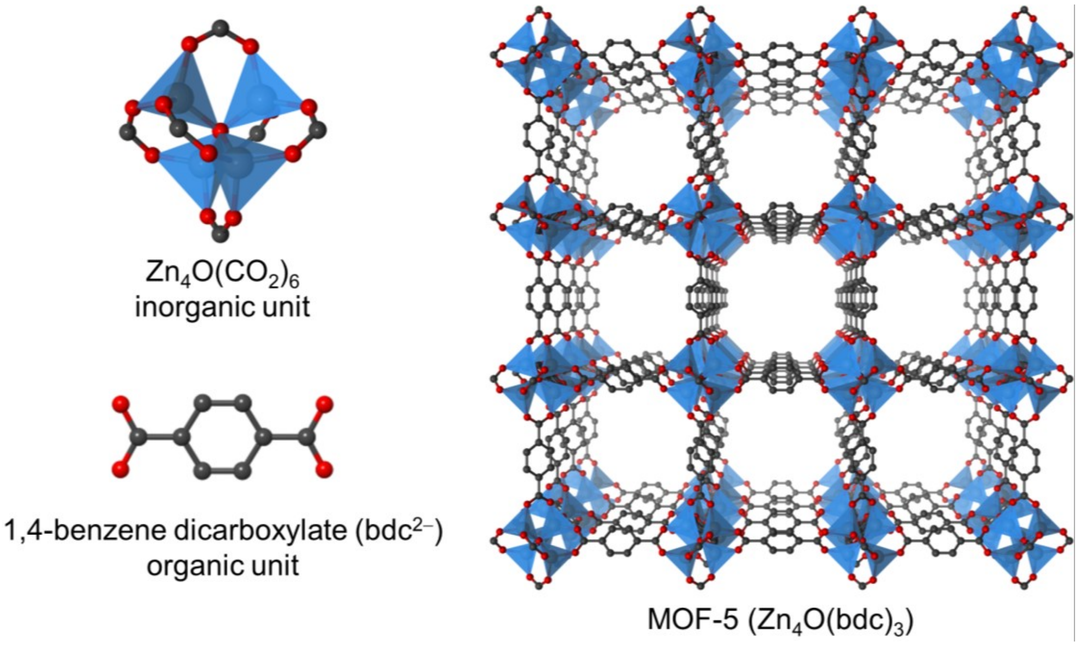

Figure 2.3: Structure and composition of MOF-5 ($Zn_4O(bdc)_3$) (CCDC deposition code 256965).

Upon elongation of the organic linker by replacing the former bdc^{2-} by 2,6-ndc^{2-} (2,6-naphthalene dicarboxylate, IRMOF-8), $bpdc^{2-}$ (4,4'-biphenyl dicarboxylate, IRMOF-10) or $tpdc^{2-}$ (terphenyl dicarboxylate, IRMOF-16) the framework was expanded resulting in an increase in the free crystallographic volume fraction from 79.2% (MOF-5) up to 91.1% (IRMOF-16) (Figure 2.4).[28] Furthermore, the MOF-5/IRMOF-1 material platform allows for the incorporation of different functionalized bdc^{2-} variants, bearing, e.g., bromo (IRMOF-2, Figure 2.4), amino (IRMOF-3, Figure 2.4) and other moieties. This early study already suggested great potential for the modification of MOFs and later on in 2010, up to eight differently functionalized bdc^{2-} derivatives could be installed in the MOF-5 structure type at the same time, producing the so-called multivariate MOFs (materials, which would be classified as multi-component solid solutions in traditional solid state chemistry).[29] Today, arising from the isoreticular chemistry principle and a huge library of available inorganic and organic building units, the highly tuneable nature of MOF materials is considered one of their unique selling points compared to other porous materials, such as for example zeolites.[30]

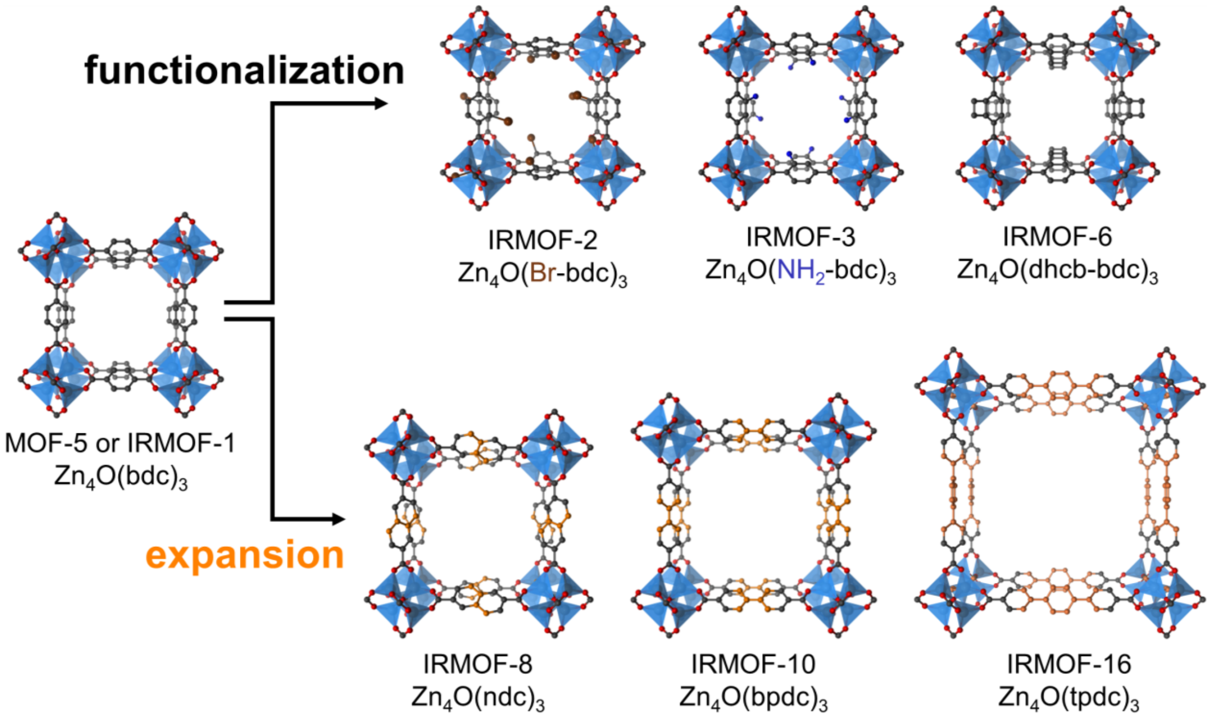

Figure 2.4: Representation of the isoreticular expansion and functionalization of the IRMOF-n series,[28] $dhcb^{2-}$ = 1,2-dihydrocyclobutabenzene-3,6-dicarboxylate. Disorder was removed for clarity. As there is no SCXRD structure of IRMOF-10 available, the model presented here was created from the SCXRD structure of IRMOF-14 (CCDC deposition codes 256965 (MOF-5), 175573 (IRMOF-2), 175574 (IRMOF-3), 175579 (IRMOF-8), 175583 (IRMOF-14), 175585 (IRMOF-16)).

2.2 Flexible MOFs

An important subclass of MOFs are the so-called Soft Porous Crystals (SPCs),[31] or simply flexible MOF,[32] which are bi- or multi stable materials characterized by the ability to undergo reversible structural changes induced by an external stimulus. Here, typical stimuli are changes in temperature[33] or mechanical pressure[34,35], and guest-uptake[36,37], but structural changes upon light irradiation[38] and electric fields[39,40] have also been reported. In the process of structural transformation, the underlying connectivity of the MOF is retained, i.e., it is displacive in nature (no chemical bonds are broken during the structural transformation). For the majority of flexible MOFs these transformations occur in a crystalline-to-crystalline fashion, but they can also involve non-crystalline MOF phases, which lack long-range order despite still possessing its original connectivity.[31] Their unique properties render these materials interesting for applications in the fields of gas storage[41], separations[42], chemical sensing[24,43] and controlled drug release[44] or as shock absorbers[45].

Commonly, the flexibility of MOFs is classified according to the occurrence of a change in the unit cell volume of the MOF and the type of structural dynamics upon application of the stimulus. In this context, the term *breathing* refers to a specific flexibility mode, which involves reversible large-magnitude changes in the crystallographic unit cell volume and the pore size of the MOF as a function of guest ad- or desorption (see Figure 2.5).[31,32] In this work, "large-magnitude" will refer to volumetric changes greater than 5% as the literature is not giving a minimum volume change required to assign the structural transition to a breathing behaviour. Sometimes the term breathing is applied more broadly, e.g., describing also thermally induced transitions without guest uptake or release as breathing,[46,47] for reasons of accuracy such broad usage of the term *breathing* will be avoided herein.

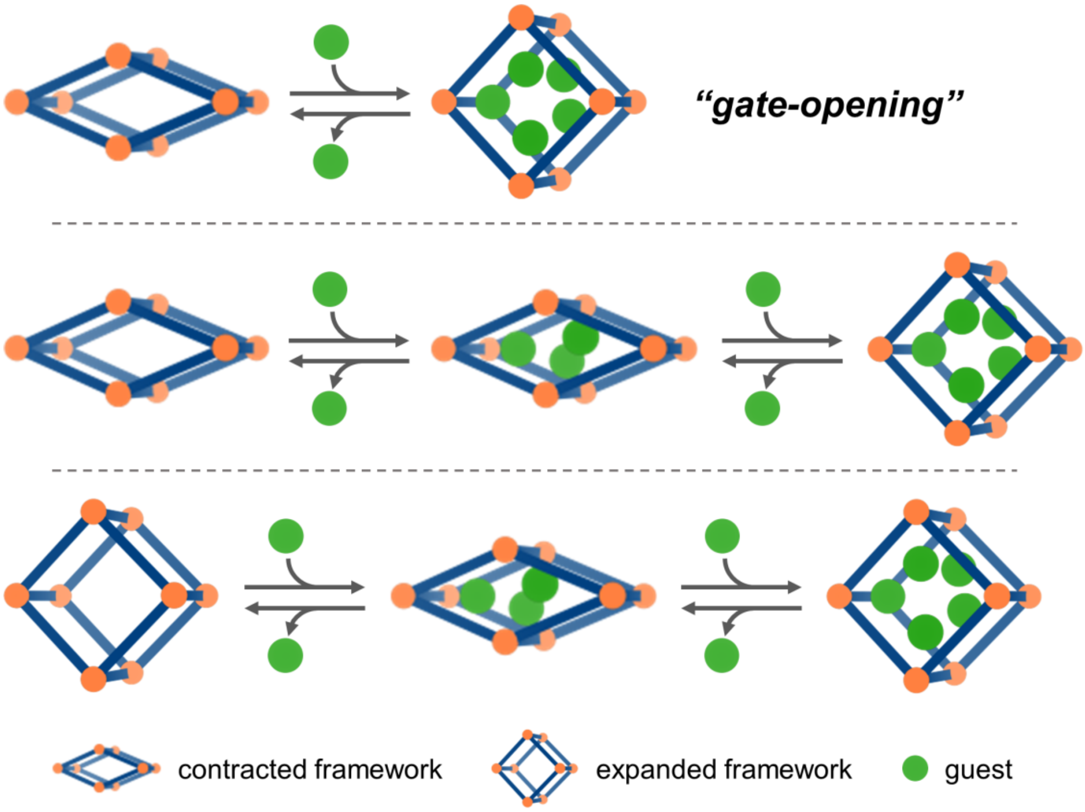

Figure 2.5: Illustration of a few exemplary breathing transitions of flexible MOFs. In the top row, the special case of the gate-opening transition is presented, where the starting of guest-uptake is coupled with the breathing transformation of the framework.

A flexible MOF exhibiting breathing behaviour may switch between a contracted and one or more other, expanded MOF phases as illustrated in Figure 2.5. There are different types of breathing behaviours as a function of the guest loading amongst the flexible MOF materials. Arising from the distinct structural response to guest ad- and desorption, the corresponding sorption isotherms of breathing MOF materials exhibit characteristic stepped shapes (Figure 2.6), which, however, deviate depending on the particular type of breathing behaviour. Here, mainly two scenarios are distinguished, (i) when a contracted phase of a flexible MOF is non-porous and there is no guest uptake until the transition to the porous expanded phase occurs at the critical pressure p_{trans} followed by a vast uptake of guest molecules (gate-opening, see Figure 2.6, left).[48,49] And (ii), when the contracted form of the flexible MOF is porous (Figure 2.6, right), resulting in guest uptake before the structural expansion at p_{trans}.[49]

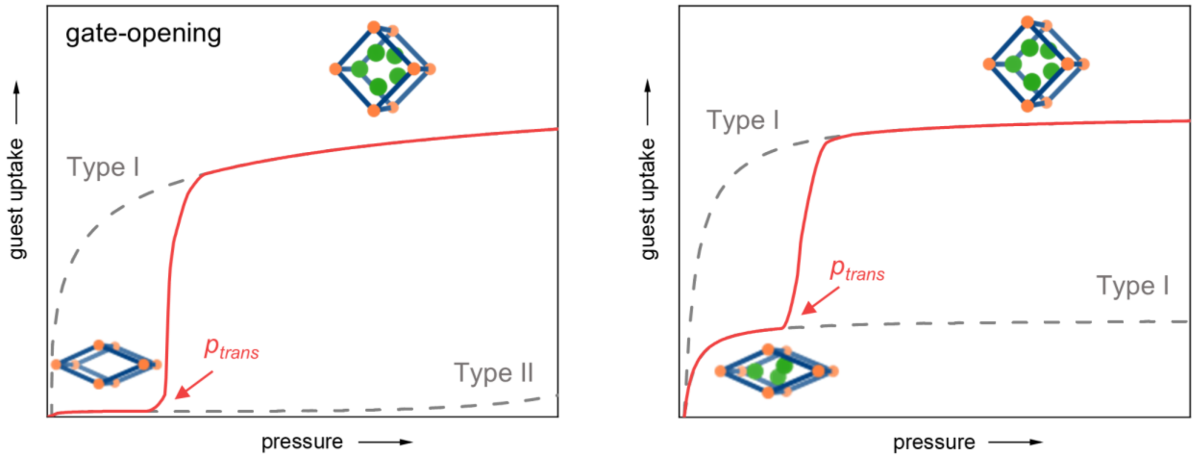

Figure 2.6: Schematic adsorption isotherms (red lines) of a potential flexible MOF exhibiting a breathing behaviour between a non-porous and a porous MOF phase (gate-opening, left) or a less-porous and a more-porous MOF phase (right). Both isotherms can be interpreted as a combination of the individual isotherms of both contracted and expanded MOF phases (see grey dashed lines), which correspond to either type I (if porous) or type II (if non-porous) isotherms according to the IUPAC classification.[50]

With potential applications in gas storage/release in mind, particularly the gate-opening type of breathing behaviours bears the advantage of a higher usable gas capacity within a limited, technically relevant operating pressure range (see Figure 2.7, left).[41,51] Furthermore, the gate-opening behaviour may differ with respect to different guest molecules (see Figure 2.7, right), which can be made use of, e.g., in separations of gas mixtures.[52,53]

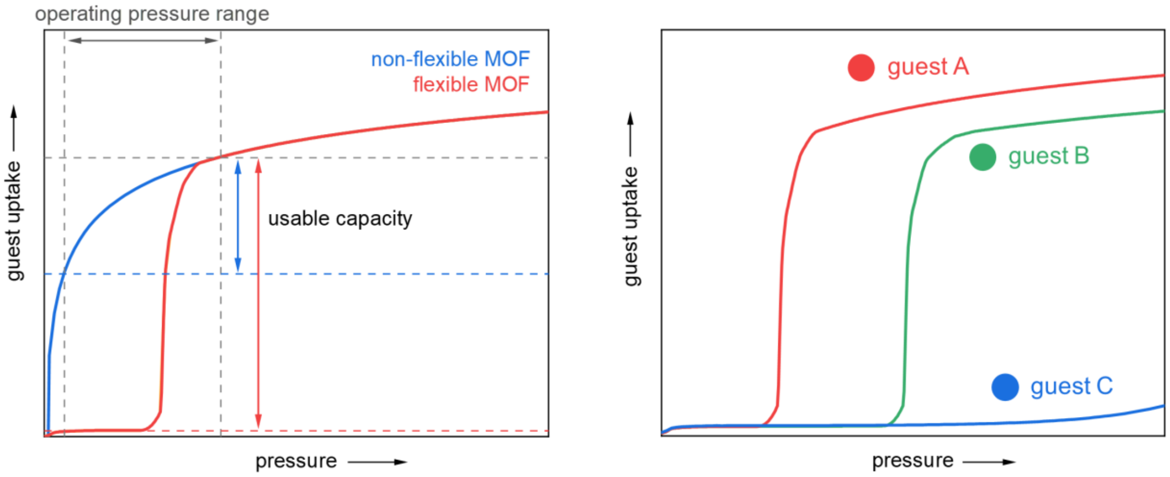

Figure 2.7: Comparison of the usable gas capacity within the operating pressure range between a flexible and a non-flexible MOF (left). Gate-opening and the general sorption behaviour may differ strongly between various guest molecules adsorbed in the same flexible MOF material (right).

In general, the complex behaviour of flexible MOFs emerges from a delicate balance between enthalpic (e.g. dipolar or intra-framework dispersion interactions) and entropic contributions (e.g. vibrational and configurational entropy) to the free energy landscape of the MOF.[47,54–59] To further understand the interactions and underlying thermodynamics of a flexible MOF and which structural requirements need to be met, these issues will be discussed with an exemplary case study of a prototypical flexible MOF system, MIL-53.

As one of the first discovered and most studied flexible MOF platforms to date, MIL-53 ([M(OH)(bdc)], M^{3+} = Cr^{3+}[60], Al^{3+}[61], Fe^{3+}[62], Sc^{3+}[63], Ga^{3+}[64], In^{3+}[65]) has been subject to over 400 publications already by 2014.[32] It is constructed of chains of MO_6 octahedra axially bridged by μ_2-OH^- groups, which are then interconnected by bdc^{2-} linkers to form a framework of sra topology with distinctive rhombic channels, also called wine rack structure motif (Figure 2.8).[66]

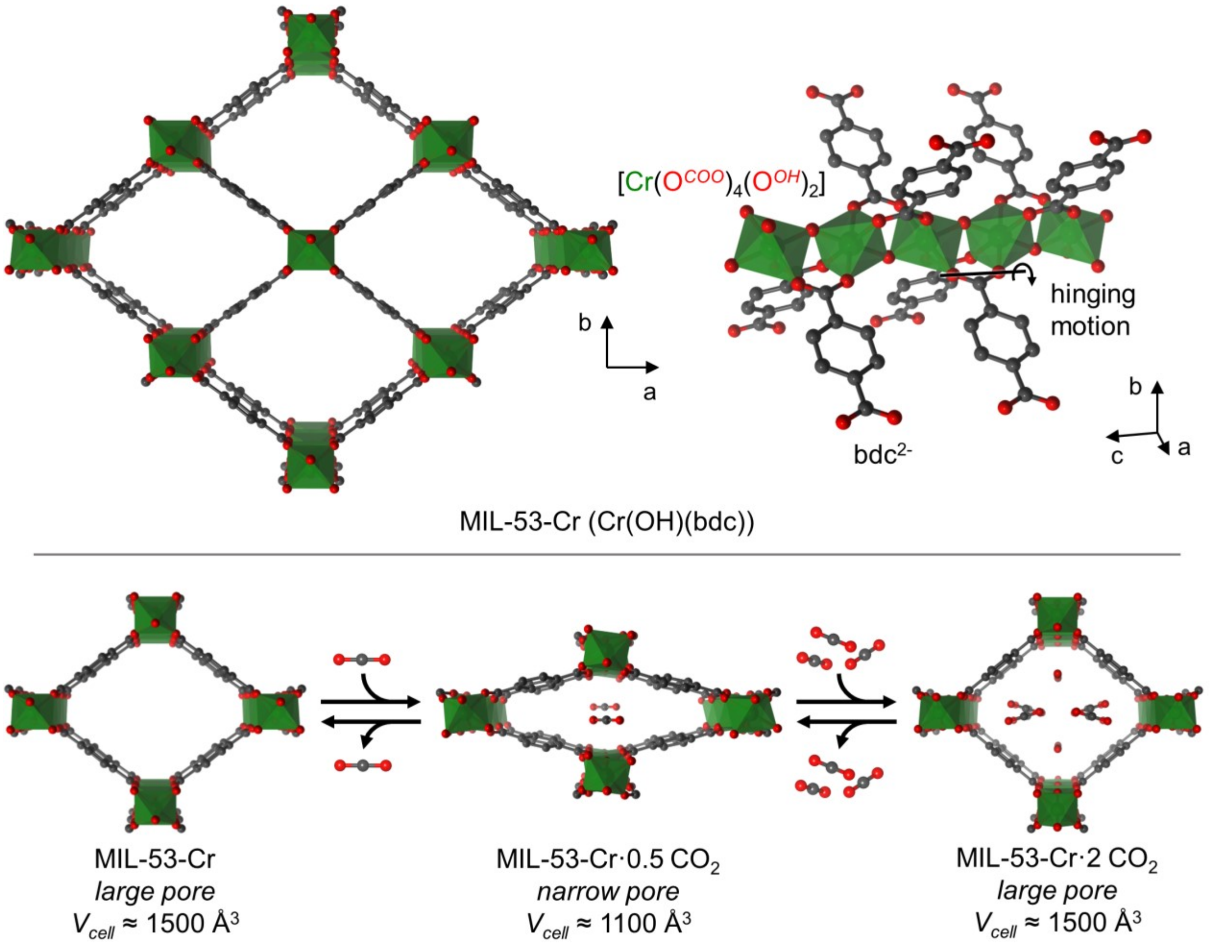

Figure 2.8: Crystal structure of guest-free MIL-53-Cr (space group *Imcm*, CCDC deposition code 1429699) in view along the rhombic channels (top, left) and with emphasis on the construction of its inorganic unit and the hinge-like motion of the carboxylate groups (top, right).[67] MIL-53-Cr exhibits large→narrow→large pore phase (breathing) transitions upon sorption of CO_2 (bottom, MIL-53-Cr·0.5CO_2 crystallizes in space group $C2/c$).[68] Please note that the structure of MIL-53-Cr·2CO_2 technically belongs to the CO_2-filled large pore phase of MIL-53-Fe.[69] However, for both Fe and Cr variants these particular phases are very similar and here the Fe variant was used for the better data quality.

MIL-53 exhibits a breathing behaviour upon the ad- and desorption of guest molecules, such as H_2O,[60,61] CO_2,[68,70] alcohols[71] and alkanes,[72,73] characterized by a contraction and expansion along the diagonals of its rhombic channels (Figure 2.8, bottom). In the process of CO_2 adsorption, MIL-53 undergoes structural transitions from a guest-free large pore to a contracted narrow pore phase, when adsorbing small amounts of CO_2 and expands again to a large pore phase when more CO_2 is adsorbed. These transitions involve volume changes of up to roughly 50% relative to the volume of its contracted phase. The driving forces of the structural contraction at low CO_2 loading have been identified as host-guest interactions, i.e., strong polar interactions and hydrogen bonding between the CO_2 guests and the μ_2-OH^- groups of the inorganic unit of both opposing sides of the rhombic channels.[68,74] By contrast, at higher CO_2 pressures, the guest-filled large pore phase becomes thermodynamically favoured due to the enthalpy gain by increased host-guest and guest-guest interactions.

Furthermore, MIL-53-M (M = Al, Ga) exhibits thermally induced flexible behaviour.[33,64,75] In case of MIL-53-Al, its guest-free large pore phase transforms into a strongly contracted narrow pore phase (sometimes also referred to as closed pore phase) when cooled to temperatures below 150 K and returns to the large pore phase from 325 K (Figure 2.9). Experimental and theoretical studies revealed that this bistability is governed by mainly two factors, (i) attractive dispersion and π-π interactions, which stabilize the contracted phase, and (ii) vibrational entropy, i.e., thermal motions (low-frequency modes) of the phenyl rings, which render the expanded phase energetically favoured at high temperatures.[33,47,54,64] Importantly, this balance of contributions is fundamental to many flexible MOFs and pivotal to understanding their behaviour.[55,56,76]

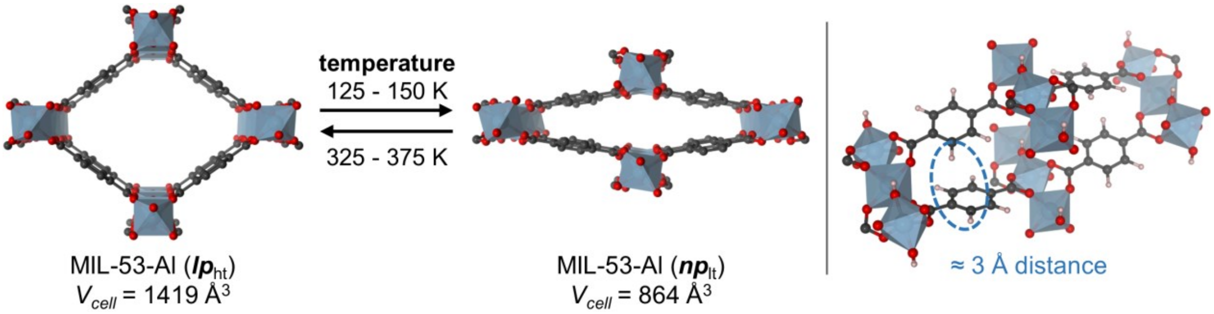

Figure 2.9: Temperature-depending flexibility of MIL-53-Al (left, space group *Imma* or *C*2/*c* for the ***lp***$_{ht}$ or ***np***$_{lt}$ phase, respectively).[33] Close distances (≈ 3 Å) between the phenyl rings of the narrow pore phase indicate attractive π-π and π-H interactions between them.

Mechanically, the flexible behaviour of MIL-53 emerges from the ability of the carboxylate groups to perform rotations around the O-O-axis resulting in a hinge-like motion (see Figure 2.8, top right).[68,77] Sometimes this ability is also referred to as “knee-cap”.[77] However, since not every carboxylate-based MOF is flexible, there must be other factors, which govern the occurrence of flexibility as well. One of these is the topology. The role of the topology is easily understood from a comparison of MIL-53 with its non-flexible polymorph, MIL-68 ([M(OH)(bdc)], $M^{3+} = Ga^{3+}$, In^{3+},[78] Fe^{3+},[79] Al^{3+},[80] Sc^{3+})[81], which is constructed of the same building units, but features a different Kagome-like topology (see Figure 2.10) composed solely of 3- and 6-rings. Here, the presence of equilateral 3-rings inhibits a flexible behaviour while maintaining an ordered structure since the angles of the 3-rings cannot vary as opposed to the rhombic motif of MIL-53 (notice that the edge lengths of the triangles, rhombus or hexagons are basically fixed, since elongation or contraction of the edges would require expansion or compression of covalent and coordinative bonds).[77]

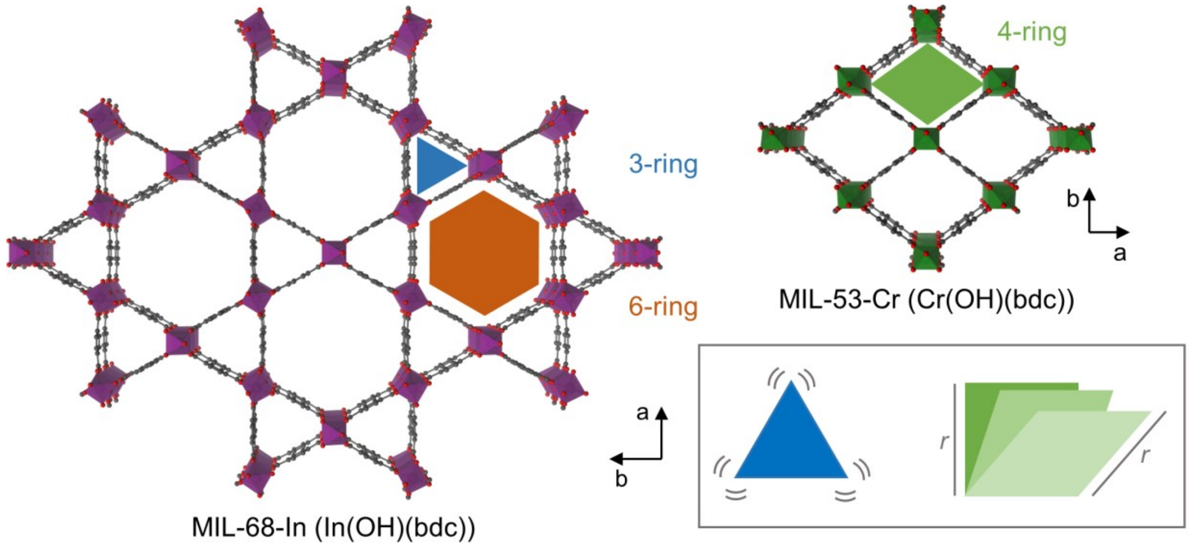

Figure 2.10: Representation of the SCXRD structure of MIL-68-In (left, space group *Cmcm*, CCDC deposition code 691619) and MIL-53-Cr (space group *Imcm*, CCDC deposition code 1429699) with 3-, 4- and 6-rings marked.

Besides the topology, the geometry of the inorganic building unit itself is considered to have a huge impact on the potential for flexible behaviour of a MOF material. In a frequently cited analysis by FÈREY and SERRE the possibility of flexibility of carboxylate-based MOFs was linked with the presence of mirror symmetry in the inorganic building unit.[77,82] If mirror symmetry of the building unit is given, concerted hinging motions of the carboxylate groups are possible (see Figure 2.11). These can facilitate structural changes of the framework without the necessity to distort the inorganic building unit by elongation or contraction of chemical bonds.

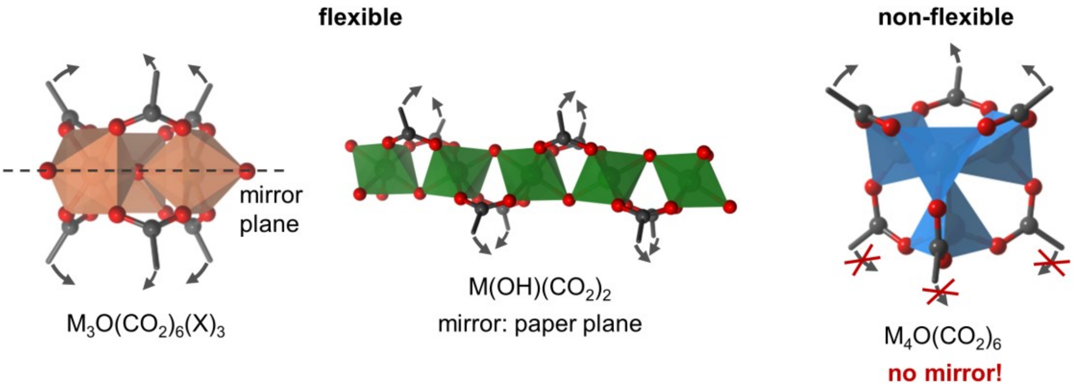

Figure 2.11: Examples of inorganic building units considered flexible (left, CCDC deposition codes 1415803 and 1429699) and non-flexible (right, CCDC deposition code 256965) due to the presence or absence of mirror symmetry, respectively.

Finally, it should be addressed that a present flexible behaviour of a MOF might be tuned by taking advantage of the principle of isoreticular synthesis, which was outlined under Section 2.1. In this regard, the exemplary MIL-53 has been prepared with a wide range of bdc^{2-} derivatives bearing functional moieties such as NH_2, NO_2, Cl, Br, CH_3, OH, and COOH groups.[83–85] These functional groups have a profound impact on the free energy landscape of the MIL-53 materials as they feature different electronic structures as well as individual steric bulks and interactions with the framework backbone or adsorbed guest molecules (e.g., H-bonding, π-H, dipolar or dispersion interactions).[83,84] This results in different breathing characters of the respective materials. For example, simply amino-functionalized MIL-53 features an improved preference for adsorbing CO_2 over CH_4 in comparison to its non-functionalized counterpart,[86] which was applied to the separation of an equimolar mixture of both gases.[87] Simultaneously, the stronger host-guest interactions stabilize the contracted phase so that higher pressures of CO_2 are required to trigger the transition to the large pore structure.[87]

Hence, chemical functionalization is a powerful tool to modulate the properties of flexible MOFs. In the following study this approach will be applied to, (i) tune the behaviour of a flexible MOF platform and, (ii) to generate fundamentally new properties in a very different MOF material deemed structurally rigid thus far.

3 Flexible Alkyl-functionalized DMOF-1 Materials

3.1 Introduction

A canonical example from the family of flexible MOFs is the pillared-layered framework $Zn_2(bdc)_2(dabco)$ (bdc^{2-} = 1,4-benzenedicarboxylate; dabco = 1,4-diazabicyclo[2.2.2]octane), also termed DMOF-1, which consists of 2D-square grid layers formed by binuclear M_2-paddlewheel units and bdc^{2-}-linkers stacked into the third dimension by dabco pillars to form a framework of **pcu** topology (Figure 3.1, top).[88]

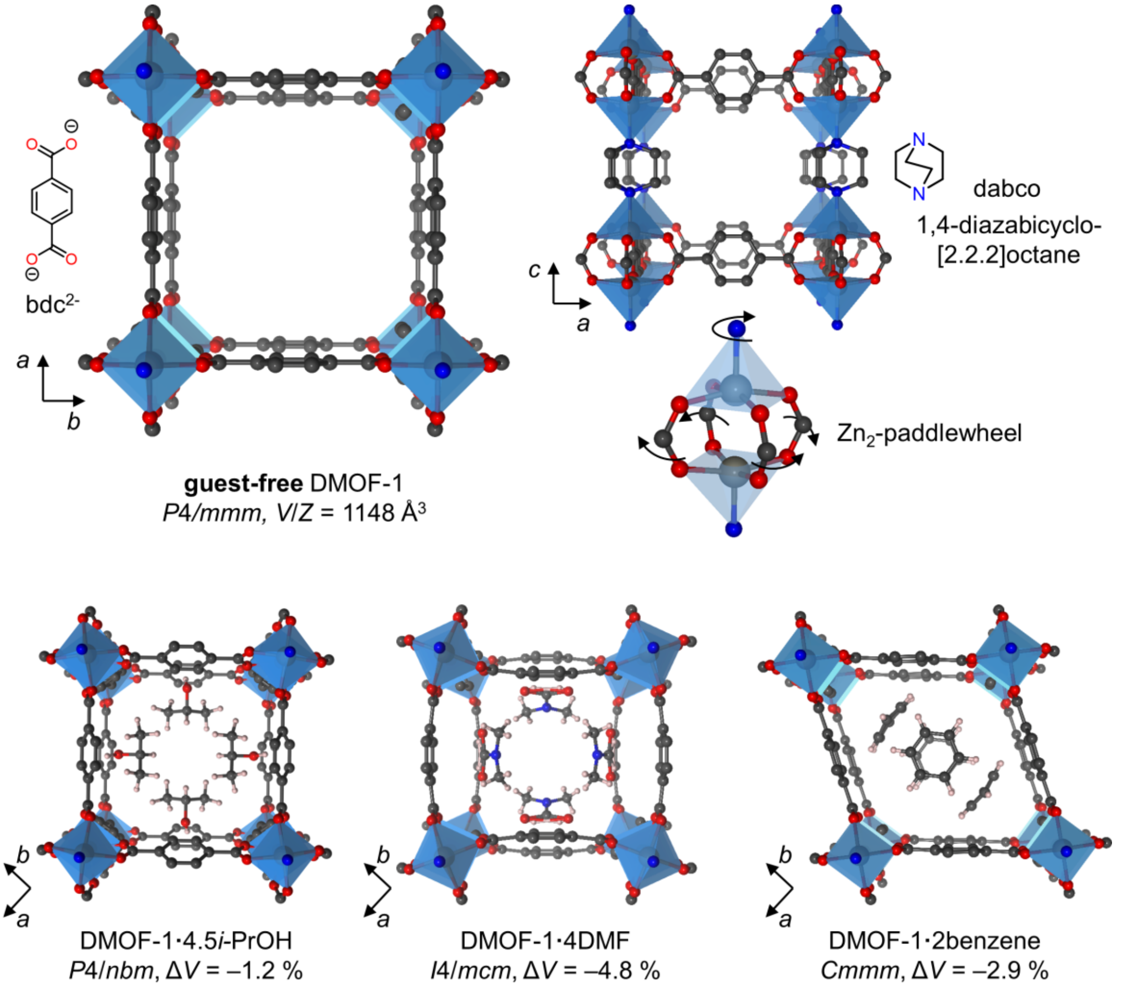

Figure 3.1: Top: SCXRD structure and building units of guest-free DMOF-1 (CCDC deposition code 238860). Possible flexibility modes at the Zn_2-paddlewheel unit are highlighted with arrows. Bottom: SCXRD structures of DMOF-1 solvated with *i*-PrOH, DMF and benzene (CCDC deposition codes 639940, 238859 and 238861, respectively). The solvent-induced volume changes of the reduced unit cell, ΔV, are given with respect to the guest-free phase of DMOF-1.

This MOF is known for its adaptive behaviour towards different guest species, such as *N*,*N*-dimethylformamide (DMF), benzene[89] and ethanol[90] (Figure 3.1, bottom) and is capable of performing *breathing* transitions upon ad- and desorption of *iso*-propanol involving unit cell volume changes of 21% in this process.[91,92] Recently, the guest-free DMOF-1 has been suggested as a mechanical shock adsorber material due to its flexible structural behaviour.[93]

The flexibility of the DMOF-1 architecture arises from the structural features of the M$_2$-paddlewheel units, which allows for cooperative hinging motions of the carboxylate groups and also for rotations along the axis of the dabco pillar (Figure 3.1).
Moreover, DMOF-1 was shown to be an excellent platform for a systematic fine-tuning of the responsive framework behaviour either via substitution of the Zn^{2+} ions against others (i.e., Cu^{2+}, Co^{2+} or Ni^{2+})[94–96] and via functionalization of the bdc^{2-} linker.[97–103] In particular, implementation of various types of 2,5-alkoxy-functionalized bdc-linkers (**RO**-bdc, **R** = alkoxy-alkyl, alkyl, alkenyl, alkynyl) in place of conventional bdc^{2-} generates a series of isoreticular Zn$_2$(**RO**-bdc)$_2$(dabco) materials (here denoted DMOF-1-**OR**) with significantly enhanced responsive behaviour as demonstrated by reversible transitions between a large pore (***lp***) phase and a contracted narrow pore (***np***) phase as a function of guest-content (*breathing*), temperature or mechanical pressure (Figure 3.2).[57,58,99]

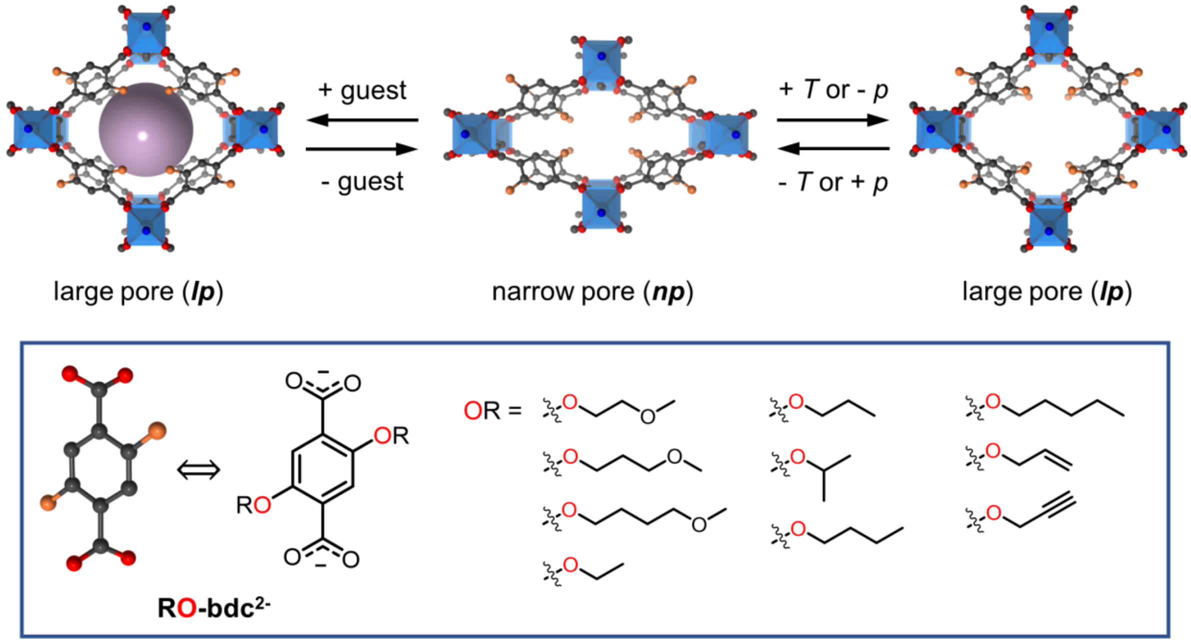

Figure 3.2: Schematic representation of the guest-, temperature- and pressure-depending flexibility of alkoxy-functionalized DMOF-**OR** materials. The orange spheres represent the implemented RO-groups. Molecular structures of the alkoxy-functionalized **RO**-bdc^{2-} linkers of previous studies are shown in the frame. Structures were either created on the basis of a published SCXRD structure (***lp*** phase, CCDC deposition code 844640) or a model created on the basis of refined unit cell parameters (***np*** phase)[99].

Utilizing this approach, the magnitude of the volume change associated with the ***lp***→***np*** phase transition can be precisely tuned by the choice of the functional RO-group leading to values of up to 28% contraction.[100,104] The fundamental driving forces behind the structural bistability in response to guest adsorption are attractive dispersion (and in some cases also dipolar) interactions between the flexible functional groups (or: dispersion energy donors, DEDs) and the backbone of the framework, which have a drastic influence on the free energy landscape of the MOF.[104,105] The unusual heating induced ***np***→***lp*** phase transitions of the guest-free DMOF-1-**OR** derivatives in turn is driven by entropic contributions.[58] Unfortunately, the flexible RO-substituents are typically very disordered in the crystal structures of the ***lp*** phases of these materials and the macroscopic strain evolving upon the transition to the contracted

np phase results in deterioration of the DMOF-1-**OR** single crystals, thus impeding detailed structural insights into the involved phases and particularly into the role of the flexible substituents.[104] The only structural information of the various ***np*** phases of the DMOF-1-**OR** derivatives known is their unit cell parameters (extracted from structureless profile fits to powder X-ray diffraction data). Atomistic structural details, especially concerning the orientation and positioning of the flexible substituents in the ***lp*** and the ***np*** phase of these responsive MOFs, are urgently needed to provide valuable insights on the nature of the interactions of the side chains with each other and the framework backbone. Such insights would (i) improve the general understanding of these complex responsive materials and (ii) allow for the extraction design principles for tuning responsiveness and phase change behaviour also in other MOF systems.[106]

In the present study, the range of responsive DMOFs is extended by three simply alkyl-functionalized derivatives, based on 2,5-dialkyl-bdc^{2-} linkers (**CX**-bdc^{2-}, alkyl = ethyl (**X** = 2), propyl (**X** = 3), butyl (**X** = 4)), lacking the phenolic ether-oxygen atom of the DMOF-1-**OR** reported so far (Figure 3.3).

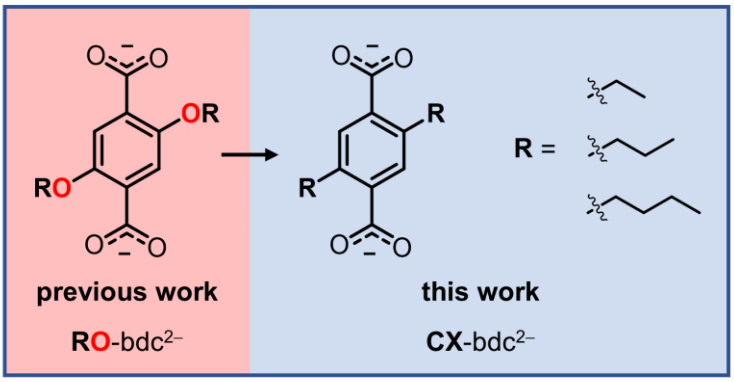

Figure 3.3: Alkoxy-functionalized **RO**-bdc^{2-} linkers of previous works and purely alkyl-functionalized **CX**-bdc^{2-} linkers, which are the main object of this study.

Remarkably, the novel DMOF-1-**CX** materials allow for an in-depth characterization via single crystal and powder X-ray diffraction (SCXRD and PXRD) of both, their guest-containing ***lp*** and contracted guest-free (*dry*) ***np*** phases, offering structural details on the flexible substituents and the framework backbone in the ***np*** phases as well as differently solvated ***lp*** states for the first time for this important class of stimuli-responsive MOFs. Additionally, striking differences are found in the CO_2 sorption and thermo-responsive behaviour compared to their alkoxy-functionalized pendants, which were comprehensively analysed by means of gas sorption experiments and differential scanning calorimetry together with elaborate *in-situ* PXRD experiments. Furthermore, as experimental data on the hydrocarbon sorption behaviour of such DED functionalized flexible DMOF-1 based systems remain scarce,[107] the sorption of industrially relevant **C_3** and **C_4** hydrocarbons by the DMOF-1-**CX** materials was explored via isothermal sorption and *in-situ* PXRD experiments, revealing a discriminative gating and breathing behaviour. Finally, these results were compared to those of the corresponding alkoxy-functionalized relatives.

3.2 Linker Synthesis

Three 2,5-dialkyl-1,4-benzenedicarboxylic acids (with alkyl = ethyl (**C2**-bdcH$_2$), propyl (**C3**-bdcH$_2$) or butyl (**C4**-bdcH$_2$), **CX**-bdcH$_2$) were prepared in a three-step synthesis adopted from the literature (Figure 3.4).[108,109] Starting from the respective 1,4-dialkyl benzenes, aromatic bromination in the using Br$_2$ at 0 °C under exclusion of light yields the 1,4-Dibromo-2,5-dialkylbenzenes. Followingly, the di-bromides are converted into the corresponding di-cyanides by means of the Rosenmund-von-Braun reaction with CuCN in *N*,*N*-dimethylformamide (DMF). In the third step, the cyanide groups are hydrolyzed under basic conditions in diethylene glycol at high temperatures giving the desired 2,5-dialkyl-1,4-benzenedicarboxylic acids. For details on the full synthetic procedures, see Materials &Methods, section 6.1.2.

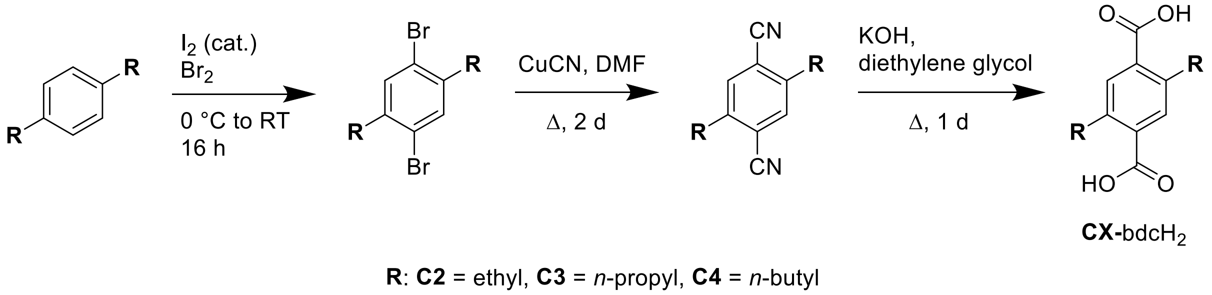

Figure 3.4: Synthesis of the 2,5-dialkyl-1,4-benzenedicarboxylic acid linkers used in this chapter.

The second type of functionalized bdc^{2-} linkers employed later in this chapter are bearing an additional phenolic O-atom connector to the functional groups. The corresponding 2,5-dialkoxy-1,4-benzenedicarboxylic acids (with alkoxy = methoxy (**C1**), ethoxy (**C2**) and *n*-propoxy (**C3**), **CYO**-bdcH$_2$) were prepared by established and well-optimized procedures[98] via Williamson etherification of 2,5-dihydroxy-1,4-benzenedicarboxylic acid dimethyl ester with the respective *n*-bromo alkanes, followed by basic cleavage of the methyl ester protecting group (Figure 3.5). For details on the full synthetic procedures, see Materials & Methods, section 6.1.2.

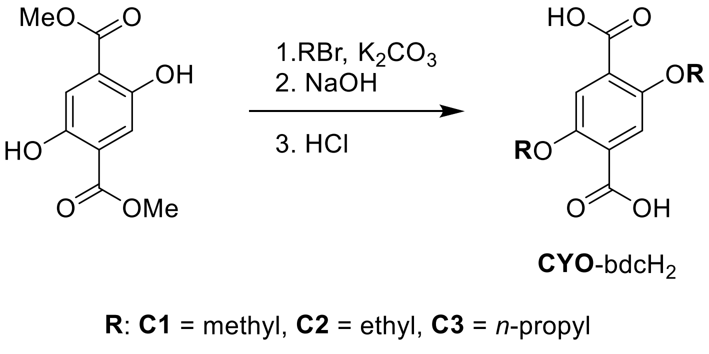

Figure 3.5: Synthesis of the 2,5-dialkoxy-1,4-benzenedicarboxylic acid linkers used in this chapter.

3.3 MOF Synthesis & Structural Characterization

The linkers in their acid form were then reacted under solvothermal conditions with $Zn(NO_3)_2 \cdot 6H_2O$ and dabco (= 1,4-diazabicyclo[2.2.2]octane) in DMF at 120 °C for 48 h to yield the corresponding DMOF-1-**CX** of the general chemical composition $[Zn_2(\mathbf{CX}\text{-bdc})_2(\text{dabco})]$ (with **X** = 1, 2 or 3) as a mixture of large colourless crystals and microcrystalline powder. Detailed synthetic procedures of the DMOF-1-**CX** are given in the Materials & Methods section 6.1.2. Taken from the freshly prepared material, the crystals of the DMOF-1-**CX** in their as-synthesized (*as*, DMF containing) state proved suitable for single crystal X-ray diffraction (SCXRD) analysis, which produced solid state structures confirming the DMOF-1-**CX** to be of the expected isoreticular pillared-layered framework architecture (Figure 3.6).

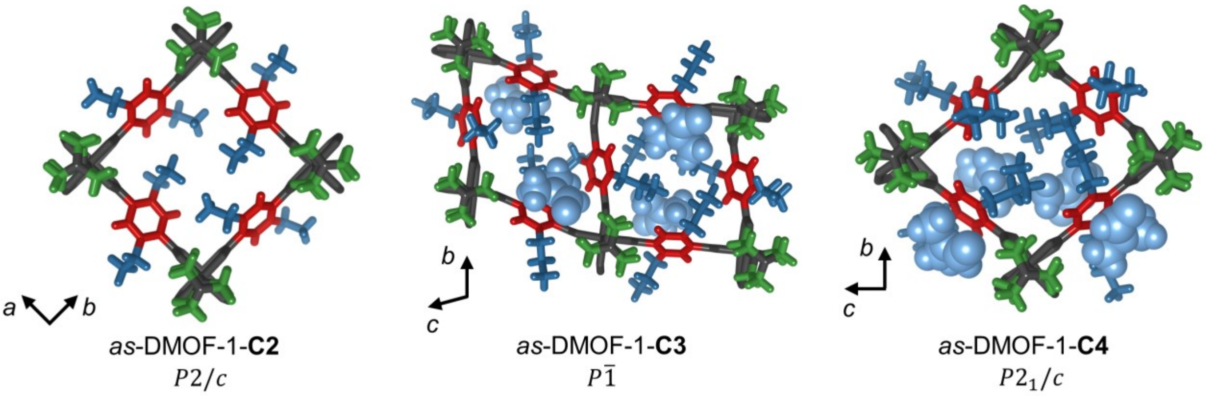

Figure 3.6: Depictions of the SCXRD structures of DMOF-1-**C2** to DMOF-1-**C4** in their as-synthesized state, in view along the dabco axis (top) or focused on the interactions between the MOF and the DMF guests (bottom). The DMF guest molecules with the disorder removed that are resolved in the electron density map are shown as space-filling models in light blue (top). C and H atoms of the phenyl-rings, dabco units and alkyl chains are coloured in red, green and blue to highlight the attractive interactions between these groups. The Zn, O and C atoms of the paddlewheel units are coloured in grey.

The *as*-DMOF-1-**C2**, *as*-DMOF-1-**C3** and *as*-DMOF-1-**C4** crystallize in the monoclinic or triclinic space groups $P2/c$ ($Z = 2$), $P\bar{1}$ ($Z = 2$) and $P2_1/c$ ($Z = 4$), respectively, where Z corresponds to one $[Zn_2(\mathbf{CX}\text{-bdc})_2(\text{dabco})]$ framework repeating unit. The space group symmetry of these structures is significantly lower than that of their alkoxy-functionalized relatives, namely the variants bearing methoxy-ethoxy, ethoxy to butoxy, *i*-propoxy or propargyloxy groups, which either crystallize in the $C2/m$ or $P4/mmm$ space group symmetries.[98] This high symmetry is reasoned by the fact, that these compounds suffer from extensive disorder of the framework backbone (phenyl rings and dabco), the flexible substituents and the guest molecules. In contrast to the alkoxy-functionalized relatives of comparable side chain length[98], here, the framework backbones are fully ordered and the flexible alkyl substituents are well-resolved in the SCXRD structures (see Figure 3.6, crystallographic data are given in the Appendix section 8.1.2).

Still, in the SCXRD structure of *as*-DMOF-1-**C4** ¼ of the alkyl-substituents show disorder over two positions and *as*-DMOF-1-**C2** features disorder of ½ of the alkyl groups and dabco units over two positions, the latter possibly due to the higher measurement temperature compared to the others. The SCXRD data of *as*-DMOF-1-**C2** had to be collected at 290 K, since acquisition at 100 K resulted in data that could not be solved, likely due to a complex ordering of the framework parts and guests. However, the data of *as*-DMOF-**C3** and *as*-DMOF-**C4** collected at 100 K and 273 K, respectively, gave high-quality SCXRD structures (Figure 3.6).

Here, the DMF guest molecules in the pores of *as*-DMOF-1-**C3** and *as*-DMOF-1-**C4** could also be fully resolved, while this was not possible for the structure of *as*-DMOF-1-**C2** collected at the higher temperature. For both *as*-DMOF-1-**C3** and *as*-DMOF-1-**C4**, two DMF molecules per MOF repeating unit were found to be included in the structure. As expected, these DMF guests are strictly ordered upon minimization of interaction enthalpy (see Figure 3.7), i.e., the less polar methyl groups of the DMF arrange close to the phenyl rings and alkyl moieties, while its carbonyl oxygen atom points towards the positively polarized α-CH$_2$ groups of the dabco unit (≈ 2.5 – 3.0 Å interaction distances are found in both cases).

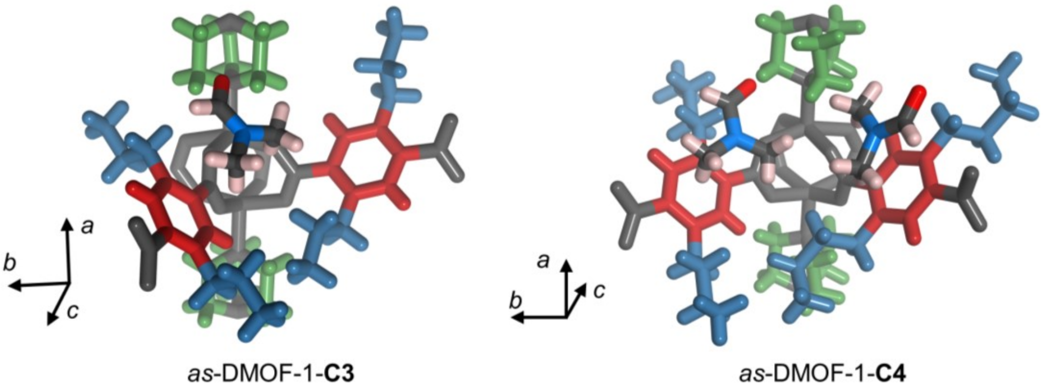

as-DMOF-1-**C3**

as-DMOF-1-**C4**

Figure 3.7: Excerpts of the SCXRD structures of DMOF-1-**C3** and DMOF-1-**C4** in their as-synthesized state highlighting the interactions between the MOF and the DMF guests. Disorder of the alkyl groups and DMF molecules was removed for clarity. The colour code of the MOF was adopted from Figure 3.6, while the DMF guest molecules are shown in conventional atom colouring (C: black, O: red, N: blue and H: white colour).

Table 3.1: Selected parameters of the SCXRD structures of the *as*-DMOF-1-**CX**.

	as-DMOF-1-**C2**	*as*-DMOF-1-**C3**	*as*-DMOF-1-**C4**
space group	$P2/c$	$P\bar{1}$	$P2_1/c$
a / Å	10.9004(6)	9.5967(5)	9.6523(5)
b / Å	10.9331(4)	10.8601(6)	28.1466(15)
c / Å	19.2435(8)	21.5316(11)	16.6332(9)
α / °	90	104.310(2)	90
β / °	89.824(5)	92.443(2)	95.248(3)
γ / °	90	95.573(2)	90
V / Å^3	2293.33(18)	2159.0(2)	4500.0(4)
Z	2	2	4
V_{void} / %	44.1	28.0	23.0
T_{meas} / K	290(5)	100(2)	273(2)
gof	1.107	1.176	1.069
R$_1$	0.1067	0.0440	0.0556
wR$_2$	0.2512	0.0850	0.1495
DMF per repeating unit	-	2	2

The guest accessible void space in the frameworks, V_{void} (Table 3.1), which was calculated after removing the DMF guests from and resolving the disorder in the model, is calculated to be 44.1% for *as*-DMOF-1-**C2**, 28.0% for *as*-DMOF-1-**C3** and 23.0% for *as*-DMOF-1-**C4**.*

Based on the obtained single crystal structures, the phase purity of the bulk material of each DMOF-1-**CX** was confirmed via structureless profile refinement (Pawley method[110]) of powder X-ray diffraction (PXRD) data (Figure 3.8, black patterns, for the Pawley fits, see Appendix section 8.1.1).

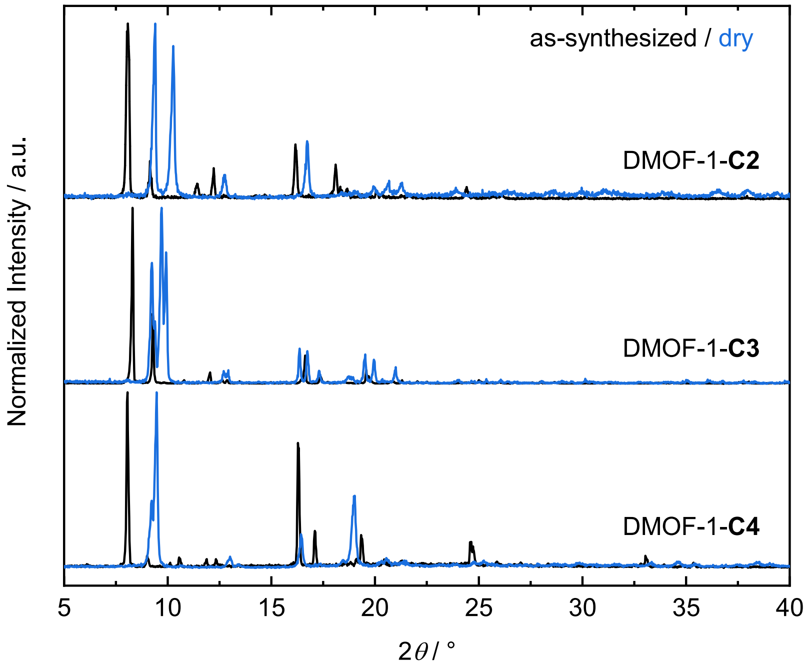

Figure 3.8: Overlay of the powder X-ray diffraction (PXRD) patterns of DMOF-1-**C2** to -**C4** in their as-synthesized (DMF-containing, black) and guest-free (*dry*, blue) states (right), which indicate the transition from a large pore (***lp***) to a narrow pore (***np***) form of the MOFs due to the shift of the prominent reflections towards higher angles $2\theta\,(\lambda = 1.54178$ Å).

To activate the materials, *as*-DMOF-1-**C2** to -**C4** were washed with DMF, and the solvent was replaced by fresh dichloromethane (DCM). Subsequent drying at 100 °C in dynamic vacuum ($\approx 10^{-4}$ kPa) for 24 h afforded the guest-free MOFs *dry*-DMOF-1-**C2** to -**C4**. The complete activation of the MOFs was proven by Fourier transform infrared (FT-IR) spectroscopy by the absence of the distinct asymmetric stretching vibration band of the carbonyl group of DMF.[111] Furthermore, the samples were investigated by solution ^{1}H NMR spectroscopy after digestion in a DCl/D_2O mixture in DMSO-d_6. The full ^{1}H NMR and FT-IR spectra are given in the Appendix sections 8.1.3 and 8.1.4.

A first visual inspection of the PXRD data of *dry*-DMOF-1-**C2**- to *dry*-DMOF-1-**C4** reveals distinct differences of the diffraction patterns in relation to their as-synthesized counterparts, namely a shift of the first strong reflection of the diffraction patterns towards higher scattering angles, which is clearly indicative of the presence of structurally contracted guest-free narrow

---

* Void volumes discussed in this work were calculated from the contact surface of a probe of a radius of 1.2 Å and a grid spacing of 0.2 Å, except where noted.

pore (***np***) phases (Figure 3.8, compare the black and blue PXRD patterns), similar to what has been observed for the related alkoxy-functionalized DMOF-1-**OCY** derivatives [Zn$_2$(**CYO**-bdc)$_2$(dabco)].[99,100,104]

Remarkably, although the crystals of *dry*-DMOF-1-**C2** to *dry*-DMOF-1-**C4** shatter upon drying as a consequence of the strain caused by the structural changes,[98] single crystals of *dry*-DMOF-1-**C2** to *dry*-DMOF-1-**C4** of sufficient quality for SCXRD experiments could still be obtained (for details, see Appendix section 8.1.2).

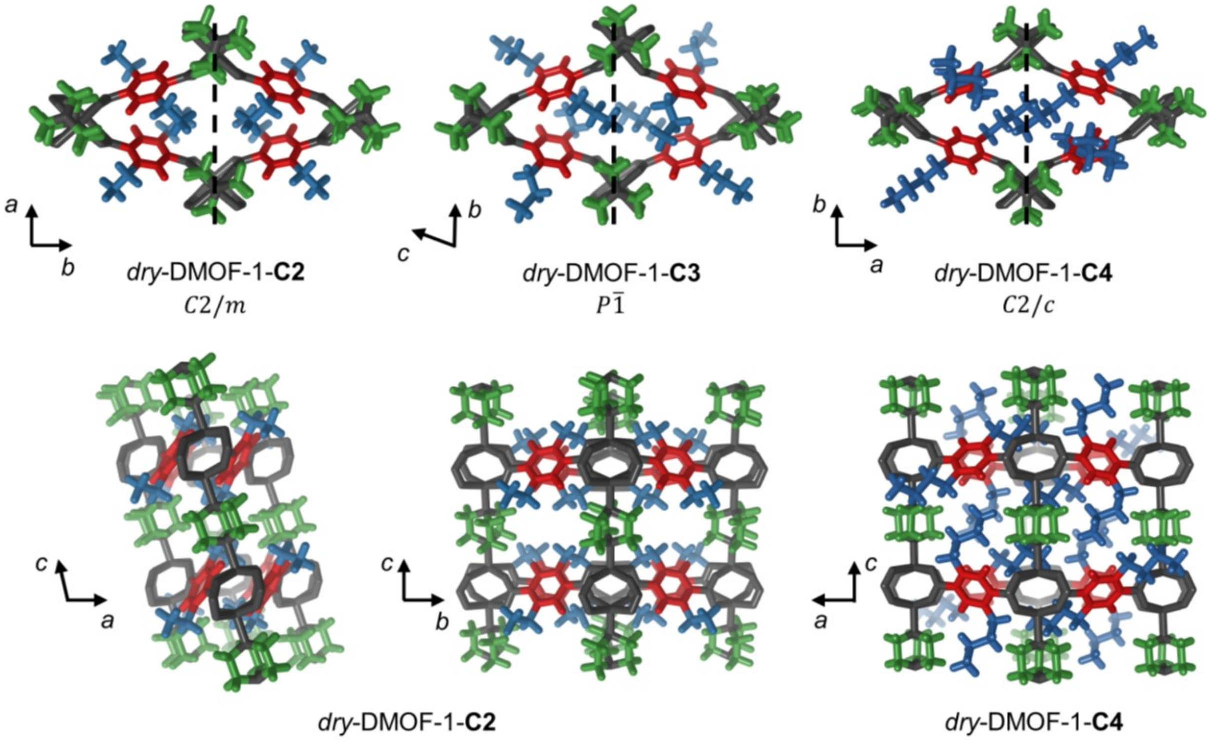

Figure 3.9: Depictions of the SCXRD structures of DMOF-1-**C2** to DMOF-1-**C4** in their dried (*dry*) states, in view along the dabco axis (top row). For a better visualization of the guest-free structures of *dry*-DMOF-1-**C2** and *dry*-DMOF-1-**C4**, additional views along the crystallographic *a* or *b* directions are given in the bottom row. The dashed line in the *dry*-DMOF-1-**CX** structure depictions (top row) was inserted as a guide to the eye to elucidate the lower symmetry of the mode of distortion in *dry*-DMOF-1-**C3** compared to *dry*-DMOF-1-**C2** and *dry*-DMOF-1-**C4**. The colour code was adopted from the previous depictions of the SCXRD structures.

From the given unit cell volumes of *dry*-DMOF-1-**C2**, *dry*-DMOF-1-**C3** and *dry*-DMOF-1-**C4**, a change in V/Z of –27%, –17% and –16% in comparison with the SCXRD data of *as*-DMOF-1-**C2**, *as*-DMOF-1-**C3** and *as*-DMOF-1-**C4** becomes evident (see Table 3.2, notice that SCXRD data of *as*- and *dry*-DMOF-1-**C2** and -**C4** were collected at different temperatures and are therefore not directly comparable).

Table 3.2: Selected parameters of the SCXRD structures of the *dry*-DMOF-1-**CX**. The *as*- and *dry*-structures were collected at different temperatures, where marked by an asterisk (*).

	dry-DMOF-1-**C2**	*dry*-DMOF-1-**C3**	*dry*-DMOF-1-**C4**
space group	$C2/m$	$P\bar{1}$	$C2/c$
a / Å	9.5105(6)	9.537(2)	18.8377(13)
b / Å	19.0806(11)	9.914(2)	10.4128(7)
c / Å	9.5140(6)	10.539(2)	19.1803(11)
α / °	90	63.798(11)	90
β / °	103.491(3)	85.076(12)	92.085(4)
γ / °	90	83.500(14)	90
V / Å^3	1678.83(18)	887.6(4)	3759.8(4)
Z	2	1	4
V_{void} / %	14.1	8.7	-
T_{meas} / K	100(2)	100(2)	100(2)
gof	1.123	1.066	1.045
R_1	0.0501	0.1487	0.0712
wR_2	0.1153	0.2869	0.1697
$\Delta V_{as\text{-}dry}$ / %	–27*	–17	–16*

After solution and refinement, the resulting SCXRD structures feature fully resolved alkyl chains and are almost fully devoid of disorder (only one of the two symmetrically independent alkyl chains of *dry*-DMOF-1-**C3** shows disorder over two positions with a ratio of 1/3 to 2/3), which allows for the first time detailed structural insights into the *narrow pore* (***np***) phases of such kind of functionalized DMOFs with due regard for the nature of the dispersion interactions of the alkyl substituents, that drive the structural contraction of the frameworks upon guest removal (Figure 3.10).[54,58,112]

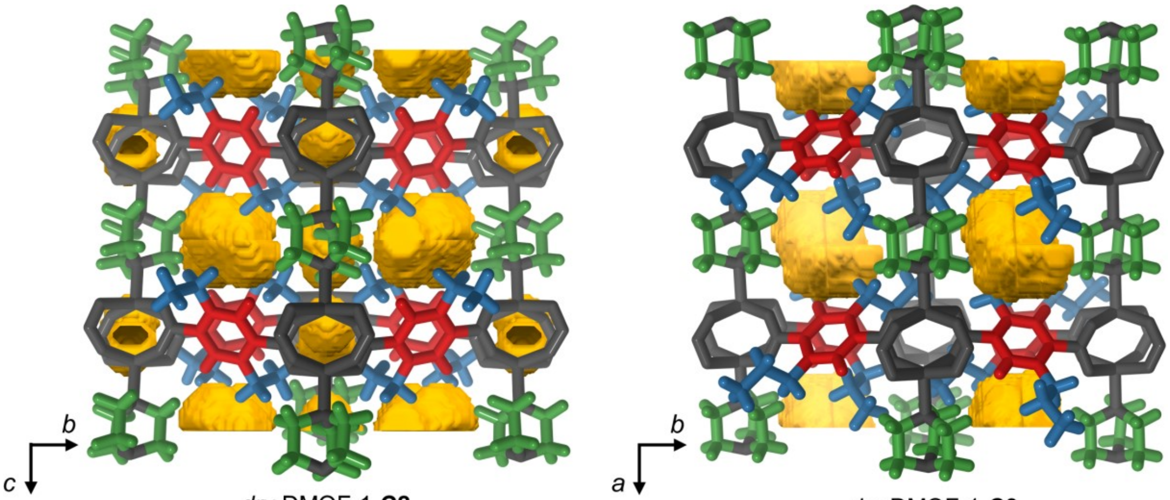

dry-DMOF-1-**C2**

dry-DMOF-1-**C3**

Figure 3.10: SCXRD structures of *dry*-DMOF-1-**C2** and *dry*-DMOF-1-**C3** in view along the diagonal of the Zn_2(**CX**-bdc)$_2$ layers in the established colour code including void maps, which were created from the contact surface of a probe of a radius of 1.2 Å.

dry-DMOF-1-**C2** and *dry*-DMOF-1-**C4** were found to crystallize in the monoclinic space groups $C2/m$ ($Z = 2$) and $C2/c$ ($Z = 4$), whereas *dry*-DMOF-1-**C3** was assigned to the lower symmetry space group $P\bar{1}$ ($Z = 1$). Although the strong structural distortion, the structures of *dry*-DMOF-1-**C2** and *dry*-DMOF-1-**C3** still own void volumes of 119 Å^3/Z (14.1% of the unit cell volume) and 73 Å^3/Z or 77 Å^3/Z (8.3% or 8.7% of the unit cell volume, depending on which fraction of the alkyl-chain disorder is removed), respectively (see Figure 3.10). On the contrary, *dry*-DMOF-1-**C4** has no residual porosity, as its pores are entirely populated by the flexible butyl groups.

In the most drastic case, the (guest-free) ***np*** form of DMOF-1-**C2**, close inter-bdc-layer contacts of the ethyl groups are facilitated by a strong distortion of the geometry of the Zn_2-paddlewheels along the crystallographic *a*-axis leading to a Zn-Zn-N angle of 160.6° instead of the 180.0° for the ideal paddlewheel. This distortion results in a displacement of the Zn_2bdc_2-layers resulting in a slipped stacking mode, effectively reducing the distance between them in order to increase intra-framework dispersion interactions (Figure 3.9, bottom left). This finds expression in the comparatively large monoclinic angle β of 103.5° of the unit cell of *dry*-DMOF-1-**C2** (see Table 3.2). By contrast, the monoclinic angle β of the unit cell of *dry*-DMOF-1-**C4** is 92.0°, which can be traced back to an almost eclipsed stacking of Zn_2bdc_2-layers, as the alkyl chains are sufficiently long to establish dispersion interactions with the phenyl rings of the **C4**-bdc^{2-}-linkers in the layer below, combined with the increased steric demand of the elongated alkyl chains (Figure 3.9, bottom right). In this regard, *dry*-DMOF-1-**C3** features an intermediate contraction along the dabco axis, which lies between *dry*-DMOF-1-**C2** and *dry*-DMOF-1-**C4**, but more interestingly, the size of steric bulk of the propyl substituents seems to fall into a regime, that favours a contraction of the Zn_2bdc_2-layer off the square-grid diagonals, resulting in the lower $P\bar{1}$ space group symmetry (Figure 3.9, top middle). Altogether, the SCXRD structures elucidate how manifold the various organic (phenyl rings, alkyl chains and dabco units) and inorganic (Zn_2-paddlewheel) building parts of the MOFs can conformationally adapt in order to maximize intra-framework dispersion interactions and to minimize free volumes in the ***np*** phases of *dry*-DMOF-1-**C2**- to *dry*-DMOF-1-**C4** (see Figure 3.9 and Table 3.2).

Table 3.3: Volume contraction of the DMOF-1-**CX** and their alkoxy counterparts of the same chain length ([Zn_2(2,5-**RO**-bdc)$_2$(dabco)], DMOF-1-**OCY** (**Y** = **X** – 1), **R** = Methyl (**C1**), Ethyl (**C2**), Propyl (**C3**)) with reference to their as-synthesized states. The data on the alkoxy-functionalized DMOF-1 derivatives was taken from the literature.[104] Unfortunately, no data are available for DMOF-1-**OC1**. The volume contraction was determined from PXRD data.

DMOF-1-**CX**		DMOF-1-**OCY**	
X	ΔV / %	ΔV / %	Y
2	24%	-	**1**
3	18%	22%	**2**
4	15%	20%	**3**

Finally, it was clarified that the obtained single crystal structures indeed do represent the bulk of the *dry*-DMOF-1-**C2** to -**C4** materials by means of Pawley fitting of the PXRD data using the respective unit cell and space group from SCXRD (for the full Pawley fits, see Appendix section 8.1.1, Figure 8.1 and Figure 8.2). Based on these fits, the magnitude of the volume change between the *as*- and *dry*-phases of DMOF-1-**C2**- to -**C4** under ambient conditions and, importantly, the same conditions, was determined as 24% (**C2**), 18% (**C3**) and 15% (**C4**), which is slightly less than that of the alkoxy-functionalized relatives[98], but does obey a similar trend that the volume contraction is inversely proportional to the substituent chain length (Table 3.3).

In accordance with the related alkoxy compounds[98], DMOF-1-**C2** to DMOF-1-**C4** show complete reversibility of the ***lp→np*** phase transition, since addition of fresh DMF to the dried materials results in a full retransformation of DMOF-1-**C2** to DMOF-1-**C4** to the initial phase of the as-synthesized state, which was validated by PXRD and Pawley refinement (for the full Pawley fits, see Appendix section 8.1.1, Figure 8.1 and Figure 8.2).

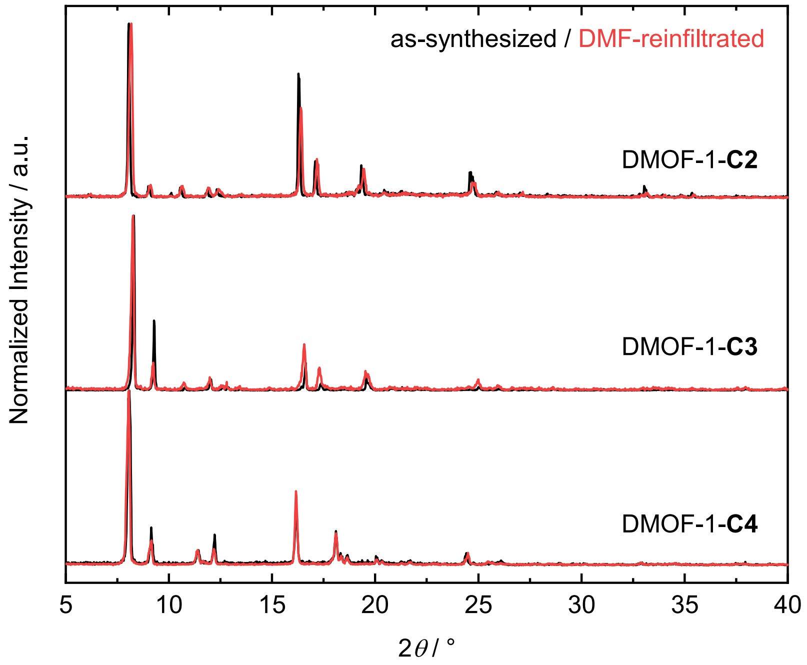

Figure 3.11: Overlay of the powder X-ray diffraction (PXRD) patterns of DMOF-1-**C2** to -**C4** in their as-synthesized (black) and DMF-reinfiltrated (red) states, which indicate the full reversibility of the ***lp→np*** transition due to the strong resemblance of both PXRD patterns ($\lambda = 1.54178$ Å).

3.4 Guest-depending Conformational Flexibility of DMOF-1-**C3**

The structural response of DMOF-1-**C3** towards a selection of different solvent guests, i.e., the rather polar acetonitrile and acetone (μ_{MeCN} = 3.93 D and μ_{acetone} = 2.88 D)[113], and the non-polar benzene and *n*-octane ($\mu_{n\text{-oct}}$ = 0 D and μ_{benzene} = 0 D) was investigated by the collection of SCXRD data from crystals of DMOF-1-**C3** that were immersed in these solvents. Experimental details on the preparation of the single crystals and the crystallographic data are given in the Materials & Methods section 6.1.2 and the Appendix section 8.1.2, respectively. Depending on the enclosed guest, the materials crystallize in either $P\bar{1}$ (acetonitrile, acetone, and *n*-octane) or $P4_2/mbc$ (benzene) space group symmetry with $Z = 1$ or $Z = 8$, respectively (Figure 3.12). Furthermore, the obtained structures show slight variations in the reduced unit cell volumes (V/Z) ranging from 1075 to 1123 Å^3 and reveal moreover a precise arrangement of the different MOF building units with respect to the individual guest resulting in a perfect host-to-guest fit. This is visualized by the highly individual shapes of the void volumes, which closely resemble the molecular geometry of the encapsulated guest molecules (Figure 3.12, yellow shapes on the right of each structure depiction). The voids were calculated after removing the guests from the structural models using the contact surface of a probe of a given radius (see Figure 3.12 and caption, for details). Here, the wide range of accessible framework conformations, i.e., phenyl ring torsions, distortions of Zn-paddlewheel units and carboxylate-to-zinc coordination angles (for details, see Table 3.4), in use to adapt to the respective guest molecule, suggests a very flat conformational energy landscape for this kind of flexible MOF.

Table 3.4: Selected angles and dihedral angles (both normalized to the smallest, positive value) extracted from the SCXRD structures of DMOF-1-**C3** solvated with either DMF (*as*), acetonitrile (MeCN), acetone, benzene, or *n*-octane.

DMOF-1-**C3**	COO-Ph / °	Zn-Zn-N / °	C-O-Zn / °	**C3**-chain-torsion / °	**C3**-chain-ph-torsion / °
as	32/36/35/40	170	121/122/124/129/132/133	175/176/179	66/72
·2MeCN	44/45	173	121/124/130	176/179	66/77
·2acetone	46/44	175	126/127/128/131	176/180	65/76
·2benzene	37/38	180	122/123/126/127	177/179/180	67/70
·*n*-octane	31/37	167	114/128/126/141	178	70/76

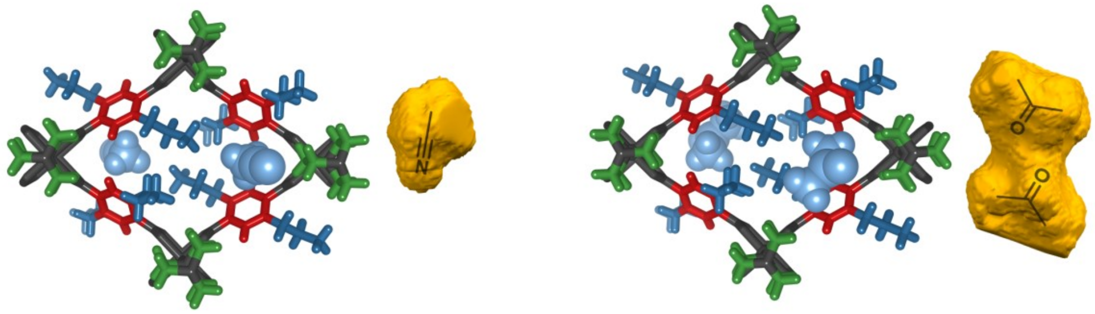

DMOF-1-**C3**·2MeCN
$P\bar{1}$, V/Z = 1078 Å^3

DMOF-1-**C3**·2acetone
$P\bar{1}$, V/Z = 1075 Å^3

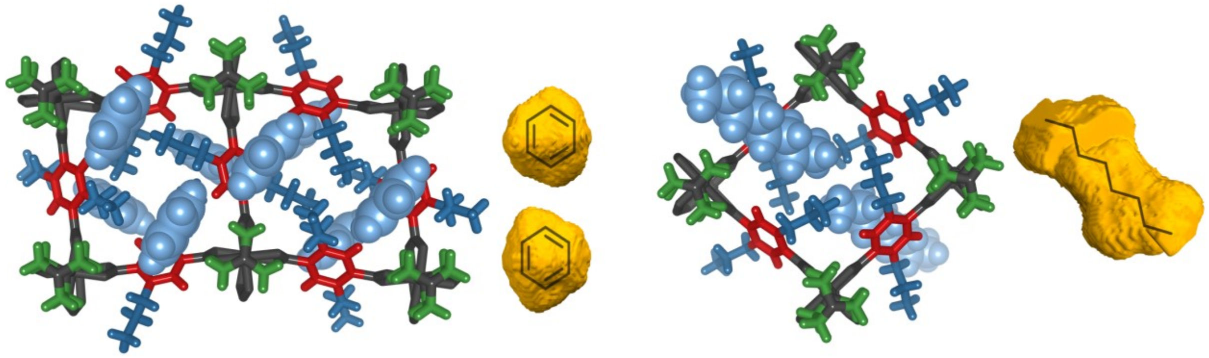

DMOF-1-**C3**·2benzene
$P4_2/mbc$, V/Z = 1123 Å^3

DMOF-1-**C3**·*n*-octane
$P\bar{1}$, V/Z = 1109 Å^3

Figure 3.12: Views of the SCXRD structures of DMOF-1-**C3** solvated with acetonitrile (MeCN), acetone, benzene, or *n*-octane along the dabco axis. The previously established colour code was utilized. Disorder in the SCXRD structures was removed for clarity. Mappings of the voids (probe radius 1.2 Å, 1.3 Å for DMOF-1-**C3**·*n*-octane and grid spacing of 0.2 Å), which contain the guest molecules, are given right of the respective structures to illustrate the adaptive nature of the flexible MOF system. The voids were calculated under retention of alkyl chain disorder.

3.5 N_2 and CO_2 Sorption in Comparison to the DMOF-1-**OCY**

As to how the guest-responsive behavior changes between alkoxy and alkyl substituents was assessed by a comparison of the sorption behavior of these compounds towards N_2 (77 K) and CO_2 (195 K), since the properties of the alkoxy-functionalized DMOF-1-**OCY** [Zn_2(2,5-**CYO**-bdc)$_2$(dabco)] (with **Y** = 1 (methoxy), 2 (ethoxy), 3 (propoxy), etc.) towards these guest molecules have been extensively investigated in the past.[99–101,104,114] Herein, the DMOFs with the same number of segments in the substituent chain are compared, i.e. the DMOF-1-**OC2** vs. DMOF-1-**C3** and the DMOF-1-**OC3** vs. DMOF-1-**C4**. The comparison DMOF-1-**OC1**- vs. DMOF-1-**C2** was not performed, since DMOF-1-**OC1** is known to at least partially decompose upon activation.[100]

For the propoxy/butyl pair, nearly no N_2 uptake at 77 K is observed at all, which complements the SCXRD structure of *dry*-DMOF-1-**C4** being devoid of any void space. *dry*-DMOF-1-**C3** and its ethoxy-equivalent, *dry*-DMOF-1-**OC2**, adsorb only small amounts of N_2 ($\approx$ 40 cm^{3}g^{-1} for propyl and $\approx$ 15 cm^{3}g^{-1} for ethoxy, see Figure 3.13), where the adsorbed amount of *dry*-DMOF-1-**C3** nicely relates to the void space calculated from the SCXRD structure of the guest-free contracted (***np***) phase (Figure 3.13, left (red dots), and Table 3.5, on the extraction of the pore volumes, see Materials & Methods 6.10). Apparently, there is even less pore space available in the ***np*** phase of the ethoxy-equivalent, in line with the significantly smaller reduced unit cell volume of ethoxy compared to propyl (V/Z(**OC2**) = 888 Å^3 vs. V/Z(**C3**) = 925 Å^3 at RT).[104] Likewise, *dry*-DMOF-1-**C2** adsorbs comparably small amounts of N_2 ($\approx$ 60 cm^{3}g^{-1}) appropriate to the free volume of its crystal structure, which is only slightly more than for *dry*-DMOF-1-**C3** (Figure 3.13, left, dark grey dots, and Table 3.5).

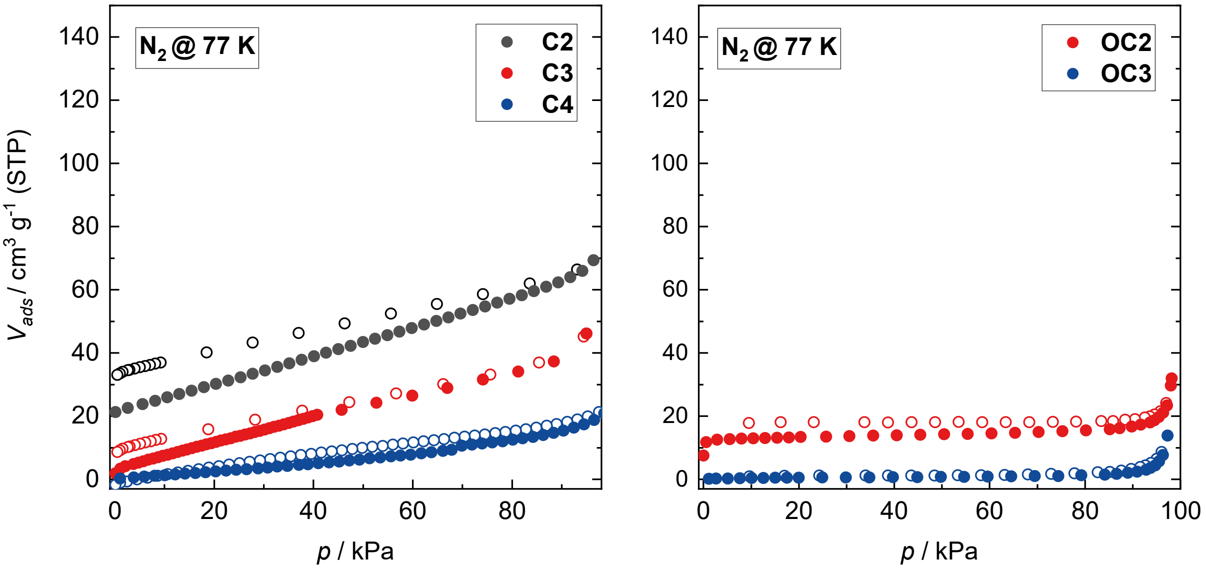

Figure 3.13: N_2 sorption isotherms of *dry*-DMOF-1-**C2** to -**C4** (left) and *dry*-DMOF-1-**OC2** and -**OC3** (right) recorded at 77 K. Adsorption and desorption branches are shown with closed and open symbols. For *dry*-DMOF-1-**CX** and *dry*-DMOF-1-**OCY** with the same length of the functional group, the same colours were used. The data on the alkoxy materials were taken from the literature.[104]

Table 3.5: Total pore volumes V_{exp} of *dry*-DMOF-1-**C2** and *dry*-DMOF-1-**C3** obtained from the N_2 isotherms at pressures around a $p/p_0 \approx 0.9$ ($p_0 = 100$ kPa for N_2 at 77 K). For comparison, the expected pore volumes V_{theo}, as obtained from the SCXRD structures of the ***np*** phases of *dry*-DMOF-1-**C2** and *dry*-DMOF-1-**C3**, are given as well.

dry-DMOF-1-**CX**	$V_{\mathrm{pore,exp}}$ / $\mathrm{cm^3g^{-1}}$	$V_{\mathrm{pore,theo}}$ / $\mathrm{cm^3g^{-1}}$
C2	$0.97 \cdot 10^{-1}$	$1.05 \cdot 10^{-1}$
C3	$0.58 \cdot 10^{-1}$	$0.60 \cdot 10^{-1}$

Note the comparably linear slope of the N_2-isotherms of *dry*-DMOF-1-**C2** and -**C3** and the hysteresis on the desorption branch although long measurement times of 60 h for *dry*-DMOF-1-**C2** and 26 h for *dry*-DMOF-1-**C3**, which is ascribed to diffusion limitations of the N_2 probe at the low measurement temperatures (77 K) into the pores of the MOF and also the discrete shape of the pore space (see Figure 3.10). Hence, the behaviour of the *dry*-DMOF-1-**CX** towards the stronger interacting CO_2 probe molecule (larger quadrupole moment of CO_2 compared to N_2), which is known to trigger breathing transitions in the related DMOF-1-**OCY** materials[104], was investigated up next.

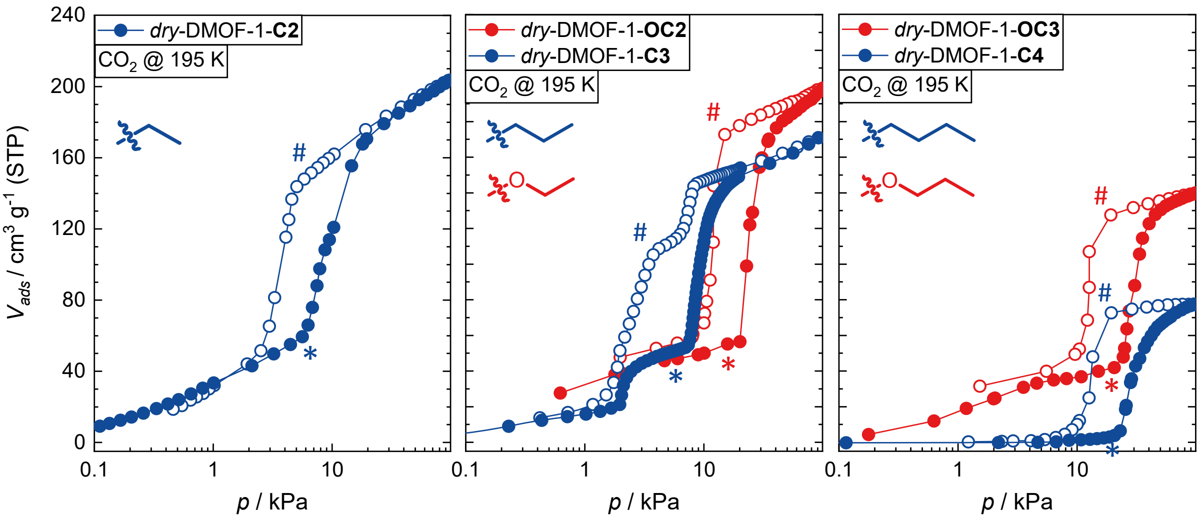

Figure 3.14: CO_2 sorption isotherms at 195 K of *dry*-DMOF-1-**C2**, *dry*-DMOF-1-**C3**, *dry*-DMOF-1-**C4** (blue symbols and lines, from left to right) and the respective alkoxy-counterparts *dry*-DMOF-1-**OC2** and *dry*-DMOF-1-**OC3** variants (red symbols and lines). Solid symbols correspond to the adsorption and empty symbols to the desorption branches of the isotherms, points of the ***np*→*lp*** or ***lp*→*np*** transitions are marked with an asterisk (adsorption) or a hash (desorption), respectively. Lines are just a guide to the eye. The data on the *dry*-DMOF-1-**OCY** materials were taken from the literature.[104]

All the alkyl functionalized DMOFs feature a stepped CO_2 sorption isotherm profile, indicating transitions from ***np*** phases to ***lp*** phases at certain threshold CO_2 pressures (Figure 3.14, marked by a blue asterisk). In more detail, the *dry*-DMOF-1-**C2** and *dry*-DMOF-1-**C4** exhibit the well-known hysteretic two-step behaviour, whereas the CO_2 isotherm of *dry*-DMOF-1-**C3** stands out due to the presence of multiple steps, on which will be further elaborated later in the text. As expected, from *dry*-DMOF-1-**C2** to *dry*-DMOF-1-**C4** the total volume uptake of CO_2 decreases from about 200 $\mathrm{cm^3g^{-1}}$ to 80 $\mathrm{cm^3g^{-1}}$ with an increasing sidechain (or DED) volume. The total pore volumes of DMOF-1-**C2** to DMOF-1-**C4** in their CO_2-filled ***lp*** phases as determined from the CO_2 uptake at $p \approx 90$ kPa are given in Table 3.6. For details on their extraction, see Materials & Methods Section 6.10.

Table 3.6: Compiled total pore volumes, V_{pore}, of the *dry*-DMOF-1-**CX** and -**OCY** in their CO_2-filled states calculated from the CO_2 uptake at $p \approx 90$ kPa, V_{ads}, and the pressure of the transition to the ***lp*** phase, p_{trans}. The value in brackets corresponds to the pore volume calculated from the SCXRD structure of *as*-DMOF-1-**C2** for comparison as there is no *in-situ* PXRD data available for this compound.

CX	V_{pore} / cm^3g^{-1}	V_{ads} / cm^3g^{-1}	p_{trans} / kPa	**OCY**	V_{pore} / cm^3g^{-1}	V_{ads} / cm^3g^{-1}	p_{trans} / kPa
C2	0.38(0.42)	202	6	**OC1**	-	-	-
C3	0.32	171	8	**OC2**	0.37	196	22
C4	0.15	77	23	**OC2**	0.26	139	25

In accordance with the N_2 sorption data, only *dry*-DMOF-1-**C2** and *dry*-DMOF-1-**C3** exhibit significant porosity towards CO_2 in their contracted phases prior to the transformation to their ***lp*** phases. Furthermore, the critical CO_2 pressure required for the transitions to the ***lp*** phase (p_{trans}) is increasing from *dry*-DMOF-1-**C2** ($p_{trans} = 6$ kPa) to *dry*-DMOF-1-**C4** ($p_{trans} = 23$ kPa), likely due to the increasing hydrophobicity and density of the ***np*** phases.

Comparing the CO_2 sorption behaviour of the alkyl-functionalized DMOFs with their alkoxy counterparts reveals that both *dry*-DMOF-1-**C3** and *dry*-DMOF-1-**C4** show the lower maximum uptake of CO_2 (Figure 3.14, middle and right, blue symbols and lines, Table 3.6), which is ascribed to the reduced volume requirements of the alkoxy groups and the dipolar nature of these groups, facilitating stronger interactions of the sidechains with CO_2. Interestingly, *dry*-DMOF-1-**OC3** adsorbs significant amounts of CO_2 (≈ 40 cm^3g^{-1}) in a not-open form before transforming to the fully open ***lp*** form, contrasting *dry*-DMOF-1-**C4** (Figure 3.14, right). This striking difference between the ***np*** phases of DMOF-1-**C4** and its propoxy relative can again be rationalized by the more dipolar nature of the alkoxy groups, leading to stronger framework-CO_2 interactions, while the non-polar butyl groups of DMOF-1-**C4** efficiently block the pores of the *np* phase. However, both *dry*-DMOF-1-**C4** and -**OC3** start transforming into the ***lp*** form at very similar CO_2 pressures $p_{trans} = 23$ and 25 kPa and the hysteresis loops are also of comparable magnitude.

For *dry*-DMOF-1-**C3** p_{trans} for the transition to the ***lp*** phase is found at a considerably lower value ($p_{trans} = 8$ kPa), than for the *dry*-DMOF-1-**OC2** ($p_{trans} = 22$ kPa). But the most striking difference between the CO_2 isotherms of the two materials is their overall shapes. The *dry*-DMOF-1-**OC2** material shows a one-step sorption isotherm typical for breathing MOFs, whereas the isotherm of *dry*-DMOF-1-**C3** features multiple steps with significant differences between the ad- and desorption profiles (Figure 3.14, middle). The two-step adsorption and desorption profiles signify the presence of additional intermediate pore (***ip***) phases besides the established ***np*** and ***lp*** phases. Strikingly, the plateaus for the ***ip*** phases are at very different sorption capacities for the ad- and desorption, thus suggesting the presence of different ***ip*** phases, depending on the sorption history of the material.

In order to catch the structural changes behind the stepped CO_2 isotherms of *dry*-DMOF-1-**C4** and especially *dry*-DMOF-1-**C3**, their breathing behaviour was monitored by means of *in-situ* PXRD experiments under variable CO_2 gas pressure at 195 K, which were performed at beamline P02.1 of DESY (Deutsches Elektronen-Synchrotron, Hamburg, Germany). Indeed, the CO_2 isotherms of both compounds could be well reproduced and followed by the *in-situ* PXRD experiment, allowing for an assignment of ***np*** and ***lp*** phases for *dry*-DMOF-1-**C4** and even separate ***ip*** phases in the case of *dry*-DMOF-1-**C3** to the different plateaus of the ad- and desorption branches of the CO_2 isotherms. Unfortunately, no *in-situ* CO_2 sorption PXRD data are available for *dry*-DMOF-1-**C2**. Firstly, the *in-situ* data on *dry*-DMOF-1-**C4** will be discussed, followed by the more elaborate case of *dry*-DMOF-1-**C3**.

The *in-situ* CO_2 sorption PXRD data of *dry*-DMOF-1-**C4** were collected in each 10 kPa step size from vacuum ($2 \cdot 10^{-3}$ kPa) to 100 kPa on the adsorption branch, whereas less PXRD patterns were recorded during desorption. The CO_2 pressures of all measured points are given in the caption of Figure 3.14. Not until a CO_2 pressure of 40 kPa (Figure 3.15, blue asterisk), *dry*-DMOF-1-**C4** starts to transform from the ***np*** phase to a ***lp*** phase, as signified by the constant growth of the reflections belonging to the ***lp*** phase over the pressure range up to 100 kPa, where only traces of the reflections of the ***np*** phase remain present. Consequently, the PXRD pattern recorded at 100 kPa CO_2 pressure showing the most complete phase transition was used to identify the ***lp*** phase via indexing and subsequent structureless profile refinement (Pawley method) of the pattern (Pawley fits are given in the Appendix section 8.1.5).

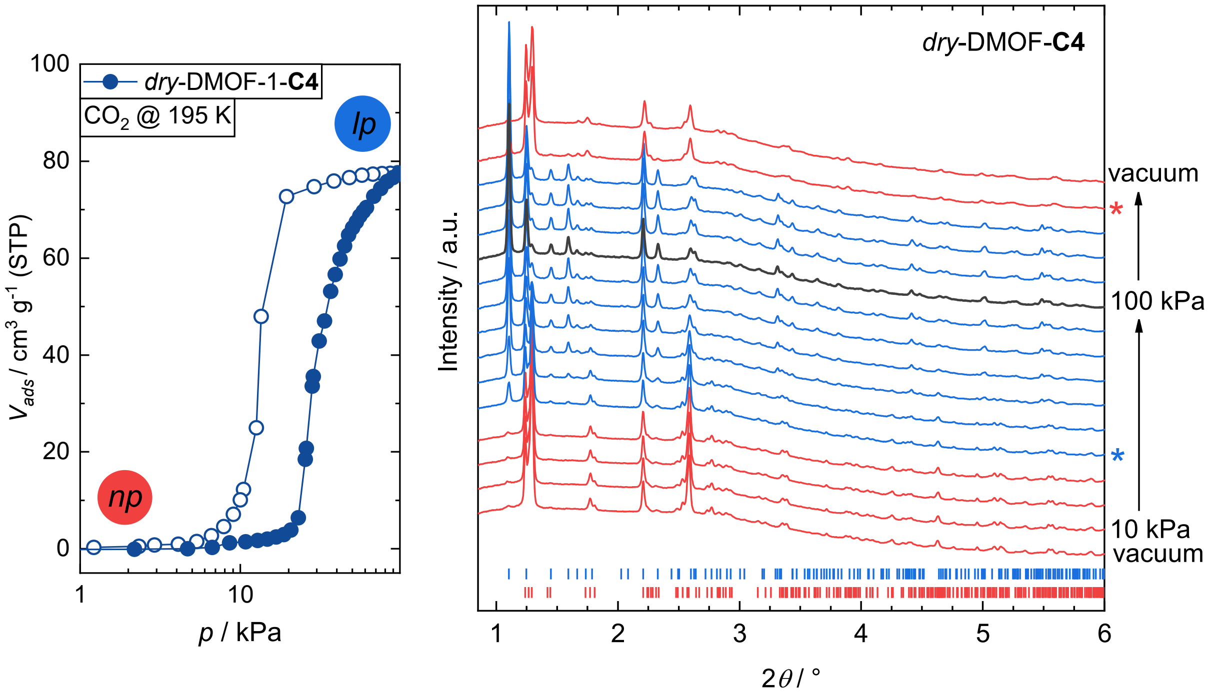

Figure 3.15: *In-situ* CO_2 sorption PXRD data of *dry*-DMOF-1-**C4** recorded from vacuum ($2 \cdot 10^{-3}$ kPa) to 100 kPa CO_2 pressure (P02.1 of DESY, $\lambda = 0.2073$ Å) with the corresponding CO_2 sorption isotherm. PXRD patterns of the adsorption branch were collected in 10 kPa steps and desorption data were collected at CO_2 pressures of 50, 10, 5 and 2 kPa and vacuum. Tick marks in red or blue correspond to positions of allowed reflections of the ***np*** or ***lp*** phase of *dry*-DMOF-1-**C4**, respectively, as extracted from the PXRD patterns by structureless profile fitting (Pawley method).

Table 3.7: Unit cell parameters and volumes of the ***np*** (adsorption branch) and CO_2-filled ***lp*** form of *dry*-DMOF-1-**C4** as determined from structureless profile refinement (Pawley method) of the *in-situ* PXRD patterns. The full profile fits are given in the Appendix section 8.1.5, Figure 8.12.

dry-DMOF-1-**C4**	**vacuum** (ads)	**100 kPa CO_2**
crystal system	monoclinic	monoclinic
space group	$C2/c$	$C2/m$
form	***np***	***lp***
a / Å	18.786(5)	16.5211(17)
b / Å	10.558(3)	14.2909(11)
c / Å	19.200(5)	9.6079(6)
α / °	90	90
β / °	92.43(3)	97.682(17)
γ / °	90	90
Z	4	2
V/Z / Å^3	951.2(18)	1124.1(3)
$\Delta V_{np \to lp}$	-	+18%
R_{wp}	0.52	0.58
R_{exp}	1.33	1.89
χ^2	0.39	0.31

The CO_2-filled ***lp*** phase of *dry*-DMOF-1-**C4** crystallizes in $C2/m$ space group symmetry with $Z = 2$ and $V/Z = 1124$ Å^3 and therefore in a different unit cell and space group symmetry than in the DMF-containing as-synthesized state. Followingly, upon adsorbing CO_2 and structural transformation, the volume per repeating unit of DMOF-1-**C4** changes by +18% in relation to its ***np*** form. On the desorption branch of the *in-situ* experiment, the ***lp→np*** back transformation is completed at 2 kPa CO_2 pressure (Figure 3.15, red asterisk).

Interestingly, the large region of the ***np→lp*** phase transition on the adsorption branch, despite equilibration times of 20-30 min per measuring point, clearly indicates slow kinetics of this transformation, in line with the shape of the step in the isotherm of *dry*-DMOF-1-**C4**, which exhibits the smallest gradient with respect to pressure of the *dry*-DMOF-1-**CX** and **-CYO** materials investigated herein (Figure 3.14). This can be ascribed to the structural features of the *np* form, where all pore space and the framework parts, which attractively interact with CO_2 guests, are blocked by the **C4**-DEDs.

As already evident from the mere shape of its CO_2 sorption isotherm, *dry*-DMOF-1-**C3** displays a surprisingly complex phase behaviour upon ad- and desorbing CO_2, which is rationalized with the help of the *in-situ* CO_2 sorption PXRD data in the following passage. The *in-situ* PXRD data were analysed by means of structureless profile refinement (Pawley method) to extract the appropriate unit cell parameters and Rietveld refinement,[115] where possible, to gain a plausible structural model of the corresponding MOF phase. The final refinement data and detailed refinement procedures are given in the Appendix section 8.1.5.

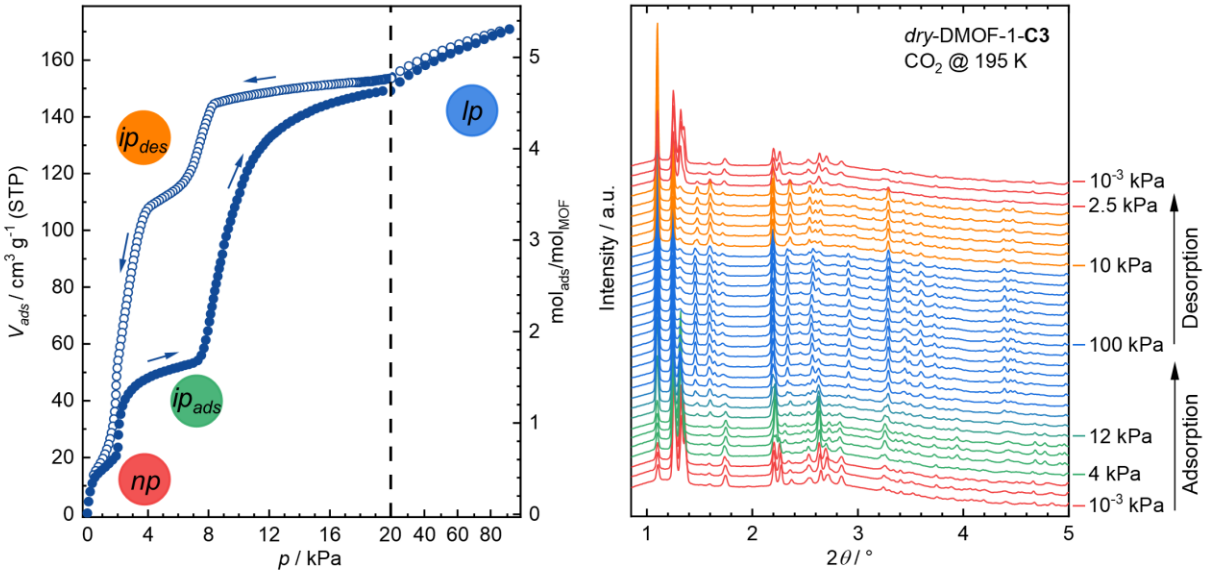

Figure 3.16: Zoom-in of the CO_2 sorption isotherm (195 K) of *dry*-DMOF-1-**C3** (left) and *in-situ* PXRD patterns under variable CO_2 pressure recorded at 195 K (P02.1 of DESY, $\lambda = 0.2073$ Å) (right). The plateaus of the isotherm are marked with a dot in a colour, which assigns them to the different phases observed during the *in-situ* PXRD experiment.

Starting in the established ***np*** form of *dry*-DMOF-1-**C3** (space group $P\bar{1}$; $V/Z = 909$ Å^3; Figure 3.16, red PXRD patterns), which shows small CO_2 uptake of about 20 cm^3/g, corresponding to about 0.5 CO_2 molecules per framework repeating unit. The PXRD pattern recorded at 2 kPa CO_2 pressure was employed in a Rietveld refinement using the SCXRD structure of *dry*-DMOF-1-**C3** as a starting model, where the present void space was filled with a CO_2 molecule (Figure 3.17, for crystallographic data and refinement procedures, see Appendix, section 8.1.5).

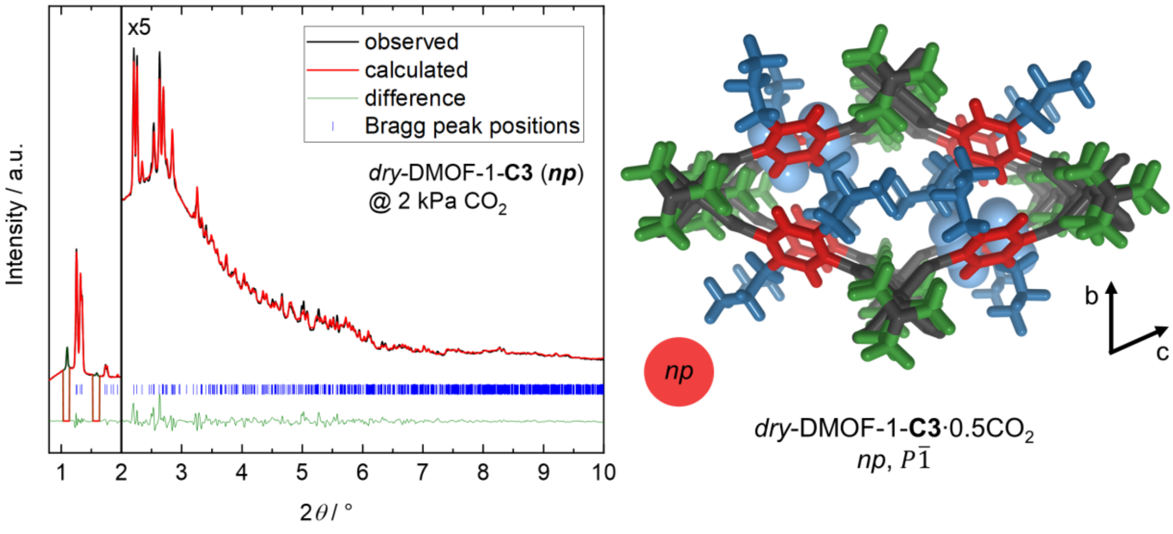

Figure 3.17: The final Rietveld plot of the refinement of the ***np*** phase of *dry*-DMOF-1-**C3** at 2 kPa CO_2 pressure on the adsorption branch of the experiment (P02.1 of DESY, $\lambda = 0.2073$ Å, left). Note that due to remaining ***lp*** phase in the material, the three 2*θ* regions 1.04-1.13 and 1.54-1.63 were excluded from the fit. Right: Structural model of the ***np*** phase of *dry*-DMOF-1-**C3** as obtained from Rietveld refinement. H atoms were added at idealized geometric positions since they were not included in the refinement.

The adsorption branch proceeds over a transformation to a slightly more expanded intermediate pore (***ip***$_{\textbf{ads}}$) phase of higher symmetry (space group $C2/m$; $V/Z = 937$ Å^3, 103% of the volume of the ***np*** phase; Figure 3.16, green PXRD patterns). The *in-situ* PXRD pattern collected at a CO_2 pressure of 6 kPa was employed in a Rietveld refinement based on a rough starting model obtained from 3D electron diffraction (3DED) of *dry*-DMOF-1-**C3** to yield a structural model for the ***ip***$_{\textbf{ads}}$ phase of *dry*-DMOF-1-**C3** (Figure 3.18, top, see Appendix section 8.1.5 for the detailed refinement procedure and Table 8.12 for the crystallographic data, for details on the 3DED data collection, see Appendix section 8.1.6).

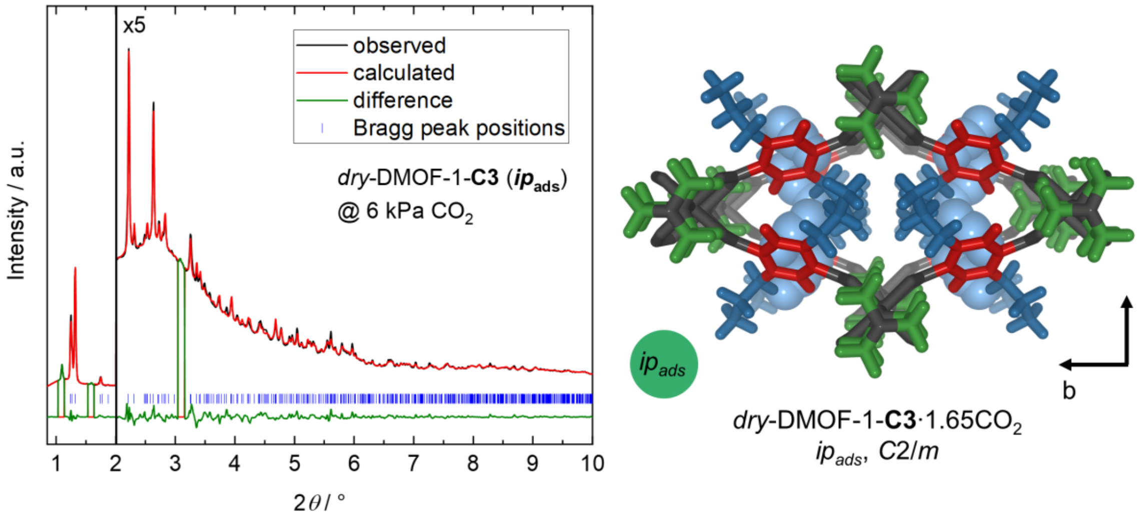

Figure 3.18: The final Rietveld plot of the refinement of the ***ip***$_{\textbf{ads}}$ phase of *dry*-DMOF-1-**C3** at 6 kPa CO_2 pressure on the adsorption branch of the experiment (P02.1 of DESY, $\lambda = 0.2073$ Å, left). Note that due to remaining ***lp*** phase in the material, the three 2θ regions 1.04-1.13, 1.54-1.63 and 3.05-3.15 were excluded from the fit. Right: Structural model of the ***ip***$_{\textbf{ads}}$ phase of *dry*-DMOF-1-**C3** as obtained from Rietveld refinement. H atoms were added at idealized geometric positions since they were not included in the refinement.

It was possible to locate the CO_2 guest molecules in the Fourier difference map and to refine their positions by setting their crystallographic occupancies to values in accordance with the CO_2 uptake observed in the sorption isotherm at 6 kPa. Evidently, in the ***ip***$_{\textbf{ads}}$ phase the adsorption of CO_2 guests is only occurring in the pore space between the Zn_2(**C3**-bdc)$_2$-layers due to the steric bulk of the propyl groups, which arrange in the centre of the pores of the Zn_2(C3-bdc)$_2$ square grid layers. This fact indicates comparably weak interactions of the propyl side chains with the CO_2 guest molecules and that the latter preferably arrange close to the polarized CH_2-groups of the dabco and on top of the phenyl rings, which have also been identified as the main spots of incorporated guest molecules (compare Figure 3.7).
From 8 kPa onward *dry*-DMOF-1-**C3** shows a steep increase in the adsorption of CO_2 caused by the transformation to a ***lp*** form, which was identified from structureless profile refinement (Pawley method, Figure 3.19, fit parameters are given in Appendix section 8.1.5) of a PXRD pattern recorded at 100 kPa CO_2 pressure. The ***lp*** phase could be indexed in an almost fully expanded unit cell (space group $C2/m$; $V/Z = 1144$ Å^3, 126% of the volume of the ***np*** phase; Figure 3.16, blue PXRD patterns), demonstrating the opening of the framework via expansion along the short diagonal and contraction of the long diagonal of the rhomb-shaped channels.

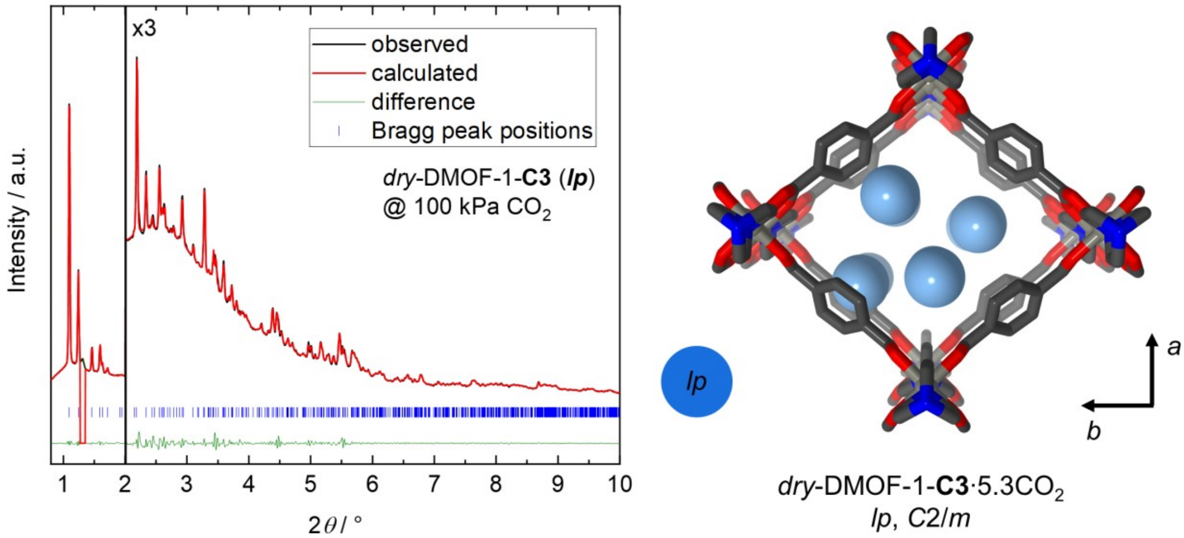

dry-DMOF-1-**C3**·5.3CO_2
lp, *C*2/*m*

Figure 3.19: Structureless profile fit (Pawley method) of the *in-situ* CO_2 sorption PXRD pattern of *dry*-DMOF-1-**C3** at a CO_2 pressure of 100 kPa (P02.1 of DESY, $\lambda = 0.2073$ Å, left). The model of the ***lp*** phase (right) was created on the mere basis of the extracted unit cell parameters to represent the opening of the framework structure, hence, the likely heavily disordered components, i.e., DEDs and CO_2 guests, are left out and are represented by the blue spheres. Here, a standard atom colouring is used (black: C, red: O, blue: N, grey: Zn) and no H-atoms are displayed.

Unfortunately, Rietveld refinement of the PXRD pattern collected at 100 kPa CO_2 pressure to gain more detailed structural insights into the fully expanded phase, also using lower symmetry starting models, did not lead to satisfactory results. This is likely to be a consequence of pronounced disorder of the phenyl rings, DEDs and guest molecules within the expanded ***lp*** phase.

Following the desorption branch of the CO_2 sorption isotherm, a different intermediate phase (***ip***$_{\text{des}}$) than the ***ip***$_{\text{ads}}$ of the adsorption branch is encountered at CO_2 pressures of about 8 kPa, as indicated by a plateau with considerably higher CO_2 uptake of about 3.5 CO_2 per MOF repeating unit in relation to the about 1.5 CO_2 adsorbed in the ***ip***$_{\text{ads}}$ phase (compare Figure 3.16). Analysis of the *in-situ* PXRD data in the pressure region corresponding to the ***ip***$_{\text{des}}$ phase (Figure 3.16, right, yellow patterns) reveals, that the ***ip***$_{\text{des}}$ phase indeed is structurally very different from the ***ip***$_{\text{ads}}$ phase of *dry*-DMOF-1-**C3**. The ***ip***$_{\text{des}}$ phase of *dry*-DMOF-1-**C3** was indexed in the monoclinic space group $P2/c$ and, importantly, the reduced unit cell volume $V/Z = 1135$ Å^3 only changes by about 9 Å^3 compared to the ***lp*** phase, despite a comparably large amount of desorbed CO_2 molecules (≈ 2 CO_2 molecules per MOF repeating unit). Moreover, a detailed chemically sensible structural model of the ***ip***$_{\text{des}}$ phase of *dry*-DMOF-1-**C3** could be derived by Rietveld refinement of the *in-situ* PXRD pattern recorded at a CO_2 pressure of 5 kPa (for details, see Appendix, section 8.1.5). Interestingly, once the CO_2 pressure drops below about 3.5 kPa in the isotherm, the material immediately transfers back into its fully contracted *np* form, without traversing to the ***ip***$_{\textit{ads}}$ phase (Figure 3.16, left), which is also corroborated by the *in-situ* PXRD data (Figure 3.16, right, red patterns). Structureless profile fits (Pawley method) with the corresponding crystallographic data of the ***np*** phase on the desorption branch are given in the Appendix section 8.1.5, Figure 8.13 and Table 8.13.

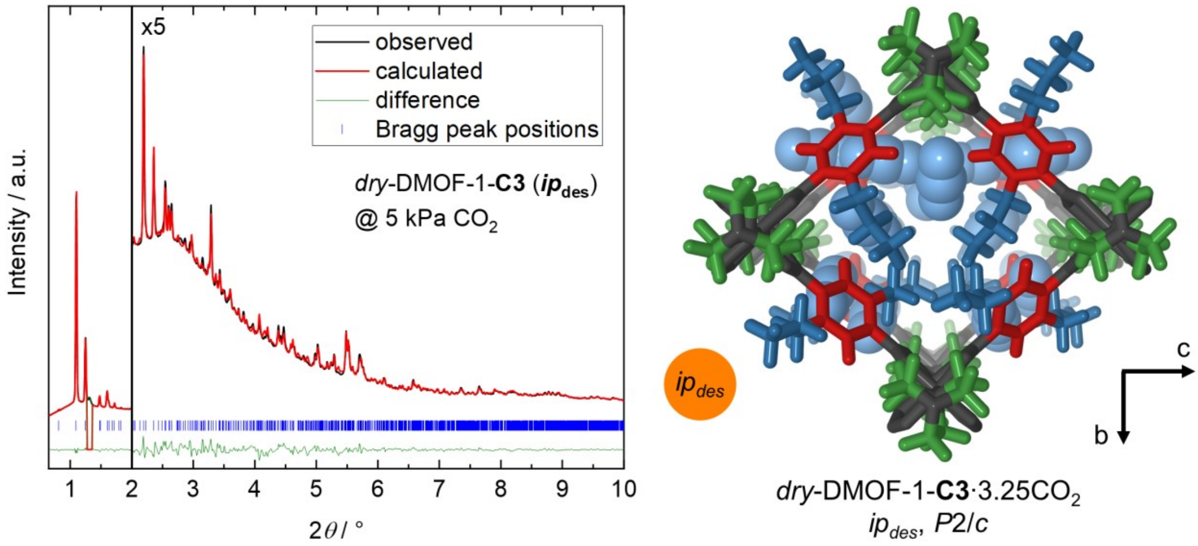

Figure 3.20: The final Rietveld plot of the refinement of the ***ip***$_{\text{des}}$ phase of *dry*-DMOF-1-**C3** at 5 kPa CO_2 pressure on the desorption branch of the experiment (P02.1 of DESY, λ = 0.2073 Å, left). The resulting structural model is displayed on the right. H atoms were added at idealized geometric positions since they were not included in the refinement. Note, that CO_2 molecules included here possess an occupancy of about 0.5 each.

For all phases encountered in course of the ad- and desorption of CO_2 in *dry*-DMOF-1-**C3**, the unit cell parameters that were extracted from the *in-situ* PXRD patterns are summarized in Table 3.8. Together with the structural models derived by Rietveld refinement, these will be discussed to generate a more comprehensive picture of the CO_2 sorption behaviour of *dry*-DMOF-1-**C3** in the following.

Table 3.8: Collected unit cell parameters of the different phases of *dry*-DMOF-1-**C3** during the ad- and desorption of CO_2 at 195 K. Furthermore, the direction of the Zn_2(**C3**-bdc)$_2$-layer parallel displacements with respect to the layer diagonals, d_{diagonal}, as described in the text is given below.

dry-DMOF-1-**C3**	***np***	***ip***$_{\text{ads}}$	***lp***	***ip***$_{\text{des}}$	***np***
crystal system	triclinic	monoclinic	monoclinic	monoclinic	triclinic
space group	$P\bar{1}$	$C2/m$	$C2/m$	$P2/c$	$P\bar{1}$
a / Å	9.587(4)	10.3475(14)	14.660(2)	9.6049(6)	9.625(13)
b / Å	10.133(5)	18.875(2)	16.290(2)	14.6583(14)	10.218(13)
c / Å	10.586(6)	9.6197(10)	9.6301(8)	16.2256(15)	10.615(15)
α / °	62.962(6)	90	90	90	62.622(19)
β / °	84.64(4)	94.581(15)	95.72(2)	96.228(11)	84.84(12)
γ / °	83.50(2)	90	90	90	82.72(13)
V/Z / Å^3	909(1)	937(4)	1144(4)	1135(3)	919(2)
V / %	100	103	126	125	101
d_{diagonal}	long/short	short	short	long	long/short

The analysis will stick to the changes in the directions of the parallel displacements of the Zn_2(**C3**-bdc)$_2$-layers with respect to their neighbouring layers, as these are symptomatic of the structural pathway of the CO_2 sorption process. In case of the monoclinic ***ip***$_{\text{ads}}$, ***lp*** and ***ip***$_{\text{des}}$ phases (Z = 2), the angle β, as it is formed by the pillar axis and either the long- or short diagonal of the Zn_2(**C3**-bdc)$_2$-layers (see Table 3.8), represents this displacement and its direction is evident (see Figure 3.21).

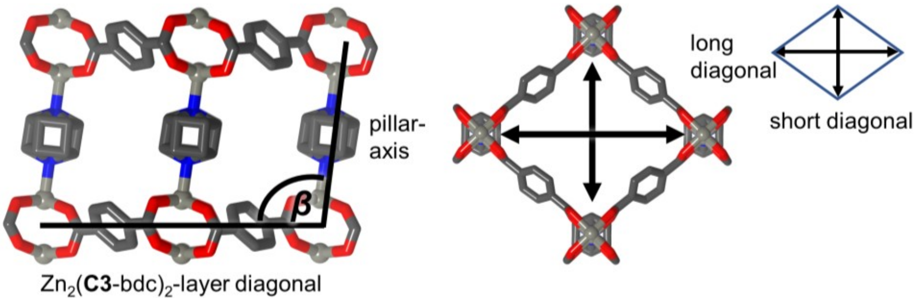

Figure 3.21: Parallel displacement of the Zn_2(**C3**-bdc)$_2$ layers as in the monoclinic ***ip***$_{\mathbf{ads}}$, ***lp*** and ***ip***$_{\mathbf{des}}$ phases (left). Long- and short diagonals through the Zn_2(**C3**-bdc)$_2$ layers (right). The model presented in Figure 3.19 is used as an example here.

Indicated by its triclinic symmetry ($Z = 1$), the ***np*** phase features a different displacement of the Zn_2(**C3**-bdc)$_2$ layers proceeding along both the long and short layer diagonals. Hence, starting from this, the layer displacement changes towards solely the short diagonal upon transformation to the slightly expanded ***ip***$_{\mathbf{ads}}$ phase. This is related to the more symmetric arrangement of the DEDs in the ***ip***$_{\mathbf{ads}}$ phase, which renders pore space in between the Zn_2(**C3**-bdc)$_2$-layers available as the flexible DEDs are now found centred in these layers (see Figure 3.18). Upon further expanding to the ***lp*** phase, where now the Zn_2(**C3**-bdc)$_2$-layers are open, their displacement direction parallel to the short diagonal of the rhombic grids is retained. In this regard, the ***ip***$_{\mathbf{des}}$ form of *dry*-DMOF-1-**C3** is different, as the displacement of the Zn_2(**C3**-bdc)$_2$-layers is parallel to the direction of the long diagonal of the Zn_2(**C3**-bdc)$_2$-layer here (Figure 3.22).

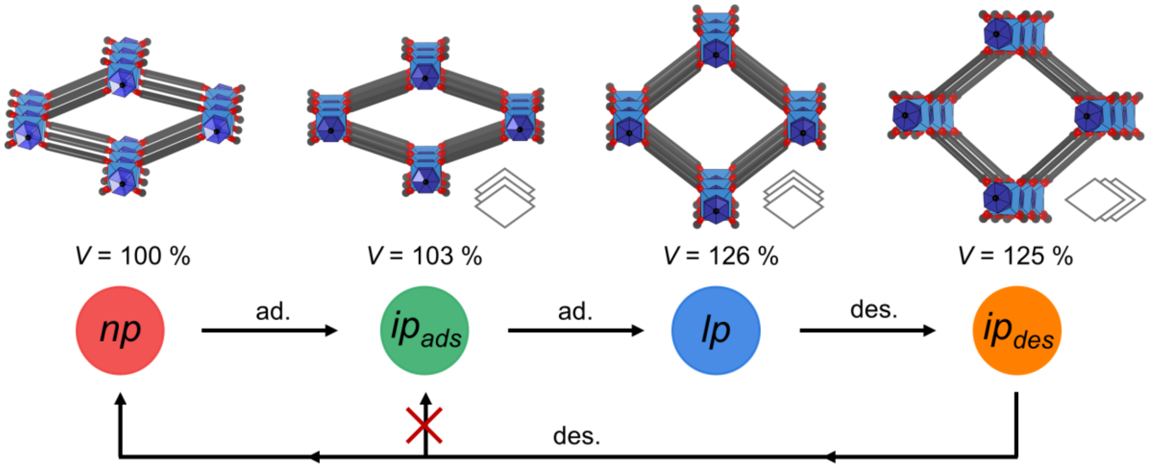

Figure 3.22: Schematic representation of the framework backbone of *dry*-DMOF-1-**C3** in the ***np***, ***ip***$_{\mathbf{ads}}$, ***lp*** and ***ip***$_{\mathbf{des}}$ phases during CO_2 sorption. Herein, the Zn_2(C3-bdc)$_2$-layer of the framework is depicted in parallel to the paper plane to picture the direction of the displacement of the next neighbouring layers with respect to the long or short diagonal of the rhombic grid as introduced in Figure 3.21.

Moreover, the structural model of the ***ip***$_{\mathbf{des}}$ phase of *dry*-DMOF-1-**C3** derived by Rietveld refinement (Figure 3.20, right) reveals ordered propyl groups residing in designated quarters of the MOF cavities. By contrast, the propyl groups are likely disordered in the ***lp*** phase, as no structural model could be fitted to this phase, while the corresponding PXRD pattern indicates rather high symmetry (space group $C2/m$). Hence, one can rationalize, that the rearrangement of the propyl groups from a disordered to an ordered state drives the transition from the ***lp*** to the ***ip***$_{\mathbf{des}}$ phase upon the release of CO_2 molecules and in turn unblocking of pore space. The aggregation of the propyl groups in the ***ip***$_{\mathbf{des}}$ phase requires a 60°-flip of 50% of the **C3**-bdc^{2-} linkers in the materials, so that the propyl sidechains can cluster in one quarter of the cavity, while leaving the opposite cavity quarter open for CO_2 molecules. The clustering of the non-polar sidechains is likely to be a consequence of relatively less favourable interactions of the latter with the CO_2 molecules in comparison with the interactions among themselves and the framework backbone. The resulting change in the direction of the Zn_2(**CX**-bdc)$_2$-layer displacement from towards the short to the long layer diagonal at the same time facilitates these interactions by bringing the propyl DEDs into closer proximity, hence allowing for stronger inter-sidechain dispersion interactions. Importantly, in the ***ip***$_{\mathbf{des}}$ phase, the configuration of the **C3**-bdc^{2-} linkers with respect to the phenyl ring tilting and the DED orientation is considerably different from that of the other structurally documented phases, i.e., the ***np*** and ***ip***$_{\mathbf{ads}}$ phases. Altogether this predetermines the structural pathway of the CO_2 desorption branch over the ***ip***$_{\mathbf{des}}$ directly to the ***np*** phase. A transition from the ***ip***$_{\mathbf{des}}$ to the ***ip***$_{\mathbf{ads}}$ therefore is kinetically hindered due to the different Zn_2(**C3**-bdc)$_2$-layer displacements and linker configurations in both phases. The same is true for the adsorption branch, where the ***ip***$_{\mathbf{ads}}$ phase directly converts to the less ordered ***lp*** phase without traversing the ***ip***$_{\mathbf{des}}$ phase.

In this study, the gas sorption behaviour of a DED functionalized MOF could be explored in extraordinary detail for the first time. However, there are still aspects of the CO_2 sorption behaviour of *dry*-DMOF-1-**C3** remaining to be addressed, especially about the underlying thermodynamics, for example regarding the question of the more stable one the two ***ip*** phases at a defined CO_2 pressure. But with the structural data gathered herein, the underlying thermodynamics might be assessed via theoretical simulations to generate a full picture of the peculiar structural behaviour of *dry*-DMOF-1-**C3** during CO_2 sorption.

3.6 Hydrocarbon Sorption

In practice, the separation of light hydrocarbons, e.g., the ethylene/ethane and propylene/propane pairs, is mainly achieved via energy intensive high-cost distillation processes run at cryogenic temperatures and high pressures,[116,117] due to their very similar physical properties.[118] In this regard, processes involving a chemical separation by adsorption using porous materials such as MOFs may pose an energy and cost saving alternative to the traditional procedures.[118] However, there are only relatively few data available on the sorption behaviour of the flexible DED-functionalized kind of materials presented herein, in particular on the C3 hydrocarbons propane and propylene and *n*-butane.[107,119,120] In addition to that, due to their chemical nature these adsorptive might provoke fundamentally different responses of flexible materials than the previously discussed N_2 and CO_2 probes. Hence, the response of the *dry*-DMOF-1-**CX** materials will be evaluated in the following and subsequently compared to their alkoxy pendants.

3.6.1 *n*-Butane

Investigation of the sorption of *n*-butane conducted at 273 K (p_0 = 103 kPa)[121] reveals stepped isotherms for all three *dry*-DMOF-1-**CX**, which yet indicate transformations from the ***np*** to the ***lp*** phases of these materials (Figure 3.23).

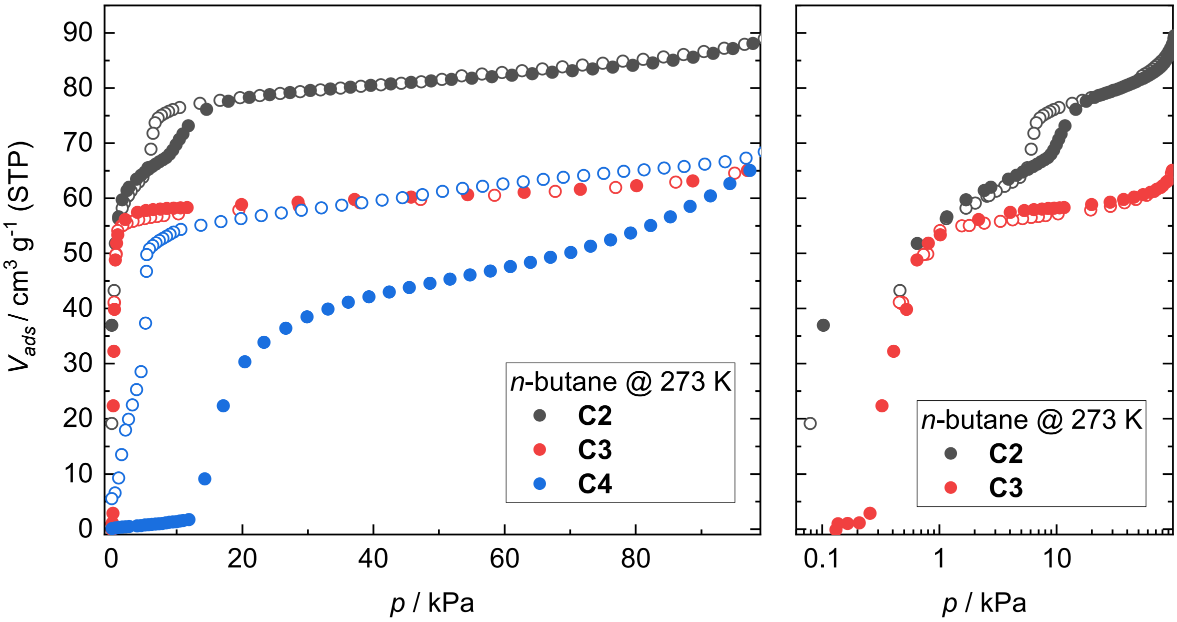

Figure 3.23: *n*-Butane sorption isotherms of *dry*-DMOF-1-**C2** to -**C4** recorded at 273 K. Furthermore, on the right the isotherms of *dry*-DMOF-1-**C2** and *dry*-DMOF-1-**C3** are shown with a logarithmic pressure axis to emphasize the low-p region of the isotherm. Note, that the isotherm of *dry*-DMOF-1-**C4** suffers from the accidental use of an O-ring of a material adsorbing *n*-butane, therefore boosting the uptake from $p \approx 0.75$ kPa.

However, there are significant differences in the maximum *n*-butane uptakes, V_{ads}, and the phase transition pressures, p_{trans}, amongst the series when proceeding from *dry*-DMOF-1-**C2** to -**C4** (Table 3.9). Upon dosing only slight amounts of *n*-butane, *dry*-DMOF-1-**C2** and *dry*-DMOF-1-**C3** readily transform to their ***lp*** states as indicated by the steep increase of the isotherms at 0.1 kPa ($p/p_0 = 0.001$), the first measuring point for this experiment, and 0.3 kPa ($p/p_0 = 0.003$) of *n*-butane pressure, respectively. Interestingly, the isotherm of *dry*-DMOF-1-**C2** exhibits a further small step at 9 kPa ($p/p_0 = 0.09$). Importantly, there is nearly no *n*-butane taken up by *dry*-DMOF-1-**C3** until the $p_{\mathrm{trans}} = 0.3$ kPa is reached. Contrasting the behaviour of *dry*-DMOF-1-**C2** and -**C3**, *dry*-DMOF-1-**C4** transforms at the much higher $p_{\mathrm{trans}} = 14$ kPa ($p/p_0 = 0.14$) and exhibits the strongest hysteresis width ($\Delta p \approx 15$ kPa) of the three materials. Please note, that the further uptake in the isotherm of *dry*-DMOF-1-**C4** past $p \approx 75$ kPa and the maintained high uptake on the desorption branch traces back to the unfortunate use of the wrong O-ring material, which adsorbed *n*-butane in this experiment.

Table 3.9: Compiled transition pressures, p_{trans}, and maximum uptakes, V_{max}, of the *dry*-DMOF-1-**CX**. V_{max} were determined as the V_{ads} at 90 kPa. For the first step of *dry*-DMOF-1-**C2**, the maximum uptake was extrapolated from a Langmuir fit of the data points prior to $p = 9$ kPa. V_{max} of *dry*-DMOF-1-**C4** was determined from the uptake at 70 kPa due to the corruption of the data at higher pressures as discussed in the text.

dry-DMOF-1-**CX**	p_{trans} / kPa	p_{trans} / p/p_0	V_{max} / $\mathrm{cm^3g^{-1}}$	V_{max} / $\mathrm{mol_{ads}mol_{MOF}}^{-1}$
C2	0.1	0.001	71	2.25
	9	0.09	86	2.74
C3	0.3	0.003	63	2.17
C4	14	0.14	49	1.82

The observed differences in p_{trans} appear reasonable in the context of the structures of the ***np*** phases, which have been discussed in section 3.3 and especially Figure 3.10. Considering the accessible voids in the ***np*** phases, *dry*-DMOF-1-**C4** and -**C3** do not take up any *n*-butane until p_{trans} as there either are no voids (**C4**), or they are distinctly separated from another (**C3**), hence, inaccessible for large probes such as *n*-butane. By contrast, the voids in the ***np*** phase of *dry*-DMOF-1-**C2** being discrete at 100 K, likely have merged into continuous channels at 273 K due to the thermal expansion of the material (compare Figure 3.10), allowing access to favourable adsorption sites.[120] Furthermore, resulting from the weak interactions of the **C2** DEDs with the framework due to their short length, the ***lp*** phase can be thermodynamically favoured already at low *n*-butane pressures. In this regard, the DEDs of *dry*-DMOF-1-**C4** in its ***np*** phase are densely packed and well-ordered and further MOF building units are not as distorted, hence, p_{trans} must be higher and similarly the required activation energy, which results in the stronger hysteresis of the sorption isotherm of this material.

As expected, the maximum uptake constantly decreases from 86 $\mathrm{cm^3g^{-1}}$ for *dry*-DMOF-1-**C2** over 63 $\mathrm{cm^3g^{-1}}$ for *dry*-DMOF-1-**C3** to 49 $\mathrm{cm^3g^{-1}}$ for *dry*-DMOF-1-**C4** corresponding to 2.74, 2.17, and 1.82 adsorbed *n*-butane molecules per MOF repeating unit. Hence, the maximum number of adsorbed *n*-butane molecules drops by roughly 0.5 per carbon atom of the DEDs.

To further analyse the *n*-butane sorption behaviour, *in-situ* *n*-butane sorption PXRD experiments were conducted at BL9 of DELTA (Dortmunder Elektronenspeicherring-Anlage, Dortmund, Germany, Figure 3.24). From the collected PXRD data, unit cell parameters of the *n*-butane filled ***lp*** phases were extracted by means of structureless profile refinement (Pawley method) of patterns recorded at 200 kPa or 230 kPa *n*-butane pressure. The full fits and fit results are given in the Appendix section 8.1.7.

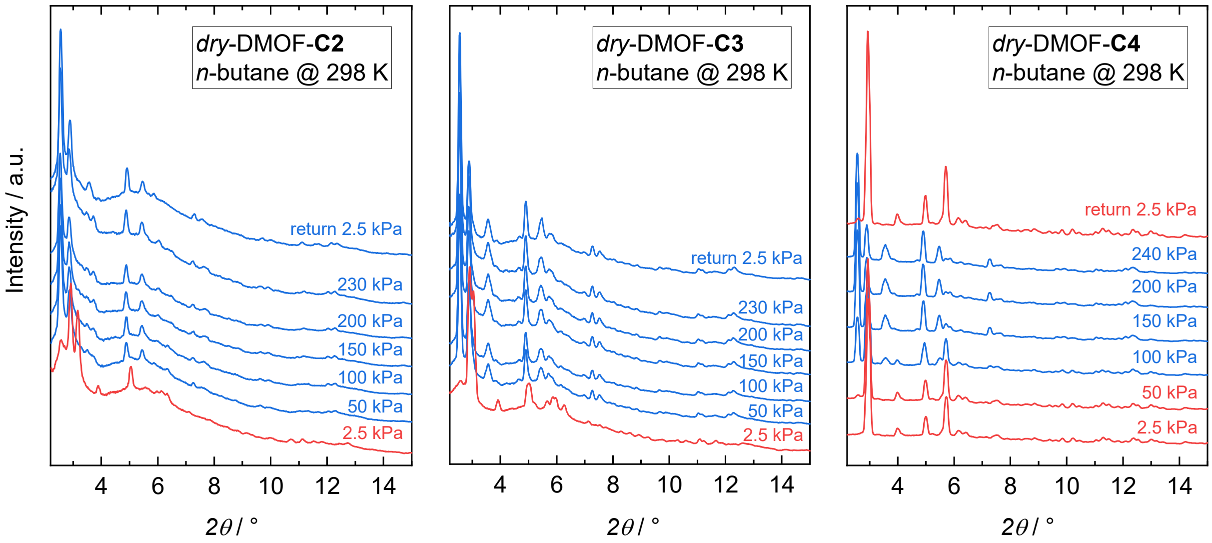

Figure 3.24: *In-situ* *n*-butane sorption PXRD data of *dry*-DMOF-1-**C2** to -**C4** recorded at 298 K (BL9 of DELTA, $\lambda = 0.4592$ Å). Employing the established colour code, red patterns correspond to the ***np*** phase, blue patterns to the ***lp*** phase.

Table 3.10: Unit cell parameters of the *dry*-DMOF-1-**CX** extracted from the *in-situ* *n*-butane sorption data collected at 298 K at BL9 of DELTA.

Compound	**C2**(***np***)	**C2**(***lp***)	**C3**(***np***)	**C3**(***lp***)	**C4**(***np***)	**C4**(***lp***)
pressure	2.5 kPa	200 kPa	2.5 kPa	230 kPa	2.5 kPa	240 kPa
crystal system	monoclinic	monoclinic	triclinic	triclinic	monoclinic	triclinic
space group	$C2/m$	$P2/c$	$P\bar{1}$	$P\bar{1}$	$C2/c$	$P\bar{1}$
a / Å	9.819(18)	10.94(3)	9.60(3)	9.61(5)	18.93(2)	9.602(4)
b / Å	18.930(13)	10.96(3)	10.28(3)	10.94(3)	10.713(17)	10.95(3)
c / Å	9.56(2)	19.35(4)	10.61(4)	10.96(5)	19.30(3)	10.96(4)
α / °	90	90	62.12(2)	88.35(16)	90	89.0(3)
β / °	100.28(10)	88.4(2)	84.4(3)	83.77(16)	93.43(11)	84.3(2)
γ / °	90	90	83.69(9)	87.06(6)	90	87.40(10)
Z	2	2	1	1	4	1
V / Å^3	1749(5)	2319(10)	919(6)	1143(9)	3907(10)	1145(5)
V/Z / Å^3	874.5	1159.5(133%)	919	1143(124%)	976.8	1145(117%)

As expected, all three DMOF-1-**CX** transform to fully expanded ***lp*** phases upon adsorbing *n*-butane. At this, the ***lp*** phase DMOF-1-**C2** can be indexed in the same unit cell and space groups as its DMF filled ***np*** phase ($P2/c$, $V/Z = 1159.5$ Å^3) and has expanded by 33% in relation to the ***np*** phase. Unfortunately, the intermediate plateau of the *n*-butane isotherm at around 9 kPa (273 K, see Figure 3.23) could not be resolved during the *in-situ* PXRD experiments. The ***lp*** phases of DMOF-1-**C3** and -**C4** were indexed in a 24% and 17% expanded unit cell similar to the one of DMOF-1-**C3**·*n*-octane (space group $P\bar{1}$, $V/Z = 1143$ and 1145 Å^3). In line with the sorption isotherms, ***lp*** DMOF-1-**C2** and DMOF-1-**C3** do not reconvert to the *np* phase under the maximum achievable vacuum in this experiment of 2.5 kPa, whereas DMOF-1-**C4** has fully reconverted under these conditions.

It has been shown for the DMOF class of materials that the lining of the pores with saturated hydrocarbon (or alkyl) groups by means of linker functionalization enhances its preference to adsorb saturated over unsaturated hydrocarbons.[119,120,122] This is important since the unsaturated hydrocarbons are the more valuable product and, hence, can be purified by sieving out undesired saturated hydrocarbons. Coupled with the gate-opening or breathing behaviour associated with flexible MOFs, the DMOF-1-**CX** materials might show potential for separation or storage applications of these gases.[123] Therefore, the behaviour of the DMOF-1-**CX** materials towards the adsorption of the light hydrocarbons propane and propylene was assessed as well and will be discussed in the following.

3.6.2 Propane & Propylene

Propane and propylene isotherms of the *dry*-DMOF-1-**CX** materials were collected at 273 K to get an overview of the sorption process of the respective gas (Figure 3.25). However, at this temperature and with an accessible $p_{\max} = 100$ kPa still only 0.17 and 0.21 p/p_0 are achievable for propylene ($p_0 = 585$ kPa) and propane ($p_0 = 474$ kPa), respectively.[121]

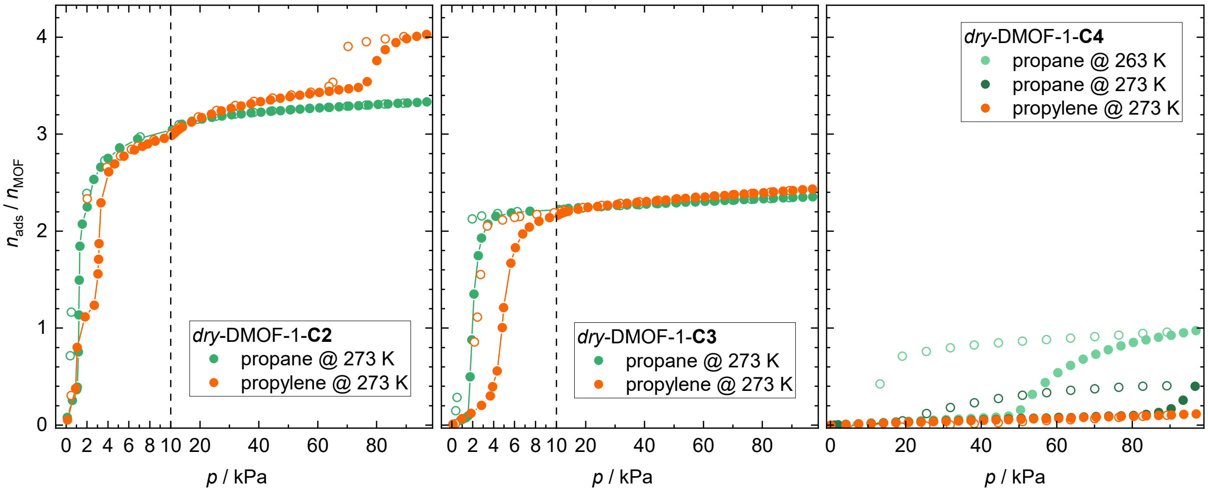

Figure 3.25: Propane (green circles) and propylene (orange circles) sorption isotherms of *dry*-DMOF-1-**C2** to -**C4** (left to right) recorded at 273 K or 263 K (propane and *dry*-DMOF-1-**C4** only). Filled circles correspond to the adsorption and empty circles to the desorption branch of the experiment. Lines were inserted only as a guide to the eye.

The propane isotherm of *dry*-DMOF-1-**C2** (Figure 3.25, left) features a one-stepped profile with only slight propane uptake (0.4 mol per mol MOF) at $p_{\text{trans}} = 1$ kPa ($p/p_0 = 2.1 \cdot 10^{-3}$) pressure, from where on up to 3.4 mol$_{\text{ads}}$ per mol$_{\text{MOF}}$ are adsorbed at 100 kPa propane pressure.

Remarkably, the corresponding propylene isotherm features a three-stepped profile with steps at $p_{\mathrm{trans}} = 1$ kPa ($p/p_0 = 0.17{\cdot}10^{-2}$), 3 kPa ($p/p_0 = 0.51{\cdot}10^{-2}$), and 79 kPa ($p/p_0 = 0.13$) and plateaus at uptakes of about 1.2, 3.4 and 4.0 mol per mol MOF. The occurrence of the further plateau at 3 kPa in the propylene sorption isotherm likely traces back to the weaker interactions of the propylene guests with the framework lined with saturated hydrocarbons, which do not yet overcome the intra-framework interactions stabilizing the contracted structure. The final step corresponds to an increase in the propylene uptake of about 18%, which equals the volume difference between the propane and the propylene molecule (Connolly solvent excluded volumes $V_{\mathrm{C3H8}} = 58.13$ Å^3 and $V_{\mathrm{C3H6}} = 49.25$ Å^3, respectively). Followingly, propylene saturation is achieved at a considerably higher pressure than for propane, indicating relatively weak interactions between the MOF and propylene compared to propane yet again.

Contrastingly, both the propane and propylene isotherms of *dry*-DMOF-1-**C3** at 273 K feature only a one-stepped isotherm profile with nearly no uptake previously to the step, indicating only one major phase transition during the adsorption of the gases (Figure 3.25, centre). Despite the overall uptake at $p \approx 100$ kPa is about 2.4 mol gas per mol MOF for propane and propylene, the values of p_{trans} are significantly different with 2 kPa ($p/p_0 = 0.42{\cdot}10^{-2}$) and 4 kPa ($p/p_0 = 0.84{\cdot}10^{-2}$), respectively. Furthermore, the gradient of the increase after p_{trans} is considerably steeper for propane indicating more favourable interactions also of the open framework with propane. Within the experimentally accessible pressure range of 100 kPa at 273 K *dry*-DMOF-1-**C4** exhibits no propane and propylene uptake except for a slight onset at about 90 kPa ($p/p_0 \approx 0.19$) of propane pressure, which might indicate the beginning of an opening of the MOF structure (Figure 3.25, right). This is proven by a propane sorption isotherm collected at 263 K, in which, even when already starting at 50 kPa, the phase transition is still not completed at 100 kPa and furthermore shows a strong hysteresis of about 30 kPa. This might be caused by the relatively long alkyl DEDs, which require ordering to facilitate the structural contraction into the ***np*** phase.

In order to follow the structural transformations of *dry*-DMOF-1-**C2** and *dry*-DMOF-1-**C3** in response to propane and propylene sorption, *in-situ* sorption PXRD experiments were carried out at BL9 of DELTA with propane and propylene at 298 K. Here, punctual snapshots at different propane or propylene pressures were recorded to catch characteristic structural changes indicated by steps in the sorption isotherms. The *in-situ* propane and propylene sorption PXRD data will be discussed compound-wise, starting with *dry*-DMOF-1-**C2**, and compared followingly. The full PXRD patterns, structureless profile fits (Pawley method), and fit data are given in the Appendix section 8.1.8.

Starting in its ***np*** form, *dry*-DMOF-1-**C2** readily begins transforming into a form with fully opened $\mathrm{Zn_2}$(**C2**-bdc)$_2$ layers, here named ***lp*₁**, upon dosing of small amounts (8 kPa) of propane in line with the corresponding propane isotherm at 298 K (Figure 3.26, green PXRD patterns). This phase is characterized by a $V/Z = 1150(3)$ Å^3 (+29% related to the ***np*** phase), crystallizes in the space group $C2/m$ ($Z = 2$), and relates to the weak plateau in the isotherm at about 10 kPa propane pressure. Ultimately, it was identified from a phase pure PXRD pattern recorded at 30 kPa immediately after dosing the gas (for unit cell parameters, see Table 3.11). Further equilibration for 5 min at this pressure point leads to the transition to the ***lp*₂** phase, which can be indexed in the space group $P2/c$ in a different unit cell setting and features about the same volume per MOF repeating unit $V/Z = 1151(4)$ Å^3. This lowering of the space group symmetry occurring with the ***lp*₁→*lp*₂** phase transition clearly points towards the ordering of flexible MOF building parts rendering additional pore space available for guest molecules. At 80 kPa the ***lp*₂** phase has further expanded to a $V/Z = 1155(5)$ Å^3 mainly by a straightening along the dabco axis of the framework as indicated by a change in the monoclinic angle β from 85.63(8)° to 86.98(6)°. Likely, this swelling-like expansion is taking place in a continuous fashion like the adsorption of propane guests in the corresponding pressure range of the isotherm. Upon reducing the pressure to vacuum (2 kPa) and desorbing propane guests, *dry*-DMOF-1-**C2** initially falls back into the ***lp*₁** phase before the ***np*** phase is partially restored after longer equilibration (25 min), which is in accordance with the isotherm, as there are still significant amounts of propane adsorbed at this pressure (Figure 3.26, red PXRD pattern).

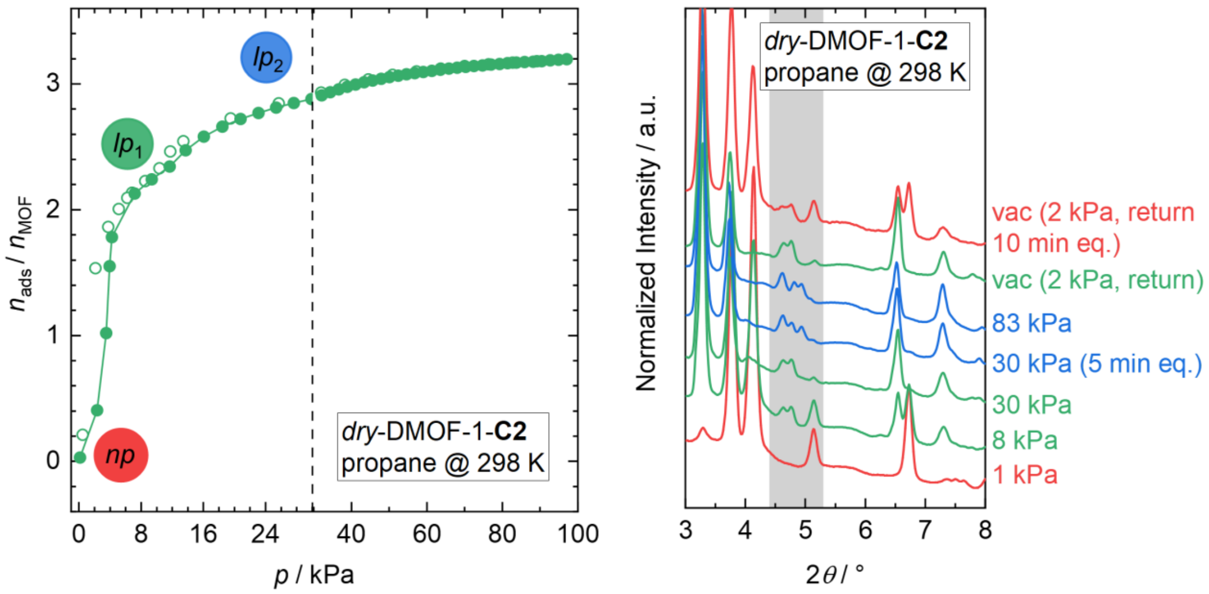

Figure 3.26: Propane sorption isotherm (298 K) of *dry*-DMOF-1-**C2** (left) and excerpt of the corresponding *in-situ* propane sorption PXRD data recorded at BL9 of DELTA ($\lambda = 0.6199$ Å, right). PXRD patterns assigned to the ***np***, ***lp*₁** and ***lp*₂** phases of *dry*-DMOF-1-**C2** during propane adsorption are marked with the same colours. The regions of the PXRD patterns between 4.4 and 5.3 2θ are highlighted in grey to elucidate the occurrence of the different phases.

Table 3.11: Unit cell parameters of *dry*-DMOF-1-**C2** extracted from the *in-situ* propane sorption data collected at 298 K at BL9 of DELTA ($\lambda = 0.6199$ Å) via structureless profile refinement. Fits and further fit data are given in the Appendix section 8.1.8.

$p(C_3H_8)$	**vac (1 kPa)**	**30 kPa**	**30 kPa (eq)**	**83 kPa**	**vac (2 kPa, return)**
phase	$\boldsymbol{np}$	$\boldsymbol{lp_1}$	$\boldsymbol{lp_2}$	$\boldsymbol{lp_2}$	$\boldsymbol{lp_1}$
crystal system	monoclinic	monoclinic	monoclinic	monoclinic	monoclinic
space group	$C2/m$	$C2/m$	$P2/c$	$P2/c$	$C2/m$
a / Å	9.880(5)	15.485(16)	10.955(14)	10.945(14)	15.497(11)
b / Å	19.050(4)	15.519(16)	10.942(12)	10.966(15)	15.490(12)
c / Å	9.626(5)	9.636(3)	19.253(10)	19.270(12)	9.6339(17)
α / °	90	90	90	90	90
β / °	100.15(3)	96.36(8)	85.63(8)	86.98(9)	96.44(4)
γ / °	90	90	90	90	90
V / Å^3	1783.4(13)	2301(3)	2301(4)	2310(5)	2298(2)
V/Z / Å^3	891.7(13)	1151(3)	1151(4)	1155(5)	1149(2)
R_{wp}	1.31	1.44	1.12	0.96	1.36
R_{exp}	3.07	6.52	2.32	2.45	4.14
χ^2	0.43	0.22	0.48	0.39	0.33

Contrasting its response to propane sorption, dosing of 20 kPa of propylene onto *dry*-DMOF-1-**C2** yields an opening of the structure into a phase, which can be indexed in a unit cell of $P2/c$ space group symmetry, hence largely corresponding to the $\boldsymbol{lp_2}$ phase known from propane sorption (see Figure 3.27 and Table 3.11). Furthermore, the V/Z is with 1149(6) Å^3 very similar. However, in contrast to propane sorption, upon increasing the propylene pressure to 83 kPa there is almost no change in the unit cell parameters except for a slight increase in the angle β (Table 3.12). As there is a further small step at 79 kPa in the propylene sorption isotherm profile at 273 K, which would be expected around 150 kPa at 298 K, pressures exceeding 100 kPa were also investigated in this *in-situ* PXRD experiment. Indeed, there is an increase in the unit cell volume of 17 Å^3 between 83 and 179 kPa propylene pressure, which is attributed to an increase in the monoclinic angle β from 85.50(4)° to 86.19(6)°, and therefore a straightening of the MOF structure along the dabco axis, but also an overall swelling of the framework since all unit cell parameters increase. Further increasing the pressure to 206 and 243 kPa does not result in a further expansion of the framework indicating the sorption plateau. Interestingly, also upon propylene pressure release and re-evacuation, *dry*-DMOF-1-**C2** initially traverses the $\boldsymbol{lp_1}$ phase (Figure 3.27, green PXRD pattern) before gradually returning to the $\boldsymbol{np}$ phase again.

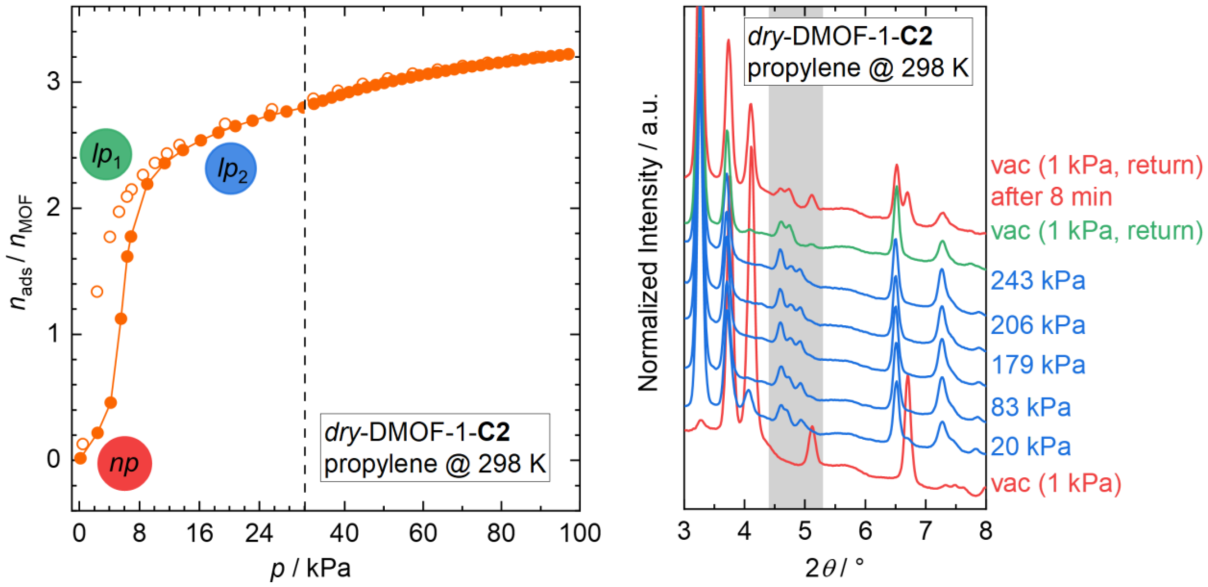

Figure 3.27: Propylene sorption isotherm (298 K) of *dry*-DMOF-1-**C2** (left) and excerpt of the corresponding *in-situ* propylene sorption PXRD data recorded at BL9 of DELTA ($\lambda = 0.6199$ Å, right). PXRD patterns assigned to the ***np***, ***lp*₁** and ***lp*₂** phases of *dry*-DMOF-1-**C2** during propylene adsorption are marked with the same colours. The regions of the PXRD patterns between 4.4 and 5.3 2θ are highlighted in grey to elucidate the occurrence of the different phases.

Table 3.12: Unit cell parameters of *dry*-DMOF-1-**C2** extracted from the *in-situ* propylene sorption PXRD data collected at 298 K at BL9 of DELTA ($\lambda = 0.6199$ Å) via structureless profile refinement. Fits and further fit data are given under Appendix section 8.1.8. * Corresponds to the adsorption branch, $^{\#}$ to the desorption branch.

$p(C_3H_6)$	vac*	20 kPa	83 kPa	179 kPa	206 kPa	243 kPa	vac#
phase	***np***	***lp*₂**	***lp*₂**	***lp*₂**	***lp*₂**	***lp*₂**	***lp*₁**
sg	$C2/m$	$P2/c$	$P2/c$	$P2/c$	$P2/c$	$P2/c$	$C2/m$
a / Å	9.885(4)	10.972(17)	10.974(10)	10.990(11)	11.00(2)	11.00(2)	15.459(4)
b / Å	19.016(4)	10.905(16)	10.918(10)	10.950(11)	10.94(2)	10.95(2)	15.503(4)
c / Å	9.604(6)	19.27(3)	19.275(18)	19.314(3)	19.34(4)	19.34(4)	9.6338(9)
a / °	90	90	90	90	90	90	90
β / °	100.16(3)	85.14(6)	85.50(4)	86.19(6)	86.32(8)	86.33(8)	96.24(3)
γ / °	90	90	90	90	90	90	90
V / Å^3	1771.0(14)	2298(6)	2302(4)	2319(3)	2323(8)	2324(8)	2295.1(9)
R_{wp}	1.07	0.65	0.47	0.60	0.82	0.82	0.56
R_{exp}	3.26	2.30	2.27	2.26	4.80	3.46	5.21
χ^2	0.33	0.28	0.21	0.27	0.17	0.24	0.11

Comparing the sorption of both gases in *dry*-DMOF-1-**C2**, the material is clearly more affine towards adsorbing propane, as indicated by the opening of the structure at lower pressures and the steeper slope of the step in the isotherm, which is a consequence of the more favourable interactions with the alkyl group lining of the pore space of the MOF. Interestingly, the opening of *dry*-DMOF-1-**C2** upon propane adsorption is characterized by traversing the high-symmetry, therefore likely disordered ***lp*₁** phase before achieving the maximum uptake in the ***lp*₂** phase. By contrast, the ***lp*₁** phase was not observed upon adsorbing propylene, hence, the occurrence of the ***lp*₁** phase during propane adsorption might relate to the faster adsorption of propane, facilitating the formation of the disordered phase. In the ***lp*$_2$** phase the material exhibits a slight swelling of the structure between 30 or 20 to 83 kPa for both gases in line with the weak slope of the isotherms in this range. On the desorption branch, the behaviour of *dry*-DMOF-1-**C2** is very similar for both gases as for each the material transforms into the ***lp*$_1$** phase and from there gradually into the ***np*** phase when evacuated at 1 kPa.

By contrast, the *in-situ* PXRD investigation of the propane and propylene sorption behaviour of *dry*-DMOF-1-**C3** reveals a distinct switching between the ***np*** phase and the ***lp*** phase, which is not followed by further swelling of the MOF structure as indicated by the identical PXRD patterns of *dry*-DMOF-1-**C3** recorded between 30 and 90 kPa propylene pressure (Figure 3.28, centre and right). This is in accordance with the profiles of the respective propane and propylene sorption isotherms, which show a sharp step with rapid uptake and a flat sorption plateau (Figure 3.28, left). The *in-situ* sorption PXRD patterns of the expanded ***lp*** phases of *dry*-DMOF-1-**C3** were both assigned to $P\bar{1}$ space group symmetry and indexed in very similar unit cells ($Z = 1$) with volumes of 1147 Å^3 and 1146 Å^3 for the propane and propylene filled phases, respectively. This corresponds to an increase of the unit cell volume by 27% in response to the adsorption of propane and propylene. Structureless profile fits of the PXRD patterns of the ***np*** phases of *dry*-DMOF-1-**C3** are given in the Appendix section 8.1.8.

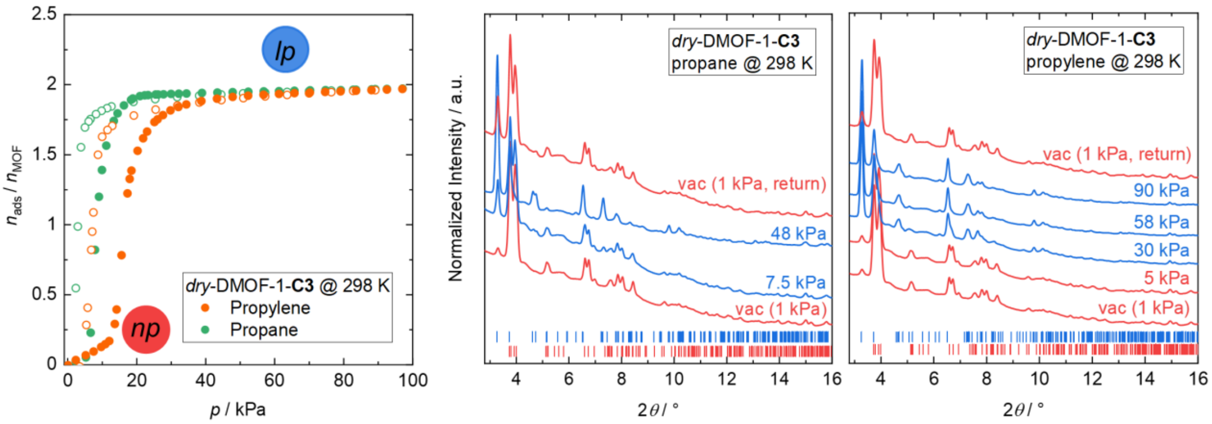

Figure 3.28: Propane and propylene sorption isotherm (298 K) of *dry*-DMOF-1-**C3** (left) and the corresponding *in-situ* propane and propylene sorption PXRD data recorded at BL9 of DELTA ($\lambda = 0.6199$ Å, centre and right). PXRD patterns assigned to the ***np*** and ***lp*** phases of *dry*-DMOF-1-**C3** during propane and propylene adsorption are marked with the same colours.

To gain more information on the chemical nature of the propane and propylene infiltrated ***lp*** phases of DMOF-1-**C3** attempts were made at a Rietveld refinement of the *in-situ* PXRD data. Due to the related unit cell and expected structural similarities, the SCXRD structure of DMOF-1-**C3**·*n*-octane (Figure 3.12), where the *n*-octane guests had been replaced by two propane or propylene molecules in accordance with the uptake in the sorption isotherms at the respective pressures, was chosen as a starting structural model for the refinement. This approach gave a good fit of the PXRD patterns recorded at 48 kPa for propane and 58 kPa for propylene. The resulting fits are given in Figure 3.29 and unit cell parameters are given in Table 3.13, for further details on the refinement procedures and refinement parameters, see Appendix section 8.1.8.

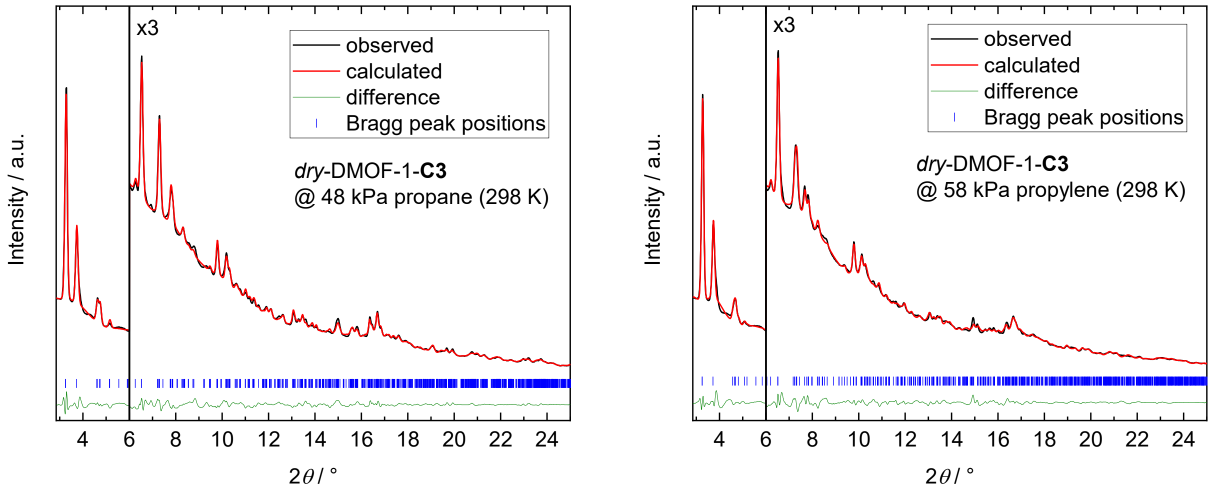

Figure 3.29: The final Rietveld plots of the refinement of *in-situ* sorption PXRD patterns (BL9 of DELTA, λ = 0.6199 Å) of the ***lp*** phases of *dry*-DMOF-1-**C3** at 48 (left) or 58 kPa (right) of propane and propylene, respectively.

Table 3.13: Unit cell parameters of the propane and propylene filled ***lp*** phases of DMOF-1-**C3** extracted from Rietveld refinement of *in-situ* sorption PXRD patterns (BL9 of DELTA, λ = 0.6199 Å). The corresponding fit and refinement parameters are given in Figure 3.29 and Appendix section 8.1.8.

pressure	**48 kPa (C_3H_8)**	**58 kPa (C_3H_6)**
crystal system	triclinic	triclinic
space group	$P\bar{1}$	$P\bar{1}$
a / Å	9.6252(12)	9.6108(15)
b / Å	10.956(4)	10.971(4)
c / Å	10.955(3)	10.940(3)
α / °	89.36(4)	88.85(3)
β / °	85.22(3)	86.94(4)
γ / °	84.86(3)	84.13(2)
V / Å^3	1146.6(5)	1145.7(5)

Inspection of the obtained Rietveld structures reveals that the conformations of phenyl rings and alkyl chains of DMOF-1-**C3** are nearly identical for the propane and propylene filled ***lp*** phases (Figure 3.30, top). Consequently, propane and propylene are each adsorbed at a very similar site, which is located mainly above a phenyl ring and in between the two dabco pillars. This site is in range of two phenyl rings, the methylene groups of two dabco units, a number of alkyl groups and therefore is highly optimized for interactions of the guests with the framework's backbone and alkyl lining. Ultimately, the propane and propylene adsorption sites add up to channels along the crystallographic [110] direction, where the channel's outer walls are formed by the alkyl DEDs (Figure 3.30, bottom). These structural information help understanding the differences in the propane and propylene sorption behaviour of *dry*-DMOF-1-**C3** as the former interacts much stronger with the narrow pore lining due to its higher number of hydrogen atoms. Additionally, electrostatic repulsion between the π-bond electrons and aromatic electrons of the phenyl rings might result in weaker interactions between propylene and the MOF. Hence, the adsorption of propane is enthalpically more favoured.

Consequently, the pressure required for the transition to the ***lp*** phase (p_{trans}) must also be lower for propane as the enthalpy of its interactions with the MOF can outbalance the intra-framework interaction enthalpy already at lower (relative) pressures compared to propylene due to its stronger interaction with the material.

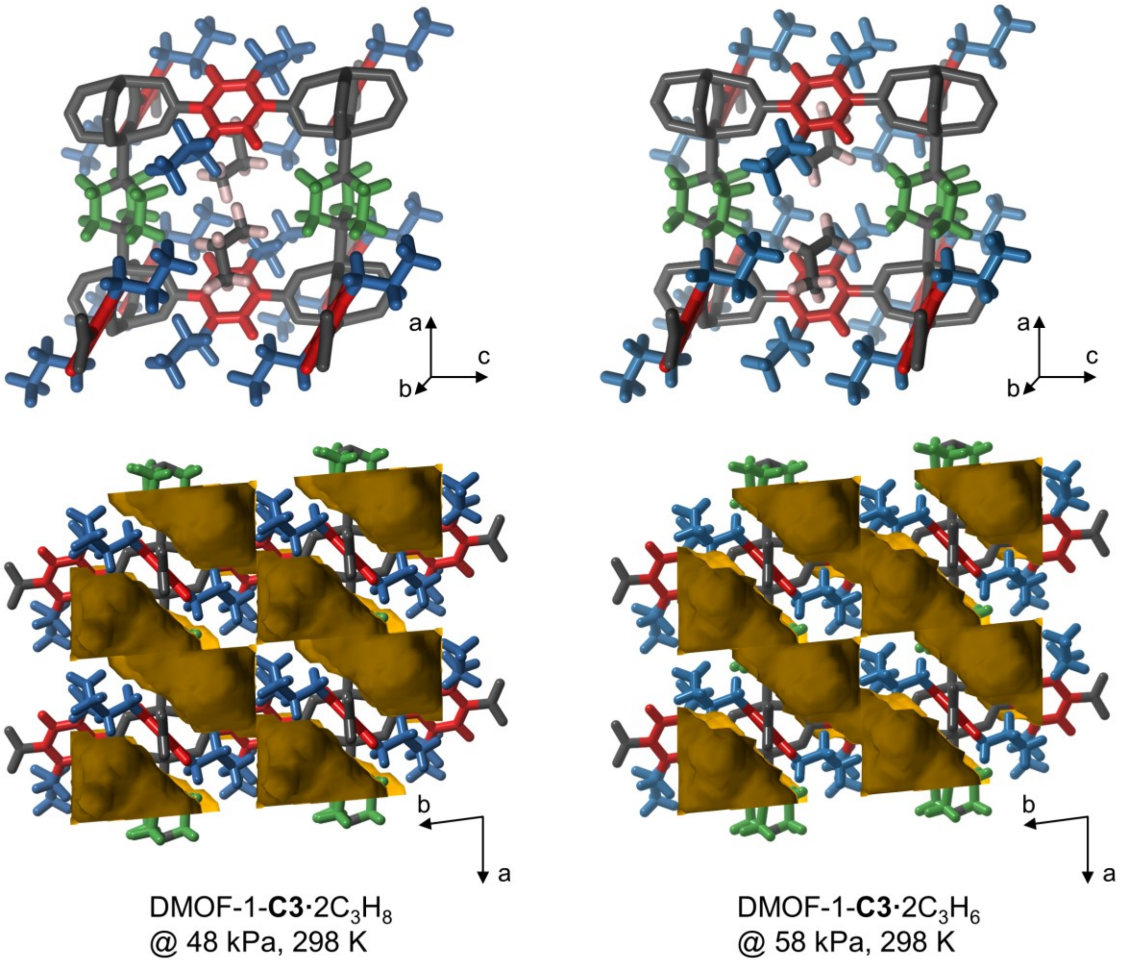

DMOF-1-**C3**·2C_3H_8
@ 48 kPa, 298 K

DMOF-1-**C3**·2C_3H_6
@ 58 kPa, 298 K

Figure 3.30: Excerpts of the structural models of propane and propylene filled DMOF-1-**C3** obtained from Rietveld refinement of *in-situ* sorption PXRD patterns (BL9 of DELTA, $\lambda = 0.6199$ Å). Structures are coloured using the established colour code with propane and propylene guests being contrasted in standard colours (C: dark grey, H: white). In the bottom, omitting the guest molecules, void maps are included, which were created from the contact surface of a probe of a radius of 1.2 Å, to highlight the channel-like shape, in which the guests are adsorbed.

A comparison of the structural model of the propane filled ***lp*** phase extracted via Rietveld refinement with the SCXRD structure of the *np* phase provides mechanistic insights into the ***np→lp*** phase transition (Figure 3.31). Besides the typical changes of the carboxylate-to-zinc coordination angle, the formation of the C_3H_8, and similarly the C_3H_6, filled ***lp*** phase occurs upon rotation of the phenyl ring about the $C_{\mathrm{carboxylate}}$-C_{phenyl} bonds of only one of the two crystallographic independent **C3**-bdc^{2-} linkers (yellow linker in Figure 3.31). By combination of the framework expansion with this rotation of about 60° across the plane of both carboxylate groups the channels running through the material incorporating the propane or propylene guests are formed.

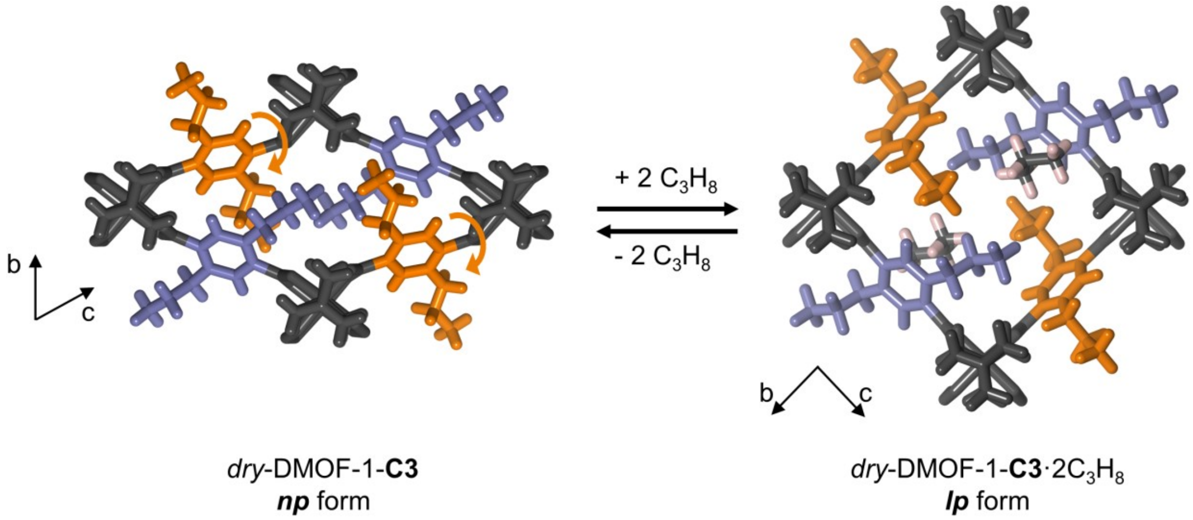

Figure 3.31: Comparison of the SCXRD structure of the ***np*** phase and the C_3H_8 filled ***lp*** phases of DMOF-1-**C3** in view along the dabco axis. The two independent **C3**-bdc^{2-} linkers are coloured in blue or orange. The orange-coloured linker undergoes a rotation upon opening to the ***lp*** phase, which is marked by orange arrows. H atoms in the structure of the propane containing ***lp*** phase have been calculated at geometrical positions as they have not been included in the structural refinement via the Rietveld method.

Based on its propane and propylene sorption behaviour, *dry*-DMOF-1-**C3** might constitute an interesting candidate for applications in the fields of gas separation or storage. These properties are, firstly, its gating effect, i.e., the absence of any significant uptake of propane or propylene until the threshold pressures of phase transition, which moreover vary by about 10 kPa (298 K) between the two gases. Secondly, in the ***lp*** phase the adsorption of propane is apparently enthalpically favoured and, hence, indicates potential for adsorptive separation of the less valuable propane from the more valuable propylene. To evaluate the suitability of *dry*-DMOF-1-**C3** for such applications, the propane and propylene sorption was investigated at higher temperatures to increase the difference in absolute pressure between the transition pressures for both gases and furthermore the tolerance towards repetitive adsorption/desorption cycles and relative humidity was studied.

Additional single component propane and propylene sorption isotherms were collected at 313 K and 323 K (Figure 3.32). By that the phase transition or gate-opening pressures are naturally shifted to higher pressures. At the same time, the window between the gate-opening pressures of propane and propylene expands from about 8 kPa at 298 K to 20 kPa at 323 K, which should be more advantageous for the discrimination between both gases.

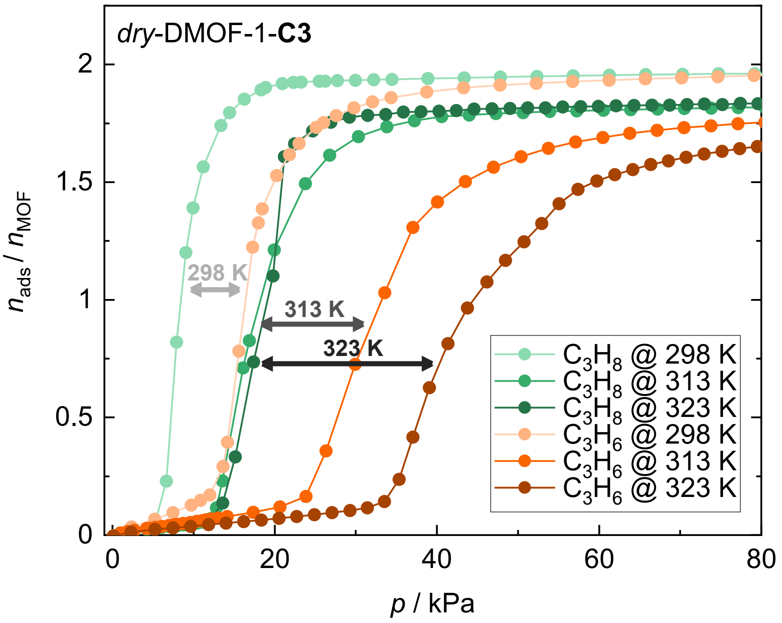

Figure 3.32: Propane (green colours) and propylene (orange colours) sorption isotherms of *dry*-DMOF-1-**C3** recorded at 298 K, 313 K, and 323 K. The pressure window between the gate-opening of *dry*-DMOF-1-**C3** is indicated by the greyscale-coloured arrows. The desorption branches of the experiments are omitted for clarity.

Nevertheless, how exactly the findings from the single-component sorption isotherms translate into real separation processes is debatable. Here, other exemplary works have both shown successful separations run by materials exhibiting gating-effects[53,124,125] and less successful attempts, where the induced gate-opening led to adsorption of both components to be separated.[126] Therefore, the C_3H_8/C_3H_6 separation ability of *dry*-DMOF-1-**C3** needs to be evaluated in practice by co-adsorption or breakthrough column experiments in the future.
If large magnitude volume changes ($> 5\%$) are involved, the textural properties of a flexible MOF might be significantly altered after no more than 10 cycles of repeated adsorption and desorption.[127] This phenomenon could be ascribed to mechanical stress-induced reduction of crystallite sizes for certain examples.[127] Due to its significance for any future application, the tolerance towards repeated adsorption and desorption cycles was investigated for *dry*-DMOF-1-**C3** as well. This was done by running 11 consecutive cycles of isothermal propane ad- and desorption at 313 K, collecting 11 points on each adsorption branch and 5 points on each desorption branch. A comparison of the first and the lastly collected sorption isotherms reveals two nearly identical isotherms, indicating high reproducibility within the 11 cycles performed (see Figure 3.33, left and centre). Besides, a PXRD pattern recorded after the sorption cycling experiment proves the structural integrity of the material (Figure 3.33, right).

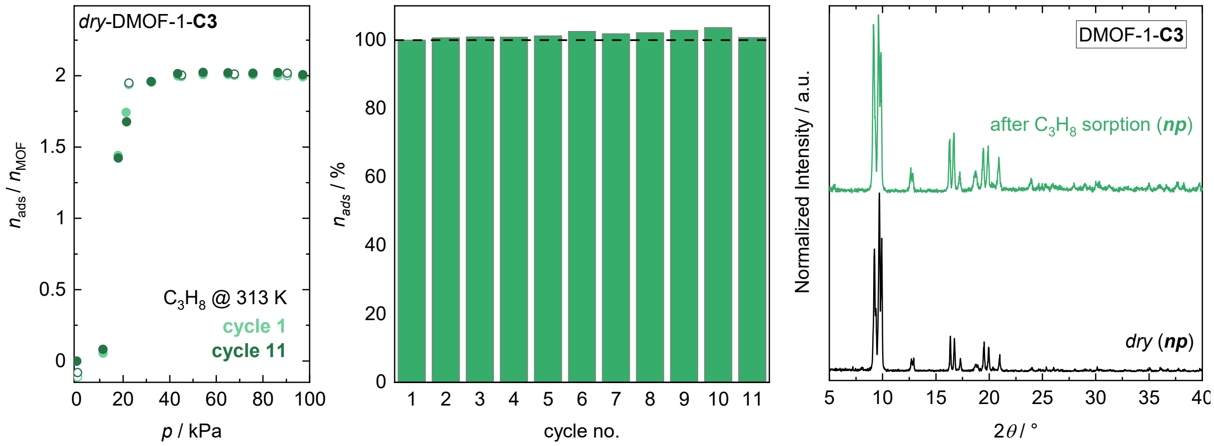

Figure 3.33: Repeated propane sorption cycling of *dry*-DMOF-1-**C3** at 313 K. Propane sorption isotherms of the first and the final (no. 11) cycle are given on the left, while the maximum uptakes (at 97 kPa) of each cycle are plotted in the centre. A PXRD pattern recorded after the cycling experiment in comparison to a PXRD of freshly prepared *dry*-DMOF-1-**C3** is given on the right.

The stability of *dry*-DMOF-1-**C3** against hydrolysis under humid atmospheres was assessed by exposing the material to an atmosphere of defined relative humidity (RH) followed by structural evaluation via PXRD. The compound was subjected to atmospheres of 100% and 52% RH, which were realized according to literature reports in a small closed space containing a vessel loaded with the sample and either pure distilled water or a saturated aqueous $Mg(NO_3)_2$ solution at 28 °C.[128,129]

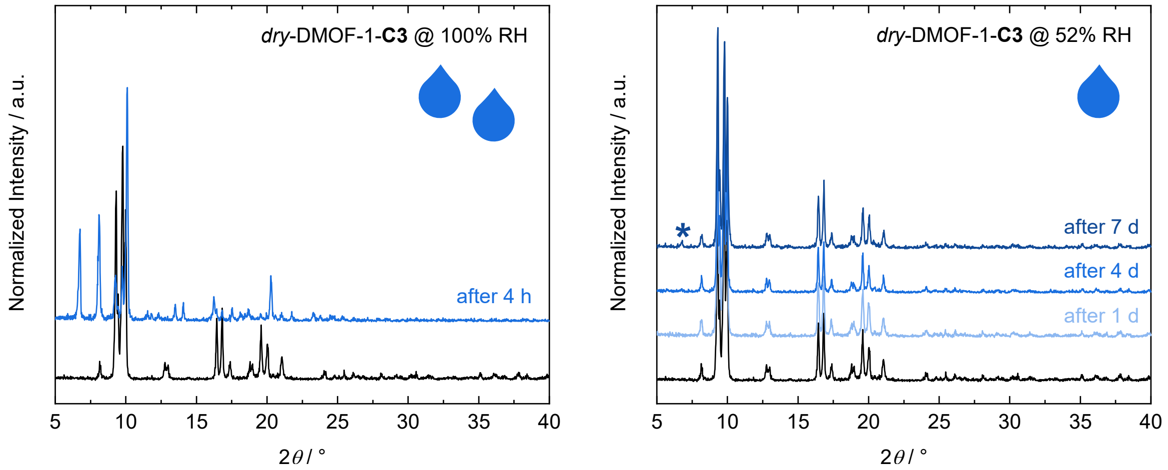

Figure 3.34: PXRD patterns ($\lambda = 1.54178$ Å) of *dry*-DMOF-1-**C3** recorded before and after subjecting the samples to 100% RH (left) and 52% RH (right) for different time intervals. A weak reflection indicating slight amounts of decomposed material is marked with an asterisk (*, right pattern).

Only after a few hours at 100% RH reflections emerge, which neither belong to the ***np*** nor the ***lp*** phase of the material, most prominently the one at $2\theta \approx 6.8°$ indicating hydrolysis and a breakdown of the MOF structure (Figure 3.34, left), hence, the material must be considered not stable at 100% RH. Interestingly, the PXRD patterns exhibit reflections, for example at $2\theta \approx 8.2°$, which are characteristic for the ***lp*** phase of DMOF-1-**C3**. By contrast, at 52% RH *dry*-DMOF-1-**C3** is significantly more resistant to hydrolysis, showing only traces of decomposed material after 7 d subjection (Figure 3.34, left, asterisk). This indicates that the

np phase of *dry*-DMOF-1-**C3** is comparably stable due to the dense packing and hydrophobicity of the structure, but, however, at high partial pressures of water it may open into the ***lp*** phase, which is then prone to hydrolysis.

3.6.3 Comparison with *dry*-DMOF-1-**OCY**

In the final paragraphs dealing with the hydrocarbon sorption, the behaviour of the *dry*-DMOF-1-**CX** materials will be compared with the corresponding alkoxy-relatives, *dry*-DMOF-1-**OC2** and *dry*-DMOF-1-**OC3**, to pinpoint the effects of the side-chain polarity. Since no experimental data is available on the sorption of C_3 and C_4 hydrocarbons on *dry*-DMOF-1-**OC2** and *dry*-DMOF-1-**OC3** both materials were synthesized and activated according to published procedures, which are very similar to the synthesis of the DMOF-1-**CX** materials described above and are given in more detail in the Materials & Methods section 6.1.2. Note, that the PXRD pattern of *dry*-DMOF-1-**OC2** could not be fully indexed in the monoclinic $C2/m$ unit cell reported in the literature[104] and also not fully applying the lower $P2_1/m$ symmetry (see Appendix Figure 8.3 and Table 8.2) with few reflections remaining not fitted. Attempts using a $P\bar{1}$ unit cell similar to the one of *dry*-DMOF-1-**C3** were not successful in improving the fit. Likely, *dry*-DMOF-1-**OC2** got partially hydrolysed during the PXRD data collection under ambient conditions due to its hydrophilic ethoxy-sidechains.[100] For DMOF-1-**OC2** and -**OC3** the full PXRD, ^{1}H NMR and IR data of digested samples are given in the Appendix sections 8.1.1, 8.1.3 and 8.1.4, respectively.

For the *dry*-DMOF-1-**OC2** and *dry*-DMOF-1-**OC3** materials *n*-butane, propane and propylene isotherms were collected at 273 K, which are again directly compared to the *dry*-DMOF-1-**C3** and *dry*-DMOF-1-**C4** materials bearing sidechains of the same length (Figure 3.35). For *n*-butane, *dry*-DMOF-1-**OC2** exhibits a slight uptake ($\approx$ 15 cm^3g^{-1}) prior to the breathing transition, which is in accordance with the published CO_2 sorption data discussed in section 3.5, similarly indicating significant porosity of its ***np*** phase. Once a pressure of 4 kPa is reached, the phase transition to a more open phase is induced. For comparison, the transformation of *dry*-DMOF-1-**C3** is taking place at the lower pressure of 0.3 kPa. Furthermore, there is another small step at about 27 kPa *n*-butane pressure after which the maximum uptake of about 81 cm^3g^{-1} is achieved being again higher than for *dry*-DMOF-1-**C3** (65 cm^3g^{-1}). For a discussion of potential causes of the higher gas uptake of *dry*-DMOF-1-**OC2** see section 3.5. Remarkably, on the desorption branch, *dry*-DMOF-1-**OC2** features another plateau at a pressure of 4 kPa with a different uptake of roughly 55 cm^3g^{-1}. In this regard, the isotherms of *dry*-DMOF-1-**C3** and *dry*-DMOF-1-**OC2** strongly differ as the latter features a multi-stepped shape, whereas the former features only one step.

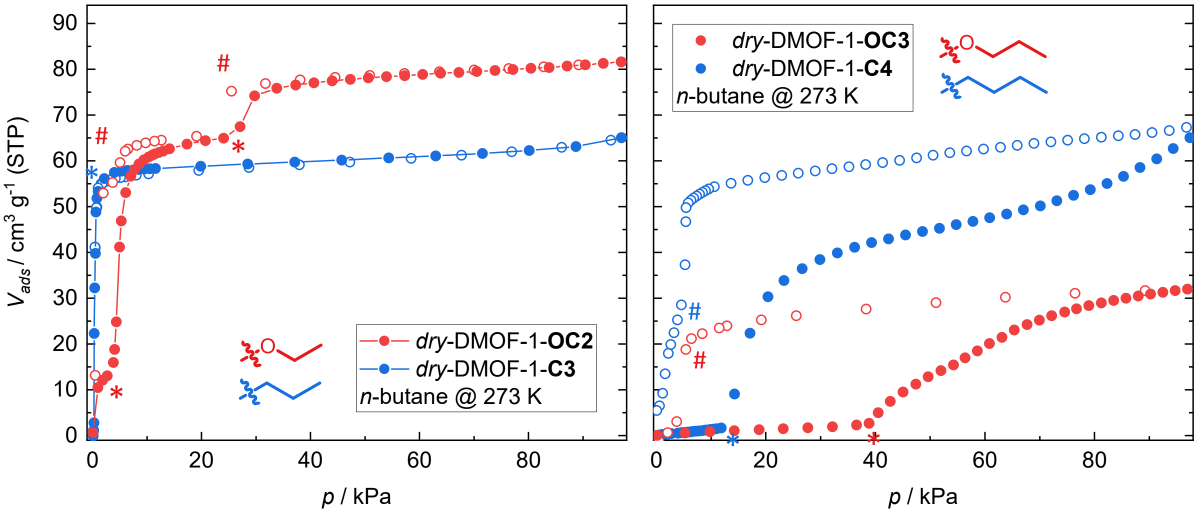

Figure 3.35: *n*-Butane sorption isotherms at 273 K of *dry*-DMOF-1-**OC2** and *dry*-DMOF-1-**C3** (left), and *dry*-DMOF-1-**OC3** and *dry*-DMOF-1-**C4** (right). Solid symbols correspond to the adsorption and empty symbols to the desorption branches of the isotherms, points of (proposed) phase transitions are marked with an asterisk (adsorption) or a hash (desorption), respectively. Lines are just a guide to the eye.

On the contrary, *dry*-DMOF-1-**C4** and *dry*-DMOF-1-**OC3** exhibit similar overall isotherm shapes with no uptake before the phase transition. However, for *dry*-DMOF-1-**OC3** the phase transition pressure is again shifted to significantly higher *n*-butane pressures (40 kPa) compared to *dry*-DMOF-1-**C4** (14 kPa). Maximum uptakes are not discussed here due to the data quality of *dry*-DMOF-1-**C4**. In addition to that, the slope of the adsorption branch after the gate-opening pressure is comparably weak. Combined with the wide hysteresis, these findings indicate a weaker affinity to adsorb *n*-butane, but also a kinetic inhibition of the sorption process, likely arising from the disordered nature of the flexible substituents of the *dry*-DMOF-1-**OC3** material.[98] Additionally, the crystallite sizes might also play a role.[130]

A more generalizing inspection of the *n*-butane sorption data reveals the trend that the breathing or gate-opening transitions of *dry*-DMOF-1-**OC2** and -**OC3**, respectively, are shifted to higher *n*-butane pressures compared to their alkyl relatives, which appears reasonable in view of the more polar sidechains. These undergo both stronger intra-framework interactions and weaker interactions with the non-polar *n*-butane guest molecules effectively resulting in a higher activation barrier for the phase transition.

This trend is similarly evident, when comparing the propane and propylene sorption behaviour of the *dry*-DMOF-1-**OCY** and *dry*-DMOF-1-**CX** at 273 K (Figure 3.36). Here, the phase transition pressures of *dry*-DMOF-1-**OC2** are found at 32 kPa propane and 66 kPa propylene, hence, also at considerably higher pressures than for *dry*-DMOF-1-**C3**. Within the accessible range of relative pressures of propane and propylene *dry*-DMOF-1-**OC3** does not take up any amounts of both gases. Apparently, the second small step observed during *n*-butane sorption in *dry*-DMOF-1-**OC2** is also not covered by the relative pressure range accessible for both gases at 273 K. Interestingly, contrasting the *n*-butane sorption behaviour, there is no additional step on the desorption branch of the propane and propylene sorption experiments.

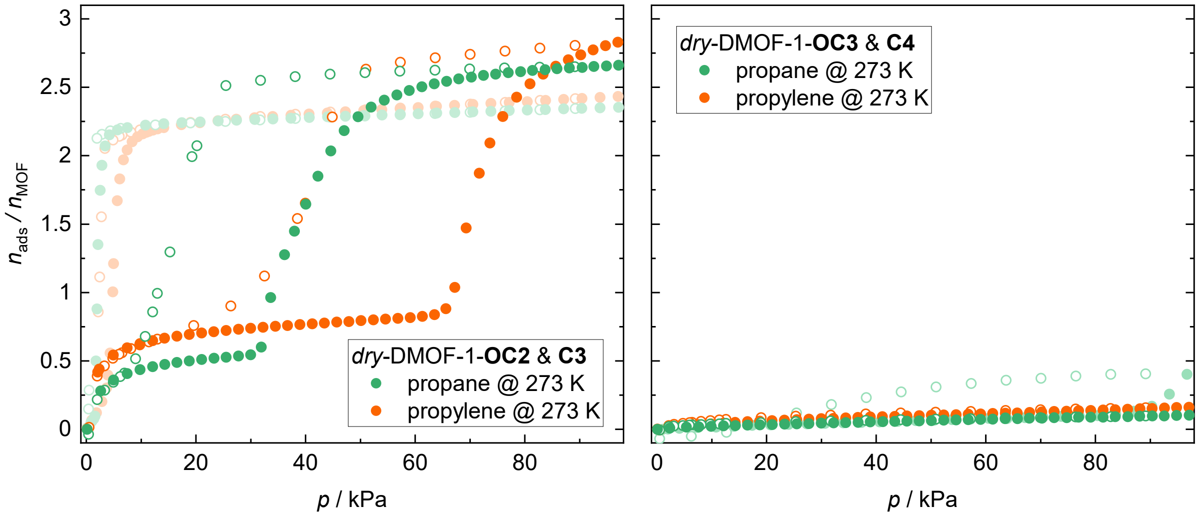

Figure 3.36: Propane (green) and propylene (orange) sorption isotherms at 273 K of *dry*-DMOF-1-**OC2** and *dry*-DMOF-1-**C3** (left), and *dry*-DMOF-1-**OC3** and *dry*-DMOF-1-**C4** (right). The dull-coloured symbols correspond to the *dry*-DMOF-1-**CX** materials. Filled symbols correspond to the adsorption and empty symbols to the desorption branches of the isotherms. Lines are just a guide to the eye.

Concluding, the *dry*-DMOF-1-**OCY** show a comparable propane and propylene sorption behaviour, also exhibiting the desired preference of adsorbing propane over propylene. Due to the less favourable interactions with hydrocarbons caused by the increased sidechain polarity, the breathing transitions are shifted to much higher pressures compared to the *dry*-DMOF-1-**CX**. These results prove the huge impact of adjusting not only the length and branching of the sidechains but also their mere polarity on the sorption of industrially relevant $\mathbf{C_3}$ and $\mathbf{C_4}$ hydrocarbons.

3.7 Thermal Behaviour

Some of the alkoxy-functionalized DMOF-1 derivatives bearing longer side chains have previously been reported to show breathing phase transitions from the ***np*** to the ***lp*** phase triggered only by temperature (i.e. driven by entropic contributions) rather than the adsorption of guest molecules.[58,101] So far, these transitions required a substituent chain length of five non-hydrogen atoms (i.e. butoxy or 2-methoxy-ethoxy chains). Shorter chain lengths, such as propoxy (four non-hydrogen atoms per chain) or ethoxy (three non-hydrogen atoms per chain) only demonstrated anisotropic thermal expansion of the rhombic motif of the ***np*** phase, but no transition to the ***lp*** phase before thermal decomposition.[58] Since the previously demonstrated diffraction and gas sorption data of the alkyl-functionalized DMOFs propose that these materials, owing to the absence of stronger dipolar interactions, have a much shallower potential energy landscape than the alkoxy-derivatives, the thermal responsiveness of these new DMOF-1-**CX** derivatives was investigated using variable temperature (VT-) powder and single crystal XRD as well as differential scanning calorimetry (DSC). Since the magnitude of the thermal response strongly correlates with the length of the flexible substituent chain, the *dry*-DMOF-1-**C3** and *dry*-DMOF-1-**C4** materials are focused on in this study.

Dry-DMOF-1-**C3** is showing strong thermal expansion by undergoing a continuous anisotropic expansion as evidenced by variable temperature (VT-)PXRD experiments (P02.1 of DESY) conducted from 300 K to 650 K. Only the PXRD data recorded in the range from 300 to 560 K are discussed here (see Figure 3.37) since the material decomposed from 560 K upwards. The full PXRD data are given in the Appendix Section 8.1.9, Figure 8.21.

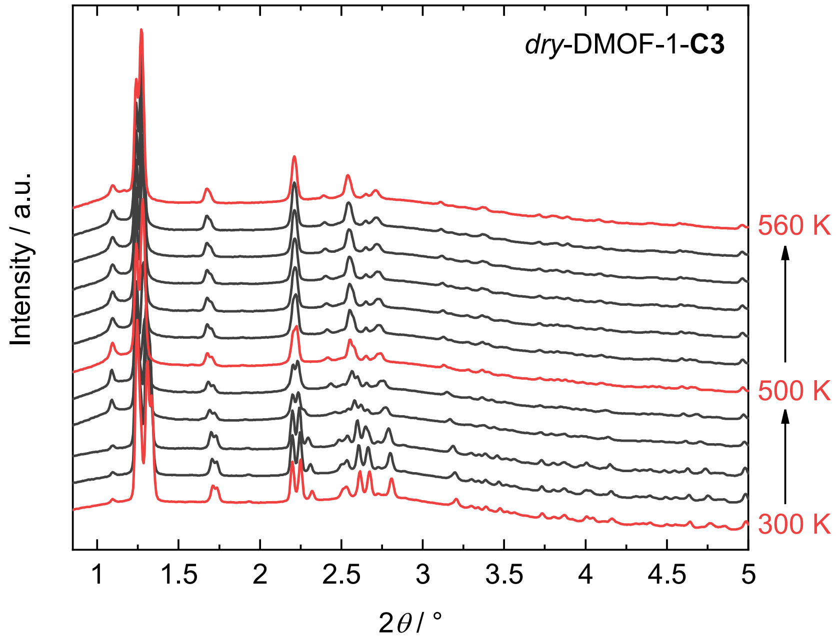

Figure 3.37: Variable temperature PXRD data of compound *dry*-DMOF-1-**C3** recorded from 300 to 560 K (P02.1 of DESY, $\lambda = 0.2073$ Å). Data in the temperature interval from 300 to 500 K were recorded in 50 K steps and from 500 K upwards with a step size of 10 K.

The collected VT-PXRD were analysed by means of structureless profile fitting (Pawley method) to extract the evolution of the unit cell parameters of *dry*-DMOF-1-**C3** as a function of temperature. The unit cell parameters and exemplary fits are given in the Appendix section 8.1.9. Here, due to the triclinic crystal symmetry, the unit cell parameters *a*, *b*, *c* do not correspond to the main directions along which the thermal expansion occurs. Hence, the direction of the principal axes of thermal expansion (X_1, X_2 and X_3) in relation to the respective unit cell parameters *a*, *b*, *c* and followingly the linear coefficients of thermal expansion (along the principal axes) α_{X1}, α_{X2} and α_{X3} and the linear volumetric coefficients of thermal expansion α_{V} were calculated using the routines of the web-based tool† PASCal.[131] The results of these calculations are given in Table 3.14 and Figure 3.38.

Table 3.14: Direction of the principal axes of thermal expansion X_1, X_2, X_3 relative to the unit cell parameters *a*, *b*, *c* of *dry*-DMOF-1-**C3**, the extracted linear thermal expansion coefficients α_{X1}, α_{X2} and α_{X3}, and the linear volumetric thermal expansion coefficient α_{V} in the range from 300 to 550 K.

	a	*b*	*c*	α / MK^{-1}
$\mathbf{X_1}$	-0.3425	0.5242	-0.7797	-51(1)
$\mathbf{X_2}$	0.8879	0.1421	-0.4375	47(4)
$\mathbf{X_3}$	0.0381	0.9862	0.1612	189(4)
V	-	-	-	188(1)

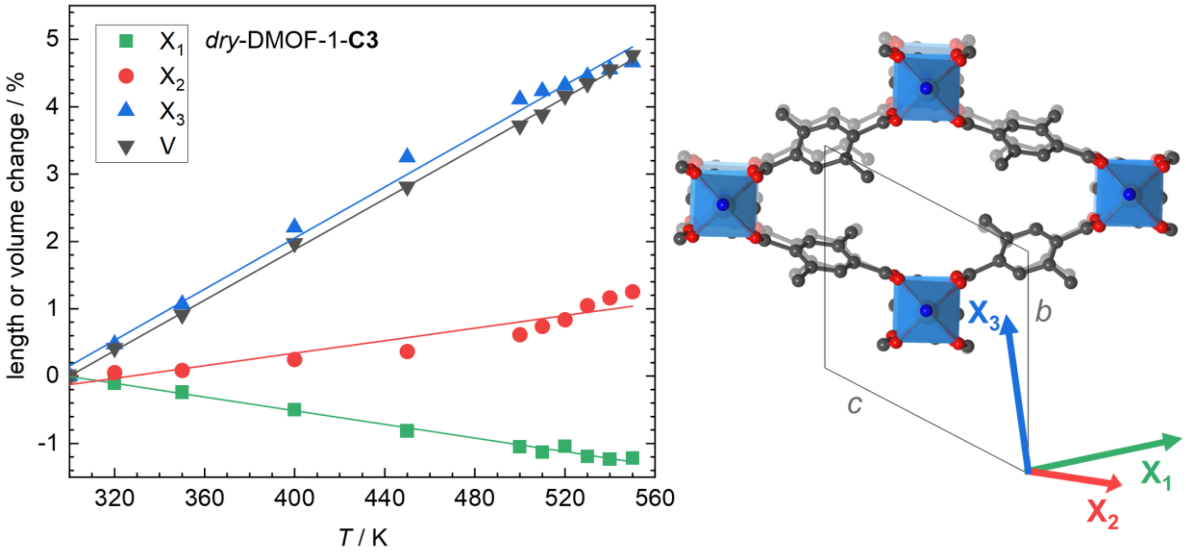

Figure 3.38: Relative changes in length of the principal axes of thermal expansion X_1, X_2 and X_3 or the unit cell volume *V* of *dry*-DMOF-1-**C3** determined from the VT-PXRD patterns recorded in the temperature range from 300 to 550 K (left). The linear fits of the data used to calculate the thermal expansion coefficients are given as well. Unit cell and simplified (H atoms and C2 and C3 of the propyl groups removed) structure of the ***np*** phase of *dry*-DMOF-1-**C3** based on the unit cell parameters extracted at 300 K and 550 K (transparent model) together with the thermal expansion vectors X_1, X_2 and X_3.

From 300 to 550 K the long diagonal of the rhombic channel contracts by approx. 1% and the short diagonal expands by approx. 4.5%. The corresponding coefficients of thermal expansion (CTEs) are –51 MK^{-1} for the direction along the long diagonal (principal axis X_1) and 189 MK^{-1} for the direction along the short diagonal (principal axis X_3, Table 3.14). These CTEs are

---

† http://pascal.chem.ox.ac.uk/

similar to the ones observed for the strongly expanding alkoxy-functionalized derivatives of DMOF, however, possess a significantly lower magnitude.[58]

At 560 K *dry*-DMOF-1-**C3** has expanded into a slightly more opened phase ($V/Z = 973$ Å^3, 5% larger volume than the ***np*** phase at 300 K), which can adequately be indexed in the monoclinic space group $C2/m$ at this point (see Appendix section 8.1.9, Table 8.23 and Figure 8.20). The transition from the triclinic ***np*** phase of *dry*-DMOF-1-**C3** to the monoclinic expanded phase appears to be continuous according to the VT-PXRD data. The 2nd order nature of the transition is also consistent with DSC data, which are featureless in that temperature range (see Appendix section 8.1.9, Figure 8.25). Heating the material further above 560 K leads to thermal decomposition starting with the loss of dabco as is evident from VT-PXRD and furthermore TG-DSC data by a mass loss of 15-20% (for details, see Appendix section 8.1.9, Figure 8.21 and Figure 8.26).

By contrast, the DSC data of *dry*-DMOF-1-**C4** clearly point towards two thermally induced first-order phase transitions occurring at 445 and 552 K, respectively, prior to the decomposition of the material at 608 K as determined from TG-DSC (for the full DSC and TG-DSC data, see Appendix section 8.1.10).

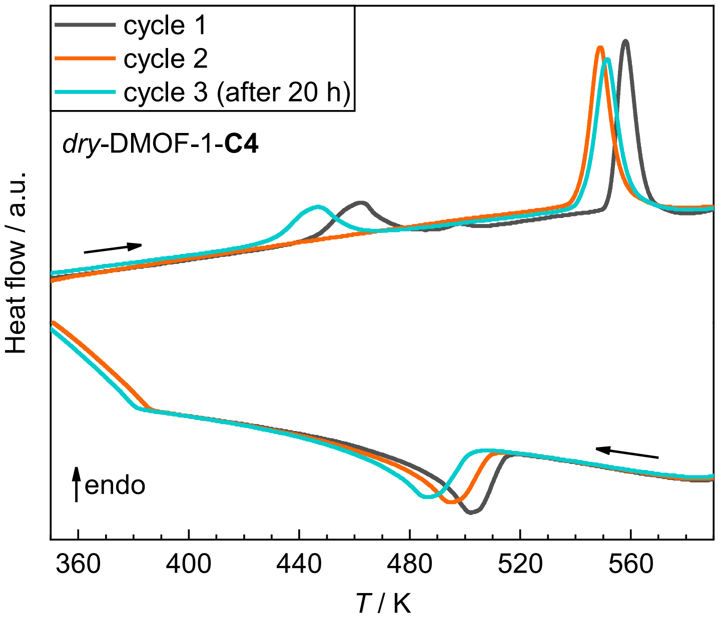

Figure 3.39: Excerpt of the DSC curves of *dry*-DMOF-1-**C4**. Cycle 1 and 2 were recorded in immediate succession, while cycle 3 was recorded 20 h after cycle 2. Note, that the ***np*→*ip*ht** transition is not present on cycle 2. The full data of the DSC experiments are given in the Appendix section 8.1.10.

With the aim to shed light on the apparently multi-step phase behaviour of *dry*-DMOF-1-**C4** VT-PXRD data in the range from 297 to 539 K were collected at BL9 of DELTA ($\lambda = 0.4592$ Å), from which unit cell parameters were extracted by means of structureless profile refinement (Pawley method). This data revealed three different phases of *dry*-DMOF-1-**C4** to occur during the heating process, of which the corresponding unit cell parameters are summarized in Table 3.15. The full fits and data are given in the Appendix section 8.1.9.

Table 3.15: Unit cell parameters of the three temperature-depending phases of *dry*-DMOF-1-**C4** extracted from structureless profile fits (Pawley method) of selected VT-PXRD patterns of (λ = 0.4592 Å, BL9 of DELTA).

$\boldsymbol{T}$	**297 K**	**492 K**	**539 K**
phase	$\boldsymbol{np}$	$\boldsymbol{ip_{ht}}$	$\boldsymbol{lp}$
crystal system	monoclinic	monoclinic	monoclinic
space group	$C2/c$	$C2/m$	$C2/m$
a / Å	18.74(3)	12.608(2)	15.295(6)
b / Å	10.764(9)	17.592(2)	15.495(6)
c / Å	19.209(19)	9.5848(13)	9.618(3)
α / °	90	90	90
β / °	93.48(8)	97.96(2)	95.88(5)
γ / °	90	90	90
V / Å^3	3867(8)	2105.4(5)	2267.3(14)
Z	4	2	2
V/Z / Å^3	967 (100%)	1053 (109%)	1134 (117%)

Followingly, the signals of the DSC curves are clearly related to transitions from the $\boldsymbol{np}$ to the $\boldsymbol{ip_{ht}}$ phase (space group $C2/m$, V/Z = 1053 Å^3 at 446 K ($\Delta H(\boldsymbol{np}\rightarrow\boldsymbol{ip}_{\mathrm{ht}})$ = 3.6 kJ mol^{-1}, $\Delta S(\boldsymbol{np}\rightarrow\boldsymbol{ip}_{\mathrm{ht}})$ = 8.1 J K^{-1} mol^{-1}) and finally from the $\boldsymbol{ip_{ht}}$ to the $\boldsymbol{lp_{ht}}$ phase (space group $C2/m$, V/Z = 1134 Å^3) at 543 K ($\Delta H(\boldsymbol{ip}_{\mathrm{ht}}\rightarrow\boldsymbol{lp_{ht}})$ = 7.7 kJ mol^{-1}, $\Delta S(\boldsymbol{ip}_{\mathrm{ht}}\rightarrow\boldsymbol{lp_{ht}})$ = 14.0 J K^{-1} mol^{-1}). The enthalpic footprints of the phase transitions during the performed two runs of DSC experiments are summarized below (Table 3.16).

Table 3.16: Thermodynamic data for the $\boldsymbol{np}\rightarrow\boldsymbol{ip}_{\mathrm{ht}}$ and $\boldsymbol{ip}_{\mathrm{ht}}\rightarrow\boldsymbol{lp}_{\mathrm{ht}}$ phase transitions of *dry*-DMOF-1-**C4** extracted from the DSC data shown above and given in the Appendix Section 8.1.10, Figure 8.27 (run 2, cycle 4). Values for ΔH were obtained by integration of the corresponding DSC peaks (up- and down scans (↑ and ↓)) after baseline subtraction. Transition temperatures were determined as the onset of the respective DSC peak.

run	*cycle*		$\Delta H_{np\rightarrow ip}$ / kJ mol^{-1}	$T_{np\rightarrow ip}$ / °C	$\Delta S_{np\rightarrow ip}$ / J K^{-1}mol^{-1}	$\Delta H_{ip\rightarrow lp}$ / kJ mol^{-1}	$T_{ip\rightarrow lp}$ / °C	$\Delta S_{ip\rightarrow lp}$ / J K^{-1}mol^{-1}
1	1	↑	3.6	445	8.1	7.7	552	14.0
		↓	-	-	-	7.7	514	15.0
	2	↑	-	-	-	8.5	542	15.7
		↓	-	-	-	7.2	509	14.1
2	3	↑	3.8	446	8.5	10.0	543	18.4
		↓	-	-	-	9.9	502	19.8
	4	↑	-	-	-	9.4	533	17.6
		↓	-	-	-	8.5	496	17.1

Interestingly, on the cooling branch of the DSC only one thermal event is present, which is clearly identified as the return transition from $\boldsymbol{lp_{ht}}$ to $\boldsymbol{ip}_{\mathrm{ht}}$ by its corresponding ΔH (see Table 3.16, cycle 2 and 4, down scans), indicating that the absent $\boldsymbol{ip_{ht}}\rightarrow\boldsymbol{np}$ back transition is kinetically hindered. This is supported by the observation that the $\boldsymbol{np}\rightarrow\boldsymbol{ip_{ht}}$ transition is still absent on a subsequent second heating-cooling cycle of the DSC experiment. Furthermore, analysis of a PXRD pattern recorded immediately after the DSC run proves that *dry*-DMOF-1-**C4** indeed remains in the $\boldsymbol{ip}_{\mathrm{ht}}$ phase (see Appendix section 8.1.1, Figure 8.4). However, if the sample is allowed to rest at room temperature for 20 h, the $\boldsymbol{np}\rightarrow\boldsymbol{ip}_{ht}$ transition again re-appears in the DSC trace, confirming that slow relaxation kinetics of the $\boldsymbol{ip}_{ht}\rightarrow\boldsymbol{np}$ transition are the origin of this effect (see Table 3.16, cycle 3). Making use of the kinetically hindered $\boldsymbol{ip}_{ht}\rightarrow\boldsymbol{np}$ transition, the $\boldsymbol{ip}_{ht}$ phase could be characterized in more detail by SCXRD (Figure 3.40). At this, a picked crystal of *dry*-DMOF-1-**C4** was heated above the $\boldsymbol{np}\rightarrow\boldsymbol{ip}_{\mathrm{ht}}$ transition temperature in an oven and then measured at 400 K, the maximum available temperature for the used single-crystal X-ray diffractometer. Further details on the crystal preparation and crystallographic data are given in the Appendix section 8.1.2, Table 8.7.

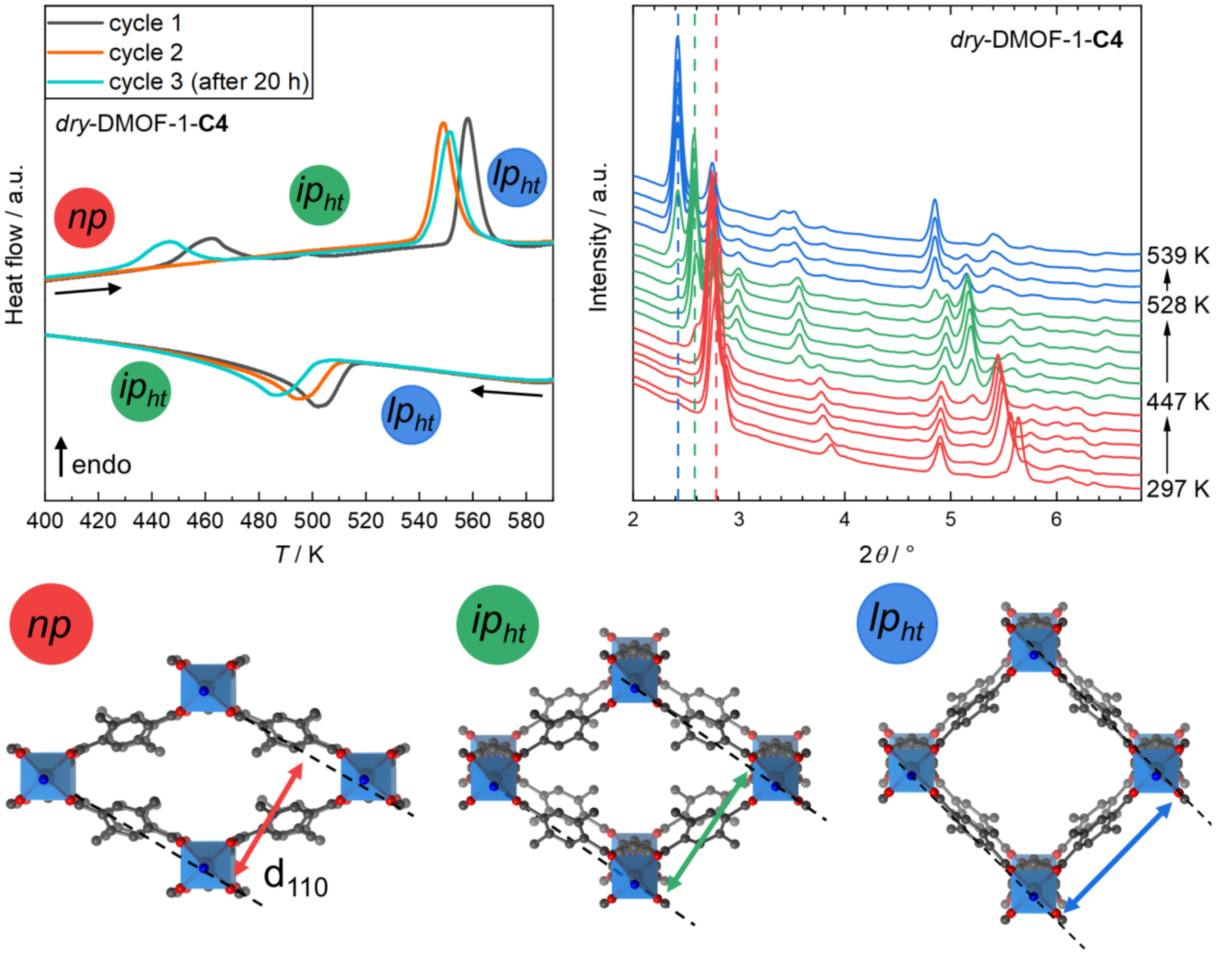

Figure 3.40: Excerpt of the DSC curves of *dry*-DMOF-1-**C4** (top, left). Note, that the $\boldsymbol{np}\rightarrow\boldsymbol{ip}_{\mathrm{ht}}$ transition is not present on cycle 2. Variable-temperature (VT-) PXRD patterns of *dry*-DMOF-1-**C4** (BL9 of DELTA, λ = 0.4592 Å, top right). The position of the 110 reflection of the different ***np***, $\boldsymbol{ip}_{\mathrm{ht}}$ and $\boldsymbol{lp}_{\mathrm{ht}}$ phases of *dry*-DMOF-1-**C4**, which are indicative of the wine rack hinging motion of the framework, are marked by dashed lines in the respective colour (red: ***np***, green: $\boldsymbol{ip}_{\mathrm{ht}}$, blue: $\boldsymbol{lp}_{\mathrm{ht}}$ phase). Furthermore, structural models are given, that relate to the experimental data (bottom). The lattice plane distance corresponding to the 110 reflections is highlighted by arrows according to the colour code given above. The model of the $\boldsymbol{lp}_{\mathrm{ht}}$ phase was created by employing extracted unit cell parameters of this phase to the SCXRD structure of the $\boldsymbol{ip}_{\mathrm{ht}}$ phase of *dry*-DMOF-1-**C4** and, hence, does not represent the likely present disorder due to rotations of the phenyl rings.

As expected, none of the carbon atoms of the flexible butyl DED except for the benzylic C1 could be resolved in the SCXRD structure of the $\boldsymbol{ip}_{\mathrm{ht}}$ of *dry*-DMOF-1-**C4**, due to the increased vibrational motions at elevated temperatures. But importantly, the Zn$_2$(**C4**-bdc)$_2$-layer of the MOF backbone has slightly opened and features no disorder, hence, full rotations of the phenyl rings appear to be not sterically or energetically feasible yet. Consequently, the $\boldsymbol{np}\rightarrow\boldsymbol{ip}_{\mathrm{ht}}$ transition is driven by an increase in vibrational entropy,[58] mainly of the flexible butyl substituents, but also due to motions of the phenyl rings, whereas the $\boldsymbol{ip}_{\mathrm{ht}}\rightarrow\boldsymbol{lp}_{\mathrm{ht}}$ transition is driven by an increase in configurational entropy,[57] caused by enabled flipping of the phenyl rings of the organic backbone of the MOF. Interestingly, the direction of the Zn$_2$(**C4**-bdc)$_2$-layer displacement of the $\boldsymbol{ip}_{\mathrm{ht}}$ has changed compared to the ***np*** phase. This is also evident from the change in the unit cell parameters upon the phase transition (Table 3.15) since the monoclinic angle β is formed between the pillar-axis (unit cell parameter c for both) and either the long (***np***) or the short ($\boldsymbol{ip}_{\boldsymbol{ht}}$) Zn$_2$(**C4**-bdc)$_2$-layer diagonal. Potentially, the Zn$_2$(**C4**-bdc)$_2$-layer displacement changes are connected with the slow relaxation kinetics of the $\boldsymbol{ip}_{\boldsymbol{ht}}\rightarrow\boldsymbol{np}$ phase transition, but also ordering processes related to phenyl ring and butyl group conformations might play a role since the ***np*** phase of *dry*-DMOF-1-**C4** features very much ordered butyl DEDs. A more detailed investigation of these particular aspects might be object of future scientific work on this topic.

The enthalpic and entropic footprints of the $\boldsymbol{np}\rightarrow\boldsymbol{ip}_{\boldsymbol{ht}}$ and the $\boldsymbol{ip}_{\boldsymbol{ht}}\rightarrow\boldsymbol{lp}_{\boldsymbol{ht}}$ transitions were finally summed up for a comparison to the related butoxy- and methoxy-ethoxy-functionalized DMOFs (*dry*-DMOF-1-**OC4** and *dry*-DMOF-1-**OC2OC1**), which feature only a single $\boldsymbol{np}\rightarrow\boldsymbol{lp}_{\boldsymbol{ht}}$ phase transition upon heating.[58] Notably, these compounds feature one additional substituent-chain segment, since the corresponding *dry*-DMOF-1-**OC3** does not undergo a thermally induced $\boldsymbol{np}\rightarrow\boldsymbol{lp}_{\boldsymbol{ht}}$ phase transition, but only anisotropic thermal expansion. Taking the rather similar values for ΔH into account, ΔS is significantly lower for *dry*-DMOF-1-**C4** (Table 3.17). This is attributed to the decreased length of the substituent chain (corresponding to a lower number of configurational states of the side chain in the open $\boldsymbol{lp}_{\boldsymbol{ht}}$ phase), since the volumetric differences between the ***np*** and $\boldsymbol{lp}_{\boldsymbol{ht}}$ phases of the compared DMOFs are of very similar magnitude (+17-19%, Table 3.17).

Table 3.17: Thermodynamic data on the $\boldsymbol{np}\rightarrow\boldsymbol{lp}_{\mathrm{ht}}$ phase transitions of *dry*-DMOF-1-**OC2OC1**, *dry*-DMOF-1-**OC4** and *dry*-DMOF-1-**C4**. For *dry*-DMOF-1-**C4**, the data for both transitions were summed up. Since *dry*-DMOF-1-**C4** undergoes multiple phase transitions towards the ***lp*** phase, for all three compounds, ΔV was determined in reference to the volumes at around 300 K. The data were always taken from the first DSC scan.

	ΔH / kJ mol^{-1}	ΔS / J K^{-1} mol^{-1}	T / K	ΔV / %
C4	11.6	22.1	445, 552	+17%
OC2OC1[58]	14.1	28.6	493	+19%
OC4[58]	13.11	32.9	398	+16%

3.8 Conclusion & Outlook

Herein, a series of three alkyl-functionalized DMOF-1-**CX** materials based on 2,5-dialkyl-1,4-benzenedicarboxylate linkers (with alkyl = ethyl (**C2**-bdc^{2-}), propyl (**C3**-bdc^{2-}) or *n*-butyl (**C4**-bdc^{2-}), **CX**-bdc^{2-}) was presented, which switch between a ***np*** and a ***lp*** phase depending on guest-content (all materials) or temperature (only the butyl-functionalized derivative). At this, the structural contraction of the ***np*** phases ranges from –24% (*dry*-DMOF-1-**C2**) to –15% (*dry*-DMOF-1-**C4**) as a function of the alkyl chain length (with respect to the volume of the ***lp*** phase). For the first time for this material class, detailed structural insights into the nature of the interactions of the guests, flexible substituents, and the framework backbone of the ***lp*** and ***np*** phases of these materials are provided by means of SCXRD and PXRD. Particularly, DMOF-1-**C3** shows a remarkable conformational flexibility regarding the encapsulation of different guest-species (i.e., DMF, acetonitrile, acetone, benzene, and *n*-octane).

The guest- and temperature responsive behaviour of the *dry*-DMOF-1-**CX** significantly differs from that of the established *dry*-DMOF-1-**OCY** of the same substituent chain lengths. Most notably, contrasting its alkoxy-pendant, *dry*-DMOF-1-**C3** features a multi-step CO_2 sorption isotherm with different ***ip*** phases occurring during ad- or desorption, which could be ultimately traced back to a re-ordering process of the propyl groups and CO_2 guests upon desorption of CO_2 from the disordered ***lp*** to the ordered $\boldsymbol{ip_{des}}$ phase.

In addition to that, an investigation of the single-component sorption of industrially relevant C_3 and C_4 hydrocarbons indicates a desired preference of adsorbing propane over propylene. In particular *dry*-DMOF-1-**C3** exhibits an interesting gating behaviour towards these gases, where the critical pressures of the transitions to the ***lp*** phase strongly differ between propane and propylene. Comparing the hydrocarbon sorption behaviour of the *dry*-DMOF-1-**CX** to their alkoxy-functionalized relatives clearly reveals the tendency of the alkoxy-functionalized derivatives to open at higher gas pressures, which is again a consequence of the higher polarity of those sidechains.

Furthermore, the thermal properties of the *dry*-DMOF-1-**CX** materials were investigated. While *dry*-DMOF-1-**C3** exhibits the characteristic anisotropic swelling with increasing temperature, *dry*-DMOF-1-**C4** shows a temperature-induced switching from the ***np*** to the $\boldsymbol{lp_{ht}}$ phase (proceeding over an $\boldsymbol{ip_{ht}}$ phase). Remarkably, the alkoxy functionalized versions *dry*-DMOF-1-**OCY** needed longer substituent chains (i.e., a linear chain of five non-hydrogen atoms) to show similar thermal phase transitions. Remarkably, the stepwise fashion of the thermally induced switching of *dry*-DMOF-1-**C4** could be ascribed to consecutive increase in, firstly, vibrational, and then configurational entropy.

Overall, the generally “softer” behaviour of the *dry*-DMOF-1-**CX** points towards a flatter free energy landscape of this family of DMOFs with respect to their alkoxy counterparts, which is in accordance with the low polarity of the alkyl substituents, which should result in weaker interactions between these groups and the framework backbone. Furthermore, the presented results demonstrate how small changes of the linker functionalization promote huge changes in the stimuli-responsive properties of the material, and therefore prove linker functionalization as a very powerful tool for tailoring the properties of stimuli-responsive MOFs.

In view of future work, a few open questions remain regarding the peculiar CO_2 sorption behaviour of *dry*-DMOF-1-**C3** and underlying thermodynamics of both ***ip*** phases on the ad- and desorption branch, which might be addressed via molecular dynamics simulations. Besides this, more detailed structural information on the DMOF-1-**OCY** materials might be accessible by means of electron diffraction techniques, which have been significantly improved within the last years.[132] This would enable a more in-depth comparison of the behaviour of the alkoxy- and alkyl functionalized derivatives discussed herein. Future works on this class of materials might focus on further evaluation of the hydrocarbon sorption data, particularly that of *dry*-DMOF-1-**C3** to study the performance of this material in a more-component sorption or breakthrough experiment.

4 Frustrated Flexibility

Large parts of the results presented in sections 4.1, 4.2, 4.3 and 4.5 of this chapter have been published in a peer-reviewed research article. Herein, text and figures of this publication are reprinted or adapted (licensed under a Creative Commons Attribution 4.0 International License, https://creativecommons.org/licenses/by/4.0/legalcode). Adaptions involve changes in compound nomenclature and rearrangements of figure parts. Reference to the publication and author contributions are given below.

R. Pallach, J. Keupp, K. Terlinden, L. Frentzel-Beyme, M. Kloß, A. Machalica, J. Kotschy, S. K. Vasa, P. A. Chater, C. Sternemann, M. T. Wharmby, R. Linser, R. Schmid, S. Henke. Frustrated flexibility in metal-organic frameworks. *Nat. Commun.* **2021**, *12*, 4097.

Publisher: Springer Nature
Date: Jul 2, 2021

Author contributions:
S.H. designed and led the project. R.P. synthesized the organic linkers and the MOFs and collected and analysed PXRD, SCXRD, IR spectroscopy, solution NMR spectroscopy, TGA/DSC, optical microscopy, and gas sorption data. K.T. contributed to the organic linker syntheses. R.P., L.F.-B., P.A.C. and S.H. performed the X-ray total scattering experiments. R.P., L.F.-B., M.K., M.T.W. and S.H. performed the variable temperature PXRD experiments. R.P., L.F.-B., A.M., M.T.W. and S.H. performed the *in-situ* PXRD experiments under CO_2 sorption. R.P., L.F.-B., M.K., C.S. and S.H. performed the *in-situ* PXRD experiments under *n*-butane sorption. J.Ke. performed the MD simulations under supervision of R.S. J.Ko. and S.K.V. performed and analysed the solid-state NMR experiments under supervision of R.L. All authors participated in discussing the data. R.P. and S.H. wrote the paper with J.Ke. and R.S. contributing the section on molecular modelling.

4.1 Introduction

In the previous chapter the influence of DED groups on the flexible behaviour of a series of functionalized materials of the DMOF-1 family was presented. Therein, a guest- and temperature-depending structural flexibility was discussed, which is characterized by phase transitions in an exclusively crystalline-to-crystalline fashion (even though some disorder of the side chains is involved in some cases). Despite the comparably well-defined structures of the crystalline state, there is growing interest in amorphous MOFs due to properties intrinsically emerging from their amorphous state.[133–136] Most prominently, these are the moldability and glass-forming ability of certain MOFs, which thus can be processed and shaped in their (supercooled) liquid state.[137–142] But in general, amorphous MOFs may bear very different properties, than their crystalline MOF relatives. For example, the crystalline MIL-100-Fe[143] (chemical composition: $Fe_3O(H_2O)_2(F)(btc)_2$, btc^{3-} = 1,3,5-benzene tricarboxylate) and its amorphous counterpart Fe-btc (chemical composition very similar to MIL-100)[144], which is commercially available under the name Basolite® F300,[145] are both constructed of largely the same inorganic and organic building units[144,146] but feature catalytic activities towards different substrates[147] and different gas sorption properties, i.e., an enhanced propane/propylene selectivity of Fe-BTC compared to MIL-100-Fe.[148] However, in general highly disordered or amorphous MOF phases, despite being described more and more frequently in the literature,[135] are rarely investigated in detail, because their disordered nature makes them much more difficult to characterize than their crystalline relatives. Especially in the field of flexible MOFs, there are only few examples undergoing reversible transitions between crystalline and non-crystalline phases, which often are only poorly understood in detail as well.[149–153]

In this chapter, a new type of flexible behaviour denoted as frustrated flexibility, which is characterized by fully reversible, displacive guest- or temperature-driven transitions between crystalline and X-ray amorphous states, will be introduced and explored in detail for a series of isoreticular MOF materials. In connection with the previous chapter, this behaviour is mediated by functional groups implemented at the framework backbone. At first, the underlying concept shall be introduced in more detail in the following.

4.2 The Concept & Design Principle of Frustrated Flexibility

The phenomenon of frustrated flexibility presented herein conceptually rests on two major pillars, of which the first one consists of the selection of an intrinsically rigid and non-responsive MOF structure type. Such one does not allow for correlated (crystalline-to-crystalline) structural changes involving a hinging or wine rack flexibility mechanism and, thus, in this regard is fundamentally different from the breathing of the DMOF-1 based materials presented in the previous chapter of this work. The second pillar is the decoration of the organic linkers of the rigid MOF scaffold with suitable dispersion energy donators (DEDs), which impact the free-energy landscape of the MOF structure. At this, the DEDs effect the materials delicate balance between enthalpic contributions, being covalent or coordinative bonding and dispersion interactions, and entropic contributions, e.g., static, and dynamic disorder. As a consequence of the additional intra-framework dispersion interactions mediated by the DEDs, the previously non-responsive MOF materials enter a state of frustration once the interacting and space-filling guest-molecules are removed from the framework's cavities. This state of frustration is caused by the incompatibility of the rigid framework lattice on the one hand and the maximization of intra-framework dispersion interactions demanding a densification of the structure on the other hand. Ultimately, the minimization of the framework enthalpy must then occur at the cost of crystalline order.

For a proof of this concept, the iconic MOF-5 (chemically $Zn_4O(bdc)_3$, bdc^{2-} = 1,4-benzenedicarboxylate) was selected as a rigid MOF platform (Figure 4.1).[2] Although there are considerable dynamics suggested to be present in this material, be it the dynamic binding of DMF (*N*,*N*-dimethyl formamide) or DEF (*N*,*N*-diethyl formamide) to its metal clusters[154,155], negative thermal expansion[156,157] or the possibility of chiral induction by guest uptake[158], it is generally considered a structurally rigid MOF.[77,159,160] This is because MOF-5 always retains its cubic symmetry and does not show any kind of volume change greater than 4%[158] upon guest removal/exchange or gas sorption. An important signature of the rigidity of MOF-5 is its fairly isotropic Young's modulus, which varies only by a factor of about 1.5 between the least stiff and the stiffest crystallographic direction, as shown by molecular dynamics simulations applying the QuickFF force field[161]. Flexible MOFs typically feature orders of magnitude differences of their Young's moduli in different crystallographic directions[162]. In view of its topology, the non-responsiveness of MOF-5 is surprising, since the **pcu** topology in principle allows for considerable degrees of freedom of a structure.[77] With the functionalized DMOF-1 derivatives of the previous chapter, we have discussed an example of a MOF family of the **pcu** topology featuring remarkable guest- and temperature-responsive phase transitions involving very large volume changes of up to 28%.[58,104,163,164] Therefore, the inherent rigidity of MOF-5 originates from a different source, the geometric features of its T_d symmetric $[Zn_4O(O_2C)_6]$ inorganic unit in the function of an octahedrally connecting node. Here, the relative orientation of the carboxylates does not allow for a cooperative hinging along the O-O axis of the carboxylates of its bdc^{2-} linkers in opposite directions. An illustration of this deformation process, for instance along the body diagonal of the cubic cavity, which corresponds to the crystallographic ⟨111⟩ direction makes clear that this is not feasible for MOF-5 (see blue arrows in Figure 4.1). Thus, large-magnitude volume changes of the crystal, as in the prominent breathing phase transitions of conventional flexible MOFs, are not feasible for MOF-5[77], since they would require major distortions of its inorganic nodes or even reversible bond breaking.

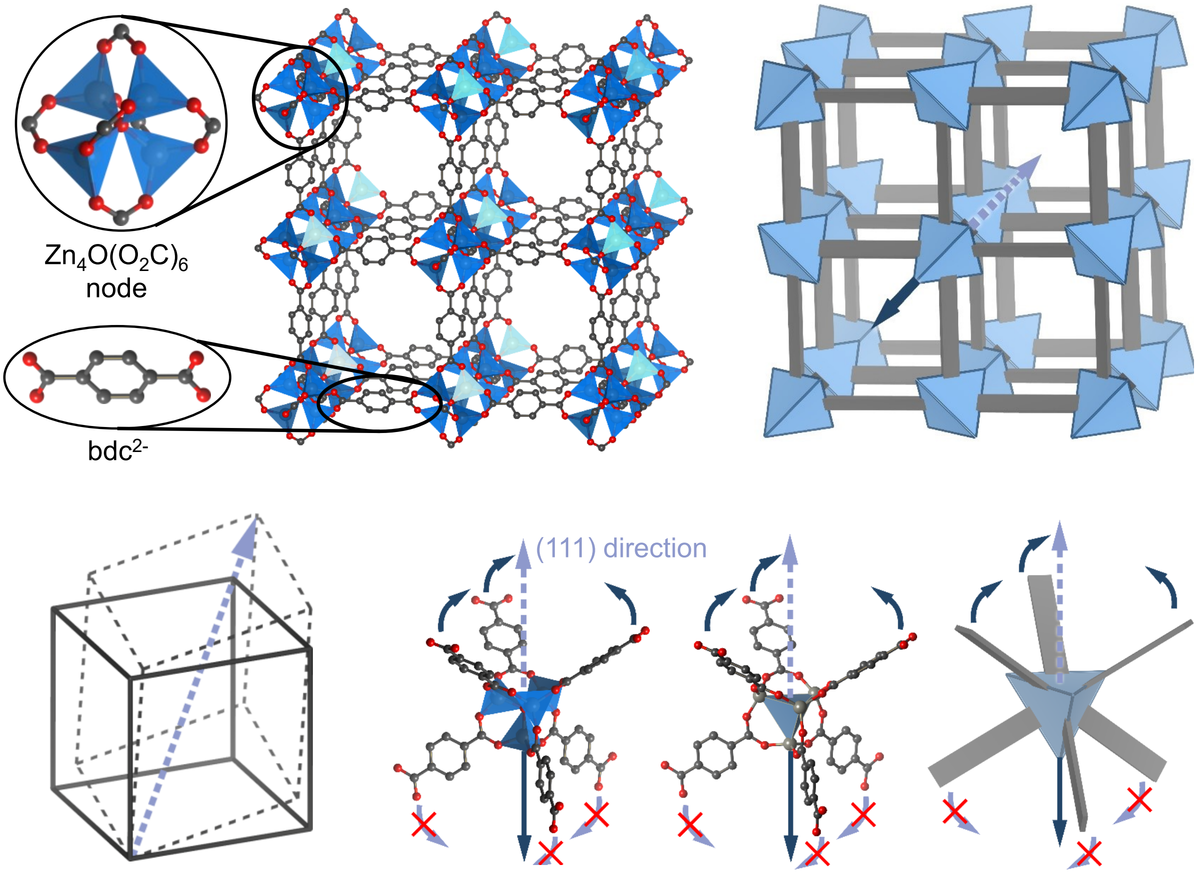

Figure 4.1: Top left: Crystal structure of MOF-5 (CCDC deposition code 256965). Zn, O and C atoms are shown in blue, red and grey, respectively. H atoms are omitted. Top right: Simplified building block representation of the structure of MOF-5 emphasizing the tetrahedral symmetry of the inorganic unit. Bottom left: Rhombohedral distortion of a cube along its body diagonal. Bottom right: Abstraction path of the actual chemical structure towards the respective geometries of its building units as shown in the simplified building block representation (top, right). Arrows symbolize the required movements of these building units (that is, $[Zn_4O]^{6+}$ and bdc^{2-}) in case of the rhombohedral contraction.

Besides its structural rigidity, the MOF-5 structure type fulfils the second requirement (or pillar) of the presented concept of frustrated flexibility by its high susceptibility to chemical functionalization of the bdc^{2-} linkers (as discussed in the Introduction, section 2.1). This allows for the decoration of the framework backbone with a huge variety of DED groups of varying length by the implementation of functionalized 2,5-alkoxy bdc^{2-} linkers. Conveniently, these linkers can be applied directly in the synthesis of the MOF materials and are furthermore easily accessible via established synthetic protocols.[104] In the systematic study presented in this chapter, the tuning of the steric bulk of the DEDs gives rise to unprecedented physical properties compared to the non-functionalized mother material MOF-5. This includes guest- and temperature-responsive structural flexibility between two crystalline phases or a crystalline and a non-crystalline phase depending on the respective DED group.

The first section deals with the structural behaviour of the MOFs as a function of the content of different guest species, which is analysed mainly by means of powder and single crystal X-ray diffraction techniques (PXRD and SCXRD). In the following section, a deeper understanding of the guest-induced changes in the local structure of the materials exhibiting frustrated flexibility is gained from solid state NMR spectroscopy, X-ray pair distribution function analysis and infrared spectroscopy. These structural investigations are then complemented by the results of molecular dynamics simulations mapping the underlying thermodynamics. Consequently, the insights into the structural behaviour were employed on understanding the physical properties in terms of the thermal and gas sorption behaviour. In the designated sections, these are analysed via the methods of differential scanning calorimetry (DSC), variable-temperature (VT-) PXRD, isothermal gas sorption (N_2, CO_2, *n*-butane) and *in-situ* gas sorption PXRD, respectively. Furthermore, the effects of increasing the DED's polarity on the structural, thermal and gas sorption behaviour are evaluated. In the final section, the concept of frustrated flexibility is transferred to other MOFs constructed of the same $[Zn_4O(CO_2)_6]$ inorganic building block and additionally its potential for MOFs with other inorganic building blocks is discussed on the basis of contemporary literature.

4.3 Frustrated Flexibility in the MOF-5-**OCX** Series

4.3.1 MOF Synthesis & Structural Behaviour

Within the scope of this study, seven functionalised MOF-5 derivatives of the general chemical composition Zn_4O(**CXO**-bdc)$_3$ (**CXO**-bdc^{2-} = 2,5-dialkoxy-1,4-benzenedicarboxylate with **X** = 2 – 8: number of carbon atoms in the alkyl chain, Figure 4.2) bearing linear alkoxy groups of variable length at the organic bdc^{2-} linker, were prepared as transparent cubic crystals (size ca. 100-500 µm), denoted *as*-MOF-5-**OCX**.[‡] Repeated solvent exchange with CH_2Cl_2 (three times) followed by careful drying under dynamic vacuum ($\approx 10^{-4}$ kPa) at 100 °C for 24 h gives the guest-free, dried materials *dry*-MOF-5-**OCX**. The influence of high surface tension effects during the drying process on the framework distortion was ruled out by exemplary activation of MOF-5-**C3** from *n*-hexane (see Appendix 8.2.1, Figure 8.39), i.e., a lower surface tension liquid (σ(20°C) = 18.35 mN m^{-1})[165] compared to DCM (σ(20°C) = 26.50 mN m^{-1})[166]. A more detailed description of all the synthetic procedures and preparational measures of the MOFs and linkers is given in the Materials & Methods Section 6.1.3.

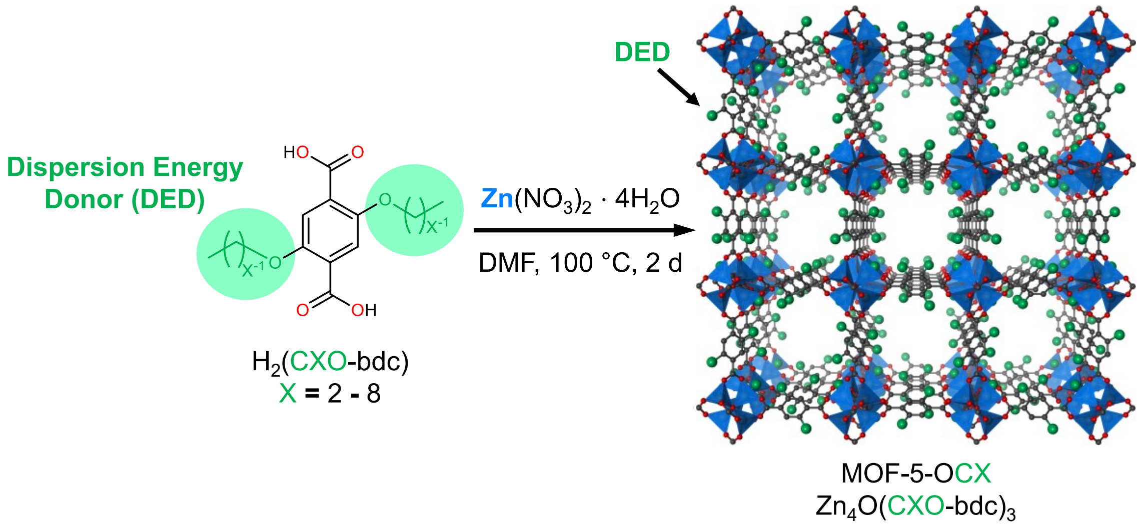

Figure 4.2: Schematic for the preparation of alkoxy-functionalized MOF-5-**OCX** derivatives. Dispersion energy donors (DEDs) are marked as green spheres. Zn, O and C atoms are shown in blue, red and grey, respectively. H atoms are omitted. The illustration is based on the SCXRD structure of MOF-5 (CCDC deposition code 256965).

The *as*-MOF-5-**OCX** (**X** = 2 – 7) crystallize in the cubic space group $Pm\bar{3}m$ with $a \approx 12.8$ Å due to disorder of both the zinc-oxo-clusters and the phenyl ring of the bdc^{2-} units (conventional MOF-5 crystallizes in the cubic space group $Fm\bar{3}m$ with $a \approx 25.7$ Å)[2]. In accordance with previous reports[99] the alkoxy-DEDs could not be resolved in the SCXRD structures. Nevertheless, the powder and single crystal X-ray diffraction (PXRD and SCXRD) data of the as-synthesized (*as*) materials *as*-MOF-5-**OC2** to *as*-MOF-5-**OC7** clearly confirm their structural analogy to prototypical MOF-5 (Figure 4.3, left, for structureless profile fits, see

---

[‡] Further MOF-**OCX** derivatives with **X** = 9, 10 were prepared within the scope of this study. For the sake of conciseness, these will, however, not be discussed any further in this chapter. For the interested reader, the experimental data gathered on these compounds are compiled in the Appendix section 8.2.10.

Appendix 8.2.1, Figure 8.29 to Figure 8.32). For a more detailed discussion of the SCXRD data, the reader is forwarded to Appendix 8.2.2.

By contrast, the material *as*-MOF-5-**OC8** possesses a different structure, as indicated by the characteristic peak splitting in its PXRD pattern, where e.g., the former 110 reflection, which is characteristic for the face diagonal of the cubic unit cell, is split into two reflections corresponding to one shorter and one longer set of *d*-spacings (Figure 4.3, left). Indeed, SCXRD verifies that *as*-MOF-5-**OC8** is a rhombohedrally distorted phase of MOF-5 with angles of 87.0° and 93.0° between neighbouring inorganic nodes (space group $R\bar{3}$) instead of 90° in the cubic parent structure (see Figure 4.3, right).[2]

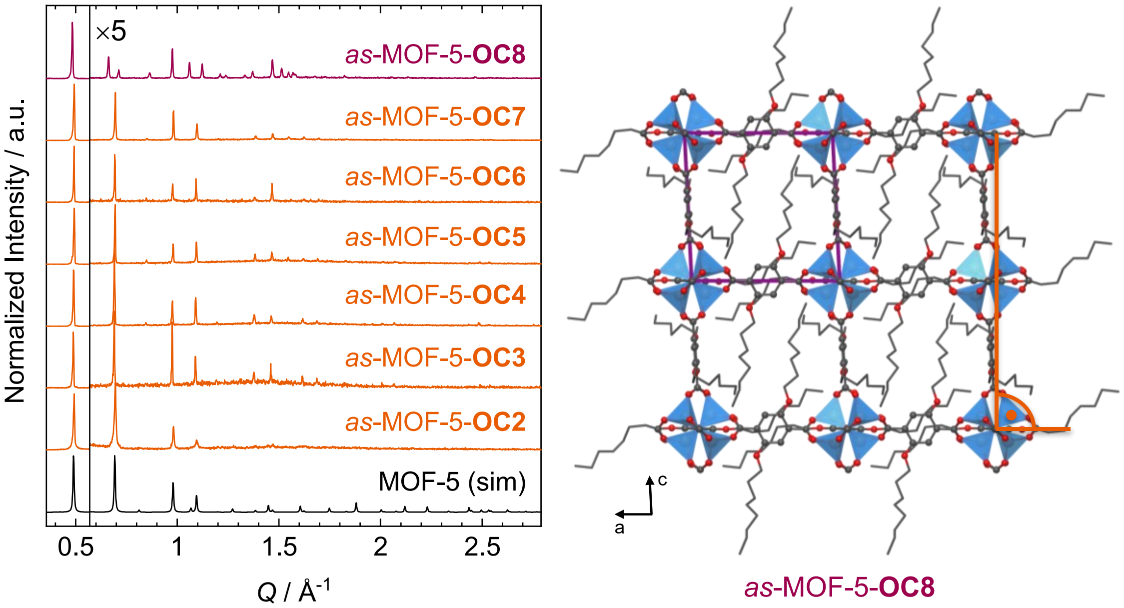

Figure 4.3: Left: PXRD data of the MOF-5-**OCX** in their *as* (as-synthesized) state in comparison to the simulated diffraction pattern of MOF-5 (CCDC deposition code 256965). Cubic and rhombohedral states are highlighted in orange or purple colour, respectively. Right: Representation of the SCXRD structure of *as*-MOF-5-**OC8** (space group $R\bar{3}$, CCDC deposition code 2040916, hydrogen atoms are omitted for clarity). A right angle (orange colour) is given to elucidate the rhombohedral distortion of the MOF structure. The Zn atoms, carboxylate groups and DEDs are statically disordered by symmetry. The second part has been removed for clarity.

Due to the geometric constraints of the $[Zn_4O(O_2C)_6]$ nodes, the rhombohedral distortion of *as*-MOF-5-**OC8** involves a slight deformation of the $[Zn_4O]^{6+}$ tetrahedron along the rhombohedral elongation axis (the body diagonal of the framework cavity), giving rise to two different kinds of Zn–O distances, three shorter ones of 1.925(1) Å and one longer one of 1.977(1) Å (Figure 4.4, left). For reference, the Zn–O bond length in MOF-5 amounts to 1.935(2) Å and lies in between the Zn–O bond lengths of the rhombohedral *as*-MOF-5-**OC8**. Remarkably, the alkoxy DEDs connected to the linker could be well resolved in the electron density map of *as*-MOF-5-**OC8**. The DEDs are located in close contact to the aromatic ring of a neighbouring bdc^{2-} linker (≈ 3.0 – 3.5 Å C_{aryl}-H_{DED} distance), giving clear evidence that dispersion interactions between these groups provide the driving force for the observed rhombohedral distortion (Figure 4.4, right).

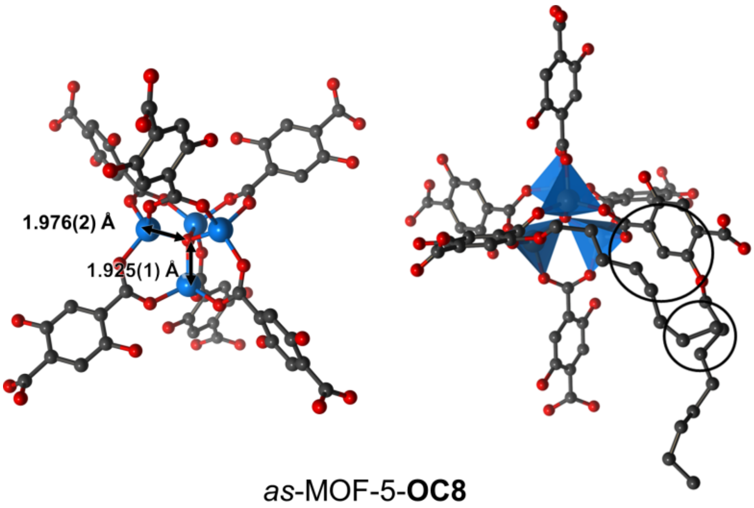

Figure 4.4: Representations of the SCXRD structure of *as*-MOF-5-**OC8** (space group $R\bar{3}$, CCDC deposition code 2040916, hydrogen atoms are omitted for clarity) showing the distorted Zn_4O node with marked Zn-O bond lengths (left, alkyl-groups omitted) and the close contact between the alky-chains and the aromatic ring of the framework backbone (right, circles). The Zn atoms, carboxylate groups and DEDs are statically disordered by symmetry. The second part has been removed for clarity.

Drying of the MOF-5-**OCX** derivatives gives rise to an unexpected structural richness as a function of the carbon chain length of the DEDs. Here, the PXRD pattern of *dry*-MOF-5-**OC8** remains largely the same, whilst *dry*-MOF-5-**OC7** now likewise features a rhombohedrally distorted structure as indicated by the same reflection splitting alike MOF-5-**OC8** (Figure 4.5).

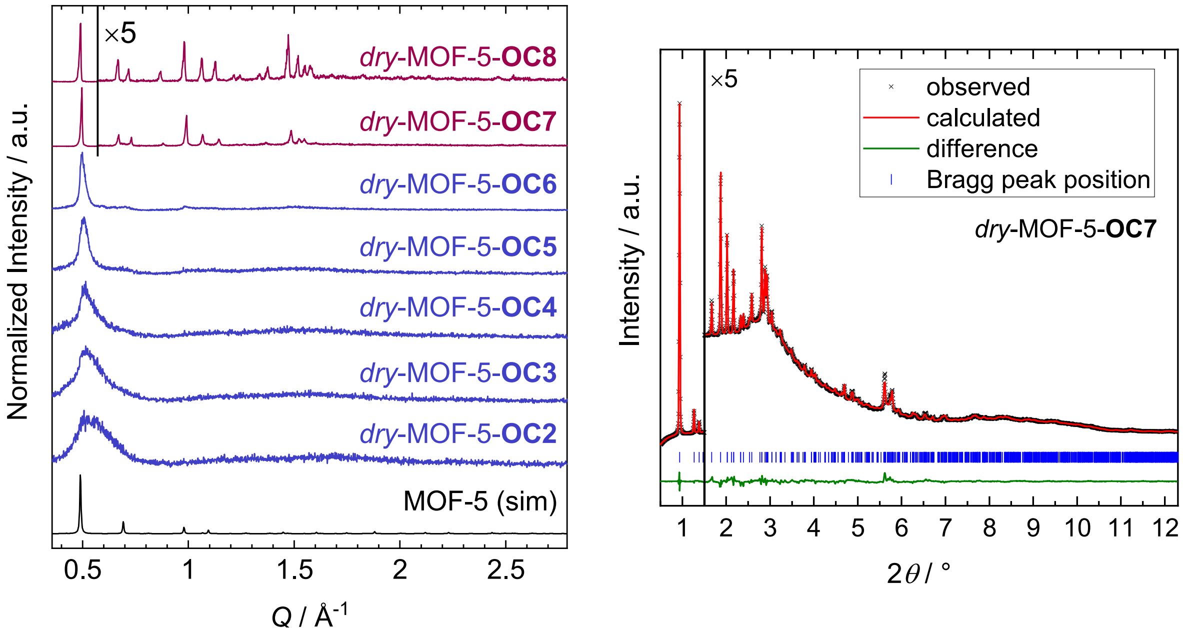

Figure 4.5: Left: PXRD data of the MOF-5-**OCX** in their *dry* (guest-free) state in comparison to the simulated diffraction pattern of MOF-5 (CCDC deposition code 256965). Rhombohedral and X-ray amorphous states are highlighted in purple or blue colour, respectively. Right: Final Rietveld fit of PXRD data of *dry*-MOF-5-**OC7** recorded at P02.1 of DESY ($\lambda = 0.2073$ Å). Final refinement parameters are $R_p = 0.930$, $R_{wp} = 1.356$, $R_{exp} = 2.398$, $\chi^2 = 0.566$ and $R_{Bragg} = 0.591$. Final unit cell parameters (space group $R\bar{3}$) are $a = 17.1950(6)$ Å, $c = 24.1731(18)$ Å and $V = 6189.7(6)$ Å^3 in the hexagonal setting and $a = 12.7860(5)$, $a = 84.507(4)$ and $V = 2063.2$ Å^3 in the rhombohedral setting (CCDC deposition code 2040923).

A detailed structural model of rhombohedral *dry*-MOF-5-**OC7** could be obtained via Rietveld refinement of high-resolution PXRD data recorded at P02.1 of DESY (Figure 4.5, right, for refinement parameters, see figure caption). At this, a modified crystallographic model of *as*-MOF-5-**OC8**, where the alkoxy group was truncated by one carbon atom (H-atoms were generally not included in the refinement), served as the starting point for the refinement. In its course, the organic building unit was described as a rigid body and a number of distance and angle restraints were applied to keep the building units in shape. Further details on the refinement procedure are given in the Appendix Section 8.2.1. This finally yields a structural model with rhombohedral angles of 84.5° and 95.5° between neighbouring $[Zn_4O(O_2C)_6]$ nodes (Figure 4.6, for further details, see Appendix section 8.2.1). Thus, this demonstrates a volume contraction of the framework by approximately 3% upon guest removal ($V_{C7,as} = 2129.8(6)$ Å^3 vs. $V_{C7,dry} = 2063.2(2)$ Å^3, Appendix 8.2.1, Table 8.27). The cubic-to-rhombohedral transition of *dry*-MOF-5-**OC7** can be reversed by adsorption of either DMF vapour (under reduced pressure at 65 °C) or liquid *n*-octane as was verified by PXRD (see Figure 4.9 below, structureless profile fits are given in the Appendix section 8.2.1, Figure 8.32).

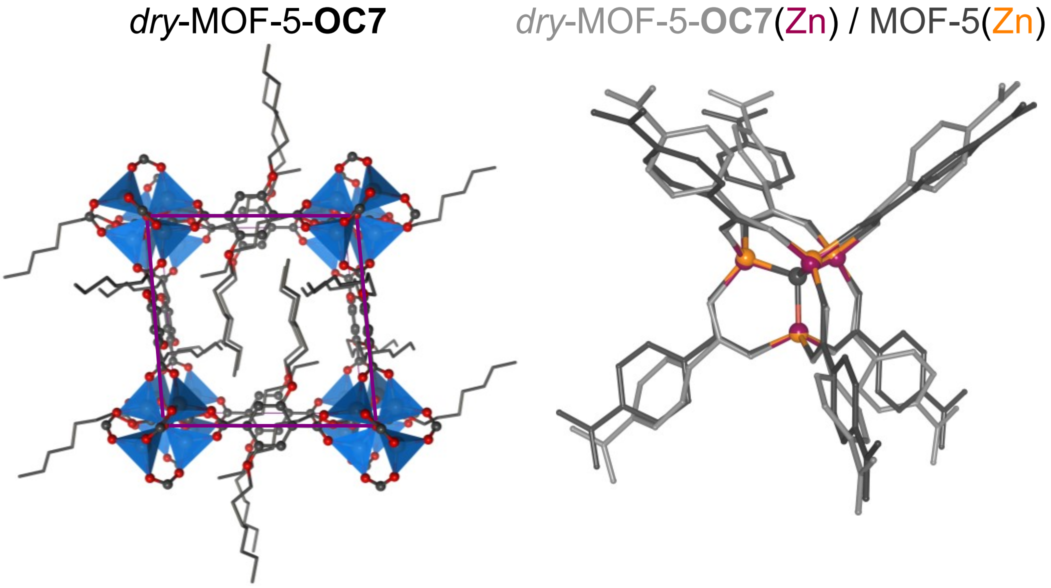

Figure 4.6: Left: Rietveld refined crystal structure of rhombohedrally distorted *dry*-MOF-5-**OC7** (space group $R\bar{3}$, unit cell edges coloured in purple, CCDC deposition code 2040923). The twofold disorder of the $[Zn_4O(O_2C)_6]$ building unit was removed for clarity. Right: Overlay of the structures of regular MOF-5 (grey, zinc cations in orange) and *dry*-MOF-5-**OC7** (light grey, zinc cations in purple) with emphasis on the relative distortion of the $[Zn_4O(O_2C)_6]$ building unit.

A drastically different behaviour is observed upon guest removal from the MOF-5-**OCX** derivatives bearing shorter DEDs at the organic linker. *Dry*-MOF-5-**OC2** to *dry*-MOF-5-**OC6** lose long-range order and transform to non-crystalline (or X-ray amorphous) states, displaying only broad diffuse scattering in their PXRD patterns. In the fields of amorphous or disordered solids (e.g., different types of glasses[167–170], red phosphorus[171]) the first scattering peak (FSP) is considered appearing as a manifestation of medium-range order (within 5 – 20 Å) of the materials.[168] Its specific interpretation thereby depends to a great extent on the respective system type under investigation. Here, the FSP is roughly at the same scattering angle of the strong 100 reflection present in the PXRD patterns of the cubic as-synthesized compounds (Figure 4.3, left). Following the sequence from *dry*-MOF-5-**OC6** to *dry*-MOF-5-**OC2**, the FSP decreases in absolute peak intensity, increases in peak width and asymmetry, and shifts towards higher scattering angles. Peak fits of the FSP using split pseudo-Voigt or PearsonVII profiles yield peak maxima ranging from Q_{FSP} = 0.496 Å^{-1} for *dry*-MOF-5-**OC6** to Q_{FSP} = 0.518 Å^{-1} for *dry*-MOF-5-**OC2** (for the full set of peak fits, see Appendix 8.2.1, Figure 8.37). According to Bragg's law, these maxima correspond to real-space distances from d_{FSP} = 12.66 Å (*dry*-MOF-5-**OC6**) to d_{FSP} = 12.12 Å (*dry*-MOF-5-**OC2**) (Figure 4.7, Table 4.1).

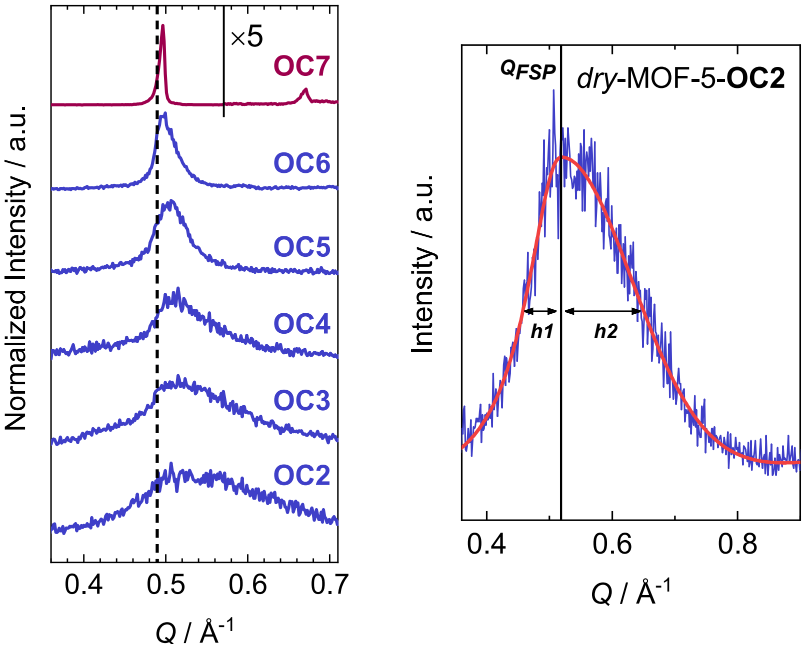

Figure 4.7: Left: Magnified PXRD data of *dry*-MOF-5-**OCX** (**X** = 2 – 7) with focus on the regions of the FSP. The Q-value corresponding to the 200 reflection of MOF-5 is marked by a dashed line for reference. Right: Legend for the extracted fit parameters (Table 4.1). Q_{FSP} is the peak maximum, *h1* and *h2* are the width at half mean of the left and right composite peak, respectively. The sum of *h1* and *h2* is the full width half mean (FWHM) of the full peak.

Furthermore, the increase of the FWHM from 0.02 Å^{-1} (*dry*-MOF-5-**OC6**) to 0.17 Å^{-1} (*dry*-MOF-5-**OC2**) suggests a drastic increase in strain and/or a decrease in domain size with decreasing alkoxy chain length. Since the position of the FSP is characteristic for the average distance between two neighbouring $[Zn_4O]^{6+}$ clusters in the solid, its shift to higher Q demonstrates a contraction of the frameworks concomitantly to the loss of long-range order. Thus, d_{FSP} corresponds to the average edge length of the MOF-5-**OCX** cages and allows for an approximation of the mean volume occupied by a single formula unit of the non-crystalline *dry*-MOF-5-**OCX** frameworks via the calculation of $(d_{\mathrm{FSP}})^3 = V_{contracted,dry}$ (Table 4.2). Comparing this to the unit cell volume of the parent crystalline *as*-MOF-5-**OCX** phases, $V_{cubic,as}$, yields an estimated volumetric contraction from –6% for *dry*-MOF-5-**OC6** up to –17% for *dry*-MOF-5-**OC2**.

Table 4.1: Parameters extracted from fits of the first scattering peak of *dry*-MOF-5-**OCX**. A Legend is given in Figure 4.7.

X	*reciprocal space*				*real space*
	Q_{FSP} / Å^{-1}	*h1* / Å^{-1}	*h2* / Å^{-1}	FWHM / Å^{-1}	d_{FSP} / Å
C2	0.518	0.0393	0.1338	0.1731	12.12
C3	0.515	0.0565	0.0925	0.1490	12.20
C4	0.510	0.0333	0.0685	0.1018	12.32
C5	0.505	0.0192	0.0262	0.0454	12.43
C6	0.496	0.0071	0.0177	0.0248	12.66

Table 4.2: Estimated volumes of the *dry*-MOF-5-**OCX**.

X	d_{FSP} / Å	$V_{\mathrm{contracted,dry}}$ / Å^3	$V_{\mathrm{cubic,as}}$ / Å^3	%change
C2	12.12	1780.4	2153.6(18)	-17
C3	12.20	1815.9	2164.3(10)	-16
C4	12.32	1870.0	2168.3(7)	-14
C5	12.43	1920.5	2157.6(3)	-11
C6	12.66	2029.1	2158.3(11)	-6

Macroscopically, with the loss of crystalline order upon desolvation, the formerly transparent crystals turn dull and cracked, due to the strain built up within the material (Figure 4.8).

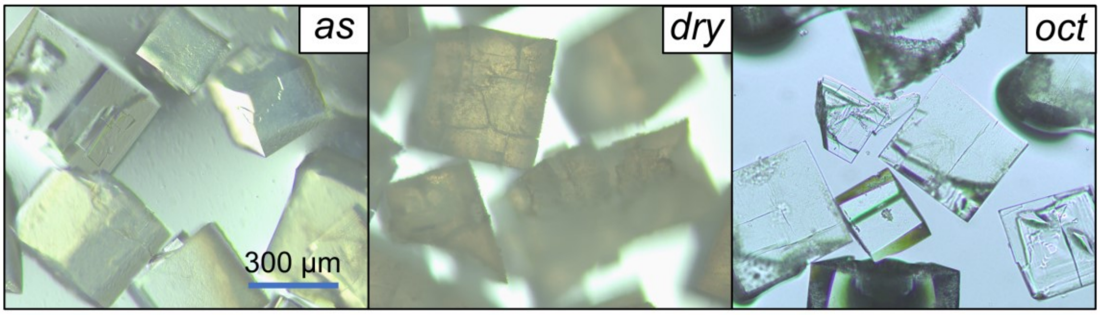

Figure 4.8: Microscopy images of *as*-, *dry*- and *oct*-MOF-5-**OC3** illustrating the visual impact of the structural transformations.

Importantly, sharp Bragg reflections, characteristic for the cubic MOF-5 structure type, re-emerge in the PXRD patterns of *dry*-MOF-5-**OCX** (**X** = 2 – 6) after adsorption of DMF (via the gaseous phase) or *n*-octane (via the liquid phase) at 65 °C for both solvents (Figure 4.9, for the corresponding profile fits of the patterns, see Appendix 8.2.1). The fact that this phenomenon occurs with *n*-octane, in which the MOFs' building blocks are not soluble, rules out solvent coordination at the inorganic building unit, which is known from DMF or DEF solvated MOF-5,[154,155] or framework reconstruction, which was reported for e.g., ethanol solvated HKUST-1,[172] as a potential cause of this effect. Note, that solvent coordination in MOF-5 will be discussed in more detail in section 4.3.2 in the context of IR spectroscopy.

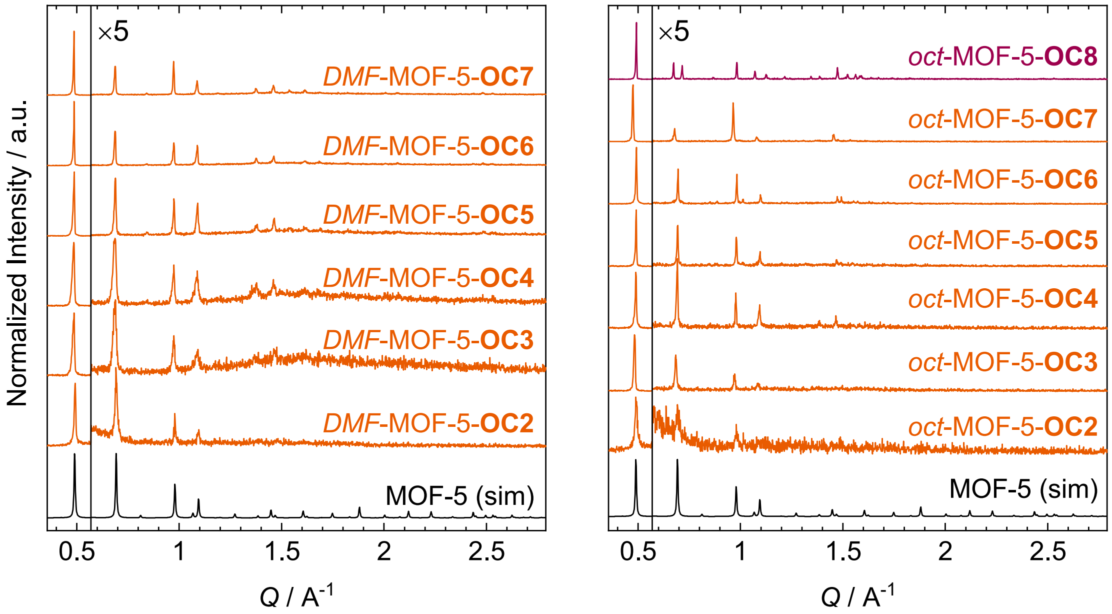

Figure 4.9: PXRD data of the MOF-5-**OCX** in their DMF- (left) and *n*-octane-resolvated (*oct*, right) states in comparison to the simulated diffraction pattern of MOF-5. Cubic and rhombohedral states are highlighted in orange or purple colour, respectively.

Most impressively, the crystalline-to-X-ray-amorphous-to-crystalline transition after DMF removal and subsequent adsorption of *n*-octane at 65 °C could even be followed by SCXRD of representative samples of MOF-5-**OC3** and MOF-5-**OC6**. Reconstructed reciprocal space sections of the *n*-octane resolvated samples *oct*-MOF-5-**OC3** and *oct*-MOF-5-**OC6** demonstrate that crystalline order is fully regained at the single-crystal level (crystal size > 300 µm) after immersion of *dry*-MOF-5-**OC3** and *dry*-MOF-5-**OC6** in *n*-octane (Figure 4.10, for details, see Appendix 8.2.2).

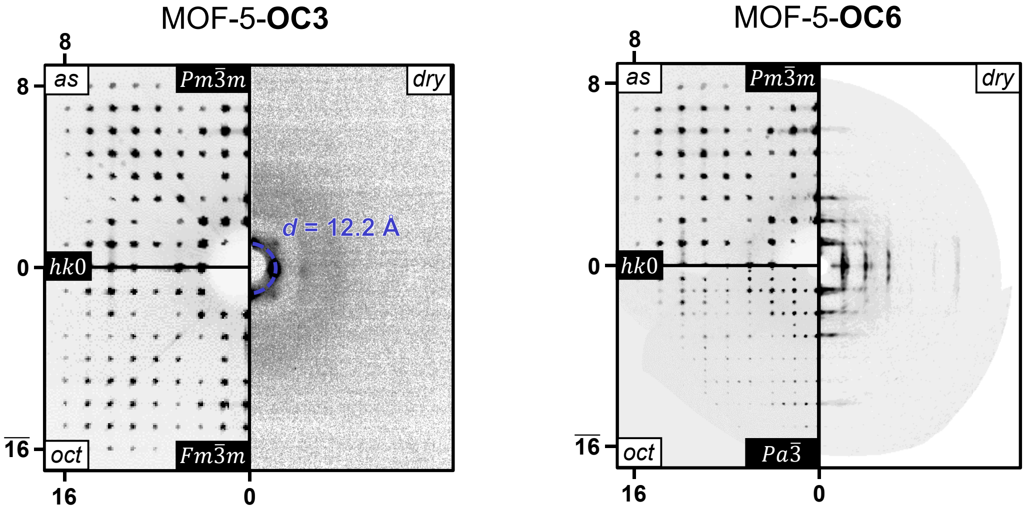

Figure 4.10: Excerpts from reconstructed reciprocal space maps of *as*- and *oct*-MOF-5-**OC3** (left) and *as*-, *dry*- and *oct*-MOF-5-**OC6** (right) showing the *hk*0 layers of reciprocal space. For *dry*-MOF-5-**OC3** a single diffraction pattern is depicted, where the four-fold symmetry of the non-crystalline structure is still visible in the diffuse scattering peaks. By contrast, reciprocal space maps of *dry*-MOF-5-**OC6** exhibits significantly more features of the cubic crystalline structure and potentially nano-crystalline domains.

Structure solution of the gathered SCXRD data reveals, that *oct*-MOF-5-**OC3** crystallizes in the cubic space group $Fm\bar{3}m$ (a = 25.7952(9) Å) and eventually features the same disordered structure as in its as-synthesized state. Interestingly, upon inclusion of the *n*-octane guest molecules *oct*-MOF-5-**OC6** adopts a slightly contracted structure (cubic space group $Pa\bar{3}$, a = 25.7145(6) Å, –1.5% volume difference per repeating unit compared to the as-synthesized state, for details on the structure solution and refinement, see Appendix 8.2.2). Taking the central O^{2-} ions of the $Zn_4O(CO_2)_6$ units as vertices, the structure of *oct*-MOF-5-**OC6** can be understood in terms of alternating acute (as in *dry*-MOF-5-**OC7** and MOF-5-**OC8**) and obtuse rhombohedra (Figure 4.11), which are constructed of the very same rhombic faces.[§] Their rhombohedral angles amount to 86.33° and 93.67°, which indicates a slightly stronger contraction of the individual rhombohedra than in the SCXRD structure of *as*-MOF-5-**OC8**, where the angles amount to 87° and 93°. Consequently, the superimposed Zn_4O-tetrahedra again feature three shorter (1.939(2) Å and 1.935(2) Å) Zn–O distances and one longer one (1.969(6) Å and 1.977(6) Å). Remarkably, this demonstrates a different crystalline-to-crystalline distortion mechanism of the MOF-5-**OCX**.

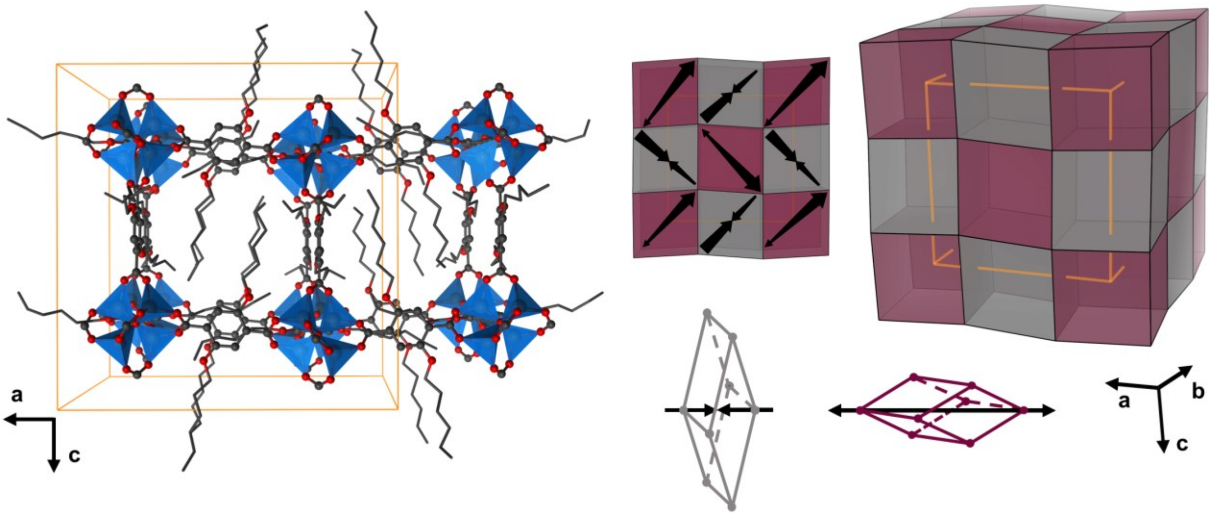

Figure 4.11: Left: SCXRD structure of *oct*-MOF-5-**OC6** (space group $Pa\bar{3}$, CCDC deposition code 2040925) with unit cell edges marked in orange colour. The two-fold disorder of the $Zn_4O(CO_2)_6$ units and the alkyl chains was removed for clarity. Right: Representations of the SCXRD structure of *oct*-MOF-5-**OC6** in front and 3-dimensional view emphasizing the alternating acute (magenta) and obtuse (grey) rhombohedral cells (i.e., the volume of one [Zn_4O(**C6O**-bdc)$_3$] repeating unit). The arrows inserted in the front view indicate the rhombohedral elongation (acute rhombohedra) or contraction (obtuse rhombohedra) axes through one of the cubic unit cells of the MOF. For further elucidation acute and obtuse rhombohedra with highlighted rhombohedral elongation or contraction axes are given at the bottom.

Moreover, the structural retransformation from the X-ray amorphous to cubic-crystalline states of *dry*-MOF-5-**OC3** and *dry*-MOF-5-**OC6** can be tracked by the naked eye from a clearing up of the formerly opaque regions of the MOF crystals (Figure 4.8). Remarkably, the mosaicity of

---

[§] An acute rhombohedron is generated by stretching (elongating) a cube along one of its four body diagonals. An obtuse rhombohedron is generated by compressing a cube along one of its four body diagonals.

the crystals does not increase after the guest-mediated crystalline-to-amorphous-to-crystalline transition (Table 4.3). This indicates that the loss of crystallinity in *dry*-MOF-5-**OCX** occurs mainly through a strain-based process, rather than cracking or bond breaking. Single crystals of the rigid $Sc_2(bdc)_3$ MOF reportedly show a similar behaviour upon reversibly transforming to an X-ray amorphous phase at pressures of 0.4 GPa.[173]

Table 4.3: Mosaicities of selected MOF-5-**OCX** single crystals.

Compound	Mosaicity / °
as-MOF-5-**OC3**	0.89
oct-MOF-5-**OC3**	0.67
as-MOF-5-**OC6**	0.86
oct-MOF-5-**OC6**	0.98

Ultimately, all the non-crystalline *dry*-MOF-5-**OCX** (**X** = 2 – 6) materials clearly recover their crystalline cubic phases when either polar or nonpolar guest molecules are reintroduced. This further demonstrates that the amorphization process upon guest-removal cannot originate from an irreversible collapse of the framework via bond dissociation but must be mediated by intra-framework dispersion interactions that are strong enough to result in a non-correlated volumetric contraction under random distortion of the framework. Furthermore, this corroborates that only small-magnitude structural distortions (such as the –3% for MOF-5-**OC7**) are feasible under retention of crystalline order. To conclude this part, the guest-depending phase behaviour of the MOF-5-**OCX** explored herein is summarized by Figure 4.12.

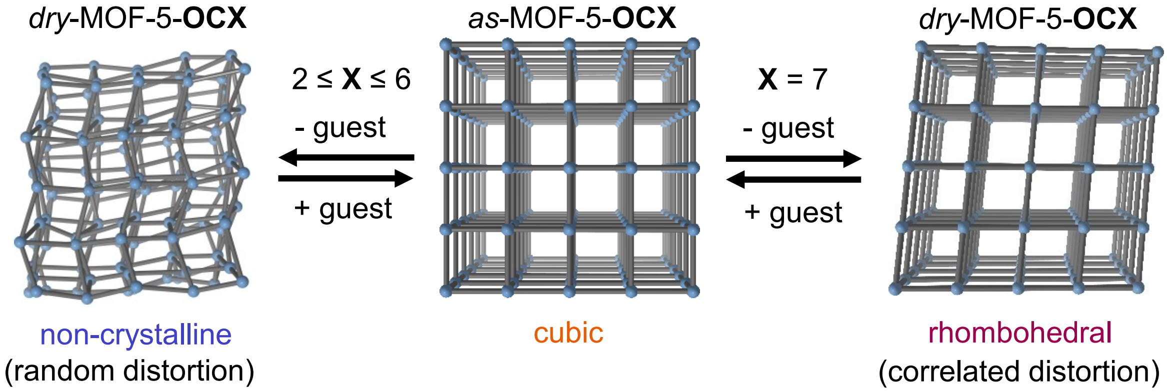

Figure 4.12: Graphical representation summarizing the guest-responsive structural behaviour of the MOF-5-**OCX** series.

4.3.2 Insights Into the Local Structure

In order to get further insights into the structural changes during the unprecedented crystalline-to-amorphous-to-crystalline transition of these MOF-5-**OCX** materials, their local structure was studied via solid-state cross polarization (CP) ^{13}C magic angle spinning nuclear magnetic resonance (MAS NMR) spectroscopy, X-ray total scattering and infrared (IR) spectroscopy. CP ^{13}C MAS NMR spectra reveal a generally heterogeneous local structure in case of non-crystalline *dry*-MOF-5-**OCX** with **X** = 2 – 5, as illustrated by the smoothly broadened signals of the carbon atoms belonging to the organic backbone of the MOFs (Figure 4.13). Heterogeneity in *dry*-MOF-5-**OC6** is apparent to a lesser extent, with defined individual features from fewer underlying configurations becoming discernible. The rhombohedral *dry*-MOF-5-**OC7** and *dry*-MOF-5-**OC8** feature sharp resonances for all carbon atoms. Apart from corroborating the above XRD data, these observations prove the overall contribution of the various MOF constituents to the amorphization at the atomic level. It is also important to note that all CP ^{13}C MAS NMR spectra establish neither breakage nor loss of the carboxylate-to-zinc coordination, even for the strongly distorted *dry*-MOF-5-**OC2** and *dry*-MOF-5-**OC3** materials, as non-coordinating carboxylate groups are expected at a chemical shift of 180-185 ppm[174].

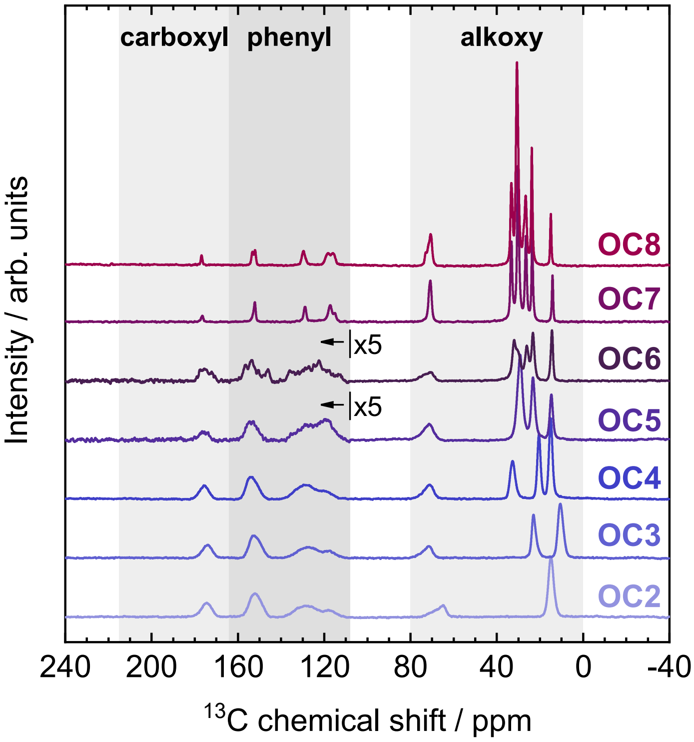

Figure 4.13: CP ^{13}C MAS NMR spectra of the *dry*-MOF-5-**OCX** with highlighted spectral regions corresponding to carboxylate, phenyl, or alkyl carbon atoms. The individual spectra are coloured according to the colour code established under section 4.3.1.

High-resolution X-ray total scattering data for all *as*-MOF-5-**OCX** and *dry*-MOF-5-**OCX** derivatives were recorded on beamline I15-1 at Diamond Light Source. From this data the total scattering structure factor *S(Q)* was obtained (the *S(Q)* functions of all materials are given in the Appendix section 8.2.4) and converted into the corresponding real-space X-ray pair distribution functions (XPDFs) in the form of *D*(*r*) by means of Fourier transformation (for details, see Materials & Methods section 6.6). For MOF-5-**OC7** there is a close resemblance of the XPDFs of the cubic (*as*) and rhombohedral (*dry*) phases up to around 15 Å, beyond which peaks originating from Zn–Zn distances across the cubic face diagonal show a characteristic change in their positions (Figure 4.14, top left).

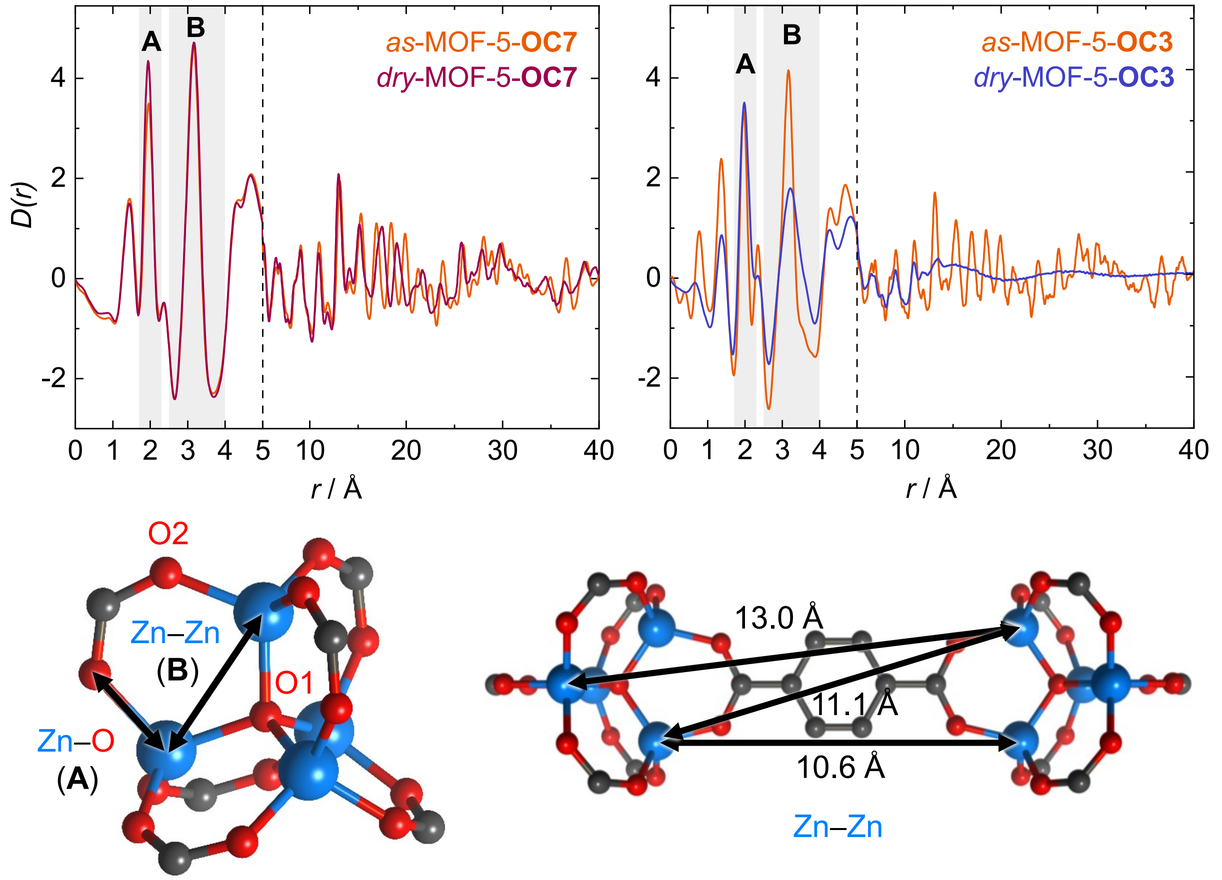

Figure 4.14: XPDFs of MOF-5-**OC7** (top, left) and MOF-5-**OC3** (top, right) in their *as*- and *dry*-states. Representations of one $[Zn_4O(O_2C)_6]$ node (bottom, left) and two $[Zn_4O(O_2C)_6]$ nodes joined by a bdc^{2-}-linker (bottom, right) with distances, within one node or between two adjacent nodes, respectively, important for the discussion marked. The latter distances correspond to the final pair-correlations observable in the XPDF of the X-ray amorphous *dry*-MOF-5-**OC3** material (top, right). Depicted structures base on the SCXRD structure of MOF-5 (CCDC deposition code 256965).

As expected for the MOF-5-**OCX** materials bearing shorter alkoxy chains (MOF-5-**OC2** to MOF-5-**OC6**), a major difference between the XPDFs of cubic (*as*) and non-crystalline (*dry*) states is found in the entire loss of correlations above $r \approx 13.5$ Å for *dry*-MOF-5-**OC2** up to $r \approx 28.3$ Å for *dry*-MOF-5-**OC6** (Figure 4.14 and Figure 4.15, Appendix section 8.2.4). The distance of 13.5 Å mainly corresponds to Zn–Zn correlations between adjacent $[Zn_4O(O_2C)_6]$ nodes (i.e., within one cavity, see Figure 4.14, bottom) since Zn–Zn pair correlations across the cubic face diagonal of one of the MOF cages possess a minimum distance of 15.0 Å, which therefore are excluded for *dry*-MOF-5-**OC2** to *dry*-MOF-5-**OC4**. The distance of 28.3 Å is in the range of two MOF cells (the term “cell”, which is defined here, refers to the volume of a single Zn_4O(**CXO**-bdc)$_3$ repeating unit of the MOF and not to a crystallographic unit cell), thus indicating the presence of very small, ordered domains of a size of about 2 × 2 × 2 MOF cells in *dry*-MOF-5-**OC6** (Figure 4.15).

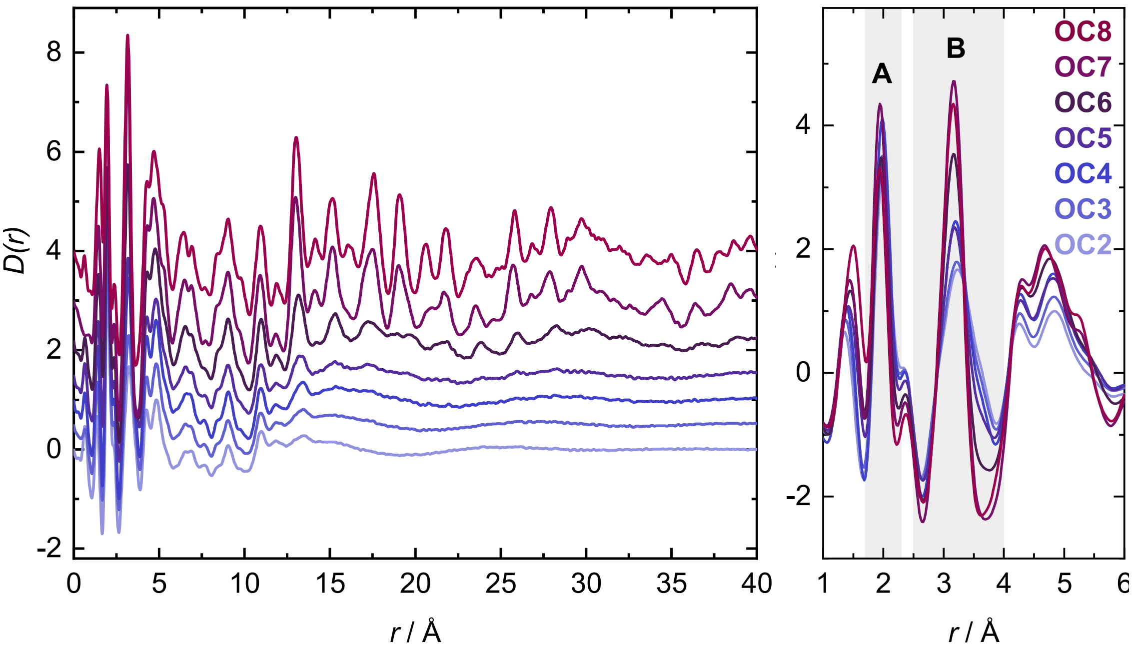

Figure 4.15: Overlay of the XPDFs of *dry*-MOF-5-**OCX** (**X** = 2 – 8) materials with emphasis on the change of the correlation length (left, XPDFs vertically offset) and the low-r region (right).

In the region below r = 4 Å, the XPDFs of all *dry*-MOF-5-**OCX** materials feature three characteristic peaks located at 1.4, 2.0 (peak **A**) and 3.1 Å (peak **B**; Figure 4.14 and Figure 4.15, right). These pair correlations are ascribed to nearest neighbour distances of C–C/C–O, Zn–O and Zn–Zn (with minor contributions from Zn–C and further Zn–O distances to the latter). Hence, these short-range distances are characteristic for the geometry of the $[Zn_4O(O_2C)_6]$ node. Guest-removal and the corresponding structural distortions induce a shift of the maximum of the Zn–Zn correlation (peak **B** in Figure 4.14 and Figure 4.15) to higher distances, while the Zn–O correlation (peak **A**) remains largely unchanged. This, in combination with a pronounced broadening of peak **B** towards higher r, clearly indicates drastic distortions of the $[Zn_4O(O_2C)_6]$ nodes in the non-crystalline frameworks. Hence, it is deduced that the loss of long-range order in these materials arises from non-correlated random distortions of these inorganic nodes, in contrast to MOF-5-**OC7** (and MOF-5-**OC8**), where the $[Zn_4O(O_2C)_6]$ nodes undergo distortions in a correlated (and thus crystalline) fashion and peak **B** consequently remains sharp and well-defined. In accordance with the PXRD data and illustrated by the peak width (Δr) of peak **B** at $D(r) = 0$, the deformation of the nodes increases with decreasing size of the DEDs (*dry*-MOF-5-**OC6**: Δr = 0.54 Å; *dry*-MOF-5-**OC2**: Δr = 0.74 Å). Furthermore, the XPDFs of n-octane-reinfiltrated samples of MOF-5-**OC3** and MOF-5-**OC6** prove that besides the recovery of the long-range correlations, the $[Zn_4O(O_2C)_6]$ nodes fully regain their structural order as well (Figure 4.16). Here, the peak **B** is even sharper than in the as-synthesized state, which is attributed to the non-coordinating nature of the n-octane guests in contrast to DMF, which is reportedly able to dynamically coordinate to the Zn^{2+} cations of the $[Zn_4O(O_2C)_6]$ nodes.[154] Since the structure of *oct*-MOF-5-**OC6** is composed of two differently rhombohedrally distorted cells, the distances of the correlations in *oct*-MOF-5-**OC6** above $r \approx 16$ Å partially resemble those of *dry*-MOF-5-**OC7** and *dry*-MOF-5-**OC8** with true rhombohedral crystallographic symmetry (Figure 4.16, right, inlet).

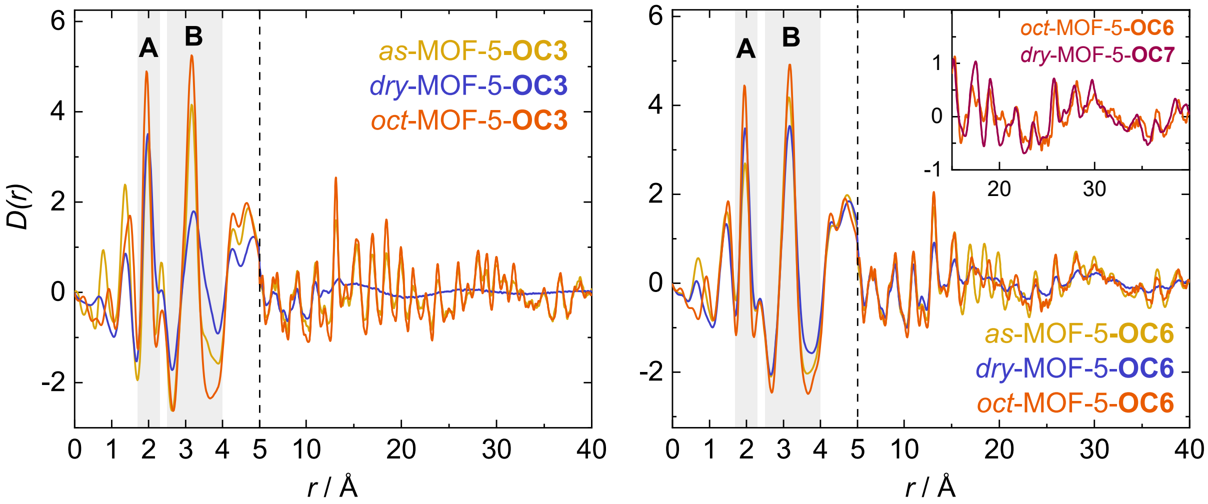

Figure 4.16: XPDFs of MOF-5-**OC3** (left) and MOF-5-**OC6** (right) in their *as*-, *dry*- and *oct*-states. Note, that the XPDFs of *as*- and *oct*-MOF-5-**OC6** show deviations in the peak positions from $r \approx 17$ Å, which is due to the different structure of *oct*-MOF-5-**OC6** (space group $Pa\bar{3}$) compared to *as*-MOF-5-**OC6** (space group $Pm\bar{3}m$) as mentioned earlier under section 4.3.1. In the inlet XPDFs of *oct*-MOF-5-**OC6** and *dry*-MOF-5-**OC7** are overlayed to elucidate the rhombohedral character of the local structures of both materials.

A similar picture can be drawn from IR spectroscopic data by analysis of the characteristic stretching modes ν_{as}(Zn-O1) and ν_s(Zn-O2) of the $[Zn_4O(O_2C)_6]$ nodes at 517 and 576 cm^{-1}, as well as ν_{as}(COO) of the coordinating carboxylates at 1571-1601 cm^{-1} (Figure 4.17, full IR spectra are given in the Appendix section 8.2.5).[175,176] Particularly, the ν_{as}(Zn-O1) vibration is considered a fingerprint mode of the $[Zn_4O(O_2C)_6]$ unit in MOF-5[175] but also for a huge variety of analogous monocarboxylate complexes ($[Zn_4O(O_2CR)_6]$, R = e.g., methyl, ethyl, *i*-butyl) of the same geometry.[176,177] Since the ν_{as}(Zn-O1) mode is threefold degenerate in case of ideal T_d symmetry of the $[Zn_4O(O_2C)_6]$ cluster, such as in guest-free MOF-5, this vibrational mode is highly affected by a lowering of its symmetry due to distortion.[176]

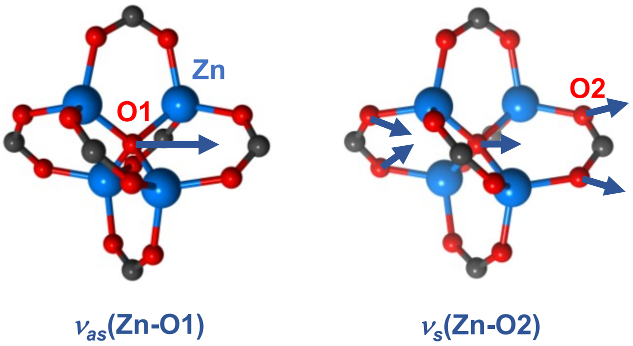

Figure 4.17: Simplified vector representation of the main contributions to the ν_{as}(Zn-O1) and ν_s(Zn-O2) stretching modes of the $[Zn_4O(O_2C)_6]$ nodes according to Civalleri, et.al.[175]

The rhombohedrally distorted *dry*-MOF-5-**OC7** and *dry*-MOF-5-**OC8** display sharp and well-defined bands of the ν_{as}(Zn-O1) and ν_{s}(Zn-O2) vibrations, whereas the non-crystalline *dry*-MOF-5-**OCX** materials feature only a broad band of increasing width when following the series from *dry*-MOF-5-**OC6** to *dry*-MOF-5-**OC2** (Figure 4.18, top left). This establishes a reduction of symmetry of the $[Zn_4O(O_2C)_6]$ nodes and might further indicate the presence of differently deformed clusters in the non-crystalline solids. In line with the XPDF data, the increasing width of the vibrational bands suggests a successively increasing distortion of the nodes from *dry*-MOF-5-**OC6** to *dry*-MOF-5-**OC2**. By contrast, resolvated (and again crystalline) *oct*-MOF-5-**OCX** display sharp bands of the ν_{as}(Zn-O1) and ν_{s}(Zn-O2) vibrations akin to those of perfectly crystalline MOF-5 (Figure 4.18, top right).

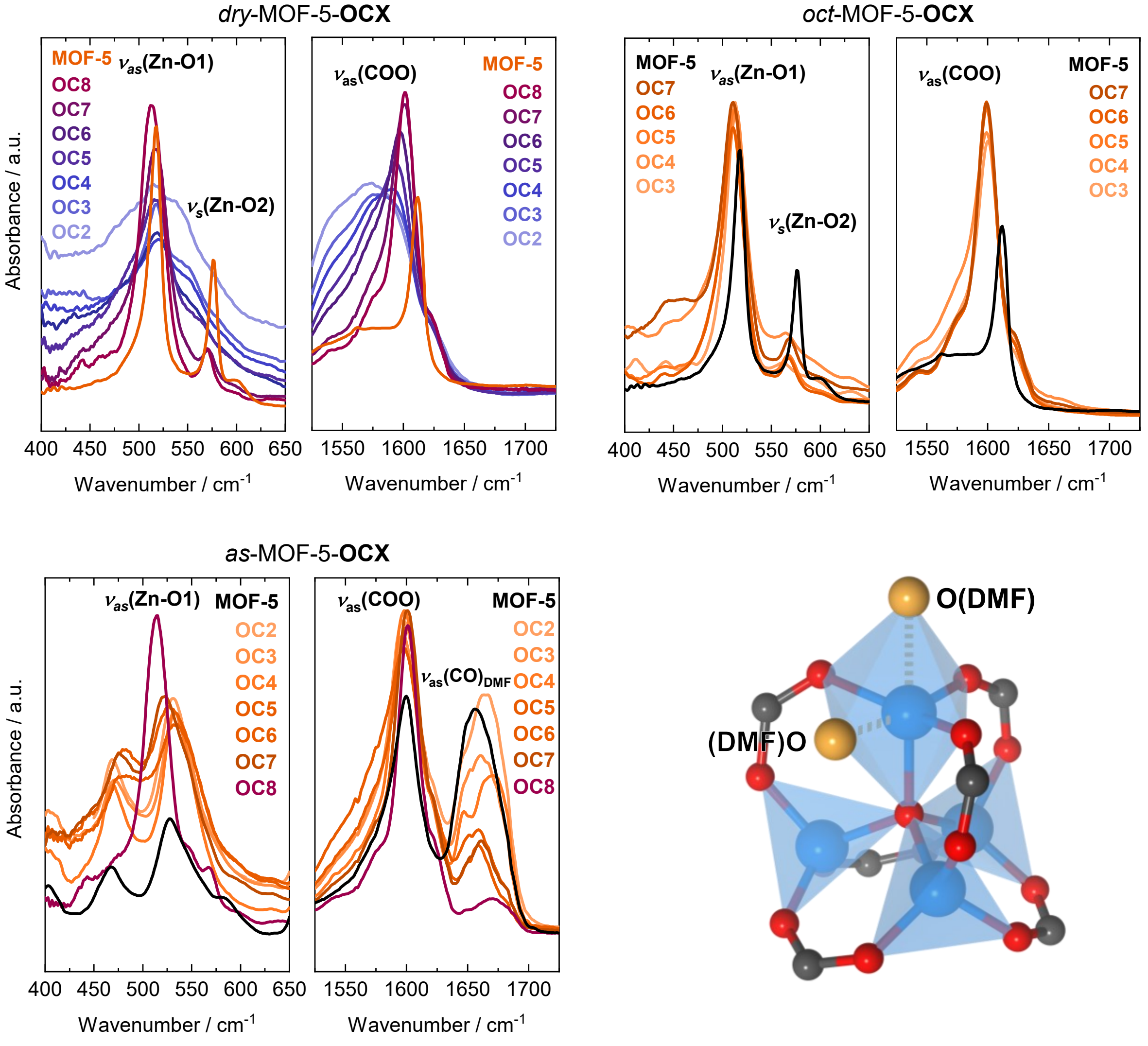

Figure 4.18: Excerpts from the IR spectral regions showing the ν_{as}(Zn-O1) and ν_{s}(Zn-O2) and the ν_{as}(COO) vibrational bands of the *dry*-MOF-5-**OCX** (top, left), the *oct*-MOF-5-**OCX** (top, right) and the *as*-MOF-5-**OCX** (bottom) in comparison with MOF-5. The ν_{as}(CO)$_{DMF}$ band was assigned according to the literature.[178] Bottom, right: Structural representation of a DMF-coordinated $Zn_4O(CO_2)_6$ unit in accordance with literature reports.[154] O atoms of the coordinating DMF molecules are coloured in yellow.

Hence, the T_d symmetry of the [$Zn_4O(O_2C)_6$] building unit is fully restored upon guest re-adsorption. Note that the spectral region of the ν_{as}(Zn-O1) and ν_s(Zn-O2) vibrations of the as-synthesized MOF-5-**OCX** features entirely different and wider bands with two apparent maxima at about 470 cm^{-1} and 530 cm^{-1} (Figure 4.18, bottom). This observation likely relates to the coordination of the DMF guest molecules to the zinc cations of the $Zn_4O(CO_2)_6$ unit causing the vibrational band patterns to change due to the reduced symmetry of the building unit and the additional band broadening by the dynamic nature of the DMF coordination.[154,155] Results of molecular dynamics (MD) simulations on this matter suggest that a single Zn^{2+} of the $Zn_4O(CO_2)_6$ unit can readily be coordinated by two DMF molecules, whereas only one Zn^{2+} of a $Zn_4O(CO_2)_6$ unit is involved in the interaction with DMF at the same time. It is also suggested, that the binding and release of DMF is highly dynamic and does not influence the structural integrity of the building unit.[154] Interestingly, *as*-MOF-5-**OC8** gives a sharp ν_{as}(Zn-O1) band indicating no interactions of the [$Zn_4O(CO_2)_6$] with DMF in this material.

Furthermore, the ν_{as}(COO) band of *dry*-MOF-5-**OCX**, which is sensitive towards the symmetry of the carboxylate-to-zinc coordination was investigated and shows a similar broadening with FWHM values spread from 47 cm^{-1} (*dry*-MOF-5-**OC6**) to 91 cm^{-1} (*dry*-MOF-5-**OC2**) as well as a simultaneous shift of the band maxima from 1597 cm^{-1} (*dry*-MOF-5-**OC6**) to 1571 cm^{-1} (*dry*-MOF-5-**OC2**) (Table 4.4). These findings further demonstrate changes in carboxylate-to-zinc coordination bonds associated with the deformation of the [$Zn_4O(O_2C)_6$] nodes[176,179].

Table 4.4: FWHM and maxima of the ν_{as}(COO) bands extracted from the IR spectra of the *dry*-MOF-5-**OCX**.

X	FWHM / cm^{-1}	$\nu_{as}(COO)_{max}$ / cm^{-1}
2	91	1571
3	88	1577
4	80	1590
5	62	1594
6	47	1597
7	39	1601
8	19	1602

Finally, the findings presented in this part demonstrate that the structural response of the *dry*-MOF-5-**OCX** (**X** = 2 – 6) is facilitated by distortions of the [$Zn_4O(O_2C)_6$] nodes on a local scale. Occurring in a non-correlated fashion as an ensemble of differently distorted clusters, this macroscopically manifests in the loss of the long-range order of these materials when devoid of guest molecules.

4.3.3 Molecular Dynamics Simulations**

To complete the thermodynamic picture and to develop an atomistic understanding of the structural behaviour of the MOF-5-**OCX** materials series molecular dynamics (MD) simulations were performed. The results of these simulations, which are crucial for the further scientific discussion are briefly summarized within this section. For further details on the MD simulation procedures, see the footnote and the references linked therein.

The MD simulations were performed using the MOF-FF[180] force field, which has been developed recently to describe structural transformations in DED-functionalized DMOF-1 based materials such as those presented in chapter 3 of this thesis.[105] Due to the numerical effort for these simulations only a limited simulation time (ca. 20 ns) was possible. Therefore, the application of pressure on the simulation cell was used to enforce the formation of the contracted states of the MOF-5-**OCX** within the timescales of the simulation.[57,112,161,181,182] Within periodic boundary conditions (pbc) small simulation cells (2x2x2) were used to extract the underlying thermodynamics, whereas larger simulation cells (8x8x8) were employed only for selected MOF-5-**OCX** (**X** = 3, 6) materials, to compare with the experimental X-ray diffraction and total scattering data.

Besides a global minimum in their cubic phase, the computed free energy profiles reveal a metastable state at a lower cell volume for the MOF-5-**OCX** materials with **X** = 2 – 5 and a shallow energy barrier connecting these states, hence, indicating the possibility of a structural deformation (Figure 4.19, left). Importantly, the driving force for this is clearly identified as the internal energy (Figure 4.19, right) mediated by the DED groups, since the extracted internal energies for all MOF-5-**OCX**, except for MOF-5-**OC8**, feature their global minimum at a volume corresponding to the contracted state.

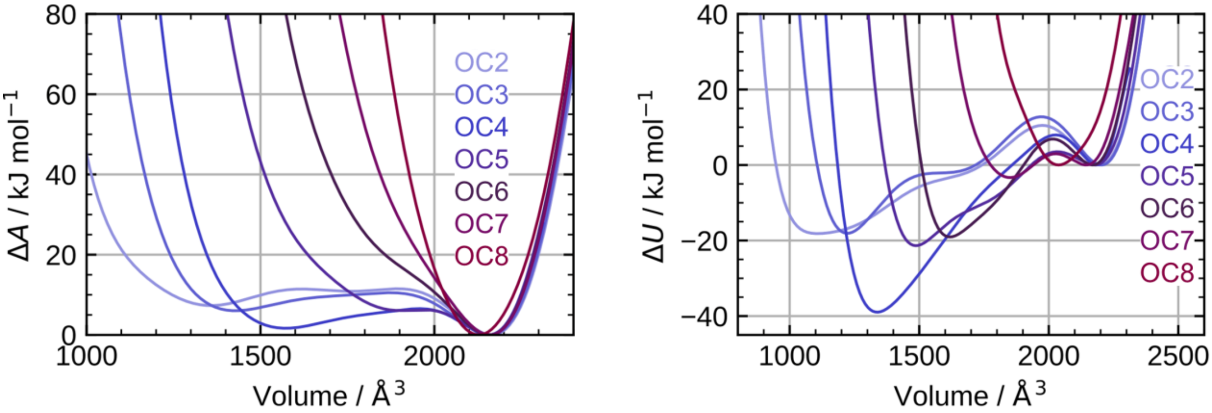

Figure 4.19: Important results from the MD simulations of the MOF-5-**OCX** materials (2x2x2 cell simulation boxes). Free energy ΔA (left) and internal energy ΔU (right) profiles with respect to volume obtained from the simulations.

** The results presented in this section arose in collaboration with J. Keupp and R. Schmid and are likewise part of the publications mentioned at the advent of this chapter. All simulations were run by J. Keupp and jointly interpreted by R. Schmid, J. Keupp, S. Henke and R. Pallach. This section is largely based on the publication part, which was written by J. Keupp and is also part of his PhD thesis: *Flexible, Responsive Metal-Organic Frameworks*: A Computational Investigation, Ruhr-Universität Bochum, 2020.

Moreover, the simulations performed with 8x8x8 cell box size show the same tendency towards a contracted phase of the MOF-5-**OC3** and MOF-5-**OC6** materials (Figure 4.20, top). From the broad distribution of individual cell volumes and angles, and their weak spatial correlation within the simulation box, a strong heterogeneity of these contracted phases is evident (Figure 4.20, middle). This corroborates the experimentally observed strong local heterogeneity and the loss of long-range order.

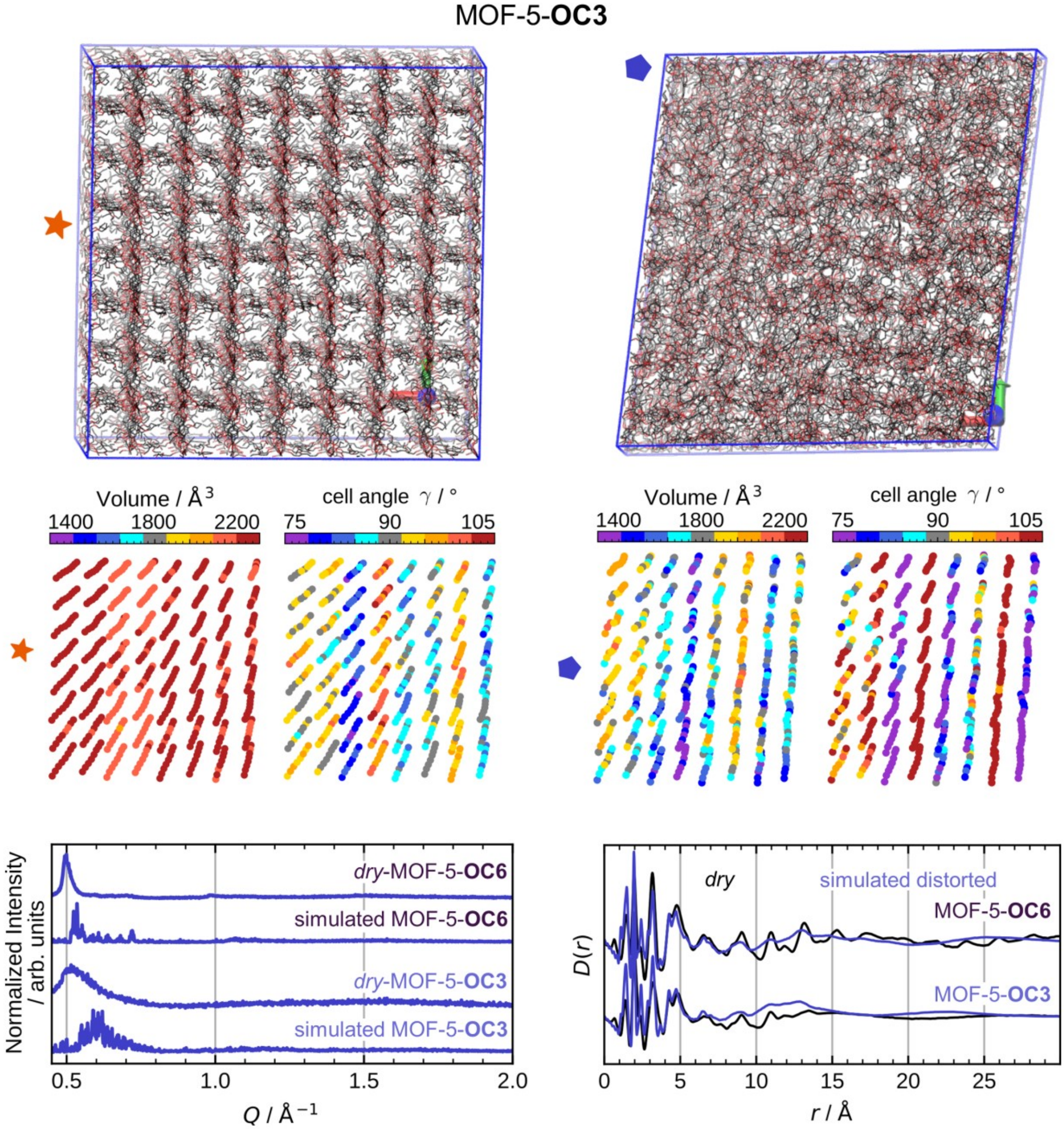

Figure 4.20: Compilation of results of the MD simulations performed for the MOF-5-**OCX** materials series. Top: Side view of a large, 8x8x8 simulation box of MOF-5-**OC3** before (orange star) and after (blue pentagon) the pressure-induced phase transformation. Middle: Individual cell volumes and angles of the MOF-5-**OC3** simulation boxes. Bottom: Simulated vs. measured PXRD patterns and XPDFs, respectively, for *dry*-MOF-5-**OC3** and -**OC6**. The simulated PXRD patterns and XPDFs were obtained via averaging of several simulation snapshots.

Remarkably, averaged PXRD patterns and XPDFs, simulated from snapshots of these contracted states, show substantial analogy to the experimental data presented above (for comparison, see Figure 4.20, bottom).
Overall, these results clearly corroborate that the postulated framework-connectivity preserving loss of long-range order driven by intra-framework dispersion forces is plausible for the MOF-5-**OCX** materials series.

4.3.4 Thermal Behaviour

The dispersion interactions introduced by the DEDs are apparently strong enough to outbalance the energetic cost for the deformation of the nodes, so that the contracted *dry*-MOF-5-**OCX** materials (either non-crystalline or rhombohedral) are enthalpically favoured in the guest-free state (Figure 4.12). Synchrotron radiation variable temperature (VT-)PXRD data recorded at DELTA (λ = 0.6199 Å) or DESY (λ = 0.2073 Å) reveal that vibrational entropy can outbalance the enthalpic stabilisation of the contracted phases, resulting in a return to the expanded cubic phases at elevated temperatures. *Dry*-MOF-5-**OC8** and *dry*-MOF-5-**OC7** undergo fully reversible rhombohedral-to-cubic phase transitions within temperature regimes of 425-450 K and 300-325 K, involving small volume changes of +1.5% and +2.0% as determined via Pawley refinement of the PXRD patters immediately before and after the phase transitions (Figure 4.21, profile fit parameters are given in the Appendix section 8.2.7).

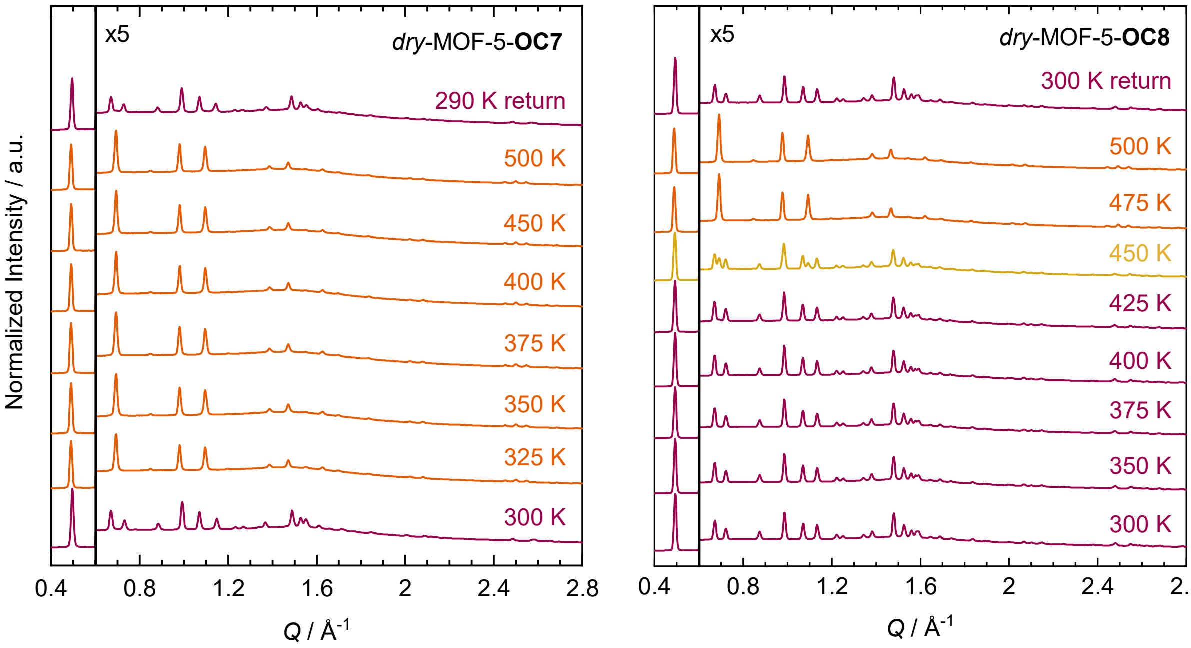

Figure 4.21: Variable temperature (VT-)PXRD data of *dry*-MOF-5-**OC7** (left) and *dry*-MOF-5-**OC8** (right) collected at DESY.

The phase transition temperatures ($T_{rh\rightarrow c}$) of the endothermic rhombohedral-to-cubic transitions were determined by DSC as 435 K and 323 K (onset temperature of the calorimetric peak) for *dry*-MOF-5-**OC8** and *dry*-MOF-5-**OC7**, respectively (Figure 4.22, Table 4.5), being in good agreement with the VT-PXRD data. Both the $T_{rh\rightarrow c}$ and the associated enthalpy and entropy changes ($\Delta H_{rh\rightarrow c}$ and $\Delta S_{rh\rightarrow c}$) are higher for *dry*-MOF-5-**OC8** compared to *dry*-MOF-5-**OC7**, indicating stronger intra-framework dispersion interactions of the material with the longer alkyl chains, which need to be overcome by means of vibrational entropy to initiate the rhombohedral-to-cubic phase transitions (Table 4.5).

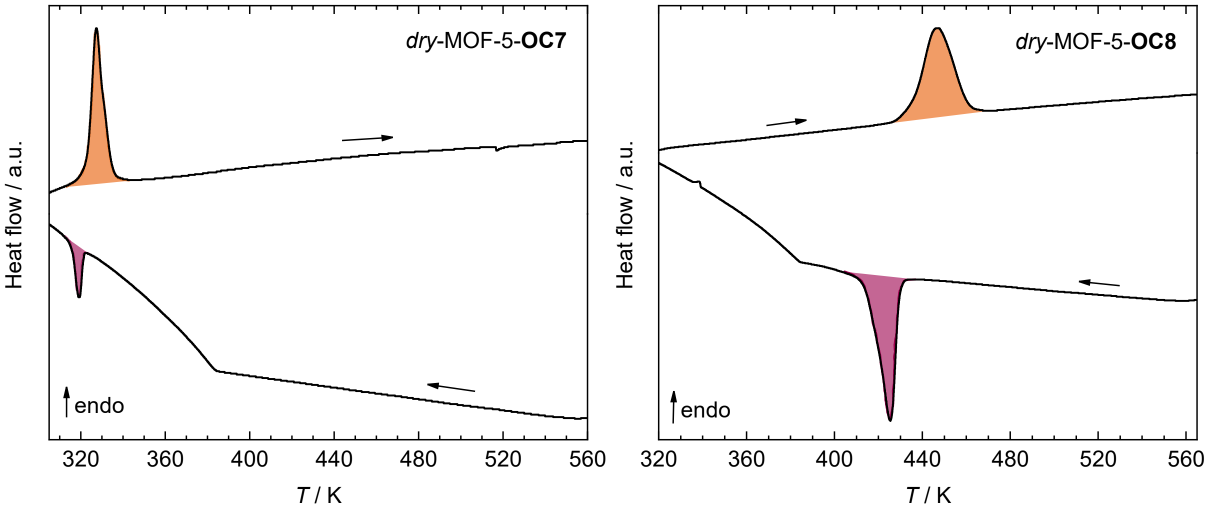

Figure 4.22: DSC data of *dry*-MOF-5-**OC7** (left) and *dry*-MOF-5-**OC8** (right) used for the determination of $T_{rh\rightarrow c}$ and $\Delta H_{rh\rightarrow c}$ recorded with a heating rate of 10 K min^{-1}.

Table 4.5: Thermodynamic data of *dry*-MOF-5-**OC7** and *dry*-MOF-5-**OC8** obtained from DSC scans. The phase transition temperatures are determined at the peak onset of the calorimetric signal.

Compound		ΔH / kJ mol^{-1}	ΔS / J K^{-1} mol^{-1}	$T_{rh\rightarrow c}$ / $T_{c\rightarrow rh}$ / K
dry-MOF-5-**OC7**	*up scan*	9.7	30.1	323
	down scan	–7.7	–23.9	321
dry-MOF-5-**OC8**	*up scan*	23.1	53.2	435
	down scan	–19.8	–46.0	429

In contrast, the non-crystalline *dry*-MOF-5-**OC6** shows a very different structural behaviour upon heating. The broad scattering peaks in its PXRD pattern constantly get sharper and increase in intensity when the material is heated from 300 to 500 K (Figure 4.23).

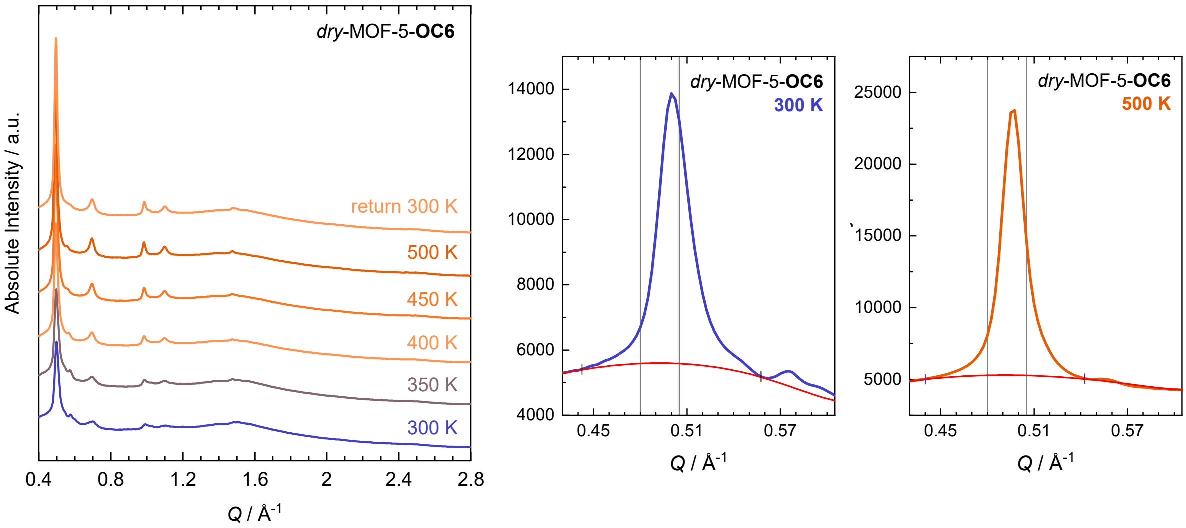

Figure 4.23: Variable temperature (VT-)PXRD data of *dry*-MOF-5-**OC6** collected at DESY. All patterns were collected with the very same exposure time. Zoomed regions of the PXRD patterns at 300 K (centred) and 500 K (right) show the FSP of *dry*-MOF-5-**OC6** with the baseline (red) used for its integration. The grey lines were added as a guide to the eye to elucidate the shift of the peak maximum.

At 500 K, fairly sharp reflections, which can be indexed in the cubic unit cell of the crystalline derivative *as*-MOF-5-**OC6** are evident. Over the range from 300 to 500 K the FSP at $Q \approx 0.5$ Å^{-1} continuously shifts to lower scattering angles, its integrated intensity increases by 72% and the peak half width decreases by over 30% (Figure 4.23, centre and right, Table 4.6).

Table 4.6: Integral, FWHM values and the maximum of the FSP of *dry*-MOF-5-**OC6** at different temperatures at identical exposure times of the same sample.

T / K	Integral / a.u.	FWHM / Å^{-1}	Q_{FSP} / Å^{-1}	d_{FSP}
300	464.7	0.026	0.501	12.57
500	797.5	0.018	0.494	12.73

Consequently, *dry*-MOF-5-**OC6** shows a continuous transformation from the non-crystalline to the cubic phase upon heating. In the absence of an exchange of latent heat in DSC experiments (Figure 4.24, left) this behaviour is interpreted as a second-order phase transition, i.e., a continuous structural change of the randomly distorted non-crystalline framework towards the crystalline cubic phase. Interestingly, the reverse transformation from the crystalline to the non-crystalline state of *dry*-MOF-5-**OC6** does not instantaneously occur upon cooling to room temperature. Instead, it takes place in a slow and gradual fashion (over about 1 d at 300 K), signifying a slow relaxation to the enthalpically favoured non-crystalline state (Figure 4.24, right).

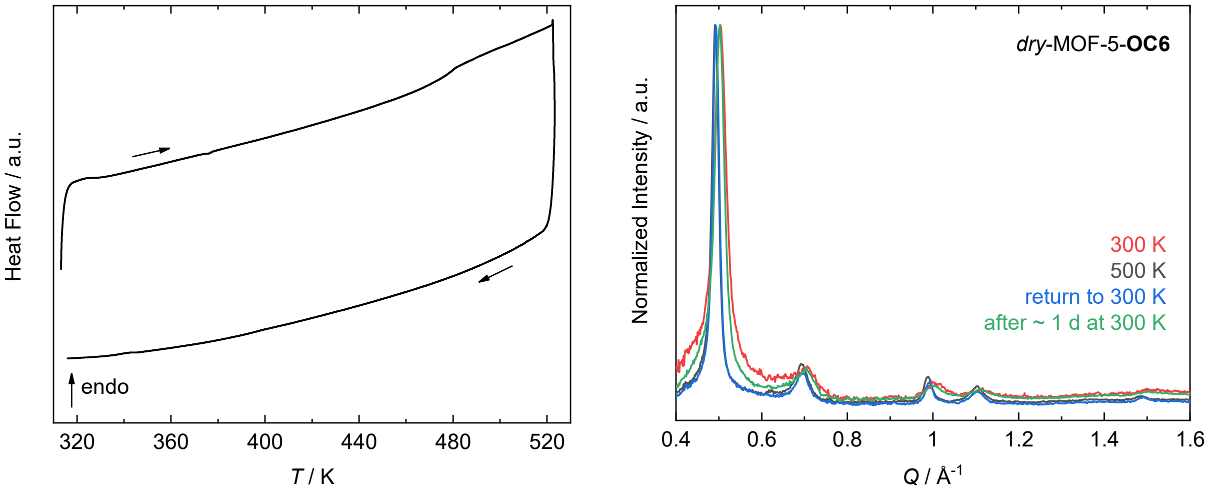

Figure 4.24: DSC data of *dry*-MOF-5-**OC6** (left). VT-PXRD data of *dry*-MOF-5-**OC6** recorded at DELTA elucidate the slow relaxation kinetics of its thermally induced non-crystalline-to-cubic transition (right). The VT-PXRD pattern collected immediately after returning to 300 K strongly resembles the one collected at 500 K. However, after letting the sample rest for about 1 d at room temperature, the PXRD pattern is very similar to the one recorded prior to the heat treatment.

Investigations of the local structure as a function of temperature via VT-XPDF similarly indicate an increase of the long-range correlations within the material at higher temperatures (Figure 4.25, for the *S(Q)* data, see Appendix Figure 8.57). Especially, this is evident from the peak emerging at $r \approx 41$ Å. Furthermore, changes in the low r regions of the PDFs, i.e., the slight sharpening of the peak B, likewise point towards the recovery of the symmetry of the $Zn_4O(CO_2)_6$ nodes with increasing temperature.

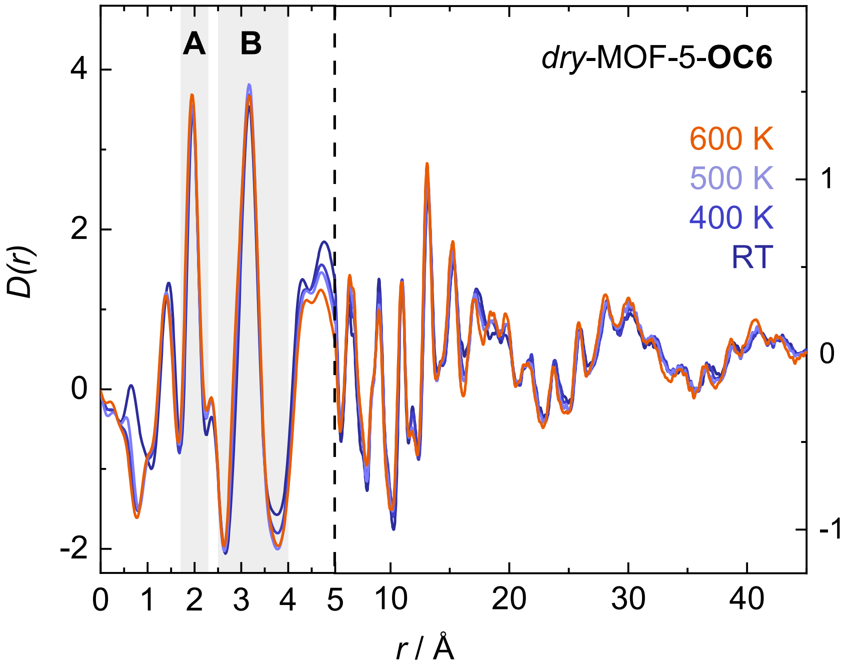

Figure 4.25: Variable-temperature (VT-) XPDFs of *dry*-MOF-5-**OC6** recorded in the range from RT to 600 K. For this data no temperature calibration was performed, hence the given temperatures are markedly overestimated (except for room temperature). The XPDF data are scaled differently from $r = 5$ Å onward to enhance the visibility of changes in the XPDFs at high r.

The thermal behaviour of *dry*-MOF-5-**OC6** is counterintuitive and inverse to the thermal behaviour of conventional materials. Materials typically lose crystallinity with rising temperature, on the most fundamental level due to increasing thermal motions, which result in the attenuation of diffracted X-rays as has been firstly described by DEBYE[183] and further refined by WALLER[184]. In addition to that, entropy-driven defect formation and eventually amorphization or melting lead to losing crystallinity at increased temperatures. For *dry*-MOF-5-OC6 the opposite behaviour is observed. Due to its frustrated framework structure, the contracted, non-crystalline phase is the enthalpically favoured ground state at room temperature. Increasing the temperature results in a population of vibrational degrees of freedom, which counteract the intra-framework dispersion interactions and thus allow the framework backbone to relax (or re-order) towards the expanded crystalline phase. Consequently, this finds expression in the form of increased Bragg-scattering intensity and a shift of the FSP towards lower scattering angles. Thus, in the case of *dry*-MOF-5-**OC6**, the crystalline high-temperature phase must have a higher entropy than the non-crystalline distorted phase. In other words, the configurational entropy of the non-crystalline phase (static disorder) is outbalanced by the vibrational entropy of the crystalline phase (dynamic disorder) at high temperature.

Importantly, the thermal behaviour of *dry*-MOF-5-**OC5** and *dry*-MOF-5-**OC4** is closely related to that of *dry*-MOF-5-**OC6**, even though the sharpening of the reflections with temperature gets less prominent with decreasing **X** (Figure 4.26). For the more heavily distorted *dry*-MOF-5-**OC3** to *dry*-MOF-5-**OC2** there could not be observed a structural response towards the elevated temperatures applied here (the corresponding VT-PXRD data are given in the Appendix section 8.2.7). Hence, it may be that the temperatures required for the transition from the non-crystalline to the cubic phase are beyond the decomposition temperatures (T_d) of the materials ($T_\mathrm{d} \approx 605$ K).[185,186]

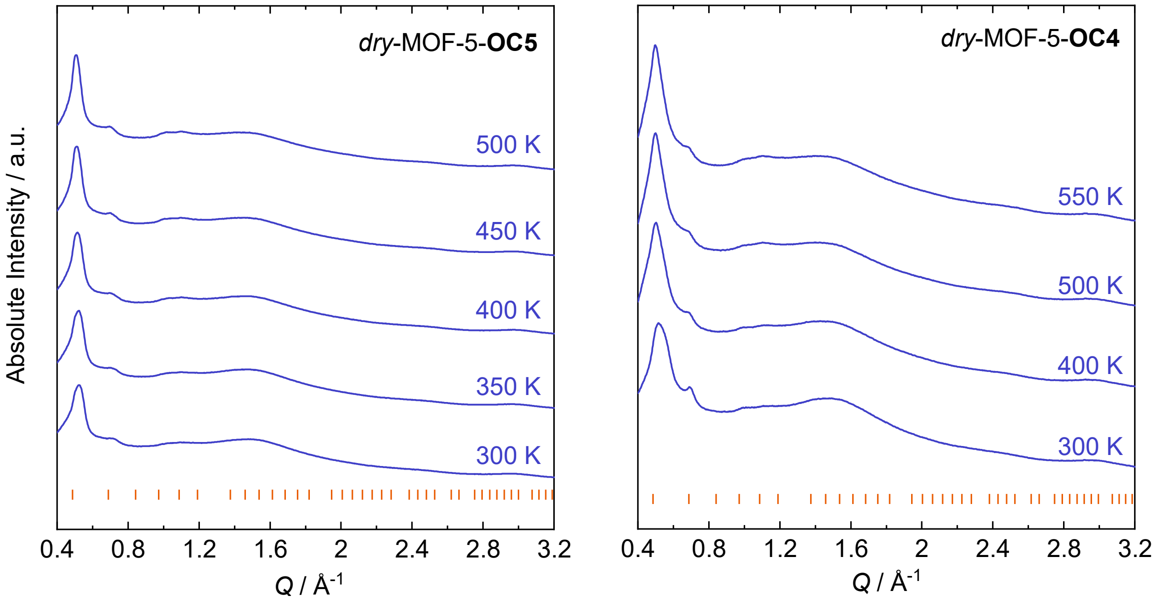

Figure 4.26: VT-PXRD patterns recorded of a dried sample of MOF-5-**OC5** and MOF-5-**OC4** recorded at DESY. Tick marks correspond to positions of allowed Bragg reflections of the corresponding as-synthesized phase of the MOFs.

Interestingly, and in accordance with their structural behaviour, the decomposition temperatures of the *dry*-MOF-5-**OCX** determined as the onset of the decomposition peak from simultaneous TG-DSC experiments decrease from *dry*-MOF-5-**OC8** to *dry*-MOF-5-**OC2** (Table 4.7, the full TG-DSC data are given in the Appendix, Section 8.2.6). Here, *dry*-MOF-5-**OC7** and *dry*-MOF-5-**OC8** possess about the same decomposition temperature, which then constantly decreases from *dry*-MOF-5-**OC6** downwards, clearly indicating that the weakening of the Zn-carboxylate bonds due to the non-correlated structural distortion of the materials facilitates the materials' decomposition.

Table 4.7: Decomposition temperatures (T_d) of the *dry*-MOF-5-**OCX** determined from TG-DSC experiments as the onset temperatures of the decomposition peak. Full TG-DSC data are given in the Appendix.

Compound	T_d / K
dry-MOF-5-**OC2**	587
dry-MOF-5-**OC3**	587
dry-MOF-5-**OC4**	592
dry-MOF-5-**OC5**	600
dry-MOF-5-**OC6**	614
dry-MOF-5-**OC7**	680
dry-MOF-5-**OC8**	681

4.3.5 Gas Sorption Properties

The porosity of the *dry*-MOF-5-**OCX** materials was analysed by N_2 (77 K), CO_2 (195 K) and *n*-butane (293 K) gas sorption experiments. Only *dry*-MOF-5-**OC2** and *dry*-MOF-5-**OC3** are able to adsorb N_2 at 77 K showing type I isotherm shape (capacity of ca. 200 – 250 cm^3 g^{-1} at saturation, for corresponding Langmuir and BET[187] surface areas, see Table 4.8, for experimental details, see Materials & Methods 6.10), whereas all other derivatives only show N_2 adsorption on the external surface (Figure 4.27, right) as evident from the low uptake (maximum uptake 20 cm^3 g^{-1}) and the nearly linear shape of the isotherms.

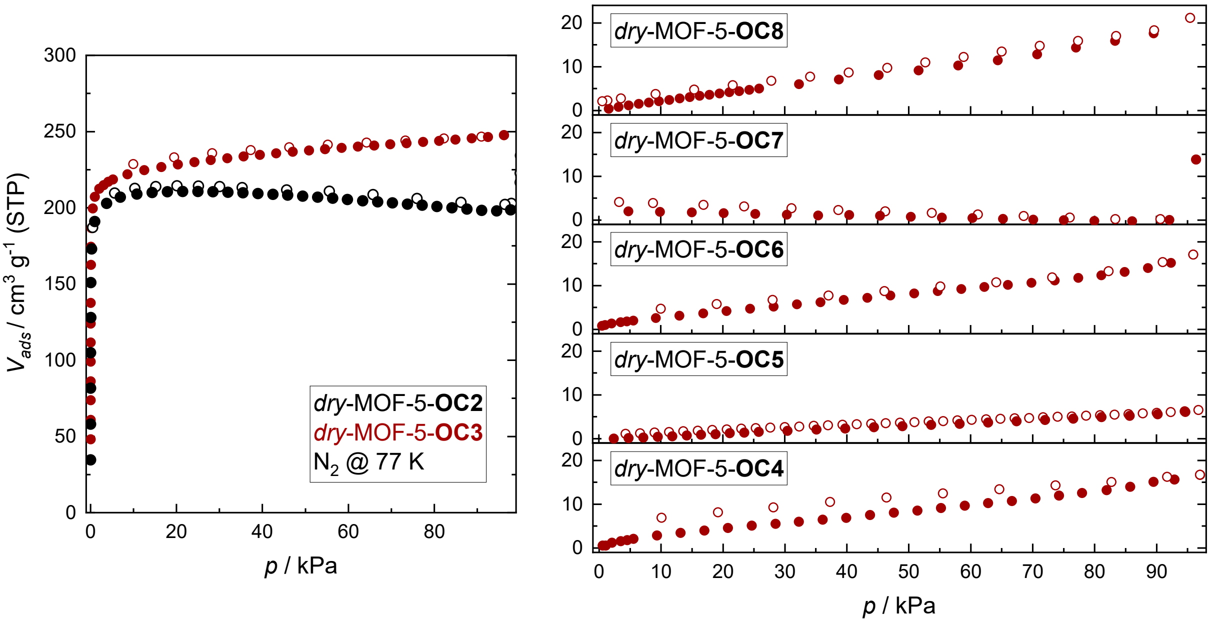

Figure 4.27: N_2 sorption isotherms of *dry*-MOF-5-**OC2** and *dry*-MOF-5-**OC3** (left) and *dry*-MOF-5-**OC4** to *dry*-MOF-5-**OC8** (right) recorded at 77 K. Adsorption and desorption branches are shown with closed and open symbols. Please note, that the drop of the N_2 uptake in the range from 30 to 100 kPa in the isotherm of *dry*-MOF-5-**OC2** is likely caused by one of the two following scenarios: (i) An error in the void volume measurement or (ii) a small leak in the measurement cell (microcrack in the glass or a faulty sealing ring). The drop in uptake amounts to about 5%. Due to this measurement error, the Langmuir and BET surface areas of *dry*-MOF-5-**OC2** (see below) are unreliable.

Table 4.8: Langmuir and BET surface areas of *dry*-MOF-5-**OC2** and *dry*-MOF-5-**OC3** calculated from the isothermal N_2 sorption data.

	S_{Langmuir} / m^{2}g^{-1}	S_{BET} / m^{2}g^{-1}
dry-MOF-5-**OC2**	919	842
dry-MOF-5-**OC3**	1159	911

However, all *dry*-MOF-5-**OCX** derivatives readily adsorb CO_2 at 195 K, featuring Type I isotherms with constantly decreasing quantities of adsorbed gas from *dry*-MOF-5-**OC2** to *dry*-MOF-5-**OC8** (Figure 4.28, left). This behaviour can be ascribed to the overall higher measurement temperature compared to N_2 resulting in faster adsorption kinetics and the slightly smaller kinetic diameter of the CO_2 molecule.[188] The corresponding BET surface areas (Table 4.9) range from 895 m^2 g^{-1} (**X** = 2) to 159 m^2 g^{-1} (**X** = 8).

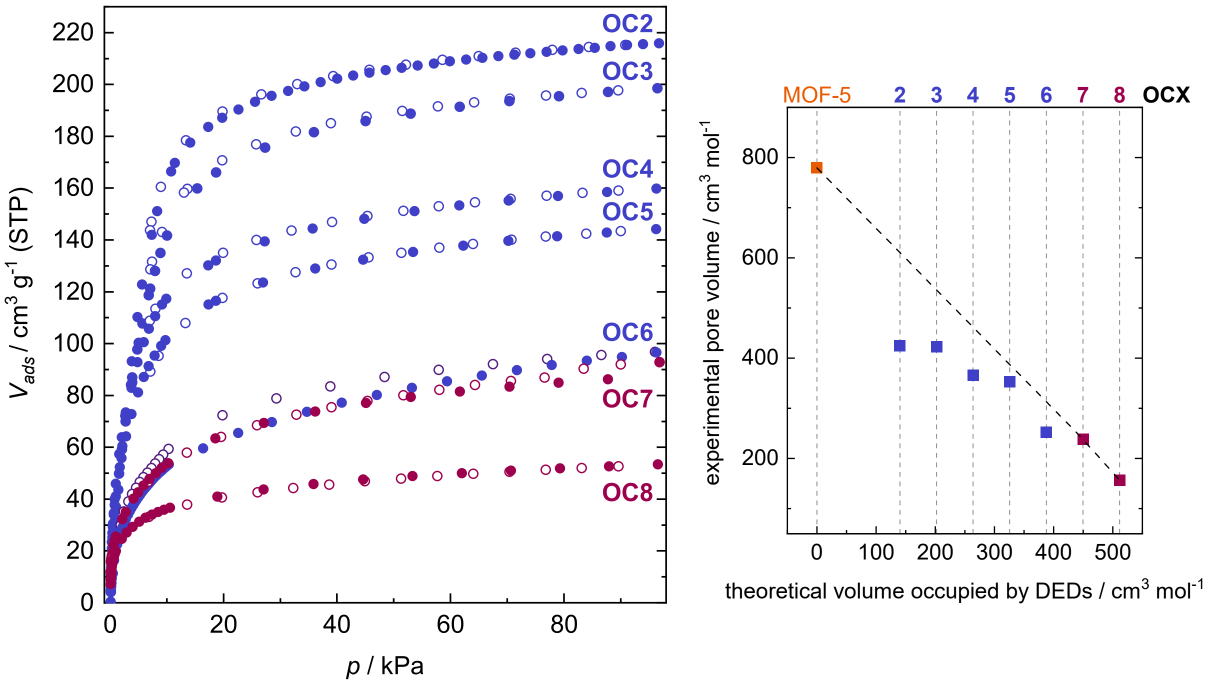

Figure 4.28: CO_2 sorption isotherms of *dry*-MOF-5-**OC2** to *dry*-MOF-5-**OC8** recorded at 195 K (left). Adsorption and desorption branches are shown with closed and open symbols. Plot of the experimental pore volumes (CO_2) vs. the theoretical volume occupied by DEDs in *dry*-MOF-5-**OCX** (right). The dashed line signifies the expected pore volumes obtained by linear interpolation from MOF-5 to *dry*-MOF-5-**OC8**.

Table 4.9: Langmuir and BET surface areas of *dry*-MOF-5-**OC2** to *dry*-MOF-5-**OC8** and MOF-5 were calculated from CO_2 sorption isotherms (195 K). The BET calculation has not been performed for MOF-5 because of the unusual shape of its CO_2 isotherm (Appendix Figure 8.88).

	S_{Langmuir} / m^{2}g^{-1}	S_{BET} / m^{2}g^{-1}
dry-MOF-5-**OC2**	1041	866
dry-MOF-5-**OC3**	978	754
dry-MOF-5-**OC4**	797	575
dry-MOF-5-**OC5**	697	517
dry-MOF-5-**OC6**	489	309
dry-MOF-5-**OC7**	427	291
dry-MOF-5-**OC8**	258	180
MOF-5	2534	-

Considering that the sorption process does not cause any substantial structural responses of the framework, as demonstrated by *in-situ* PXRD experiments under CO_2 atmosphere at 195 K (for the PXRD patterns, see Figure 4.29 and Appendix Figure 8.89), the correlation between the pore volumes determined from the CO_2 sorption isotherms (for details on the extraction of the pore volumes, see Materials & Methods 6.10) and the volumes theoretically occupied by the alkoxy groups, here in terms of their Connolly solvent-excluded volume (CSEV) (for details on their determination see Materials & Methods 6.10) was examined.

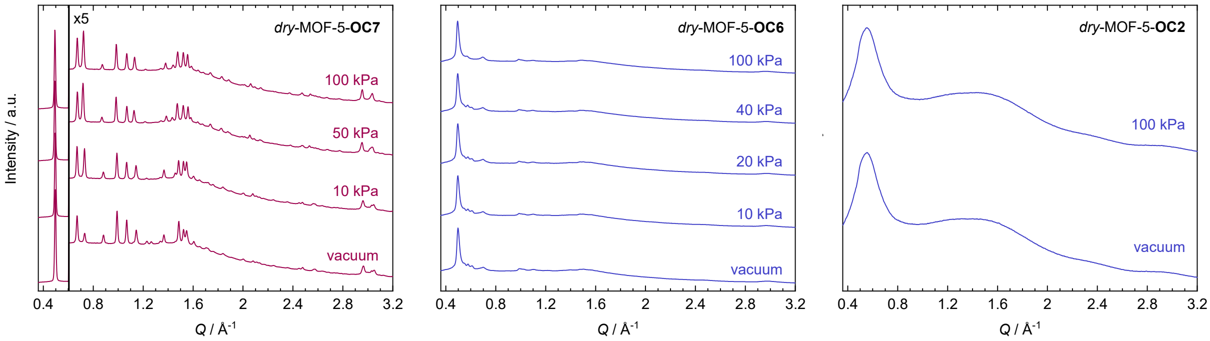

Figure 4.29: Exemplary *in-situ* CO_2 sorption PXRD patterns of *dry*-MOF-5-**OC7**, *dry*-MOF-5-**OC6** and *dry*-MOF-5-**OC2** recorded at DESY. The *in-situ* CO_2 sorption PXRD data of *dry*-MOF-5-**OC3** to **-OC5** and *dry*-MOF-5-**OC8** are given in the Appendix, Figure 8.89.

With the inclusion of MOF-5, a non-linear relationship becomes apparent, since the experimental pore volumes of the non-crystalline derivatives with shorter alkoxy substituents (**C2** - **C6**) are significantly lower than expected from the linear interpolation between MOF-5 and *dry*-MOF-5-**OC8** (Figure 4.28, right, dashed line). The latter was used for interpolation because it shows a relatively small volume contraction (approximately 1.5% compared to the cubic phase). Moreover, the deviation from the expected pore volume gets stronger with decreasing chain lengths. We ascribe this to increasing structural deformation (and thus contraction) when proceeding from *dry*-MOF-5-**OC6** to *dry*-MOF-5-**OC2**. Based on the experimental pore volumes, a volume contraction of the *dry*-MOF-5-OCX materials compared to the cubic *as*-MOF-5-**OCX** was further estimated (results are given in Table 4.10). To do so, the experimentally determined total pore volumes of the *dry*-MOF-5-**OCX** phases (V_{exp}) were compared to the expected pore volumes of a respective theoretical cubic framework (V_{theo}). Here, V_{theo} corresponds to the volumes of hypothetical crystalline cubic MOF-5-**OCX** obtained from the interpolation between MOF-5 and *dry*-MOF-5-**OC8** as mentioned before (Figure 4.28, right). The discrepancy between V_{exp} and V_{theo}, was then related to the crystallographic volume of the cubic phases, $V_{\mathrm{cryst,cub}}$, of the *as*-MOF-5-**OCX** in order to estimate how much pore volume has been lost for the *dry*-MOF-5-**OCX** materials as a consequence of non-correlated framework contraction. Subtracting V_{exp} from V_{theo} gives ΔV. ΔV is the 'missing' pore volume per mole MOF of the *dry*-MOF-5-**OCX** (**X** = 2 - 6) phases. Relating ΔV to the crystallographic volume per mole *as*-MOF-5-**OCX**, V_{cubic}, as known from PXRD, yields an estimate for the degree of contraction of the *dry*-MOF-5-**OCX** phases. The results are in good agreement to the values approximated from PXRD data (see above, Table 4.2) and range from –4% for *dry*-MOF-5-**OC6** to –14% for *dry*-MOF-5-**OC2** (Table 4.10).

Table 4.10: Estimation of the volume contraction from CO_2 sorption experiments. V_{exp} is the experimental pore volume per mole MOF. V_{theo} is the theoretical pore volume of a hypothetical crystalline cubic MOF-5-**OCX** derived via interpolation (see text above). $\Delta V = V_{theo} - V_{exp}$. $V_{cryst,cub}$ is the crystallographic volume of the corresponding cubic *as*-MOF-5-**OCX** phase. %change = ΔV / $V_{cryst,cub}$.

X	V_{exp} / cm^3mol^{-1}	V_{theo} / cm^3mol^{-1}	ΔV / cm^3mol^{-1}	$V_{cryst,cub}$ / cm^3mol^{-1}	%change
2	425	611	186	1297	-14
3	423	536	113	1303	-9
4	366	461	95	1306	-7
5	353	386	33	1299	-3
6	253	311	58	1300	-4

Application of *n*-butane as sorbate produces a strikingly different response of the materials, due to the stronger interaction of this gas with the hydrophobically lined interior of the pores (polarizability α(*n*-butane) = 8.02 Å^3 compared to $\alpha(CO_2)$ = 2.51 Å^3)[189] and the higher measurement temperature (293 K). Firstly, the full *n*-butane isotherms are given in Figure 4.30 and reveal Type I shaped isotherms for all *dry*-MOF-5-**OCX**, except for *dry*-MOF-5-**OC7**, which will be discussed in the following, with maximum uptakes constantly increasing from 16 cm^3g^{-1} for *dry*-MOF-5-**OC8** to 97 cm^3g^{-1} for *dry*-MOF-5-**OC2**.

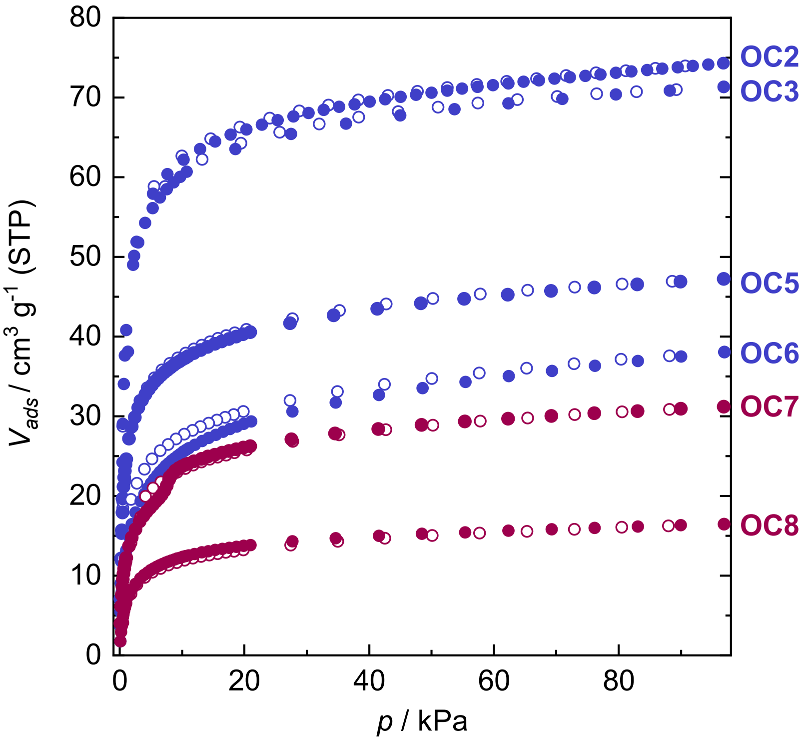

Figure 4.30: *n*-Butane sorption isotherms of *dry*-MOF-5-**OCX** derivatives recorded at 293 K. Adsorption and desorption branches are shown with closed and open symbols.

Dry-MOF-5-**OC7** displays a stepped *n*-butane sorption isotherm with a slight hysteresis, which signifies a rhombohedral-to-cubic transition at a *n*-butane pressure of 8.0 kPa ($p/p_0 \approx 0.04$) (Figure 4.31). This is confirmed by *in-situ* PXRD experiments under variable *n*-butane pressure at 298 K, although the transition is shifted to a much higher pressure (50-100 kPa,

$p/p_0 \approx$ 0.2-0.4), potentially due to too short equilibration times during the *in-situ* PXRD study, which were only 2 min per pressure point for this particular sample (for details, see Materials & Methods 6.12). The *in-situ* PXRD data further clarify that the breathing transition of *dry*-MOF-5-**OC7** during *n*-butane sorption is reversible once the *n*-butane pressure is reduced.

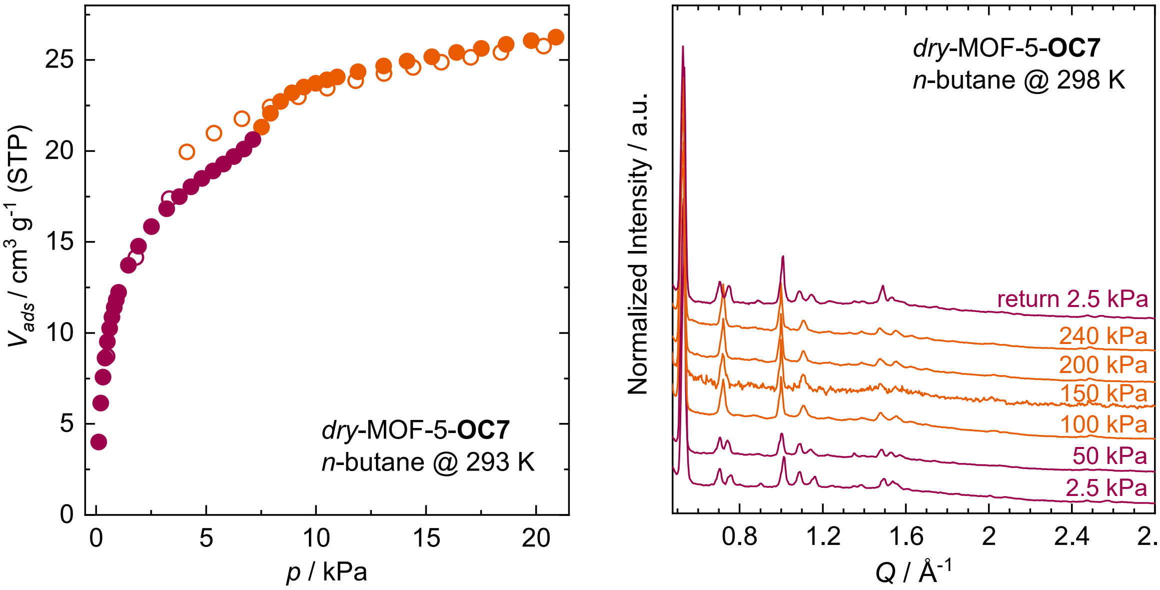

Figure 4.31: Excerpt of the *n*-butane sorption isotherm of *dry*-MOF-5-**OC7** at 293 K (left*). In-situ* *n*-butane sorption PXRD patterns of *dry*-MOF-5-**OC7** recorded at DELTA.

In contrast, *dry*-MOF-5-**OC6** features a simple Langmuir-shaped *n*-butane sorption isotherm without any obvious steps at 293 K (Figure 4.32, left). Here, *in-situ* PXRD at 298 K demonstrates that the material continuously transforms from the non-crystalline distorted phase to the crystalline cubic phase with increasing *n*-butane pressure as the prominent reflections of its cubic phase gain intensity and definition (Figure 4.32, right).

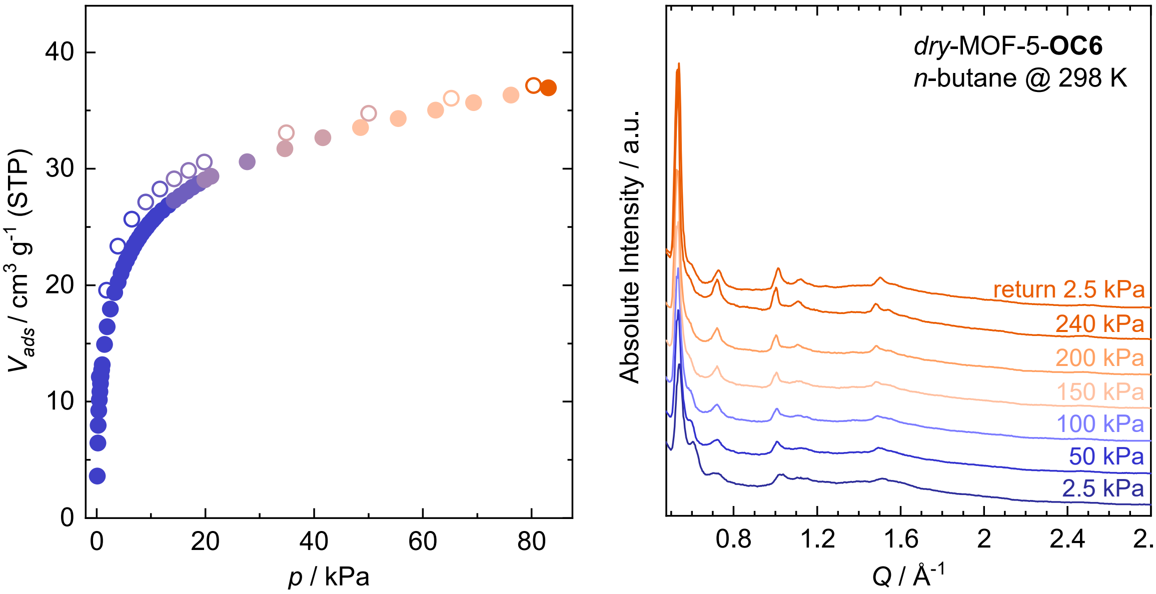

Figure 4.32: Excerpt of the *n*-butane sorption isotherm of *dry*-MOF-5-**OC6** at 293 K (left*). In-situ* *n*-butane sorption PXRD patterns of *dry*-MOF-5-**OC6** recorded at DELTA.

After pressure release, *dry*-MOF-5-**OC6** does not retransform to the non-crystalline phase on the time scale of the PXRD data collection (10 min), but largely retransforms within 17 h (Figure 4.33, left). Similar to the thermal transition of *dry*-MOF-5-**OC6**, the retransformation appears to be a gradual relaxation process and therefore must be kinetically hindered as indicated by *in-situ* *n*-butane sorption PXRD experiments. Here, the PXRD pattern recorded immediately after returning to vacuum (2.5 kPa, the lowest accessible pressure for this experiment) shows no structural retransformation, whereas the PXRD patterns collected after 17 h storage under ambient conditions clearly indicate a retransformation to the non-crystalline phase of *dry*-MOF-5-**OC6**. The behaviour of *dry*-MOF-5-**OC5** is comparable to that of *dry*-MOF-5-**OC6**, as the characteristic reflections of the cubic phase slightly sharpen, but the structural changes induced by the adsorption of *n*-butane are of a smaller extent (Figure 4.33, right).

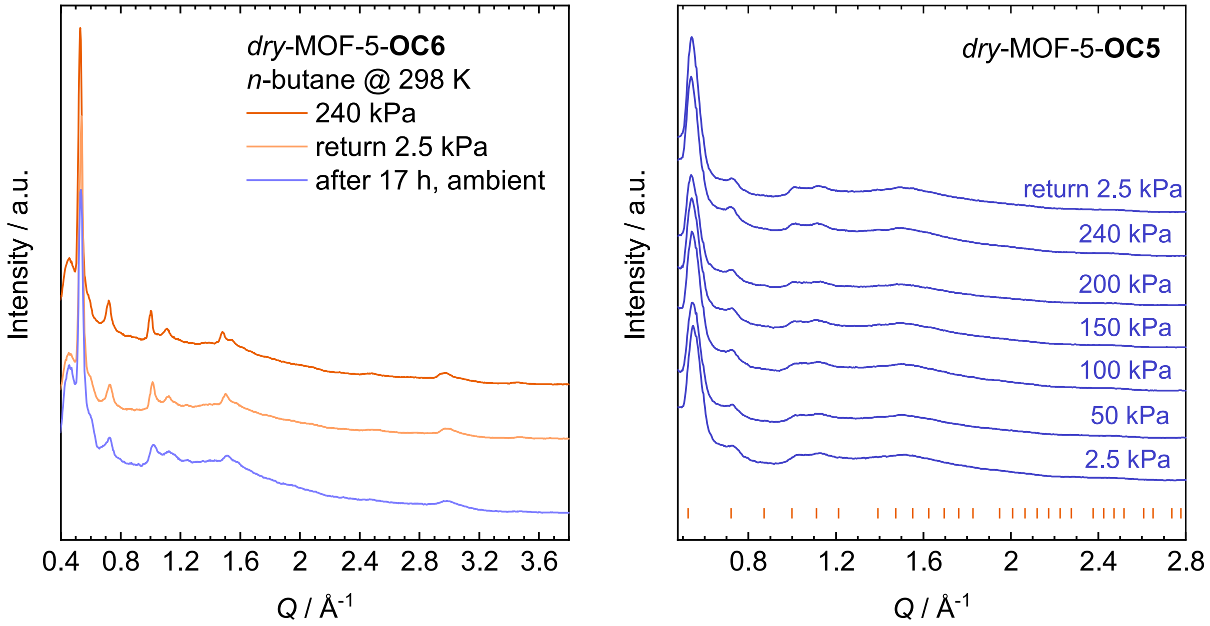

Figure 4.33: *In-situ* *n*-butane sorption PXRD patterns of *dry*-MOF-5-**OC6** recorded at saturation pressure (240 kPa), after returning to 2.5 kPa pressure and after 17 h of storage under ambient conditions after the experiment (298 K, BL9 of DELTA, left). *In-situ* *n*-butane sorption PXRD patterns of *dry*-MOF-5-**OC5** recorded at 298 K (BL9 of DELTA) with tick marks corresponding to allowed reflection positions of the cubic phase of *dry*-MOF-5-**OC5**.

Most surprisingly, propylene and propane sorption isotherms of *dry*-MOF-5-**OC6** and *dry*-MOF-5-**OC7** at 293 K indicate a clear breathing transition of both frameworks upon adsorption of these gases (Figure 4.34). For *dry*-MOF-5-**OC7** again small steps and hystereses ascribed to the rhombohedral-to-cubic transition are evident. The transition is taking place at a pressure of 31 kPa for propane ($p/p_0 \approx 0.04$), which is about the same relative pressure as for the *n*-butane inducted rhombohedral-to-cubic transition of *dry*-MOF-5-**OC7**. For propylene this transition is taking place at 22 kPa ($p/p_0 \approx 0.02$) and therefore at a much lower relative pressure, indicating stronger interactions between the probe molecule and the material. *dry*-MOF-5-**OC6** features much larger steps in the propane and propylene isotherms at ca. 15 kPa ($p/p_0 \approx 0.018$ and 0.015, respectively) and strong hystereses, thus demonstrating that the non-crystalline-to-crystalline transition of this framework is triggered once a certain threshold pressure is reached.

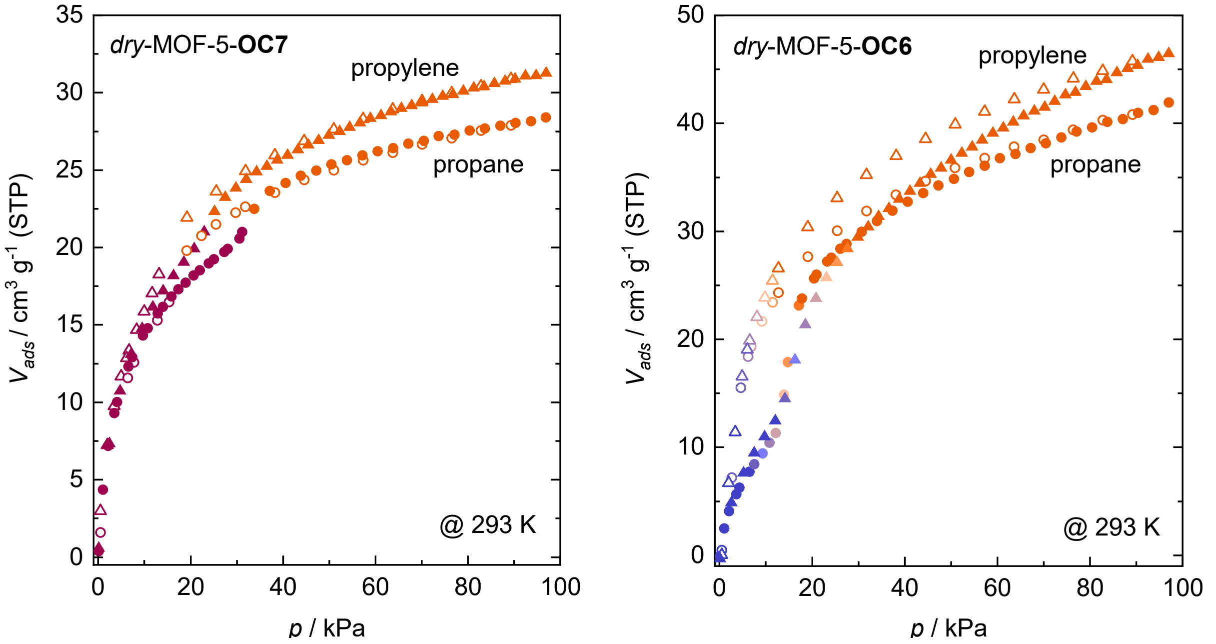

Figure 4.34: Propane (circles) and propylene (triangles) isotherms of *dry*-MOF-5-**OC7** (left) and *dry*-MOF-5-**OC6** (right) recorded at 293 K. Adsorption and desorption branches are shown as closed and open symbols, respectively.

In conclusion, these findings support the hypothesis that guest molecules which exhibit favourable interactions with the DEDs decorating the frameworks are able to induce a structural response by counterbalancing the molecular forces leading to the non-correlated or correlated deformation of the framework architecture. These structural responses take either place as a discontinuous breathing transition as in *dry*-MOF-5-**OC7** or as a continuous transition as observed for *dry*-MOF-5-**OC6** and *dry*-MOF-5-**OC5** to their respective cubic phases.

4.3.6 Conclusion

The guest- and temperature depending frustrated flexibility of a series of alkoxy-DED functionalized MOF-5-**OCX** (**X** = 2 – 8) was demonstrated. The concept of frustrated flexibility is based on the combination of a rigid framework architecture prohibiting large-scale correlated framework distortions with DED groups enthalpically favouring a contraction of the structure. Analysis via single crystal and powder X-ray diffraction techniques revealed that by tuning of the steric bulk of the DEDs a reversible guest-depending switching between either a cubic crystalline and a rhombohedrally distorted crystalline phase for small volume changes (–3%) or a cubic crystalline and an X-ray amorphous phase (MOF-5-**OC2** to MOF-5-**OC6**) for larger volume changes (–17% to –6%) occurs. In case of the latter, frustration of the frameworks arises from the conflict between the framework lattice, which is rigid due to intrinsic geometrical constraints of the inorganic building units, and intra-framework dispersion interactions, demanding a densification of the structure. Importantly, the retransformation to the cubic crystalline phase by *n*-octane resolvation excludes solvent coordination or framework reconstruction effects as a cause of this behaviour. On the local scale, as investigated by solid state NMR, X-ray total scattering PDF analysis and FT-IR spectroscopy, these structural contractions come along with correlated (rhombohedral states) or non-correlated distortions (non-crystalline states) of the $[Zn_4O(CO_2)_6]$ building units of the frameworks. MD simulations of the MOF-5-**OCX** corroborate that the structural contractions are enthalpically driven by dispersion interactions of the alkoxy-groups with themselves or the framework backbone. These interactions can be overcome either by vibrational entropy at elevated temperatures, as demonstrated for *dry*-MOF-5-**OC5** to -**OC8** via VT-PXRD and DSC experiments, or enthalpically through the adsorption of guest molecules, which strongly interact with the DED groups, as demonstrated by isothermal *n*-butane sorption and *in-situ* *n*-butane sorption PXRD experiments. At this, *dry*-MOF-5-**OC7** exhibits a breathing transition as a function of *n*-butane pressure, whereas *dry*-MOF-5-**OC5** and -**OC6** continuously transform to their cubic phases. This endows frustratedly flexible MOFs with unprecedented physical properties, such as continuous non-crystalline-to-crystalline transitions driven by entropy rather than enthalpy.

4.4 The Influence of DED-Polarity on Frustrated Flexibility

In order to assess the effects of stronger intra-framework interactions of the DED groups on frustrated flexibility and its tunability, more polar DED groups will be employed in the following and compared to the MOF-5-**OCX**.

In general, intermolecular, or supramolecular interactions are strongly influenced by the polar nature/polarity of the involved molecules or functional groups. Despite maybe different in the individual case, the general rule is that the interaction energy increases with the polarity of the interacting groups or molecules.[190] As to how macroscopic properties are impacted by this, the change of the fundamental physical properties (e.g., boiling points, densities, or vapour pressures, see Table 4.11) from *n*-hexane over 1-methoxy butane to 1,2-dimethoxy ethane serves as a practical example.

Table 4.11: Selected physical properties, i.e., the molar mass M, density under standard conditions ϱ, boiling point (bp), dipole moment μ, permittivity ε_r and polarizability α of *n*-hexane[191], 1-methoxy butane[192] and 1,2-dimethoxy ethane[193,194]. Unfortunately, no experimental data on the dipole moment of 1-methoxy butane was available, however, for the comparable compound 1-methoxy propane, a dipole moment of μ = 1.11 D[195] was found.

compound	M / g mol^{-1}	$\varrho_{25°\text{C, 1atm}}$ / g cm^{-3}	bp_{1atm} / °C	μ / D	ε_r	α / Å^3
n-hexane	86.18	0.66	68.3	0	1.89	11.9
1-methoxy butane	88.15	0.74	69.8	–	–	10.4–11.5
1,2-dimethoxy ethane	90.12	0.86	85.2	1.62	7.30	9.5

Here, the temperatures of the boiling points and the densities increase, while the vapour pressures and molar volumes decrease with increasing polarity of the molecules, thus, pointing towards increasing intermolecular forces. In order to develop a deeper understanding of the influence of the strength of intraframework interactions on frustrated flexibility, i.e., to probe the effects of sidechain (or DED) polarity, the structural behaviour and the thermal and sorption properties of alkoxy-functionalized MOF-5 now bearing additional terminal methoxy groups was investigated (Figure 4.35). Due to their enhanced ability to exhibit dipolar-dipolar and dipolar-non-polar interactions compared to the pure-alkoxy DEDs, followingly these methoxy-alkoxy groups will be denoted as Dipolar (and) Dispersion Energy Donors (DDEDs) in accordance with the naming scheme established earlier in this work.

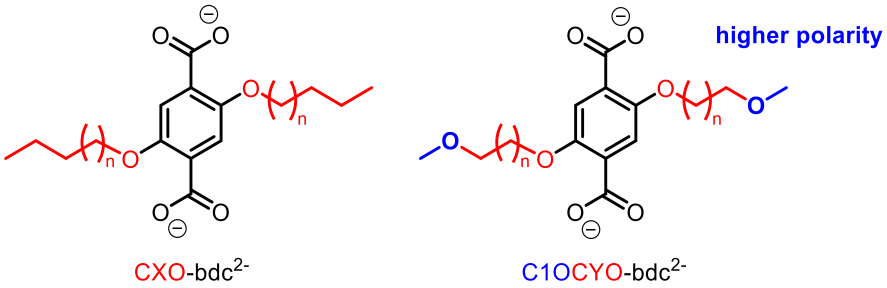

Figure 4.35: Comparison between the **CXO-** and **C1OCYO**-bdc^{2-} linkers bearing either alkoxy or methoxy-alkoxy groups regarding the polarity of the DEDs and DDEDs. Note that linkers of the same number of segments in the DED and DDED chain are yielded if **X** = n + 3 and **Y** = n + 1.

4.4.1 Synthesis and Structural Behaviour

In a similar manner to the MOF-5-**OCX** materials, a series of methoxy-alkoxy functionalized MOF-5 derivatives of the general chemical composition Zn_4O(**C1OCYO**-bdc)$_3$ (**C1OCYO**-bdc^{2-} = 2,5-dimethoxy-alkoxy-1,4-benzene dicarboxylate with **Y** = 2 – 6) was prepared, denoted in accordance with the previously introduced nomenclature as MOF-5-**OCYC1O**. The implemented organic linkers and MOFs (*as*- and *dry*-states) presented here were synthesized and dried (MOFs) according to the same protocols as established for the MOF-5-**OCX** series under section 4.3.1 (detailed procedures given under Materials & Methods 6.1.3). In analogy to the previously discussed *as*-MOF-5-**OCX** derivatives, the *as*-MOF-5-**OCYC1O** materials were obtained as large cubic crystals (size 100 – 500 µm).

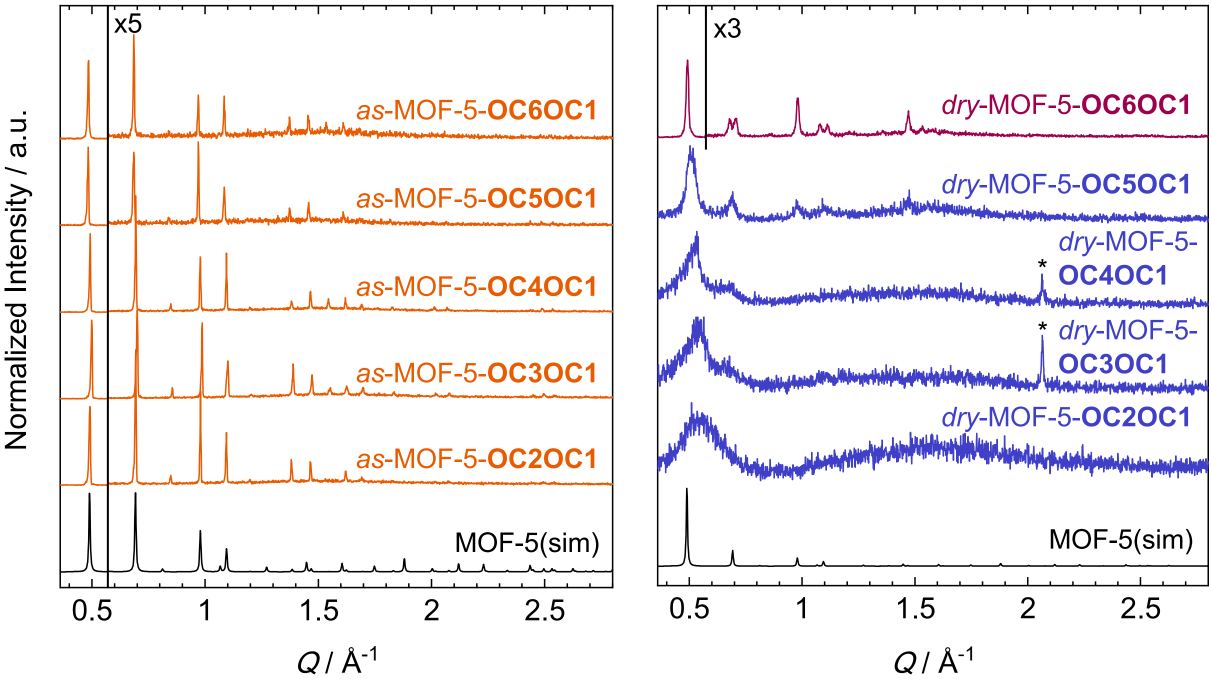

Figure 4.36: PXRD data of the MOF-5-**OCYOC1** in their as-synthesized (*as*, left) and guest-free (*dry*, right) states in comparison to a simulated PXRD pattern of guest-free MOF-5. The signals marked with an asterisk (*) originate from the material of the sample holder.

From the analysis of PXRD (structureless profile fitting, Pawley method[110]) and SCXRD data the *as*-MOF-5-**OCYC1O** prove to be of the same cubic framework structure as the mother compound MOF-5 (see Figure 4.36, left, and Appendix 8.2.1 for the Pawley fits). In conformity with their alkoxy-bearing relatives, the methoxy-alkoxy groups are severely disordered in the as-synthesized state and could not be located in the electron density maps generated during the refinement of the SCXRD data (space group $Pm\bar{3}m$). Surprisingly, despite the same number of 9 substituent chain segments as MOF-5-**OC8**, the methoxy-terminated derivative MOF-5-**OC6OC1** is cubic in the as-synthesized state and exhibits no rhombohedral distortion. Nevertheless, upon transformation to the guest-free state, *dry*-MOF-5-**OC6OC1** performs a rhombohedral contraction and therefore its structural response is rather comparable to MOF-5-**OC7** (Figure 4.36, right). Here, the rhombohedral distortion is significantly less though, since the rhombohedral angle of *dry*-MOF-5-**OC6OC1** amounts to 87.7° as determined from the PXRD data (structureless profile fit, space group $R\bar{3}$, for details see Figure 8.33 and Table 8.26), which corresponds to a volumetric contraction of 2% in relation to *as*-MOF-5-**OC6OC1**. The alkoxy-terminated derivative *dry*-MOF-5-**OC7** in turn contracts by 3% upon DMF removal and features a rhombohedral angle of 84.5°. Also, the rhombohedral angle of *dry*-MOF-5-**OC8** is with 85.5° still smaller than the one of *dry*-MOF-5-**OC6OC1**.

In line with the *dry*-MOF-5-**OCX** (**X** = 2 – 6), guest-free *dry*-MOF-5-**OC5OC1** to -**OC2OC1** transform to nanocrystalline (**Y** = 5) or non-crystalline X-ray (**Y** = 2 – 4) amorphous states, which are similarly characterized by the presence of a broad first-scattering peak (FSP) at slightly lower scattering angles as the defining 100-reflection of the crystalline materials (Figure 4.36, right).

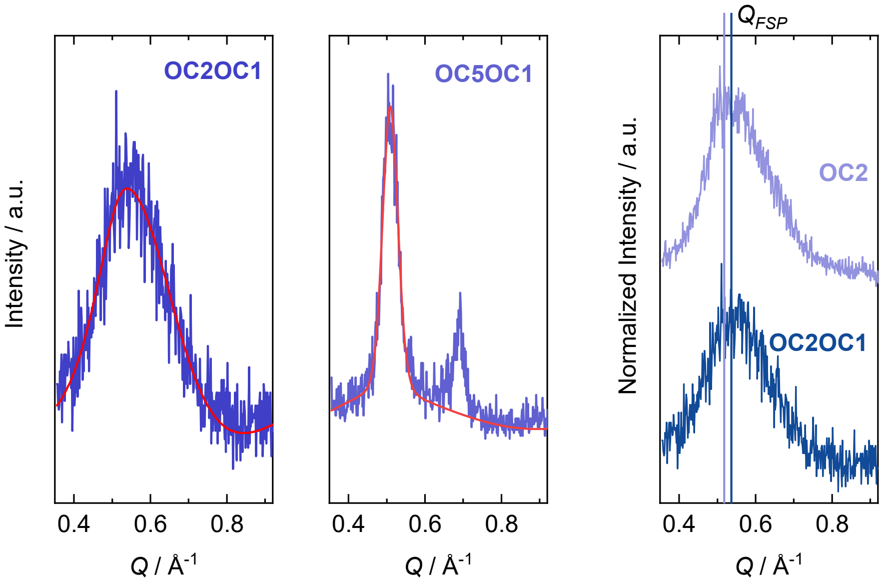

Figure 4.37: Left: Results of single peak fits of the FSP of *dry*-MOF-5-**OC2OC1** and *dry*-MOF-5-**OC5OC1**. Right: The FSP of *dry*-MOF-5-**OC2OC1** in comparison with *dry*-MOF-5-**OC2**, the sample exhibiting the strongest structural distortion within the MOF-5-**OCX** series. Maxima of the FSP, Q_{FSP}, extracted from the fits are marked by a straight line in the corresponding colour. Note, that in order to fit a proper baseline, a second peak was fitted for *dry*-MOF-5-**OC5OC1** and the *d*-spacing of its maximum is not commensurate with the d_{FSP} and cubic symmetry.

Remarkably, the maximum of the FSP, Q_{FSP}, of *dry*-MOF-5-**OC2OC1** (Q_{fsp}(**OC2OC1**) = 0.536 Å^{-1}, as determined from a peak fit using split pseudo-Voigt functions, see Appendix 8.2.1) is shifted to considerably higher scattering angles in comparison with its purely alkoxy-equivalent *dry*-MOF-5-**OC4** (Q_{FSP}(**OC4**) = 0.510 Å^{-1}) or even *dry*-MOF-5-**OC2** (Q_{FSP}(**OC2**) = 0.518 Å^{-1}), the sample exhibiting the strongest structural contraction within the MOF-5-**OCX** series (see Table 4.2). Applying the same approximation of the volumetric contraction via the calculation of $(d_{\mathrm{FSP}})^3$ as described under section 4.3.1 (Table 4.6), the corresponding d_{FSP}(**OC2OC1**) = 11.73 Å gives a volume change of –25% in relation to the cubic *as*-MOF-5-**OC2OC1**, which is a significantly larger contraction compared to the –17% approximate volume change of MOF-5-**OC2** upon guest-removal. This suggests that the more dipolar character of the methoxy-ethoxy sidechains produces much stronger intra-framework interactions, which can enthalpically outbalance a stronger structural distortion. When the

DDED chain length increases from **Y** = 2 to **Y** = 5, the peak sharpness and asymmetry of the FSP evolves differently than for the purely alkoxy-functionalized *dry*-MOF-5-**OCX**, which suggests a different mode of framework distortion to be present in these materials. The most striking feature here is the emergence of a further broad diffuse scattering peak around 0.60 $Å^{-1}$ to 0.70 $Å^{-1}$ upon elongation of the sidechains of *dry*-MOF-**OCYC1O**. However, when reaching *dry*-MOF-5-**OC5OC1**, broad but clear traces of the characteristic cubic reflections reappear, reminiscent of the behaviour of *dry*-MOF-5-**OC6** (i.e., a distorted nanocrystalline structure). Moreover, the shape of the FSP (Q_{FSP}(**OC5OC1**) = 0.506 $Å^{-1}$) allows for a single peak fit again to yield an estimation of the volumetric contraction by –11% in reference to its as-synthesized phase, which matches the regime of the contraction between *dry*-MOF-5-**OC5** and -**OC6** (–11% to –6%, respectively).

Table 4.12: Parameters extracted from fits of the first scattering peak of *dry*-MOF-5-**OC2OC1** and *dry*-MOF-5-**OC5OC1** (see Figure 4.37) with the resulting estimated volumes of the contracted materials.

OC1OCY	*reciprocal space*		*real space*	*volume contraction*		
	Q_{FSP} / $Å^{-1}$	*FWHM* / $Å^{-1}$	d_{FSP} / Å	$V_{\mathrm{contracted,dry}}$ / $Å^3$	$V_{\mathrm{cubic,as}}$ / $Å^3$	%change
OC2OC1	0.536	0.238	11.73	1614.0	2143.2(6)	-25
OC5OC1	0.506	0.0428	12.42	1915.9	2156.5(11)	-11

The cubic phase and consequently the crystalline order of the MOF-5-**OCYOC1** is recovered by the infiltration of DMF over the gas phase (performed under reduced pressure at 50 °C, Figure 4.38). Note, that the signal-to-noise ratio is comparably low, which is due to comparably high DMF content giving rise to diffuse scattering. Nevertheless, the reflections from the MOF phase are very sharp and, hence, indicate full transformation of the materials to the cubic phase. However, this is not the case if *n*-octane is added to the material via the liquid phase at 60 °C (see Appendix, Figure 8.40). Unlike the case of the purely alkoxy-functionalized MOF-5-**OCX**, here, the interactions between the polar methoxy-alkoxy side chains and the non-polar *n*-octane guest molecules are apparently too weak to overcome the strong intra-framework dispersion interactions driving the crystalline-to-amorphous transition and, thus, to mediate the recovery of the crystalline cubic phases. Nevertheless, upon reinfiltration of the MOF-5-**OCYOC1** with the dipolar guest molecule 1-methoxy-2-(2-methoxyethoxy) ethane (diglyme, μ_{diglyme} = 1.97 D, for comparison μ_{DMF} = 3.82 D, $\mu_{\mathrm{n\text{-}oct}}$ = 0 D)[196], sharp Bragg reflections re-emerge, which clearly indicate the formation of the cubic-crystalline phases of the *diglyme*-MOF-5-**OCYOC1** materials (Figure 4.38, for profile fits, see Figure 8.35, Table 8.26). Interestingly, *diglyme*-MOF-5-**OC6OC1** does not retransform to the cubic state but remains rhombohedral upon expanding to a larger rhombohedral angle of 89°, similar to the behaviour of *dry*-MOF-5-**OC8**, which does neither transform to the cubic phase upon introduction of DMF or *n*-octane. Note, that a significant fraction of *diglyme*-MOF-5-**OC2OC1** has converted into an unknown, likely hydrolysed phase, since the resolvation was performed under non-inert conditions and diglyme is well miscible with water.

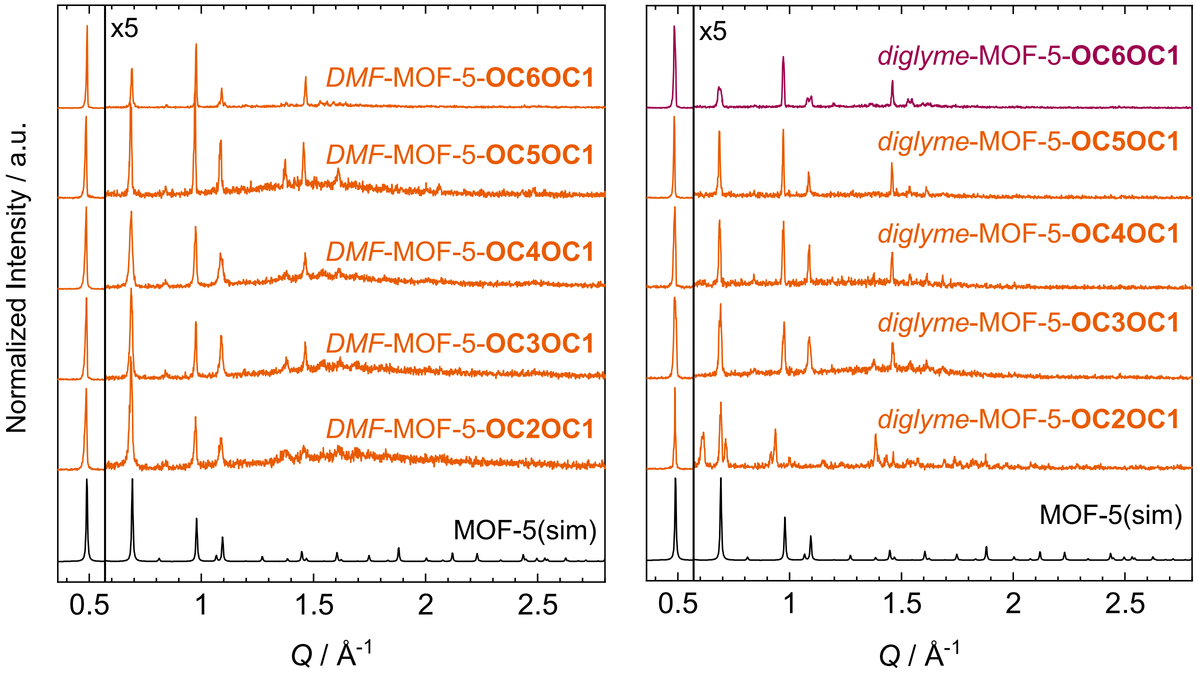

Figure 4.38: PXRD data of the MOF-5-**OCYOC1** in their DMF-reinfiltrated (*DMF*, left) and diglyme-reinfiltrated (*diglyme*, right) states in comparison to a simulated PXRD pattern of guest-free MOF-5.

As expected, the MOF-5-**OCYOC1** derivatives bearing a methoxy group as part of the linker functionalization likewise demonstrate frustrated flexibility as exhibited by the MOF-5-**OCX** materials. Nevertheless, there are significant differences to the purely alkoxy-functionalized MOF-5-**OCX**, most importantly, the generally much stronger approximate volumetric contraction of the *dry*-MOF-5-**OCYOC1** (e. g. –25% of *dry*-MOF-5-**OC2OC1** vs. –14% of *dry*-MOF-5-**OC4** or –11% of *dry*-MOF-5-**OC5OC1** (non-correlated distortion) vs. –3% of *dry*-MOF-5-**OC7** (rhombohedral distortion)). Likely this arises from the stronger intra-framework interactions due to the more polar character of the DDEDs, which has an impact on the free energy landscape of the MOF-5-**OCYOC1**. How these changes exert on a local scale will be investigated in the following by means of FT-IR spectroscopy and XPDF analysis.

4.4.2 Local Structure

High-resolution X-ray total scattering data of the *as*- and *dry*-MOF-5-**OCYOC1** with **Y** = 2 – 4 were collected on beamline I15-1 at Diamond Light Source and transformed into the corresponding real space XPDFs in the *D(r)* form (for the *S(Q)* data, see Appendix Figure 8.64 and Figure 8.65). The obtained XPDFs of the *as*- and *dry*-MOF-5-**OCYOC1** will be similarly analysed regarding the overall correlation length found in the high r region and the local geometries of the $Zn_4O(O_2C)_6$ units, which are mainly represented by the low r region of the XPDFs. As expected, investigation of the high r region of the XPDF of *dry*-MOF-5-**OC2OC1** reveals a complete loss of correlations above $r \approx 13.5$ Å (Zn-Zn correlation distance of adjacent

$Zn_4O(CO_2)_6$-nodes), indicative of the strong and non-correlated structural distortion present in this material (Figure 4.39 and Appendix Figure 8.66 and Figure 8.67).

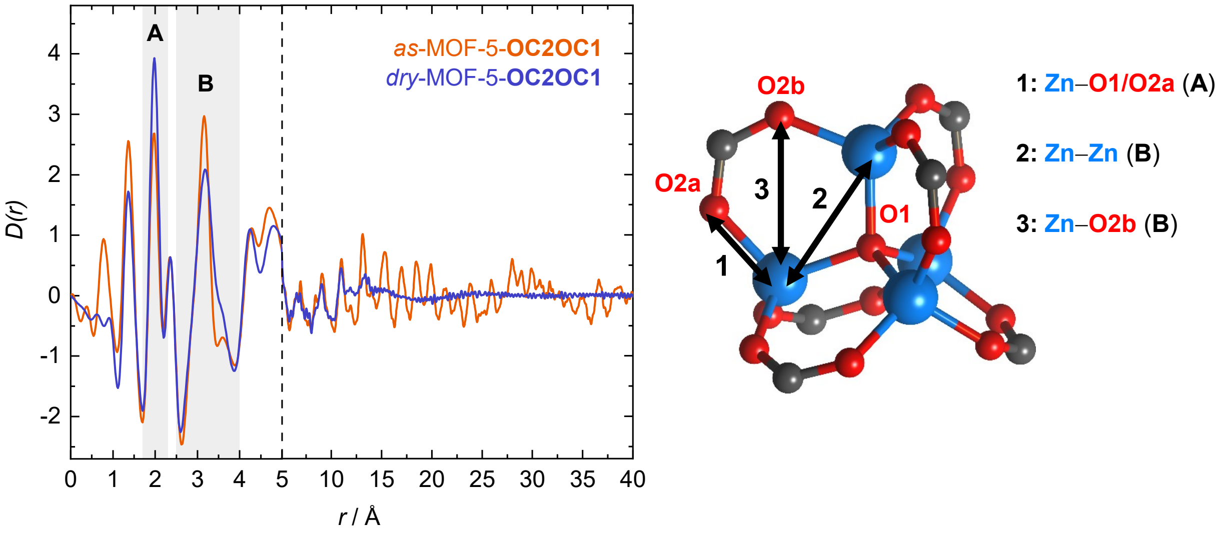

Figure 4.39: XPDFs of *as*- and *dry*-MOF-5-**OC2OC1** with the low-r region ($r = 1 - 5$ Å) highlighted (left) and a representation of the $Zn_4O(O_2C)_6$ node (CCDC deposition code 256965) with important distances marked (right), that are assigned to certain peaks in the XPDFs.

Interestingly, the XPDFs of *dry*-MOF-5-**OC3OC1** and -**OC4OC1** still show weak traces of correlations up to $r \approx 28$ Å (correlation distance of 2x2x2 MOF cells, Figure 4.40, top). Despite the differences in the correlation lengths, *dry*-MOF-5-**OC2OC1** to -**OC4OC1** share very similar low-*r* regions of their respective XPDFs. In more detail, the peak A corresponding to the nearest neighbour Zn–O distances remains largely the same as for the as-synthesized materials, whereas peak **B** exhibits the characteristic shift of the peak maximum and widening towards higher *r* due to the distortion of the $Zn_4O(CO_2)_6$ unit. Remarkably, for all *dry*-MOF-5-**OCYOC1** the widening of peak **B** towards higher *r* occurs in a more shoulder-like manner than in the case of the purely alkoxy-functionalized *dry*-MOF-5-**OCX** (**X** $\leq$ 6) (Figure 4.40, top, arrow). Since the high-*r* flank of peak **B** also includes contributions from the third nearest neighbours of the Zn atoms (i.e., Zn-carboxylate-O, distance 3 in Figure 4.39, $d_{Zn\text{-}O2b} \approx 3.3$ Å in MOF-5), it is possible that the evolution of the shoulder of peak **B** towards higher *r* arises from a tilting of the carboxylate groups upon the very heavy distortion of the $Zn_4O(CO_2)_6$ units of *dry*-MOF-5-**OC2OC1** to -**OC4OC1**. Even though a direct comparison of the widths of the peak **B** of the *dry*-MOF-5-**OCYOC1** vs. the *dry*-MOF-5-**OCX** does not appear sensible due to their differing shape in each MOF-series, the XPDF data generally suggest that there is less variation in the non-correlated distortions of the inorganic $Zn_4O(CO_2)_6$ nodes as a function of DDED chain length in the *dry*-MOF-5-**OCYOC1** (see Figure 4.40, top). Accordingly, these distortions appear similar between *dry*-MOF-5-**OC2OC1** and *dry*-MOF-5-**OC4**, whereas they differ more strongly between *dry*-MOF-5-**OC4OC1** and *dry*-MOF-5-**OC6** with the latter featuring the less distorted $Zn_4O(CO_2)_6$ nodes (for comparisons, see Figure 4.40, bottom).

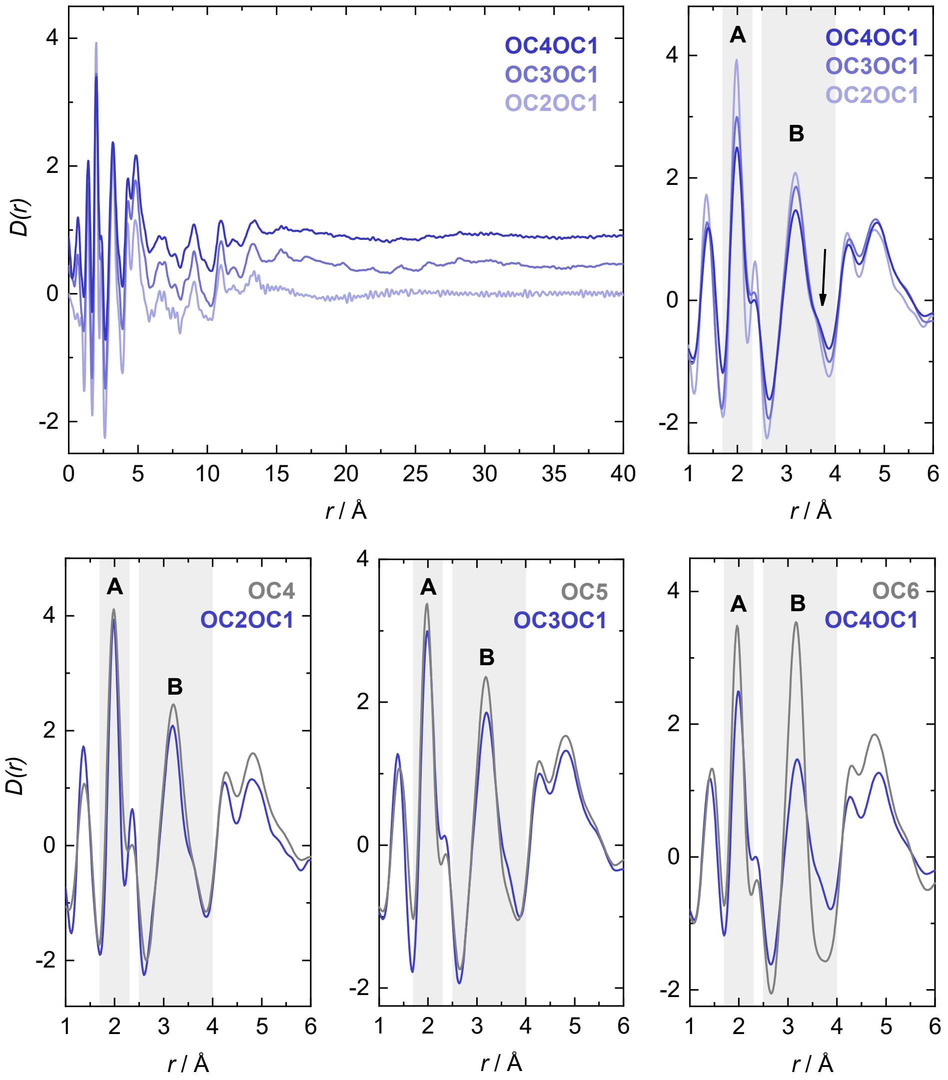

Figure 4.40: Top: Overlay of the XPDFs of *dry*-MOF-5-**OCYOC1** (**Y** = 2 – 4) with focus on the high-*r* region for the correlation length (left) or the low-*r* regions for the state of the $Zn_4O(CO_2)_6$ clusters. The high-*r* region XPDFs (top left) were stacked with a vertical offset. Bottom, from left to right: Comparisons of the low-*r* regions of the XPDFs of *dry*-MOF-5-**OC2OC1** vs. *dry*-MOF-5-**OC4** to *dry*-MOF-5-**OC4OC1** vs. *dry*-MOF-5-**OC6**.

Similar conclusions are drawn from an investigation of the FT-IR spectroscopic data of the *dry*-MOF-5-**OCYOC1** series. The full FT-IR spectra are given in the Appendix, Figure 8.76 to Figure 8.80. Here, the spectral region of the characteristic ν_{as}(Zn-O1) and ν_s(Zn-O2) vibrational bands (≈ 450 – 600 cm^{-1}) shows only one broad band for the non-crystalline materials (Y = 2 – 5) and two sharper bands at 514 and 570 cm^{-1} for the rhombohedral-crystalline *dry*-MOF-5-**OC6OC1**. As stated earlier in section 4.3.2, the reduction of the T_d symmetry of the $Zn_4O(CO_2)_6$ unit in a non-correlated fashion likely causes these bands to broaden. In accordance with the XPDF data for **Y** = 2 – 4, the bands remain very broad for the *dry*-MOF-5-**OCYOC1** with **Y** = 2 and 3 and become just slightly sharper when **Y** increases over 4 to 5. This also indicates a very similar degree of distortion of the $Zn_4O(O_2C)_6$ clusters for **Y** = 2 – 4, while **Y** = 5 being less distorted. The crystalline order remains fully preserved for *dry*-MOF-5-**OC6OC1** and the ν_{as}(Zn-O1) and ν_{s}(Zn-O2) bands appear sharp again. The heterogeneity of the *dry*-MOF-5-**OCYOC1** is similarly reflected by the broadening of the ν_{as}(COO) bands following the series from **Y** = 6 to 2 (Figure 4.41) and furthermore the evolution of the band maxima towards lower wavenumbers (from 1599 to 1582 cm^{-1}). However, this IR band changes more continuously as a function of **Y** than the ν_{as}(Zn-O1) and ν_{s}(Zn-O2) bands, which again points towards differences in the particular distortion mode compared to the *dry*-MOF-5-**OCX**.

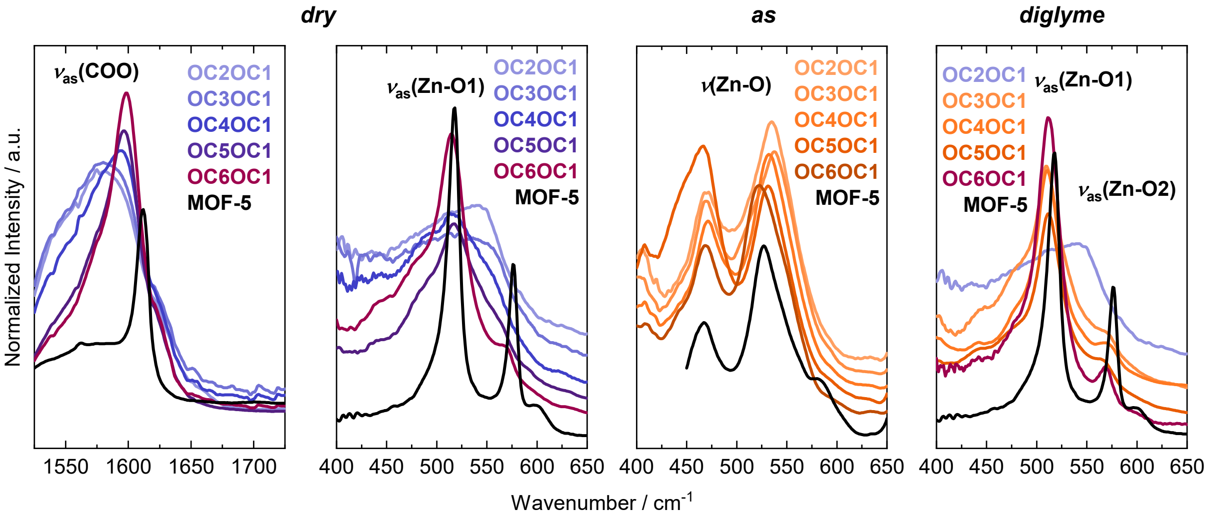

Figure 4.41: Excerpts from the IR spectral regions showing the ν_{as}(Zn-O1) and ν_{s}(Zn-O2) and the ν_{as}(COO) vibrational bands of the MOF-5-**OCYOC1** materials in their *dry*, *as* (DMF containing) and *diglyme*-reinfiltrated states.

Upon re-adsorption of diglyme, sharp bands of the ν_{as}(Zn-O1), ν_{s}(Zn-O2) and ν_{as}(COO) vibrations emerge, which closely resemble the ones of guest-free MOF-5 accompanying the recovery of crystalline order and in turn the recovery of the T_d symmetry of the $Zn_4O(O_2C)_6$ building units (Figure 4.41). Note, that the vibrational region related to the Zn_4O units does not show any sharp bands for *diglyme*-MOF-5-**OC2OC1**, which is in accordance with the partial decomposition or phase change detected via PXRD (Figure 4.38). Importantly, this concomitantly demonstrates the absence of a coordination of the ether-oxygen atoms of the diglyme guest molecules to the Zn cations of the $Zn_4O(CO_2)_6$ unit, since this would result in a reduction of the T_d symmetry of the $Zn_4O(CO_2)_6$ unit and therefore affect the ν_{as}(Zn-O1) and ν_{s}(Zn-O2) vibrational bands such as in DMF-solvated (*as*) MOF-5 or any functionalized derivative presented herein (see section 4.3.2 and Figure 4.18). Hence, this excludes solvent coordination from causing the recovery of the crystalline order upon diglyme-resolvation. Furthermore, in earlier works on MOF-5-**OC2OC1**, the coordination of the terminal ether group of the DDEDs to the Zn^{2+} cations of the inorganic units in the materials has been proposed as a major energetic contribution towards the structural transformations occurring upon guest-removal.[99,197] As the IR spectroscopic data do not suggest any substantial interactions between the diglyme or DDED ether groups and the $[Zn_4O(CO_2)_6]$ units, this can also be considered improbable.

4.4.3 Thermal Properties

As has been shown for the *dry*-MOF-5-**OCX** with **X** $= 4 - 8$, that the dispersion interaction-driven structural contractions of these materials are at least partially reversible due to increased vibrational entropy of the DEDs at elevated temperatures. Therefore, the thermal responsivity of the *dry*-MOF-5-**OCYOC1** was investigated, here focussing on the materials with **Y** $= 5, 6$. The initial DSC cycle of *dry*-MOF-5-**OC6OC1** features two thermal events (onset temperature of the respective peaks, $T_{on} = 393$ K, 471 K) on the first DSC measuring cycle, which likely correspond to the release of a small amount of residual adsorbed water molecules. Consecutive measuring cycles feature only one thermal event, which is found at around $T_{on} = 330$ K and possibly points towards a transition from the rhombohedral to the cubic phase as shown by *dry*-MOF-5-**OC7** and -**OC8**. However, the thermal signature is comparably low ($\Delta H = 2.7$ kJ mol^{-1}), since the $\Delta H_{rh \to c}$ for *dry*-MOF-5-**OC7** and -**OC8** amounts to 9.7 and 23.1 kJ mol^{-1}, respectively. The associated change in entropy of $\Delta S = 8.3$ J K^{-1} mol^{-1}, is therefore also significantly lower. Nevertheless, a weaker thermal footprint of the proposed rhombohedral-to-cubic transition can also be attributed to the even smaller volume change of *dry*-MOF-5-**OC6OC1** upon the transition. For comparison, the rhombohedral angle of *dry*-MOF-5-**OC6OC1** is 87.7°, whereas the one of *dry*-MOF-5-**OC8** amounts to 85.5°. Equally, this indicates, that the sidechains of *dry*-MOF-5-**OC6OC1** probably are already more disordered in the rhombohedral phase than in the case of *dry*-MOF-5-**OC8**. By contrast, the non-crystalline *dry*-MOF-5-**OC5OC1** shows no thermal event indicative of an exchange of latent heat in the DSC curve. Still, a kink at around 410 K on the heating branch (390 K on the cooling branch) suggests a second-order transition to the cubic phase potentially taking place from these temperature on. A second-order transition to the cubic phase is shown by *dry*-MOF-5-**OC6**, which is, however, not traceable via DSC experiments.

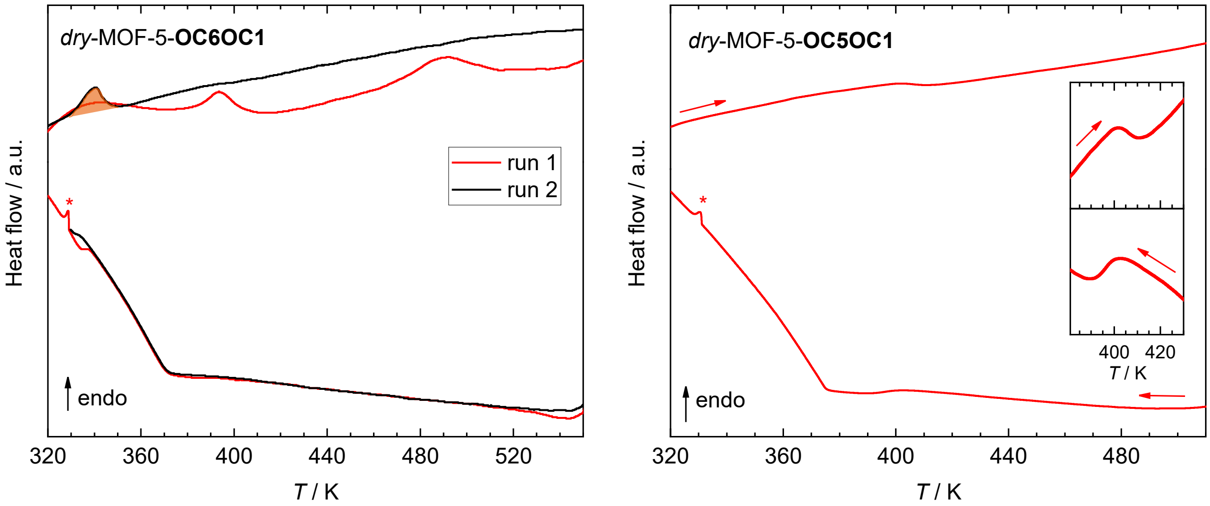

Figure 4.42: DSC data of *dry*-MOF-5-**OC6OC1** (left) and *dry*-MOF-5-**OC5OC1** (right). The peak in the DSC of *dry*-MOF-5-**OC6OC1**, which likely corresponds to a rhombohedral-to-cubic phase transition is highlighted in orange. The insets of the DSC curve of *dry*-MOF-5-**OC5OC1** show magnifications of the kinks in the heating and cooling branches of the respective data. The signal marked with an asterisk (*) is an artifact.

Table 4.13: Thermodynamic data of *dry*-MOF-5-**OC6OC1** and *dry*-MOF-5-**OC5OC1** obtained from the DSC data given above.

OCYOC1	scan	T_{on} / °C	ΔH / kJ mol^{-1}	ΔS / J K^{-1} mol^{-1}
OC6OC1	up	330	2.7	8.3
	down	332	-	-
OC5OC1	up	401	-	-
	down	401	-	-

4.4.4 Gas Sorption Properties

The porosity of the *dry*-MOF-5-**OCYOC1** materials was investigated by means of N_2 (77 K), CO_2 (195 K) and *n*-butane (293 K) gas sorption experiments, as these three probe molecules cover a wide range of host-guest interaction-types. As expected, none of the *dry*-MOF-5-**OCYOC1** materials shows any internal N_2 uptake, but only external surface adsorption with maximum uptakes of 5 to 19 cm^{3}g^{-1}, as evidenced by the nearly linear shape of the isotherms (Type III, Figure 4.43). This is a likely consequence of the diffusion limitations arising from the utilized DDED functionalization.

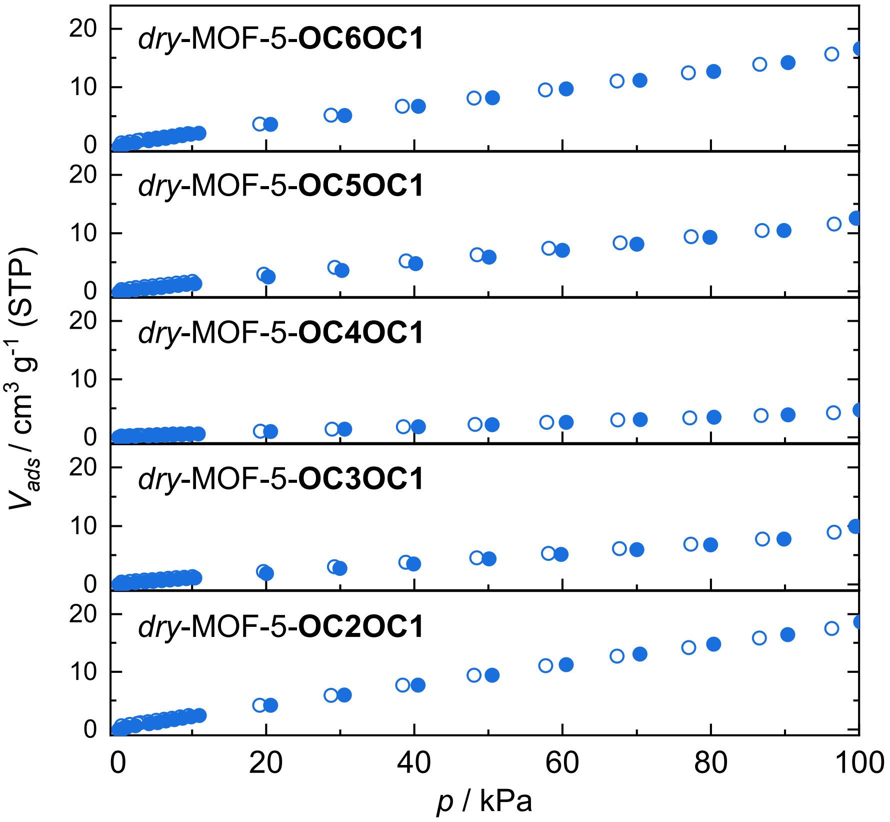

Figure 4.43: N_2 sorption isotherms of *dry*-MOF-5-**OC2OC1** to *dry*-MOF-5-**OC6OC1** recorded at 77 K. Adsorption and desorption branches are shown with closed and open symbols.

In contrast, CO_2 sorption experiments yield sorption profiles of Langmuir (Type I) shape for all the *dry*-MOF-5-**OCYOC1**, but with noticeable variability in the adsorbed amounts of CO_2 (Figure 4.44). In more detail, *dry*-MOF-5-**OC5OC1** and *dry*-MOF-5-**OC6OC1** show the highest CO_2 uptake of 73 to 75 cm^3g^{-1}, followed by *dry*-MOF-5-**OC2OC1** with 36 cm^3g^{-1}. From *dry*-MOF-5-**OC2OC1** to *dry*-MOF-5-**OC4OC1**, the CO_2 uptake is decreasing to just 11 cm^3g^{-1}. On the assumption that the sorption of CO_2 does not induce any structural response as observed for the *dry*-MOF-5-**OCX** (see section 4.3.5, Figure 4.29), the total pore volumes (extracted from the maximum uptake in the isotherms) were evaluated regarding the volumetric contraction of the *dry*-MOF-5-**OCYOC1** where no crystallographic indexing is possible (Y = 2 – 5). To gain a comparable approximation of the percentages of volume change upon contraction, the difference (ΔV) between the theoretical (V_{theo}) and experimental (V_{exp}) pore volumes were related to the crystallographic free volume of the as-synthesized phase ($V_{cub,cryst}$) utilizing the same procedure as for the *dry*-MOF-5-**OCX** under section 4.3.5 (see Figure 4.44, right, Table 4.14). The resulting estimated percentages of volume contraction amount to values ranging from –7% (*dry*-MOF-5-**OC5OC1**) to –33% (*dry*-MOF-5-**OC2OC1**). For *dry*-MOF-5-**OC5OC1** this is in reasonable agreement with the approximation from the PXRD data (–10% volume change), whereas the approximation for *dry*-MOF-5-**OC2OC1** significantly differs from that resulting from the PXRD data (–25%). This deviation likely arises from the strong structural contraction present in *dry*-MOF-5-**OC2OC1** (and probably also the -**OC3OC1** and -**OC4OC1** derivatives), which renders a large fraction of the presumably very narrow pores inaccessible to the CO_2 probe molecules. Moreover, it must be noted that the “cubic approximation” used to estimate the degree of contraction of the guest-free MOF phases may be an oversimplification, particularly if the contraction of the frameworks gets stronger. Thus, the disagreement between the values calculated form CO_2 sorption and estimated from the FSP of the PXRD data may also originate from the crude model applied to the later. Nevertheless, the CO_2 sorption behaviour of the *dry*-MOF-5-**OCYOC1** corroborates, that these materials undergo substantially stronger volumetric contractions upon guest-removal compared to their purely-alkoxy functionalized relatives.

Table 4.14: Data utilized for the estimation of the volumetric contraction of the *dry*-MOF-5-**OCYOC1** materials in relation to their as-synthesized phases. V_{exp} is the experimental pore volume per mole MOF. V_{theo} is the theoretical pore volume of a hypothetical crystalline cubic MOF-5-**OCYOC1** derived via interpolation (see text above). $\Delta V = V_{\mathrm{theo}} - V_{\mathrm{exp}}$. $V_{\mathrm{cryst,cub}}$ is the crystallographic volume of the corresponding cubic *as*-MOF-5-**OCYOC1** phase. %change = ΔV / $V_{\mathrm{cryst,cub}}$.

OCYOC1	V_{exp}/cm^3mol^{-1}	V_{theo}/cm^3mol^{-1}	ΔV/cm^3mol^{-1}	$V_{cub,cryst}$/cm^3mol^{-1}	%change
OC2OC1	84	513	429	1290	-33
OC3OC1	63	440	377	1299	-29
OC4OC1	29	367	338	1297	-26
OC5OC1	205	293	89	1298	-7

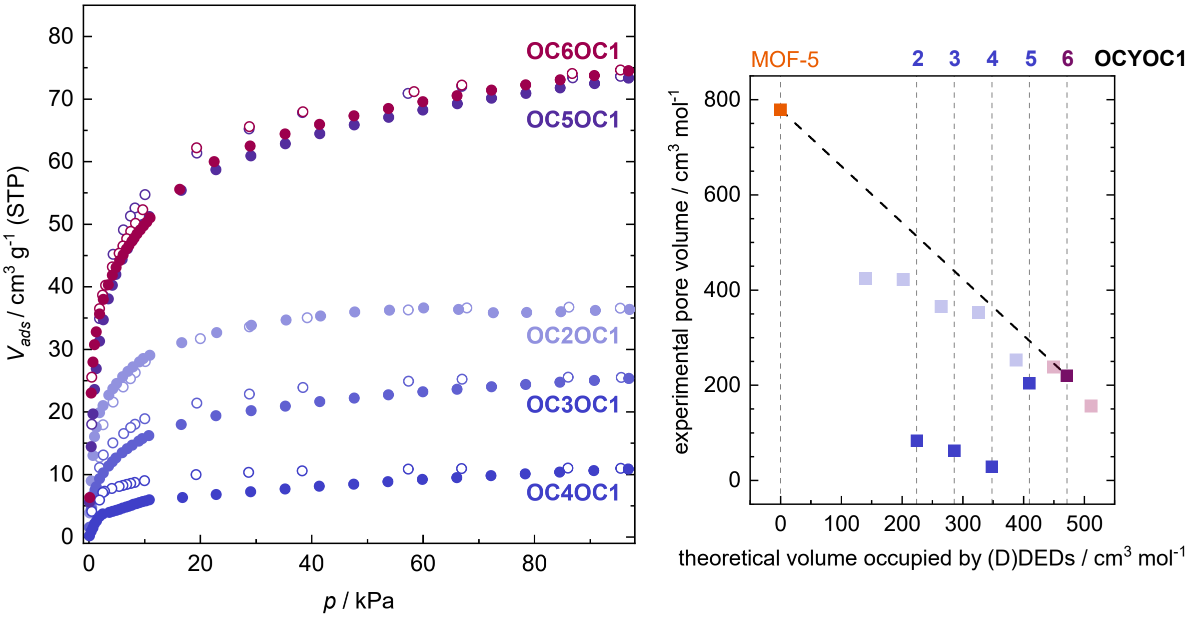

Figure 4.44: CO_2 sorption isotherms of *dry*-MOF-5-**OC2OC1** to *dry*-MOF-5-**OC6OC1** recorded at 195 K (left). Adsorption and desorption branches are shown with closed and open symbols. Plot of the experimental pore volumes (CO_2) vs. the theoretical volume occupied by (D)DEDs in *dry*-MOF-5-**OCYOC1** (right). The dashed line signifies the expected pore volumes obtained by linear interpolation from MOF-5 to *dry*-MOF-5-**OC6OC1**. Values corresponding to the *dry*-MOF-5-**OCX** are displayed in transparent colours.

In addition to N_2 and CO_2, the sorption behaviour of the *dry*-MOF-5-**OCYOC1** materials towards *n*-butane (293 K) was investigated due to the much different adsorbate-adsorbent interactions, which can provoke a distinct response, as has been shown in the previous chapter. Similarly, as with N_2 and CO_2, *dry*-MOF-5-**OC2OC1** to -**OC4OC1** do only take up small amounts of *n*-butane, which is ascribed to firstly, the heavy framework contraction and therefore limited pore accessibility of these materials and, secondly, the high polarity of the DDEDs, which only weakly interact with the non-polar *n*-butane guest-molecules (in line with the inability of *n*-octane infiltration to initiate the re-establishment of the cubic structures, Figure 4.45).

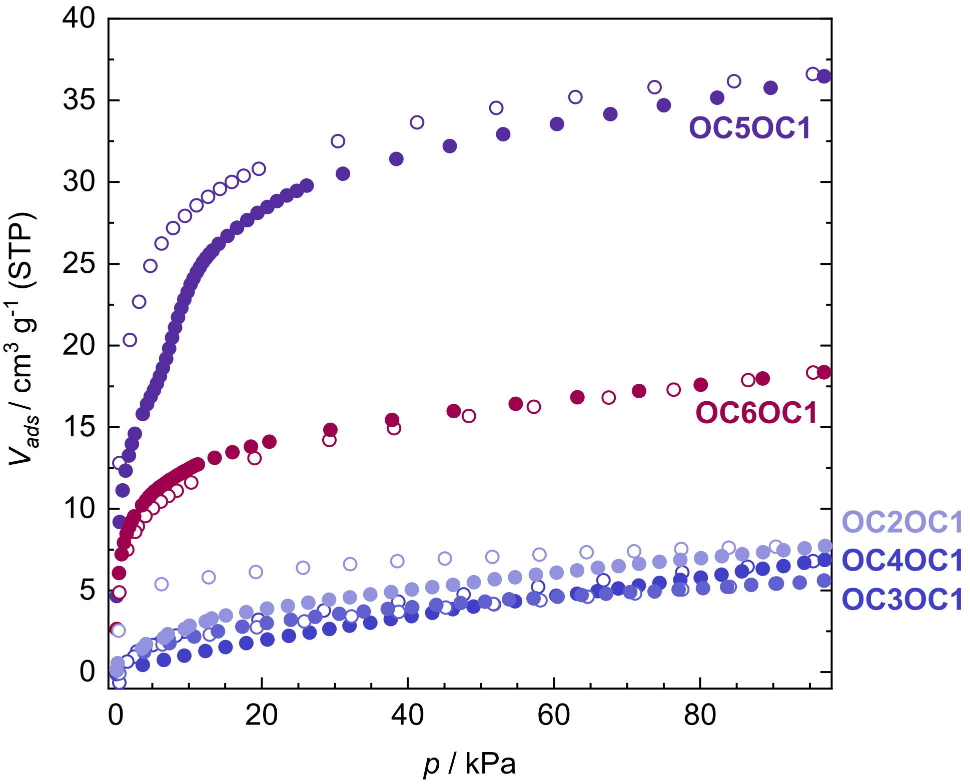

Figure 4.45: *n*-Butane sorption isotherms of *dry*-MOF-5-**OC2OC1** to *dry*-MOF-5-**OC6OC1** recorded at 293 K.

However, with increasing **Y**, as the DDED groups get less polar and with less structural contraction, there is a considerable *n*-butane uptake of 36 cm^{3}g^{-1} and 18 cm^{3}g^{-1} for the *dry*-MOF-5-**OC5OC1** and *dry*-MOF-5-**OC6OC1** materials, respectively. At this, the isotherm of *dry*-MOF-5-**OC6OC1** features a type I profile, which signifies the compound to keep its rhombohedrally distorted structure throughout *n*-butane adsorption, just as *dry*-MOF-5-**OC8** exhibiting the same (D)DED length. Interestingly, the *n*-butane isotherm of *dry*-MOF-5-**OC5OC1** features a stepped profile, hence indicating a structural response upon the adsorption of *n*-butane when a pressure of about 6 kPa is reached. A similar *n*-butane sorption behaviour is shown by *dry*-MOF-5-**OC7** due to a breathing transition from its rhombohedral to the cubic phase, which is taking place at about 8 kPa *n*-butane. For further comparison, the maximum uptakes of a virtual contracted and an expanded form were extracted via a dual-site Langmuir fitting of the isotherm parts belonging to either the contracted form, i.e., the sorption data before p_{trans}, or the expanded form of the MOF (see Figure 4.46 for the fits). This was done according to the following equation,

$$V_{ads} = \frac{V_{1,max}K_1p}{1+K_1p} + \frac{V_{2,max}K_2p}{1+K_2p}$$

where V_{ads} is the volume adsorbed at a pressure p, $V_{1,\mathrm{max}}$ and $V_{2,\mathrm{max}}$ are the volume adsorbed on site 1 or 2 and K_1 and K_2 are the equilibrium constant for the adsorption at these sites (for the fit parameters, see Table 4.15).

By contrast, for MOF-5-**OC5OC1** the difference in the maximum uptakes, $\Delta V_{ads,step}$, is considerably increased compared to MOF-5-**OC7** ($\Delta V_{ads,step}$(**OC5OC1**) = 11.2 cm^3mol^{-1}, ($\Delta V_{ads,step}$(**OC7**) = 8.7 cm^3mol^{-1}). This points towards a breathing transition between the non-crystalline and the cubic phase of MOF-**OC5OC1** as the associated contracted-to-cubic state volume change is of a larger magnitude (7-11% (**OC5OC1**) vs. 3% (**OC7**)) and the volume occupied by the (D)DEDs is 9% smaller (see Figure 4.44, right, and Figure 4.46) here. If this is indeed the case, MOF-5-**OC5OC1** undergoes a guest-induced discontinuous non-crystalline-to-cubic-crystalline phase transition, which has not been observed yet for frustrated flexible materials. Here, future studies should focus on the verification of these findings via *in-situ* PXRD experiments.

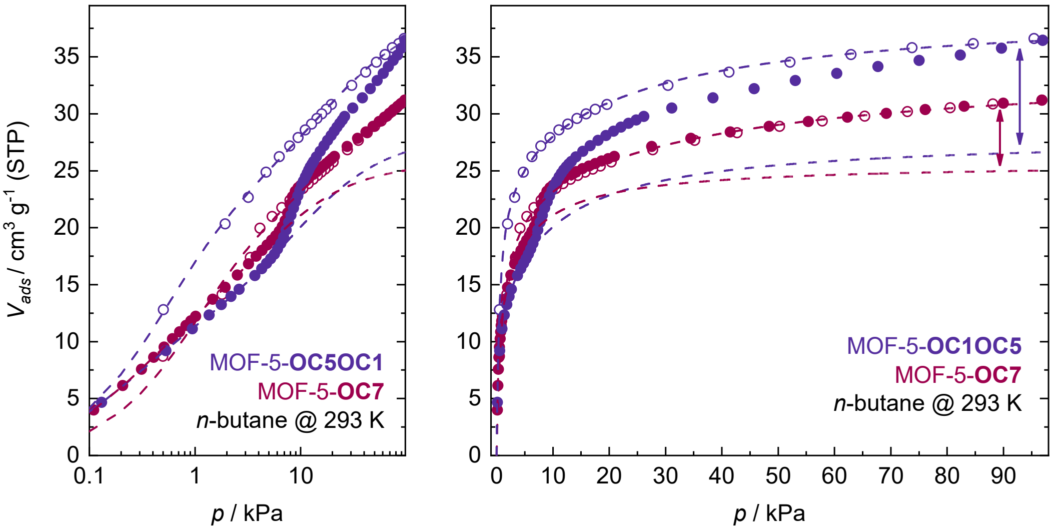

Figure 4.46: *n*-Butane sorption isotherms of *dry*-MOF-5-**OC5OC1** and *dry*-MOF-5-**OC7** (left: logarithmic pressure axis, right: linear pressure axis) with dual-site Langmuir fits of the expanded phase using the respective data of the desorption branch and the contracted phases of both materials using the sorption data up to p = 6 kPa (**OC5OC1**) or 8 kPa (**OC7**) (right, dashed lines). The difference in the maximum *n*-butane uptake due to proposed non-crystalline-to-cubic-crystalline phase transition of MOF-5-**OC5OC1** and the established rhombohedral-to-cubic phase transition of MOF-5-**OC7** is highlighted by arrows.

Table 4.15: Fit parameters of the dual-site Langmuir fit of the *n*-butane sorption isotherms of *dry*-MOF-5-**OC5OC1** and *dry*-MOF-5-**OC7**.

	$V_{1,max}$ / cm^3g^{-1}	K_1 / $cm^3g^{-1}kPa^{-1}$	$V_{2,max}$ / cm^3g^{-1}	K_2 / $cm^3g^{-1}kPa^{-1}$
OC5OC1 (contracted)	11.9(3)	4.5(2)	16.1(14)	0.11(2)
OC5OC1 (expanded)	24.4(5)	2.01(11)	14.8(3)	0.047(5)
OC7 (rhombohedral)	13.3(3)	0.21(2)	12.4(2)	3.90(9)
OC7 (cubic)	11.8(7)	0.028(10)	22.6(10)	1.02(12)

4.4.5 Final Comparison & Conclusion

The impact of a change in the (D)DED's functionality on the frustrated flexibility of a series of MOFs was investigated. Here, functionalized MOF-5 derivatives bearing methoxy-alkoxy DDEDs (MOF-5-**OCYOC1**) instead of purely alkoxy DEDs (MOF-5-**OCX**) exhibit significant differences in their frustratedly flexible behaviour. Ascribed to the higher DDED polarity, which results in stronger intra-framework interactions, the *dry*-MOF-5-**OCYOC1** tend towards a stronger structural distortion in comparison with their **OCX**-counterparts of the same DED length (–25% for **OC2OC1** vs. –14% for **OC4**, based on PXRD data). Since the framework architecture only allows for small distortions of its structure in a correlated fashion, the *dry*-MOF-5-**OCYOC1** materials remain in the regime of non-correlated distortion – displaying X-ray amorphization – with DDEDs exhibiting a linear chain of up to eight carbon/oxygen atoms. Hence, the first *dry*-MOF-5-**OCYOC1** material to show a rhombohedral distortion is *dry*-MOF-5-**OC6OC1**, bearing nine carbon/oxygen atoms in its DDED chain – one more than *dry*-MOF-5-**OC7** (chain of eight carbon/oxygen atoms). On the local scale, the structural contraction is accompanied by very strong geometrical distortions of the $Zn_4O(CO_2)_6$ clusters of the variants with **Y** = 2 – 4, which reduce from **Y** = 5, 6, as suggested by the XPDF and FT-IR data. Interestingly, a full recovery of the cubic crystalline phases of the MOF-5-**OCYOC1** is not afforded by reinfiltration with the non-polar *n*-octane guest as for the MOF-5-**OCX** but requires guests of higher polarity, such as diglyme or DMF. The CO_2 (195 K) and *n*-butane (293 K) sorption properties differ to the effect that for the -**OC2OC1** to -**OC4OC1** derivatives the gas uptakes are significantly reduced compared to their alkoxy relatives. This is ascribed to the heavier structural contraction of the *dry*-MOF-5-**OCYOC1** and the resulting inaccessibility of pore space. Remarkably, the *n*-butane sorption isotherm of *dry*-MOF-5-**OC5OC1** clearly indicates a breathing transition between its non-crystalline and cubic phase, where the associated uptake is significantly higher than for MOF-5-**OC7** due to the higher volume change upon the transition. Besides guest-induced flexibility also thermal responsiveness is indicated for *dry*-MOF-5-**OC5OC1** and -**OC6OC1**. In accordance with the rhombohedrally distorted *dry*-MOF-5-**OC7** and -**OC8**, *dry*-MOF-5-**OC6OC1** undergoes a thermally induced transition to its cubic phase, as indicated by DSC experiments. Regarding its behaviour at elevated temperatures, *dry*-MOF-5-**OC5OC1** is likely to resemble *dry*-MOF-5-**OC6** by undergoing a second order phase transition to the cubic state. Nevertheless, the detailed nature of the structural response to temperature of these two *dry*-MOF-5-**OCYOC1** derivatives is unknown so far. Hence, temperature dependent PXRD studies need to be performed in the future to shed light on the unusual responsiveness of these materials. Finally, the findings presented herein demonstrate the principal tunability of frustrated flexibility, not only by changing the chain length of the DEDs but also by their chemical modification.

4.5 Frustrated Flexibility in Other Metal-Organic Frameworks

After the exploration of guest- and temperature responsive frustrated flexibility and its tunability by chemical modification of the (D)DEDs for MOF-5 based materials, the final point remaining to be addressed in this chapter is the question of the transferability of frustrated flexibility onto other MOF platforms, which will be briefly done within this section. Here, two MOFs composed of the same $[Zn_4O(CO_2)_6]$ building block will be investigated backed by experimental data, whereas other MOFs will be discussed on a theoretical basis.

To assess the occurrence of frustrated flexibility in other MOF materials, as a first proof of concept, IRMOF-10,[28] which is an isoreticularly expanded variant of MOF-5 featuring 4,4'-biphenyldicarboxylate ($bpdc^{2-}$) linkers, and MOF-177[198] ($Zn_4O(btb)_2$, btb^{3-} = 1,3,5-benzene-tris(4'-benzoate)), of the entirely different **qom** topology were chosen as reference materials. Due to their high porosity (87% and 81% free volume for IRMOF-10 and MOF-177, respectively), linkers equipped with relatively long **OC8**-DEDs were prepared in a multi-step synthesis (**C8O**-$bpdcH_2$ and **C8O**-$btbH_3$, see Materials & Methods 6.1.3 for the full synthetic procedures). The corresponding MOFs were synthesized as large cubic or trigonal crystals (100-500 µm) from a DEF (*N,N*-diethylformamide) solution (IRMOF-10-**OC8**) or a DMF/NMP (N-methyl-2-pyrrolidone)/EtOH mixture[199] (MOF-177-**OC8**) heated at 100 °C for 48 h (for the detailed synthetic procedure see Materials & Methods 6.1.3). After washing with DMF and exchanging the solvent for benzene, the MOFs were activated by sublimation of benzene[200] at 0 °C *in vacuo* (ca. 10^{-4} kPa), followed by heating at 80 °C and 110 °C *in vacuo* for 21 h in total. The materials were proven guest-free via IR spectroscopy afterwards (Figure 4.48).

A comparison of *as*-IRMOF-10-**OC8** and *as*-MOF-177-**OC8** with simulated PXRD patterns of IRMOF-10 and MOF-177 clearly proves the analogy of the structural architecture of the MOFs (Figure 4.47). Furthermore, structureless profile refinement data are given in the Appendix section 8.2.1. Similar to the MOF-5-**OCX**, IRMOF-10-**OC8** and MOF-177-**OC8** transform from the crystalline state (*as*, guest-filled) into a non-crystalline, distorted state after guest-removal. For both compounds, the PXRD patterns only feature a broad FSP, with d_{FSP} = 15.73 Å for *dry*-IRMOF-10-**OC8** as determined by a fit using a split PearsonVII peak function (see Appendix Figure 8.38). An approximation via $(d_{FSP})^3$ yields a volume contraction of –22% for *dry*-IRMOF-10-**OC8** compared to its as-synthesized state. Due to the irregular shape of the FSP and the trigonal symmetry of the crystalline parent framework such an analysis could not be performed for *dry*-MOF-177-**OC8**.

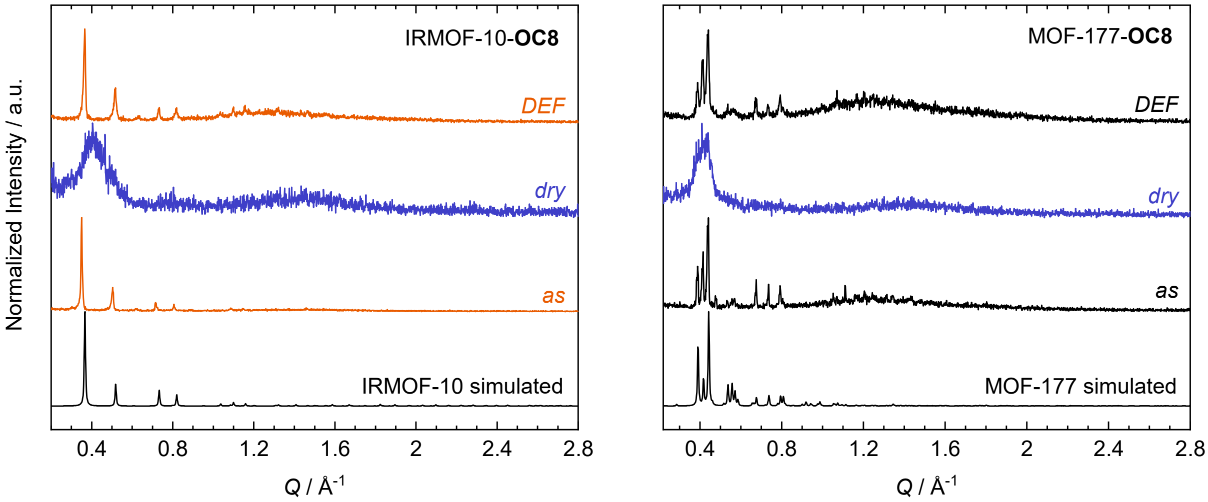

Figure 4.47: PXRD patterns of *as*-, *dry*- and DEF-reinfiltrated IRMOF-10-**OC8** and MOF-177-**OC8**.

Remarkably, *dry*-IRMOF-10-**OC8** and *dry*-MOF-177-**OC8** return to the crystalline state when DEF is added (Figure 4.47) as the sharp reflections of the as-phases re-emerge in the PXRD patterns. Particularly, for IRMOF-10-**OC8** these phase transitions can also be followed by IR spectroscopy, where the ν_{as}(COO) vibrational band at approx. 1550 cm^{-1} shows the typical broadening upon transition to the non-crystalline phase and sharpens again, when the material enters the crystalline state again (Figure 4.48).

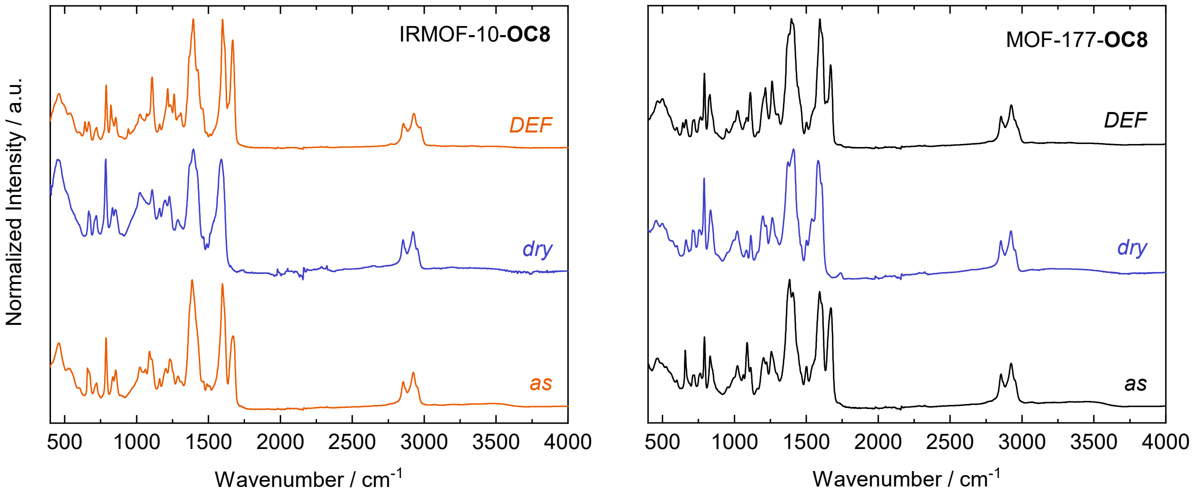

Figure 4.48: IR spectra of *as*-, *dry*- and DEF-reinfiltrated IRMOF-10-**OC8** and MOF-177-**OC8**.

It can thus be concluded that not only MOF-5-based materials, but also expanded versions of MOF-5, as well as a great number of other MOFs exhibiting the prominent [$Zn_4O(O_2C)_6$] node, may show stimuli-responsive frustrated flexibility as presented here. Note, that some of the recently reported polyMOFs, a class of MOF-5 based materials using polyether 2,5-alkoxy-bdc^{2-} linkers, likewise exhibit a dynamical loss and recovery of crystalline order in response to guest molecules.[201,202] In principle, it is likely that frustrated flexibility arises in any MOF material, if it possesses (i) a rigid framework structure, which does not allow for large-magnitude volume changes under retention of crystalline order and (ii) considerable tolerance towards functionalization of the MOF backbone with DED groups to appropriately manipulate the underlying free-energy landscape of the MOF materials. Finally, three other suitable MOF structure types, which meet these requirements and, hence, show potential for frustrated flexibility are briefly discussed in the following.

The first example consists in the well-known MIL-101 family of MOFs of the general chemical composition $[M_3O(X)(H_2O)_2(bdc)_3]$ ($X = OH^-$ or F^-, $M^{3+} = Cr^{3+}$, Fe^{3+})[203],[204] exhibiting the zeolitic 5- and 6-ring based **mtn** topology constructed of SBU-linker super tetrahedra, providing a rigid framework architecture with two different mesopores of ≈ 29 Å and ≈ 34 Å diameter. Importantly, MIL-101 is reported to allow for the implementation of a huge variety of functionalized bdc derivatives in the MOF synthesis,[205–208] including 2,5-di-fu-bdc^{2-} with fu = F, CH_3 and OCH_3,[207] which are chemically very similar to the **CXO**-bdc^{2-} type linkers used herein (Figure 4.49, top).

As a second example, the prominent isoreticular UiO-66/67/68[209] series is proposed, which is constructed of $Zr_6O_4(OH)_4(CO_2)_{12}$ clusters interconnected by bdc^{2-}, bpdc^{2-} or terphenyl dicarboxylate (tpdc^{2-}) linkers, respectively, as this class of materials has been demonstrated suitable for the functionalization of the organic linkers.[108,210–214] Their up to 12-fold interconnection at the inorganic building unit results in naturally rigid framework structures of fcu topology (Figure 4.49, middle).[161,215,216] However, upon inclusion of additional functional groups, their propensity for defect formation (e.g., missing linker defects)[217–219] might lead to a lower connectivity, which can further facilitate the appearance of frustrated flexibility in the material. Taking the formation of missing linker defects further, Zr_6O_4-node based MOFs of lower, e.g., 6-fold connectivity can be generated as in the case of MOF-808, which acts as the third example to be mentioned here. Pristine MOF-808[220] is of the general chemical composition $Zr_6O_4(OH)_4(btc)_2(HCOO)_6$ (btc^{3-} = 1,3,5-benzene tricarboxylate) and featuring the spn topology (Figure 4.49, bottom). Its most prominent quality is the exchangeability of the six formate anions of the inorganic unit by other carboxylates, which has been made use of to anchor amino acids or even copper amine complexes to the framework backbone.[221,222] By this approach, the confined pore space of this MOF-type could be decorated with suitable DED groups potentially turning the balance of framework energetics towards the occurrence of frustrated flexibility.

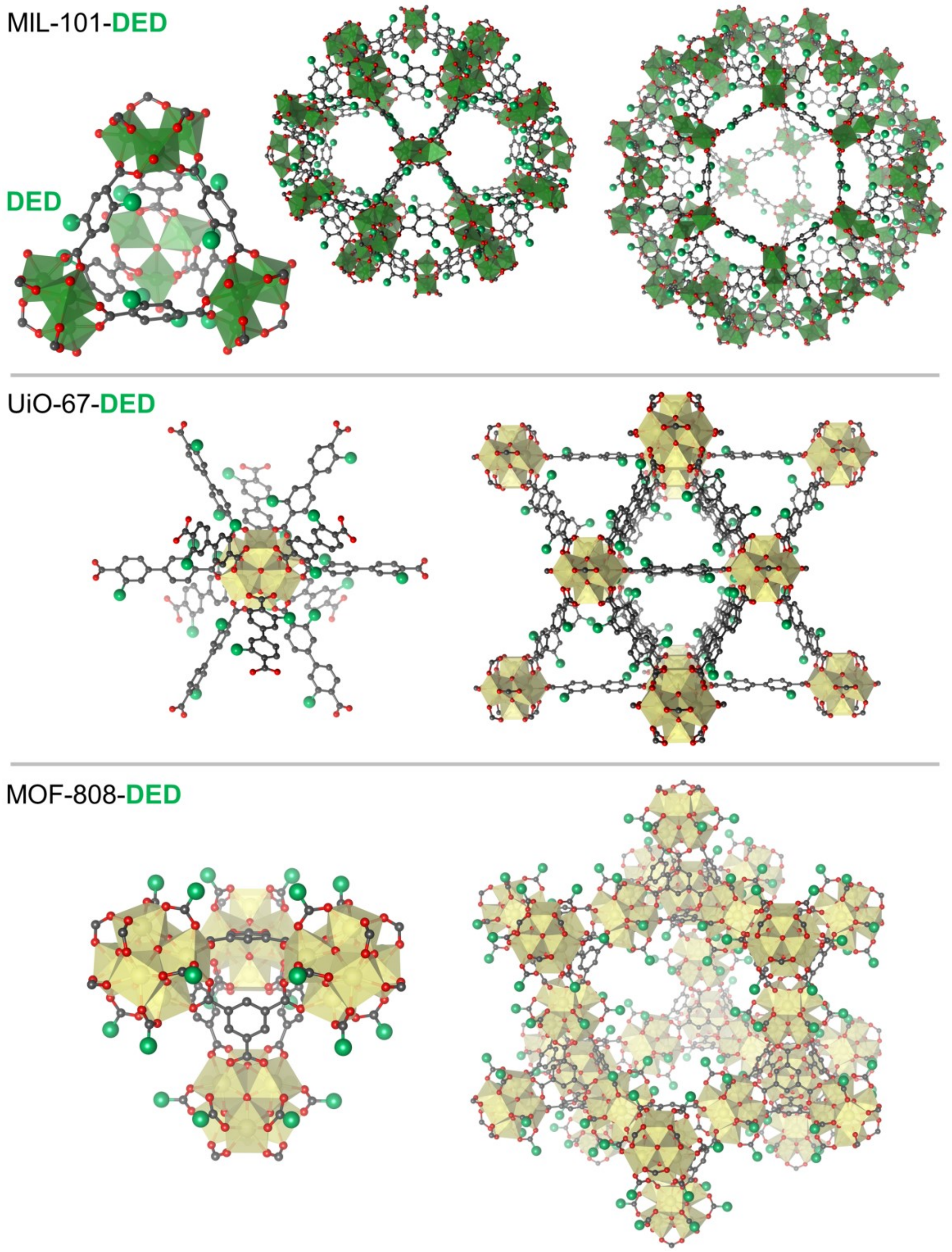

Figure 4.49: Representations of potential DED-functionalized variants of MIL-101 (top), UiO-67 (middle) and MOF-808 (bottom) in the style of Figure 4.2. DED groups are depicted as green spheres and Cr or Zr are depicted as green or light-yellow spheres and polyhedrons, respectively. For MIL-101 only the small one of the two pores of the framework is shown. The representations were created based on the SCXRD or Rietveld-refined structures of unfunctionalized MIL-101 (CCDC deposition code 605510), dimethyl functionalized UiO-67 (CCDC deposition code 1422392) and MOF-808 with bound histidine (CCDC deposition code 1886178).

In principle, frustrated flexibility may be an unrecognized feature of a number of other MOF structure types, which so far are deemed to be structurally rigid but could straightforwardly be functionalized with suitable DEDs.[159,161] Moreover, it might be the case that frustrated flexibility, i.e. the incompatibility of intra-framework forces with the geometrical constraints of the MOF's building units, is a fundamental principle behind the frequently reported amorphization of MOFs upon guest removal.[149,223–225] In this regard, future work may focus on discovering the consequences of frustrated flexibility for existing and well-studied MOF families, such as the three examples mentioned above. Overall, inducing frustrated flexibility into rigid MOF materials might generate exciting, unconventional, and potentially useful responsive properties in these materials.

5 General Summary & Outlook

In this thesis, the modulation of the behaviour of flexible MOFs by means of chemical functionalization using alkyl-, alkoxy-, and methoxy-alkoxy groups, which are covalently joined at the organic bdc^{2-} linkers of the framework, was studied. These groups have a huge impact on the free energy landscape of the investigated materials as they undergo dipolar and dispersion interactions with the framework backbone, guest molecules and themselves. This type of functionalization was applied to two MOF platforms with fundamentally different properties regarding the structural conditions for a flexible behaviour and, hence, show a fundamentally different response to the functionalization.

In chapter 3, the first material platform discussed is DMOF-1, which is intrinsically flexible through hinging along the O–O axes of the carboxylates. For these materials it is known from the literature that a functionalization with alkoxy groups leads to a guest-depending switching between ***lp*** and ***np*** phases. In this work, the library of functionalized derivatives of this type was extended by three purely alky (ethyl, propyl, and butyl) functionalized compounds devoid of a phenolic ether O-atom. These three compounds, denoted DMOF-1-**CX** (**X** = 2 – 4), exhibit a similar guest-depending phase behaviour as their alkoxy relatives. Notably, by means of SCXRD and *in-situ* gas sorption PXRD very detailed structural insights into the chemical nature (i.e., interactions between various building units, host-guest interactions, configuration of the side chains, torsion of the phenyl rings of the linkers with respect to the carboxylate groups, porosity) of the expanded guest-filled ***lp*** and contracted guest-free ***np*** phases of this material class is provided for the first time (Figure 5.1, left). Compared to their alkoxy relatives, the DMOF-1-**CX** exhibit a smaller volumetric contraction of their ***np*** states, which is attributed to the weaker interactions of the non-polar alkyl side chains compared to the previously used alkoxy side chains. Importantly, SCXRD structures of DMOF-1-**C3** including different solvents prove the high conformational flexibility of the side chains for efficient encapsulation of various guest molecules, which in turn suggests a flat conformational energy landscape for this material (Figure 5.1, right).

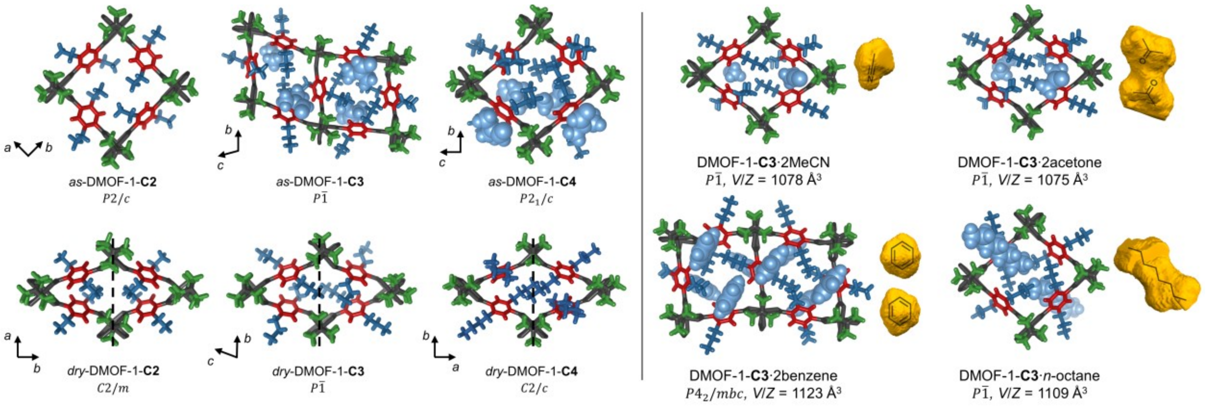

Figure 5.1: Selected SCXRD structures of the DMOF-1-**CX** presented in this thesis. Structures of the *as*- and *dry* states are displayed on the left, while the SCXRD structures of DMOF-1-**C3** filled with different solvents are given on the right.

The new alkyl-functionalized DMOF-1-**CX** were investigated regarding their gas sorption and thermal behaviour and subsequently compared to their alkoxy relatives of the same overall substituent chain length. Upon sorption of CO_2 all DMOF-1-**CX** display the expected stepped isotherms with a slightly lower maximum CO_2 uptake than their alkoxy relatives, which likely relates to less strong interactions with the adsorbate molecules compared to the DMOF-1-**OCY**.

However, the CO_2 sorption behaviour of DMOF-1-**C3** is remarkably different as its isotherm features a multi-stepped shape with deviating profiles depending on the history (ad- or desorption) of the material (Figure 5.2, left). *In-situ* CO_2 sorption PXRD experiments and subsequent Rietveld refinements revealed that both opening and closing of the structure proceeds about two different intermediate pore ($\boldsymbol{ip_{ads}}$ or $\boldsymbol{ip_{des}}$) phases. The extracted structural data suggest that the propyl groups of the MOF are strongly involved here due to comparably unfavourable interactions with the CO_2 guest molecules (Figure 5.2, right).

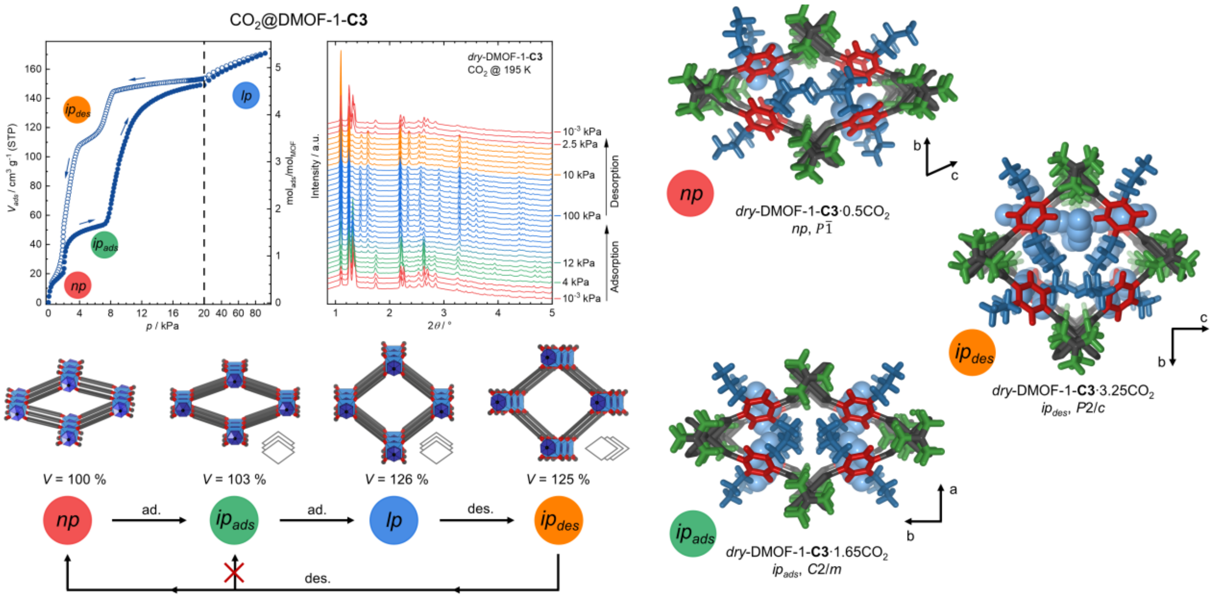

Figure 5.2: Summary of the CO_2 sorption behaviour of DMOF-1-**C3**. The CO_2 sorption isotherm and corresponding *in-situ* PXRD data with simplified models of the assigned phases are given on the left. Structural models extracted by Rietveld refinement are given on the right.

The industrial separation of light hydrocarbons such as propane and propylene still remains an energy and cost intensive procedure. Hence, the sorption behaviour of the DMOF-1-**CX** materials towards the hydrocarbons *n*-butane, propane, and propylene (273 K, 298 K) was assessed with a particular focus on the potential for propane/propylene separation. It was found that DMOF-1-**C2** to -**C4** all exhibit a preference of adsorbing propane over propylene (Figure 5.3, top), which is beneficial for a potential separation application since propane is the less valuable product to be filtered out. Upon adsorbing the hydrocarbons, the three materials transform to expanded ***lp*** forms, where the phase transition pressures increase from DMOF-1-**C2** to DMOF-1-**C4** related to the free volume fraction in the ***np*** structures. Here, DMOF-1-**C4** barely transforms to the ***lp*** phase only upon adsorbing propane under the applied experimental conditions (maximum pressure 100 kPa, 273 K). In particular DMOF-1-**C3** proves interesting for propane/propylene separation as it shows a distinct ***np*→*lp*** gate-opening transition with a clear pressure difference for both gases within a sensible pressure range (Figure 5.3, bottom). This was investigated by *in-situ* gas sorption PXRD, which further allowed Rietveld refinement of structural models of both propane and propylene filled ***lp*** phases. For both gases the facile formation of channels throughout the material during the ***np*→*lp*** phase transition by about 60° rotations of the phenyl rings of 50% of all linkers, gives an explanation for the vast transformation after reaching the transition pressure. Furthermore, DMOF-1-**C3** shows excellence tolerance towards repetitive ad-/desorption cycling and the exposition to humid atmosphere of up to 50% RH (Figure 5.3, bottom).

A comparison of the hydrocarbon sorption behaviour of the DMOF-1-**CX** with their alkoxy counterparts revealed that the latter transform to their ***lp*** phases at significantly higher pressures, which is reasonable in the light of the higher polarity of the alkoxy side chains. Moreover, all alkoxy-based derivatives adsorb significant amounts of hydrocarbon gases already in their ***np*** phases, while the ***np*** phases of DMOF-1-**C3** and DMOF-1-**C4** are inaccessible to those gases. Due to this feature, DMOF-1-**C3** provides the highest working capacities for a small pressure swing of all materials studied here.

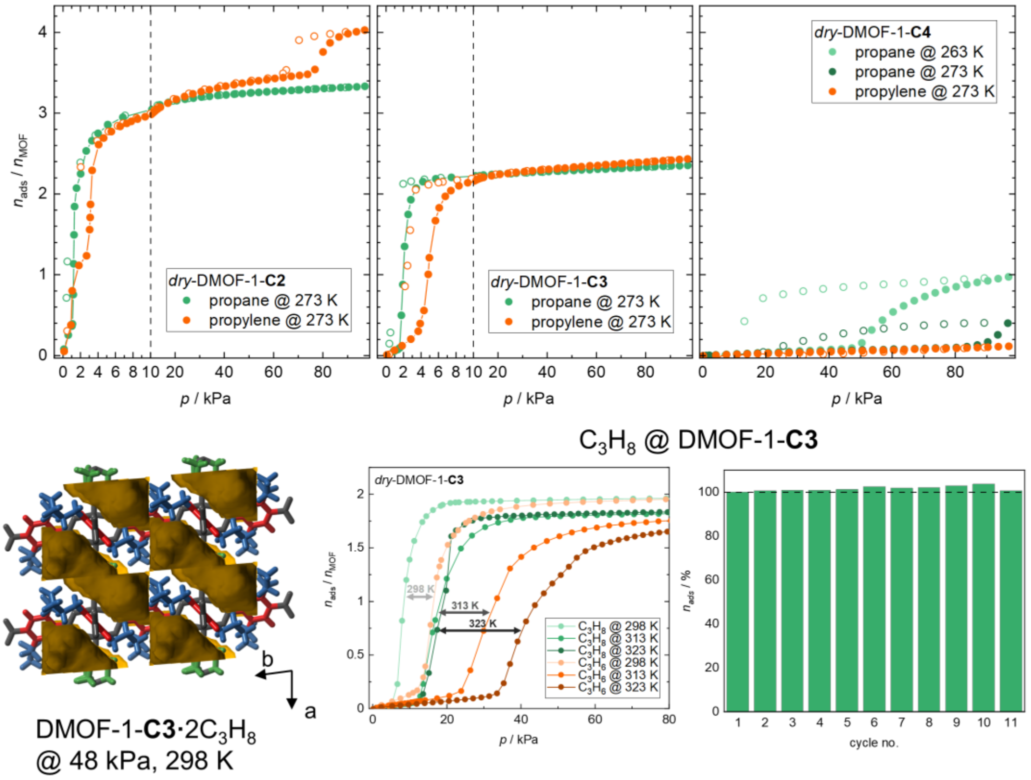

Figure 5.3: Selected propane and propylene sorption data of the DMOF-1-**CX** (top). The structural model and further propane and propylene sorption data recorded from 298 to 323 K for DMOF-1-**C3** (bottom, left and centre, respectively). Furthermore, the propane uptake of DMOF-1-**C3** in repeated sorption cycles in given (bottom, right).

The thermal behaviour of DMOF-1-**C3** and -**C4** was investigated and compared to their alkoxy relatives as well. Here, DMOF-1-**C3** exhibits the typical anisotropic thermal expansion without a structural transformation to the ***lp*** phase, similar to reports on DMOF-1-**OC2** (Figure 5.4, left). By contrast, DMOF-1-**C4** undergoes a stepwise transition from the ***np*** over an ***ip*** to the ***lp*** phase at elevated temperatures (Figure 5.4, right). Crystallographic analyses indicated that the ***np***→***ip*** phase transition relates to the increase of the vibrational entropy of the alkyl chains, while the ***ip***→***lp*** transition corresponds to an increase in configurational entropy facilitated by phenyl ring rotations.

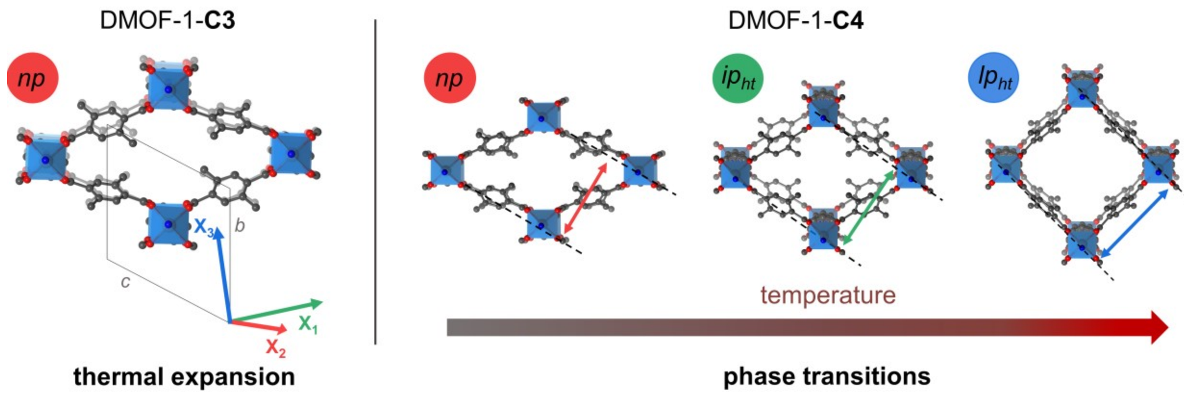

Figure 5.4: Summarized thermal phase behaviour of DMOF-1-**C3** (left) and DMOF-1-**C4** (right).

Interestingly, for the DMOF-1-**OCY** materials thermally induced ***np***→***lp*** phase transitions are only possible when the side chain is longer by one more non-hydrogen atom. In combination with the other results obtained herein, this indicates that, compared to the alkoxy relatives, the purely alkyl functionalized materials feature a considerably flatter free energy landscape as they undergo less strong intra-framework interactions due to the reduced polarity of the side chains. The flatter free energy landscape gives access to multiple phase transitions upon guest uptake (i.e., CO_2 sorption in DMOF-1-**C3**) or increases in temperature (i.e., DMOF-1-**C4**).

In chapter 4 the new concept of frustrated flexibility was presented. By contrast to the previous chapter, it is based on a rigid, non-responsive MOF structure type, not allowing any concerted hinging movements of its building parts (here MOF-5, see Figure 5.5, left). This is decorated at the organic building unit with dispersion energy donating alkoxy groups, which impact the free energy landscape of the MOF so that a contraction of the structure becomes energetically favoured. Ultimately, in such a rigid material this can only occur upon loss of crystalline order, entering a state of frustration.

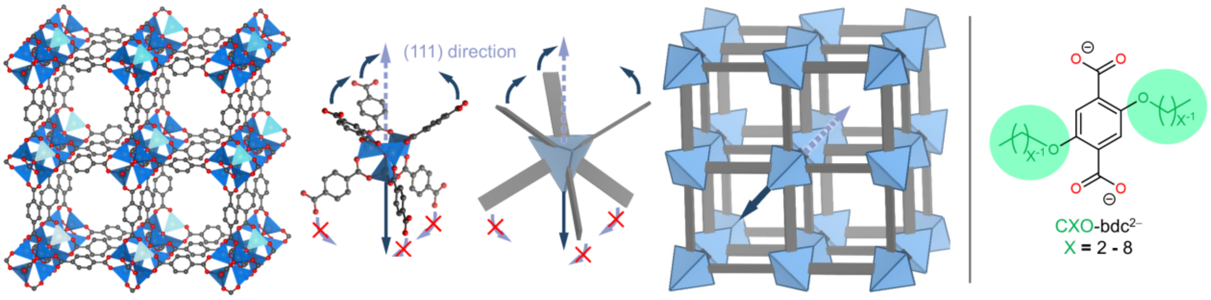

Figure 5.5: Structural features of the $Zn_4O(CO_2)_6$ building units, which render MOF-5 a rigid material (left). Alkoxy-functionalized bdc^{2-} linkers used to induce frustrated flexibility (right). DED groups are marked in green.

This concept was demonstrated for a series of alkoxy-functionalized MOF-5-**OCX** ($\mathrm{Zn_4O}$(**CXO**-bdc)$_3$ (**CXO**-bdc^{2-} = 2,5-dialkoxy-1,4-benzenedicarboxylate)) with **X** = 2 – 8 (Figure 5.5, right). As investigated by single crystal and powder X-ray diffraction techniques, these materials exhibit guest-induced structural transformations between either a cubic and a rhombohedral phase for small volume changes (–3%) or a cubic and a non-crystalline phase (*dry*-MOF-5-**OC2** to *dry*-MOF-5-**OC6**) for volume changes of greater extent (–17% to –6%). In case of the latter, the stronger structural contraction mediated by the DED groups requires the entering of the frustrated state. Both types of phase transitions are displacive in nature since solvent coordination or framework reconstruction could be ruled out as a cause of this behaviour by means of *n*-octane infiltration, which afforded the recovery of the cubic phases (Figure 5.6).

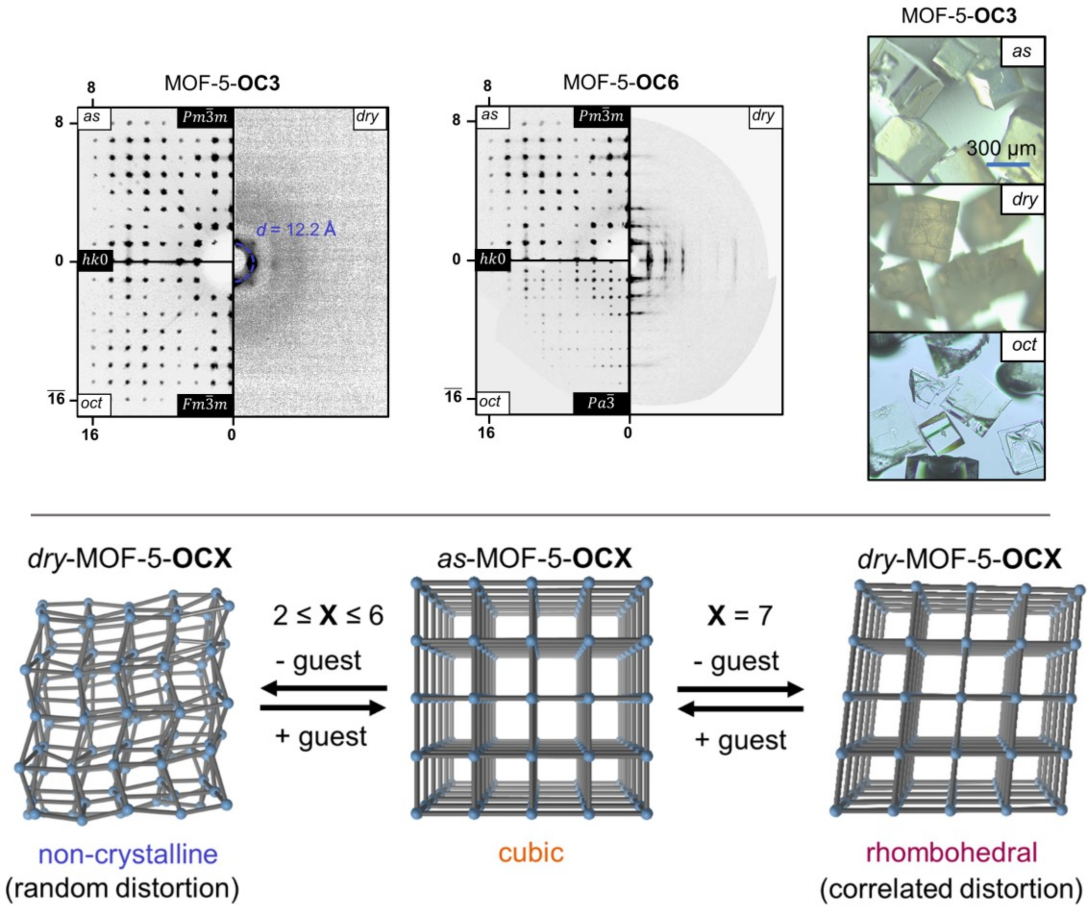

Figure 5.6: SCXRD data of MOF-5-**OC3** and **-OC6** in their *as*-, *dry*-, and *oct*-states (top, left and centre) and the visual impact of the structural transformations on crystals of MOF-5-**OC3** (top, right). The guest-depending structural behaviour of the MOF-5-**OCX** (**X** = 2 – 7) materials is summarized at the bottom.

Furthermore, the local structure of the MOF-5-**OCX** series was investigated by means of solid-state NMR, X-ray total scattering PDF, and FT-IR spectroscopic analysis. This revealed that the local structure of the non-crystalline *dry*-MOF-5-**OCX** can be understood in terms of an ensemble of differently distorted, non-correlated [$\mathrm{Zn_4O(CO_2)_6}$] building units, where the degree of distortion increases with decreasing length of the alkoxy group (Figure 5.7).

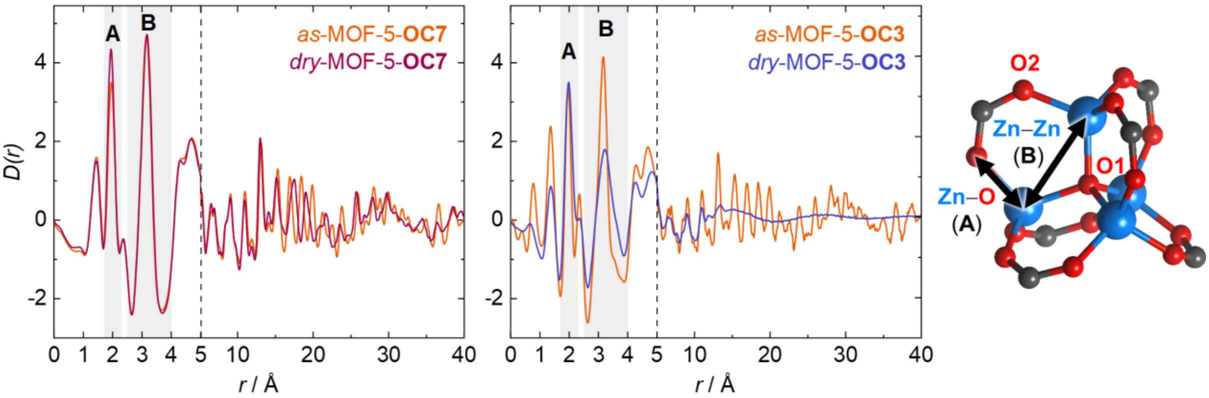

Figure 5.7: Different changes in the local structures of MOF-5-**OC7** and -**OC3** between their *as*- and *dry*-states examined by XPDF analysis.

The structural behaviour could be reproduced by MD simulations, which were performed by J. KEUPP and R. SCHMID, and furthermore allow for thermodynamic insights into the MOF-5-**OCX** materials. These corroborate that the structural contractions are indeed enthalpically driven by dispersion interactions between the DED groups with themselves and the framework backbone. As shown via DSC and variable-temperature PXRD experiments, these interactions are overcome by vibrational entropy at elevated temperatures. This results in either discontinuous (rhombohedral-to-cubic) for *dry*-MOF-5-**OC7** and -**OC8** or continuous (non-crystalline-to-cubic) transformations for *dry*-MOF-5-**OC6** and -**OC5**. Besides, the adsorption of guest molecules, in particular *n*-butane (273 K), leads to similar, but here enthalpically driven transformations to the cubic phases of *dry*-MOF-5-**OC5** to -**OC7**. At this, *dry*-MOF-5-**OC7** exhibits again a discontinuous breathing transition, while *dry*-MOF-5-**OC6** and -**OC5** continuously transform to the cubic phases.

By the novel approach presented herein, frustratedly flexible MOFs, which were previously deemed rigid, are now endowed with unprecedented physical properties, such as continuous non-crystalline-to-crystalline transitions driven by entropy rather than enthalpy.

How these properties are tuned by modulating the polarity of the (D)DED (dipolar and dispersion energy donator) groups was investigated for a series of MOF-5 derivatives bearing methoxy-alkoxy groups (MOF-5-**OCYOC1**) instead of purely alkoxy DEDs. Due to their higher polarity and therefore stronger interactions of the DDEDs the MOF-5-**OCYOC1** exhibit a significantly different behaviour (Figure 5.8). Firstly, in their guest-free state, the *dry*-MOF-5-**OCYOC1** feature a stronger structural distortion than their alkoxy relatives with roughly the same chain length (–25% for **OC2OC1** vs. –14% for **OC4**, based on PXRD data). Followingly, the regime of non-correlated structural distortion extends to a higher number of (D)DED chain atoms since only small contractions of the MOF-5 platform are feasible maintaining crystalline order. Here, MOF-5-**OC5OC1** still transforms to a poorly crystalline state upon guest removal, while *dry*-MOF-5-**OC7** is rhombohedral.

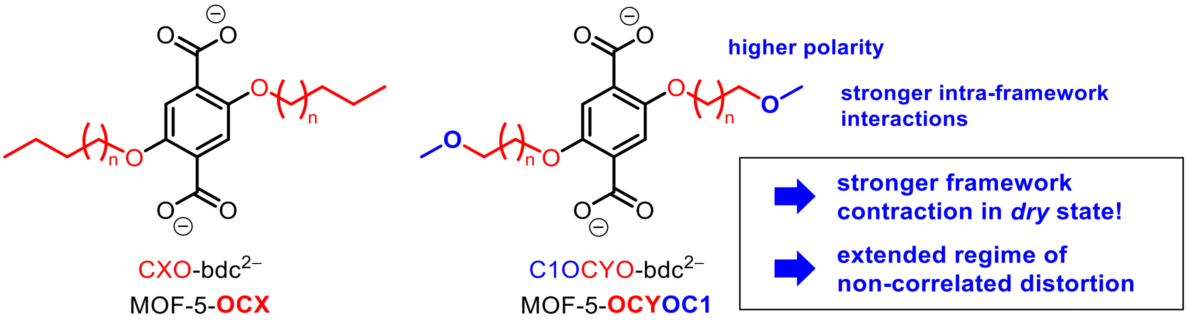

Figure 5.8: The impact of higher polarity of the side chains of the MOF-5-**OCYOC1** materials with respect to their MOF-5-**OCX** relatives.

On the local scale, the structural contractions of the *dry*-MOF-5-**OCYOC1** come along with strong distortions of the $[Zn_4O(CO_2)_6]$ building units of comparable magnitude for $\mathbf{Y} = 2 - 4$, which successively reduces from $\mathbf{Y} = 5$ to $\mathbf{Y} = 6$.

In line with the increased polarity of the DDEDs, the structural distortion of the *dry*-MOF-5-**OCYOC1** could not be reversed by reinfiltration with *n*-octane but requires the usage of the more polar guest molecules diglyme or DMF to transform to the cubic state again. Due to their strong structural contraction, hence, potential pore blocking and higher DDED polarity *dry*-MOF-5-**OC2OC1** to -**OC4OC1** exhibit significantly lower porosity towards CO_2 (195 K) and none towards *n*-butane (273 K). Remarkably, the *n*-butane sorption isotherm of *dry*-MOF-5-**OC5OC1** suggests a breathing between the non-crystalline and cubic phases of this compound. Related to the greater volume difference between both phases compared to *dry*-MOF-5-**OC7**, the uptake associated with the phase transition is significantly higher for *dry*-MOF-5-**OC5OC1**.

The collected DSC data further suggest a thermal responsiveness of *dry*-MOF-5-**OC5OC1** and *dry*-MOF-5-**OC6OC1**, where the former undergoes a continuous transformation from the non-crystalline to the cubic phase very similar to *dry*-MOF-5-**OC6**. For the latter, a transformation from the rhombohedral to the cubic phase is indicated in accordance with the behaviour of *dry*-MOF-5-**OC7** and -**OC8**. However, the *n*-butane and thermally induced flexibility still needs to be verified by *in-situ* PXRD experiments.

Finally, the concept of frustrated flexibility was successfully applied to other MOF platforms based on $[Zn_4O(CO_2)_6]$ building units. Here, the isoreticularly expanded variant of MOF-5, IRMOF-10, and MOF-177 of the completely different **qom** topology were endowed with **OC8**-alkoxy groups, which resulted in a similar reversible guest-depending switching between a crystalline guest-filled and a non-crystalline phase devoid of guest molecules. Finally, other potential candidates for frustrated flexibility, which fulfil the two main criteria, i.e., a rigid MOF structure and suitable tolerance towards functionalization of the organic linker, namely MIL-101, UiO-67 and MOF-808, were picked from the literature and discussed. These examples might be investigated in detail in future studies on frustrated flexibility.

In summary, the results presented in this thesis showcase that the functionalization of the organic linkers with alkyl or alkoxy side chains is a powerful tool for manipulating the stimuli responsive phase behaviour of MOF materials. At this, the balance between enthalpic and entropic contributions to the free energy landscape of the MOF materials is changed depending on the chemical nature of functional groups. Utilizing this approach allows for, (i) precise and systematic tuning of existing flexibility in a MOF system or (ii) giving rise to completely new flexible behaviours in otherwise structurally rigid and non-responsive MOFs. Importantly, the latter opens the field to endow in principle any MOF, particularly those previously considered rigid, with fundamentally new and exotic responsive properties, as long as they are tolerant towards suitable chemical functionalization.

Such alike functionalized materials come with flat free energy landscapes resulting in guest- and temperature-induced multiple phase transition behaviours, which are controlled by the chemical nature of the functional groups (i.e., polarity, steric bulk). Consequently, these materials can be modulated to act highly guest-specific, which is very beneficial for applications such as gas storage or separation. Furthermore, the emerging unusual thermal behaviours render these functionalized MOF materials interesting candidates for applications in the fields of energy storage and transfer.

Ultimately, this constitutes a good example of how the modular nature of MOFs can be exploited to change essential materials properties, which is not possible for conventional porous materials.

6 Materials & Methods

6.1 Materials Synthesis

6.1.1 General Considerations

All chemicals used herein were purchased from commercial suppliers (Sigma-Aldrich, abcr, Alfa-Aesar, etc.) and used without further purification.

6.1.2 Synthetic Procedures to Chapter 3

Synthesis of the **CX**-bdcH_2

All three **CX**-bdcH_2 derivatives were synthesized using the same procedures. Hence, only an exemplary synthesis of **C3**-bdcH_2 is described below.

A Schlenk tube was loaded with 1,4-dipropyl benzene (4.30 g, 26.50 mmol, 1.0 eq.) and Iodine (0.034 g, 0.13 mmol, 0.005 eq.) was added. The mixture was cooled to 0 °C and under exclusion of light, Bromine (8.47 g, 53 mmol, 2.0 eq.) was added dropwise over a period of 1 h. After warming up to room temperature overnight, 30 ml of 25% aqueous KOH were added, and the reaction mixture stirred for about 15 min until full decolorization. The precipitating solid was filtered off and dissolved in 75 ml of EtOH at 75 °C. This solution was cooled to −7 °C overnight to give white needle-shaped crystals, which were filtered off and dried *in vacuo* to give the pure 1,4-Dibromo-2,5-dipropyl benzene (4.33 g, 51%).
1,4-Dibromo-2,5-diethyl benzene, ^{1}H NMR (400 MHz, DMSO-d_6) δ 7.54 (s, 1H, Ar-H), 2.65 (q, J = 7.2 Hz, 2H, CH_2), 1.14 (t, J = 7.2 Hz, 3H, CH_3). *1,4-Dibromo-2,5-dipropyl benzene*, ^{1}H NMR (600 MHz, DMSO-d_6) δ 7.53 (s, 1H, Ar-H), 2.61 (t, J = 7.7 Hz, 2H, Ar-CH_2), 1.59-1.51 (m, 2H, CH_2), 0.91 (t, J = 7.3 Hz, 3H, CH_3). *1,4-Dibromo-2,5-dibutyl benzene*, ^{1}H NMR (500 MHz, DMSO-d_6) δ 7.52 (s, 1H, Ar-H), 2.63 (t, J = 7.7 Hz, 2H, Ar-CH_2), 1.55 – 1.47 (m, 2H, CH_2), 1.36 – 1.28 (m, 2H, CH_2CH_3), 0.90 (t, J = 7.3 Hz, 3H, CH_3).

In argon atmosphere, to a solution of 1,4-dibromo-2,5-dipropyl benzene (4.33 g, 13.53 mmol, 1 eq.) in 60 ml DMF, Copper(I) cyanide (3.63 g, 40.53 mmol, 3 eq.) was added to give a greenish suspension, that was refluxed for 2 d. After cooling to room temperature, the reaction mixture was poured into 25% aqueous NH_3, resulting in the precipitation of an off-white solid from a deep-blue solution. The solid was filtered off and washed with further 150 ml of 25% aqueous NH_3 and 200 ml water. Soxhlet extraction using Acetone and subsequent drying *in vacuo* afforded a pure product (2.25 g, 78%). On occasions, where the product was not sufficiently pure for further use, additional recrystallization from ethanol or acetone gave the pure product.

1,4-Dicyano-2,5-diethyl benzene, ^{1}H NMR (400 MHz, DMSO-*d$_6$*) δ 7.96 (s, 1H, Ar-H), 2.80 (q, J = 7.6 Hz, 2H, CH$_2$), 1.22 (t, J = 7.6 Hz, 3H, CH$_3$). *1,4-Dicyano-2,5-dipropyl benzene,* ^{1}H NMR (500 MHz, DMSO-*d$_6$*) δ 7.94 (s, 1H, Ar-H), 2.76 (t, J = 7.6 Hz 2H, Ar-CH$_2$), 1.68 – 1.59 (m, 2H, CH$_2$), 0.91 (t, J = 7.3 Hz, 3H, CH$_3$). *1,4-Dicyano-2,5-dibutyl benzene*, ^{1}H NMR (500 MHz, DMSO-*d$_6$*) δ 7.95 (s, 1H, Ar-H), 2.78 (t, J = 7.7 Hz, 2H, Ar-CH$_2$), 1.62 – 1.54 (m, 2H, CH$_2$), 1.35 – 1.25 (m, 2H, C*H$_2$*CH$_3$), 0.90 (t, J = 7.3 Hz, 3H, CH$_3$).

A suspension of 1,4-dicyano-2,5-dipropyl benzene (2.25 g, 10.59 mmol, 1 eq.) and KOH (1.79 g, 32.49 mmol, 3 eq.) in 30 ml diethylene glycol was refluxed for 1 d. After cooling to room temperature, the resulting dark-brown mixture was diluted with 45 ml water and acidified using 10% aqueous HCl. The precipitate was filtered off and washed with 150 ml water and dried *in vacuo* at 80 °C. Recrystallization from ethyl acetate and acetonitrile afforded the pure off-white product (1.26 g, 48%).

2,5-Diethyl-1,4-benzenedicarboxylic acid (C2-bdcH$_2$), ^{1}H NMR (400 MHz, DMSO-*d$_6$*) δ 13.11 (s, 2H, COO-H), 7.65 (s, 2H, Ar-H), 2.89 (q, J = 7.4 Hz, 4H, CH$_2$), 1.15 (t, J = 7.4 Hz, 6H, CH$_3$); ^{13}C NMR (100 MHz, DMSO-*d$_6$*) δ 168.4, 141.8, 133.2, 131.4, 26.1, 15.9. *2,5-Dipropyl-1,4-benzenedicarboxylic acid* (C3-bdcH$_2$), ^{1}H NMR (500 MHz, DMSO-*d$_6$*) δ 13.09 (s, 2H, COO-H), 7.62 (s, 2H, Ar-H), 2.84 (t, J = 7.5 Hz, 4H, Ar-CH$_2$), 1.57 – 1.48 (m, 4H, CH$_2$), 0.88 (t, J = 7.6 Hz, 3H, CH$_3$); ^{13}C NMR (126 MHz, DMSO-*d$_6$*) δ 168.56, 140.18, 133.24, 132.10, 34.88, 24.40, 13.95. *2,5-Dibutyl-1,4-benzenedicarboxylic acid* (C4-bdcH$_2$), ^{1}H NMR (500 MHz, DMSO-*d$_6$*) δ 13.07 (s, 2H, COO-H), 7.61 (s, 2H, Ar-H), 2.90 – 2.82 (t, J = 7.5 Hz, 4H, Ar-CH$_2$), 1.52 – 1.45 (m, 4H, CH$_2$), 1.33 – 1.26 (m, 4H, C*H$_2$*CH$_3$), 0.88 (t, J = 7.3 Hz, 6H, CH$_3$). ^{13}C NMR (126 MHz, DMSO-*d$_6$*) δ 168.56, 140.37, 133.22, 132.04, 33.48, 32.57, 22.13, 13.80.

Synthesis and Activation of DMOF-1-**CX**

All alkyl functionalized DMOFs investigated herein were synthesized using the same procedure. One exemplary procedure is shown below.

To a solution of Zn(NO$_3$)$_2$ · 6H$_2$O (0.17 g, 0.56 mmol) and the corresponding 2,5-dialkyl-1,4-benzenedicarboxylic acid (0.14 g, 0.56 mmol) in DMF, a solution of 1,4-diazabicyclo[2.2.2]octan (0.03 g, 0.28 mmol) in DMF was added, giving a volume of 10 ml in sum. This solution was then heated at 120 °C for 2 d. After cooling to room temperature, the crystalline material was characterized by PXRD, SCXRD and IR spectroscopy. Subsequently, the mother liquor was decanted and exchanged by 10 ml of fresh DMF. The DMF was replaced by 10 ml of DCM and kept overnight. Afterwards, the DCM was removed and the remaining solid dried in vacuo (ca. 10^{-2} mbar) at 100 °C overnight. Until further manipulation or characterization the materials were stored under Argon atmosphere by use of Schlenk technique. The analytical procedures described herein were carried out under ambient conditions.

Synthesis and Activation of DMOF-1-**OCY**

The alkoxy functionalized DMOFs investigated herein were synthesized using literature known procedures, which only slightly differ for DMOF-1-**OC2**[100] and DMOF-1-**OC3**[98]. Linker synthesis procedures are described under Materials & Methods section 6.1.3 below.

Synthesis and activation of DMOF-1-**OC2** and DMOF-1-**OC3** in brackets. To a solution of $Zn(NO_3)_2 \cdot 6H_2O$ (0.13 g, 0.42 mmol) and the corresponding 2,5-dialkoxy-1,4-benzenedicarboxylic acid (0.42 mmol) in DMF, a solution of 1,4-diazabicyclo[2.2.2]octan (0.05 g, 0.42 mmol (0.22 mmol)) in DMF was added, giving a volume of 15 ml (12.5 ml) in sum. This solution was then heated at 120 °C for 2 d. After cooling to room temperature, the crystalline material was characterized by PXRD and IR spectroscopy. Subsequently, the mother liquor was decanted and exchanged by 15 ml of fresh DMF. The DMF was replaced by 10 ml of DCM and kept overnight. Afterwards, the DCM was removed and the remaining solid dried in vacuo (ca. 10^{-2} mbar) at 100 °C overnight. Until further manipulation or characterization the materials were stored under Argon atmosphere by use of Schlenk technique. The analytical procedures described herein were carried out under ambient conditions.

Preparation of Single Crystals

The preparation of the single crystals used for the collection of the SCXRD data is described below:

- Single crystals of the *as*-DMOF-1-**CX** were taken from the freshly synthesized material (typically grown on the walls of the synthesis vial) and kept in the mother liquor until being measured.
- Single crystals of *dry*-DMOF-1-**C2** and *dry*-DMOF-1-**C4** were picked from the bulk materials, which was obtained by the typical drying method described above. The measured single crystals of *dry*-DMOF-1-**C3** were obtained by drying straight from DMF skipping the solvent exchange by DCM, which significantly decreased the crystallite sizes and quality. Other procedures involving multiple solvent exchange steps before the drying *in vacuo* were less successful in producing suitable single crystals of *dry*-DMOF-1-**C3**.

- Single crystals of solvated DMOF-1-**C3** were obtained either by resolvating previously dried crystals (DMOF-1-**C3**·2MeCN) or by solvent exchange of as-synthesized (DMF-containing) material over 1 d (DMOF-1-**C3**·2acetone, DMOF-1-**C3**·2benzene). Due to immiscibility of *n*-octane and DMF, crystals of DMOF-1-**C3**·*n*-octane were obtained from the benzene-solvated materials by exchanging the solvent for *n*-octane for 1 d.
- Single crystals of DMOF-1-**C3**·DMF/THF were obtained as a side-product of attempts to generate sufficient single crystals of *dry*-DMOF-1-**C3**. At this, crystals of *as*-DMOF-1-**C3** were immersed in THF, which was decanted after 1 d. Followingly, the crystals were kept in an argon stream for several h with the idea to smoothly evaporate the THF from the pores.
- To obtain a measurable single crystal of the $\boldsymbol{ip_{ht}}$ phase of *dry*-DMOF-1-**C4**, the slow relaxation of the transition from the $\boldsymbol{ip_{ht}}$ to the ***np*** phase of DMOF-1-**C4** was utilized (for further details see DSC data of *dry*-DMOF-1-**C4**). In more detail, a crystal of *dry*-DMOF-1-**C4** was mounted on a loop by use of oil and checked for sufficient quality by performing a fast scan at RT. Afterwards, the loop with the mounted crystal was heated at 473 K in an oven (under air) for 15 min and then measured at 400 K (maximum available temperature of the used cryo stream) on the single crystal diffractometer.

6.1.3 Synthetic procedures to Chapter 4

Synthesis of the **CXO**-bdcH$_2$ and **C1OCYO**-bdcH$_2$

All *alkoxy*-functionalized 2,5-diOC$_x$H$_{2x+1}$-bdcH$_2$ (H$_2$(**CXO**-bdc)) and 2,5-diMeOC$_y$H$_{2y}$-bdcH$_2$ (H$_2$(**C1OCYO**-bdc)) linkers were prepared by use of Williamson ether synthesis starting from 2,5-dihydroxy-terephthalic acid dimethyl ester and the corresponding *n*-bromoalkane according to the literature.[98] A typical synthesis procedure is described below.

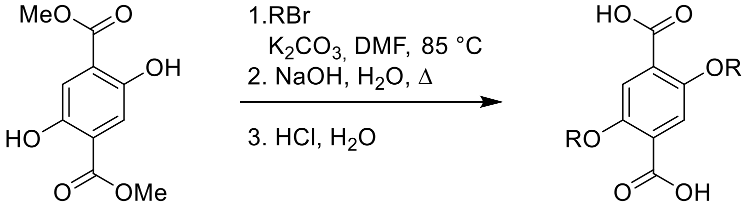

To a suspension of 2,5-dihydroxy-terephthalic acid dimethyl ester (1.00 g, 4.42 mmol) and K$_2$CO$_3$ (3.06 g, 22.11 mmol) in 30 ml DMF, RBr (13.26 mmol) was added dropwise, and the mixture was heated at 85 °C for 4 h. The solvent was removed *in vacuo*, 50 mL of aqueous NaOH (50.0 mmol) were added and the reaction mixture was refluxed for 14 h. At room temperature, the solution was acidified by dropwise addition of aqueous HCl (15%). The precipitate was filtered off and thoroughly washed with water. Afterwards, the solid was dried under dynamic vacuum at 80 °C for 16 h. The product was obtained as an off-white powder in yields of 90% averaged. In rare cases, when the product contained unreacted educts, recrystallisation from EtOAc or DMF afforded pure products.

2,5-Diethoxy-1,4-benzenedicarboxylic acid, H_2(**C2O**-bdc), ^{1}H NMR (500 MHz, DMSO-d_6): δ 12.93 (s, 2 H, COO–H), 7.26 (s, 2 H, Ar–H), 4.04 (q, J = 7.0 Hz, 4 H, OCH_2), 1.29 (t, J = 6.87 Hz, 6 H, CH_3) ppm; ^{13}C NMR (125.75 MHz, DMSO-d_6): δ 166.86, 150.30, 125.56, 115.64, 64.92, 14.70 ppm.

2,5-Dipropoxy-1,4-benzenedicarboxylic acid (H_2(**C3O**-bdc), ^{1}H NMR (500 MHz, DMSO-d_6): δ12.89 (s, 2 H, COO–H), 7.26 (s, 2 H, Ar–H), 3.94 (t, J = 6.4 Hz, 4 H, OCH_2), 1.73-1.66 (m, 4 H, CH_2), 0.97 (t, J = 7.34 Hz, 6 H, CH_3) ppm; ^{13}C NMR (125.75 MHz, DMSO-d_6): δ 166.89, 150.43, 125.43, 115.49, 70.57, 22.12, 10.39 ppm.

2,5-Dibutoxy-1,4-benzenedicarboxylic acid (H_2(**C4O**-bdc), ^{1}H NMR (500 MHz, DMSO-d_6): δ12.88 (s, 2 H, COO–H), 7.26 (s, 2 H, Ar–H), 3.98 (t, J = 6.4 Hz, 4 H, OCH_2), 1.69-1.63 (m, 4 H, CH_2), 1.47-1.40 (m, 4 H, CH_2), 0.91 (t, J = 7.3 Hz, 6 H, CH_3) ppm; ^{13}C NMR (125.75 MHz, DMSO-d_6): δ 166.91, 150.41, 125.44, 115.43, 68.80, 30.81, 18.63, 13.71 ppm.

2,5-Dipentoxy-1,4-benzenedicarboxylic acid (H_2(**C5O**-bdc), ^{1}H NMR (600 MHz, DMSO-d_6): δ12.89 (s, 2 H, COO–H), 7.25 (s, 2 H, Ar–H), 3.97 (t, J = 6.2 Hz, 4 H, OCH_2), 1.70–1.65 (m, 4 H, CH_2), 1.42–1.37 (m, 4 H, CH_2), 1.36–1.29 (m, 4 H, CH_2), 0.88 (t, J = 7.0 Hz, 6 H, CH_3) ppm; ^{13}C NMR (150.94 MHz, DMSO-d_6): δ 166.84, 150.41, 125.48, 115.49, 69.13, 28.36, 27.53, 21.79, 13.91 ppm.

2,5-Dihexyloxy-1,4-benzenedicarboxylic acid (H_2(**C6O**-bdc), ^{1}H NMR (600 MHz, DMSO-d_6): δ12.91 (s, 2 H, COO–H), 7.25 (s, 2 H, Ar–H), 3.97 (t, J = 6.4 Hz, 4 H, OCH_2), 1.69-1.64 (m, 4 H, CH_2), 1.44-1.39 (m, 4 H, CH_2), 1.33-1.25 (m, 8 H, CH_2), 0.87 (t, J = 7.0 Hz, 6 H, CH_3) ppm; ^{13}C NMR (150.94 MHz, DMSO-d_6): δ 166.83, 150.41, 125.45, 115.49, 69.12, 30.89, 28.63, 24.97, 22.04, 13.87 ppm.

2,5-Diheptyloxy-1,4-benzenedicarboxylic acid (H_2(**C7O**-bdc), ^{1}H NMR (600 MHz, DMSO-d_6): δ12.91 (s, 2 H, COO–H), 7.24 (s, 2 H, Ar–H), 3.96 (t, J = 6.4 Hz, 4 H, OCH_2), 1.69-1.64 (m, 4 H, CH_2), 1.44-1.38 (m, 4 H, CH_2), 1.33-1.22 (m, 12 H, CH_2), 0.86 (t, J = 6.8 Hz, 6 H, CH_3) ppm; ^{13}C NMR (150.94 MHz, DMSO-d_6): δ 166.85, 150.41, 125.54, 115.49, 69.12, 31.24, 28.69, 28.35, 25.28, 22.01, 13.95 ppm.

2,5-Dioctyloxy-1,4-benzenedicarboxylic acid (H_2(**C8O**-bdc), ^{1}H NMR (600 MHz, DMSO-d_6): δ 7.11 (s, 2 H, Ar–H), 3.92 (t, J = 6.4 Hz, 4 H, OCH_2), 1.67-1.63 (m, 4 H, CH_2), 1.41-1.37 (m, 4 H, CH_2), 1.31-1.22 (m, 16 H, CH_2), 0.85 (t, J = 7.0 Hz, 6 H, CH_3) ppm; ^{13}C NMR (150.94 MHz, DMSO-d_6): δ 167.82, 150.71, 127.14, 115.76, 69.63, 31.72, 29.27, 29.21, 29.17, 25.86, 22.58, 14.43 ppm.

2,5-Dimethoxy-alkoxy-1,4-benzenedicarboxylic acid (H_2(**C1OC2O**-bdc), ^{1}H NMR (500 MHz, DMSO-d_6): δ12.91 (s, 2 H, COO–H), 7.30 (s, 2 H, Ar–H), 4.12 (t, J = 5.0 Hz, 4 H, CH_2), 3.63

(t, $J = 5.0$ Hz, 4 H, CH_2), 3.31 (s, 6 H, OCH_3) ppm; ^{13}C NMR (125.75 MHz, DMSO-d_6): δ 166.72, 150.53, 125.70, 116.04, 70.37, 69.15, 58.35 ppm.

2,5-Dimethoxy-alkoxy-1,4-benzenedicarboxylic acid (H_2(**C1OC3O**-bdc), ^1H NMR (400 MHz, DMSO-d_6): δ 12.92 (s, 2 H, COO–H), 7.28 (s, 2 H, Ar–H), 4.03 (t, $J = 6.4$ Hz, 4 H, OCH_2), 3.48 (t, $J = 6.4$ Hz, 4 H, OCH_2), 3.23 (s, 6 H, OCH_3), 1.94-1.87 (m, 4 H, CH_2) ppm; ^{13}C NMR (125.75 MHz, DMSO-d_6): δ 166.78, 150.47, 125.45, 115.60, 68.43, 66.29, 57.94, 28.94 ppm.

2,5-Dimethoxy-alkoxy-1,4-benzenedicarboxylic acid (H_2(**C1OC4O**-bdc), ^1H NMR (400 MHz, DMSO-d_6): δ 12.91 (s, 2 H, COO–H), 7.26 (s, 2 H, Ar–H), 3.99 (t, $J = 6.4$ Hz, 4 H, OCH_2), 3.35 (t, $J = 6.4$ Hz, 4 H, OCH_2), 3.22 (s, 6 H, OCH_3), 1.74-1.61 (m, 8 H, CH_2) ppm; ^{13}C NMR (100.64 MHz, DMSO-d_6): δ 166.83, 150.83, 125.45, 115.48, 71.51, 68.91, 57.75, 25.50 ppm.

2,5-Dimethoxy-alkoxy-1,4-benzenedicarboxylic acid (H_2(**C1OC5O**-bdc), ^1H NMR (400 MHz, DMSO-d_6): δ 12.89 (s, 2 H, COO–H), 7.26 (s, 2 H, Ar–H), 3.97 (t, $J = 6.4$ Hz, 4 H, OCH_2), 3.31 (t, $J = 6.4$ Hz, 4 H, OCH_2), 3.21 (s, 6 H, OCH_3), 1.72-1.65 (m, 4 H, CH_2), 1.57-1.50 (m, 4 H, CH_2), 1.47-1.40 (m, 4 H, CH_2) ppm; ^{13}C NMR (100.64 MHz, DMSO-d_6): δ 166.83, 150.43, 125.49, 115.54, 71.83, 69.11, 57.78, 28.64, 22.14 ppm.

2,5-Dimethoxy-alkoxy-1,4-benzenedicarboxylic acid (H_2(**C1OC6O**-bdc), ^1H NMR (400 MHz, DMSO-d_6) δ 12.93 (s, 2 H, COO–H), 7.25 (s, 2 H, Ar-H), 3.97 (t, $J = 6.4$ Hz, 4 H, OCH_2), 3.29 (t, $J = 6.5$, 4 H, OCH_2), 3.20 (s, 6 H, OCH_3), 1.78 – 1.64 (m, 4H, CH_2), 1.54 – 1.46 (m, 4 H, CH_2), 1.45 - 1.38 (m, 4 H, CH_2), 1.36 – 1.30 (m, 4 H, CH_2) ppm; ^{13}C NMR (101 MHz, DMSO-d_6) δ 166.84, 150.43, 125.48, 115.52, 71.80, 69.07, 57.78, 28.98 –25.15 ppm.

Synthesis of H_2(**C8O**-bpdc)

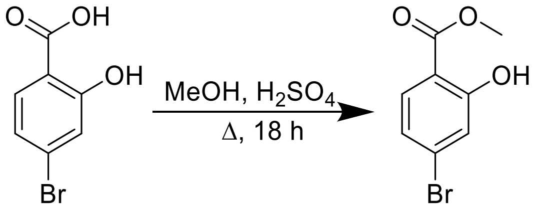

4-bromo-2-hydroxybenzoic acid (23.8 g, 0.109 mol, 1 eq.) was dissolved in methanol (300 mL) and conc. sulfuric acid (8 mL) was added dropwise. The mixture was refluxed overnight. The solvent was evaporated, and water (250 mL) was added. The resulting solid was filtered and washed with water multiple times. Recrystallization from methanol gave methyl 4-bromo-2-hydroxybenzoate (13.847 g, 0.059 mmol, 55%) as a white solid.

4-Bromo-2-hydroxybenzoate, ^1H NMR (700 MHz, $CDCl_3$): δ 10.82 (s, 1H), 7.68 (d, $J = 8.5$ Hz, 1H), 7.18 (d, $J = 1.9$ Hz, 1H), 7.02 (dd, $J = 8.5$, 1.9 Hz, 1H), 3.95 (s, 3H) ppm; ^{13}C NMR (101 MHz, $CDCl_3$): δ 170.2, 162.1, 131.0, 130.0, 122.8, 120.9, 111.5, 52.6 ppm.

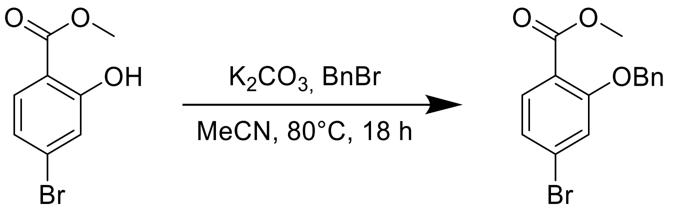

The synthesis was inspired by a procedure from the literature[226]. Methyl 4-bromo-2-hydroxybenzoate (7 g, 30.3 mmol, 1 eq.) and potassium carbonate (8.37 g, 60.59 mmol, 2 eq.) were added to acetonitrile (75 mL). Benzyl bromide (3.6 mL, 30.30 mmol, 1 eq.) were added dropwise and the mixture was refluxed overnight. The solids were filtered, and the solvents removed from the filtrate to give methyl 2-(benzyloxy)-4-bromobenzoate (9.4 g, 29.2 mmol, 97%) as a clear oil.

Methyl 2-(benzyloxy)-4-bromobenzoate, ^{1}H NMR (400 MHz, CDCl$_3$): δ 7.71 (d, J = 8.3 Hz, 1H), 7.49 (ddt, J = 7.5, 1.4, 0.7 Hz, 2H), 7.40 (ddd, J = 7.6, 6.8, 1.3 Hz, 2H), 7.36 – 7.30 (m, 1H), 7.19 (d, J = 1.8 Hz, 1H), 7.15 (dd, J = 8.3, 1.7 Hz, 1H), 5.17 (s, 2H), 3.89 (s, 3H) ppm. ^{13}C NMR (101 MHz, CDCl$_3$): δ 166.1, 158.8, 136.1, 133.1, 128.7, 128.1, 127.6, 126.9, 123.9, 119.7, 117.4, 71.0, 52.3 ppm.

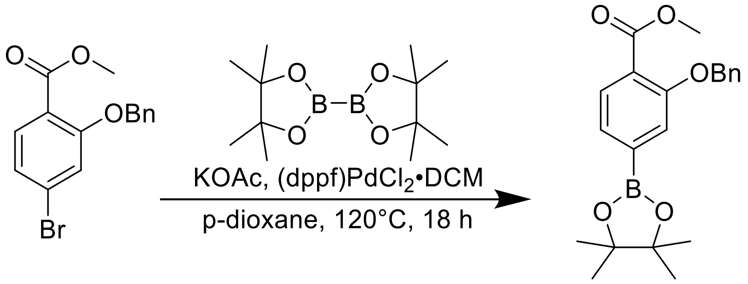

The synthesis was inspired by a procedure from the literature[226]. Under argon atmosphere methyl 2-(benzyloxy)-4-bromobenzoate (9.4 g, 29.2 mmol, 1 eq.), Bis(pinacolato)diboron (8.15 g, 32.1 mmol, 1.1 eq.) and potassium acetate (8.6 g, 87.6 mmol, 3 eq.) were suspended in *p*-dioxane and degassed with argon for 15 minutes. Then [1,1'- bis(diphenylphosphino) ferrocene] dichloropalladium(II) · dichloromethane ((dppf)PdCl$_2$ · DCM, 0.48 g, 0.58 mmol, 0.02 eq.) was added and the mixture was heated to 120 °C overnight. After cooling to room temperature, the mixture was filtered over a plug of Cellite® and the solids were washed with EtOAc. After removing the solvents under reduced pressure 100 mL EtOAc and 2 spoons charcoal were added. The suspension was refluxed for 15 minutes before removing the solids and evaporating the solvents. The resulting solid was recrystallized from hexane giving methyl 2-(benzyloxy)-4-(4,4,5,5-tetramethyl-1,3,2-dioxaborolan-2-yl) benzoate (6.3 g, 17 mmol, 59%) as a light brown solid.

^{1}H NMR (400 MHz, $CDCl_3$): δ 7.73 (d, J = 7.6 Hz, 1H), 7.48 – 7.44 (m, 2H), 7.42 – 7.29 (m, 4H), 7.27 – 7.21 (m, 1H), 5.15 (s, 2H), 3.83 (s, 3H), 1.29 (s, 12H) ppm. ^{13}C NMR (101 MHz, $CDCl_3$): δ 167.0, 157.5, 137.0, 131.0, 128.6, 127.8, 127.1, 127.0, 123.3, 119.5, 84.3, 70.8, 52.1, 25.0 ppm.

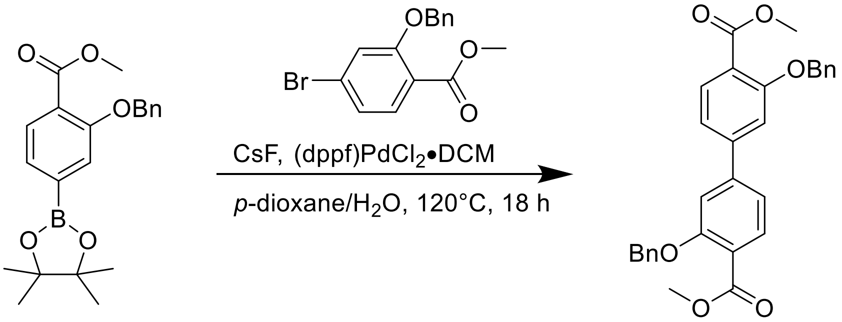

The synthesis was inspired by a procedure from the literature[226]. Under argon atmosphere, methyl 2-(benzyloxy)-4-bromobenzoate (5 g, 15.6 mmol, 1 eq.), methyl 2-(benzyloxy)-4-(4,4,5,5-tetramethyl-1,3,2-dioxaborolan-2-yl) benzoate (6.3 g, 17.1 mmol, 1.1 eq.) and CsF (7.1 g, 46.7 mmol, 3 eq.) were dissolved in a *p*-dioxane/water mixture (2:1, 120 mL). The mixture was degassed with argon for overall 15 minutes, whereas after 10 minutes of degassing (dppf)$PdCl_2 \cdot$ DCM (1 g, 1.3 mmol, 0.05 eq.) was added. The mixture was stirred at 80 °C overnight. Water (100 mL) was added, and the mixture subsequently cooled to 4 °C. The resulting grey solid was filtered off over an approx. 1 cm thick layer of Cellite® and then washed with cold distilled water. The wash solution was disposed of and the Cellite® filter subsequently washed with DCM dissolving the grey solid. The solvents were then removed under reduced pressure, resulting in a grey-brown residue. The residue was washed with cold EtOAc and dried under dynamic vacuum. Dimethyl 3,3'-bis(benzyloxy)-[1,1'-biphenyl]-4,4'-dicarboxylate (6.2 g, 12.8 mmol, 82%) was obtained as a grey solid.

Dimethyl 3,3'-bis(benzyloxy)-[1,1'-biphenyl]-4,4'-dicarboxylate, ^{1}H NMR (400 MHz, $CDCl_3$): δ 7.91 (d, J = 8.1 Hz, 2H), 7.55 – 7.50 (m, 4H), 7.44 – 7.38 (m, 4H), 7.37 – 7.30 (m, 2H), 7.16 (dd, J = 8.0, 1.6 Hz, 2H), 7.09 (d, J = 1.6 Hz, 2H), 5.23 (s, 4H), 3.93 (s, 6H) ppm. ^{13}C NMR (101 MHz, $CDCl_3$): δ 166.5, 158.6, 145.4, 136.7, 132.5, 128.7, 128.0, 127.0, 120.3, 119.6, 113.1, 70.9, 52.2 ppm.

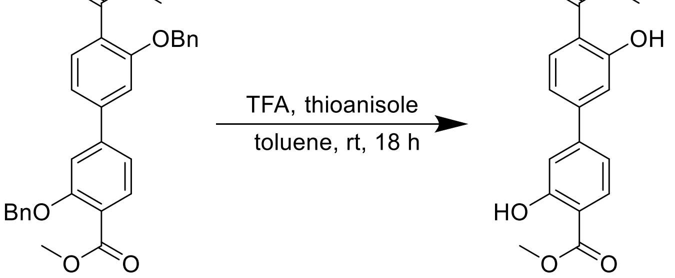

The synthesis was inspired by a procedure from the literature[227]. Under argon atmosphere, dimethyl 3,3'-dihydroxy-[1,1'-biphenyl]-4,4'-dicarboxylate (5.67 g, 11.8 mmol, 1 eq.), trifluoroacetic acid (136.6 ml, 1.76 mol, 150 eq.) and thioanisole (8.3 mL, 70.6 mmol, 6 eq.) were dissolved in toluene (500 mL) and stirred at room temperature overnight. The solution was transferred to a separation funnel and distilled water (800 mL) was added. The aqueous phase was washed with DCM (3 x 200 mL). The combined organic phases were dried with $MgSO_4$, and the solvents removed under reduced pressure, upon which a grey suspension was obtained. The solids were filtered off and washed with Et_2O. Drying under dynamic vacuum yielded dimethyl 3,3'-dihydroxy-[1,1'-biphenyl]-4,4'-dicarboxylate (2.53 g, 8.3 mmol, 71%).

Dimethyl 3,3'-dihydroxy-[1,1'-biphenyl]-4,4'-dicarboxylate, ^{1}H NMR (500 MHz, $CDCl_3$): δ 10.8 (s, 2H), 7.90 (d, J = 8.3 Hz, 2H), 7.22 (d, J = 1.8 Hz, 2H), 7.13 (dd, J = 8.3, 1.8 Hz, 2H), 3.98 (s, 6H) ppm. ^{13}C NMR (126 MHz, $CDCl_3$): δ 170.4, 161.9, 146.9, 130.5, 118.3, 116.2, 112.2, 52.5 ppm.

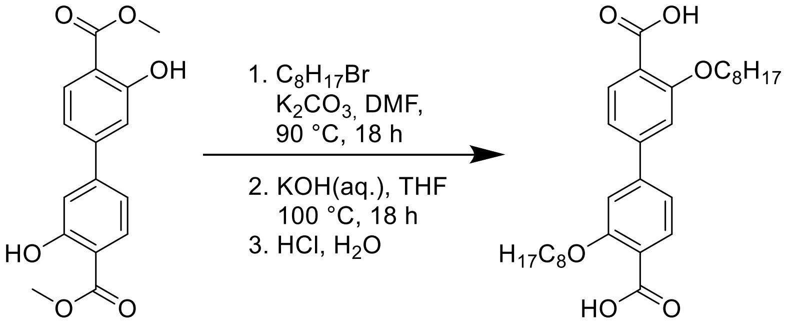

The synthesis was inspired by a procedure from the literature[214]. Dimethyl 3,3'-dihydroxy-[1,1'-biphenyl]-4,4'-dicarboxylate (300 mg, 0.99 mmol, 1 eq.) and K_2CO_3 (686 mg, 4.96 mmol, 5 eq.) were suspended in DMF (20 mL). *n*-Octylbromide (0.98 g, 4.96 mmol, 5 eq.) was added slowly and the mixture was stirred at 90 °C overnight. After cooling to room temperature, the solids were filtered off and the solvents were removed under reduced pressure. For saponification of the ester groups an aqueous solution of KOH (10 wt%, 30 mL) and 15 mL THF was added. The mixture was stirred at 100 °C overnight. After cooling down, an aqueous solution of HCl (10%) was added dropwise, until a solid precipitated (pH = 1). The solid was filtered off and washed with distilled water. Drying under dynamic vacuum gave 3,3'-dioctyloxy-(1,1'-biphenyl)-4,4'-dicarboxylic acid as a white powder in quantitative yield (99%).

3,3'-Dioctyloxy-(1,1'-Biphenyl)-4,4'-dicarboxylic acid, ^{1}H NMR (400 MHz, DMSO-d_6): δ 12.64 (s, 2H), 7.70 (d, J = 7.9 Hz, 2H), 7.36 – 7.29 (m, 4H), 4.15 (t, J = 6.4 Hz, 4H), 1.79 – 1.66 (m, 4H), 1.46 (dq, J = 9.4, 6.7 Hz, 4H), 1.35 – 1.22 (m, 16H), 0.89 – 0.83 (m, 6H) ppm. ^{13}C NMR (101 MHz, DMSO-d_6): δ 167.2, 157.8, 143.7, 131.1, 121.4, 118.7, 112.0, 68.3, 31.2, 28.7, 28.7, 28.6, 25.4, 22.1, 13.9 ppm.

Synthesis of H_3(**C8O**-btb)

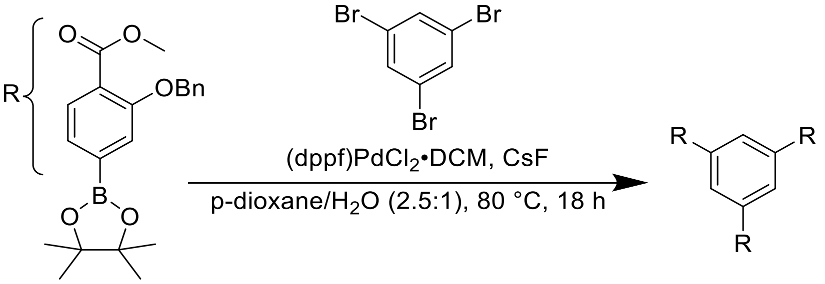

Under argon atmosphere 1,3,5-tribromobenzene (1.66 g, 5.26 mmol, 1 eq.), methyl 2-(benzyloxy)-4-(4,4,5,5-tetramethyl-1,3,2-dioxaborolan-2-yl) benzoate (6.2 g, 16.84 mmol, 3.2 eq.) and caesium fluoride (5 g, 33.15 mmol, 6.3 eq.) were suspended in a *p*-dioxane/water-mixture (120 mL/48 mL) and degassed with argon for 15 minutes. Then [1,1′- bis(diphenylphosphino)ferrocene] dichloropalladium(II) · DCM (0.34 g, 0.42 mmol, 0.1 eq.) was added and the mixture was heated to 80 °C overnight. After cooling to room temperature water (100 mL) was added and the mixture was filtered over a plug of Cellite®. The solids were washed with water and cold EtOAc. Then, the filter was washed with DCM and collected separately from the previous washing solvents. The solvents were removed under reduced pressure to give Dimethyl 3,3''-bis(benzyloxy)-5'-(3-(benzyloxy)-4-(methoxycarbonyl) phenyl)-[1,1':3',1''-terphenyl]-4,4''-dicarboxylate (3.32 g, 4.16 mmol, 79%) as a light grey solid.

Dimethyl 3,3''-bis(benzyloxy)-5'-(3-(benzyloxy)-4-(methoxycarbonyl)phenyl)-[1,1':3',1''-terphenyl]-4,4''-dicarboxylate, ^{1}H NMR (400 MHz, DMSO-d$_6$) δ 8.02 (s, 3H), 7.86 (d, J = 8.0 Hz, 3H), 7.67 (d, J = 1.7 Hz, 3H), 7.55 (ddd, J = 7.7, 6.2, 1.6 Hz, 9H), 7.44 – 7.38 (m, 6H), 7.34 – 7.29 (m, 3H), 5.42 (s, 6H), 3.85 (s, 9H). ^{13}C NMR (101 MHz, DMSO-d$_6$) δ 168.5, 165.8, 161.0, 157.8, 144.9, 143.0, 140.7, 137.0, 131.5, 128.3, 127.6, 126.9, 119.4, 69.8, 51.9.

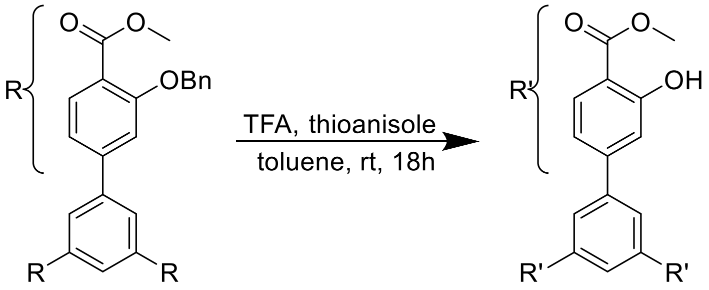

The synthesis was inspired by a procedure from the literature[227]. Under argon atmosphere dimethyl 3,3''-bis(benzyloxy)-5'-(3-(benzyloxy)-4-(methoxycarbonyl) phenyl)-[1,1':3',1''-terphenyl]-4,4''-dicarboxylate (2.6 g, 3.29 mmol, 1 eq.), thioanisole (3.5 mL, 29.6 mmol, 9 eq.) and trifluoroacetic acid (38 mL, 493.74 mmol, 150 equiv.) were dissolved in toluene (180 mL) and stirred at room temperature overnight. Then, water (100 mL) was added, and the solution was extracted with DCM (3 x 50 mL). The combined organic phases were washed with brine (1x 50 mL) and dried over $MgSO_4$. The solvents were removed under reduced pressure as far as possible. The resulting suspension was heated to 110 °C and toluene was added slowly until everything was dissolved. The solution was cooled to 4 °C for 3 days before filtering off and drying the product Dimethyl 3,3''-dihydroxy-5'-(3-hydroxy-4-(methoxycarbonyl) phenyl)-[1,1':3',1''-terphenyl]-4,4''-dicarboxylate (1.17 g, 2.22 mmol, 67%) as a white solid.

Dimethyl 3,3''-dihydroxy-5'-(3-hydroxy-4-(methoxycarbonyl)phenyl)-[1,1':3',1''-terphenyl]-4,4''-dicarboxylate, ^{1}H NMR (500 MHz, $CDCl_3$): δ 10.84 (s, 3H), 7.91 (d, J = 8.2 Hz, 3H), 7.80 (s, 3H), 7.27 (d, J = 1.7 Hz, 3H), 7.17 (dd, J = 8.3, 1.8 Hz, 3H), 3.99 (s, 9H) ppm. ^{13}C NMR (126 MHz, $CDCl_3$): δ 170.4, 161.9, 141.1, 130.6, 130.5, 129.0, 126.1, 118.2, 116.0, 52.4 ppm.

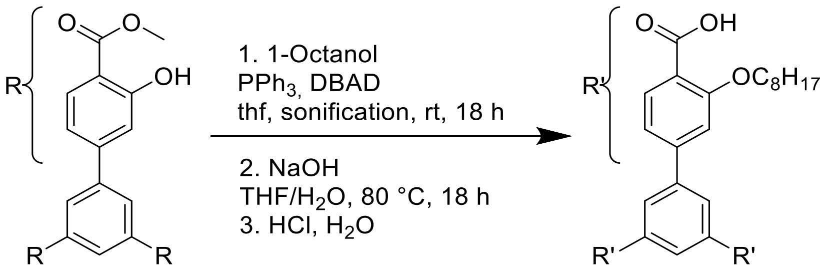

The synthesis was inspired by a procedure from the literature[99]. Under argon atmosphere the starting compound dimethyl 3,3''-dihydroxy-5'-(3-hydroxy-4-(methoxycarbonyl) phenyl)-[1,1':3',1''-terphenyl]-4,4''-dicarboxylate (300 mg, 0.57 mmol, 1 eq.), PPh_3 (522 mg, 1.99 mmol, 3.5 eq.) and di-*tert*-butyl azodiformate (DBAD) (458 mg, 1.99 mmol, 3.5 eq.) were dissolved in THF (8 mL) under sonification. The aliphatic alcohol (1.99 mmol, 3.5 eq.) was added and the mixture sonificated at room temperature for 3 hours. Then sodium hydroxide (40 mL, 10 wt% in water) was added, and the solution refluxed overnight. The majority of the organic solvents were removed under reduced pressure giving a clear colourless solution. The solution was extracted with EtOAc (3x 50 mL), and the solvent was removed from the combined organic phases. Sodium hydroxide (20 mL, 10 wt% in water) and THF (20 mL) were added, and the mixture was refluxed overnight. The resulting phases were separated, and hydrochloric acid was added to the organic phase while stirring vigorously. The resulting solid was washed with water and dried under vacuum giving the product 1,3,5-tris(3'-octyloxy-4'-carboxyphenyl) benzene (251 mg, 304 mmol, 60%) as a white solid.

1,3,5-tris(3'-octyloxy-4'-carboxyphenyl)benzene, ^{1}H NMR (400 MHz, $CDCl_3$): δ 10.95 (s, 3H), 8.31 (d, J = 8.3 Hz, 3H), 7.81 (s, 3H), 7.46 – 7.40 (m, 3H), 7.30 – 7.28 (m, J = 1.5 Hz, 3H), 4.36 (t, J = 6.4 Hz, 6H), 1.97 (tt, J = 7.3 Hz, 6.4 Hz, 6H), 1.52 (tt, J = 7.3 Hz, 6.9 Hz, 6H), 1.44 – 1.24 (m, 24H), 0.89 (t, J = 6.9 Hz, 9H) ppm. ^{13}C NMR (101 MHz, $CDCl_3$): δ 165.0, 158.0, 147.2, 141.6, 134.5, 126.6, 121.2, 117.1, 111.6, 70.7, 31.7, 29.2, 29.1, 29.0, 25.9, 22.6, 14.1 ppm.

Synthesis and Activation of MOF-5-**OCX** and MOF-5-**OCYOC1**

All MOF-5-**OCX** and MOF-5-**OCYOC1** materials were prepared under the same reaction conditions. In a typical synthesis 0.756 g $Zn(NO_3)_2 \cdot 4\ H_2O$ (2.89 mmol) and the appropriate H_2(**CXO**-bdc) or H_2(**C1OCYO**-bdc) linker precursor (0.666 mmol) were weighted in an 100 ml screw cap vial and 50 ml DMF were added. The reaction mixture was sonicated until the components were completely dissolved, giving a clear solution, which was heated at 100 °C for 48 h. After cooling to room temperature, the mother liquor was decanted, and the colourless cubic crystals were immersed in fresh DMF (3 × 50 ml) over several hours. Analytics referred to as *'as-synthesized'* were undertaken at this point. For activation of the MOFs, the DMF was decanted and replaced by DCM (50 ml) and the crystals were kept in DCM overnight. This procedure was repeated two times. Following, the solvent was decanted, and the crystals dried in dynamic vacuum (10^{-3} mbar) at 100 °C for 20 h. The dried MOFs were stored in a Schlenk tube under argon atmosphere prior to sample characterization of the *'dried'* (*dry*) materials.

The amount of incorporated DMF molecules in the pores of the *as*-MOF-5-**OCX** was determined by solution ^{1}H NMR spectroscopy. In order to do so, DMF-washed crystals of *as*-MOF-5-**OCX** were shortly put on a filter paper to remove excess DMF from the surface of the crystals. These crystals were then digested in a mixture of DMSO-*d6* and DCl/D_2O for ^{1}H NMR spectroscopy. Resulting amounts of incorporated DMF molecules per repeating unit are given below.

Table 6.1: Chemical composition (including contained DMF) of *as*-MOF-5-**OCX** as obtained from ^{1}H NMR spectroscopy of digested samples of the *as*-MOF-5-**OCX**.

OCX	Chemical composition
OC2	$[Zn_4O($**C2O**-bdc$)_3]\cdot7.5DMF$
OC3	$[Zn_4O($**C3O**-bdc$)_3]\cdot6.6DMF$
OC4	$[Zn_4O($**C4O**-bdc$)_3]\cdot5.1DMF$
OC5	$[Zn_4O($**C5O**-bdc$)_3]\cdot3.9DMF$
OC6	$[Zn_4O($**C6O**-bdc$)_3]\cdot3.6DMF$
OC7	$[Zn_4O($**C7O**-bdc$)_3]\cdot2.4DMF$
OC8	$[Zn_4O($**C8O**-bdc$)_3]\cdot1.5DMF$

MOF-5-**OCX** reinfiltration

For the reinfiltration of a MOF utilizing DMF, a glass weight boat was loaded with a powdered sample of the dried MOF of choice and another weight boat with a small amount of DMF (ca. 1 ml). Both weight boats were placed in a Schlenk tube. The Schlenk tube was evacuated for a short time, sealed under reduced pressure, and heated at 65 °C for 16 h.

Re-infiltration experiments using *n*-octane were performed by immersing dried crystals of the MOF in ca. 2 ml *n*-octane in a 12 ml screw cap vial, followed by heating at 65 °C for 16 h. Analytics were performed immediately after cooling to room temperature.

Synthesis and Activation of IRMOF-10-**OC8**

Based on a published procedure[28], in a typical synthesis 0.115 g $Zn(NO_3)_2 \cdot 4\ H_2O$ (0.44 mmol) and 0.04 g 3,3'-dioctyloxy-(1,1'-biphenyl)-4,4'-dicarboxylic acid (0.08 mmol) were dissolved in 12 ml DEF and heated at 100 °C for 48 h. After cooling to room temperature, the mother liquor was washed with DMF (3 × 15 ml). The activation procedure was inspired by a published freeze drying method using benzene[200]. The DMF was exchanged for benzene (3 × 15 ml), kept overnight and exchanged once again. Following this, the benzene was frozen at 0 °C and sublimed at a pressure of 10^{-3} mbar for 2 h. Afterwards the sample was heated at 80 °C *in vacuo* for 15 h and then heated at 110 °C for 6 h. After cooling to room temperature, the sample was stored in a Schlenk flask under Argon atmosphere prior to sample analysis of the *'dried'* material.

Synthesis and Activation of MOF-177-**OC8**

Based on a published procedure[199], the compound was prepared from a solution of 0.088 g $Zn(NO_3)_2 \cdot 4\ H_2O$ (0.34 mmol) and 0.037 g 1,3,5-tris(3'-octyloxy-4'-carboxyphenyl)benzene (0.05 mmol) in 3.75/3.75/0.75 ml DMF/NMP/EtOH. This solution was heated at 100 °C for 48 h. The resulting crystals were washed with DMF (3 × 10 ml). The dried material was obtained via the same procedure as IRMOF-10-**OC8**.

Synthesis and Activation of MOF-5

Based on a published procedure[228], the compound was prepared from a solution of 1.80 g $Zn(NO_3)_2 \cdot 6H_2O$ (6.1 mmol) and 0.33 g 1,4-benzenedicarboxylic acid (2.0 mmol) in 50 ml freshly distilled DEF, which was heated at 80 °C for 3 d. The resulting crystals were washed with dry DMF (3 × 50 ml, dried over 4 Å molecular sieve) and the solvent was exchanged for DCM (3 × 50 ml) with 5 h between each exchanging step. The crystals were filtered off and dried in vacuo (10^{-2} mbar) at 100 °C for 20 h. The dried samples were kept in a Schlenk tube under argon atmosphere.

6.2 Powder X-ray Diffraction

Powder X-ray diffraction data of as-synthesized, dried and resolvated materials were collected on a Siemens D5005 diffractometer in Bragg-Brentano geometry using CuKα radiation in a range from 2.5° or 5.0° to 50° 2Θ with a stepsize of 0.02°. All samples were finely ground and placed on either a glass holder or a zero-background sample holder made of single crystalline silicon (cut along the (610)-plane) or, if mentioned, on a holder made of plastic. Further diffraction data were collected at beamline P02.1 at DESY (Deutsches Elektronen-Synchrotron, Hamburg, Germany) with a monochromatic X-ray beam ($\lambda = 0.2073$ Å) using a Perkin Elmer XRD1621 flat panel detector. The samples were finely ground and measured using 0.7- or 1.0-mm diameter quartz capillaries. Data were integrated using the DAWN[229,230] software package.

In general, structureless profile fitting (Pawley method[110]) and Rietveld refinements[115] were performed using the routines provided by the TOPAS-*academic v6* software package[231], where the peak shapes were fitted utilizing the Thompson-Cox-Hastings profile[232] and Chebychev polynomials were used as a function for the background. Details on the Rietveld refinement procedures can be found in the respective parts of the Appendix. If not already published via the Cambridge Crystallographic Data Centre (CCDC, accessible on the internet via https://www.ccdc.cam.ac.uk/, deposition codes are given in the crystallographic data tables), related crystallographic information files are provided on the enclosed CD.

Fitting of the first scattering peak (FSP) of the materials *dry*-MOF-5-**OC2** to *dry*-MOF-5-**OC6** was performed using split pseudo-Voigt (**OC3**-**OC6**) or PearsonVII (**OC2**) peak profile functions as implemented in the TOPAS-*academic v6* software package. In this process only the first scattering peak and the corresponding background function were refined.

6.3 Single Crystal X-ray Diffraction

Single crystal X-ray diffraction data (SCXRD) for all compounds were collected on either an Oxford Diffraction Xcalibur or a Bruker D8 Venture diffractometer using either MoKα ($\lambda = 0.7107$ Å) or CuKα ($\lambda = 1.5418$ Å) radiation, further equipped with an Oxford liquid nitrogen cryostream to keep the sample environment at the respective temperature in the range from 100 to 400 K. The raw data was processed with the APEX3 suite or the CrysAlisPro software package. The structure solution and refinement processes were conducted with the Olex2[233] interface using SHELXS, SHELXT and SHELXL[234]. Further details on the individual structure refinement procedures are given in the Appendix together with the final crystal structure data. If not already published via the Cambridge Crystallographic Data Centre (CCDC, accessible on the internet via https://www.ccdc.cam.ac.uk/, deposition codes are given in the crystallographic data tables), related crystallographic information files are provided on the enclosed CD.

All given precession images were reconstructed from processed experimental diffraction data using the APEX3 software. Diffraction images of *dry*-MOF-5-**OC3** were collected using CuKα (λ = 1.5418 Å) radiation. Precession images of *dry*-MOF-5-**OC6** were calculated from diffraction images collected at 100 K during a 180° φ scan with an angular step size of 1° and 1 s exposure time using CuKα ($\lambda = 1.5418$ Å) radiation.

Furthermore, all crystal mosaicities were obtained using the APEX3 software.

6.4 Solution ^{1}H NMR Spectroscopy

^{1}H and ^{13}C NMR spectroscopy was performed on digested MOF samples (in DMSO-d_6 with DCl/D$_2$O, 35% weight, $<$ 0.1 ml)) and synthesized organic linkers (DMSO-d_6 or CDCl$_3$) utilizing Bruker DPX-300, DPX-500, or Agilent DD2 500 spectrometers. The data were processed using the ACD/Labs or Mestrenova softwares. ^{1}H and ^{13}C NMR spectra were referenced to the respective residual solvent signal and chemical shifts are given with respect to tetramethylsilane.

6.5 Solid State NMR Spectroscopy

Solid state NMR experiments were carried out using a 2.5 mm triple-resonance (^{1}H, ^{13}C, ^{15}N channels) MAS probe on a 700 MHz Bruker Avance Neo spectrometer and a spinning frequency of 33.33 kHz at an overall effective sample temperature of 5 °C. The temperature calibration was performed externally with KBr powder.[235] For 1D ^{13}C Cross-polarization NMR experiments, data acquisition was performed for 19.93 ms with a recycle delay of 3 s and total number of scans (NS) of around 6000-7000. The applied decoupling sequence was Swept-frequency two-pulse phase modulation (SWf-TPPM).

6.6 X-ray Pair Distribution Function (XPDF) Analysis

In conventional PXRD analysis techniques, e.g., Pawley or Rietveld methods, only intensity from Bragg scattering is considered, whereas diffuse scattering contributions are typically discarded by applying an arbitrary background function. But especially for highly disordered materials, the diffuse scattering holds important structural information, which are not represented by the Bragg scattering. In the *total scattering* approach, both Bragg and diffuse scattering are treated on an equal basis, summarized in the total scattering structure function (sometimes also denoted as total scattering structure factor)[236] $S(Q)$, where Q is the wavevector change in the scattering experiment, which is defined according to:[237]

$$|Q| = \frac{4\pi \sin\theta}{\lambda}$$

with the scattering angle θ and the X-ray wavelength λ. To experimentally obtain the $S(Q)$, the raw data are firstly corrected for air- and sample container scattering, multiple scattering, X-ray fluorescence, absorption, beam polarization or Compton (inelastic) scattering[238] and finally normalized by the average scattering power of the material.[237] Hence, it is important to know the exact chemical composition of the material under investigation.

By means of Fourier transformation, the $S(Q)$ is then converted to real-space by means of Fourier transformation according to the following equation:[237]

$$D(r) = \frac{2}{\pi} \int_{Q_{min}}^{Q_{max}} Q[S(Q) - 1] \sin(Qr)\, dQ$$

where $Q_{\min}$ and $Q_{\max}$ are the limits of the Q-range over which the Fourier transform is performed. The resulting $D(r)$ is a radial atomic pair distribution function (PDF), i.e., a measure of the probability of finding two atoms separated by a distance r within the material.[239] The limits of the Fourier transform already imply that high-Q-range experimental data are mandatory to catch all features in the resulting PDF, which is one of the reasons why often high-energy scattering data from dedicated synchrotron beamlines are employed.[239]

Besides the $D(r)$ form mentioned above, there are various forms of normalizations of PDFs commonly used in the literature, of which each has its individual pros and cons.[236] However, the $D(r)$ form is consistently used herein as it is characterized by an emphasis on the mid- and high-r regions of the PDF.

Within the scope of this thesis, X-ray total scattering experiments were performed at beamline I15-1 at DLS (Diamond Light Source, UK) using a monochromatic X-ray beam with an energy of 76.7 keV ($\lambda = 0.161669$ Å). Finely ground samples were loaded into 1.5 mm (outer diameter) borosilicate glass capillaries. Scattering data from an empty capillary was used for background subtraction. Corrections for background, multiple, container, fluorescence and Compton scattering as well as absorption were done with the GudrunX program. The pair distribution functions on the form of $D(r)$ were obtained via Fourier transform of the normalized reciprocal space data $S(Q)$.[236,238]

For the as-synthesized materials, the correct chemical compositions were determined by use ^{1}H NMR spectroscopy, since the pores of the MOF-5-**OCX** are filled with a number of DMF molecules (see Materials & Methods section 6.1.3).

6.7 Fourier-Transform Infrared (FT-IR) Spectroscopy

IR spectra were recorded on a Perkin Elmer Spectrum Two Fourier transform IR spectrometer ($\tilde{\nu} = 400 - 4000$ cm^{-1}) in reflection mode using a diamond ATR (attenuated total reflectance) unit. All measurements were conducted under ambient conditions. As-synthesized samples were shortly dried on a filter paper to remove surface DMF. For *n*-octane reinfiltrated samples, excess *n*-octane was removed past loading the sample onto the diamond crystal to avoid solvent evaporation from the pores of the compounds under investigation.

6.8 Thermal Analysis

Simultaneous thermogravimetric analysis and differential scanning calorimetry (TG-DSC) experiments were performed using a STA504 by TA instruments under a constant Argon flow (4 l h^{-1}). Measurements for all *as* and *dry* MOFs were carried out from 30 to 770 °C with a heating rate of 10 K min^{-1}. Furthermore, the TG-DSC data of *dry*-MOF-5-**OC6OC1** were collected using a SDT 650 by TA Instruments under a constant N_2 flow (100 ml min^{-1}). The measurement was carried out within a temperature range from 30 to 600 °C with a heating rate of 10 °C min^{-1}.

Further DSC experiments were performed using a TA DSC-25 instrument under a constant N_2 flow (50 ml min^{-1}). ΔH of MOF-5-**OC7** and MOF-5-**OC8** were extracted from experimental data (up- and downscans) collected over a temperature range from 25 to 250 °C with a heating/cooling rate of 10 K min^{-1}. ΔH was determined as the integral area of the corresponding calorimetric peak following baseline subtraction. Furthermore, the DSC data of *dry*-MOF-5-**OC6** were collected using a TA Instruments DSC Q200 under a constant N_2 flow.

6.9 Variable-Temperature Powder X-ray Diffraction (VT-PXRD)

Powder X-ray diffraction data at various temperatures were collected at beamline P02.1 at DESY (Deutsches Elektronen-Synchrotron, Hamburg, Germany) with a monochromatic X-ray beam ($\lambda = 0.2073$ Å) using a Perkin Elmer XRD1621 flat panel detector. All samples were finely ground, filled into 0.7 or 1.0 mm diameter quartz capillaries and heated or cooled using a combined setup of an Oxford CryoStream ($T \leq 500$ K) and an Oxford HotAirBlower (from $T > 500$ K). Temperature calibration was conducted by reference PXRD measurements using Al. Data were integrated using the DAWN software package. Further experiments of the samples *dry*-MOF-5-**OC2** and *dry*-MOF-5-**OC6** were performed at BL9 of DELTA (Dortmunder Elektronenspeicherring-Anlage, Dortmund, Germany) with a monochromatic X-ray beam ($\lambda = 0.6199$ Å) using a MAR345 image plate detector. Finely ground samples were sealed in quartz capillaries and heated using an Oxford CryoStream in the range from 300 to 500 K. Data were integrated using the DAWN software package.

The integration of the FSP of *dry*-MOF-5-**OC6** at 300 K and 500 K was performed using the Origin 2020 Pro software package.

6.10 Isothermal Gas Sorption

Sorption experiments were undertaken with a Quantachrome ASiQ MP porosimeter using only high-purity adsorptive gases (N_2: 99.999%, CO_2: 99.995%, *n*-butane: 99.95%, propane: 99.95%, propylene: 99.95%). Sample quantities of at least 40 mg were used for the experiments. Prior to the measurements each sample was carefully grinded and afterwards degassed in dynamic vacuum ($p \approx 10^{-5}$ kPa) at 100 °C. Sorption isotherms were measured for the gases N_2 and CO_2 at 77 K and 195 K and for *n*-butane, propane, and propylene at 293 K, respectively.

Evaluation of Pore Volumes

On the assumption that the (micro-) pores of the material are completely filled with liquid-state adsorbate at relative pressures of about $p/p_0 \approx 0.9$ (N_2) or $p/p_0 \approx 0.5$ (CO_2), where the slope of the isotherm is ≈ 0, the total pore volume of the material can be determined from the maximum gas uptake $V_{\mathrm{ads,max}}$ in this region of the isotherm, which is converted into the liquid-state volume of the adsorbate V_{liq}. The experimental total pore volumes (V_{exp}) were calculated from the maximum CO_2 uptake (in cm^3 CO_2 / mol MOF at standard temperature and pressure) at the maximum pressures $p \approx 95$ kPa ($p/p_0 \approx 0.5$), where the plateau of the isotherm indicates saturation of the pores with CO_2. Here, a liquid density of $\rho(CO_2) = 1.032$ g cm^{-3} (–29 °C)[240] was applied in accordance with previous reports.[241] These calculations were undertaken by use of the *ASiQwin* (Version 5.2) software package according to the following equation:

$$V_{exp} = V_{liq} = \frac{p_a V_{ads} V_m}{RT}$$

where p_{a} and T are the ambient temperature and pressure and V_{m} is the molar volume of the respective adsorbate.

To subtract out the volume occupied by the alkoxy DEDs in the estimation of the volume contraction between the *as*- and *dry*-MOF-5-**OCX** or -**OCYOC1** (as described under Section 4.3.5), the Connolly Solvent Excluded Volumes of the alkoxy substituents used here were calculated using the routines implemented in the Perkin Elmer *Chem3D* software with a probe radius $r = 1.4$ Å. At this, benzene was used as a model compound, to which at first two ethoxy moieties were added in 2,5-positions, that were successively elongated by CH_2-groups at both arms. For each step, the resulting CSEV was obtained, and the respective volume of benzene was subtracted from it. By this procedure, the space requirement of the alkoxy chains of each length was determined for one repeating unit of the framework.

Evaluation of Surface Areas

The BET-model[187] was derived by Brunauer, Emmett and Teller to complement the Langmuir model[242] by taking multi-layer adsorption of the adsorbate molecules into account. Assuming that adsorption sites within the same adsorbate layer are equivalent and that there are no interactions between, an isotherm is represented by the BET-equation, here in its linearized form:

$$\frac{p}{N(p_0 - p)} = \frac{1}{N_m C} + \frac{C-1}{N_m C}\frac{p}{p_0}$$

where the N is the amount adsorbed, N_m is the amount adsorbed in the first layer and C is the empirical BET-constant, which is related to adsorbent-adsorbate- and adsorbate-adsorbate interactions. By plotting $p/(N(p_0\text{-}p))$ vs. p/p_0, the amount adsorbed in the monolayer, N_m, can be extracted and converted to the corresponding BET-surface area, S_BET, via the area covered by a single adsorbate molecule, which is represented by its molecular cross-sectional area σ and the Avogadro constant N_A

$$S_{BET} = N_m N_A \sigma$$

Typically, mono-layer coverage is expected to occur in the range from 0.05 to 0.3 p/p_0 where the BET-plot is applied.[50] Note, that for microporous MOFs mono-layer coverage can be achieved at even lower p/p_0 than 0.05 when using N_2 as a probe.[243,244]

Here, the Langmuir and BET surface areas of MOF-5 (only Langmuir) and the *dry*-MOF-5-**OCX** were calculated from CO_2 sorption isotherms (195 K). In accordance to previous reports, a molecular cross-sectional area of $\sigma = 17.00$ Å^2 was used for CO_2.[241] For the calculation of the BET plots to yield the corresponding surface areas three data points between 0.014 and 0.05 (MOF-5-**OC3** to -**OC8**, except MOF-5-**OC6**), 0.05 to 0.21 (MOF-5-**OC6**) or 0.037 and 0.145 (MOF-5-**OC2**) p/p_0 (p_0 = 188 kPa)[245,246] were taken. The BET calculation has not been performed for MOF-5 because of the unusual shape of its CO_2 isotherm.

6.11 *In-situ* CO_2 Sorption Powder X-ray Diffraction

Collection of powder X-ray diffraction data as a function of CO_2 pressure was conducted at beamline P02.1 at DESY (Deutsches Elektronen-Synchrotron, Hamburg, Germany) with a monochromatic X-ray beam ($\lambda = 0.2073$ Å) using a Perkin Elmer XRD1621 flat panel detector.

The samples were finely ground, filled into 0.7 or 1.0 mm diameter quartz capillaries and mounted onto a custom-made vacuum-tight gas cell. The gas cell setup did not allow to spin the capillaries so that the data were collected statically without sample spinning. During the experiments all samples were kept at 195 K using an Oxford liquid nitrogen CryoStream. Measurements were performed within a pressure range of 10^{-2} (vacuum) and 100 kPa CO_2. High-purity CO_2 (99.995%) was used. At each pressure step the samples were equilibrated for 10-15 min.

6.12 *In-situ n*-Butane Sorption Powder X-ray Diffraction

Collection of powder X-ray diffraction data as a function of *n*-butane pressure was conducted at beamline BL9 at DELTA (Dortmunder Elektronenspeicherring-Anlage, Dortmund, Germany) with a monochromatic X-ray beam (λ = 0.4592 Å) using a MAR345 image plate detector. The samples were finely ground, filled into 1.0 mm diameter quartz capillaries (but not sealed), and placed in a custom-made vacuum-tight gas cell. The gas cell setup did not allow to spin the capillaries so that the data were collected statically without sample spinning. All measurements were performed at room temperature (about 293 K) using *n*-butane of a purity of 99.5%. At each pressure step the samples were equilibrated for 2-10 min depending on the sample. For *dry*-MOF-5-**OC2** to *dry*-MOF-5-**OC6** equilibration times of 10 min per pressure step were applied, whereas *dry*-MOF-5-**OC7** and *dry*-MOF-5-**OC8** were equilibrated for only 2 min at each step (step size 50 kPa).

7 Bibliography

[1] M. Kondo, T. Yoshitomi, K. Seki, H. Matsuzaka, S. Kitagawa, *Angew. Chem. Int. Ed.* **1997**, *36*, 1725–1727.

[2] H. Li, M. Eddaoudi, M. O'Keeffe, O. M. Yaghi, *Nature* **1999**, *402*, 276–279.

[3] S. S. Y. Chui, S. M. F. Lo, J. P. H. Charmant, A. G. Orpen, I. D. Williams, *Science* **1999**, *283*, 1148–1150.

[4] H. Li, M. Eddaoudi, T. L. Groy, O. M. Yaghi, *J. Am. Chem. Soc.* **1998**, *120*, 8571–8572.

[5] X. Zhang, Z. Chen, X. Liu, S. L. Hanna, X. Wang, R. Taheri-Ledari, A. Maleki, P. Li, O. K. Farha, *Chem. Soc. Rev.* **2020**, *49*, 7406–7427.

[6] C. Healy, K. M. Patil, B. H. Wilson, L. Hermanspahn, N. C. Harvey-Reid, B. I. Howard, C. Kleinjan, J. Kolien, F. Payet, S. G. Telfer, P. E. Kruger, T. D. Bennett, *Coord. Chem. Rev.* **2020**, *419*, 213388.

[7] R. Freund, O. Zaremba, G. Arnauts, R. Ameloot, G. Skorupskii, M. Dincă, A. Bavykina, J. Gascon, A. Ejsmont, J. Goscianska, M. Kalmutzki, U. Lächelt, E. Ploetz, C. S. Diercks, S. Wuttke, *Angew. Chem. Int. Ed.* **2021**, 2–29.

[8] S. R. Batten, N. R. Champness, X. M. Chen, J. Garcia-Martinez, S. Kitagawa, L. Öhrström, M. O'Keeffe, M. P. Suh, J. Reedijk, *Pure Appl. Chem.* **2013**, *85*, 1715–1724.

[9] F. Millange, N. Guillou, R. I. Walton, J. M. Grenèche, I. Margiolaki, G. Férey, *Chem. Commun.* **2008**, 4732–4734.

[10] N. Stock, S. Biswas, *Chem. Rev.* **2012**, *112*, 933–969.

[11] J. Klinowski, F. A. Almeida Paz, P. Silva, J. Rocha, *Dalton Trans.* **2011**, *40*, 321–330.

[12] H. Al-Kutubi, J. Gascon, E. J. R. Sudhölter, L. Rassaei, *ChemElectroChem* **2015**, *2*, 462–474.

[13] N. A. Khan, S. H. Jhung, *Coord. Chem. Rev.* **2015**, *285*, 11–23.

[14] J. L. Do, T. Friščić, *ACS Cent. Sci.* **2017**, *3*, 13–19.

[15] O. M. Yaghi, O. K. M, N. W. Ockwig, H. K. Chae, M. Eddaoudi, J. Kim, *Nature* **2003**, *423*, 705–714.

[16] N. W. Ockwig, O. Delgado-Friedrichs, M. O'Keeffe, O. M. Yaghi, *Acc. Chem. Res.* **2005**, *38*, 176–182.

[17] J. Kim, B. Chen, T. M. Reineke, H. Li, M. Eddaoudi, D. B. Moler, M. O'Keeffe, O. M. Yaghi, *J. Am. Chem. Soc.* **2001**, *123*, 8239–8247.

[18] M. Eddaoudi, D. Moler, H. Li, B. Chen, T. Reineke, M. O'Keeffe, O. Yaghi, *Acc. Chem. Res.* **2001**, *34*, 319–330.

[19] M. O'Keeffe, O. M. Yaghi, *Chem. Rev.* **2012**, *112*, 675–702.

[20] Z. Chen, H. Jiang, M. Li, M. O'Keeffe, M. Eddaoudi, *Chem. Rev.* **2020**, *120*, 8039–8065.

[21] R. Freund, S. Canossa, S. M. Cohen, W. Yan, H. Deng, V. Guillerm, M. Eddaoudi, D. G. Madden, D. Fairen-Jimenez, H. Lyu, L. K. Macreadie, Z. Ji, Y. Zhang, B. Wang, F. Haase, C. Wöll, O. Zaremba, J. Andreo, S. Wuttke, C. S. Diercks, *Angew. Chem. Int. Ed.* **2021**, *60*, 23946–23974.

[22] H. Jiang, D. Alezi, M. Eddaoudi, *Nat. Rev. Mater.* **2021**, *6*, 466–487.

[23] V. Guillerm, D. Maspoch, *J. Am. Chem. Soc.* **2019**, *141*, 16517–16538.

[24] L. E. Kreno, K. Leong, O. K. Farha, M. Allendorf, R. P. Van Duyne, J. T. Hupp, *Chem. Rev.* **2012**, *112*, 1105–1125.

[25] I. M. Hönicke, I. Senkovska, V. Bon, I. A. Baburin, N. Bönisch, S. Raschke, J. D. Evans, S. Kaskel, *Angew. Chem. Int. Ed.* **2018**, *57*, 13780–13783.

[26] H. Furukawa, N. Ko, Y. B. Go, N. Aratani, S. B. Choi, J. Kim, O. M. Yaghi, *Science* **2010**, 424–429.

[27] W. Zhou, H. Wu, T. Yildirim, *J. Am. Chem. Soc.* **2008**, *130*, 15268–15269.

[28] M. Eddaoudi, J. Kim, N. Rosi, D. Vodak, J. Wachter, M. O'Keeffe, O. M. Yaghi, *Science* **2002**, *295*, 469–472.

[29] H. Deng, C. J. Doonan, H. Furukawa, R. B. Ferreira, J. Towne, C. B. Knobler, B. Wang, O. M. Yaghi, *Science* **2010**, *327*, 846–850.

[30] A. G. Slater, A. I. Cooper, *Science* **2015**, *348*, aaa8075.

[31] S. Horike, S. Shimomura, S. Kitagawa, *Nat. Chem.* **2009**, *1*, 695–704.

[32] A. Schneemann, V. Bon, I. Schwedler, I. Senkovska, S. Kaskel, R. A. Fischer, *Chem. Soc. Rev.* **2014**, *43*, 6062–6096.

[33] Y. Liu, J. H. Her, A. Dailly, A. J. Ramirez-Cuesta, D. A. Neumann, C. M. Brown, *J. Am. Chem. Soc.* **2008**, *130*, 11813–11818.

[34] Q. Zeng, K. Wang, B. Zou, *J. Am. Chem. Soc.* **2017**, *139*, 15648–15651.

[35] P. Serra-Crespo, A. Dikhtiarenko, E. Stavitski, J. Juan-Alcañiz, F. Kapteijn, F. X. Coudert, J. Gascon, *CrystEngComm* **2015**, *17*, 276–280.

[36] A. P. Katsoulidis, D. Antypov, G. F. S. Whitehead, E. J. Carrington, D. J. Adams, N. G. Berry, G. R. Darling, M. S. Dyer, M. J. Rosseinsky, *Nature* **2019**, *565*, 213–217.

[37] F. Salles, G. Maurin, C. Serre, P. L. Llewellyn, C. Knöfel, H. J. Choi, Y. Filinchuk, L. Oliviero, A. Vimont, J. R. Long, G. Férey, *J. Am. Chem. Soc.* **2010**, 13782–13788.

[38] N. Yanai, T. Uemura, M. Inoue, R. Matsuda, T. Fukushima, M. Tsujimoto, S. Isoda, S. Kitagawa, *J. Am. Chem. Soc.* **2012**, *134*, 4501–4504.

[39] A. Ghoufi, K. Benhamed, L. Boukli-Hacene, G. Maurin, *ACS Cent. Sci.* **2017**, *3*, 394–398.

[40] A. Knebel, B. Geppert, K. Volgmann, D. I. Kolokolov, A. G. Stepanov, J. Twiefel, P. Heitjans, D. Volkmer, J. Caro, *Science* **2017**, *358*, 347–351.

[41] J. A. Mason, J. Oktawiec, M. K. Taylor, M. R. Hudson, J. Rodriguez, J. E. Bachman, M. I. Gonzalez, A. Cervellino, A. Guagliardi, C. M. Brown, P. L. Llewellyn, N. Masciocchi, J. R. Long, *Nature* **2015**, *527*, 357–361.

[42] X. Zhao, Y. Wang, D. S. Li, X. Bu, P. Feng, *Adv. Mater.* **2018**, *30*, 1705189.

[43] N. Yanai, K. Kitayama, Y. Hijikata, H. Sato, R. Matsuda, Y. Kubota, M. Takata, M. Mizuno, T. Uemura, S. Kitagawa, *Nat. Mater.* **2011**, *10*, 787–793.

[44] P. Horcajada, R. Gref, T. Baati, P. K. Allan, G. Maurin, P. Couvreur, G. Férey, R. E. Morris, C. Serre, *Chem. Rev.* **2012**, *112*, 1232–1268.

[45] P. G. Yot, L. Vanduyfhuys, E. Alvarez, J. Rodriguez, J. P. Itié, P. Fabry, N. Guillou, T. Devic, I. Beurroies, P. L. Llewellyn, V. Van Speybroeck, C. Serre, G. Maurin, *Chem. Sci.* **2016**, *7*, 446–450.

[46] Z. Liu, L. Zhang, D. Sun, *Chem. Commun.* **2020**, *56*, 9416–9432.

[47] J. Wieme, K. Lejaeghere, G. Kresse, V. Van Speybroeck, *Nat. Commun.* **2018**, *9*, 4899.

[48] S. Kitagawa, R. Kitaura, S. Noro, *Angew. Chem. Int. Ed.* **2004**, *43*, 2334–2375.

[49] S. K. Elsaidi, M. H. Mohamed, D. Banerjee, P. K. Thallapally, *Coord. Chem. Rev.* **2018**, *358*, 125–152.

[50] M. Thommes, K. Kaneko, A. V. Neimark, J. P. Olivier, F. Rodriguez-Reinoso, J. Rouquerol, K. S. W. Sing, *Pure Appl. Chem.* **2015**, *87*, 1051–1069.

[51] J. A. Mason, M. Veenstra, J. R. Long, *Chem. Sci.* **2014**, *5*, 32–51.

[52] S. Shimomura, M. Higuchi, R. Matsuda, K. Yoneda, Y. Hijikata, Y. Kubota, Y. Mita, J. Kim, M. Takata, S. Kitagawa, *Nat. Chem.* **2010**, *2*, 633–637.

[53] C. Gücüyener, J. Van Den Bergh, J. Gascon, F. Kapteijn, *J. Am. Chem. Soc.* **2010**, *132*, 17704–17706.

[54] A. M. Walker, B. Civalleri, B. Slater, C. Mellot-Draznieks, F. Corà, C. M. Zicovich-Wilson, G. Román-Pérez, J. M. Soler, J. D. Gale, *Angew. Chem. Int. Ed.* **2010**, *49*, 7501–7503.

[55] K. T. Butler, P. Vervoorts, M. G. Ehrenreich, J. Armstrong, J. M. Skelton, G. Kieslich, *Chem. Mater.* **2019**, *31*, 8366–8372.

[56] L. Vanduyfhuys, S. M. J. Rogge, J. Wieme, S. Vandenbrande, G. Maurin, M. Waroquier, V. Van Speybroeck, *Nat. Commun.* **2018**, *9*, 204.

[57] P. Vervoorts, J. Keupp, A. Schneemann, C. L. Hobday, D. Daisenberger, R. A. Fischer, R. Schmid, G. Kieslich, *Angew. Chem. Int. Ed.* **2021**, *60*, 787–793.

[58] S. Henke, A. Schneemann, R. A. Fischer, *Adv. Funct. Mater.* **2013**, *23*, 5990–5996.

[59] C. L. Hobday, G. Kieslich, *Dalton Trans.* **2021**, *50*, 3759–3768.

[60] C. Serre, F. Millange, C. Thouvenot, M. Noguès, G. Marsolier, D. Louër, G. Férey, *J. Am. Chem. Soc.* **2002**, *124*, 13519–13526.

[61] T. Loiseau, C. Serre, C. Huguenard, G. Fink, F. Taulelle, M. Henry, T. Bataille, G. Férey, *Chem. Eur. J.* **2004**, *10*, 1373–1382.

[62] T. R. Whitfield, X. Wang, L. Liu, A. J. Jacobson, *Solid State Sci.* **2005**, *7*, 1096–1103.

[63] J. P. S. Mowat, S. R. Miller, A. M. Z. Slawin, V. R. Seymour, S. E. Ashbrook, P. A. Wright, *Microporous Mesoporous Mater.* **2011**, *142*, 322–333.

[64] C. Volkringer, T. Loiseau, N. Guillou, G. Férey, E. Elkaïm, A. Vimont, *J. Chem. Soc. Dalt. Trans.* **2009**, *53*, 2241–2249.

[65] E. V Anokhina, M. Vougo-Zanda, X. Wang, A. J. Jacobson, *J. Am. Chem. Soc.* **2005**, *127*, 15000–15001.

[66] N. L. Rosi, J. Kim, M. Eddaoudi, B. Chen, M. O'Keeffe, O. M. Yaghi, *J. Am. Chem. Soc.* **2005**, *127*, 1504–1518.

[67] F. M. Mulder, B. Assfour, J. Huot, T. J. Dingemans, M. Wagemaker, A. J. Ramirez-Cuesta, *J. Phys. Chem. C* **2010**, *114*, 10648–10655.

[68] C. Serre, S. Bourrelly, A. Vimont, N. A. Ramsahye, G. Maurin, P. L. Llewellyn, M. Daturi, Y. Filinchuk, O. Leynaud, P. Barnes, G. Férey, *Adv. Mater.* **2007**, *19*, 2246–2251.

[69] N. Guillou, S. Bourrelly, P. L. Llewellyn, R. I. Walton, F. Millange, *CrystEngComm* **2015**, *17*, 422–429.

[70] S. Bourrelly, P. L. Llewellyn, C. Serre, F. Millange, T. Loiseau, G. Férey, *J. Am. Chem. Soc.* **2005**, *127*, 13519–13521.

[71] S. Bourrelly, B. Moulin, A. Rivera, G. Maurin, S. Devautour-Vinot, C. Serre, T. Devic, P. Horcajada, A. Vimont, G. Clet, M. Daturi, J. C. Lavalley, S. Loera-Serna, R. Denoyel, P. L. Llewellyn, G. Férey, *J. Am. Chem. Soc.* **2010**, *132*, 9488–9498.

[72] P. L. Llewellyn, G. Maurin, T. Devic, S. Loera-Serna, N. Rosenbach, C. Serre, S. Bourrelly, P. Horcajada, Y. Filinchuk, G. Férey, *J. Am. Chem. Soc.* **2008**, *130*, 12808–12814.

[73] P. L. Llewellyn, P. Horcajada, G. Maurin, T. Devic, N. Rosenbach, S. Bourrelly, C. Serre, D. Vincent, S. Loera-Serna, Y. Filinchuk, G. Férey, *J. Am. Chem. Soc.* **2009**, *131*, 13002–13008.

[74] F. Salles, A. Ghoufi, G. Maurin, R. G. Bell, C. Mellot-Draznieks, G. Férey, *Angew. Chem. Int. Ed.* **2008**, *47*, 8487–8491.

[75] A. Boutin, D. Bousquet, A. U. Ortiz, F. X. Coudert, A. H. Fuchs, A. Ballandras, G.

Weber, I. Bezverkhyy, J. P. Bellat, G. Ortiz, G. Chaplais, J. L. Paillaud, C. Marichal, H. Nouali, J. Patarin, *J. Phys. Chem. C* **2013**, *117*, 8180–8188.

[76] M. T. Wharmby, S. Henke, T. D. Bennett, S. R. Bajpe, I. Schwedler, S. P. Thompson, F. Gozzo, P. Simoncic, C. Mellot-Draznieks, H. Tao, Y. Yue, A. K. Cheetham, *Angew. Chem. Int. Ed.* **2015**, *54*, 6447–6451.

[77] G. Férey, C. Serre, *Chem. Soc. Rev.* **2009**, *38*, 1380–1399.

[78] C. Volkringer, M. Meddouri, T. Loiseau, N. Guillou, J. Marrot, G. Férey, M. Haouas, F. Taulelle, N. Audebrand, M. Latroche, *Inorg. Chem.* **2008**, *47*, 11892–11901.

[79] A. Fateeva, P. Horcajada, T. Devic, C. Serre, J. Marrot, J. M. Grenèche, M. Morcrette, J. M. Tarascon, G. Maurin, G. Férey, *Eur. J. Inorg. Chem.* **2010**, *68*, 3789–3794.

[80] Q. Yang, S. Vaesen, M. Vishnuvarthan, F. Ragon, C. Serre, A. Vimont, M. Daturi, G. De Weireld, G. Maurin, *J. Mater. Chem.* **2012**, *22*, 10210–10220.

[81] L. Mitchell, B. Gonzalez-Santiago, J. P. S. Mowat, M. E. Gunn, P. Williamson, N. Acerbi, M. L. Clarke, P. A. Wright, *Catal. Sci. Technol.* **2013**, *3*, 606–617.

[82] G. Férey, *Dalton Trans.* **2016**, *45*, 4073–4089.

[83] T. Devic, P. Horcajada, C. Serre, F. Salles, G. Maurin, B. Moulin, D. Heurtaux, G. Clet, A. Vimont, J. M. Grenéche, B. Le Ouay, F. Moreau, E. Magnier, Y. Filinchuk, J. Marrot, J. C. Lavalley, M. Daturi, G. Férey, *J. Am. Chem. Soc.* **2010**, *132*, 1127–1136.

[84] S. Biswas, T. Ahnfeldt, N. Stock, *Inorg. Chem.* **2011**, *50*, 9518–9526.

[85] F. Millange, R. I. Walton, *Isr. J. Chem.* **2018**, *58*, 1019–1035.

[86] L. Hamon, P. L. Llewellyn, T. Devic, A. Ghoufi, G. Clet, V. Guillerm, G. D. Pirngruber, G. Maurin, C. Serre, G. Driver, W. Van Beek, E. Jolimaître, A. Vimont, M. Daturi, G. Férey, *J. Am. Chem. Soc.* **2009**, *131*, 17490–17499.

[87] S. Couck, J. F. M. Denayer, G. V. Baron, T. Rémy, J. Gascon, F. Kapteijn, *J. Am. Chem. Soc.* **2009**, *131*, 6326–6327.

[88] D. N. Dybtsev, H. Chun, K. Kim, *Angew. Chem. Int. Ed.* **2004**, *43*, 5033–5036.

[89] Y. Kim, R. Haldar, H. Kim, J. Koo, K. Kim, *Dalton Trans.* **2016**, *45*, 4187–4192.

[90] G. Turner, S. C. McKellar, D. R. Allan, A. K. Cheetham, S. Henke, S. A. Moggach, *Chem. Sci.* **2021**, *12*, 13793–13801.

[91] K. Uemura, Y. Yamasaki, Y. Komagawa, K. Tanaka, H. Kita, *Angew. Chem. Int. Ed.* **2007**, *46*, 6662–6665.

[92] J. S. Grosch, F. Paesani, *J. Am. Chem. Soc.* **2012**, *134*, 4207–4215.

[93] J. Wieme, S. M. J. Rogge, P. G. Yot, L. Vanduyfhuys, S. K. Lee, J. S. Chang, M. Waroquier, G. Maurin, V. Van Speybroeck, *J. Mater. Chem. A* **2019**, *7*, 22663–22674.

[94] R. Kitaura, F. Iwahori, R. Matsuda, S. Kitagawa, Y. Kubota, M. Takata, T. C.

Kobayashi, *Inorg. Chem.* **2004**, *43*, 6522–6524.

[95] L. G. Zhu, H. P. Xiao, *Zeitschrift fur Anorg. und Allg. Chemie* **2008**, *634*, 845–847.

[96] P. Maniam, N. Stock, *Inorg. Chem.* **2011**, *50*, 5085–5097.

[97] Z. Wang, S. M. Cohen, *J. Am. Chem. Soc.* **2009**, *131*, 16675–16677.

[98] S. Henke, A. Schneemann, A. Wütscher, R. A. Fischer, *J. Am. Chem. Soc.* **2012**, *134*, 9464–9474.

[99] S. Henke, R. Schmid, J. D. Grunwaldt, R. A. Fischer, *Chem. Eur. J.* **2010**, *16*, 14296–14306.

[100] I. Schwedler, S. Henke, M. T. Wharmby, S. R. Bajpe, A. K. Cheetham, R. A. Fischer, *Dalton Trans.* **2016**, *45*, 4230–4241.

[101] A. Schneemann, P. Vervoorts, I. Hante, M. Tu, S. Wannapaiboon, C. Sternemann, M. Paulus, D. C. F. Wieland, S. Henke, R. A. Fischer, *Chem. Mater.* **2018**, *30*, 1667–1676.

[102] M. Mendt, P. Vervoorts, A. Schneemann, R. A. Fischer, A. Pöppl, *J. Phys. Chem. C* **2019**, *123*, 2940–2952.

[103] K. Uemura, Y. Yamasaki, F. Onishi, H. Kita, M. Ebihara, *Inorg. Chem.* **2010**, *49*, 10133–10143.

[104] S. Henke, A. Schneemann, A. Wütscher, R. A. Fischer, *J. Am. Chem. Soc.* **2012**, *134*, 9464–9474.

[105] J. Keupp, J. P. Dürholt, R. Schmid, *Faraday Discuss.* **2021**, *225*, 324–340.

[106] R. Pallach, J. Keupp, K. Terlinden, L. Frentzel-Beyme, M. Kloß, A. Machalica, J. Kotschy, S. K. Vasa, P. A. Chater, C. Sternemann, M. T. Wharmby, R. Linser, R. Schmid, S. Henke, *Nat. Commun.* **2021**, *12*, 1–12.

[107] A. Schneemann, E. D. Bloch, S. Henke, P. L. Llewellyn, J. R. Long, R. A. Fischer, *Chem. Eur. J.* **2015**, *21*, 18764–18769.

[108] C. Yu, S. Bourrelly, C. Martineau, F. Saidi, E. Bloch, H. Lavrard, F. Taulelle, P. Horcajada, C. Serre, P. L. Llewellyn, E. Magnier, T. Devic, *Dalton Trans.* **2015**, *44*, 19687–19692.

[109] M. Rehahn, A. D. Schlüter, W. J. Feast, *Synth.* **1988**, *1988*, 386–388.

[110] G. S. Pawley, *J. Appl. Cryst.* **1981**, *14*, 357–361.

[111] P. J. Linstrom, W. G. Mallard, Eds. , *NIST Chemistry WebBook, NIST Standard Reference Database Number 69*, National Institute Of Standards And Technology, Gaithersburg MD, 20899, **2022**.

[112] J. Keupp, R. Schmid, *Adv. Theory Simul.* **2019**, *2*, 1900117.

[113] D. R. Lide, Ed. , in *CRC Handb. Chem. Phys.*, Taylor And Francis, Boca Raton, FL, **2006**, pp. 9–50, 9–49.

[114] S. Henke, D. C. Florian Wieland, M. Meilikhov, M. Paulus, C. Sternemann, K. Yusenko, R. A. Fischer, *CrystEngComm* **2011**, *13*, 6399–6404.

[115] H. M. Rietveld, *J. Appl. Cryst.* **1969**, *2*, 65–71.

[116] S. Chu, Y. Cui, N. Liu, *Nat. Mater.* **2016**, *16*, 16–22.

[117] D. S. Sholl, R. P. Lively, *Nature* **2016**, *532*, 6–9.

[118] A. B. de Haan, H. B. Eral, B. Schuur, *Industrial Separation Processes*, De Gruyter, Berlin, **2020**.

[119] Y. Wu, Z. Liu, J. Peng, X. Wang, X. Zhou, Z. Li, *ACS Appl. Mater. Interfaces* **2020**, *12*, 51499–51505.

[120] A. Schneemann, Y. Jing, J. D. Evans, T. Toyao, Y. Hijikata, Y. Kamiya, K. I. Shimizu, N. C. Burtch, S. I. Noro, *Dalton Trans.* **2021**, *50*, 10423–10435.

[121] D. R. Lide, Ed. , in *CRC Handb. Chem. Phys.*, Taylor And Francis, Boca Raton, FL, **2006**, pp. 6–91.

[122] X. Wang, Z. Niu, A. M. Al-Enizi, A. Nafady, Y. Wu, B. Aguila, G. Verma, L. Wojtas, Y. S. Chen, Z. Li, S. Ma, *J. Mater. Chem. A* **2019**, *7*, 13585–13590.

[123] K. Chen, S. H. Mousavi, R. Singh, R. Q. Snurr, G. Li, P. A. Webley, *Chem. Soc. Rev.* **2022**, *51*, 1139–1166.

[124] L. Li, R. Krishna, Y. Wang, J. Yang, X. Wang, J. Li, *J. Mater. Chem. A* **2016**, *4*, 751–755.

[125] D. L. Chen, N. Wang, F. F. Wang, J. Xie, Y. Zhong, W. Zhu, J. K. Johnson, R. Krishna, *J. Phys. Chem. C* **2014**, *118*, 17831–17837.

[126] X. Y. Tian, H. L. Zhou, X. W. Zhang, C. Wang, Z. H. Qiu, D. D. Zhou, J. P. Zhang, *Inorg. Chem.* **2020**, *59*, 6047–6052.

[127] V. Bon, N. Kavoosi, I. Senkovska, S. Kaskel, *ACS Appl. Mater. Interfaces* **2015**, *7*, 22292–22300.

[128] M. C. De Goffau, X. Yang, J. M. Van Dijl, H. J. M. Harmsen, *Environ. Microbiol.* **2009**, *11*, 809–822.

[129] C. Fiorio, *J. Res. Natl. Bur. Stand. (1934).* **1976**, *81*, 89–96.

[130] L. Abylgazina, I. Senkovska, R. Engemann, S. Ehrling, T. E. Gorelik, N. Kavoosi, U. Kaiser, S. Kaskel, *Front. Chem.* **2021**, *9*, 1–10.

[131] M. J. Cliffe, A. L. Goodwin, *J. Appl. Cryst.* **2012**, *45*, 1321–1329.

[132] T. Gruene, J. J. Holstein, G. H. Clever, B. Keppler, *Nat. Rev. Chem.* **2021**, *5*, 660–668.

[133] T. D. Bennett, A. K. Cheetham, *Acc. Chem. Res.* **2014**, *47*, 1555–1562.

[134] T. D. Bennett, S. Horike, *Nat. Rev. Mater.* **2018**, *3*, 431–440.

[135] J. Fonseca, T. Gong, L. Jiao, H. L. Jiang, *J. Mater. Chem. A* **2021**, *9*, 10562–10611.

[136] T. D. Bennett, A. K. Cheetham, A. H. Fuchs, F. X. Coudert, *Nat. Chem.* **2016**, *9*, 11–16.

[137] S. Li, R. Limbach, L. Longley, A. A. Shirzadi, J. C. Walmsley, D. N. Johnstone, P. A. Midgley, L. Wondraczek, T. D. Bennett, *J. Am. Chem. Soc.* **2019**, *141*, 1027–1034.

[138] R. Gaillac, P. Pullumbi, K. A. Beyer, K. W. Chapman, D. A. Keen, T. D. Bennett, F.-X. Coudert, *Nat. Mater.* **2017**, *16*, 1149–1155.

[139] H. Tao, T. D. Bennett, Y. Yue, *Adv. Mater.* **2017**, *29*, 1601705.

[140] T. D. Bennett, J. C. Tan, Y. Yue, E. Baxter, C. Ducati, N. J. Terrill, H. H. M. Yeung, Z. Zhou, W. Chen, S. Henke, A. K. Cheetham, G. N. Greaves, *Nat. Commun.* **2015**, *6*, 8079.

[141] L. Frentzel-Beyme, M. Kloß, R. Pallach, S. Salamon, H. Moldenhauer, J. Landers, H. Wende, J. Debus, S. Henke, *J. Mater. Chem. A* **2019**, *7*, 985–990.

[142] L. Frentzel-Beyme, M. Kloß, P. Kolodzeiski, R. Pallach, S. Henke, *J. Am. Chem. Soc.* **2019**, *141*, 12362–12371.

[143] P. Horcajada, S. Surblé, C. Serre, D. Y. Hong, Y. K. Seo, J. S. Chang, J. M. Grenèche, I. Margiolaki, G. Férey, *Chem. Commun.* **2007**, *100*, 2820–2822.

[144] A. F. Sapnik, I. Bechis, S. M. Collins, D. N. Johnstone, G. Divitini, A. J. Smith, P. A. Chater, M. A. Addicoat, T. Johnson, D. A. Keen, K. E. Jelfs, T. D. Bennett, *Nat. Commun.* **2021**, *12*, 1–12.

[145] Sigma-Aldrich, “Basolite F300, Fe-BTC,” can be found under https://www.sigmaaldrich.com/DE/de/product/aldrich/690872, n.d.

[146] L. Sciortino, A. Alessi, F. Messina, G. Buscarino, F. M. Gelardi, *J. Phys. Chem. C* **2015**, *119*, 7826–7830.

[147] A. Dhakshinamoorthy, M. Alvaro, P. Horcajada, E. Gibson, M. Vishnuvarthan, A. Vimont, J. M. Grenèche, C. Serre, M. Daturi, H. Garcia, *ACS Catal.* **2012**, *2*, 2060–2065.

[148] A. F. Sapnik, C. W. Ashling, L. K. Macreadie, S. J. Lee, T. Johnson, S. G. Telfer, T. D. Bennett, *J. Mater. Chem. A* **2021**, *9*, 27019–27027.

[149] J. W. Xiu, G. E. Wang, M. S. Yao, C. C. Yang, C. H. Lin, G. Xu, *Chem. Commun.* **2017**, *53*, 2479–2482.

[150] B. Bueken, F. Vermoortele, M. J. Cliffe, M. T. Wharmby, D. Foucher, J. Wieme, L. Vanduyfhuys, C. Martineau, N. Stock, F. Taulelle, V. Van Speybroeck, A. L. Goodwin, D. De Vos, *Chem. Eur. J.* **2016**, *22*, 3264–3267.

[151] S. Krause, J. D. Evans, V. Bon, I. Senkovska, S. Ehrling, P. Iacomi, D. M. Többens, D. Wallacher, M. S. Weiss, B. Zheng, P. G. Yot, G. Maurin, P. L. Llewellyn, F. X. Coudert, S. Kaskel, *Chem. Sci.* **2020**, *11*, 9468–9479.

[152] K. Uemura, S. Kitagawa, K. Fukui, K. Saito, *J. Am. Chem. Soc.* **2004**, *126*, 3817–3828.

[153] N. Yanai, W. Kaneko, K. Yoneda, M. Ohba, S. Kitagawa, *J. Am. Chem. Soc.* **2007**, *129*, 3496–3497.

[154] C. K. Brozek, V. K. Michaelis, T. C. Ong, L. Bellarosa, N. López, R. G. Griffin, M. Dincă, *ACS Cent. Sci.* **2015**, *1*, 252–260.

[155] Z. Akimbekov, D. Wu, C. K. Brozek, M. Dincə, A. Navrotsky, *Phys. Chem. Chem. Phys.* **2015**, *18*, 1158–1162.

[156] N. Lock, Y. Wu, M. Christensen, L. J. Cameron, V. K. Peterson, A. J. Bridgeman, C. J. Kepert, B. B. Iversen, *J. Phys. Chem. C* **2010**, *114*, 16181–16186.

[157] L. H. N. Rimmer, M. T. Dove, A. L. Goodwin, D. C. Palmer, *Phys. Chem. Chem. Phys.* **2014**, *16*, 21144–21152.

[158] S. Y. Zhang, D. Li, D. Guo, H. Zhang, W. Shi, P. Cheng, L. Wojtas, M. J. Zaworotko, *J. Am. Chem. Soc.* **2015**, *137*, 15406–15409.

[159] L. Sarkisov, R. L. Martin, M. Haranczyk, B. Smit, *J. Am. Chem. Soc.* **2014**, *136*, 2228–2231.

[160] A. Marmier, K. E. Evans, *Dalton Trans.* **2016**, *45*, 4360–4369.

[161] S. M. J. Rogge, M. Waroquier, V. Van Speybroeck, *Acc. Chem. Res.* **2018**, *51*, 138–148.

[162] A. U. Ortiz, A. Boutin, A. H. Fuchs, F. X. Coudert, *Phys. Rev. Lett.* **2012**, *109*, 195502.

[163] N. Klein, H. C. Hoffmann, A. Cadiau, J. Getzschmann, M. R. Lohe, S. Paasch, T. Heydenreich, K. Adil, I. Senkovska, E. Brunner, S. Kaskel, *J. Mater. Chem.* **2012**, *22*, 10303.

[164] H. C. Hoffmann, B. Assfour, F. Epperlein, N. Klein, S. Paasch, I. Senkovska, S. Kaskel, G. Seifert, E. Brunner, *J. Am. Chem. Soc.* **2011**, *133*, 8681–8690.

[165] Dortmund Data Bank, "Dortmund Data Bank (DDB)," **2020**.

[166] J. Debgupta, B. A. Kakade, V. K. Pillai, *Phys. Chem. Chem. Phys.* **2011**, *13*, 14668–14674.

[167] S. R. Elliott, *Phys. Rev. Lett.* **1991**, *67*, 711–714.

[168] S. R. Elliott, *Nature* **1991**, *354*, 445–452.

[169] P. S. Salmon, *Proc. R. Soc. A Math. Phys. Eng. Sci.* **1994**, *445*, 351–365.

[170] G. Lucovsky, J. C. Phillips, *Phys. Status Solidi Basic Res.* **2009**, *246*, 1806–1812.

[171] J. M. Zaug, A. K. Soper, S. M. Clark, *Nat. Mater.* **2008**, *7*, 890–899.

[172] G. Majano, O. Martin, M. Hammes, S. Smeets, C. Baerlocher, J. Pérez-Ramírez, *Adv. Funct. Mater.* **2014**, *24*, 3855–3865.

[173] A. J. Graham, A. M. Banu, T. Düren, A. Greenaway, S. C. McKellar, J. P. S. Mowat, K. Ward, P. A. Wright, S. A. Moggach, *J. Am. Chem. Soc.* **2014**, *136*, 8606–8613.

[174] T. D. Bennett, T. K. Todorova, E. F. Baxter, D. G. Reid, C. Gervais, B. Bueken, B. Van De Voorde, D. De Vos, D. A. Keen, C. Mellot-Draznieks, *Phys. Chem. Chem. Phys.* **2016**, *18*, 2192–2201.

[175] B. Civalleri, F. Napoli, Y. Noël, C. Roetti, R. Dovesi, *CrystEngComm* **2006**, *8*, 364–371.

[176] O. Berkesi, P. Berenji, I. Dreveni, T. Körtvélyesi, J. A. Andor, J. Mink, P. L. Goggin, *Vib. Spectrosc.* **2007**, *43*, 227–236.

[177] O. Berkesi, J. A. Andor, U. A. Jayasooriya, R. D. Cannon, *Spectrochimica Acta Part A* **1992**, *48*, 147–149.

[178] G. Durgaprasad, D. N. Sathyanarayana, C. C. Patel, *Bull. Chem. Soc. Jpn.* **1971**, *44*, 316–322.

[179] V. Zeleňák, Z. Vargová, K. Györyová, *Spectrochimica Acta Part A* **2007**, *66*, 262–272.

[180] S. Bureekaew, S. Amirjalayer, M. Tafipolsky, C. Spickermann, T. K. Roy, R. Schmid, *Phys. Status Solidi Basic Res.* **2013**, *250*, 1128–1141.

[181] S. M. J. Rogge, M. Waroquier, V. Van Speybroeck, *Nat. Commun.* **2019**, *10*, 4842.

[182] J. D. Evans, L. Bocquet, F. X. Coudert, *Chem* **2016**, *1*, 873–886.

[183] P. Debye, *Ann. Phys.* **1912**, *348*, 59–92.

[184] I. Waller, *Zeitschrift für Phys.* **1923**, *17*, 398–408.

[185] T. D. Bennett, J. C. Tan, Y. Yue, E. Baxter, C. Ducati, N. J. Terrill, H. H. M. Yeung, Z. Zhou, W. Chen, S. Henke, A. K. Cheetham, G. N. Greaves, *Nat. Commun.* **2015**, *6*, 8079.

[186] R. Gaillac, P. Pullumbi, F. X. Coudert, *J. Phys. Chem. C* **2018**, *122*, 6730–6736.

[187] S. Brunauer, P. H. Emmett, E. Teller, *J. Am. Chem. Soc.* **1938**, *60*, 309–319.

[188] K. A. Cychosz, M. Thommes, *Engineering* **2018**, *4*, 559–566.

[189] "NIST Computational Chemistry Comparison and Benchmark Database, NIST Standard Reference Database Number 101,Release 20, August 2019, Editor: Russell D. Johnson III http://cccbdb.nist.gov/," **2019**.

[190] P. W. Atkins, *Atkins' Physical Chemistry*, Oxford University Press, Oxford, **2006**.

[191] D. R. Lide, Ed. , in *CRC Handb. Chem. Phys.*, Taylor And Francis, Boca Raton, FL, **2006**, pp. 3–282, 6–71, 6–142.

[192] D. R. Lide, Ed. , in *CRC Handb. Chem. Phys.*, Taylor And Francis, Boca Raton, FL, **2006**, pp. 3–82, 6–68.

[193] D. R. Lide, Ed. , in *CRC Handb. Chem. Phys.*, Taylor And Francis, Boca Raton, FL,

2006, pp. 3–188, 6–66, 6–138.

[194] A. Lago, M. A. Rivas, J. Legido, T. P. Iglesias, *J. Chem. Thermodyn.* **2009**, *41*, 257–264.

[195] D. R. Lide, Ed. , in *CRC Handb. Chem. Phys.*, Taylor And Francis, Boca Raton, FL, **2006**, pp. 9–51.

[196] D. R. Lide, Ed. , in *CRC Handb. Chem. Phys.*, Taylor And Francis, Boca Raton, FL, **2006**, pp. 9–53, 9–50.

[197] S. Henke, Metal-Organic Frameworks with Additional Flexible Substituents: Modulating Responsiveness, Gas Sorption Selectivity & Network Topologies, Ruhr-Universität Bochum, **2011**.

[198] H. K. Chae, D. Y. Siberio-Pérez, J. Kim, Y. B. Go, M. Eddaoudi, A. J. Matzger, M. O'Keeffe, O. M. Yaghi, *Nature* **2004**, *427*, 523–527.

[199] Y. B. Zhang, H. Furukawa, N. Ko, W. Nie, H. J. Park, S. Okajima, K. E. Cordova, H. Deng, J. Kim, O. M. Yaghi, *J. Am. Chem. Soc.* **2015**, *137*, 2641–2650.

[200] L. Ma, A. Jin, Z. Xie, W. Lin, *Angew. Chem. Int. Ed.* **2009**, *48*, 9905–9908.

[201] S. Ayala, K. C. Bentz, S. M. Cohen, *Chem. Sci.* **2019**, *10*, 1746–1753.

[202] Z. Zhang, H. T. H. Nguyen, S. A. Miller, S. M. Cohen, *Angew. Chem. Int. Ed.* **2015**, *54*, 6152–6157.

[203] G. Férey, C. Mellot-Draznieks, C. Serre, F. Millange, J. Dutour, S. Surblé, I. Margiolaki, *Science* **2005**, *309*, 2040–2042.

[204] K. M. L. Taylor-Pashow, J. Della Rocca, Z. Xie, S. Tran, W. Lin, *J. Am. Chem. Soc.* **2009**, *131*, 14261–14263.

[205] M. Lammert, S. Bernt, F. Vermoortele, D. E. De Vos, N. Stock, *Inorg. Chem.* **2013**, *52*, 8521–8528.

[206] P. Horcajada, H. Chevreau, D. Heurtaux, F. Benyettou, F. Salles, T. Devic, A. Garcia-Marquez, C. Yu, H. Lavrard, C. L. Dutson, E. Magnier, G. Maurin, E. Elkaïm, C. Serre, *Chem. Commun.* **2014**, *50*, 6872–6874.

[207] A. Buragohain, P. Van Der Voort, S. Biswas, *Microporous Mesoporous Mater.* **2015**, *215*, 91–97.

[208] A. Buragohain, S. Couck, P. Van Der Voort, J. F. M. Denayer, S. Biswas, *J. Solid State Chem.* **2016**, *238*, 195–202.

[209] J. H. Cavka, S. Jakobsen, U. Olsbye, N. Guillou, C. Lamberti, S. Bordiga, K. P. Lillerud, *J. Am. Chem. Soc.* **2008**, *130*, 13850–13851.

[210] S. J. Garibay, S. M. Cohen, *Chem. Commun.* **2010**, *46*, 7700–7702.

[211] Z. Hu, Y. Peng, Z. Kang, Y. Qian, D. Zhao, *Inorg. Chem.* **2015**, *54*, 4862–4868.

[212] S. Øien-ØDegaard, B. Bouchevreau, K. Hylland, L. Wu, R. Blom, C. Grande, U. Olsbye, M. Tilset, K. P. Lillerud, *Inorg. Chem.* **2016**, *55*, 1986–1991.

[213] C. Kutzscher, G. Nickerl, I. Senkovska, V. Bon, S. Kaskel, *Chem. Mater.* **2016**, *28*, 2573–2580.

[214] N. X. Zhu, Z. W. Wei, C. X. Chen, D. Wang, C. C. Cao, Q. F. Qiu, J. J. Jiang, H. P. Wang, C. Y. Su, *Angew. Chem. Int. Ed.* **2019**, *58*, 17033–17040.

[215] P. G. Yot, K. Yang, F. Ragon, V. Dmitriev, T. Devic, P. Horcajada, C. Serre, G. Maurin, *Dalton Trans.* **2016**, *45*, 4283–4288.

[216] H. Wu, T. Yildirim, W. Zhou, *J. Phys. Chem. Lett.* **2013**, *4*, 925–930.

[217] L. Valenzano, B. Civalleri, S. Chavan, S. Bordiga, M. H. Nilsen, S. Jakobsen, K. P. Lillerud, C. Lamberti, *Chem. Mater.* **2011**, *23*, 1700–1718.

[218] H. Wu, Y. S. Chua, V. Krungleviciute, M. Tyagi, P. Chen, T. Yildirim, W. Zhou, *J. Am. Chem. Soc.* **2013**, *135*, 10525–10532.

[219] C. A. Trickett, K. J. Gagnon, S. Lee, F. Gándara, H. B. Bürgi, O. M. Yaghi, *Angew. Chem. Int. Ed.* **2015**, *54*, 11162–11167.

[220] H. Furukawa, F. Gándara, Y. B. Zhang, J. Jiang, W. L. Queen, M. R. Hudson, O. M. Yaghi, *J. Am. Chem. Soc.* **2014**, *136*, 4369–4381.

[221] J. Baek, B. Rungtaweevoranit, X. Pei, M. Park, S. C. Fakra, Y. S. Liu, R. Matheu, S. A. Alshmimri, S. Alshehri, C. A. Trickett, G. A. Somorjai, O. M. Yaghi, *J. Am. Chem. Soc.* **2018**, *140*, 18208–18216.

[222] H. Lyu, O. I. Chen, N. Hanikel, M. I. Hossain, R. W. Flaig, X. Pei, A. Amin, M. D. Doherty, R. K. Impastato, T. G. Glover, D. R. Moore, O. M. Yaghi, *J. Am. Chem. Soc.* **2022**, *144*, 2387–2396.

[223] D. A. Burns, E. M. Press, M. A. Siegler, R. S. Klausen, V. S. Thoi, *Angew. Chem. Int. Ed.* **2020**, *59*, 763–768.

[224] Y. Song, A. E. Khudozhitkov, J. Lee, H. Kang, D. I. Kolokolov, A. G. Stepanov, M. Yoon, *Chem. Commun.* **2020**, *56*, 4468–4471.

[225] D. Matoga, B. Gil, W. Nitek, A. D. Todd, C. W. Bielawski, *CrystEngComm* **2014**, *16*, 4959–4962.

[226] S. Grunder, C. Valente, A. C. Whalley, S. Sampath, J. Portmann, Y. Y. Botros, J. F. Stoddart, *Chem. Eur. J.* **2012**, *18*, 15632–15649.

[227] P. T. Fletcher, Steven; Gunning, *Tetrahedron Lett.* **2008**, *49*, 4817–4819.

[228] S. S. Kaye, A. Dailly, O. M. Yaghi, J. R. Long, *J. Am. Chem. Soc.* **2007**, *129*, 14176–14177.

[229] M. Basham, J. Filik, M. T. Wharmby, P. C. Y. Chang, B. El Kassaby, M. Gerring, J. Aishima, K. Levik, B. C. A. Pulford, I. Sikharulidze, D. Sneddon, M. Webber, S. S.

Dhesi, F. Maccherozzi, O. Svensson, S. Brockhauser, G. Náray, A. W. Ashton, *J. Synchrotron Radiat.* **2015**, *22*, 853–858.

[230] J. Filik, A. W. Ashton, P. C. Y. Chang, P. A. Chater, S. J. Day, M. Drakopoulos, M. W. Gerring, M. L. Hart, O. V. Magdysyuk, S. Michalik, A. Smith, C. C. Tang, N. J. Terrill, M. T. Wharmby, H. Wilhelm, *J. Appl. Cryst.* **2017**, *50*, 959–966.

[231] A. A. Coelho, *J. Appl. Cryst.* **2018**, *51*, 210–218.

[232] P. Thompson, D. E. Cox, J. B. Hastings, *J. Appl. Cryst.* **1987**, *20*, 79–83.

[233] O. V. Dolomanov, L. J. Bourhis, R. J. Gildea, J. A. K. Howard, H. Puschmann, *J. Appl. Cryst.* **2009**, *42*, 339–341.

[234] G. M. Sheldrick, *Acta Cryst. C* **2015**, *71*, 3–8.

[235] K. R. Thurber, R. Tycko, *J. Magn. Reson.* **2009**, *196*, 84–87.

[236] D. A. Keen, *J. Appl. Cryst.* **2001**, *34*, 172–177.

[237] S. J. L. Egami, Takeshi; Billinge, *Underneath the Bragg Peaks: Structural Analysis of Complex Materials*, Pergamon, Burlington, **2012**.

[238] A. K. Soper, E. R. Barney, *J. Appl. Cryst.* **2011**, *44*, 714–726.

[239] S. J. L. Billinge, in *Powder Diffr.* (Eds.: S.J.L. Billinge, R.E. Dinnebier), Royal Society Of Chemistry, Cambridge, **2008**, pp. 464–493.

[240] R. C. Weast, Ed. , *CRC Handbook of Chemistry and Physics*, CRC Publishing, Cleveland, OH, **1970**.

[241] W. Yang, A. J. Davies, X. Lin, M. Suyetin, R. Matsuda, A. J. Blake, C. Wilson, W. Lewis, J. E. Parker, C. C. Tang, M. W. George, P. Hubberstey, S. Kitagawa, H. Sakamoto, E. Bichoutskaia, N. R. Champness, S. Yang, M. Schröder, *Chem. Sci.* **2012**, *3*, 2993–2999.

[242] I. Langmuir, *J. Am. Chem. Soc.* **1918**, *40*, 1361–1403.

[243] K. S. Walton, R. Q. Snurr, *J. Am. Chem. Soc.* **2007**, *129*, 8552–8556.

[244] D. A. Gómez-Gualdrón, P. Z. Moghadam, J. T. Hupp, O. K. Farha, R. Q. Snurr, *J. Am. Chem. Soc.* **2016**, *138*, 215–224.

[245] J. Medek, *Fuel* **1977**, *56*, 131–133.

[246] P. J. Branton, P. G. Hall, M. Treguer, K. S. W. Sing, *J. Chem. Soc. Faraday Trans.* **1995**, *91*, 2041–2043.

[247] M. O. Cichocka, J. Ångström, B. Wang, X. Zou, S. Smeets, *J. Appl. Cryst.* **2018**, *51*, 1652–1661.

[248] W. Kabsch, *Acta Crystallogr. Sect. D Biol. Crystallogr.* **2010**, *66*, 125–132.

[249] G. M. Sheldrick, *Acta Crystallogr. Sect. A Found. Crystallogr.* **2015**, *71*, 3–8.

[250] G. M. Sheldrick, *Acta Crystallogr. Sect. A Found. Crystallogr.* **2008**, *64*, 112–122.

[251] S. Amirjalayer, R. Schmid, *J. Phys. Chem. C* **2008**, *112*, 14980–14987.

[252] A. L. Spek, *J. Appl. Cryst.* **2003**, *36*, 7–13.

8 Appendix

8.1 Additional Experimental Data and Information to Chapter 3

8.1.1 Powder X-ray Diffraction

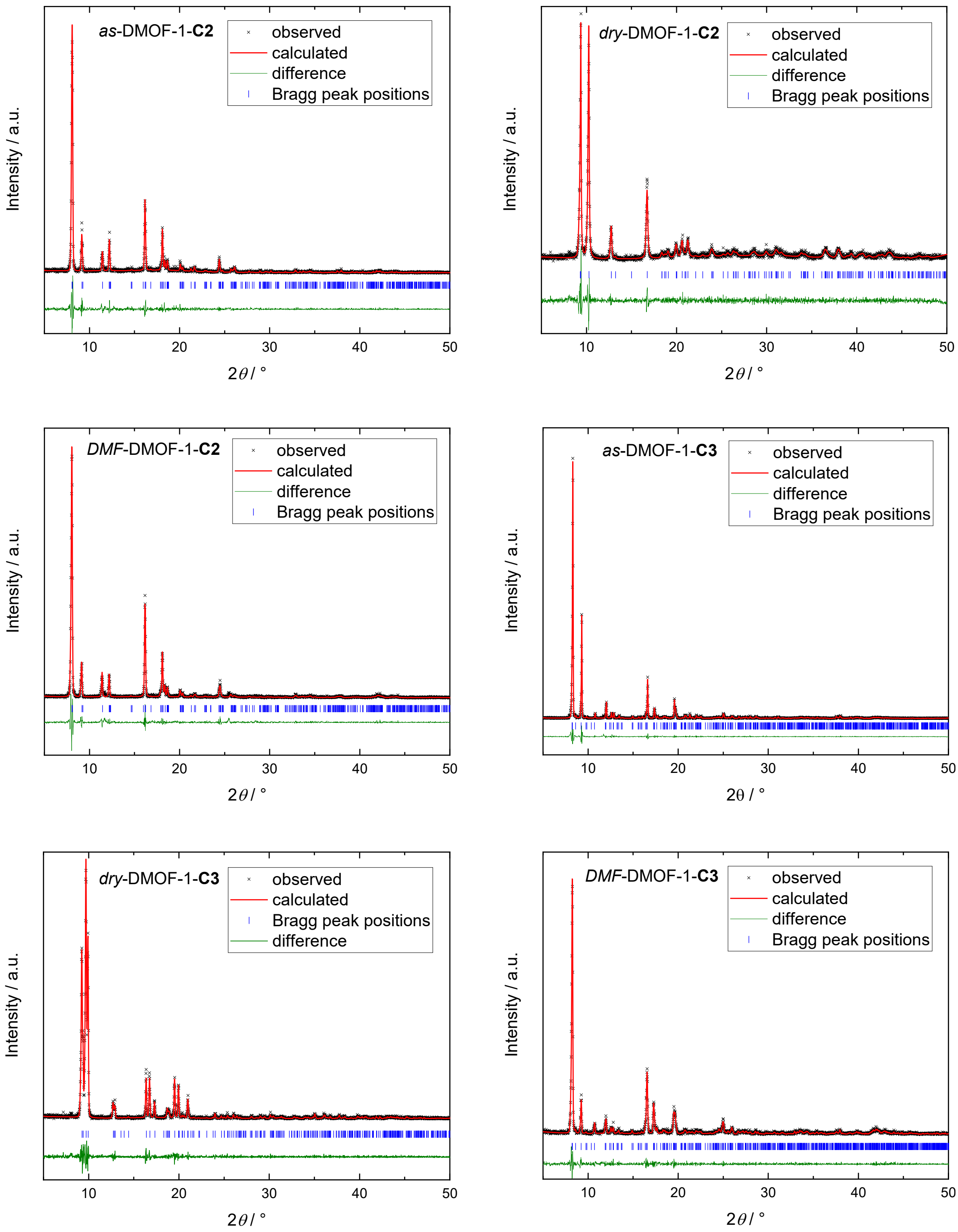

Figure 8.1: PXRD patterns with profile fits (Pawley method) of DMOF-1-**C2** and DMOF-1-**C3** in their as synthesized (*as*), guest-free (*dry*) and DMF-reinfiltrated (*DMF*) states.

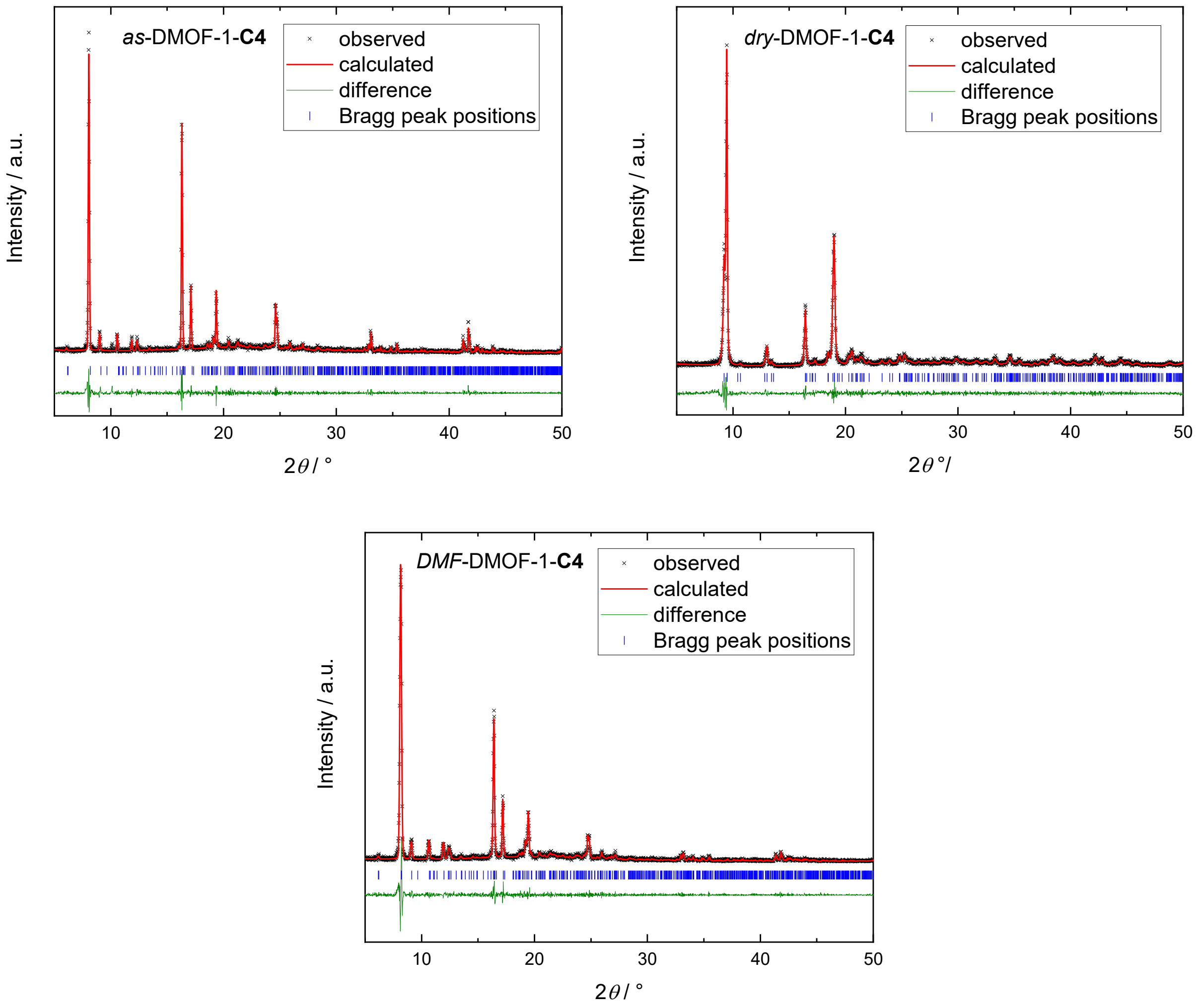

Figure 8.2: PXRD patterns with profile fits (Pawley method) of DMOF-1-**C4** in its as synthesized (*as*), guest-free (*dry*) and DMF-reinfiltrated (*DMF*) states.

Table 8.1: Unit cell parameters *a*, *b*, *c* and cell volume *V* determined by profile fitting (Pawley method) of the PXRD patterns and the corresponding R_{wp}, R_{exp} and χ^2 values for DMOF-1-**C2**, DMOF-1-**C3** and DMOF-1-**C4** in their as-synthesized (*as*), guest-free (*dry*) and DMF re-solvated (*DMF*) states.

Compound	*as*-DMOF-1-**C2**	*dry*-DMOF-1-**C2**	*DMF*-DMOF-1-**C2**
crystal system	monoclinic	monoclinic	monoclinic
space group	$P2/c$	$C2/m$	$P2/c$
a / Å	10.8978(3)	9.819(6)	10.915(5)
b / Å	10.960(2)	18.992(7)	10.956(5)
c / Å	19.302(4)	9.581(6)	19.283(10)
α / °	90	90	90
β / °	89.52(3)	100.36(4)	89.50(7)
γ / °	90	90	90
V / Å^3	2305.4(9)	1757. 5(17)	2305(2)
R_{wp}	27.82	22.00	27.23
R_{exp}	23.57	18.53	20.42
χ^2	1.18	1.19	1.33

Compound	*as*-DMOF-1-**C3**	*dry*-DMOF-1-**C3**	*DMF*-DMOF-1-**C3**
crystal system	triclinic	triclinic	triclinic
space group	$P\bar{1}$	$P\bar{1}$	$P\bar{1}$
a / Å	9.6379(18)	9.6172(15)	9.634(9)
b / Å	10.9137(17)	10.2964(16)	10.922(7)
c / Å	22.703(4)	10.6401(15)	22.709(16)
α / °	109.058(14)	62.219(8)	109.08(4)
β / °	91.97(2)	84.26(2)	91.90(10)
γ / °	94.83(2)	83.586(19)	94.89(9)
V / Å^3	2244.2(7)	925.0(3)	2245(3)
R_{wp}	22.73	26.88	28.63
R_{exp}	16.17	23.63	22.35
χ^2	1.41	1.14	1.28

Compound	*as*-DMOF-1-**C4**	*dry*-DMOF-1-**C4**	*DMF*-DMOF-1-**C4**
crystal system	monoclinic	monoclinic	monoclinic
space group	$P2_1/c$	$C2/c$	$P2_1/c$
a / Å	9.7011 (17)	18.705(15)	9.706(3)
b / Å	28.433(4)	10.774(8)	28.400(7)
c / Å	16.606(2)	19.233(18)	16.602(2)
α / °	90	90	90
β / °	94.235(16)	93.40(5)	94.45(2)
γ / °	90	90	90
V / Å^3	4568.0(12)	3869(6)	4562(2)
R_{wp}	20.14	17.47	22.79
R_{exp}	15.37	15.31	17.10
χ^2	1.31	1.14	1.33

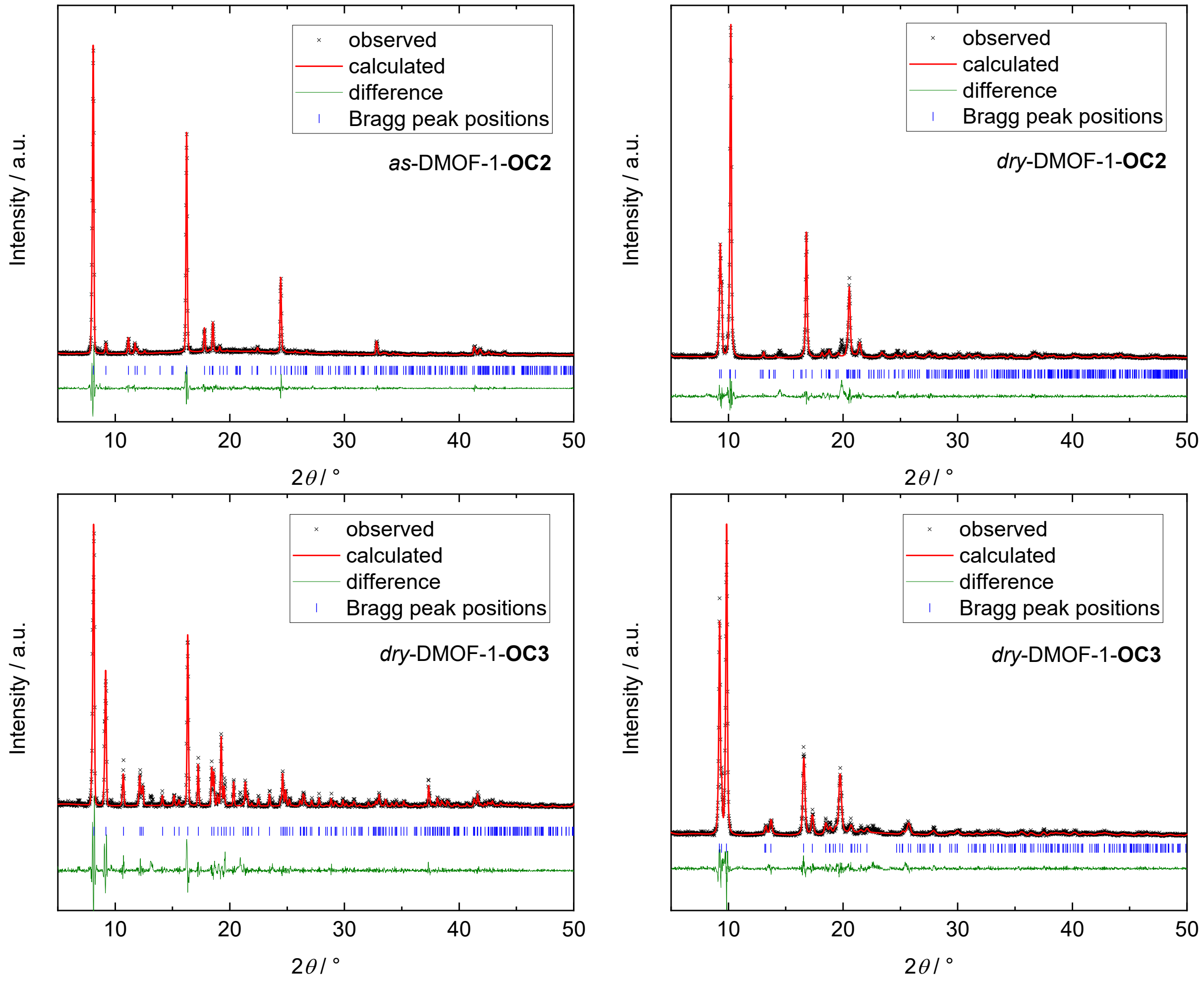

Figure 8.3: PXRD patterns with profile fits (Pawley method) of DMOF-1-**OC2** and DMOF-1-**OC3** in their as-synthesized (*as*) and guest-free (*dry*) states.

Table 8.2: Unit cell parameters a, b, c and cell volume V determined by profile fitting (Pawley method) of the PXRD patterns and the corresponding R_{wp}, R_{exp} and χ^2 values for DMOF-1-**OC2** and DMOF-1-**OC3** in their as-synthesized (as) and guest-free (*dry*) states.

Compound	*as*-DMOF-1-**OC2**	*dry*-DMOF-1-**OC2**	*as*-DMOF-1-**OC3**	*dry*-DMOF-1-**OC3**
crystal system	monoclinic	monoclinic	monoclinic	monoclinic
space group	$C2/m$	$P2_1/m$	$C2/m$	$C2/m$
a / Å	15.893(3)	18.892(7)	14.397(2)	10.249(4)
b / Å	15.071(2)	9.783(6)	16.491(2)	18.817(5)
c / Å	9.639(3)	9.589(5)	9.6261(11)	9.605(4)
α / °	90	90	90	90
β / °	94.53(4)	93.30(7)	91.620(15)	92.14(6)
γ / °	90	90	90	90
V / Å^3	2301.5(10)	1769.2(15)	2284.5(5)	1851.2(11)
R_{wp}	22.06	26.80	32.48	25.13
R_{exp}	18.08	19.33	23.19	20.49
χ^2	1.33	1.39	1.40	1.23

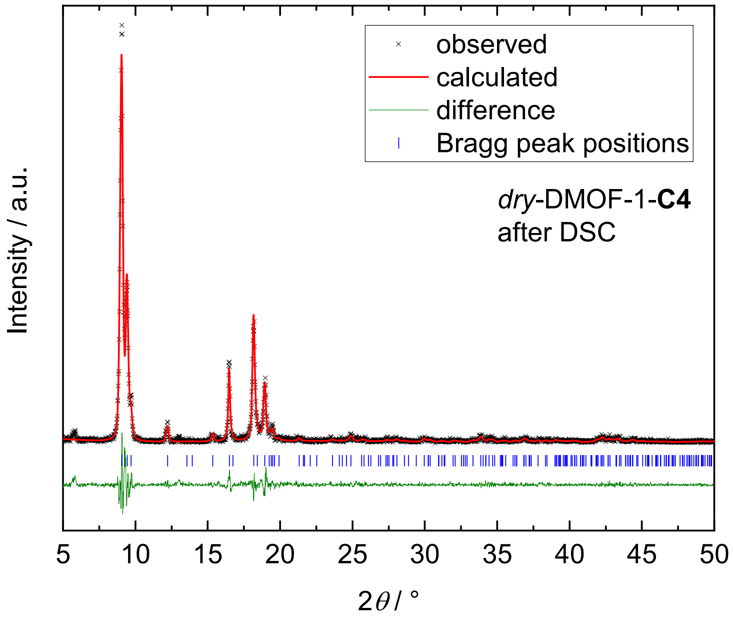

Figure 8.4: PXRD pattern with profile fit (Pawley method) of *dry*-DMOF-1-**C4** recorded 2 h after a DSC run.

Table 8.3: Unit cell parameters a, b, c, cell volume V and the corresponding R_{wp}, R_{exp} and χ^2 as determined by profile fitting (Pawley method) of the PXRD pattern of *dry*-DMOF-1-**C4** 2 h after a DSC run.

Compound	*dry*-DMOF-1-**C4** after DSC
crystal system	monoclinic
space group	$C2/m$
a / Å	11.686(4)
b / Å	18.213(5)
c / Å	9.477(3)
α / °	90
β / °	98.83(6)
γ / °	90
V / Å^3	1993.1(12)
R_{wp}	25.52
R_{exp}	20.04
χ^2	1.27

8.1.2 Single Crystal X-ray Diffraction

Table 8.4: Crystallographic data of *as*-DMOF-1-**C2**, *as*-DMOF-1-**C3** and *as*-DMOF-1-**C4**.

Compound	*as*-DMOF-1-**C2**	*as*-DMOF-1-**C3**	*as*-DMOF-1-**C4**
Empirical formula	$C_{30}H_{36}N_2O_8Zn_2$	$C_{40}H_{58}N_4O_{10}Zn_2$	$C_{44}H_{66}N_4O_{10}Zn_2$
Formula weight / g·mol^{-1}	683.35	885.64	941.74
Temperature / K	290(5)	100(2)	273(2)
Crystal system	monoclinic	triclinic	monoclinic
Space group	$P2/c$	$P\bar{1}$	$P2_1/c$
a / Å	10.9004(6)	9.5967(5)	9.6523(5)
b / Å	10.9331(4)	10.8601(6)	28.1466(15)
c / Å	19.2435(8)	21.5316(11)	16.6332(9)
a / °	90	104.310(2)	90
β / °	89.824(5)	92.443(2)	95.248(3)
γ / °	90	95.573(2)	90
Volume / Å^3	2293.33(18)	2159.0(2)	4500.0(4)
Z	2	2	4
ϱ_{calc} g/cm^3	0.990	1.362	1.390
μ / mm^{-1}	1.080	1.169	1.805
F(000)	708.0	932.0	1992.0
Crystal size / mm^3	0.33 × 0.312 × 0.293	0.076 × 0.161 × 0.302	0.055 × 0.073 × 0.138
Radiation	MoKα (λ = 0.71073)	MoKα (λ = 0.71073)	CuKα (λ = 1.54178)
2Θ range for data collection / °	5.278 to 59.504	4.576 to 70.154	6.192 to 119.996
Index ranges	-15 ≤ h ≤ 11, -14 ≤ k ≤ 15, -20 ≤ l ≤ 26	-14 ≤ h ≤ 15, -17 ≤ k ≤ 17, -34 ≤ l ≤ 34	-10 ≤ h ≤ 10, -31 ≤ k ≤ 31, -18 ≤ l ≤ 18
Reflections collected	16110	151838	92930
Independent reflections	5723 [R_{int}= 0.0363, R_{sigma}= 0.0472]	18886 [R_{int}= 0.0445, R_{sigma}= 0.0306]	6677 [R_{int}= 0.2453, R_{sigma}= 0.0872]
Data/restraints/parameters	5723/70/221	18886/4/543	6677/14/628
Goodness-of-fit on F^2	1.107	1.176	1.069
Final R indexes [I ≥ 2σ(I)]	R_1= 0.0745, wR_2= 0.2250	R_1= 0.0440, wR_2= 0.0850	R_1= 0.0556, wR_2= 0.1495
Final R indexes [all data]	R_1= 0.1067, wR_2= 0.2512	R_1= 0.0440, wR_2= 0.0850	R_1= 0.0556, wR_2= 0.1495
Largest diff. peak/hole / e·Å^{-3}	1.73/-0.70	0.85/-1.94	0.82/-0.69
CCDC deposition number	-	-	-

Table 8.5: Crystallographic data of *dry*-DMOF-1-**C2**, *dry*-DMOF-1-**C3** and *dry*-DMOF-1-**C4**.

Compound	*dry*-DMOF-1-**C2**	*dry*-DMOF-1-**C3**	*dry*-DMOF-1-**C4**
Empirical formula	$C_{30}H_{36}N_2O_8Zn_2$	$C_{34}H_{44}N_2O_8Zn_2$	$C_{38}H_{52}N_2O_8Zn_2$
Formula weight / g·mol^{-1}	683.34	739.45	795.55
Temperature / K	100(2)	103(2)	100(2)
Crystal system	monoclinic	triclinic	monoclinic
Space group	$C2/m$	$P\bar{1}$	$C2/c$
a / Å	9.5105(6)	9.537(2)	18.8377(13)
b / Å	19.0806(11)	9.914(2)	10.4128(7)
c / Å	9.5140(6)	10.539(2)	19.1803(11)
α / °	90	63.798(11)	90
β / °	103.491(3)	85.076(12)	92.085(4)
γ / °	90	83.500(14)	90
Volume / Å^3	1678.83(18)	887.6(4)	3759.8(4)
Z	2	1	4
ϱ_{calc} g/cm^3	1.352	1.383	1.405
μ / mm^{-1}	2.154	2.078	2.001
F(000)	708.0	386.0	1672.0
Crystal size / mm^3	0.129 × 0.053 × 0.040	0.066 × 0.063 × 0.038	0.096 × 0.082 × 0.027
Radiation	CuKα (λ = 1.54178)	CuKα (λ = 1.54178)	CuKα (λ = 1.54178)
2Θ range for data collection / °	9.27 to 150.59	9.34 to 129.926	9.228 to 146.19
Index ranges	$-11 \leq h \leq 11$, $-23 \leq k \leq 23$, $-11 \leq l \leq 11$	$-11 \leq h \leq 11$, $-11 \leq k \leq 11$, $-12 \leq l \leq 12$	$-23 \leq h \leq 21$, $-12 \leq k \leq 12$, $-23 \leq l \leq 23$
Reflections collected	15466	16217	36979
Independent reflections	1777 [R_{int}= 0.0750, R_{sigma}= 0.0418]	2909 [R_{int}= 0.1487, R_{sigma}= 0.1004]	3729 [R_{int}= 0.1620, R_{sigma}= 0.0752]
Data/restraints/parameters	1777/51/152	2909/0/214	3729/0/260
Goodness-of-fit on F^2	1.123	1.066	1.045
Final R indexes [I ≥ 2σ(I)]	R_1= 0.0459, wR_2= 0.1128	R_1= 0.1130, wR_2= 0.2653	R_1= 0.0712, wR_2= 0.1697
Final R indexes [all data]	R_1= 0.0501, wR_2= 0.1153	R_1= 0.1487, wR_2= 0.2869	R_1= 0.0712, wR_2= 0.1697
Largest diff. peak/hole / e·Å^{-3}	1.04/-0.46	1.74/-1.76	1.52/-0.43
CCDC deposition number	-	-	-

Table 8.6: Crystallographic data of DMOF-1-**C3** solvated with acetone, benzene, and acetonitrile.

Compound	DMOF-1-**C3**·2acetone	DMOF-1-**C3**·2benzene	DMOF-1-**C3**·2MeCN
Empirical formula	$C_{40}H_{56}N_2O_{10}Zn_2$	$C_{46}H_{50}N_2O_8Zn_2$	$C_{36}H_{47}N_2O_8Zn_2$
Formula weight / g·mol^{-1}	855.60	889.62	821.56
Temperature / K	100(2)	100(2)	100(2)
Crystal system	triclinic	tetragonal	triclinic
Space group	$P\bar{1}$	$P4_2/mbc$	$P\bar{1}$
a / Å	9.5672(4)	21.6725(7)	9.5700(4)
b / Å	10.8263(5)	21.6725 (7)	10.8480(5)
c / Å	10.8524(5)	19.1187(7)	10.8519(5)
α / °	73.454(3)	90	73.867(3)
β / °	87.226(3)	90	86.441(3)
γ / °	86.458(3)	90	85.590(3)
Volume / Å^3	1074.90(8)	8980.0(7)	1078.05(9)
Z	1	8	1
ϱ_{calc} g/cm^3	1.322	1.316	1.265
μ / mm^{-1}	1.823	1.740	1.777
F(000)	450.0	3712.0	430.0
Crystal size / mm^3	0.061 × 0.042 × 0.034	0.063 × 0.051 × 0.043	0.063 × 0.032 × 0.027
Radiation	CuKα (λ = 1.54178)	CuKα (λ = 1.54178)	CuKα (λ = 1.54178)
2Θ range for data collection / °	8.504 to 150.254	5.766 to 149.44	8.49 to 119.958
Index ranges	$-11 \le h \le 11$, $-13 \le k \le 13$, $-13 \le l \le 13$	$-27 \le h \le 27$, $-26 \le k \le 27$, $-23 \le l \le 23$	$-10 \le h \le 10$, $-11 \le k \le 12$, $-12 \le l \le 12$
Reflections collected	29167	159840	20867
Independent reflections	4246 [R_{int}= 0.2175, R_{sigma}= 0.0992]	4745 [R_{int}= 0.2015, R_{sigma}= 0.0481]	3190 [R_{int} = 0.2497, R_{sigma} = 0.1875]
Data/restraints/parameters	4246/0/283	4745/57/315	3190/45/304
Goodness-of-fit on F^2	1.030	1.124	1.042
Final R indexes [I ≥ 2σ(I)]	R_1= 0.0637, wR_2= 0.1642	R_1= 0.0795, wR_2= 0.1744	R_1 = 0.0653, wR_2 = 0.1619
Final R indexes [all data]	R_1= 0.0947, wR_2= 0.1839	R_1= 0.1054, wR_2= 0.1900	R_1 = 0.1134, wR_2 = 0.1810
Largest diff. peak/hole / e·Å^{-3}	0.80/-1.01	0.67/-0.56	1.03/-0.81
CCDC deposition number	-	-	-

Table 8.7: Crystallographic data of DMOF-1-**C3** solvated with *n*-octane and DMF/THF (for preparation details see above) and the ***ip***$_{\mathbf{ht}}$ phase of *dry*-DMOF-1-**C4**.

Compound	DMOF-1-**C3**·*n*-octane	DMOF-1-**C3**·DMF/THF	*dry*-DMOF-1-**C4** (***ip***$_{\mathbf{ht}}$)
Empirical formula	$C_{42}H_{62}N_2O_8Zn_2$	$C_{37}H_{55}N_3O_9Zn_2$	$C_{38}H_{52}N_2O_8Zn_2$
Formula weight / g·mol^{-1}	853.67	816.58	795.55
Temperature / K	100(2)	273(2)	400(2)
Crystal system	Triclinic	monoclinic	monoclinic
Space group	$P\bar{1}$	$P2/c$	$C2$/m
a / Å	9.5727(4)	9.5617(2)	12.3369(19)
b / Å	10.8237(5)	15.4447(3)	17.778(3)
c / Å	10.9048(5)	15.3731(3)	9.5969(18)
α / °	82.828(15)	90	90
β / °	88.609(7)	98.2830(10)	98.418(5)
γ / °	81.737(7)	90	90
Volume / Å^3	1109.40(3)	2246.58(8)	2082.1(6)
Z	1	2	2
ϱ_{calc} g/cm^3	1.278	1.207	1.269
μ / mm^{-1}	1.728	1.709	1.807
F(000)	452.0	860.0	836.0
Crystal size / mm^3	0.063 × 0.034 × 0.030	0.076 × 0.066 × 0.051	0.095 × 0.08 × 0.035
Radiation	CuKα (λ = 1.54178)	CuKα (λ = 1.54178)	CuKα (λ = 1.54178)
2Θ range for data collection / °	8.172 to 134.956	5.722 to 134.952	8.788 to 129.972
Index ranges	-11 ≤ h ≤ 11, -12 ≤ k ≤ 12, -13 ≤ l ≤ 13	-11 ≤ h ≤ 11, -18 ≤ k ≤ 18, -18 ≤ l ≤ 18	--14 ≤ h ≤ 14, -20 ≤ k ≤ 20, -11 ≤ l ≤ 11
Reflections collected	40196	38132	12358
Independent reflections	3904 [R_{int}= 0.1259, R_{sigma}= 0.0632]	4044 [R_{int}= 0.1475, R_{sigma}= 0.0629]	1770 [R_{int} = 0.0947, R_{sigma} = 0.0631]
Data/restraints/parameters	3904/0/282	4044/18/290	1770/0/98
Goodness-of-fit on F^2	1.125	1.074	1.123
Final R indexes [I ≥ 2σ(I)]	R_1= 0.0590, wR_2= 0.1173	R_1= 0.0612, wR_2= 0.1661	R_1 = 0.1353, wR_2 = 0.3138
Final R indexes [all data]	R_1= 0.0860, wR_2= 0.1358	R_1= 0.0887, wR_2= 0.1853	R_1 = 0.1556, wR_2 = 0.3289
Largest diff. peak/hole / e·Å^{-3}	0.71/-1.16	0.86/-0.52	0.89/-0.79
Flack parameter			

8.1.3 Solution ^{1}H NMR Spectroscopy

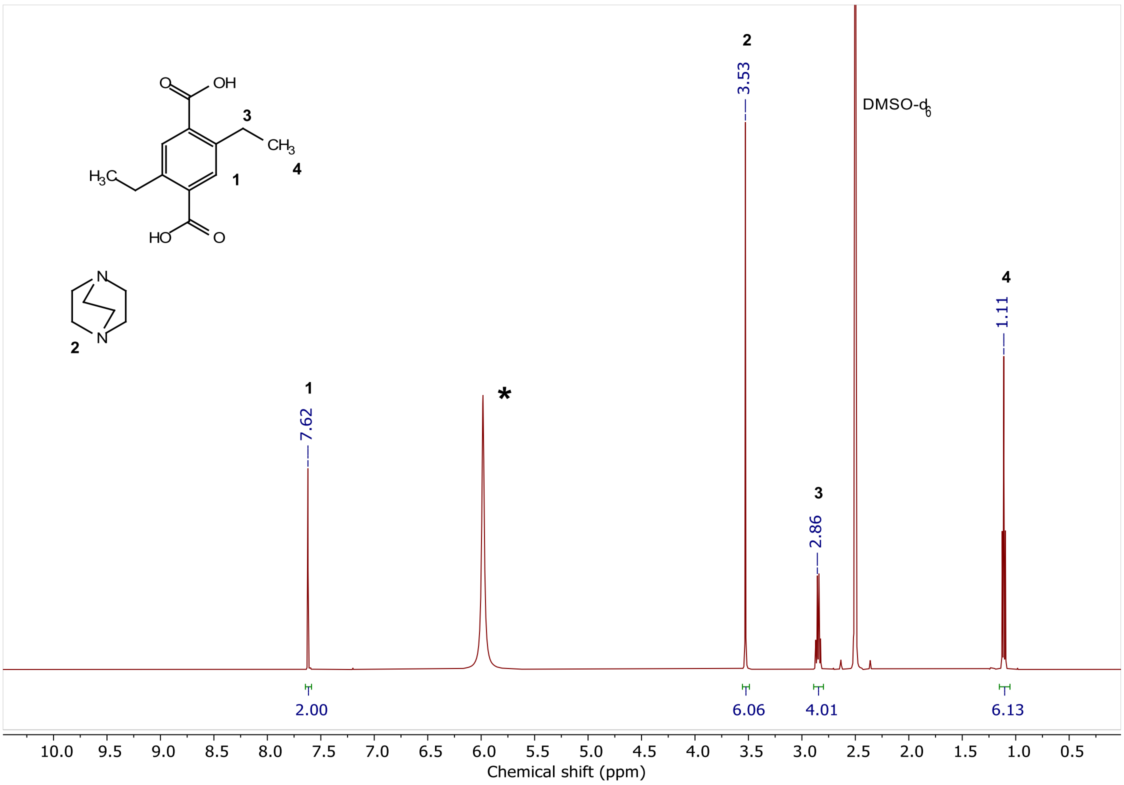

Figure 8.5: ^{1}H NMR spectrum of a digested sample of *dry*-DMOF-**C2**. The D_2O signal is marked with an asterisk (*).

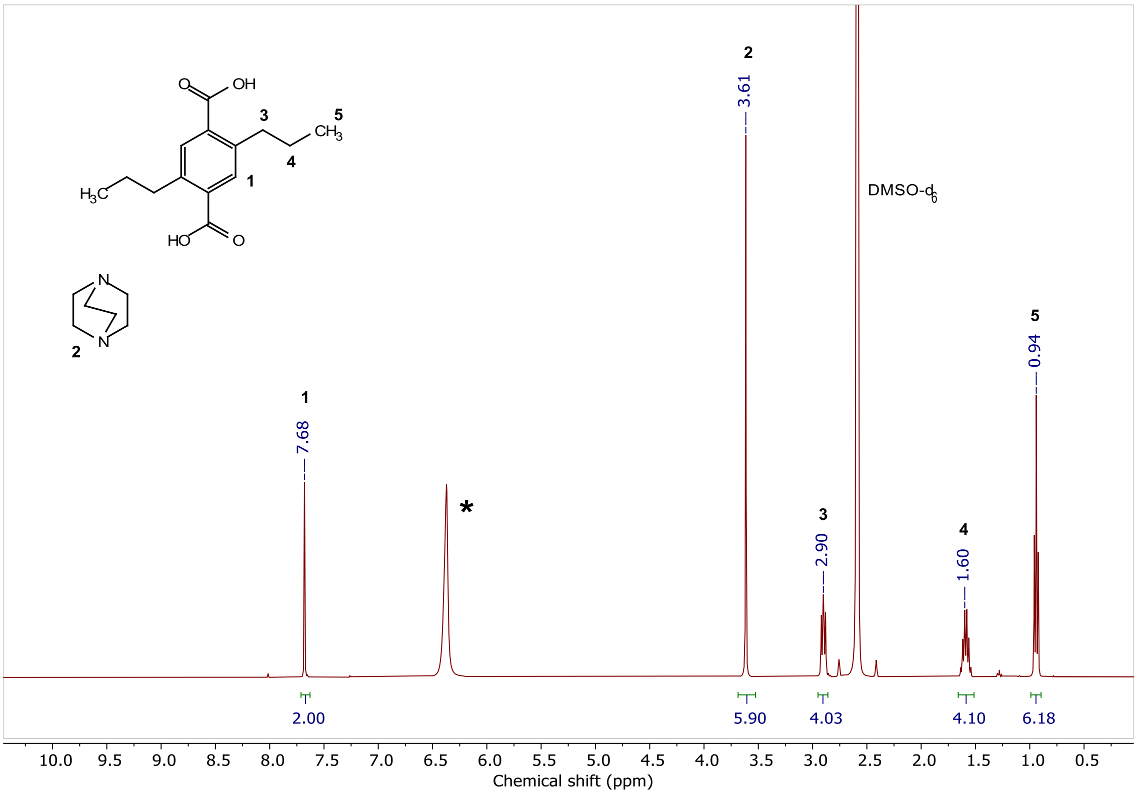

Figure 8.6: ^{1}H NMR spectrum of a digested sample of *dry*-DMOF-**C3**. The D_2O signal is marked with an asterisk (*).

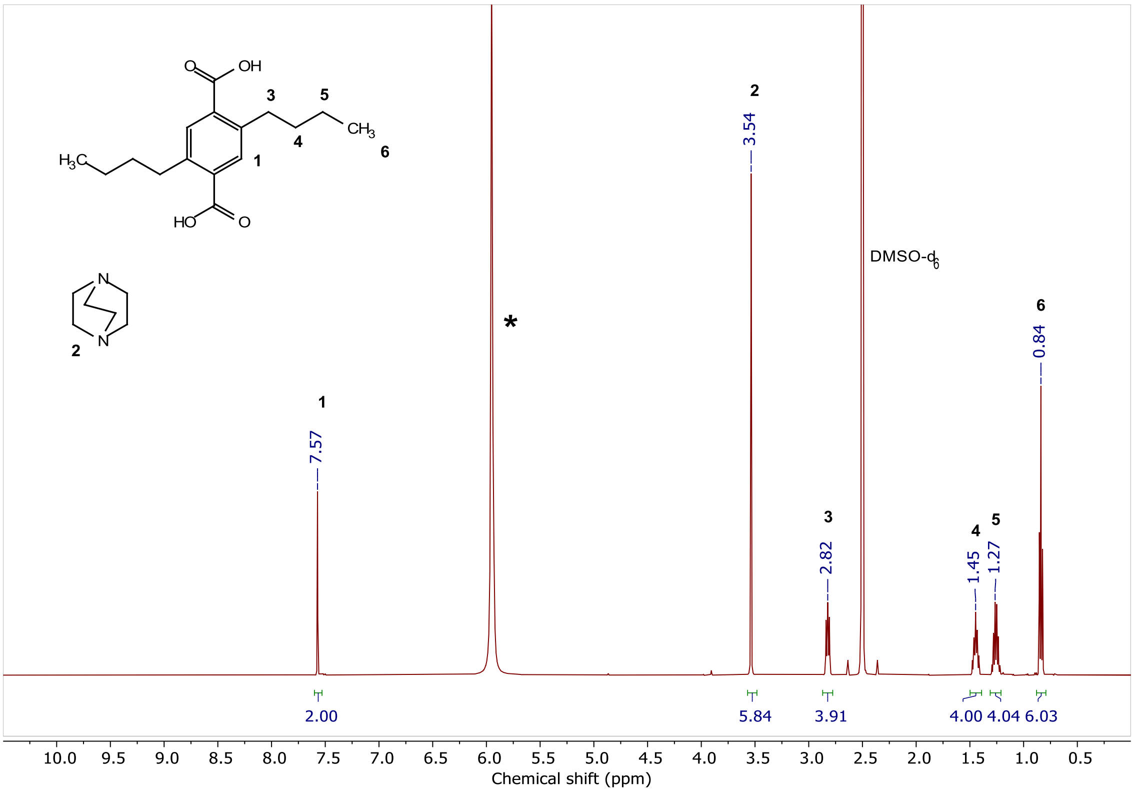

Figure 8.7: ^{1}H NMR spectrum of a digested sample of *dry*-DMOF-**C4**. The D$_2$O signal is marked with an asterisk (*).

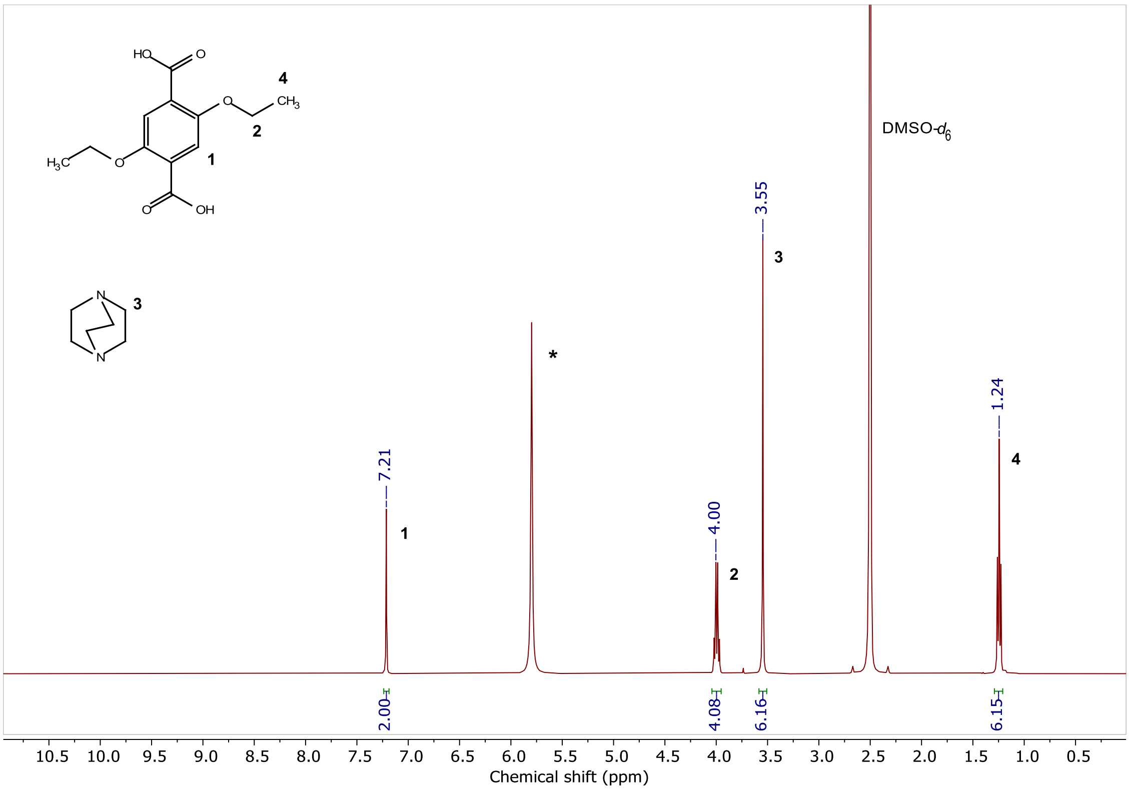

Figure 8.8: ^{1}H NMR spectrum of a digested sample of *dry*-DMOF-**OC2**. The D$_2$O signal is marked with an asterisk (*).

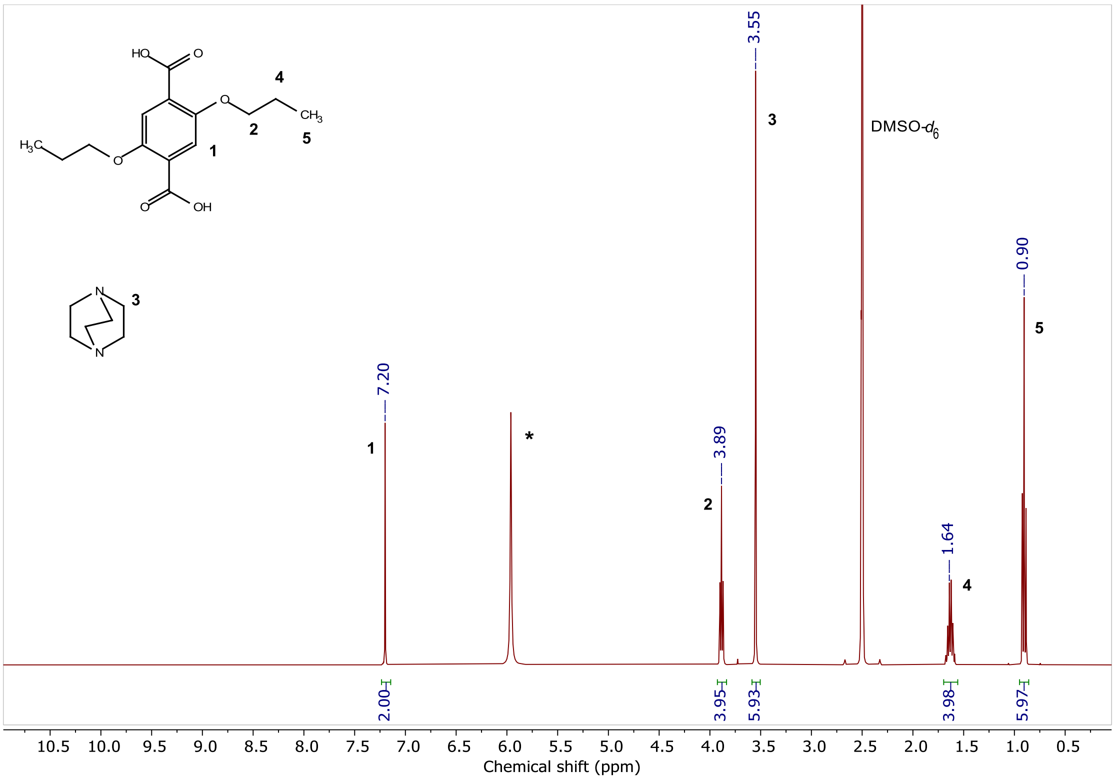

Figure 8.9: ^{1}H NMR spectrum of a digested sample of *dry*-DMOF-**OC3**. The D_2O signal is marked with an asterisk (*).

8.1.4 Fourier Transform-Infrared (FT-IR) Spectroscopy

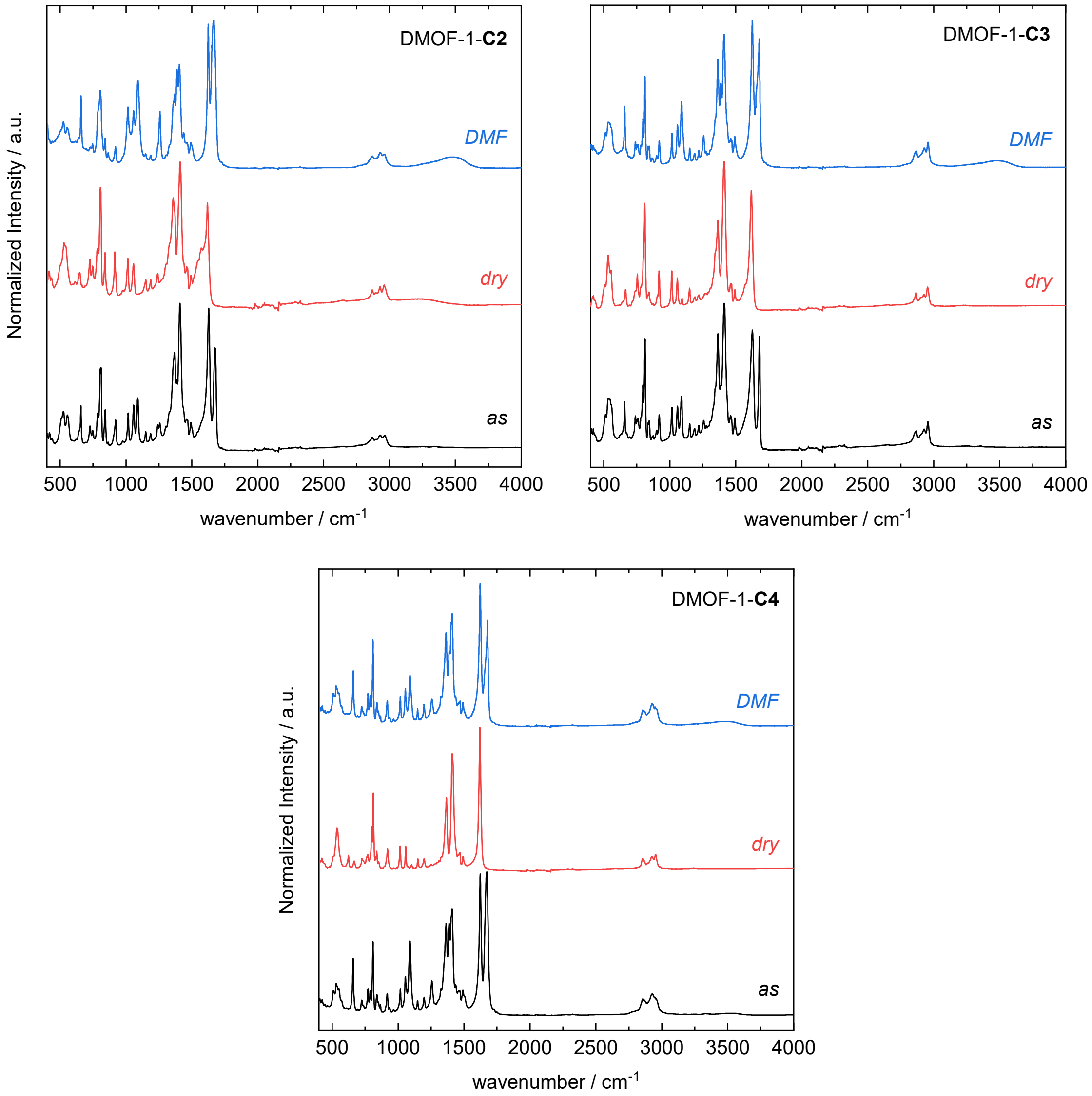

Figure 8.10: FT-IR spectra of DMOF-1-**CX** in their as-synthesized (*as*), guest-free (*dry*) and DMF-reinfiltrated (*DMF*) states.

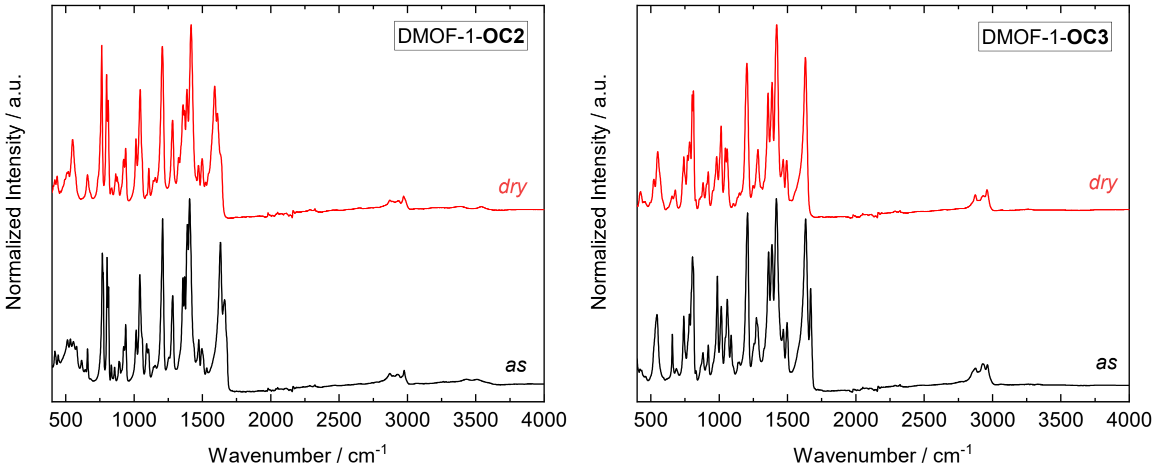

Figure 8.11: FT-IR spectra of DMOF-1-**OCY** in their as-synthesized (*as*) and guest-free (*dry*) states.

8.1.5 *In-situ* CO_2 Sorption PXRD

Pawley Fits of *dry*-DMOF-1-**C4**

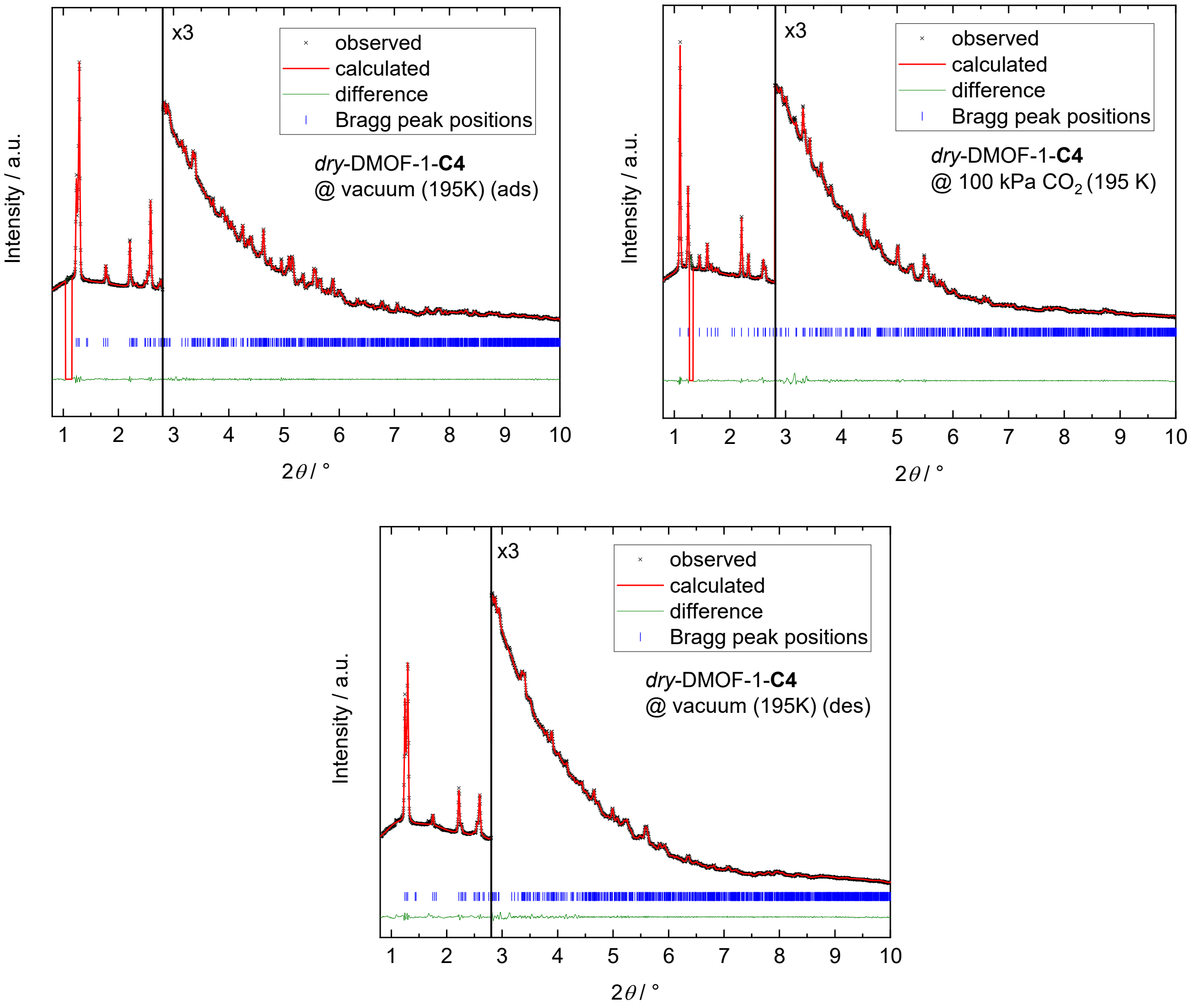

Figure 8.12: *In-situ* CO_2 sorption PXRD patterns (DESY, λ = 0.2073 Å) with Pawley fits of *dry*-DMOF-1-**C4** recorded at vacuum (***np*** phase, adsorption branch), 100 kPa CO_2 pressure (***lp*** phase) and again at vacuum (***np*** phase, desorption branch). The corresponding fit data are given below.

Table 8.8: Unit cell parameters *a*, *b*, *c* and cell volume *V* determined by profile fitting (Pawley method) of the PXRD patterns and the corresponding R_{wp}, R_{exp} and χ^2 values for *dry*-DMOF-1-**C4** at CO_2 pressures of $2{\cdot}10^{-3}$ kPa (vacuum) and 100 kPa (adsorption branch) and again $2{\cdot}10^{-3}$ kPa (vacuum).

Compound	**$2{\cdot}10^{-3}$ kPa (ads)**	**100 kPa CO_2**	**$2{\cdot}10^{-3}$ kPa (des)**
crystal system	monoclinic	monoclinic	monoclinic
space group	$C2/c$	$C2/m$	$C2/c$
a / Å	18.786(5)	16.5211(17)	18.680(3)
b / Å	10.558(3)	14.2909(11)	10.517(3)
c / Å	19.200(5)	9.6079(6)	19.098(6)
α / °	90	90	90
β / °	92.43(3)	97.682(17)	91.98(5)
γ / °	90	90	90
V / Å^3	3804.9(18)	2248.1(3)	3749.6(18)
R_{wp}	0.52	0.58	0.54
R_{exp}	1.33	1.89	1.23
χ^2	0.39	0.31	0.44

Rietveld Refinement of the ***np*** phase of *dry*-DMOF-1-**C3**

From the PXRD pattern recorded at a CO_2 pressure of 2 kPa, featuring the maximum CO_2 filling of this phase (≈ 0.5 CO_2 molecules per MOF repeating unit), the unit cell parameters, space group, peak shape function and background parameters were extracted by structureless profile fitting (Pawley method), which were used and kept fixed in the initial Rietveld refinement steps.

The starting structural model consisted of the SCXRD structure of the ***np*** phase *dry*-DMOF-1-**C3** with the disorder of one of the independent alkyl-DEDs and all H-atoms removed. Throughout the Rietveld refinement, both independent bdc^{2-}-linkers and the dabco unit were constrained as rigid bodies using a z-matrix description with zero-occupancy dummy atoms fixing their positions relative to special positions (inversion centres). Furthermore, the shape of the Zn_2-paddlewheel unit was kept intact with a number of restraints listed in Table 8.9.

Table 8.9: Values and tolerances of distance and angle restraints applied on the Zn_2-paddlewheel unit during the Rietveld refinement of the ***np*** phase of *dry*-DMOF-1-**C3**.

Distances	Value / Å	Tolerance / Å
Zn1-O1/O3, Zn1-O2'/O4'	2.00	0.05
Zn1-N1	2.05	0.05
Zn1-Zn1'	2.9	0.05
Angles		
O1-Zn1-O2‘, O3-Zn-O4‘	160	5
O1-Zn-O3, O3-Zn-O2',...	90	5
N1-Zn1-Zn1'	172	1
Zn1-N1-dummy	180	3

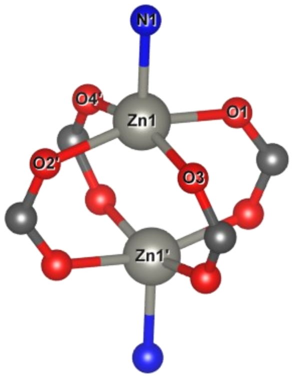

In the first refinement cycles the rigid bodies were allowed to rotate and the Zn allowed to move along the *a*, *b,* and *c* directions. Thereafter, the dihedral angles of the propyl groups were allowed to change, while maintaining the C-C-C angles, and phenyl rings could rotate as well. Afterwards, the CO_2 molecules were added at positions indicated by the Fourier difference map, treated as rigid bodies using a z-matrix description, and were freely rotated and translated under the application of anti-bump restraints with a minimum distance of 2.8 Å to neighbouring carbon atoms. Resulting conformations of the flexible parts of the structure, i.e., the propyl groups, phenyl ring torsions and CO_2 molecules were randomized based on their approximate errors for multiple refinement cycles to ensure the global minimum structure. In the final cycle, the unit cell parameters, space group, peak shape function and background parameters were refined alongside. The final Rietveld plot is given in the main text in Figure 3.17 and the crystallographic data are listed in Table 8.10.

Table 8.10: Crystallographic data for the Rietveld refinement of the ***np*** phase of *dry*-DMOF-1-**C3** at 2 kPa CO_2 pressure.

Compound	*dry*-DMOF-1-**C3** (***np***) @ 2 kPa CO_2
Empirical formula	$C_{34}H_{44}N_2O_8Zn_2 \cdot 0.5CO_2$
Formula weight	759.50
Calclulated density	1.2934(3)
space group	$P\bar{1}$
Crystal system	triclinic
a / Å	9.5995(10)
b / Å	10.2296(10)
c / Å	10.6377(12)
α / °	62.471(6)
β / °	84.633(18)
γ / °	84.604(15)
V / Å^3	920.8(2)
Z	1
Diffractometer	P02.1, Deutsches Elektronen Synchrotron, Hamburg, Germany
Temperature / K	195
Wavelength / Å	0.2073
No. Reflections	1323
No. Atoms	29
No. Restraints	18
R_p	1.356
R_{exp}	2.138
R_{wp}	1.938
χ^2	0.906
R_{Bragg}	1.069

Rietveld Refinement of the ***ip***$_{\mathbf{ads}}$ phase of *dry*-DMOF-1-**C3**

The PXRD pattern recorded at a CO_2 pressure of 6 kPa on the adsorption branch of the *in-situ* experiment was indexed in a monoclinic cell with the $C2/m$ space group. Structureless profile fitting (Pawley method) provided refined unit cell parameters, peak shape function parameters and the background curve used for the refinement.

The starting model for the Rietveld refinement was obtained via 3DED (see Appendix section 8.1.6 for details) of a dried crystal of *dry*-DMOF-1-**C3** and taken over after the following modifications were made:

- As unit cell parameters from ED are typically overestimated by 5-10%, the unit cell parameters were set to the values determined from structureless profile fitting.
- The dabco unit could not be fully resolved in the 3DED structure, therefore a dabco unit of a chemically reasonable geometry was added to the structural model. Additionally, the disorder of the dabco linker over two positions, as common for this type of MOF structure, was introduced.
- The C2 and C3 carbon atoms of the propyl groups were also not included in the 3DED structure, which were thus added manually using the Mercury software.

To constrain the positions of the atoms of the **C3**-bdc^{2-} and dabco linkers, dummy atoms were placed on the special positions located in the centre of the linkers (inversion centres). These dummy atoms were followingly used as the pivot of the z-matrix description of the **C3**-bdc^{2-} and dabco units (or their part of the asymmetric unit). Before the initial refinement cycles, the internal distances and angles of the Zn_2-paddlewheel were restrained to chemically reasonable values (see Table 8.11) and a soft flatten restraint was applied to the carboxylate-Zn moiety. Also, certain atomic distances (C2-C3, C1-O1, C1-O2) were optimized.

Table 8.11: Values and tolerances of distance and angle restraints applied on the Zn_2-paddlewheel unit during the Rietveld refinement of the ***ip***$_{\mathbf{ads}}$ phase of *dry*-DMOF-1-**C3**.

Distances	Value / Å	Tolerance / Å
Zn1-O1’, Zn1-O2	2.05	0.05
Zn1-N1	2.05	0.05
Zn1-Zn1’	2.9	0.05
Zn1-O1	3.35	0.05
Zn1-O2’	3.05	0.05
Angles		
O2-Zn1-O1‘‘‘, O1‘-Zn-O2‘‘‘	160	3
O2-Zn-O1’	90	2
N1-Zn1-Zn1’	172	3
Zn1-N1-dummy	180	2

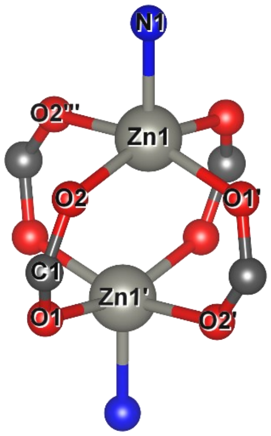

In the first refinement cycles, the rigid bodies were allowed to rotate (dabco only along the b-axis) and the dihedral angles between the carboxylate moieties and the phenyl ring of the bdc linkers were refined within an interval of 25-50°. In addition to that, the propyl group atom positions were refined with fixed C-C atom distances (1.51 Å) and constrained C-C-C angles

(109.5-113.5°), and the atomic coordinates of the Zn were refined (with y fixed at 0.5). Subsequently, the CO_2 molecules were added to the structural model according to electron density peaks in the Fourier difference map, described as a rigid body (one CO_2 per asymmetric unit) with a fixed occupancy of 0.385, that was set according to in-house CO_2 sorption data. After a refinement of the rotational and translational coordinates of the CO_2 molecules (using 2.5 Å Anti-bump restraints), its occupancy was also refined within an interval of 0.35 to 0.42.

In order to find the global minimum for the configuration of the "flexible parts" of the structure (i.e., the propyl groups, the CO_2 molecules and the carboxylate-phenyl dihedral angle), their parameters were randomized based on their approximate errors for multiple refinement cycles. In the final refinement cycle, unit cell, peak shape function and background function parameters were refined once again. The final Rietveld fit is given in Section 3.5, Figure 3.18 and the crystallographic data in Table 8.12.

Table 8.12: Crystallographic data for the Rietveld refinement of the ***ip*$_{\text{ads}}$** phase of *dry*-DMOF-1-**C3** at 6 kPa CO_2 pressure.

Compound	*dry*-DMOF-1-**C3** (***ip*$_{ads}$**) @ 6 kPa CO_2
Empirical formula	$C_{34}H_{44}N_2O_8Zn_2 \cdot 1.65CO_2$
Formula weight	812.11
Calclulated density	1.412(3)
space group	$C2/m$
Crystal system	monoclinic
a / Å	10.3475(14)
b / Å	18.875(2)
c / Å	9.6197(10)
α / °	90
β / °	94.581(15)
γ / °	90
V / Å^3	1872.9(4)
Z	2
Diffractometer	P02.1, Deutsches Elektronen Synchrotron, Hamburg, Germany
Temperature / K	195
Wavelength / Å	0.2073
No. Reflections	1655
No. Atoms	17
No. Restraints	16
R_{p}	1.438
R_{exp}	2.148
R_{wp}	2.039
χ^2	0.953
R_{Bragg}	1.164

Pawley-fit of the ***np*** and ***lp*** Phase of *dry*-DMOF-1-**C3**

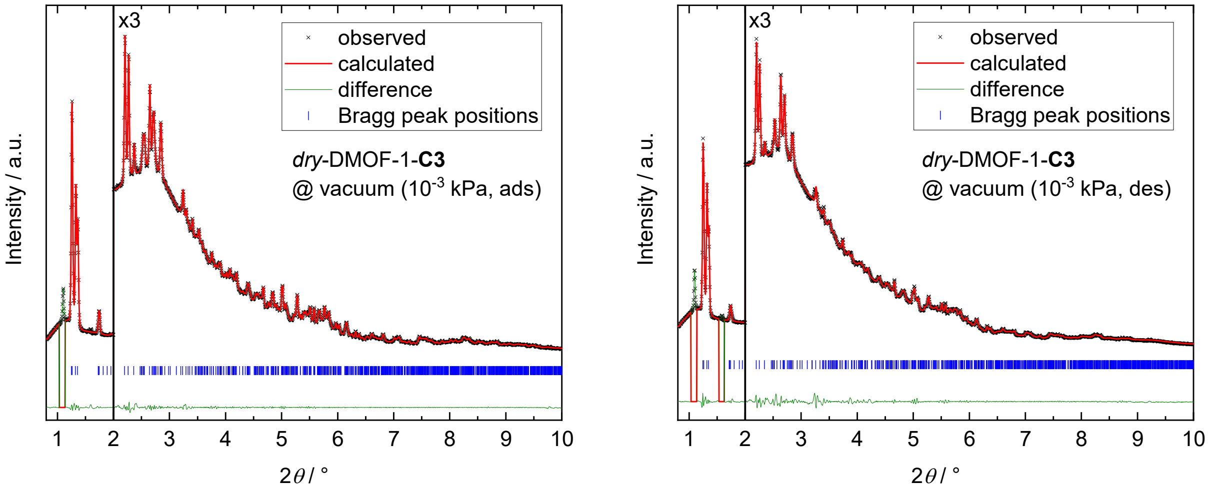

Figure 8.13: Structureless profile fits (Pawley method) of *in-situ* CO_2 sorption PXRD pattern of *dry*-DMOF-1-**C3** at 10^{-3} kPa pressure on the adsorption branch and desorption branch (P02.1 of DESY, $\lambda = 0.2073$ Å). Fit parameters are given below.

Table 8.13: Unit cell parameters *a*, *b*, *c* and cell volume *V* determined by profile fitting (Pawley method) of the PXRD patterns and the corresponding R_{wp}, R_{exp} and χ^2 values for *dry*-DMOF-1-**C3** at CO_2 pressures of $2{\cdot}10^{-3}$ kPa (***np*** phase, adsorption branch), 100 kPa (***lp*** phase) and $2{\cdot}10^{-3}$ kPa (***np*** phase, desorption branch). The corresponding fits of the np phases are given above, while the fit of the ***lp*** phase is given in the main text (Figure 3.19).

Compound	**$2{\cdot}10^{-3}$ kPa (ads)**	**100 kPa CO_2**	**$2{\cdot}10^{-3}$ kPa (des)**
crystal system	triclinic	monoclinic	triclinic
space group	$P\bar{1}$	$C2/m$	$P\bar{1}$
a / Å	9.587(4)	14.660(2)	9.625(13)
b / Å	10.133(5)	16.290(2)	10.218(13)
c / Å	10.586(6)	9.6301(8)	10.615(15)
α / °	62.962(6)	90	62.622(19)
β / °	84.64(4)	95.72(2)	84.84(12)
γ / °	83.50(2)	90	82.72(13)
V / Å^3	909.1(8)	2288. 5(4)	919(2)
R_{wp}	0.60	1.05	0.88
R_{exp}	1.14	1.60	1.21
χ^2	0.52	0.65	0.73

Rietveld Refinement of the ***ip***$_{\mathbf{des}}$ Phase of *dry*-DMOF-1-**C3**

Due to the appearance of additional weak reflections at around 1.8 to 2.1° 2θ, that could not be indexed in the $C2/m$ space group, the diffraction pattern was indexed in the lower symmetry space group $P2/c$ (changed setting). Following, the unit cell, background and peak shape function parameters were extracted by structureless profile fitting (Pawley method) of the PXRD pattern and were carried over into the Rietveld refinement.

The starting structural model was based on a SCXRD structure of a DMF-solvated ***lp*** phase of compound *dry*-DMOF-1-**C3**, which was also found to crystallize in $P2/c$ symmetry (see Appendix section 8.1.2, Table 8.7). To obtain the starting structure, DMF molecules were removed, such as the disorder in the alkyl groups and dummy atoms were placed on special positions (i.e., the center of the dabco pillar (2-fold axis through 0, y, ¼) and the centers of the phenyl ring of the bdc-linkers (inversion center)). To fix the internal distances of the organic building units of the framework, the symmetry independent halves of the bdc-linkers and the dabco pillar were described as rigid bodies using z-matrices, including the dummy atoms mentioned above. The beq parameters were fixed to values of 1.0 for Zn and N, 2.0 for all backbone C atoms and 3.5 or 4.0 for the alkyl C atoms throughout the refinement. In order to keep the geometry of the Zn-paddlewheel unit, all of the Zn-O, Zn-N and Zn-Zn distances and several O-Zn-O and Zn-Zn-N angles were restrained to reasonable values (see Table 8.14). Additionally, a soft flatten restraint was applied to the carboxylate-Zn moiety.

Table 8.14: Values and tolerances of distance and angle restraints applied on the Zn_2-paddlewheel unit during the Rietveld refinement of the ***ip***$_{\mathbf{des}}$ phase of *dry*-DMOF-1-**C3**.

Distances	Value / Å	Tolerance / Å
Zn1-O1/O3 Zn1'-O2/O4	2.0	0.05
Zn1-N1	2.0	0.05
Zn1-Zn1'	2.9	0.02
Zn1-O1/O3	3.3	0.1
Zn1-O2'/O4'	3.1	0.1
Angles		
O1-Zn1-O3, O3-Zn1-O4', O4'-Zn1-O2', O2'-Zn1-O1	90	5
O1-Zn-O4', O3-Zn-O2'	160	5
N1-Zn1-Zn1'	172	3
Zn1-N1-dummy	180	3

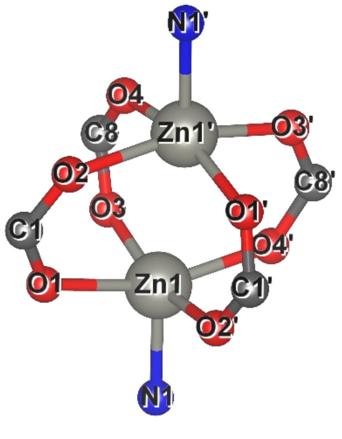

In the first cycle of the refinement, unit cell parameters were changed to the ones obtained from Pawley refinement, as the basing SCXRD structure consists of different b and c unit cell parameters and a different monoclinic angle β. In this refinement cycle, the rigid bodies describing the dabco and bdc-linkers were allowed to be rotated and the atomic coordinates of the Zn were refined as well. In the following cycle, the dihedral angles between carboxylate groups and phenyl rings were refined within an interval of 20° to 45°, as well as the conformations of the alkyl chains by refining the dihedral angles between C6-C5-C4-C3, C7-C6-C5-C4, C13-C12-C11-C10 and C14-C13-C12-C11, while leaving bond distances and angles fixed. In the next step, the CO_2 molecules were added to the structural model successively (with a fixed occupancy of 0.5) and positioned according to electron density peaks in the Fourier difference map. These CO_2 molecules were treated as rigid bodies, that could be freely rotated and translated. With the introduction of the CO_2 molecules to the structural model, anti-bump restraints were applied, when necessary, to set intermolecular distances between the CO_2 and carbon atoms of the MOF to a minimum of 2.5 Å. In later cycles, the occupancies of the CO_2 molecules were refined. In the final cycle of the refinement, unit cell, peak shape function and background function parameters were also refined once again. The final Rietveld plot and the resulting refinement parameters are given in Section 3.5 (Figure 3.20) and Table 8.15.

Table 8.15: Crystallographic data for the Rietveld refinement of the ***ip*** $_{\mathrm{des}}$ phase of *dry*-DMOF-1-**C3** at 50 mbar CO_2 pressure.

Compound	*dry*-DMOF-1-**C3** (***ip*** $_{des}$) @ 5 kPa CO_2
Empirical formula	$C_{34}H_{44}N_2O_8Zn_2 \cdot 3.25CO_2$
Formula weight	880.32
Calclulated density	1.22603(19)
space group	$P2/c$
Crystal system	monoclinic
a / Å	9.6049(6)
b / Å	14.6583(14)
c / Å	16.2256(16)
α / °	90
β / °	96.228(11)
γ / °	90
V / Å^3	2270.9(4)
Z	2
Diffractometer	P02.1, Deutsches Elektronen Synchrotron, Hamburg, Germany
Temperature / K	195
Wavelength / Å	0.2073
No. Reflections	1655
No. Atoms	38
No. Restraints	23
R_{p}	1.248
R_{exp}	2.248
$R_{w\mathrm{p}}$	1.746
χ^2	0.777
R_{Bragg}	1.293

8.1.6 3D Electron Diffraction[††]

Three-dimensional electron diffraction (3DED) data were gathered on crystals of *dry*-DMOF-1-**C3** using a JEOL JEM-2100 LaB_6 transmission electron microscope operating at an acceleration voltage of 200 kV, equipped with an Amsterdam Scientific Instruments Timepix detector. Data collection was carried out using Instamatic[247], with data reduction being performed using XDS[248]. Structure solution was done using SHELXT[249] whereafter a preliminary refinement was done against the acquired 3DED data using SHELXL[250]. The acquired model was then used as a starting point for further refinement against powder X-ray diffraction data of *dry*-DMOF-1-**C3** at 60 mbar CO_2 pressure as described under Appendix section 8.1.5.

Table 8.16: Crystallographic table for electron diffraction data of *dry*-DMOF-1-**C3**.

Empirical formula	$C_{14}NO_5Zn$
Wavelength	0.0251 Å
Crystal system	Monoclinic
Space group	$C2/m$ (No. 12)
Unit cell dimensions	a = 10.62 Å
	b = 20.26 Å
	c = 10.15 Å
	β = 94.91
Volume	2177 Å^3
Z	4
Rotation range	106.19° (-59.26 to 46.93°)
Index ranges	$-11 \leq h \leq 12$
	$-23 \leq k \leq 24$
	$-12 \leq l \leq 12$
Reflections collected	1776
Independent reflections	779642
	[R(int) = 0.1892]
Completeness (to 0.8 Å resolution)	80 %
R_1 (ED model) [I > 4σ(I)]	0.3237

[††] Please note, that the 3D electron diffraction experiments were conducted and analyzed by Erik Svensson Grape and Andrew K. Inge as part of a scientific collaboration.

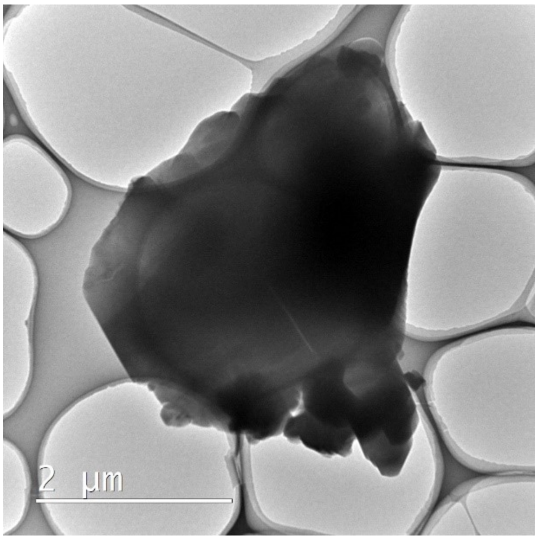

Figure 8.14: Image of a crystal of *dry*-DMOF-1-**C3** used for the 3DED data acquisition.

8.1.7 *In-situ n*-Butane Sorption PXRD

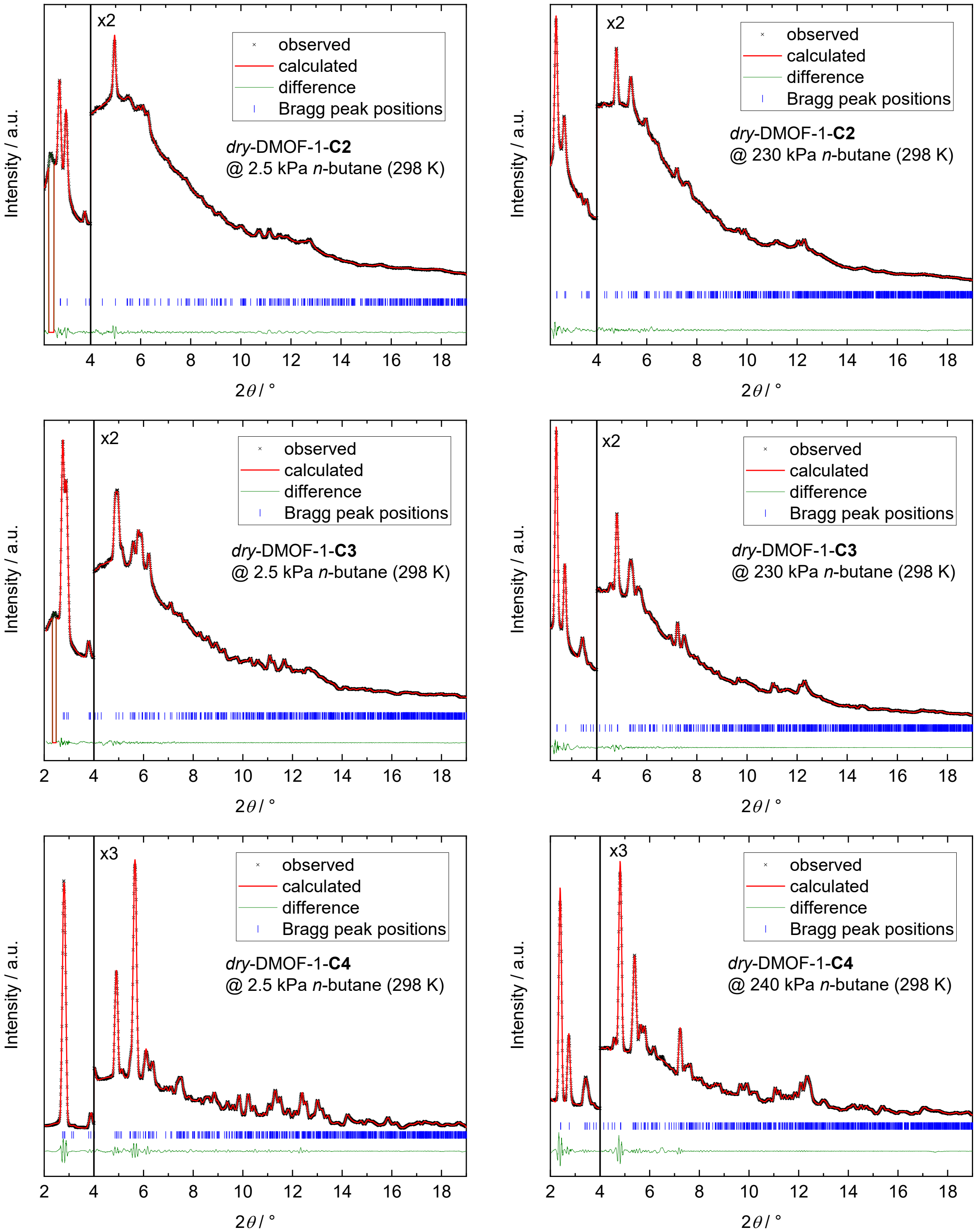

Figure 8.15: *In-situ n*-butane sorption PXRD patterns (BL9 of DELTA, $\lambda = 0.4592$ Å) with Pawley fits of the *dry*-DMOF-1-**CX** recorded at vacuum (***np*** phase, 2.5 kPa) and 230 or 240 kPa pressure (***lp*** phase). The corresponding fit data are given below.

Table 8.17: Unit cell parameters *a*, *b*, *c* and cell volume *V* determined by profile fitting (Pawley method) of the PXRD patterns and the corresponding R_{wp}, R_{exp} and χ^2 values for the *dry*-DMOF-1-**CX** at vacuum (***np*** phase, 2.5 kPa) and 230 or 240 kPa pressure (***lp*** phase).

Compound	**C2**(***np***)	**C2**(***lp***)	**C3**(***np***)	**C3**(***lp***)	**C4**(***np***)	**C4**(***lp***)
pressure	2.5 kPa	200 kPa	2.5 kPa	230 kPa	2.5 kPa	240 kPa
crystal system	monoclinic	monoclinic	triclinic	triclinic	monoclinic	triclinic
space group	$C2/m$	$P2/c$	$P\bar{1}$	$P\bar{1}$	$C2/c$	$P\bar{1}$
a / Å	9.819(18)	10.94(3)	9.60(3)	9.61(5)	18.93(2)	9.602(4)
b / Å	18.930(13)	10.96(3)	10.28(3)	10.94(3)	10.713(17)	10.95(3)
c / Å	9.56(2)	19.35(4)	10.61(4)	10.96(5)	19.30(3)	10.96(4)
α / °	90	90	62.12(2)	88.35(16)	90	89.0(3)
β / °	100.28(10)	88.4(2)	84.4(3)	83.77(16)	93.43(11)	84.3(2)
γ / °	90	90	83.69(9)	87.06(6)	90	87.40(10)
V / Å^3	1749(5)	2319(10)	919(6)	1143(9)	3907(10)	1145(5)
R_{wp}	0.70	0.69	0.48	0.76	2.23	2.53
R_{exp}	1.75	1.62	1.46	1.30	2.00	1.86
χ^2	0.40	0.42	0.33	0.59	1.11	1.36

8.1.8 *In-situ* Propane & Propylene Sorption PXRD

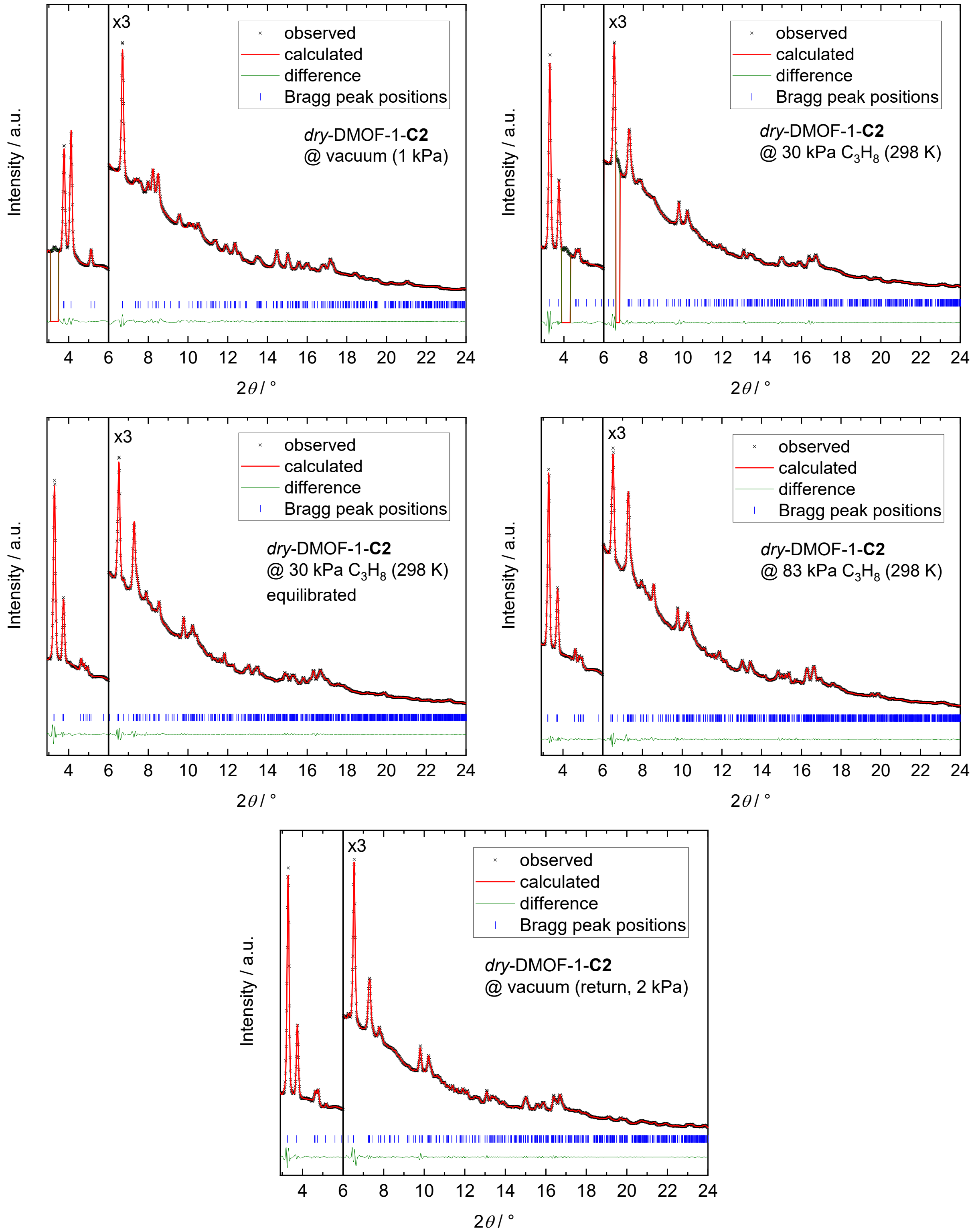

Figure 8.16: *In-situ* propane sorption PXRD patterns (BL9 of DELTA, $\lambda = 0.6199$ Å) with Pawley fits of *dry*-DMOF-1-**C2** recorded at vacuum (start and return) and various propane pressures. The corresponding fit data are given below.

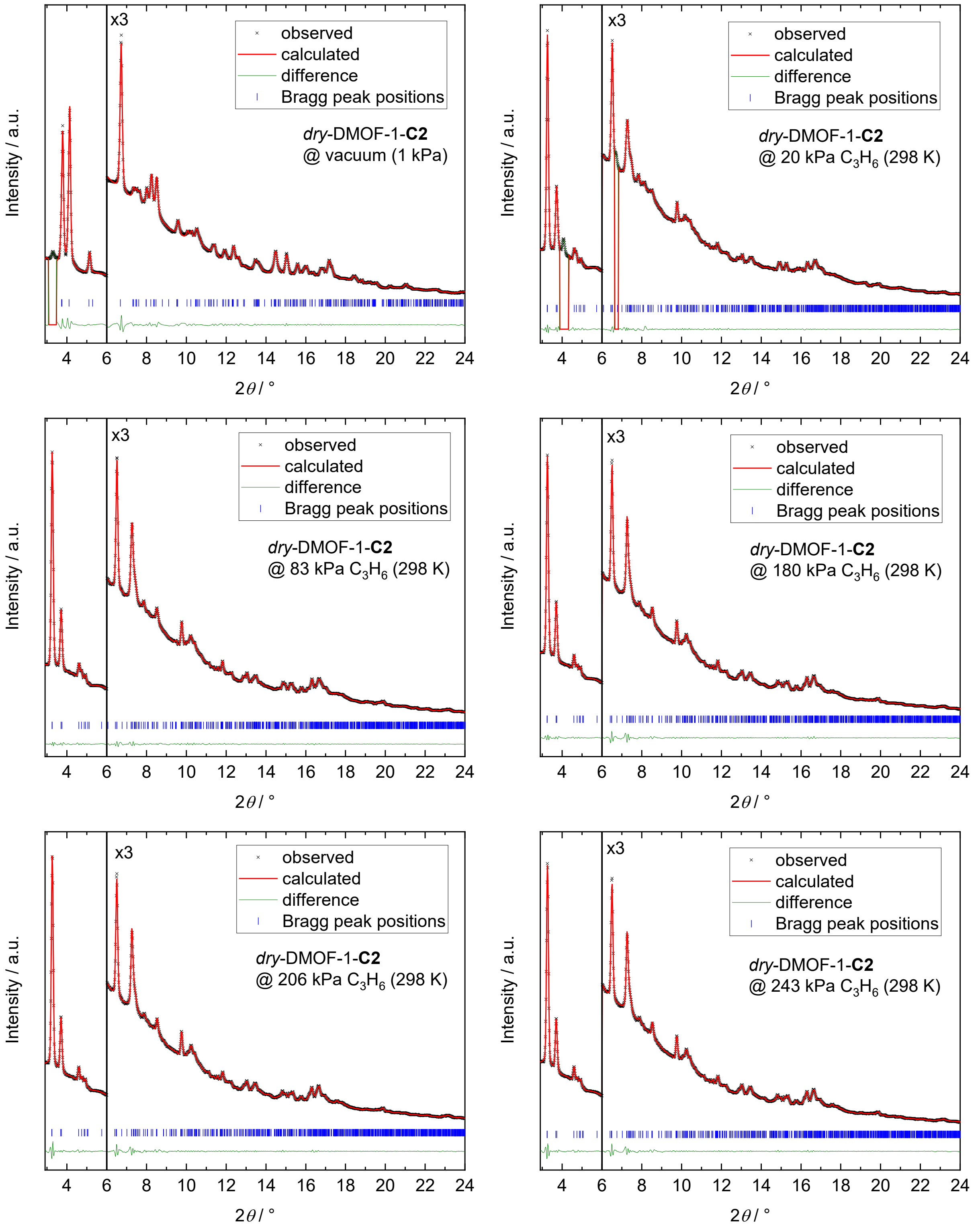

Figure 8.17: *In-situ* propylene sorption PXRD patterns (BL9 of DELTA, $\lambda = 0.6199$ Å) with Pawley fits of *dry*-DMOF-1-**C2** recorded at vacuum and various pressures. The corresponding fit data are given below.

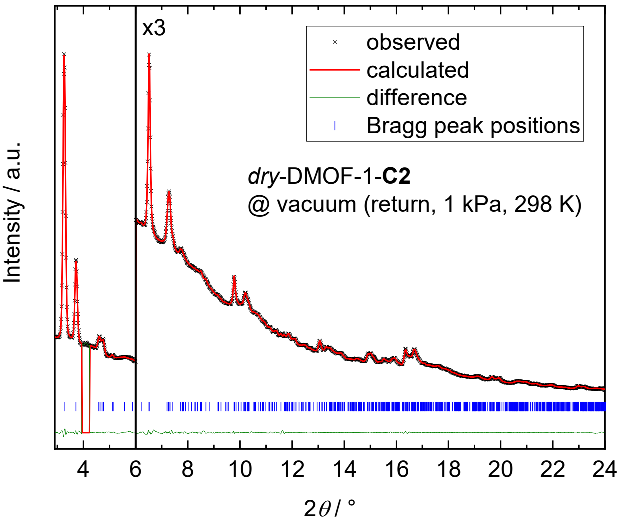

Figure 8.18: *In-situ* propylene sorption PXRD pattern (BL9 of DELTA, λ = 0.6199 Å) with Pawley fit of *dry*-DMOF-1-**C2** recorded at vacuum (return). The corresponding fit data are given below.

Table 8.18: Unit cell parameters a, b, c and cell volume V determined by profile fitting (Pawley method) of the *in-situ* gas sorption PXRD patterns (BL9 of DELTA, λ = 0.6199 Å) and the corresponding R_{wp}, R_{exp} and χ^2 values for *dry*-DMOF-1-**C2** under various propane pressures.

C_3H_8 pressure	**vac (1 kPa)**	**30 kPa**	**30 kPa (eq)**	**83 kPa**	**return (1 kPa)**
crystal system	monoclinic	monoclinic	monoclinic	monoclinic	monoclinic
space group	$C2/m$	$C2/m$	$P2/c$	$P2/c$	$C2/m$
a / Å	9.880(5)	15.485(16)	10.955(14)	10.945(14)	15.497(11)
b / Å	19.050(4)	15.519(16)	10.942(12)	10.966(15)	15.490(12)
c / Å	9.626(5)	9.636(3)	19.253(10)	19.270(12)	9.6339(17)
a / °	90	90	90	90	90
β / °	100.15(3)	96.36(8)	85.63(8)	86.98(9)	96.44(4)
γ / °	90	90	90	90	90
V / Å^3	1783.4(13)	2301(3)	2301(4)	2310(5)	2298(2)
R_{wp}	1.31	1.44	1.12	0.96	1.36
R_{exp}	3.07	6.52	2.32	2.45	4.14
χ^2	0.43	0.22	0.48	0.39	0.33

Table 8.19: Unit cell parameters *a*, *b*, *c* and cell volume *V* determined by profile fitting (Pawley method) of the *in-situ* gas sorption PXRD patterns (BL9 of DELTA, λ = 0.6199 Å) and the corresponding R_{wp}, R_{exp} and χ^2 values for *dry*-DMOF-1-**C2** under various propylene pressures.

C_3H_6 pressure	**vacuum (1 kPa)**	**20 kPa**	**83 kPa**	**179 kPa**	**206 kPa**
crystal system	monoclinic	monoclinic	monoclinic	monoclinic	monoclinic
space group	$C2/m$	$P2/c$	$P2/c$	$P2/c$	$P2/c$
a / Å	9.885(4)	10.972(17)	10.974(10)	10.990(11)	11.00(2)
b / Å	19.016(4)	10.905(16)	10.918(10)	10.950(11)	10.94(2)
c / Å	9.604(6)	19.27(3)	19.275(18)	19.314(3)	19.34(4)
α / °	90	90	90	90	90
β / °	100.16(3)	85.14(6)	85.50(4)	86.19(6)	86.32(8)
γ / °	90	90	90	90	90
V / Å^3	1771.0(14)	2298(6)	2302(4)	2319(3)	2323(8)
R_{wp}	1.07	0.65	0.47	0.60	0.82
R_{exp}	3.26	2.30	2.27	2.26	4.80
χ^2	0.33	0.28	0.21	0.27	0.17

Table 8.20: Unit cell parameters *a*, *b*, *c* and cell volume *V* determined by profile fitting (Pawley method) of the *in-situ* gas sorption PXRD patterns (BL9 of DELTA, λ = 0.6199 Å) and the corresponding R_{wp}, R_{exp} and χ^2 values for *dry*-DMOF-1-**C2** under various propylene pressures.

C_3H_6 pressure	**243 kPa**	**return (1 kPa)**
crystal system	monoclinic	monoclinic
space group	$P2/c$	$C2/m$
a / Å	11.01(2)	15.459(4)
b / Å	10.95(2)	15.503(4)
c / Å	19.35(4)	9.6338(9)
α / °	90	90
β / °	86.33(9)	96.24(3)
γ / °	90	90
V / Å^3	2327(9)	2295.1(9)
R_{wp}	0.84	0.56
R_{exp}	3.46	5.21
χ^2	0.24	0.11

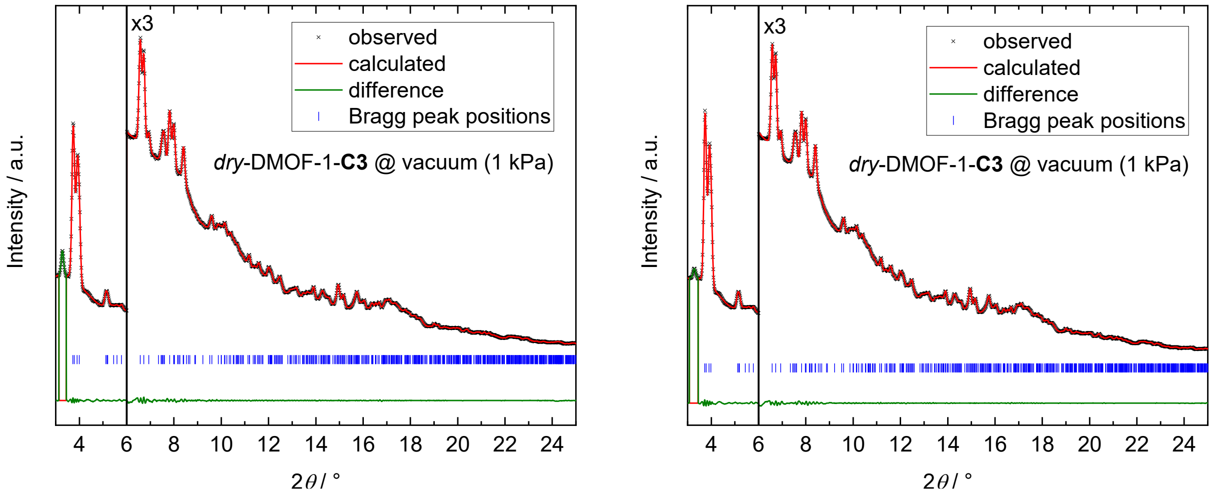

Figure 8.19: *In-situ* propylene sorption PXRD patterns (BL9 of DELTA, λ = 0.6199 Å) with Pawley fits of *dry*-DMOF-1-**C3** (***np***) recorded at vacuum before the propane (left) and propylene (right) sorption experiment. The corresponding fit data are given below.

Table 8.21: Unit cell parameters a, b, c and cell volume V determined by profile fitting (Pawley method) of the *in-situ* gas sorption PXRD patterns (BL9 of DELTA, λ = 0.6199 Å) and the corresponding R_{wp}, R_{exp} and χ^2 values for *dry*-DMOF-1-**C3** (***np***) at vacuum before the propane and propylene sorption experiment.

pressure	**C_3H_8, vacuum (1 kPa)**	**C_3H_6, vacuum (1 kPa)**
crystal system	triclinic	triclinic
space group	$P\bar{1}$	$P\bar{1}$
a / Å	9.617(4)	9.617(4)
b / Å	10.317(3)	10.321(3)
c / Å	10.651(3)	10.652(3)
α / °	62.145(8)	62.126(8)
β / °	84.36(6)	84.41(5)
γ / °	83.62(3)	83.62(3)
V / Å^3	927.3(6)	927.6(5)
R_{wp}	0.37	0.39
R_{exp}	4.02	2.10
χ^2	0.09	0.19

Rietveld refinement of C_3H_8 and C_3H_6 infiltrated DMOF-1-**C3**

The PXRD patterns were recorded at propane and propylene pressures of 48 and 58 kPa on the adsorption branch of the *in-situ* experiment were indexed in a triclinic unit cell with the $P\bar{1}$ space group. Structureless profile fitting (Pawley method) provided refined unit cell parameters, peak shape function parameters and the background curve used for the initial refinement cycle.

The starting structural model was based on a SCXRD structure of the *n*-octane solvated ***lp*** phase of *dry*-DMOF-1-**C3**, which was likewise found to crystallize in $P\bar{1}$ symmetry (see Appendix section 8.1.2, Table 8.7). In the starting structural model, the half *n*-octane molecule contained in the asymmetric unit was removed to be replaced by a propane or propylene molecule and tied to its position in initial refinement cycles using a dummy atom placed on 1 0.5 0 later on in the refinement. Further dummy atoms were placed on special positions (i.e., the centre of the dabco pillar (inversion centre) and the centres of the phenyl ring of the bdc-linkers (inversion centre)). To fix the internal distances of the organic building units of the framework, the symmetry independent halves of the bdc-linkers and the dabco pillar were described as rigid bodies using z-matrices, including the dummy atoms mentioned above. The beq parameters were taken over from the starting model and kept fixed throughout the refinement. In order to keep the geometry of the Zn-paddlewheel unit, all of the Zn-O (2±0.05, 3.1±0.1, 3.3±0.1 Å), Zn-N (2±0.05 Å) and Zn-Zn (2.9±0.05 Å) distances, furthermore Zn-Zn-N (172±3°) and Zn-N-dummy (180±3°) angles were restrained.

In the first cycle of the refinement, unit cell parameters were changed to the ones obtained from Pawley refinement, as the basing SCXRD structure consists of different b and c unit cell parameters and different angles α, β, γ. In this refinement cycle, the rigid bodies describing the dabco, bdc-linkers were allowed to be rotated and the atomic coordinates of the Zn were refined as well. In the following cycle, the dihedral angles between carboxylate groups and phenyl rings were refined within an interval of –20° to 20° from their starting positions, as well as the conformations of the alkyl chains by refining the dihedral angles between C6-C5-C4-C3, C7-C6-C5-C4, C13-C12-C11-C10 and C14-C13-C12-C11, while leaving bond distances and angles fixed. In the next step, the propane and propylene molecules, described as rigid bodies including the dummy atom as described above, were added to the structural model (at first with a fixed occupancy of 0.5). The propane/propylene molecules were followingly freely rotated and translated. For the introduced the propane and propylene molecules no anti-bump restraints had to be applied. In later cycles, the occupancies of the propane/propylene molecules were set according to the respective sorption isotherms. In order to find the global minimum for the configuration of the “flexible parts” of the structure (i.e., the propyl groups, the propane/propylene molecules and the carboxylate-phenyl dihedral angle), their parameters were randomized based on their approximate errors for multiple refinement cycles. In the final refinement cycle, unit cell, peak shape function and background function parameters were refined once again. The final Rietveld plot and the resulting refinement parameters are given in the corresponding main text section and Table 8.22.

Table 8.22: Crystallographic data for the Rietveld refinement of the propane or propylene filled ***lp*** phases of *dry*-DMOF-1-**C3** at 48 or 58 kPa propane or propylene pressure.

dry-DMOF-1-**C3**	@ 48 kPa C_3H_8 (***lp***)	@ 58 kPa C_3H_6 (***lp***)
Empirical formula	$C_{34}H_{44}N_2O_8Zn_2 \cdot 2C_3H_8$	$C_{34}H_{44}N_2O_8Zn_2 \cdot 2C_3H_6$
Formula weight	827.69	823.66
Calclulated density	1.1111(5)	1.1120(5)
space group	$P\bar{1}$	$P\bar{1}$
Crystal system	triclinic	triclinic
a / Å	9.6252(12)	9.6108(15)
b / Å	10.956(4)	10.971(4)
c / Å	16.955(3)	10.940(3)
α / °	89.36(4)	88.85(3)
β / °	85.22(3)	86.94(4)
γ / °	84.86(3)	84.13(4)
V / Å^3	1146.9(4)	1145.7(5)
Z	1	1
Diffractometer	BL9, Dortmunder Elektronen Speicherring Anlage, Dortmund, Germany	
Temperature / K	298	298
Wavelength / Å	0.6199	0.6199
No. Reflections	860	864
No. Atoms	29	29
No. Restraints	12	12
R_p	1.330	1.817
R_{exp}	3.472	2.859
R_{wp}	1.741	1.251
χ^2	0.501	0.635
R_{Bragg}	0.634	0.565

8.1.9 Variable Temperature PXRD

dry-DMOF-1-**C3**

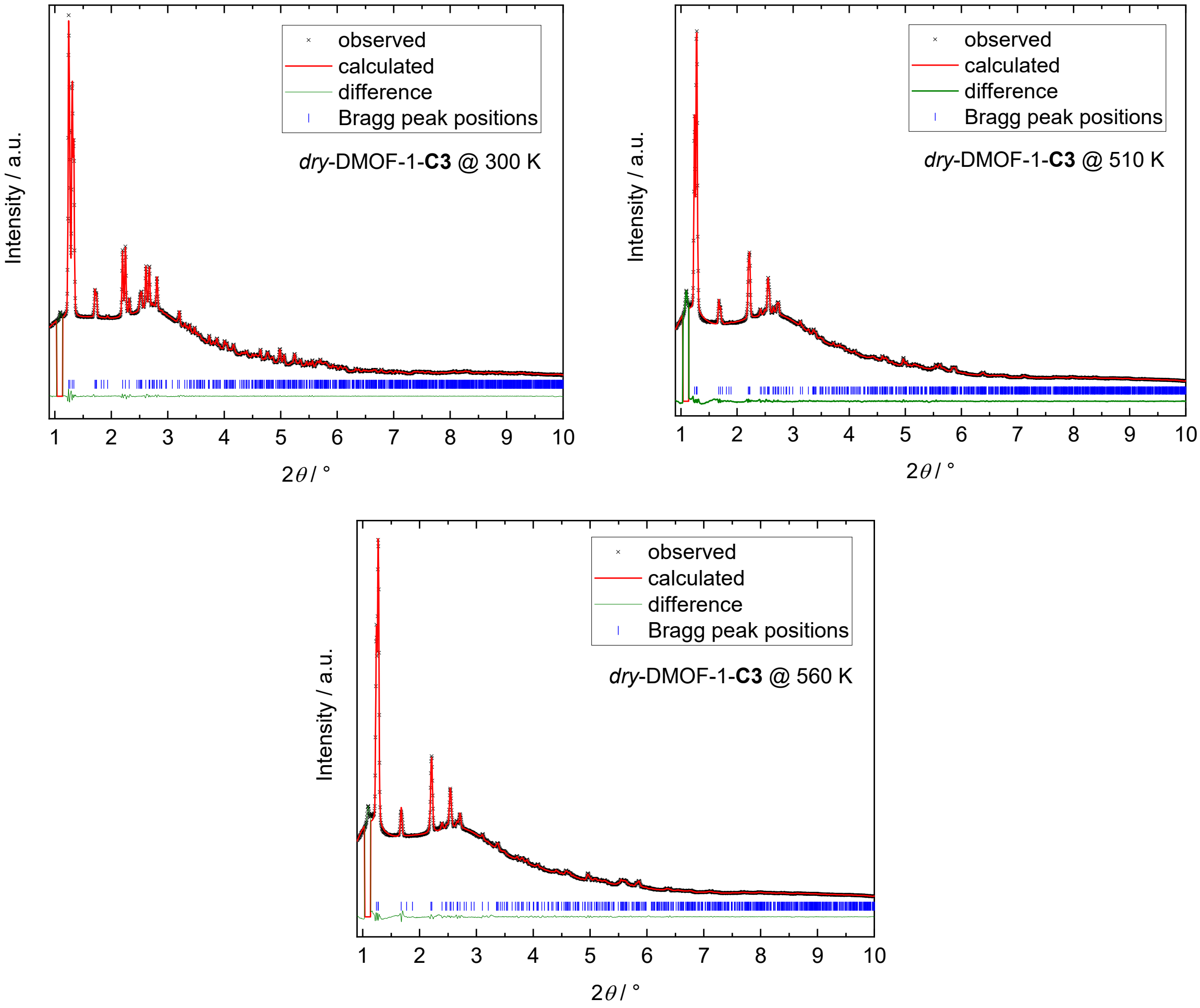

Figure 8.20: Exemplary VT-PXRD patterns (P02.1 of DESY, $\lambda = 0.2073$ Å) of *dry*-DMOF-1-**C3** at 300, 510 and 560 K with corresponding profile fits (Pawley method). Fitted unit cell parameters are listed in Table 8.23. $R_{wp} = 0.67$, $R_{exp} = 1.25$, $\chi^2 = 0.53$ (300 K); $R_{wp} = 0.96$, $R_{exp} = 1.25$, $\chi^2 = 0.77$ (510 K); $R_{wp} = 1.18$, $R_{exp} = 1.95$, $\chi^2 = 0.60$ (560 K).

Table 8.23: Lattice parameters extracted from structureless profile fitting (Pawley method) of the VT-PXRD data (P02.1 of DESY) of *dry*-DMOF-1-**C3**, that were used for determination of the thermal expansion coefficients.

T / K	sg	a	b	c	α	β	γ	V / A^3
300	$P\bar{1}$	9.6252(9)	10.3200(9)	10.6422(8)	62.108(4)	84.29(3)	83.651(14)	927.20(14)
320	$P\bar{1}$	9.6307(7)	10.3671(8)	10.6537(9)	61.897(6)	84.23(4)	83.62(2)	931.07(15)
350	$P\bar{1}$	9.6343(6)	10.4269(8)	10.6678(8)	61.633(5)	84.25(3)	83.56(2)	935.67(13)
400	$P\bar{1}$	9.6495(9)	10.5428(18)	10.6943(13)	61.158(9)	84.26(4)	83.43(4)	945.5(2)
450	$P\bar{1}$	9.6552(10)	10.649(3)	10.7142(18)	60.737(13)	84.34(4)	83.27(4)	953.3(3)
500	$P\bar{1}$	9.663(10)	10.735(4)	10.751(3)	60.370(18)	84.53(4)	83.15(4)	961.7(5)
510	$P\bar{1}$	9.6655(9)	10.746(4)	10.762(4)	60.29(2)	84.65(4)	83.16(3)	963.2(5)
520	$P\bar{1}$	9.6690(10)	10.753(3)	10.782(3)	60.27(2)	84.69(4)	83.16(4)	965.8(5)
530	$P\bar{1}$	9.6702(10)	10.765(4)	10.794(3)	60.23(3)	84.83(4)	83.03(4)	967.5(5)
540	$P\bar{1}$	9.6734(11)	10.775(4)	10.804(4)	60.20(4)	84.88(5)	82.97(4)	969.4(6)
550	$P\bar{1}$	9.6757(11)	10.786(4)	10.812(4)	60.21(4)	84.91(5)	82.93(4)	971.4(6)
560	*C2/m*	10.824(3)	18.743(7)	9.6752(9)	90	97.30(3)	90	1947.0(10)

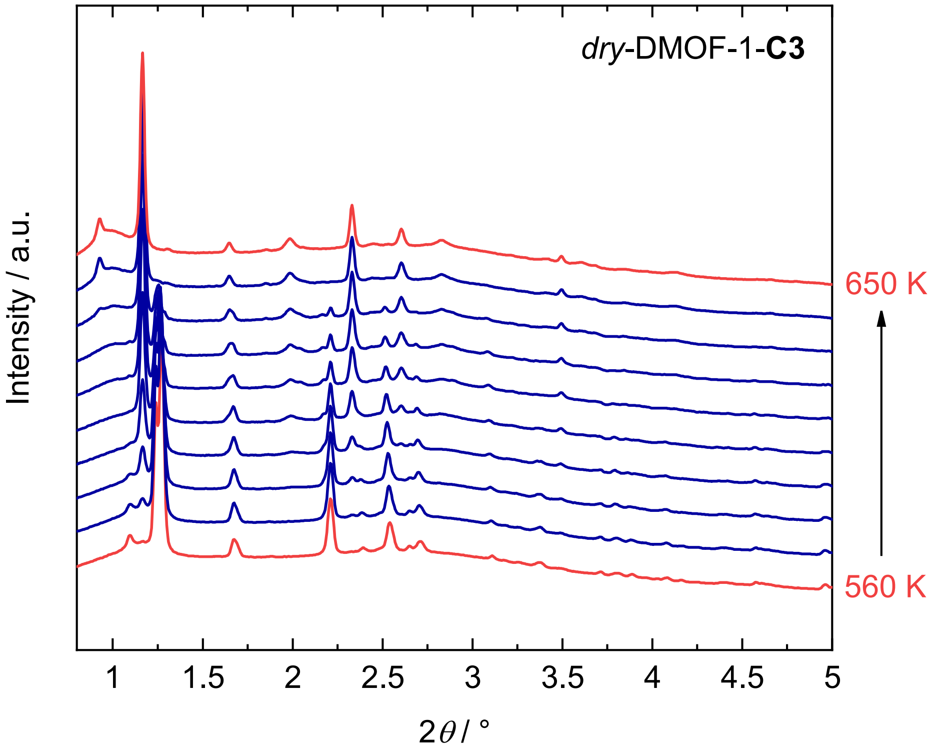

Figure 8.21: Variable temperature PXRD data of compound *dry*-DMOF-1-**C3** recorded from 560 to 650 K (λ = 0.2073 Å) showing the thermal decomposition starting from 560 K. The vanishing of the reflection at ≈ 1.3° 2θ (corresponding to the distance between the Zn_2(**C3**-bdc)$_2$-layers along the dabco-axis) indicates the loss of dabco, which is likely to occur as the first event of the decomposition process as similarly indicated by a 15-20% weight loss in TG-DSC (see Figure 8.26).

dry-DMOF-1-**C4**

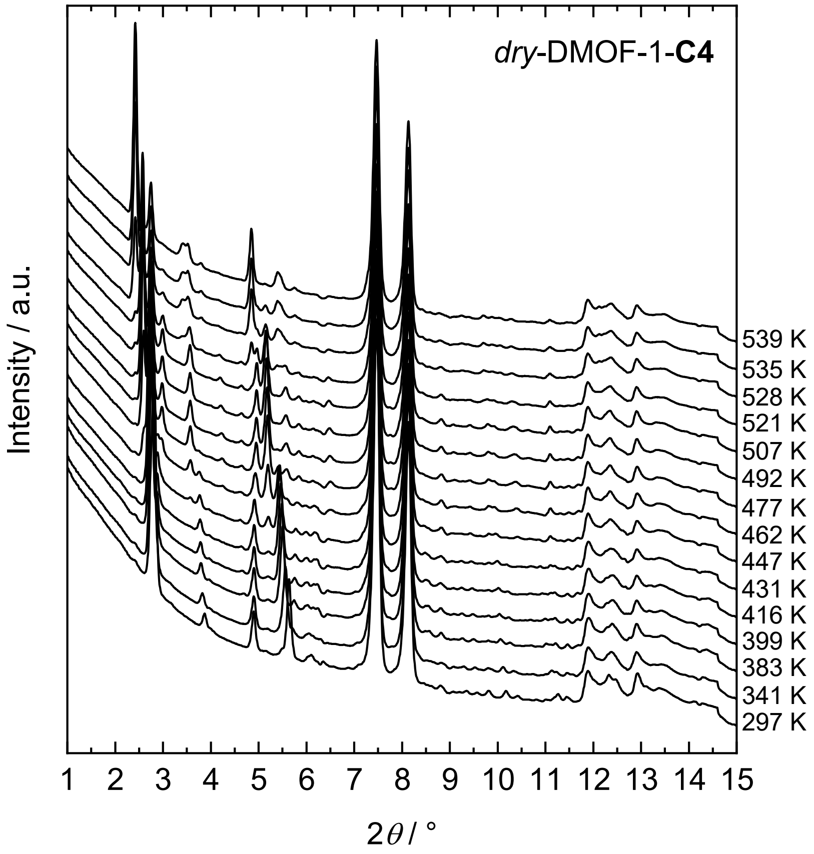

Figure 8.22: The full set of VT-PXRD patterns of *dry*-DMOF-1-**C4** recorded at BL9 of DELTA (λ = 0.4592 Å) with measurement temperatures given on the right of each pattern. Note that the strong reflections in the range from 7 – 9° 2θ and 11.5 – 14.5° 2θ emerge from the graphite dome used in this experiment.

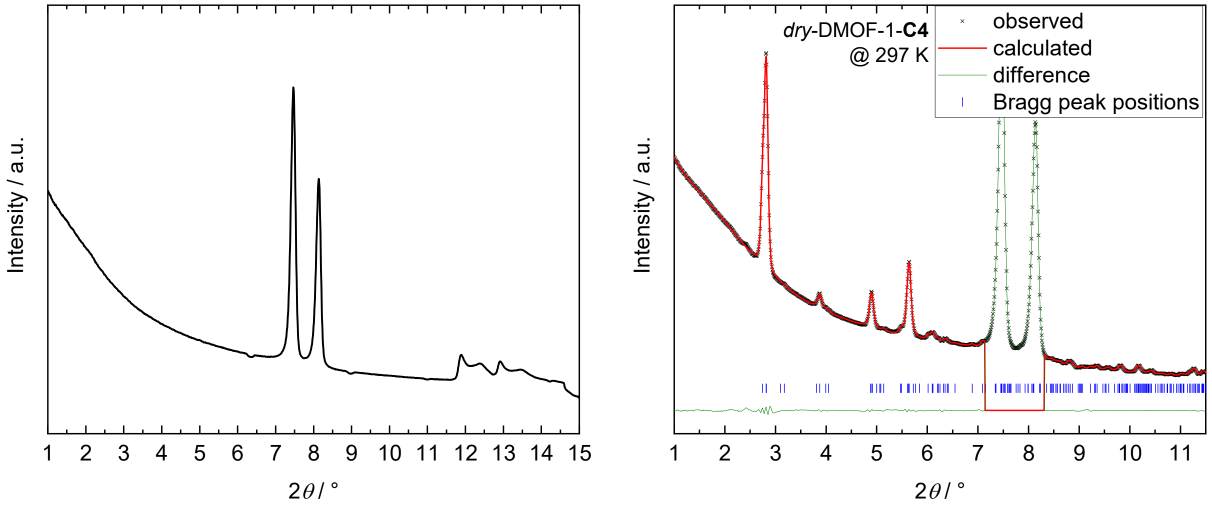

Figure 8.23: Left: PXRD pattern of the graphite dome without sample recorded at RT at BL9 of DELTA (λ = 0.4592 Å). Right: VT-PXRD pattern with profile fit (Pawley method) of *dry*-DMOF-1-**C4** recorded at 297 K at BL9 of DELTA (λ = 0.4592 Å). The regions with the signals originating from the graphite dome have been excluded from the fit. Fit data are given below (Table 8.24).

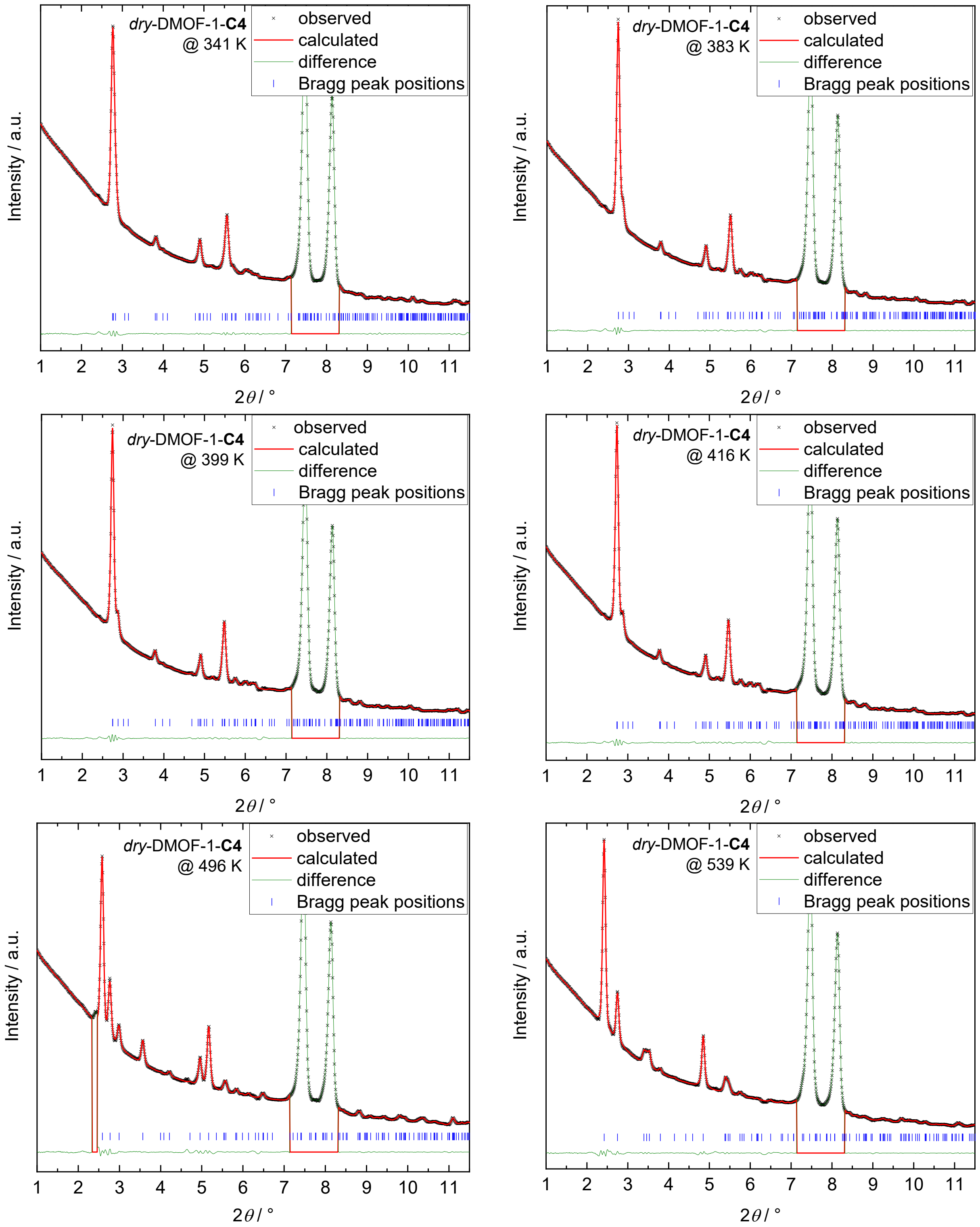

Figure 8.24: VT-PXRD pattern with profile fit (Pawley method) of *dry*-DMOF-1-**C4** recorded at the given temperatures at BL9 of DELTA ($\lambda = 0.4592$ Å). The regions with the signals originating from the graphite dome have been excluded from the fit. Fit data are given below (Table 8.24).

Table 8.24: Lattice and fit parameters extracted from structureless profile fitting (Pawley method) of selected VT-PXRD patterns of *dry*-DMOF-1-**C4** recorded at BL9 of DELTA ($\lambda = 0.4592$ Å).

T	297 K	341 K	383 K	399 K	416 K	492 K	539 K
phase	***np***	***np***	***np***	***np***	***np***	***ip*$_{ht}$**	***lp***
crystal system	monoclinic	monoclinic	monoclinic	monoclinic	monoclinic	monoclinic	monoclinic
space group	$C2/c$	$C2/c$	$C2/c$	$C2/c$	$C2/c$	$C2/m$	$C2/m$
a / Å	18.74(3)	18.59(2)	18.412(6)	18.368(7)	18.317(7)	12.608(2)	15.295(6)
b / Å	10.764(9)	10.998(6)	11.191(9)	11.228(10)	11.325(6)	17.592(2)	15.495(6)
c / Å	19.209(19)	19.116(18)	19.209(12)	19.262(14)	19.254(10)	9.5848(13)	9.618(3)
a / °	90	90	90	90	90	90	90
β / °	93.48(8)	94.33(8)	95.31(6)	95.24(6)	95.22(6)	97.96(2)	95.88(5)
γ / °	90	90	90	90	90	90	90
V / Å^3	3867(8)	3897(6)	3941(4)	3956(4)	3977(4)	2105.4(5)	2267.3(14)
R_{wp}	0.53	0.50	0.53	0.56	0.59	0.79	0.71
R_{exp}	3.27	3.37	3.35	3.46	3.54	3.85	3.92
χ^2	0.16	0.15	0.16	0.16	0.17	0.20	0.18

8.1.10 DSC & TG-DSC

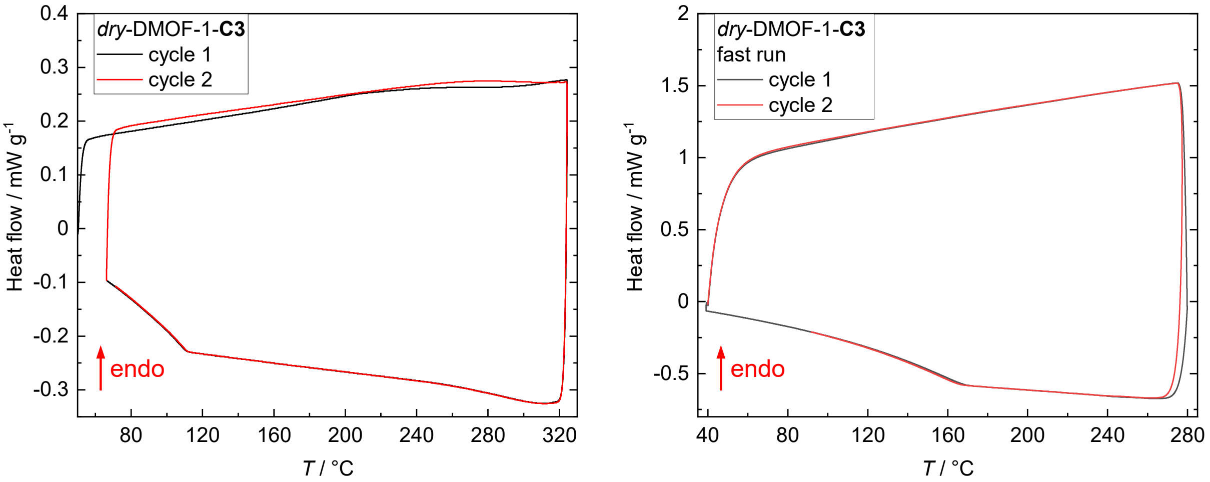

Figure 8.25: DSC curves of *dry*-DMOF-1-**C3**. Left: The data were collected in the range from 50 to 325 °C with a heating and cooling rate of 10 °C/min and measuring cycle 2 was performed immediately after a 1 min isothermal segment at the end of measuring cycle 1. Right: The data were collected in the range from 40 to 280 °C using a heating rate of 50 °C/min and a cooling rate of 20 °C/min and measuring cycle 2 was performed immediately after a 1 min isothermal segment and equilibration at 40 °C at the end of measuring cycle 1.

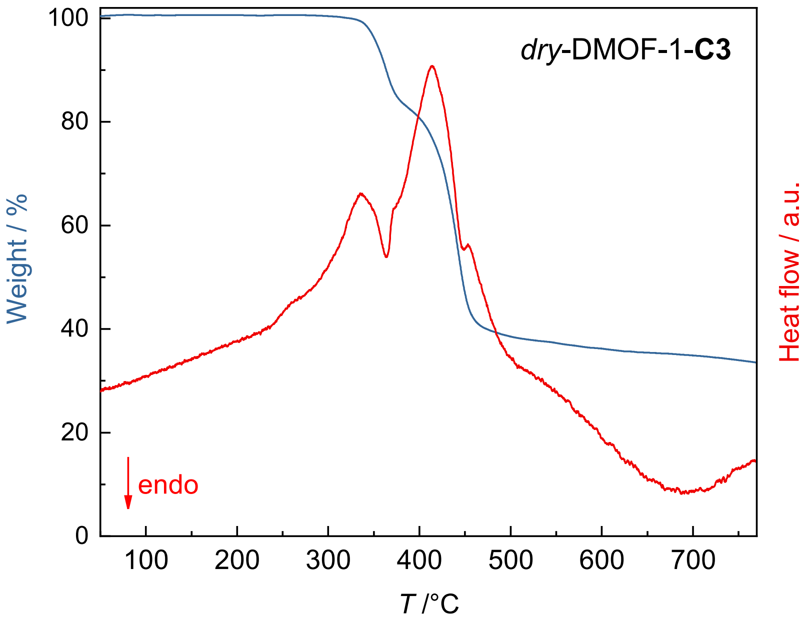

Figure 8.26: TG-DSC data of *dry*-DMOF-1-**C3**. The decomposition temperature was determined as T_d = 301 °C (574 K) from this data.

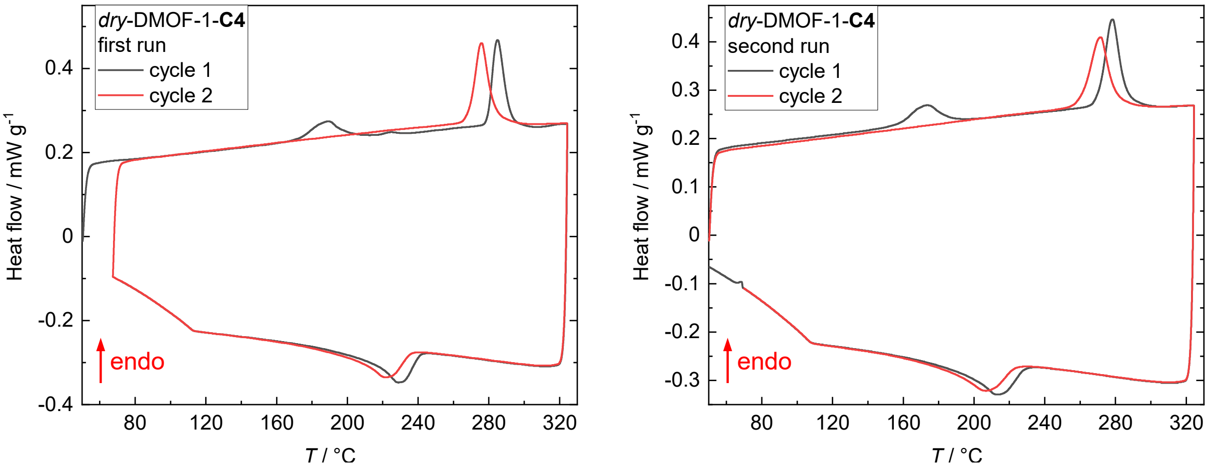

Figure 8.27: DSC curves of the first (left) and second run (right) of *dry*-DMOF-1-**C4**. For both runs, the data were collected in the range from 50 to 325 °C with a heating and cooling rate of 10 °C/min. For run 1 data collection of measuring cycle 2 was performed immediately after a 1 min isothermal segment at the end of measuring cycle 1, whereas for run 2 the temperature was further equilibrated at 50 °C before the second measuring cycle. Note that run 2 was performed with exactly the same sample 20 h after run 1.

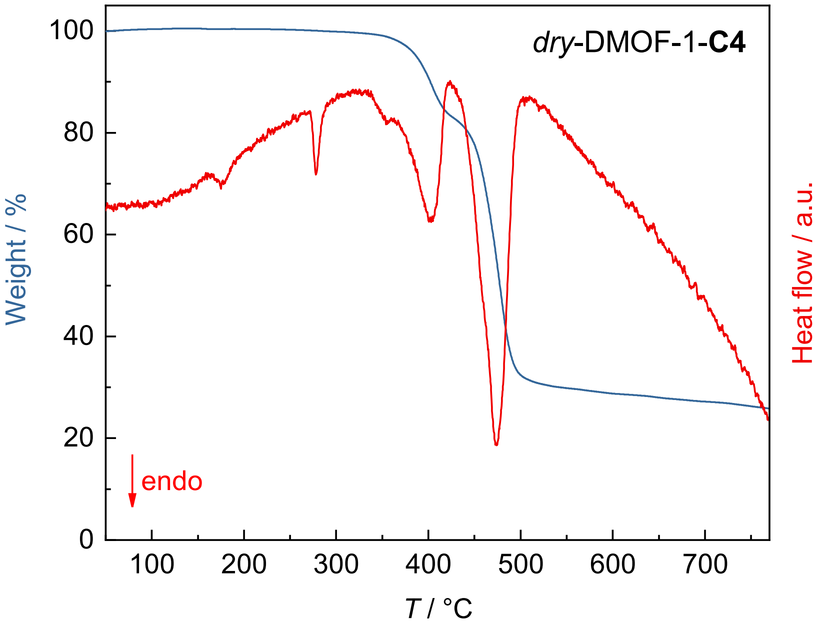

Figure 8.28: TG-DSC data of *dry*-DMOF-1-**C4**. The decomposition temperature was determined as T_d = 335 °C (608 K) from this data.

8.2 Additional Experimental Data and Information to Chapter 4

8.2.1 Powder X-ray Diffraction

Structureless profile fits (Pawley method)

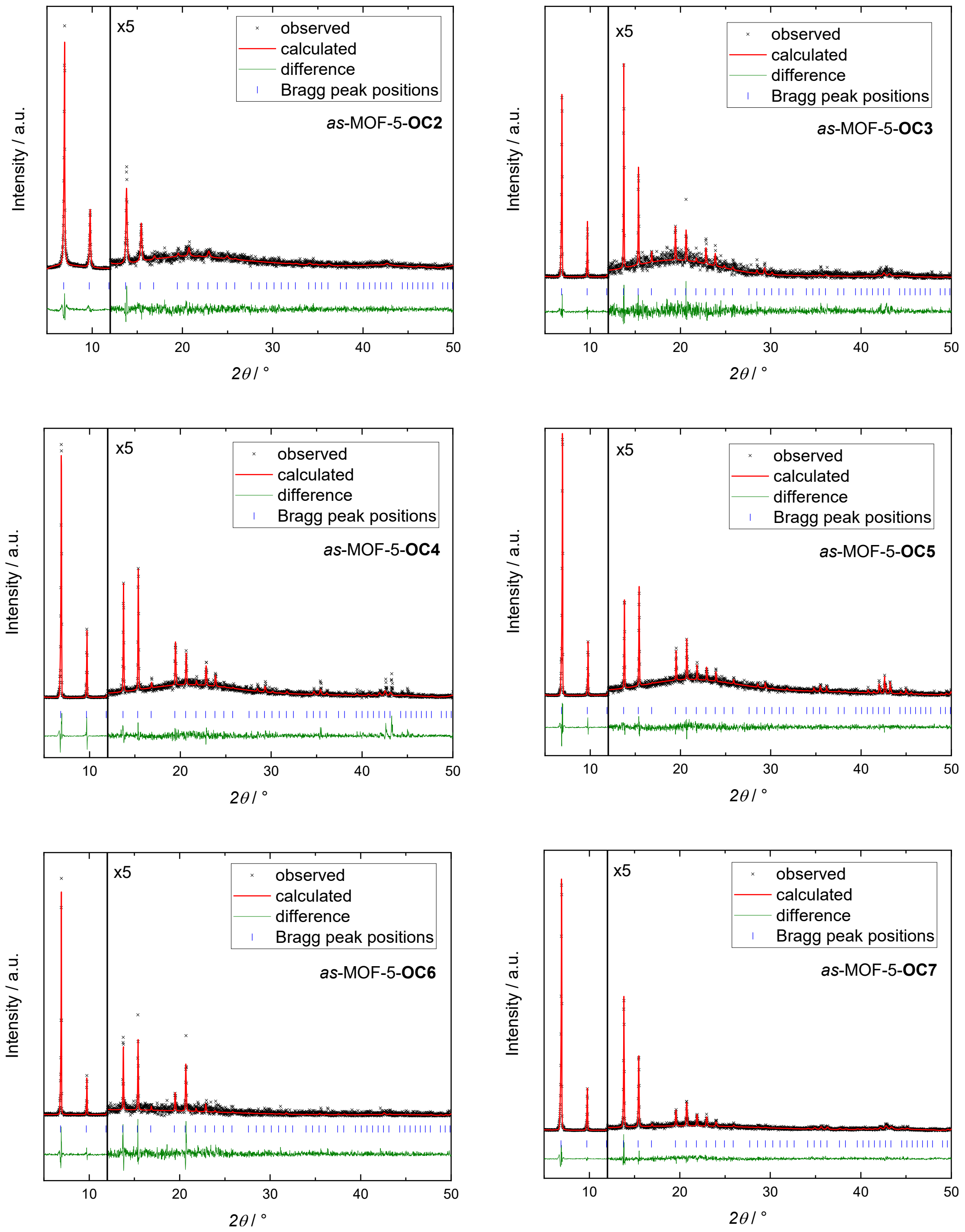

Figure 8.29: PXRD patterns with profile fits (Pawley method) of as-synthesized MOF-5-**OC2** to MOF-5-**OC7**.

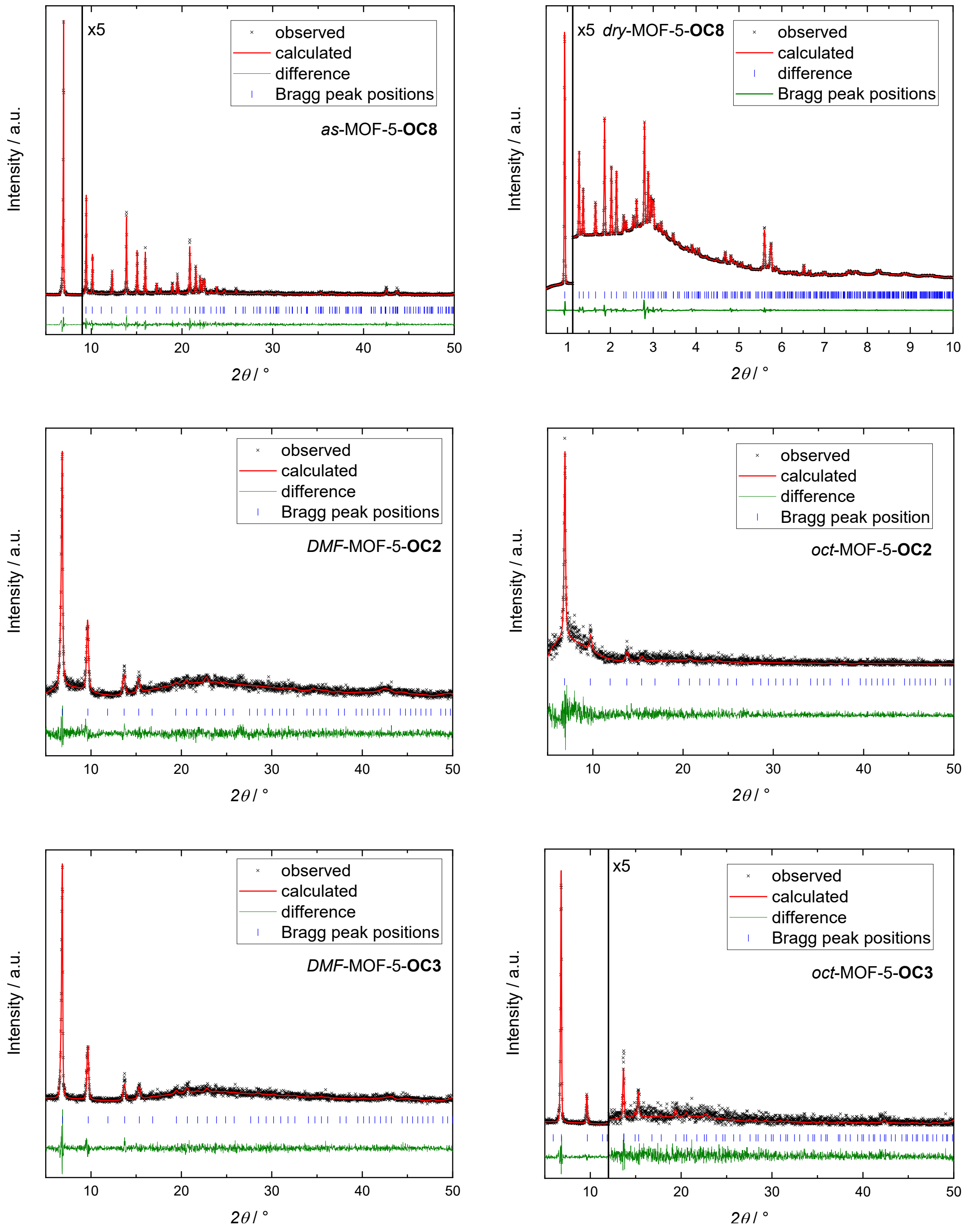

Figure 8.30: PXRD patterns with profile fits (Pawley method) of as-synthesized and *dry*-MOF-5-**OC8** (top row). The pattern of *dry*-MOF-5-**OC8** was recorded at beamline P02.1 at DESY (Deutsches Elektronen-Synchrotron, Hamburg, Germany) with a monochromatic X-ray beam (λ = 0.2073 Å). Furthermore, PXRD patterns with profile fits (Pawley method) of MOF-5-**OC2** (middle row) and MOF-5-**OC3** (bottom row) reinfiltrated with DMF (left) or *n*-octane (right) are shown.

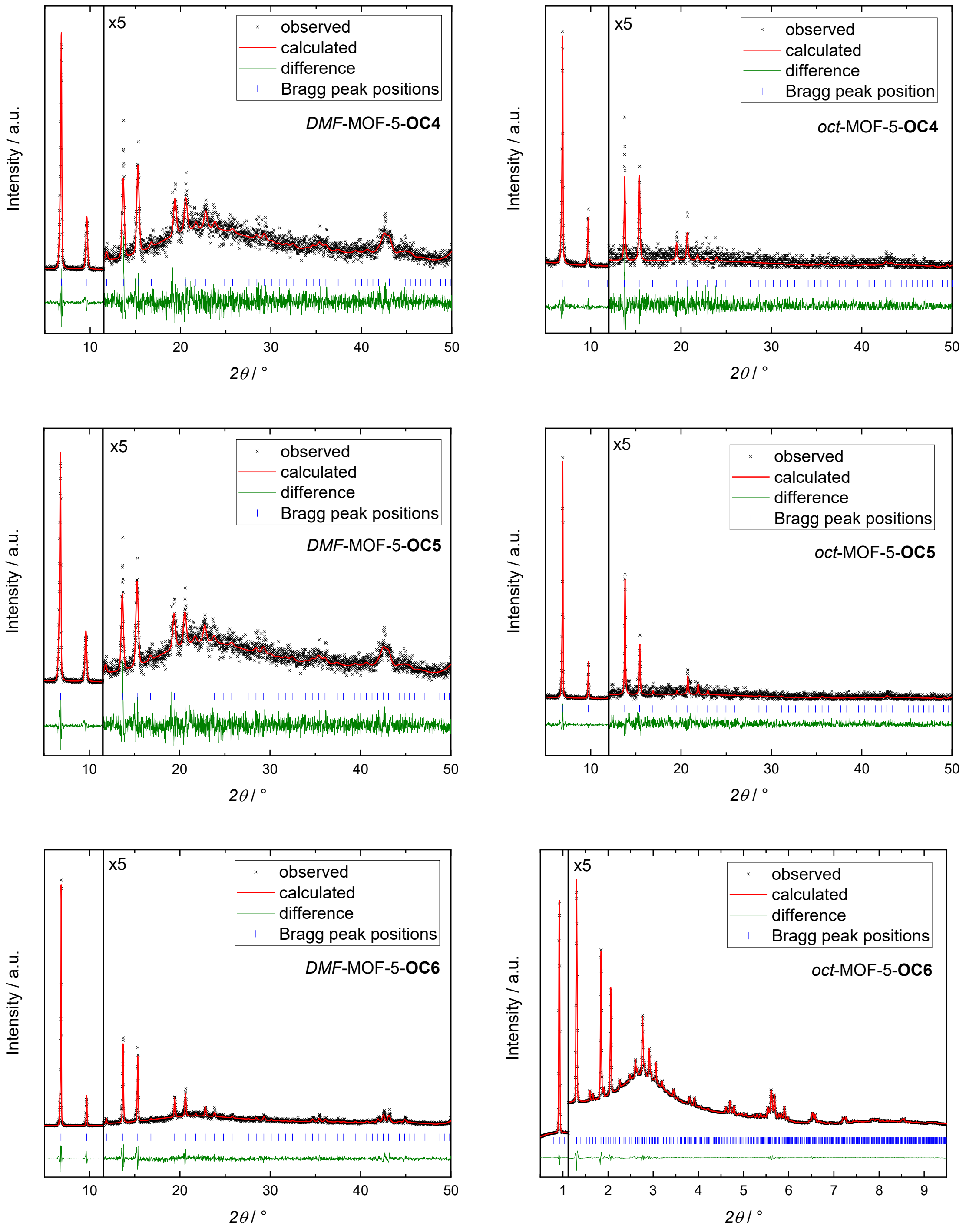

Figure 8.31: PXRD patterns with profile fits (Pawley method) of MOF-5-**OC4** to MOF-5-**OC6** reinfiltrated with DMF (left) or *n*-octane (right). The pattern of *oct*-MOF-5-**OC6** was recorded at beamline P02.1 at DESY (Deutsches Elektronen-Synchrotron, Hamburg, Germany) with a monochromatic X-ray beam ($\lambda = 0.2073$ Å).

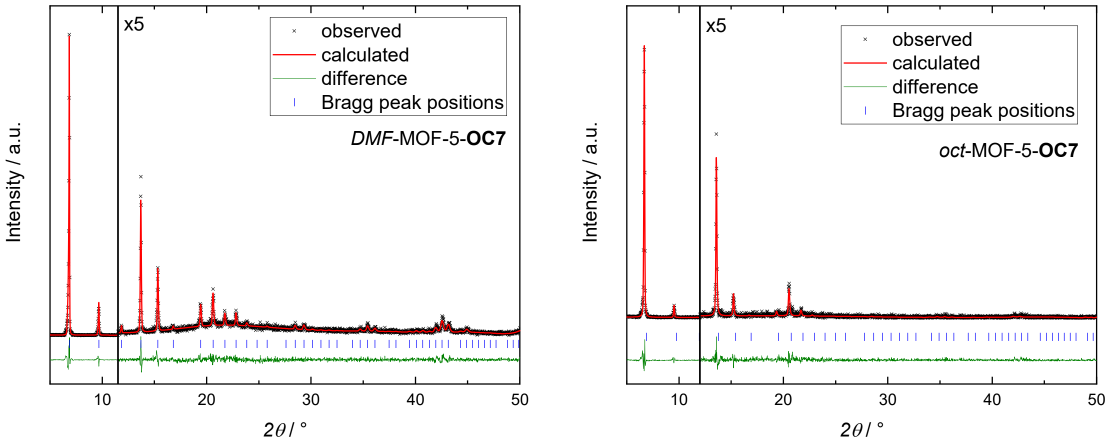

Figure 8.32: PXRD patterns with profile fits (Pawley method) of MOF-5-**OC7** reinfiltrated with DMF (left) or *n*-octane (right).

Tables 8.25: Unit cell parameters *a*, *b*, *c*, and cell volume *V* determined by profile fitting (Pawley method) of the PXRD patterns and the corresponding R_{wp}, R_{exp} and χ^2 values for the MOF-5-**OCX** in various solvated states.

Compound	*as*-MOF-5-**OC2**	*DMF*-MOF-5-**OC2**	*oct*-MOF-5-**OC2**
crystal system	cubic	cubic	cubic
space group	$Pm\bar{3}m$	$Pm\bar{3}m$	$Pm\bar{3}m$
a / Å	12.913(3)	12.952(10)	12.8604(2)
b / Å	12.913(3)	12.952(10)	12.860(2)
c / Å	12.913(3)	12.952(10)	12.860(2)
a / °	90	90	90
β / °	90	90	90
γ / °	90	90	90
V / Å^3	2153.6(18)	2173(5)	2127.0(12)
R_{wp}	20. 55	18.62	39.84
R_{exp}	16.19	17.12	38.75
χ^2	1.61	1.18	1.06

Compound	*as*-MOF-5-**OC3**	*DMF*-MOF-5-**OC3**	*oct*-MOF-5-**OC3**
crystal system	cubic	cubic	cubic
space group	$Pm\bar{3}m$	$Pm\bar{3}m$	$Fm\bar{3}m$
a / Å	12.934(2)	12.895(7)	25.852(13)
b / Å	12.934(2)	12.895(7)	25.852 (13)
c / Å	12.934(2)	12.895(7)	25.852(13)
a / °	90	90	90
β / °	90	90	90
γ / °	90	90	90
V / Å^3	2163.8(10)	2144(4)	17277(27)
R_{wp}	29.92	21.55	36.65
R_{exp}	26.56	19.77	32.75
χ^2	1.27	1.19	1.25

Compound	*as*-MOF-5-**OC4**	*DMF*-MOF-5-**OC4**	*oct*-MOF-5-**OC4**
crystal system	cubic	cubic	cubic
space group	$Pm\bar{3}m$	$Pm\bar{3}m$	$Pm\bar{3}m$
a / Å	12.9395(13)	12.933(5)	12.889(5)
b / Å	12.9395(13)	12.933(5)	12.889(5)
c / Å	12.9395(13)	12.933(5)	12.889(5)
α / °	90	90	90
β / °	90	90	90
γ / °	90	90	90
V / Å^3	2166.5(7)	2163(2)	2141(2)
R_{wp}	22.72	18.46	40.18
R_{exp}	15.29	16.72	37.00
χ^2	2.21	1.22	1.18

Compound	*as*-MOF-5-**OC5**	*DMF*-MOF-5-**OC5**	*oct*-MOF-5-**OC5**
crystal system	cubic	cubic	cubic
space group	$Pm\bar{3}m$	$Pm\bar{3}m$	$Pm\bar{3}m$
a / Å	12.9202(6)	12.900(2)	12.853(3)
b / Å	12.9202(6)	12.900(2)	12.853(3)
c / Å	12.9202(6)	12.900(2)	12.853(3)
α / °	90	90	90
β / °	90	90	90
γ / °	90	90	90
V / Å^3	2156.8(3)	2146.8(9)	2123(2)
R_{wp}	18.03	19.27	38.40
R_{exp}	14.75	15.38	35.96
χ^2	1.49	1.57	1.14

Compound	*as*-MOF-5-**OC6**	*DMF*-MOF-5-**OC6**	*oct*-MOF-5-**OC6**
crystal system	cubic	cubic	cubic
space group	$Pm\bar{3}m$	$Pm\bar{3}m$	$Pa\bar{3}$
a / Å	12.924(2)	12.9294(14)	25.7329(2)
b / Å	12.924(2)	12.929414)	25.7329(2)
c / Å	12.924(2)	12.9294(14)	25.7329(2)
α / °	90	90	90
β / °	90	90	90
γ / °	90	90	90
V / Å^3	2158.5(11)	2161.4(7)	17039.9(9)
R_{wp}	38.75	19.76	1.74
R_{exp}	33.97	13.62	0.55
χ^2	1.30	2.10	1.52

Compound	*as*-MOF-5-**OC7**	*DMF*-MOF-5-**OC7**	*oct*-MOF-5-**OC7**
crystal system	cubic	cubic	cubic
space group	$Pm\bar{3}m$	$Pm\bar{3}m$	$Pm\bar{3}m$
a / Å	12.8660(12)	12.9182(12)	12.843(2)
b / Å	12.8660(12)	12.9182(12)	12.843(2)
c / Å	12.8660(12)	12.9182(12)	12.843(2)
α / °	90	90	90
β / °	90	90	90
γ / °	90	90	90
V / Å^3	2129.8(6)	2155.8(6)	2118.5(11)
R_{wp}	21.02	18.51	31.62
R_{exp}	16.58	13.74	26.93
χ^2	1.61	1.81	1.38

Compound	*as*-MOF-5-**OC8**		*dry*-MOF-5-**OC8**	
crystal system	trigonal	rhombohedral	trigonal	rhombohedral
space group	$R\bar{3}$		$R\bar{3}$	
a / Å	17.485(2)	12.862(2)	17.4115(9)	12.8204(5)
b / Å	17.485(2)	12.862(2)	17.4115(9)	12.8204(5)
c / Å	23.913(2)	12.862(2)	23.870(2)	12.8204(5)
α / °	90	85.639 (8)	90	85.539(5)
β / °	90	85.639 (8)	90	85. 539(5)
γ / °	120	85.639 (8)	120	85. 539(5)
V / Å^3	6331.0(16)	2110.3(5)	6267.1(9)	2089.0(3)
R_{wp}	23.74		1.41	1.41
R_{exp}	18.85		1.09	1.09
χ^2	1.59		1.68	1.68

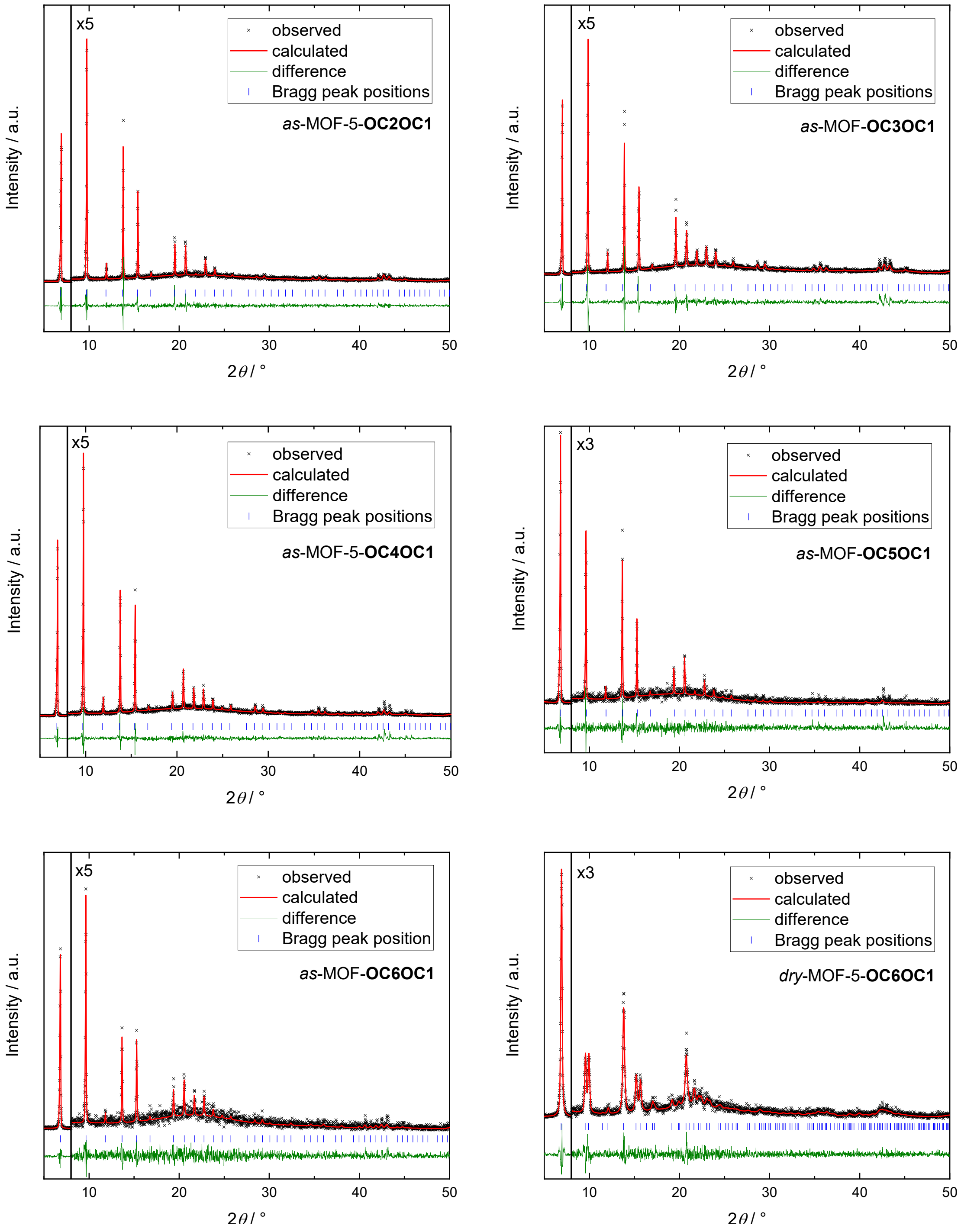

Figure 8.33: PXRD patterns with profile fits (Pawley method) of as-synthesized MOF-5-**OC2OC1** to MOF-5-**OC6OC1** and *dry*-MOF-5-**OC6OC1**.

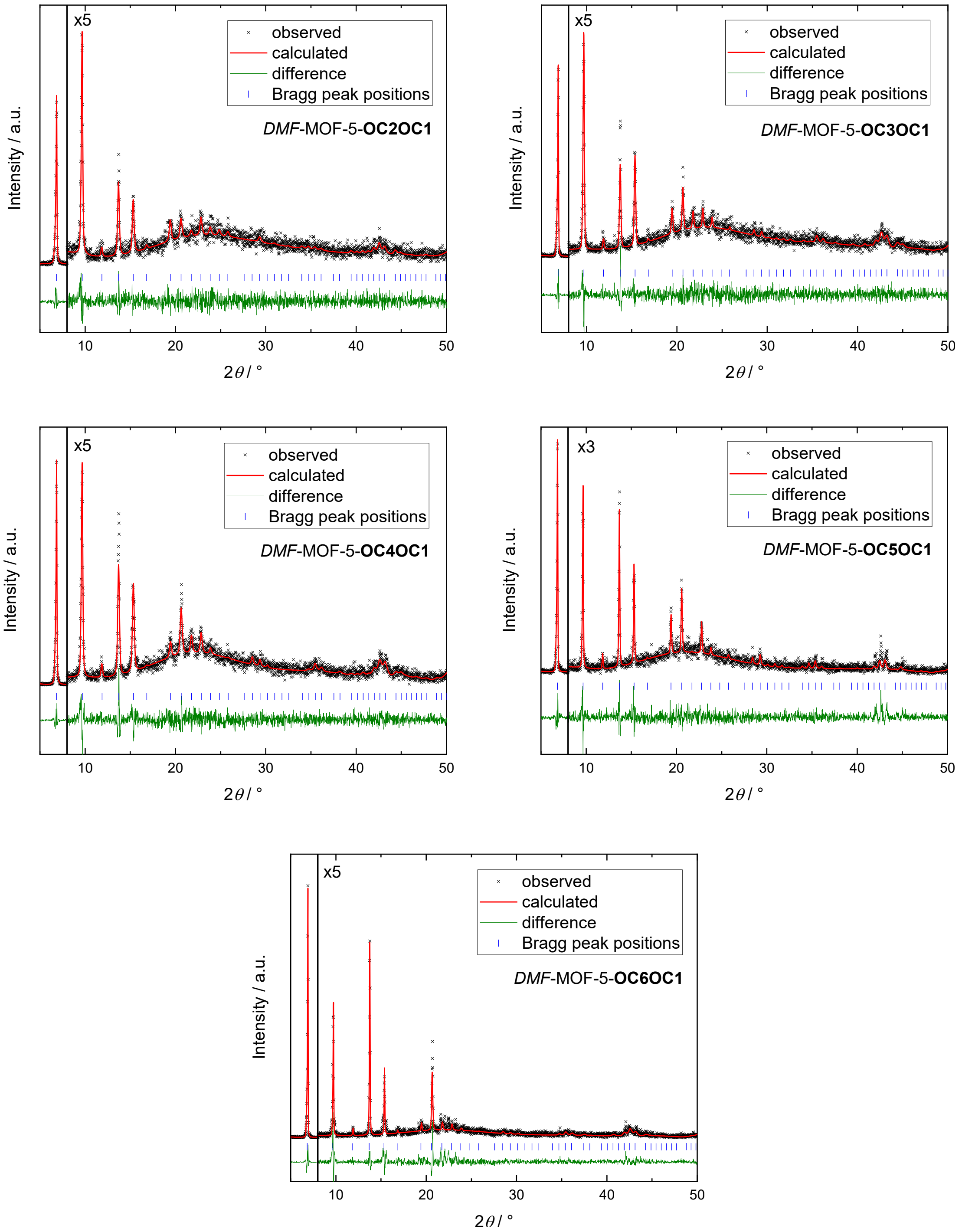

Figure 8.34: PXRD patterns with profile fits (Pawley method) of MOF-5-**OC2OC1** to MOF-5-**OC6OC1** reinfiltrated with DMF.

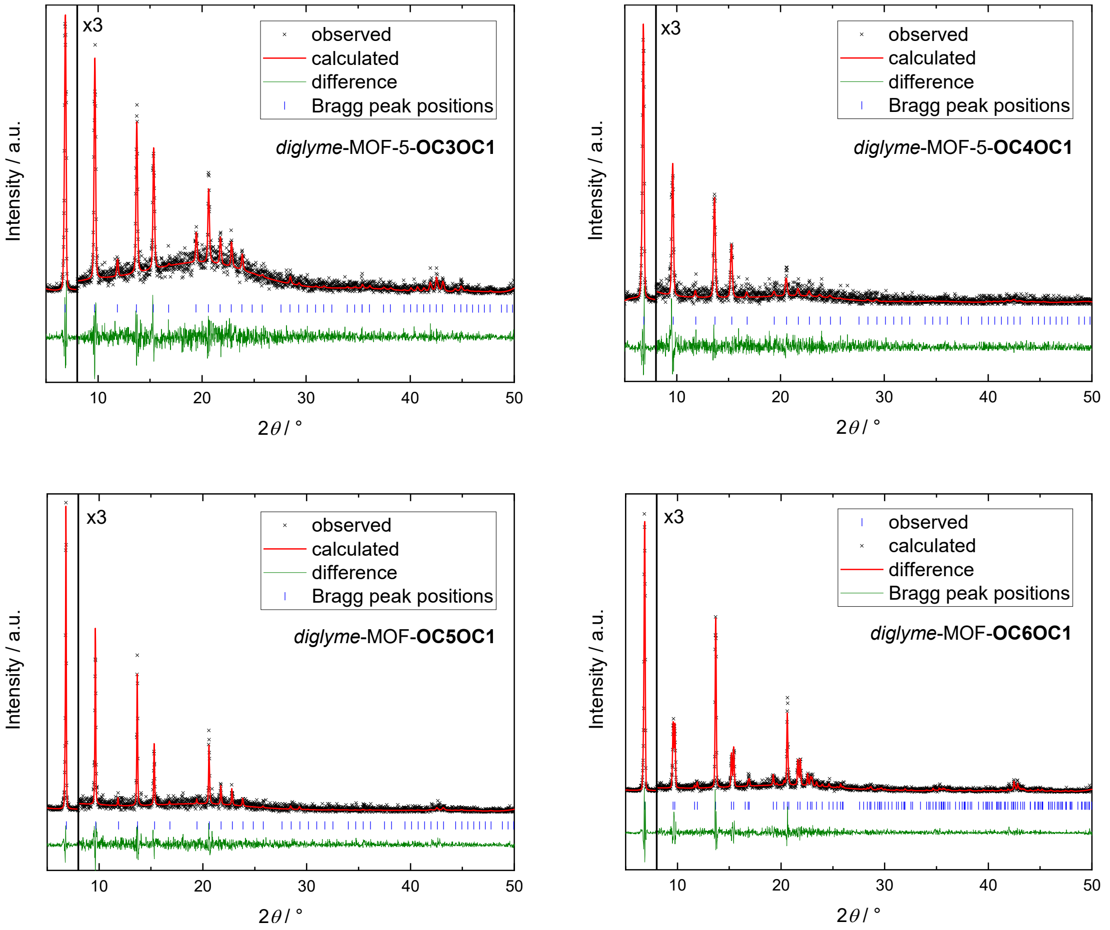

Figure 8.35: PXRD patterns with profile fits (Pawley method) of MOF-5-**OC3OC1** to MOF-5-**OC6OC1** reinfiltrated with diglyme.

Table 8.26: Unit cell parameters *a*, *b*, *c*, and cell volume *V* determined by profile fitting (Pawley method) of the PXRD patterns and the corresponding R_{wp}, R_{exp} and χ^2 values for the MOF-5-**OCYOC1** in various solvated states.

Compound	*as*-MOF-5-**OC2OC1**	*as*-MOF-5-**OC3OC1**	*as*-MOF-5-**OC4OC1**
crystal system	cubic	cubic	cubic
space group	$Pm\bar{3}m$	$Pm\bar{3}m$	$Pm\bar{3}m$
a / Å	12.8930(12)	12.9206(12)	12.9141(9)
b / Å	12.8930(12)	12.9206(12)	12.9141(9)
c / Å	12.8930(12)	12.9206(12)	12.9141(9)
α / °	90	90	90
β / °	90	90	90
γ / °	90	90	90
V / Å^3	2143.2(6)	2157.0(6)	2153.7(5)
R_{wp}	22.38	21.56	20.83
R_{exp}	15.93	13.29	15.06
χ^2	1.41	1.62	1.38

Compound	*as*-MOF-5-**OC5OC1**	*as*-MOF-5-**OC6OC1**	*dry*-MOF-5-**OC6OC1**	
crystal system	cubic	cubic	rhombohedral	trigonal
space group	$Pm\bar{3}m$	$Pm\bar{3}m$	$R\bar{3}$	
a / Å	12.920(2)	12.952(2)	12.868(5)	17.840(7)
b / Å	12.920(2)	12.952(2)	12.868(5)	17.840(7)
c / Å	12.920(2)	12.952(2)	12.868(5)	23.138(13)
α / °	90	90	87.77(2)	90
β / °	90	90	87.77(2)	90
γ / °	90	90	87.77(2)	120
V / Å^3	2156.5(11)	2172.7(12)	2130(2)	6377(6)
R_{wp}	32.60	30.31	21.32	
R_{exp}	28.36	27.33	19.68	
χ^2	1.15	1.11	1.08	

Compound	*DMF*-MOF-5-**OC2OC1**	*DMF*-MOF-5-**OC3OC1**	*DMF*-MOF-5-**OC4OC1**
crystal system	cubic	cubic	cubic
space group	$Pm\bar{3}m$	$Pm\bar{3}m$	$Pm\bar{3}m$
a / Å	12.917(4)	12.894(3)	12.897(3)
b / Å	12.917(4)	12.894(3)	12.897(3)
c / Å	12.917(4)	12.894(3)	12.897(3)
α / °	90	90	90
β / °	90	90	90
γ / °	90	90	90
V / Å^3	2155(2)	2143.6(14)	2145.0(15)
R_{wp}	19.11	19.99	18.57
R_{exp}	18.07	17.61	16.19
χ^2	1.06	1.14	1.15

Compound	*DMF*-MOF-5-**OC5OC1**	*DMF*-MOF-5-**OC6OC1**
crystal system	cubic	cubic
space group	$Pm\bar{3}m$	$Pm\bar{3}m$
a / Å	12.939(2)	12.9269(18)
b / Å	12.939(2)	12. 9269(18)
c / Å	12.939(2)	12. 9269(18)
α / °	90	90
β / °	90	90
γ / °	90	90
V / Å^3	2166.2(11)	2160.1(9)
R_{wp}	27.50	30.05
R_{exp}	23.58	22.11
χ^2	1.17	1.36

Compound	*diglyme*-MOF-5-**OC3OC1**	*diglyme*-MOF-5-**OC4OC1**	*diglyme*-MOF-5-**OC5OC1**
crystal system	cubic	cubic	cubic
space group	$Pm\bar{3}m$	$Pm\bar{3}m$	$Pm\bar{3}m$
a / Å	12.931(2)	12.941(3)	12.909(2)
b / Å	12.931(2)	12.941(3)	12.909(2)
c / Å	12.931(2)	12.941(3)	12.909(2)
α / °	90	90	90
β / °	90	90	90
γ / °	90	90	90
V / Å^3	2162.4(11)	2167.0(12)	2151.1(11)
R_{wp}	25.41	33.85	35.13
R_{exp}	22.37	32.03	33.00
χ^2	1.14	1.06	1.06

Compound	*diglyme*-MOF-5-**OC6OC1**	
crystal system	rhombohedral	trigonal
space group	$R\bar{3}$	
a / Å	12.935(2)	18.133(3)
b / Å	12.935(2)	18.133(3)
c / Å	12.935(2)	22.788(4)
α / °	89.008(11)	90
β / °	89.008(11)	90
γ / °	89.008(11)	120
V / Å^3	2163.2(6)	6489(2)
R_{wp}	30.12	
R_{exp}	26.62	
χ^2	1.28	

Rietveld refinement of *dry*-MOF-5-**OC7**

The starting structural model was based on the single crystal structure of rhombohedral *as*-MOF-5-**OC8**, which was modified by reducing the linker carbon chain lengths from -**OC8** to -**OC7**. A profile fit (Pawley method) gave unit cell and background parameters, which were taken over into the refinement using the Rietveld method.

The obtained model was refined against synchrotron powder diffraction data (Deutsches Elektronen Synchrotron, DESY, beamline P02.1, λ = 0.2073 Å) in a 2θ range from 0.5° to

12.3°. In initial refinement steps, only zinc and oxygen atom positions were refined applying bond distance (Zn–O, Zn–Zn) and angle (Zn–O–Zn, O–Zn–O) restraints according to values of the crystal structure of *as*-MOF-5-**OC8**. The organic linker (except for the carboxylate-oxygen atoms) of the framework was described as a rigid body (using a Z-matrix expression) of which the carbon atom positions (except for those belonging to the alkyl groups) were refined previously using distance and angle restraints as before. Additionally, a dummy atom was placed on the centre of inversion located at the centre of the linker's phenyl ring to further restrain the associated carbon atom positions using distance restraints. Within later cycles, all alkyl carbon atom positions were refined by variation of their corresponding Z-matrix parameters. At this, C–C bond distances and angles were restrained to an interval of 1.51-1.55 Å and 108-112°, respectively, while the O(ether)–C distance was limited to range from 1.28 to 1.36 Å. Further, translational, and torsional movement of the rigid body was enabled during this stage of the refinement. Displacement parameters (b_{eq}) were refined as three groups of equal values ((1) zinc atoms, (2) all oxygen and phenyl- and carboxylate carbon atoms, (3) alkyl chain carbon atoms. The final Rietveld plot and resulting crystallographic data are given below.

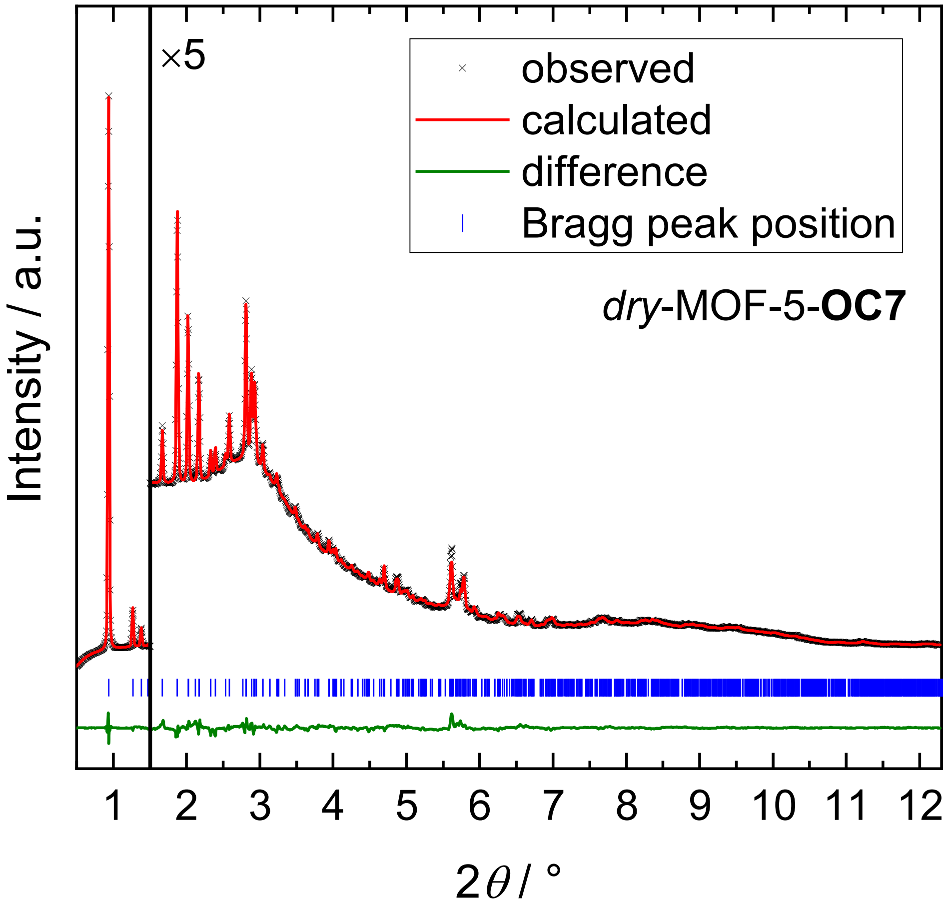

Figure 8.36: Final Rietveld fit of PXRD data of *dry*-MOF-5-**OC7** (λ = 0.2073 Å).

Table 8.27: Crystallographic data for the Rietveld refinement of *dry*-MOF-5-**OC7** (CCDC deposition number 2040923).

Compound	*dry*-MOF-5-**OC7**	
Empirical formula	$C_{66}H_{96}O_{19}Zn_4$	
Formula weight	1454.90	
Calculated density	1.093	
space group	$R\bar{3}$	
Crystal system	trigonal	rhombohedral
a / Å	17.1950(6)	12.7860(5)
b / Å	17.1950(6)	12.7860(5)
c / Å	24.1731(18)	12.7860(5)
α / °	90	84.507(4)
β / °	90	84.507(4)
γ / °	120	84.507(4)
V / Å^3	6189.7(6)	2063.2
Z	3	1
Diffractometer	P02.1, Deutsches Elektronen Synchrotron, Hamburg, Germany	
Temperature / K	300	
Wavelength / Å	0.2073	
No. Reflections	1791	
No. Atoms	19	
No. Restraints	59	
R_p	0.930	
R_{exp}	2.398	
$R_{w\mathrm{p}}$	1.356	
χ^2	0.320	
R_{Bragg}	0.591	

Fitting of the FSP of *dry*-MOF-5-**OC2** to -**OC6** and *dry*-MOF-5-**OC2OC1** and *dry*-MOF-5-**OC5OC1**

The first scattering peak (FSP) found for the materials *dry*-MOF-5-**OC2** to *dry*-MOF-5-**OC6** was fitted using split pseudo-Voigt (**OC3**-**OC6**) or PearsonVII (**OC2**) peak profile functions as implemented in the TOPAS-*academic v6* software package. In this process only the first scattering peak and the corresponding background function were refined. The obtained parameters are given below.

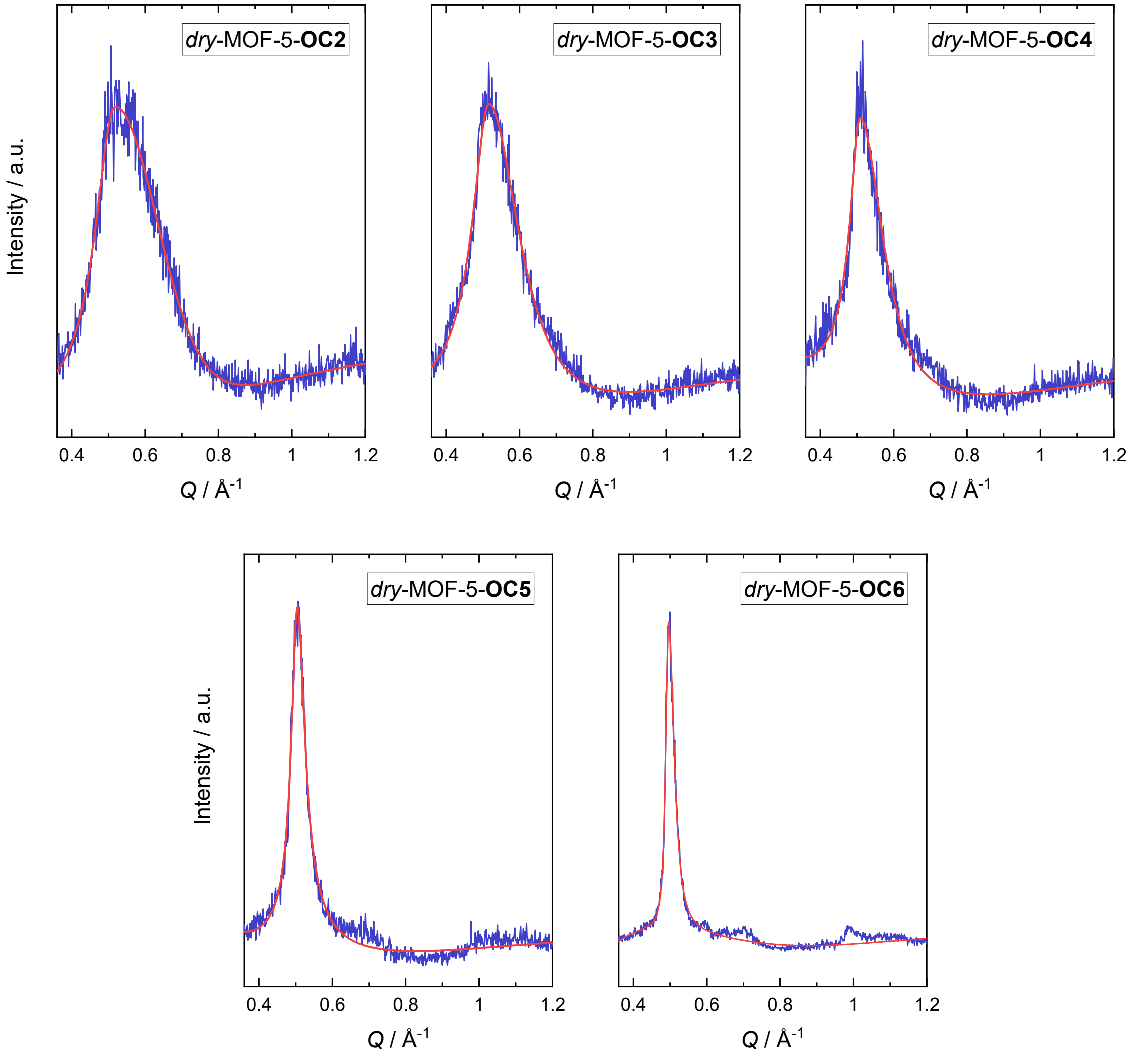

Figure 8.37: PXRD pattern with fit of the single FSP of *dry*-MOF-5-**OC2** to *dry*-MOF-5-**OC6**.

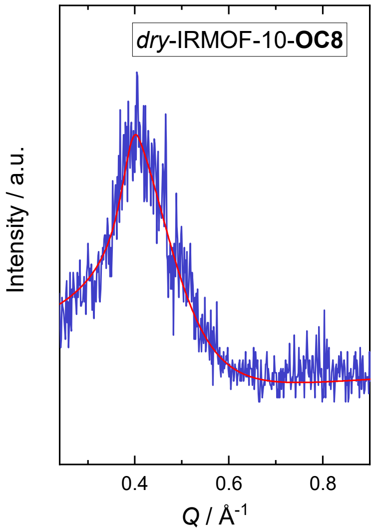

Figure 8.38: PXRD pattern with fit of the single FSP of *dry*-IRMOF-10-**OC8**.

PXRD pattern of *dry*-MOF-5-**OC3** activated from *n*-hexane

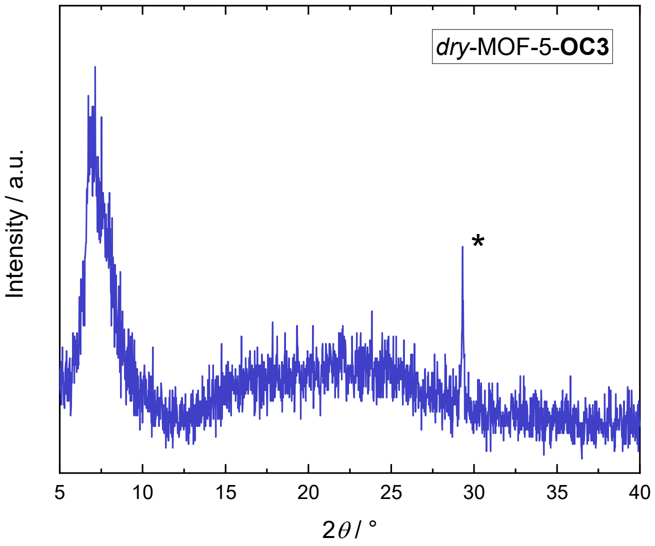

Figure 8.39: PXRD pattern of *dry*-MOF-5-**OC3** activated from the low surface tension liquid *n*-hexane. The marked reflection (*) stems from the material of the plastic sample holder used to record the pattern.

PXRD pattern of *dry*-MOF-5-**OCYOC1** treated with *n*-octane

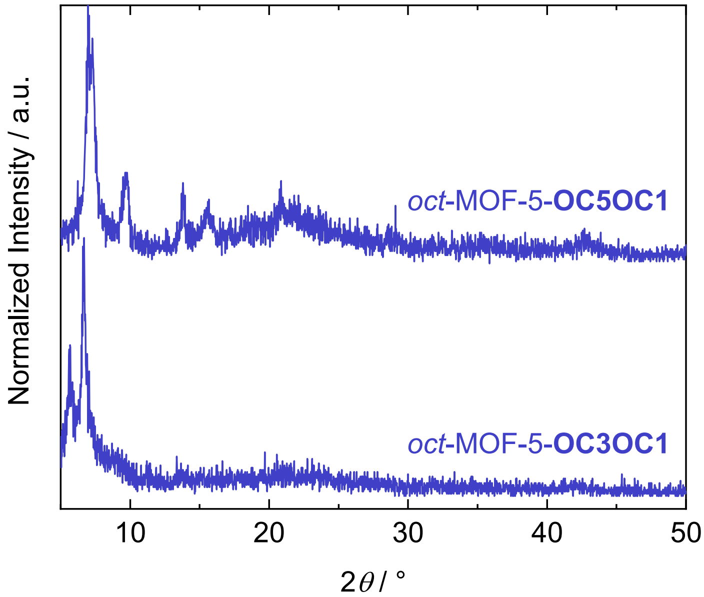

Figure 8.40: PXRD pattern of *dry*-MOF-5-**OC3OC1** and *dry*-MOF-5-**OC5OC1** solvated with *n*-octane. Apparently, the materials remain in their distorted non-crystalline phases.

8.2.2 Single Crystal X-ray Diffraction

Single Crystal Structure Determination

All cubic *as-synthesized* MOF-5-**OCX** (**X** = 2 – 7) and -**OCYOC1** (**Y** = 5 – 6) crystallize in the cubic space group $Pm\bar{3}m$ as a result of disorder of both the zinc-oxo-clusters and the phenyl ring of the bdc units. Therefore, the Zn and carboxylate O atoms are equally disordered by symmetry over two sites as well as the phenyl rings. Additionally, all ether O atoms are equally disordered over 4 sites. Solvent molecules or the alkyl chains could not be located due to severe disorder, consequently, if present, the corresponding electron density within the pores was subtracted from the experimental data by use of solvent masking as implemented in Olex2[233] (the number of masked electrons per unit cell are given in Table 8.28 to Table 8.31).

The crystal structure of *as*-MOF-5-**OCX** (**X** = 2 – 7) in the space group $Pm\bar{3}m$ feature a unit cell with lattice parameter $a \approx 12.8$ Å. Hence, the unit cell of these structures is about 8-times smaller than the unit cell of conventional MOF-5 ($a \approx 25.7$ Å, space group symmetry $Fm\bar{3}m$). The resulting two-fold static disorder of the Zn_4O clusters and the organic linkers about the 4-fold rotation axis oriented along the $\langle 100 \rangle$ direction, has previously been observed for several other MOF-5 derivatives[99], including IRMOF-5[28], which is identical to *as*-MOF-5-**OC5**. The static disorder potentially allows for the presence of a twisted configuration of the carboxylate groups of the bdc-type linkers, which generates a translational symmetry instead of inversion symmetry between neighbouring $[Zn_4O]^{6+}$ clusters. Nevertheless, previous theoretical calculations indicated that the twisted bdc-confirmation of MOF-5 is significantly higher in energy, even for symmetrically substituted bdc-type linkers[251]. This finding is corroborated by the fact that the *as*-MOF-5-**OCX** crystal structures (with **X** = 2 – 7) show very weak and diffuse superstructure reflections on the {hk½} planes. These reflections can be indexed in the larger $Fm\bar{3}m$ unit cell (with $a \approx 25.7$ Å), thus strongly suggesting that the structures of *as*-MOF-5-**OCX** locally feature the same inversion symmetry between neighboring $[Zn_4O]^{6+}$ clusters and no twisted configuration. Note that an all-twisted bdc-configuration exhibiting only translational symmetry between the $[Zn_4O]^{6+}$ clusters would crystallize in a small primitive unit cell (with $a \approx 12.8$ Å) in the polar $P\bar{4}3m$ space group. Thus, the diffuse superstructure reflections are a clear indication of a locally higher symmetry commensurate with a non-twisted structure. Nevertheless, inclusion of the weak and diffuse superstructure reflections in the structure refinement by applying the large unit cell with $Fm\bar{3}m$ symmetry yields the same disordered structural model as in the smaller $Pm\bar{3}m$ cell. Thus, the simpler models of $Pm\bar{3}m$ symmetry are more appropriate to describe the global crystal structures of *as*-MOF-5-**OCX** (**X** = 2 – 7) and are reported here.

Rhombohedral *as*-MOF-5-**OC8** crystallizes in space group $R\bar{3}$ displaying a likewise disordered inorganic building unit. The phenyl ring of the linker is not disordered. The alkyl chains could be resolved and were refined applying a number of bond distance and angle restraints. All carbon atoms of the alkyl chain, except for the ones named C8 and C9, are disordered over two sites and their occupancies were fixed to 0.5 during the refinement. Solvent molecules could not be resolved, and their corresponding electron density was likewise subtracted by masking.

oct-MOF-5-**OC3** was found to crystallize in the face centered cubic space group $Fm\bar{3}m$ as a consequence of the disorder of the Zn and carboxylate O atoms over two sites with fractional occupancies of 0.73/0.27 (instead of the fractional occupancies of 0.5/0.5 found for the other materials crystallizing in the smaller $Pm\bar{3}m$ cell), similar as initially found by M. Eddaoudi *et al.*[28] The fractional occupancies of 0.73/0.27 are also a strong indication that neighboring $[Zn_4O]^{6+}$ clusters are related by inversion symmetry on a local scale. The phenyl ring carbon atoms and ether O atoms of the linker are disordered by symmetry over two and four sites, respectively. Solvent molecules or alkyl chains could not be located due to severe disorder and were therefore subtracted from the experimental data by use of the solvent masking routines of Olex2.

oct-MOF-5-**OC6** was found to crystallize in the primitive cubic space group $Pa\bar{3}$. The crystal used for data collection was twinned, therefore the experimental data were refined applying the merohedral twin law (-1 0 0 0 0 1 0 1 0) and the twinning factor of 0.482(3), which were determined using the TwinRotMat implementation of the PLATON[252] software. Structurally, the Zn and carboxylate O atoms of the inorganic units are disordered over two sites, similar to all the other structures reported above. Free refinement of the occupancies of these sites gave values very close to 0.5, consequently the occupancies were set to fix values of 0.5. Interestingly, and similar to the rhombohedral structure of *as*-MOF-5-**OC8**, the phenyl rings of the bdc type linker are not disordered here. The alkyl chains could be resolved (with disorder over two positions, except for carbon atoms C9, C15 and C16) and were refined applying a number of bond distance and angle restraints. Occupancies of the disordered carbon atoms of the alkyl chains could not be refined freely and were set to fixed values of 0.5/0.5 or 0.35/0.65. Solvent molecules could not be located. Further details to the SCXRD structures of the MOF-5-**OCX** materials can be found in the provided crystallographic information files (CCDC deposition numbers 2040916 to 2040922, 2040924 and 2040925).

Crystal Structure Data

Table 8.28: Crystallographic data of as-synthesized MOF-5-**OC2** to MOF-5-**OC4**.

Compound	*as*-MOF-5-**OC2**	*as*-MOF-5-**OC3**	*as*-MOF-5-**OC4**
Empirical formula	$C_{36}H_{36}O_{19}Zn_4$	$C_{42}H_{48}O_{19}Zn_4$	$C_{48}H_{60}O_{19}Zn_4$
Formula weight / g·mol^{-1}	1034.13	1118.28	1202.44
Temperature / K	250.0(2)	254(2)	293(2)
Crystal system	cubic	cubic	cubic
Space group	$Pm\bar{3}m$	$Pm\bar{3}m$	$Pm\bar{3}m$
a / Å	12.813(2)	12.8791(4)	12.8018(12)
b / Å	12.813(2)	12.8791(4)	12.8018(12)
c / Å	12.813(2)	12.8791(4)	12.8018(12)
α / °	90	90	90
β / °	90	90	90
γ / °	90	90	90
Volume / Å^3	2103.7(10)	2136.3(2)	2098.0(6)
Z	1	1	1
ϱ_{calc} g/cm^3	0.816	0.876	0.952
μ / mm^{-1}	1.164	1.159	1.175
F(000)	524.0	577.0	620.0
Crystal size / mm^3	0.24 × 0.236 × 0.222	0.437 × 0.427 × 0.396	0.479 × 0.444 × 0.284
Radiation	MoKα (λ = 0.71073)	MoKα (λ = 0.71073)	MoKα (λ = 0.71073)
2Θ range for data collection / °	5.506 to 54.98	4.472 to 54.994	5.512 to 54.924
Index ranges	$-16 \leq h \leq 16$, $-16 \leq k \leq 16$, $-16 \leq l \leq 16$	$-16 \leq h \leq 16$, $-16 \leq k \leq 16$, $-16 \leq l \leq 16$	$-4 \leq h \leq 16$, $-16 \leq k \leq 16$, $-11 \leq l \leq 16$
Reflections collected	25791	50399	4002
Independent reflections	544 [R_{int}= 0.1614, R_{sigma}= 0.0726]	548 [R_{int}= 0.0714, R_{sigma}= 0.0142]	541 [R_{int}= 0.0772, R_{sigma}= 0.0432]
Data/restraints/parameters	544/13/29	548/13/32	541/20/26
Goodness-of-fit on F^2	1.209	1.220	1.176
Final R indexes [I ≥ 2σ(I)]	R_1= 0.0974, wR_2= 0.2799	R_1= 0.0947, wR_2= 0.2836	R_1= 0.1200, wR_2= 0.3425
Final R indexes [all data]	R_1= 0.1275, wR_2= 0.3612	R_1= 0.1119, wR_2= 0.3160	R_1= 0.1511, wR_2= 0.3885
Largest diff. peak/hole / e·Å^{-3}	0.46/-0.92	0.53/-0.58	0.47/-0.60
Number of masked electrons	246.0	0.0	108.6
CCDC deposition number	2040917	2040918	2040919

Table 8.29: Crystallographic data of as-synthesized MOF-5-**OC5** to MOF-5-**OC7**.

Compound	*as*-MOF-5-**OC5**	*as*-MOF-5-**OC6**	*as*-MOF-5-**OC7**
Empirical formula	$C_{54}H_{72}O_{19}Zn_4$	$C_{60}H_{84}O_{19}Zn_4$	$C_{66}H_{96}O_{19}Zn_4$
Formula weight / g·mol^{-1}	1286.59	1370.75	1454.90
Temperature / K	284.78(2)	250.0(2)	110.02(2)
Crystal system	cubic	cubic	cubic
Space group	$Pm\bar{3}m$	$Pm\bar{3}m$	$Pm\bar{3}m$
a / Å	12.8898(15)	12.9040(12)	12.8526(5)
b / Å	12.8898(15)	12.9040(12)	12.8526(5)
c / Å	12.8898(15)	12.9040(12)	12.8526(5)
α / °	90	90	90
β / °	90	90	90
γ / °	90	90	90
Volume / Å^3	2141.6(7)	2148.7(6)	2123.1(2)
Z	1	1	1
ϱ_{calc} g/cm^3	0.998	1.068	1.138
μ / mm^{-1}	1.154	1.163	1.740
F(000)	668.0	722.0	764.0
Crystal size / mm^3	0.23 × 0.18 × 0.124	0.41 × 0.336 × 0.29	0.223 × 0.16 × 0.119
Radiation	MoKα (λ = 0.71073)	MoKα (λ = 0.71073)	CuKα (λ = 1.54178)
2Θ range for data collection / °	4.468 to 54.09	5.468 to 57.392	9.732 to 148.906
Index ranges	$-16 \le h \le 15$, $-15 \le k \le 16$, $-16 \le l \le 11$	$-17 \le h \le 16$, $-16 \le k \le 17$, $-17 \le l \le 9$	$-13 \le h \le 12$, $-15 \le k \le 15$, $-16 \le l \le 10$
Reflections collected	7925	8092	10658
Independent reflections	532 [R_{int}= 0.0462, R_{sigma}= 0.0204]	611 [R_{int}= 0.0565, R_{sigma}= 0.0249]	490 [R_{int}= 0.0264, R_{sigma}= 0.0112]
Data/restraints/parameters	532/13/29	611/1/32	490/7/32
Goodness-of-fit on F^2	1.584	1.119	1.137
Final R indexes [$I \ge 2\sigma(I)$]	R_1= 0.0972, wR_2= 0.3011	R_1= 0.0819, wR_2= 0.2352	R_1= 0.0616, wR_2= 0.1780
Final R indexes [all data]	R_1= 0.1258, wR_2= 0.3729	R_1= 0.0982, wR_2= 0.2717	R_1= 0.0632, wR_2= 0.1835
Largest diff. peak/hole / e·Å^{-3}	0.57/-0.78	0.34/-0.72	0.29/-0.35
Number of masked electrons	0.0	328.0	84.8
CCDC deposition number	2040920	2040921	2040922

Table 8.30: Crystallographic data of as-synthesized MOF-5-**OC8** and *n*-octane resolvated MOF-5-**OC3** and MOF-5-**OC6**.

Compound	*as*-MOF-5-**OC8**	*oct*-MOF-5-**OC3**	*oct*-MOF-5-**OC6**
Empirical formula	$C_{72}H_{108}O_{19}Zn_4$	$C_{42}H_{48}O_{19}Zn_4$	$C_{60}H_{84}O_{19}Zn_4$
Formula weight / g·mol^{-1}	1539.06	1118.28	1370.75
Temperature / K	293(2)	250(2)	250(2)
Crystal system	trigonal	cubic	cubic
Space group	$R\bar{3}$	$Fm\bar{3}m$	$Pa\bar{3}$
a / Å	17.7158(10)	25.7952(9)	25.7145(6)
b / Å	17.7158(10)	25.7952(9)	25.7145(6)
c / Å	23.4128(11)	25.7952(9)	25.7145(6)
α / °	90	90	90
β / °	90	90	90
γ / °	120	90	90
Volume / Å^3	6363.6(8)	17163.9(18)	17003.3(12)
Z	3	8	8
ϱ_{calc} g/cm^3	1.606	0.866	1.071
μ / mm^{-1}	1.568	1.145	1.712
F(000)	3248.0	4576.0	5728.0
Crystal size / mm^3	0.208 × 0.196 × 0.162	0.208 × 0.205 × 0.133	0.187 × 0.145 × 0.076
Radiation	MoKα ($\lambda = 0.71073$)	MoKα ($\lambda = 0.71073$)	CuKα ($\lambda = 1.54178$)
2Θ range for data collection / °	4.376 to 64.906	4.466 to 60.968	3.436 to 144.808
Index ranges	$-26 \leq h \leq 25$, $-26 \leq k \leq 25$, $-35 \leq l \leq 35$	$-36 \leq h \leq 23$, $-35 \leq k \leq 35$, $-34 \leq l \leq 33$	$-21 \leq h \leq 31$, $-29 \leq k \leq 31$, $-31 \leq l \leq 23$
Reflections collected	17446	19056	90399
Independent reflections	4735 [R_{int}= 0.0578, R_{sigma}= 0.0615]	1356 [R_{int}= 0.0588, R_{sigma}= 0.0234]	5804 [R_{int} = 0.1027, R_{sigma} = 0.0390]
Data/restraints/parameters	4735/53/149	1356/6/46	5804/60/275
Goodness-of-fit on F^2	1.031	1.129	1.123
Final R indexes [I ≥ 2σ(I)]	R_1= 0.0923, wR_2= 0.2707	R_1= 0.0777, wR_2= 0.2353	R_1 = 0.1031, wR_2 = 0.2738
Final R indexes [all data]	R_1= 0.0923, wR_2= 0.2707	R_1= 0.1017, wR_2= 0.2860	R_1 = 0.1160, wR_2 = 0.2873
Largest diff. peak/hole / e·Å^{-3}	0.79/-0.45	0.59/-1.15	0.48/-0.41
Number of masked electrons	36.1	0.0	-
CCDC deposition number	2040916	2040924	2040925

Table 8.31: Crystallographic data of as-synthesized MOF-5-**OC5OC1** and MOF-5-**OC6OC1**.

Compound	*as*-MOF-5-**OC5OC1**	*as*-MOF-5-**OC6OC1**
Empirical formula	$C_{60}H_{84}O_{25}Zn_4$	$C_{66}H_{96}O_{25}Zn_4$
Formula weight / g·mol^{-1}	1466.75	1550.90
Temperature / K	293(2)	250(2)
Crystal system	cubic	cubic
Space group	$Pm\bar{3}m$	$Pm\bar{3}m$
a / Å	12.7929(9)	12.8798(2)
b / Å	12.7929(9)	12.8798(2)
c / Å	12.7929(9)	12.8798(2)
α / °	90	90
β / °	90	90
γ / °	90	90
Volume / Å^3	2093.7(4)	2136.62(10)
Z	1	1
ϱ_{calc} g/cm^3	1.163	1.205
μ / mm^{-1}	1.194	1.814
F(000)	764.0	812.0
Crystal size / mm^3	0.267 × 0.216 × 0.151	0.113 × 0.093 × 0.071
Radiation	MoKα (λ = 0.71073)	CuKα (λ = 1.54178)
2Θ range for data collection / °	4.502 to 58.458	9.712 to 144.358
Index ranges	$-6 \leq h \leq 17$, $-13 \leq k \leq 14$, $-16 \leq l \leq 7$	$-15 \leq h \leq 11$, $-14 \leq k \leq 15$, $-15 \leq l \leq 11$
Reflections collected	4129	11019
Independent reflections	607 [R_{int} = 0.0375, R_{sigma} = 0.0236]	480 [R_{int} = 0.0401, R_{sigma} = 0.0192]
Data/restraints/parameters	607/6/35	480/6/35
Goodness-of-fit on F^2	0.933	1.176
Final R indexes [I ≥ 2σ(I)]	R_1 = 0.0601, wR_2 = 0.1753	R_1 = 0.0712, wR_2 = 0.2143
Final R indexes [all data]	R_1 = 0.0954, wR_2 = 0.2069	R_1 = 0.0747, wR_2 = 0.2253
Largest diff. peak/hole / e·Å^{-3}	0.20/-0.24	0.45/-0.48
Number of masked electrons	65.4	84.3
CCDC deposition number	-	-

Full Precession Images

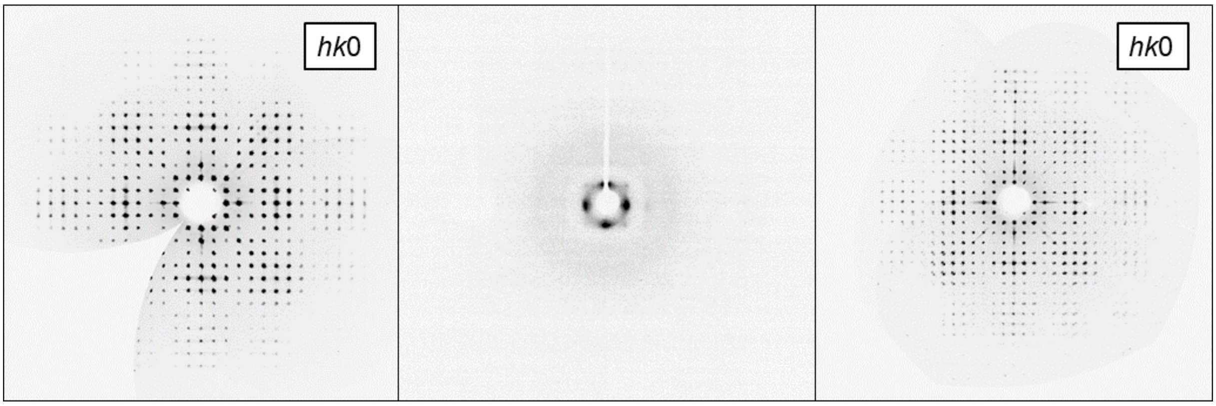

Figure 8.41: Reconstructed precession images of *as*-MOF-5-**OC3** (left) and *oct*-MOF-5-**OC3** (right) showing the *hk*0 layers of reciprocal space. In the middle, a single diffraction pattern of *dry*-MOF-5-**OC3** is shown.

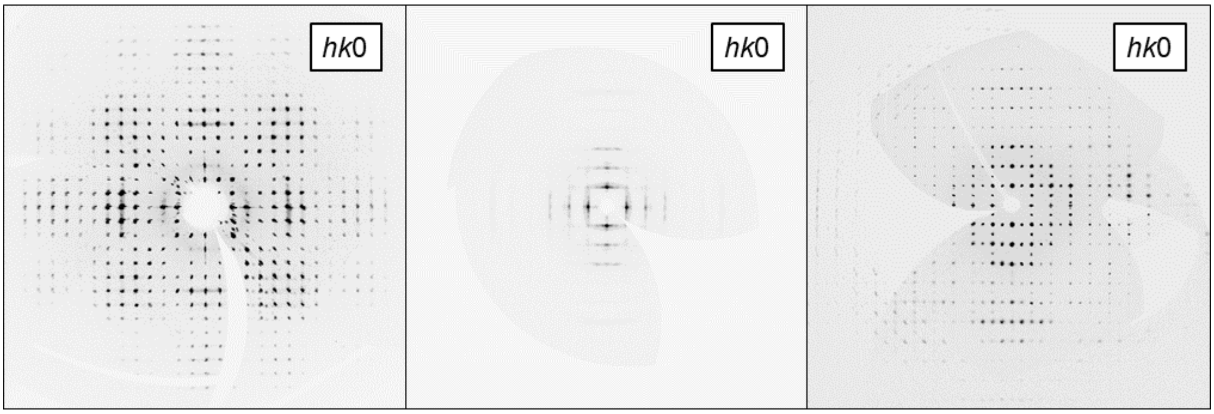

Figure 8.42: Reconstructed precession images of *as*-, *dry*- and *oct*-MOF-5-**OC6** (from left to right) showing the *hk*0 layers of reciprocal space.

8.2.3 Solution ^{1}H NMR Spectroscopy

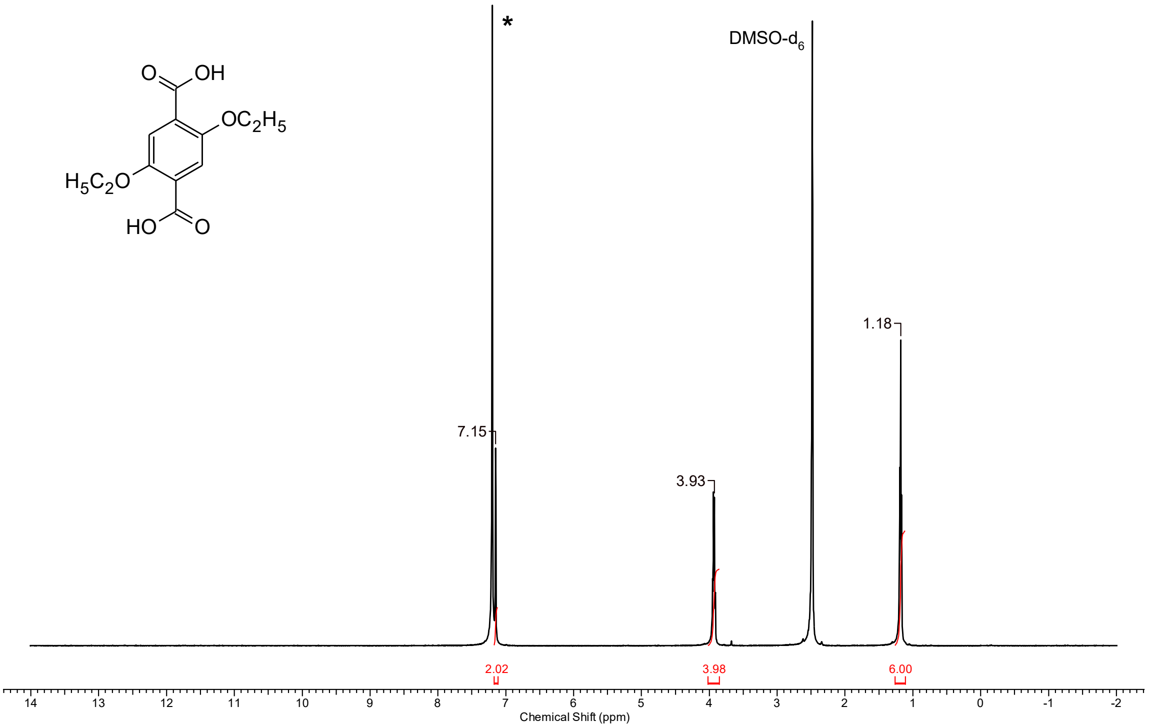

Figure 8.43: ^{1}H NMR spectrum of a digested sample of *dry*-MOF-5-**OC2**. The D_2O signal is marked with an asterisk (*).

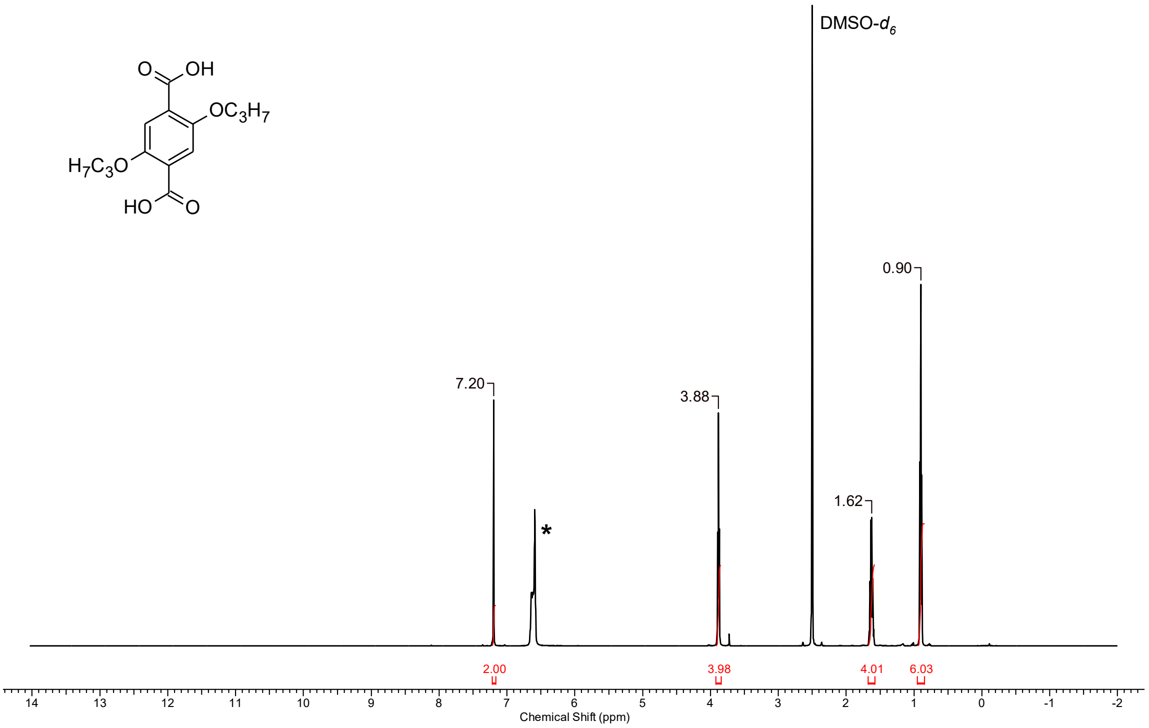

Figure 8.44: ^{1}H NMR spectrum of a digested sample of *dry*-MOF-5-**OC3**. The D_2O signal is marked with an asterisk (*).

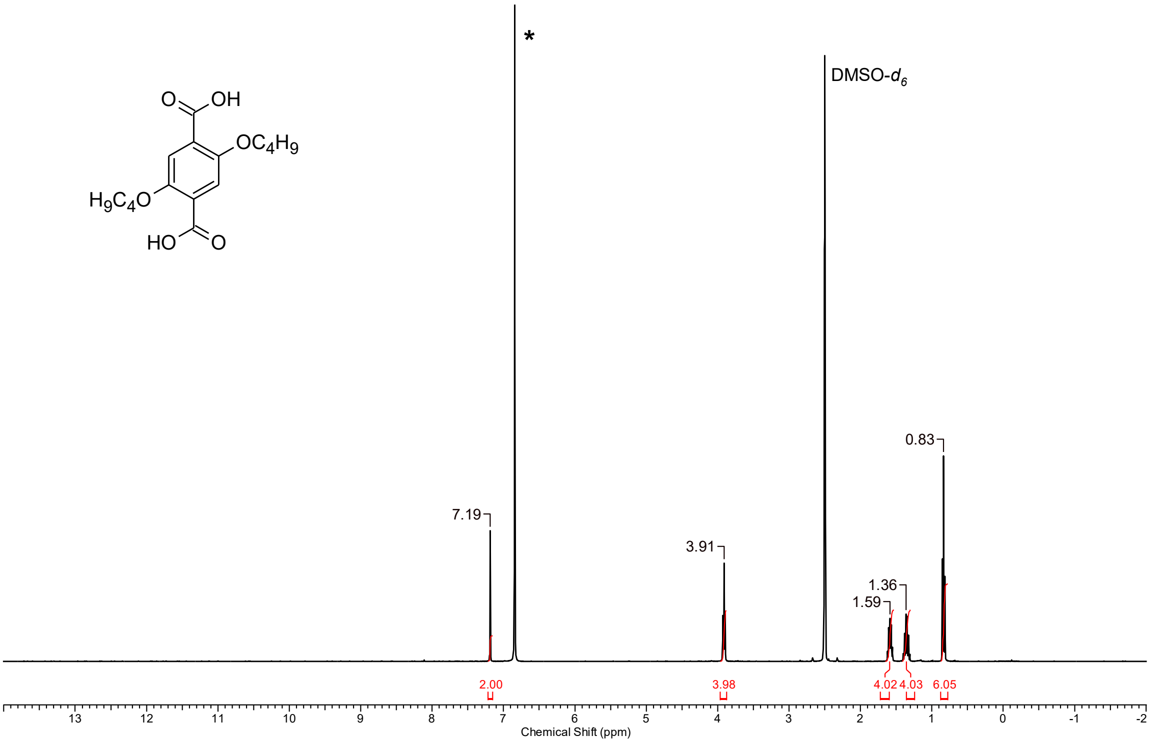

Figure 8.45: ^{1}H NMR spectrum of a digested sample of *dry*-MOF-5-**OC4**. The D_2O signal is marked with an asterisk (*).

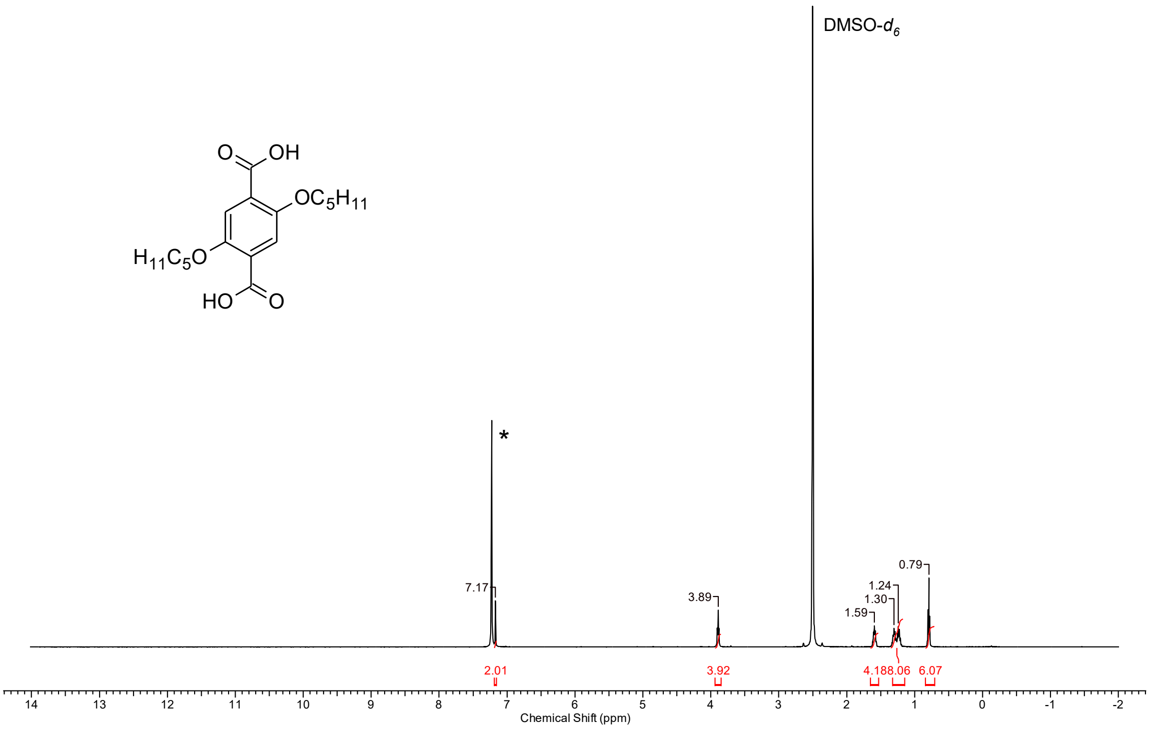

Figure 8.46: ^{1}H NMR spectrum of a digested sample of *dry*-MOF-5-**OC5**. The D_2O signal is marked with an asterisk (*).

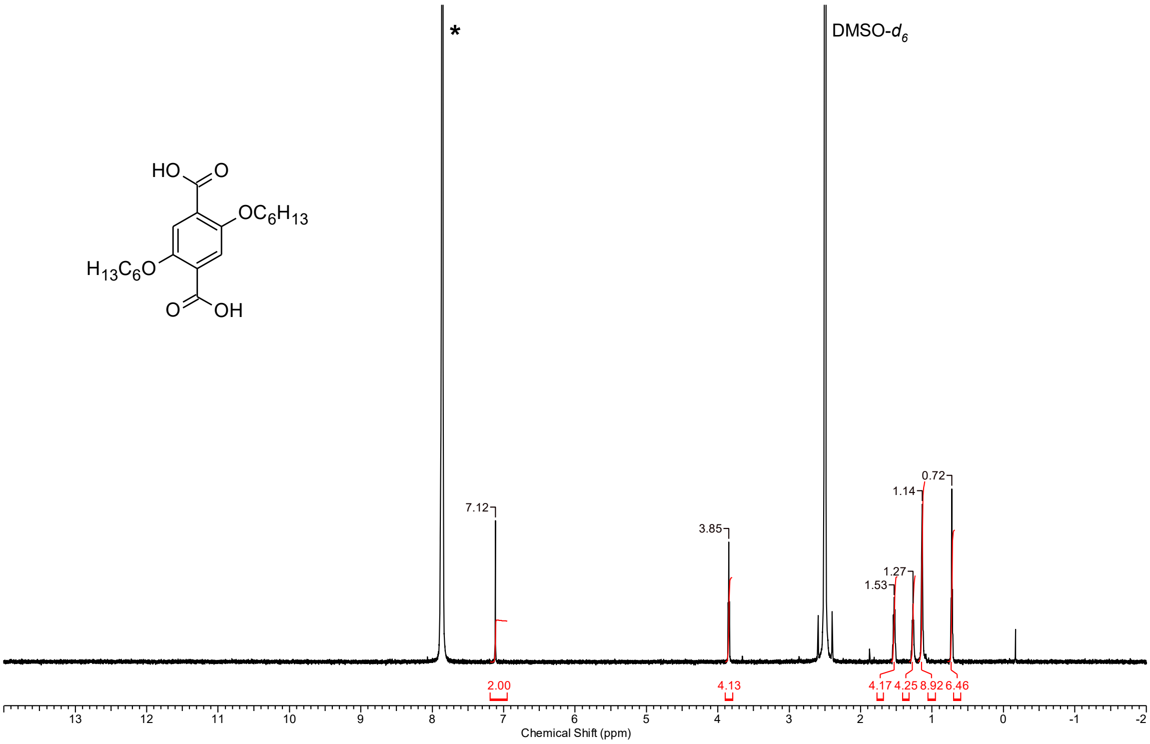

Figure 8.47: ^{1}H NMR spectrum of a digested sample of *dry*-MOF-5-**OC6**. The D_2O signal is marked with an asterisk (*).

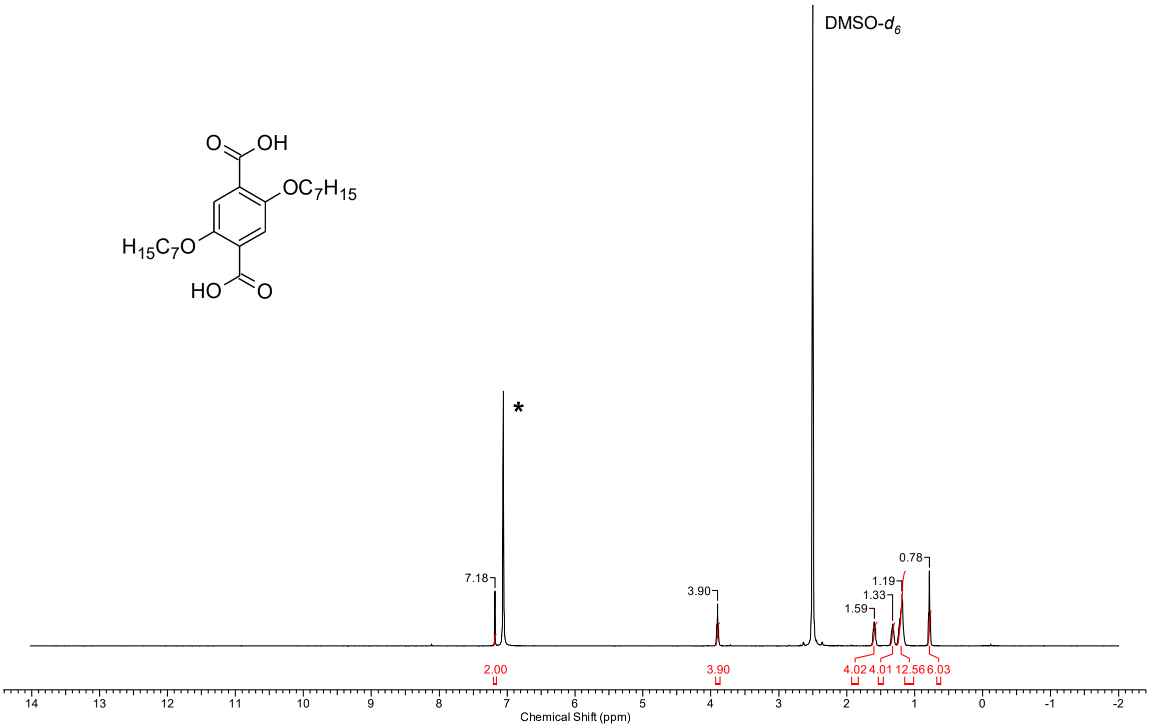

Figure 8.48: ^{1}H NMR spectrum of a digested sample of *dry*-MOF-5-**OC7**. The D_2O signal is marked with an asterisk (*).

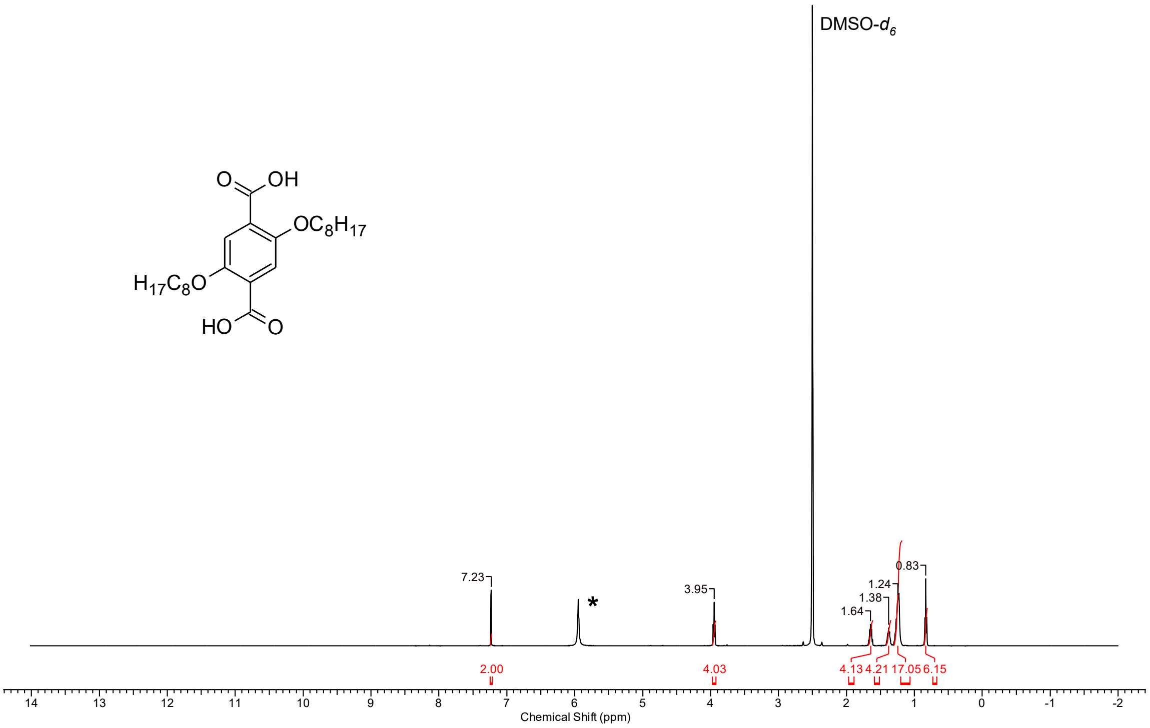

Figure 8.49: ^{1}H NMR spectrum of a digested sample of *dry*-MOF-5-**OC8**. The D$_2$O signal is marked with an asterisk (*).

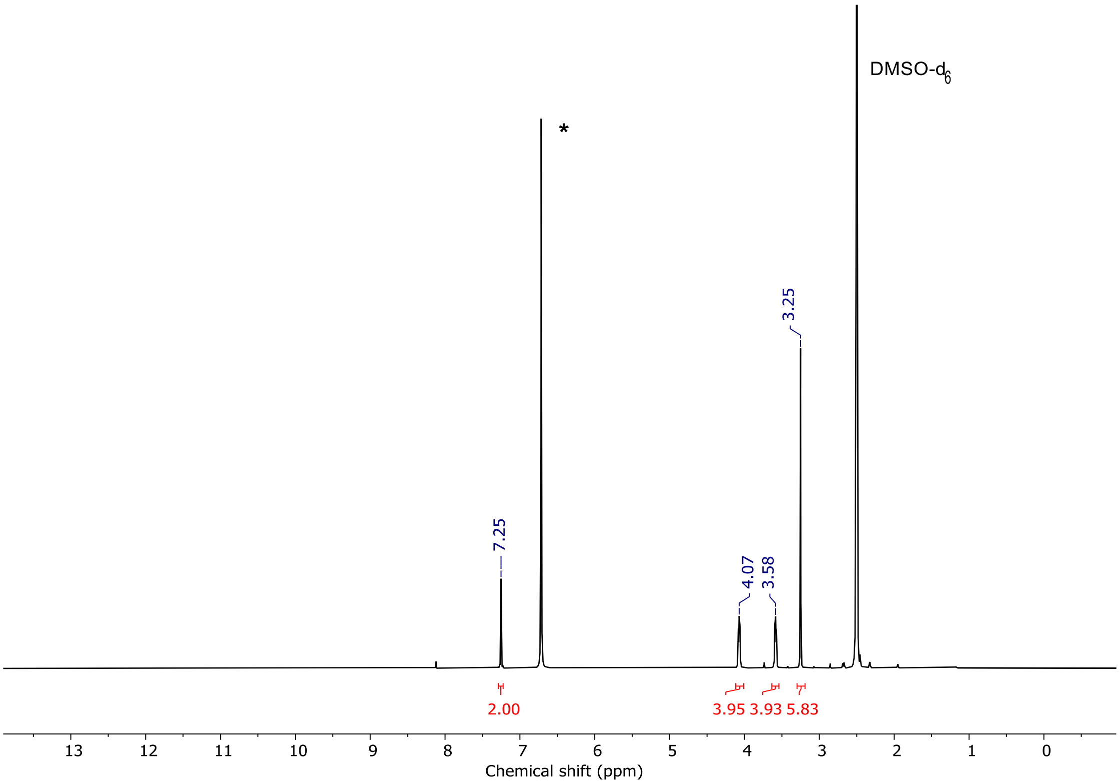

Figure 8.50: ^{1}H NMR spectrum of a digested sample of *dry*-MOF-5-**OC2OC1**. The D$_2$O signal is marked with an asterisk (*).

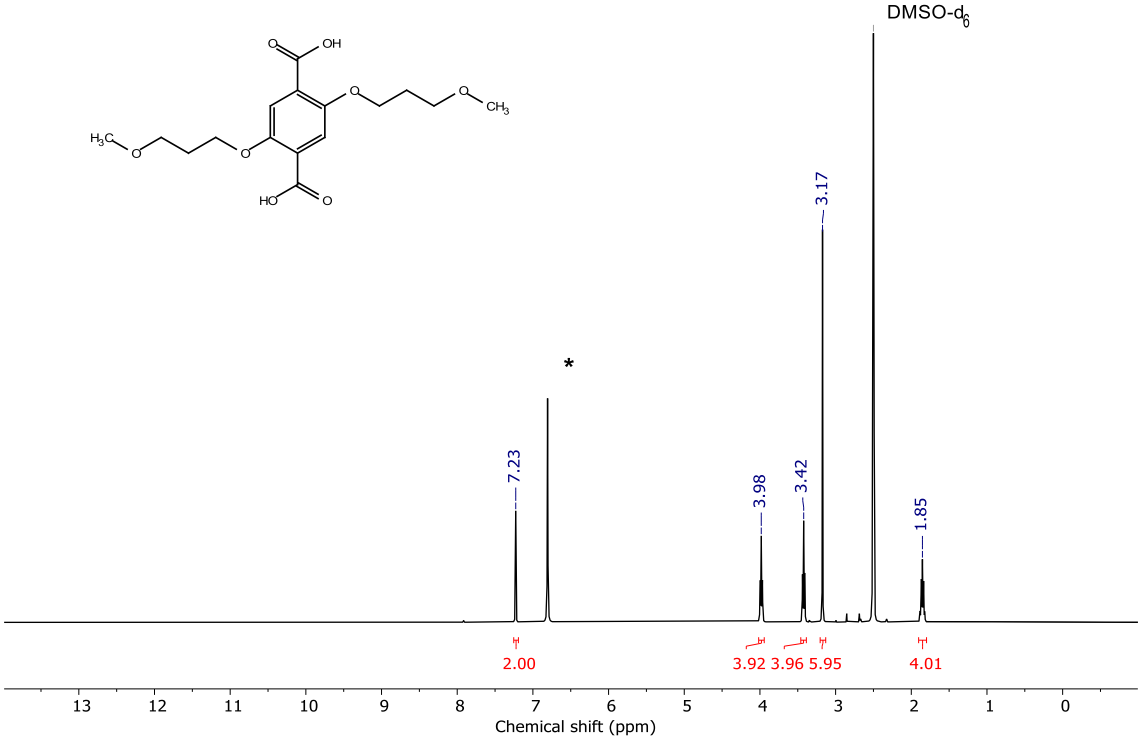

Figure 8.51: ^{1}H NMR spectrum of a digested sample of *dry*-MOF-5-**OC3OC1**. The D_2O signal is marked with an asterisk (*).

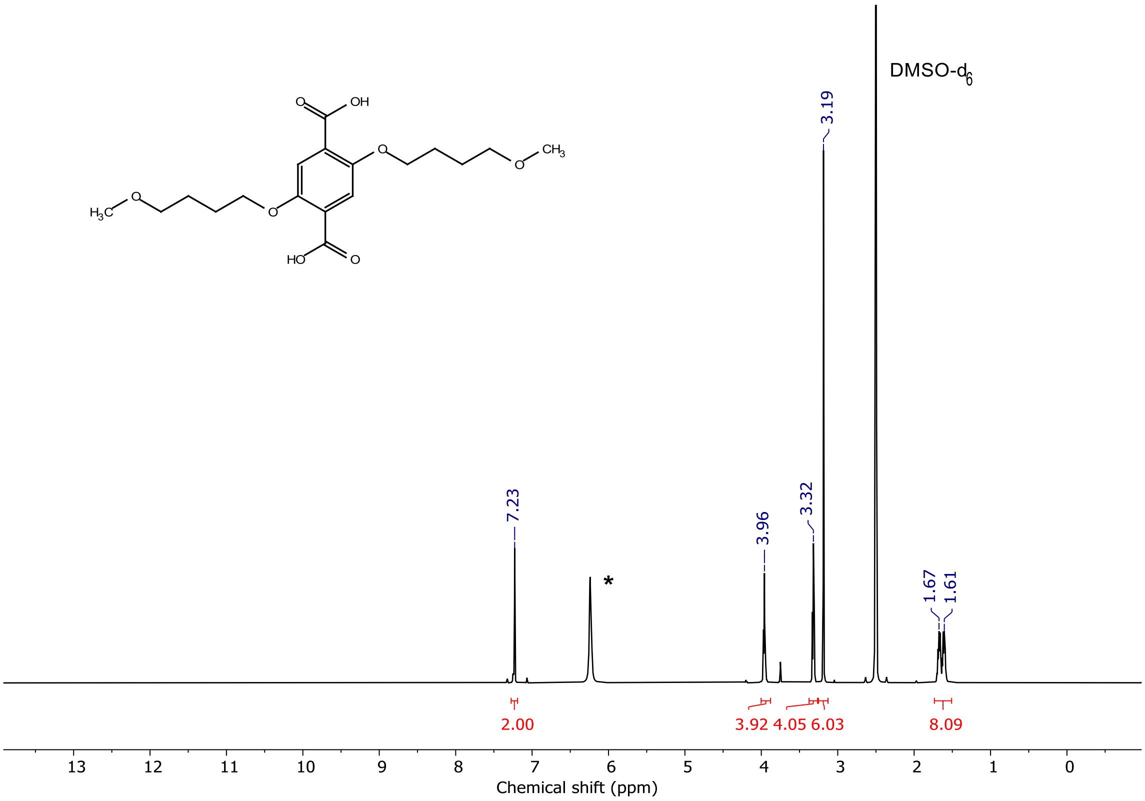

Figure 8.52: ^{1}H NMR spectrum of a digested sample of *dry*-MOF-5-**OC4OC1**. The D_2O signal is marked with an asterisk (*).

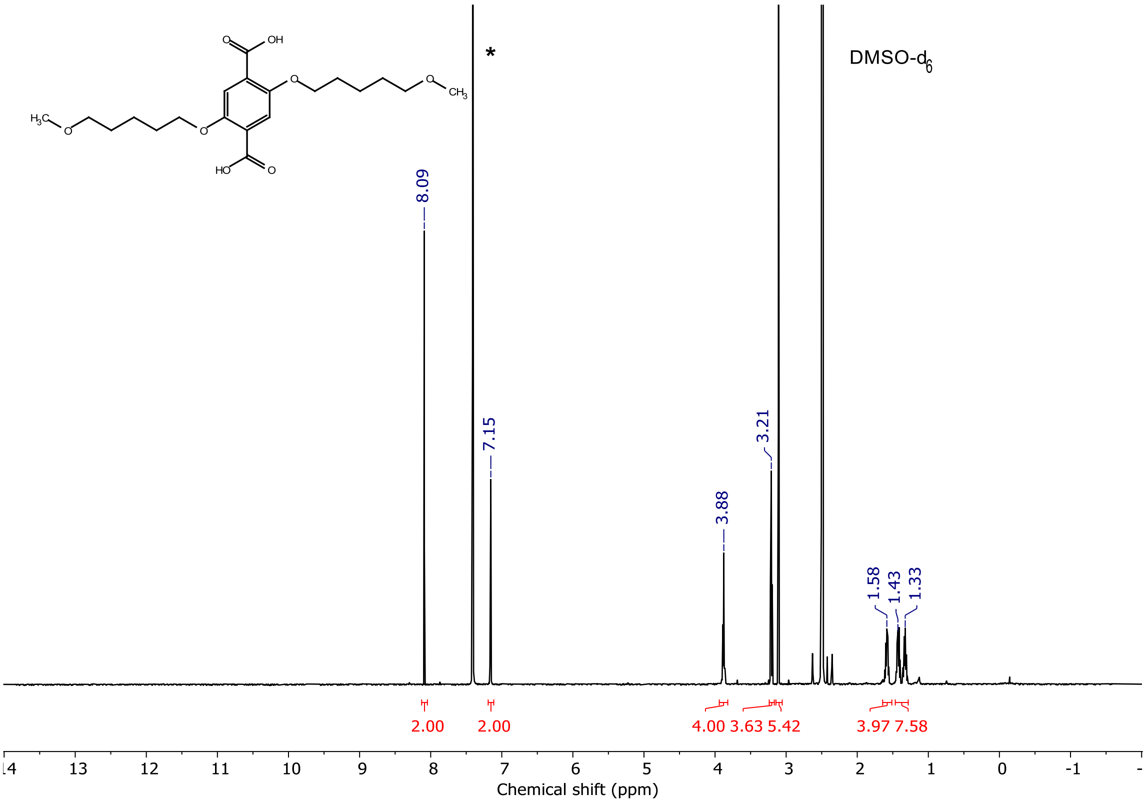

Figure 8.53: ^{1}H NMR spectrum of a digested sample of *dry*-MOF-5-**OC5OC1**. The D_2O signal is marked with an asterisk (*).

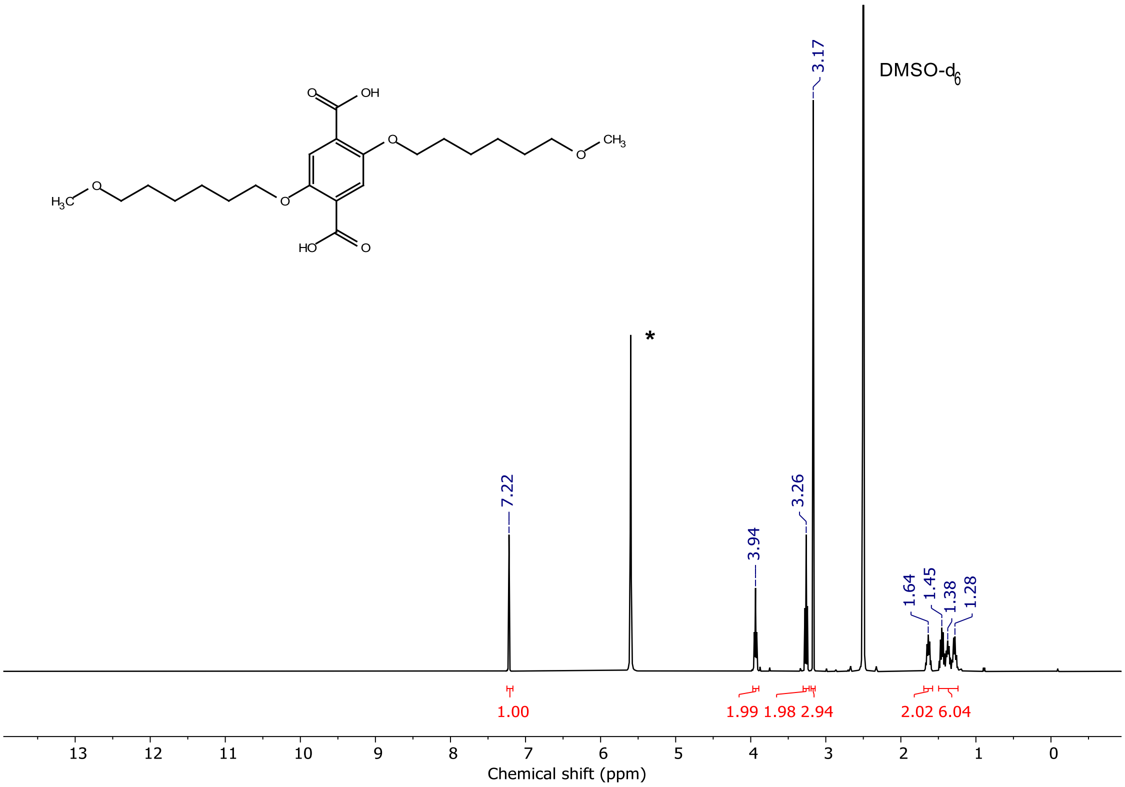

Figure 8.54: ^{1}H NMR spectrum of a digested sample of *dry*-MOF-5-**OC6OC1**. The D_2O signal is marked with an asterisk (*).

8.2.4 X-ray Pair Distribution Function (XPDF) Analysis

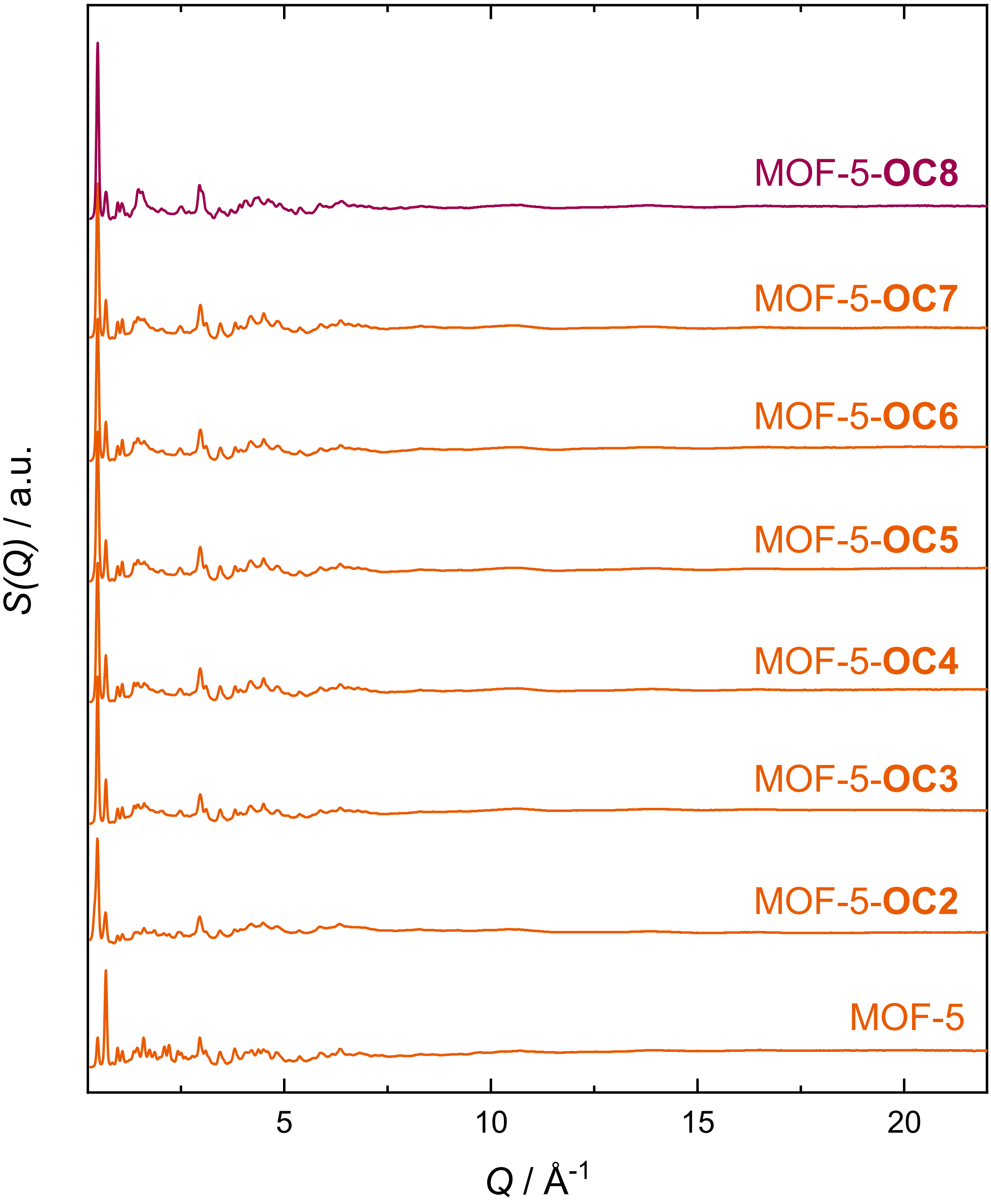

Figure 8.55: X-ray scattering factors *S(Q)* for as-synthesized MOF-5 and the *as*-MOF-5-**OCX** determined from total scattering experiments at I15-1 of Diamond Light Source.

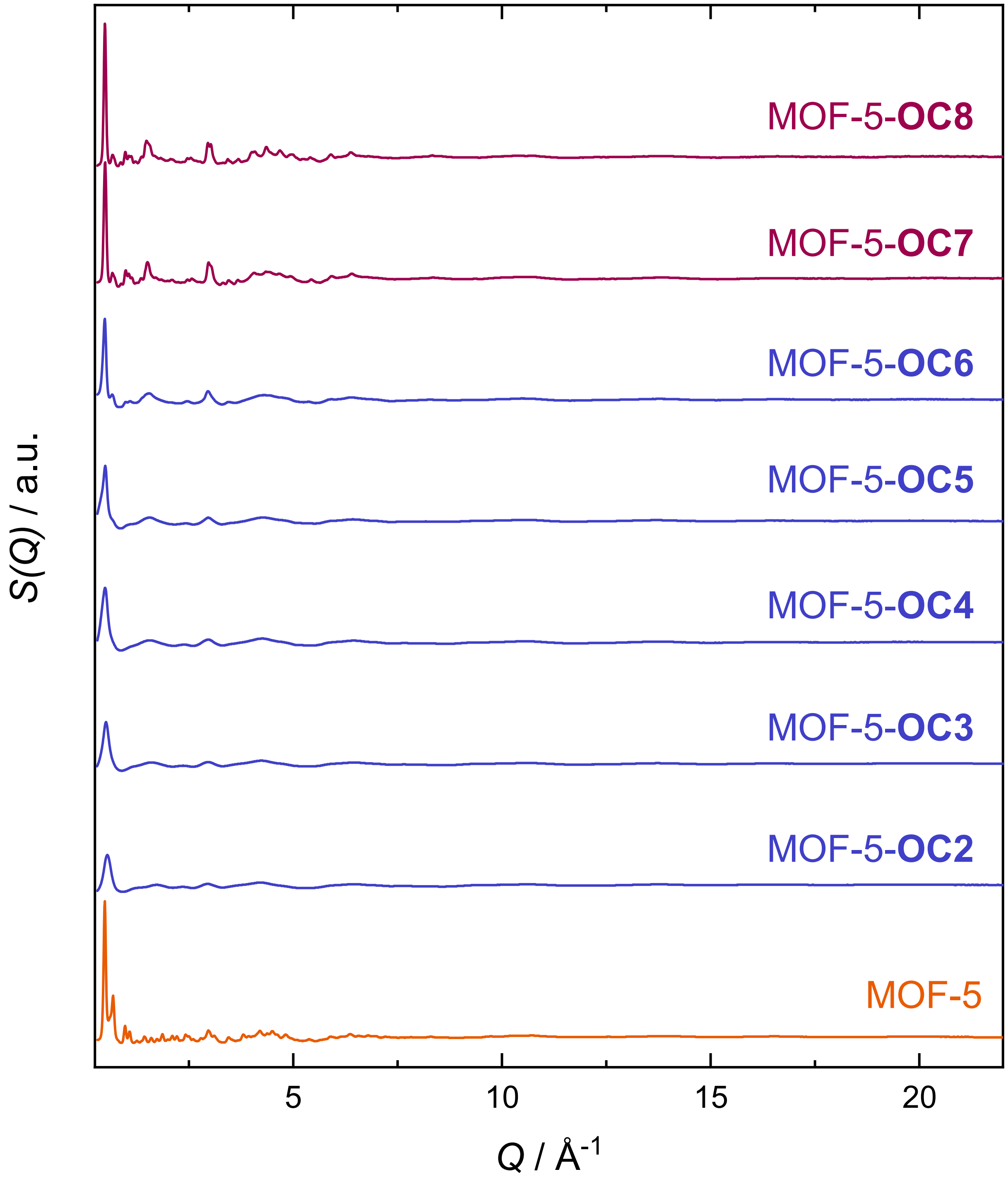

Figure 8.56: X-ray scattering factors *S(Q)* for dried MOF-5 and the *dry*-MOF-5-**OCX** determined from total scattering experiments at I15-1 of Diamond Light Source.

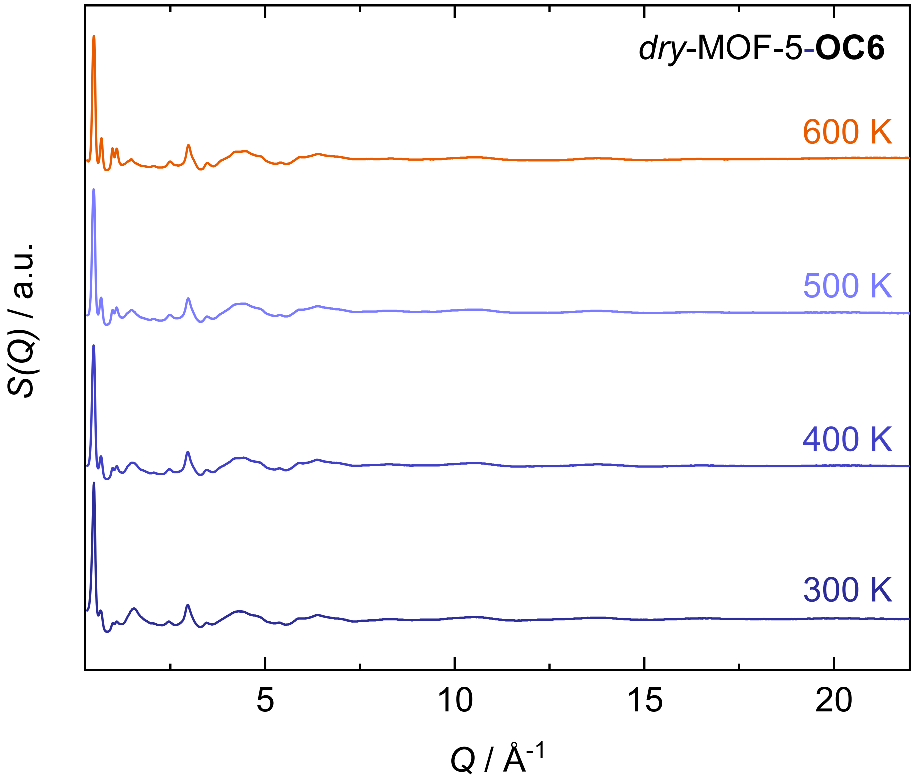

Figure 8.57: X-ray scattering factors *S(Q)* for *dry*-MOF-5-**OC6** at different temperatures determined from total scattering experiments at I15-1 of Diamond Light Source.

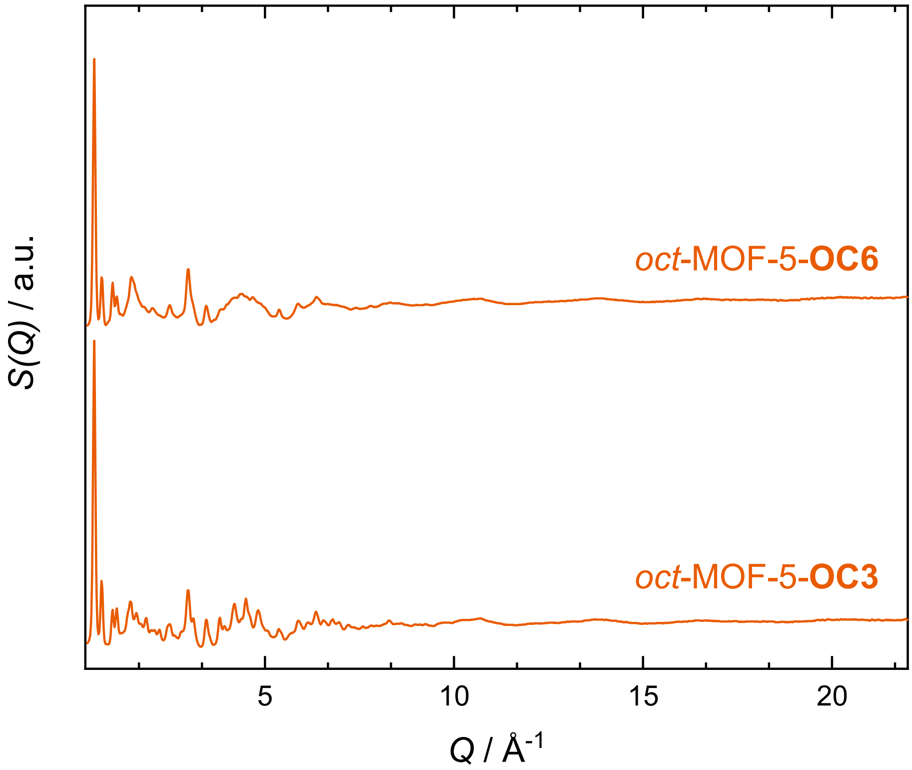

Figure 8.58: X-ray scattering factors *S(Q)* for *oct*-MOF-5-**OC3** and *oct*-MOF-5-**OC6** determined from total scattering experiments at I15-1 of Diamond Light Source.

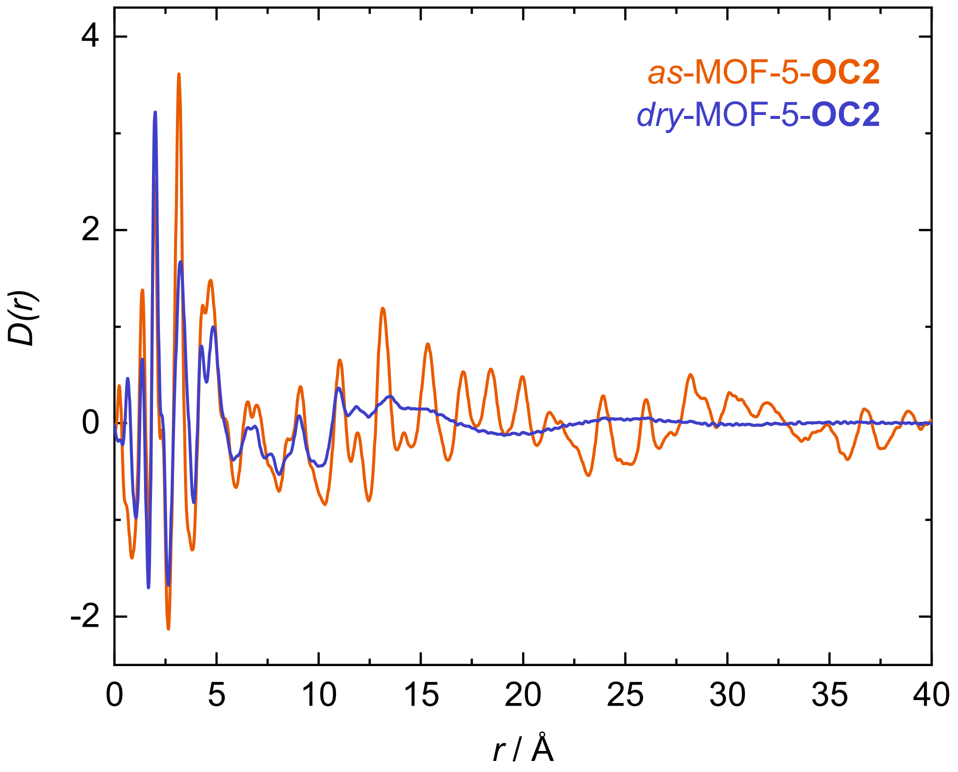

Figure 8.59: X-ray pair distribution functions *D(r)* of *as*- and *dry*-MOF-5-**OC2** obtained via Fourier transform of the *S(Q)* shown above.

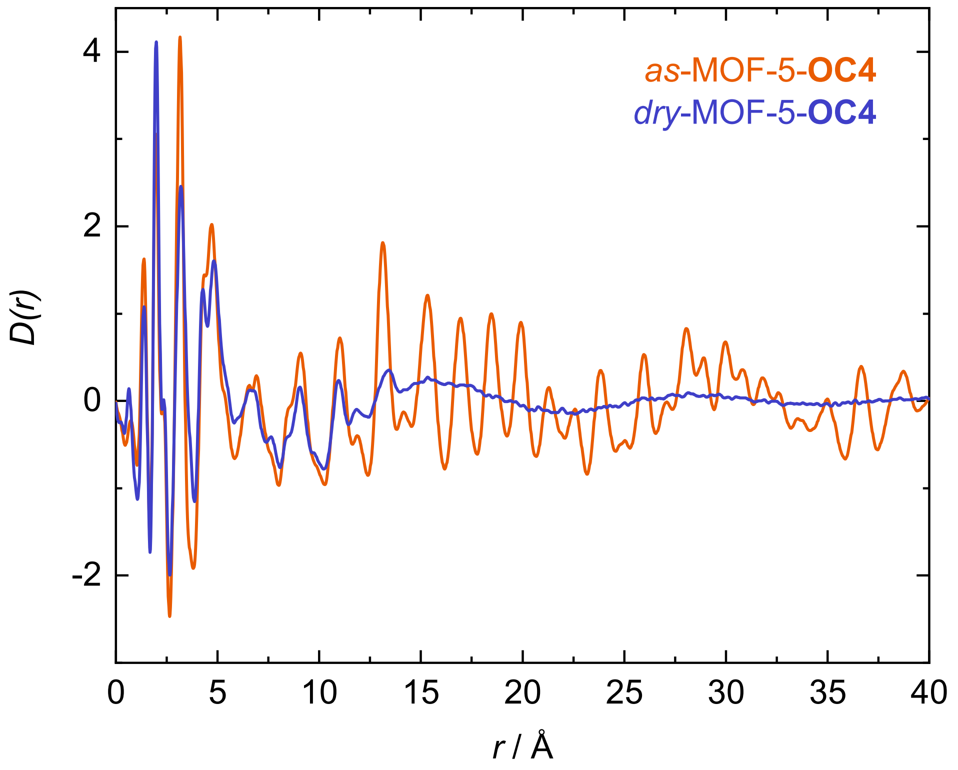

Figure 8.60: X-ray pair distribution functions *D(r)* of *as*- and *dry*-MOF-5-**OC4** obtained via Fourier transform of the *S(Q)* shown above.

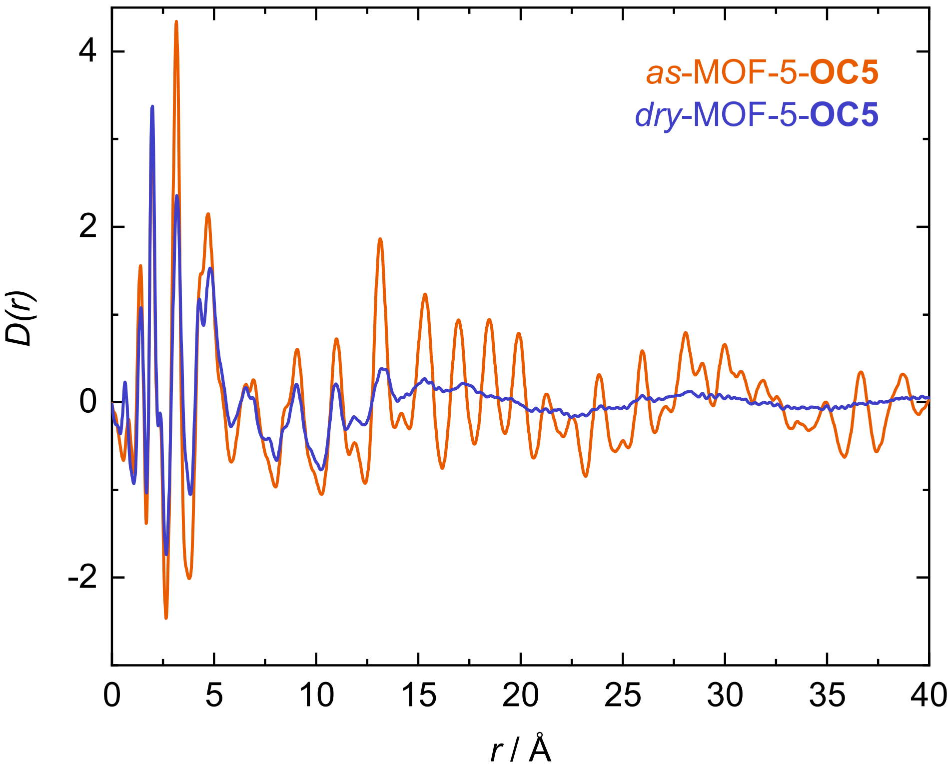

Figure 8.61: X-ray pair distribution functions *D(r)* of *as*- and *dry*-MOF-5-**OC5** obtained via Fourier transform of the *S(Q)* shown above.

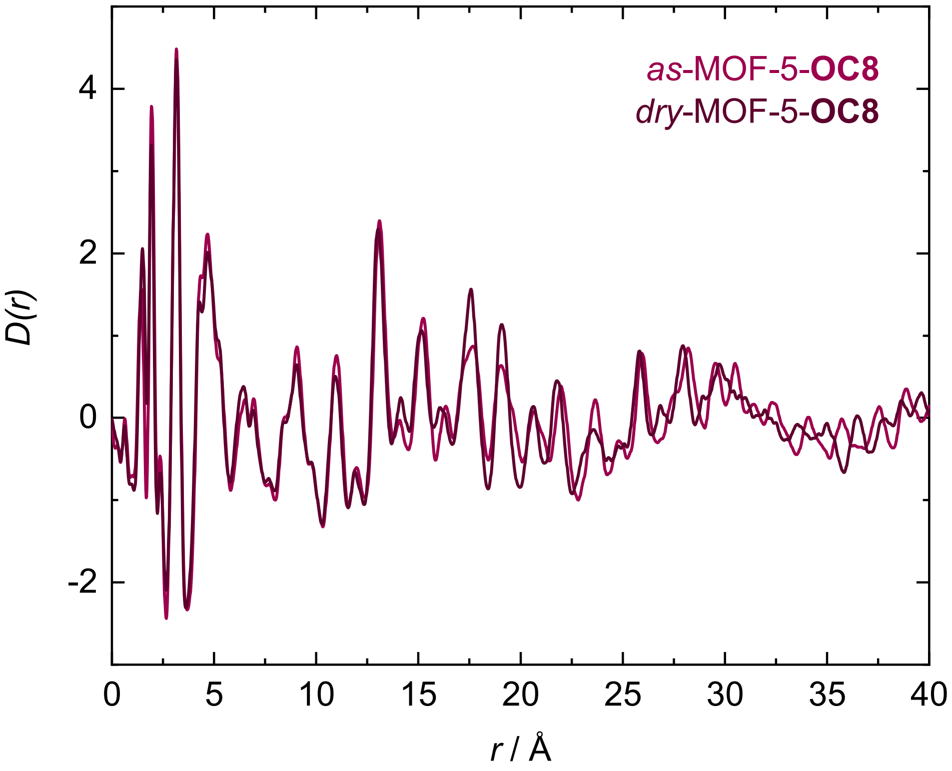

Figure 8.62: X-ray pair distribution functions *D(r)* of *as*- and *dry*-MOF-5-**OC8** obtained via Fourier transform of the *S(Q)* shown above.

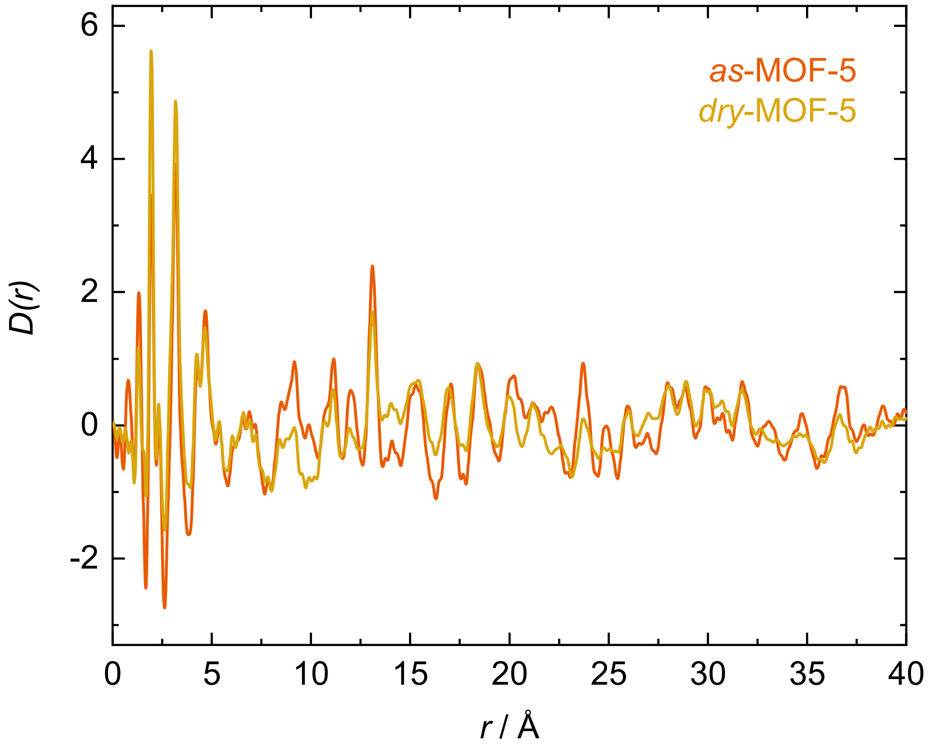

Figure 8.63: X-ray pair distribution functions *D(r)* of *as*- and *dry*-MOF-5 obtained via Fourier transform of the *S(Q)* shown above.

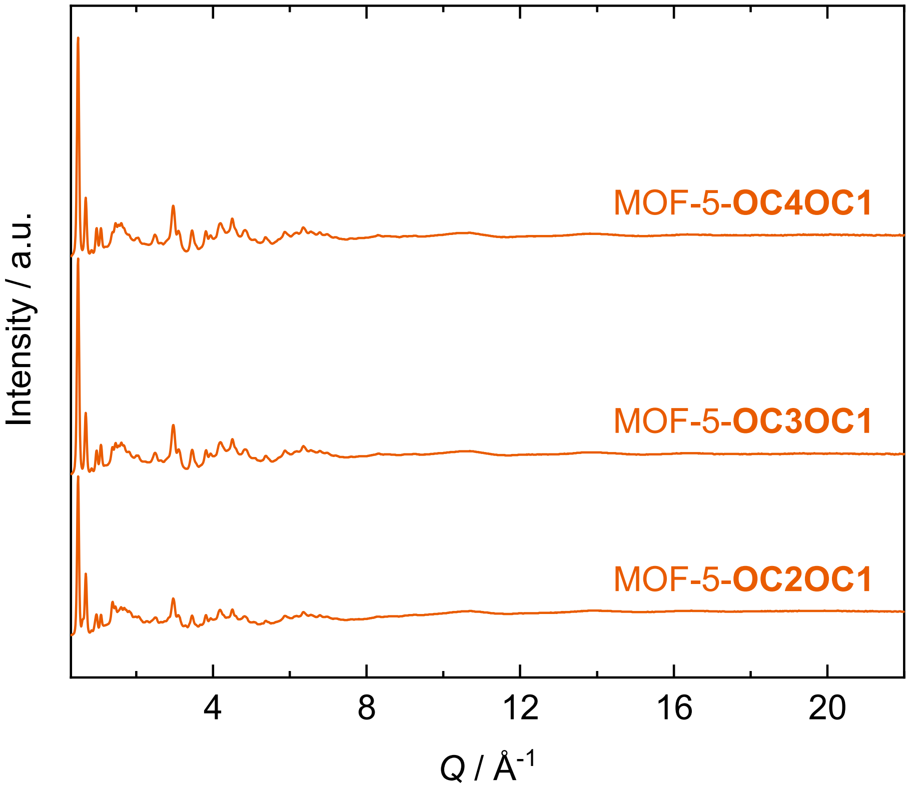

Figure 8.64: X-ray scattering factors *S(Q)* for the *as*-MOF-5-**OCYOC1** determined from total scattering experiments at I15-1 of Diamond Light Source.

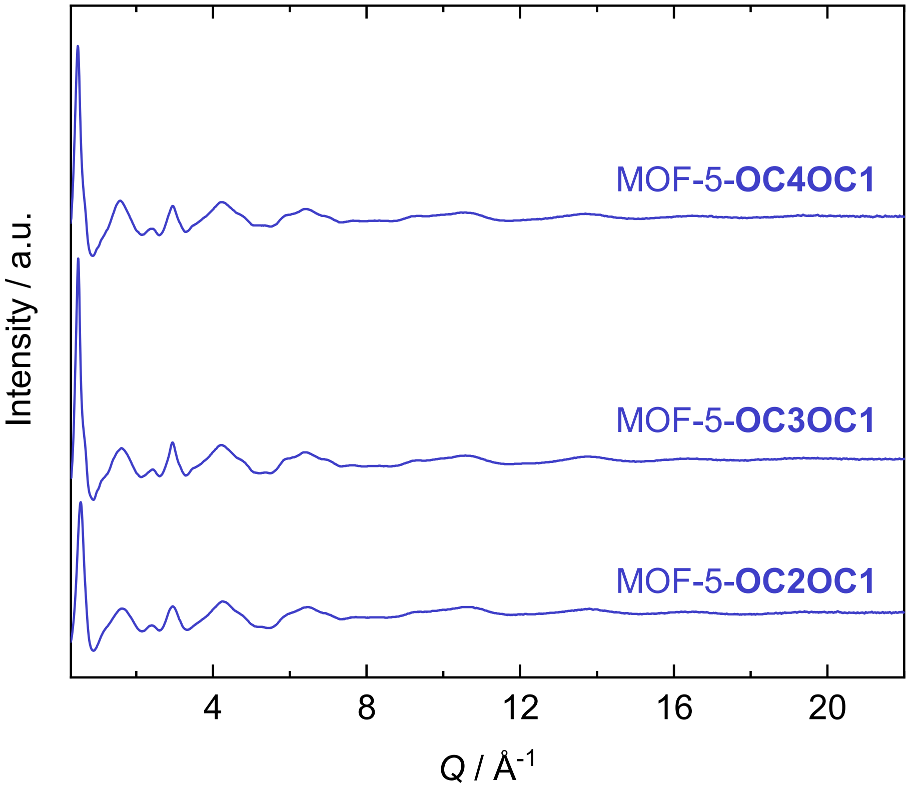

Figure 8.65: X-ray scattering factors *S(Q)* for the *dry*-MOF-5-**OCYOC1** determined from total scattering experiments at I15-1 of Diamond Light Source.

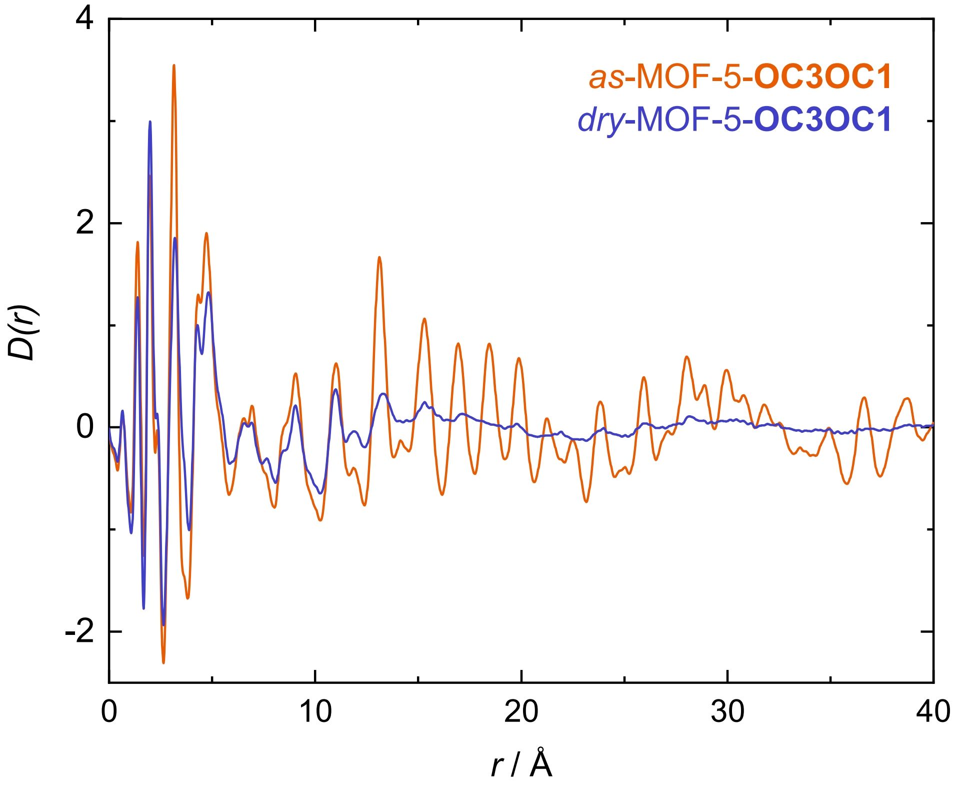

Figure 8.66: X-ray pair distribution functions *D(r)* of *as*- and *dry*-MOF-5-**OC3OC1** obtained via Fourier transform of the *S(Q)* shown above.

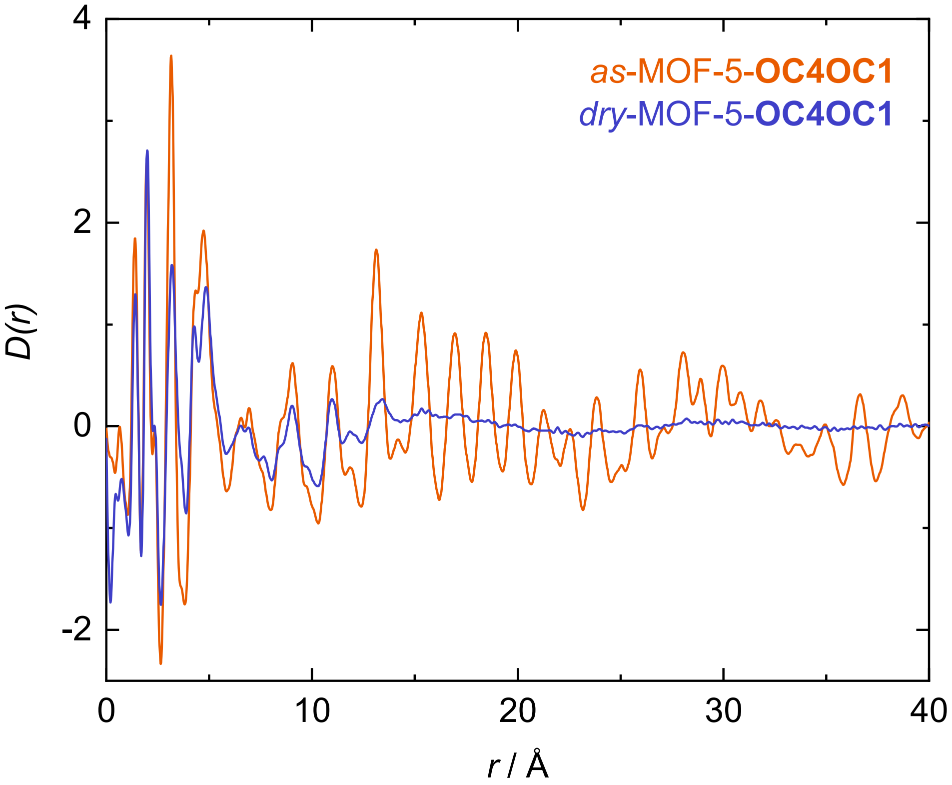

Figure 8.67: X-ray pair distribution functions *D(r)* of *as*- and *dry*-MOF-5-**OC4OC1** obtained via Fourier transform of the *S(Q)* shown above.

8.2.5 Fourier Transform-Infrared (FT-IR) Spectroscopy

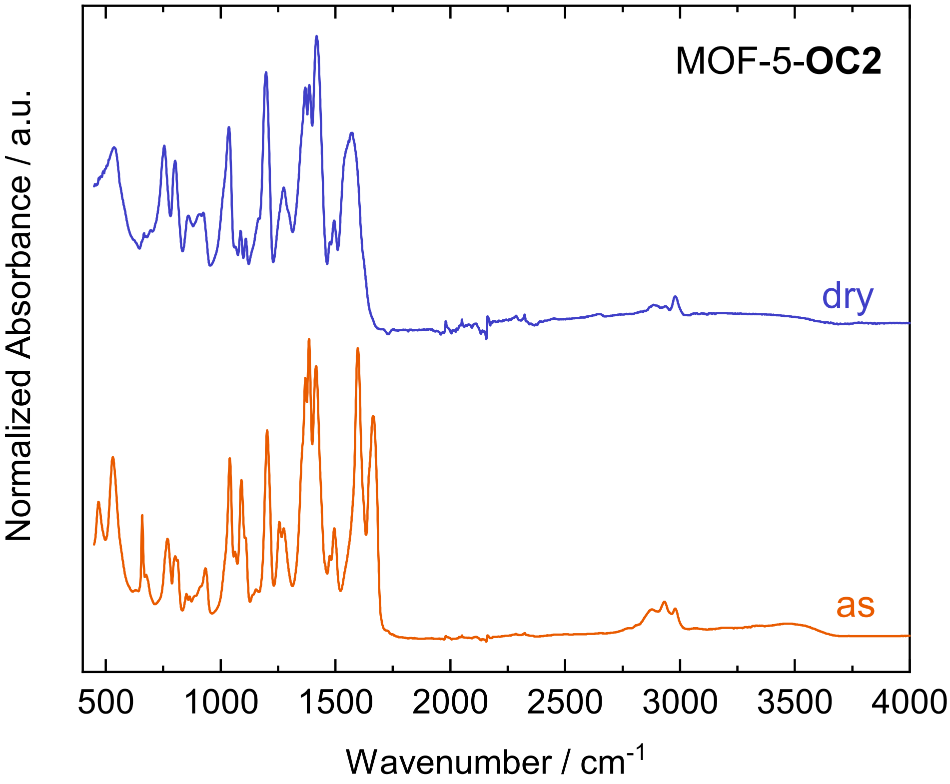

Figure 8.68: FT-IR spectra of *as*-MOF-5-**OC2** and *dry*-MOF-5-**OC2**.

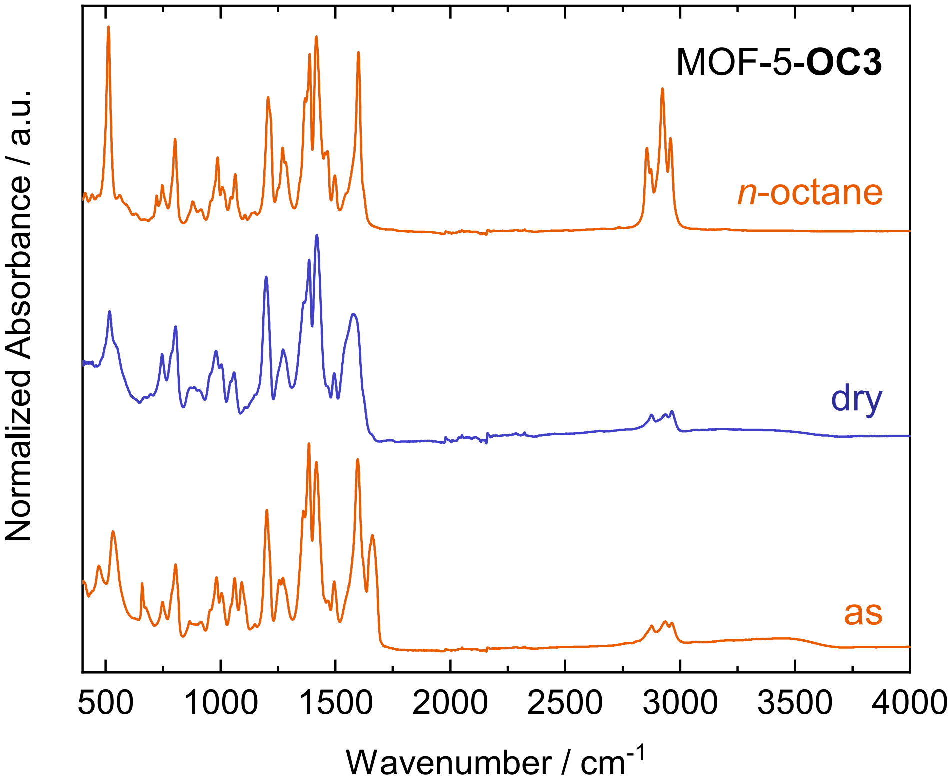

Figure 8.69: FT-IR spectra of *as*-, *dry*- and *n*-octane reinfiltrated MOF-5-**OC3**.

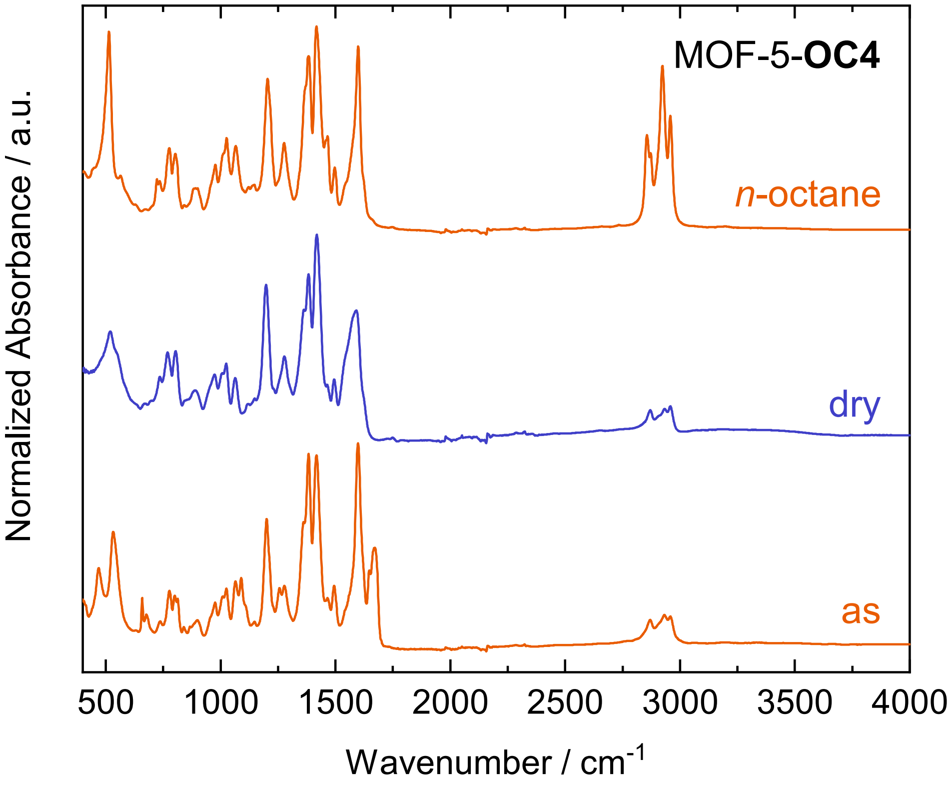

Figure 8.70: FT-IR spectra of *as*-, *dry*- and *n*-octane reinfiltrated MOF-5-**OC4**.

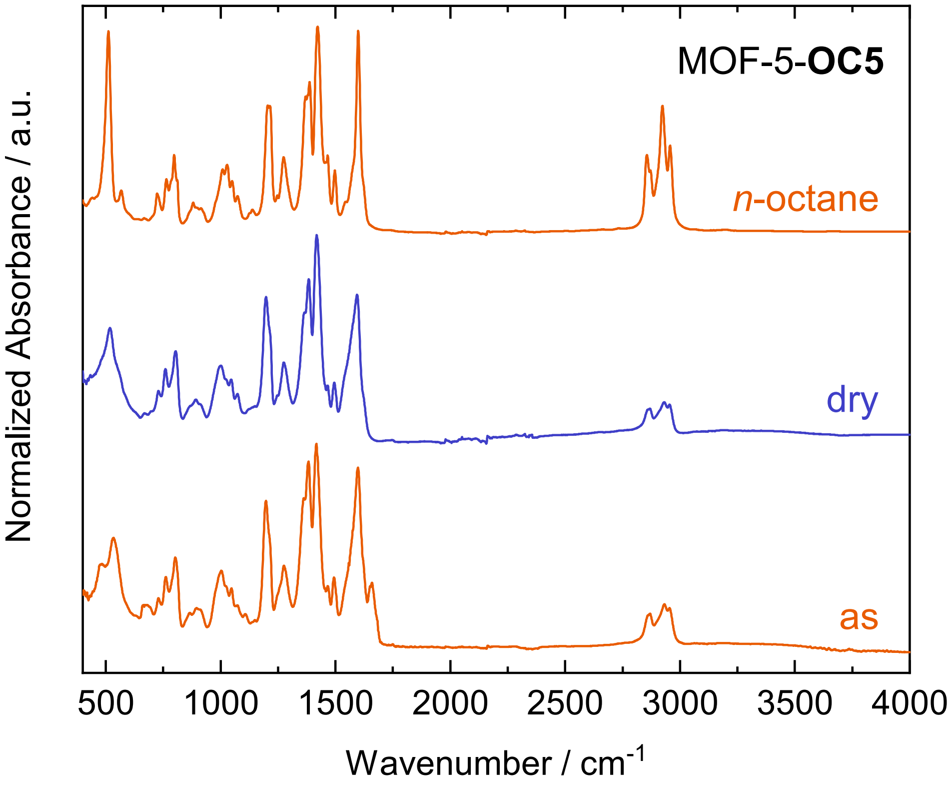

Figure 8.71: FT-IR spectra of *as*-, *dry*- and *n*-octane reinfiltrated MOF-5-**OC5**.

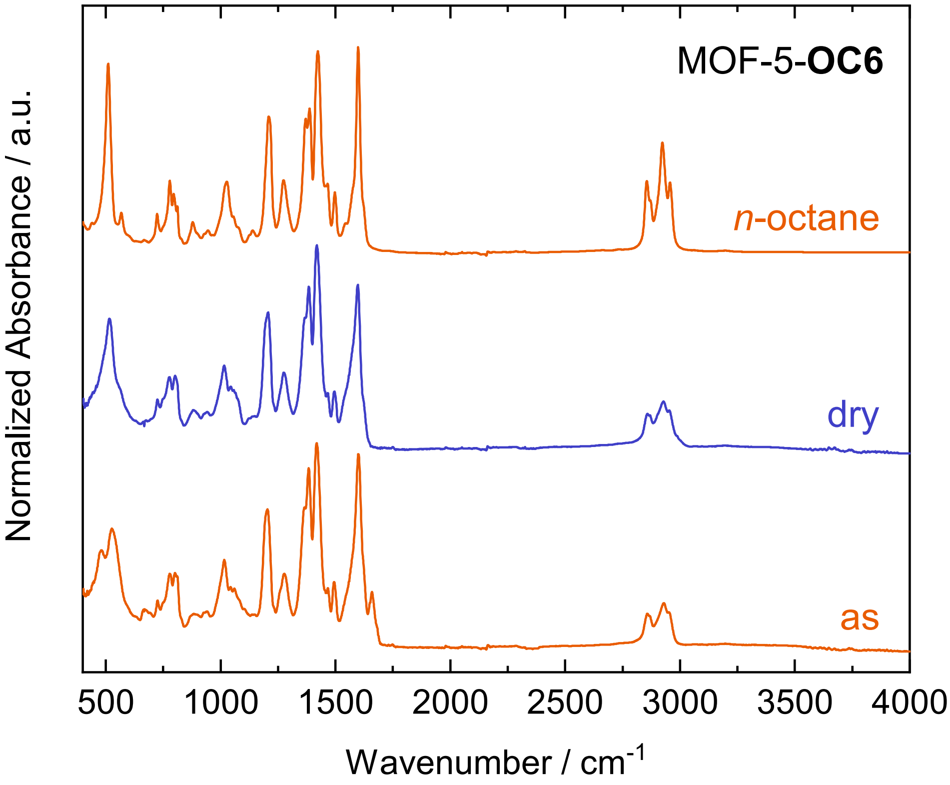

Figure 8.72: FT-IR spectra of *as*-, *dry*- and *n*-octane reinfiltrated MOF-5-**OC6**.

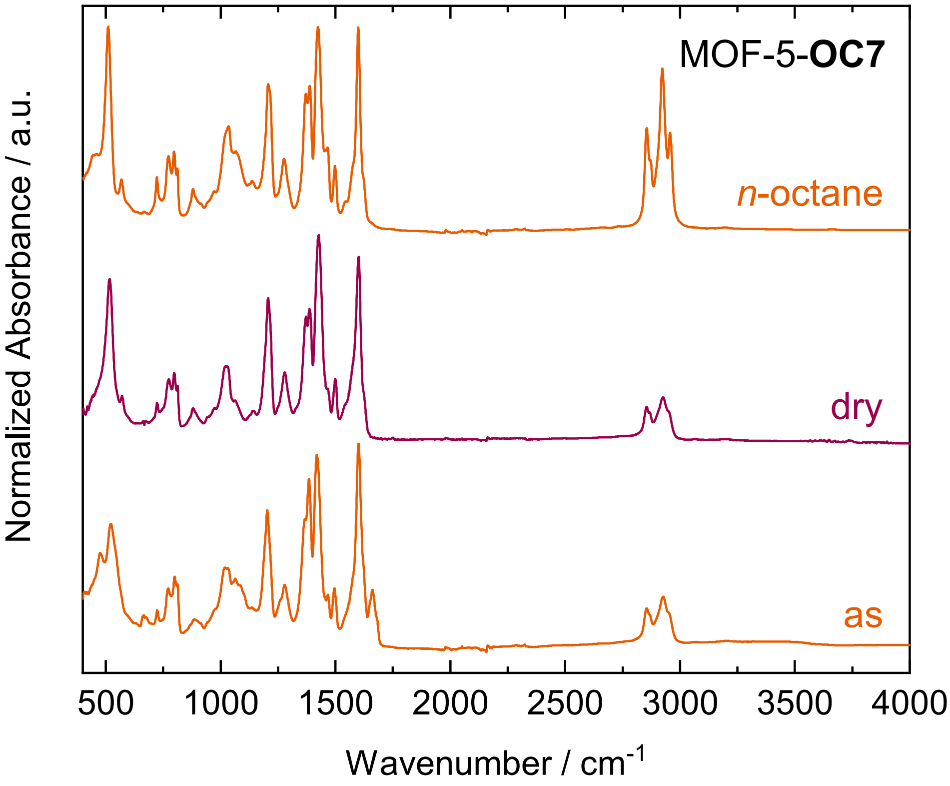

Figure 8.73: FT-IR spectra of *as*-, *dry*- and *n*-octane reinfiltrated MOF-5-**OC7**.

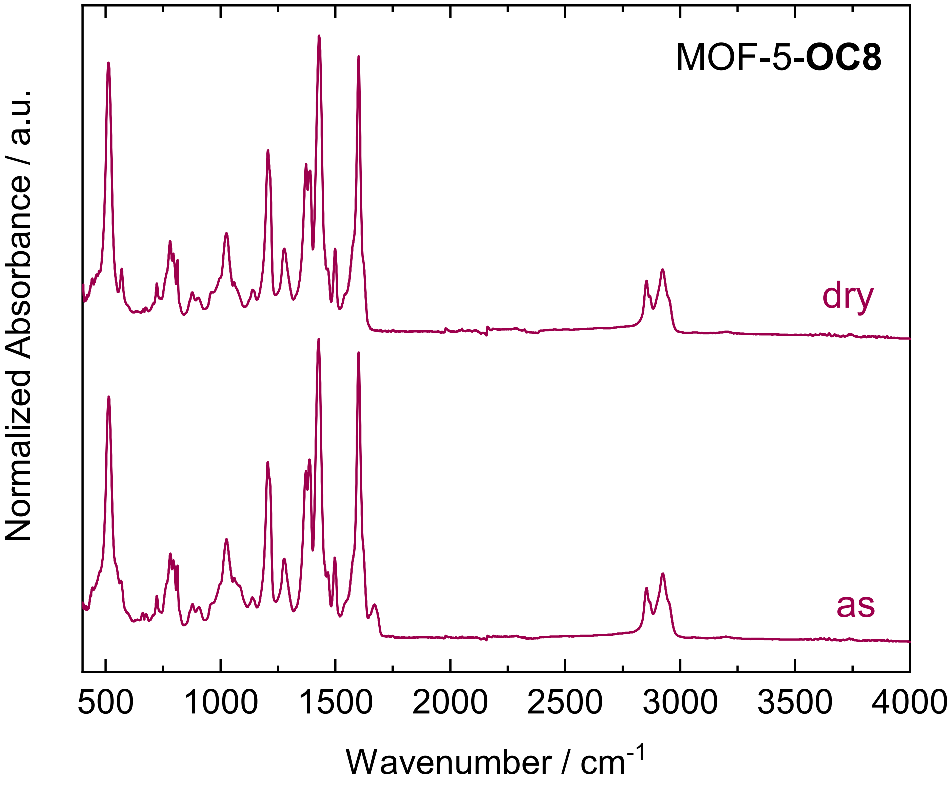

Figure 8.74: FT-IR spectra of *as*-MOF-5-**OC8** and *dry*-MOF-5-**OC8**.

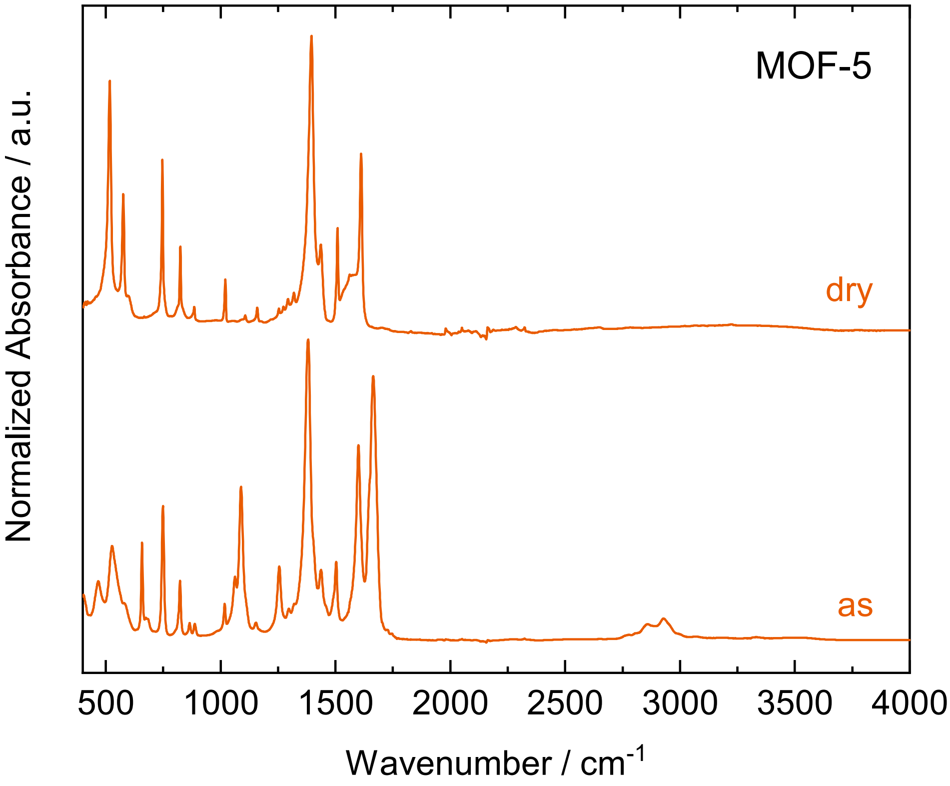

Figure 8.75: FT-IR spectra of *as*-MOF-5 and *dry*-MOF-5.

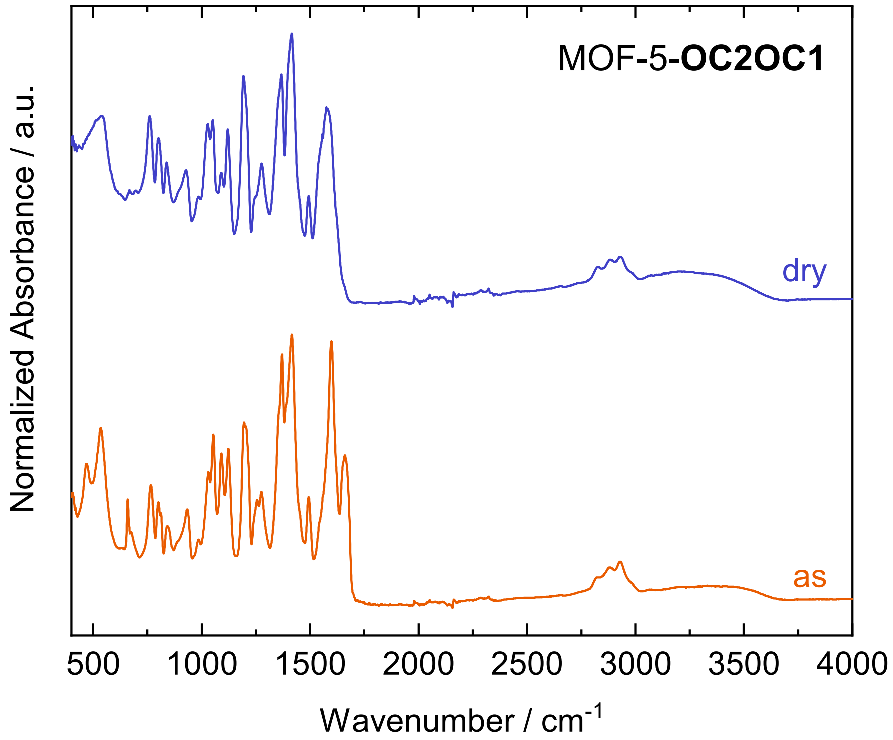

Figure 8.76: FT-IR spectra of *as*- and *dry*-MOF-5-**OC2OC1**.

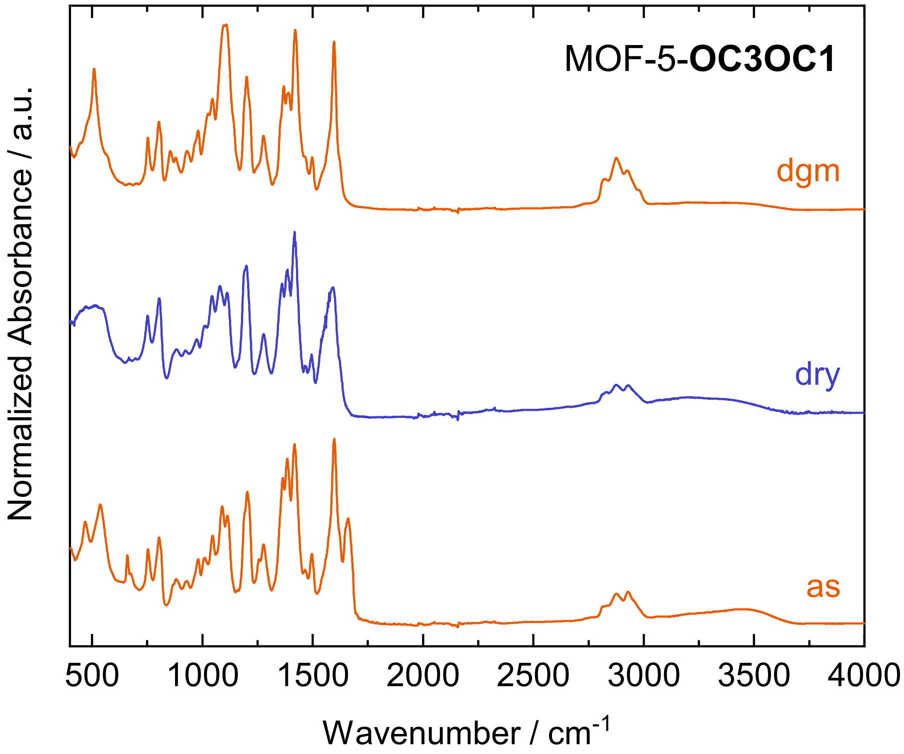

Figure 8.77: FT-IR spectra of *as*-, *dry*- and *diglyme*-MOF-5-OC3OC1.

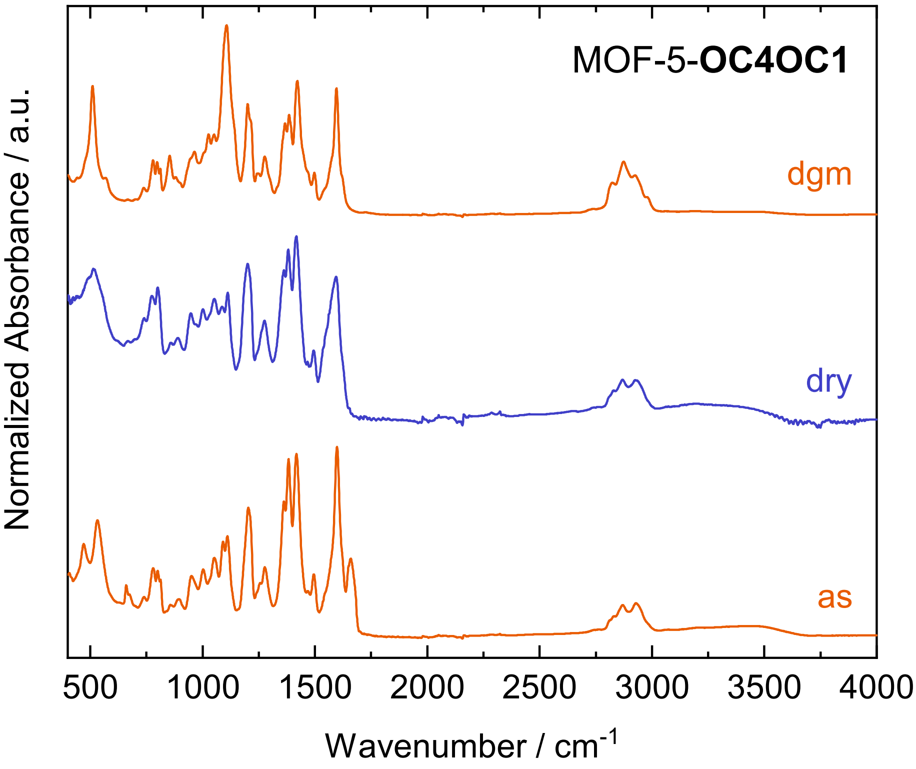

Figure 8.78: FT-IR spectra of *as*-, *dry*- and *diglyme*-MOF-5-**OC4OC1**.

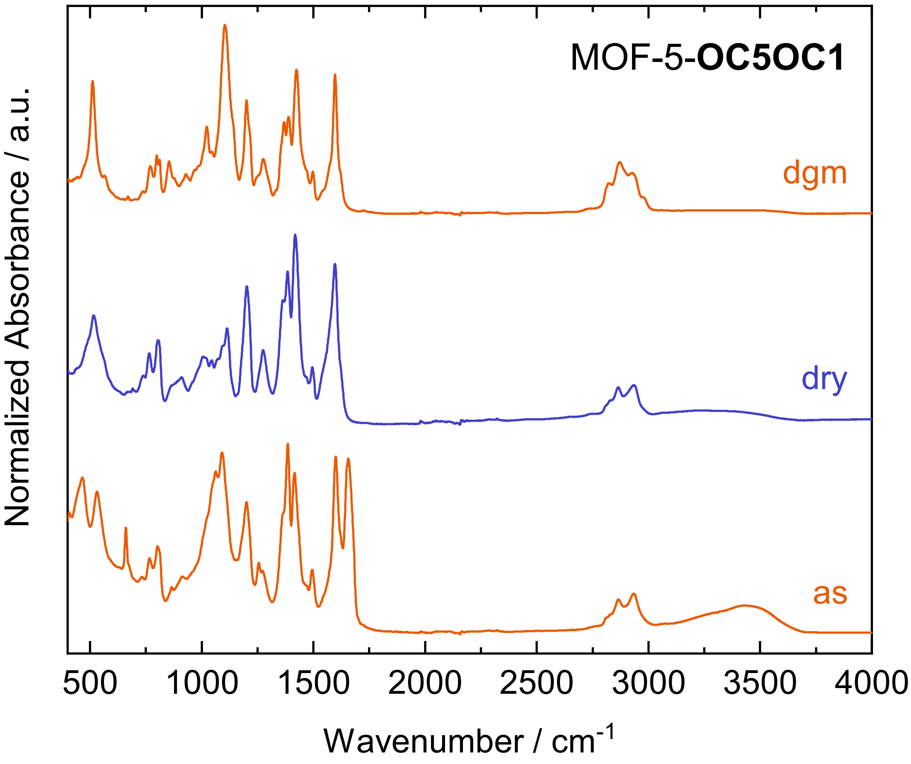

Figure 8.79: FT-IR spectra of *as*-, *dry*- and *diglyme*-MOF-5-**OC5OC1**.

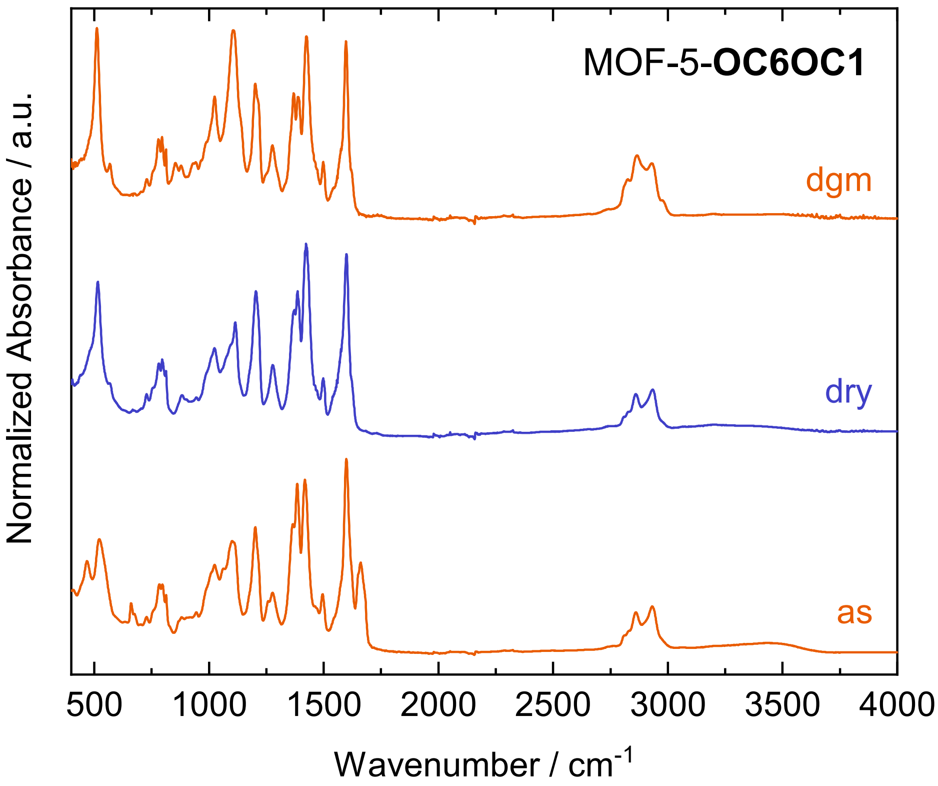

Figure 8.80: FT-IR spectra of *as*-, *dry*- and *diglyme*-MOF-5-**OC6OC1**.

8.2.6 Thermal Analysis

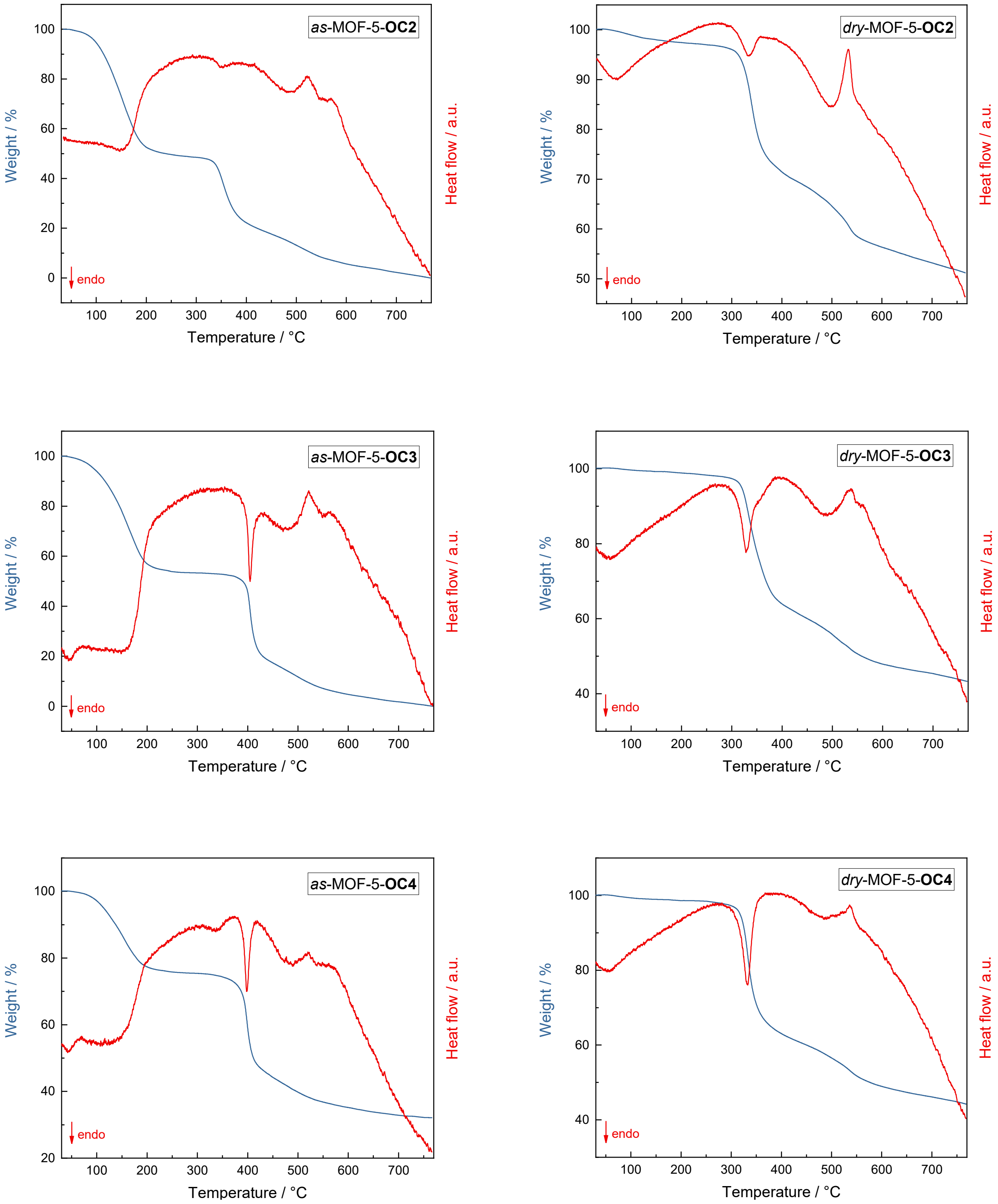

Figure 8.81: TG-DSC data of as-synthesized (left) and dried (right) MOF-5-**OC2** to MOF-5-**OC4**.

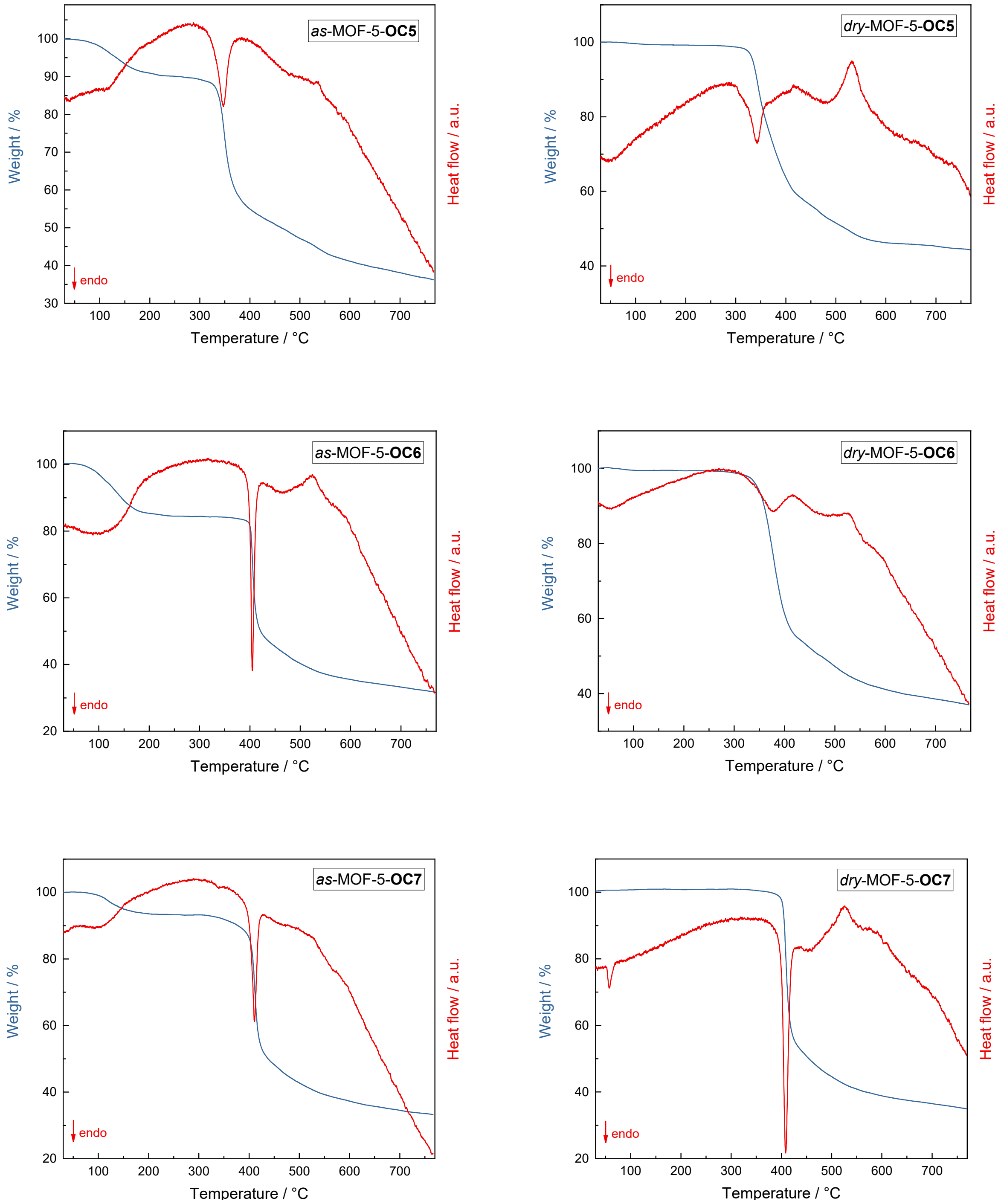

Figure 8.82: TG-DSC data of as-synthesized (left) and dried (right) MOF-5-**OC5** to MOF-5-**OC7**.

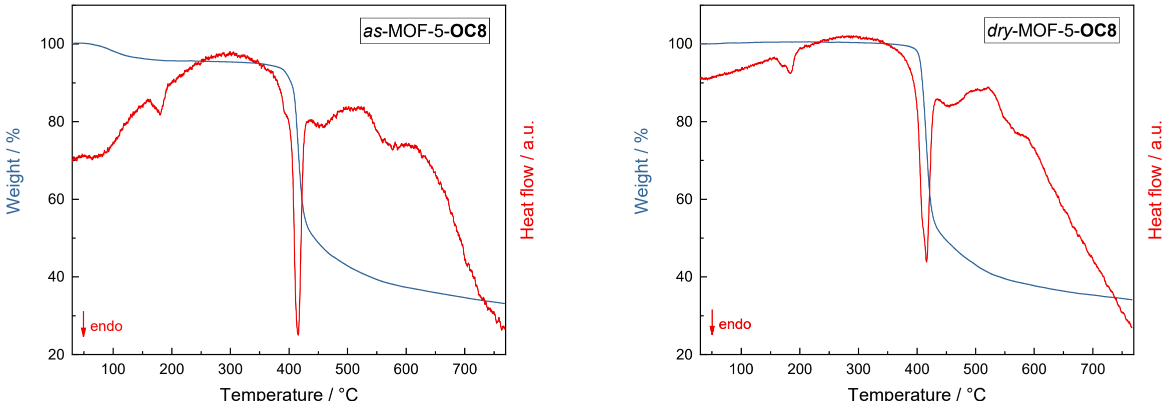

Figure 8.83: TG-DSC data of as-synthesized (left) and dried (right) MOF-5-**OC8**.

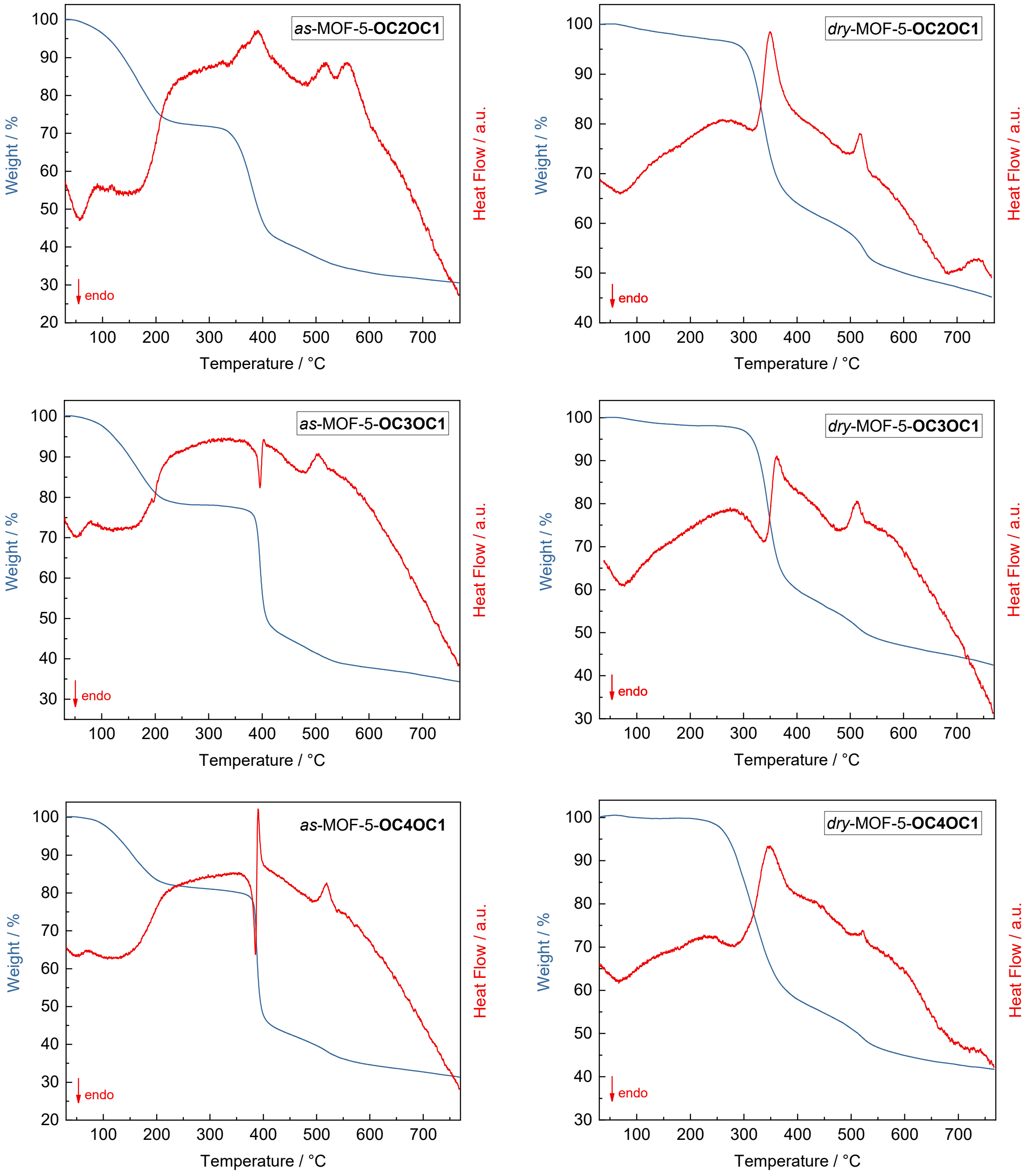

Figure 8.84: TG-DSC data of the *as-* (left) and *dry-* (right) MOF-5-**OCYOC1** (**Y** = 2 – 4).

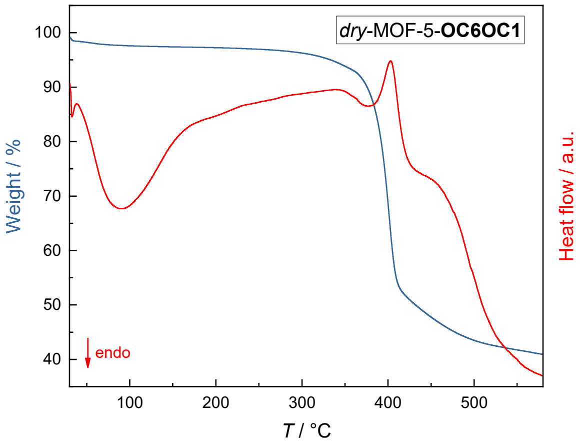

Figure 8.85: TG-DSC data of *dry*-MOF-5-**OC6OC1**.

8.2.7 Variable-Temperature Powder X-ray Diffraction (VT-PXRD)

Profile Fit Data of *dry*-MOF-5-**OC7** and *dry*-MOF-5-**OC8**

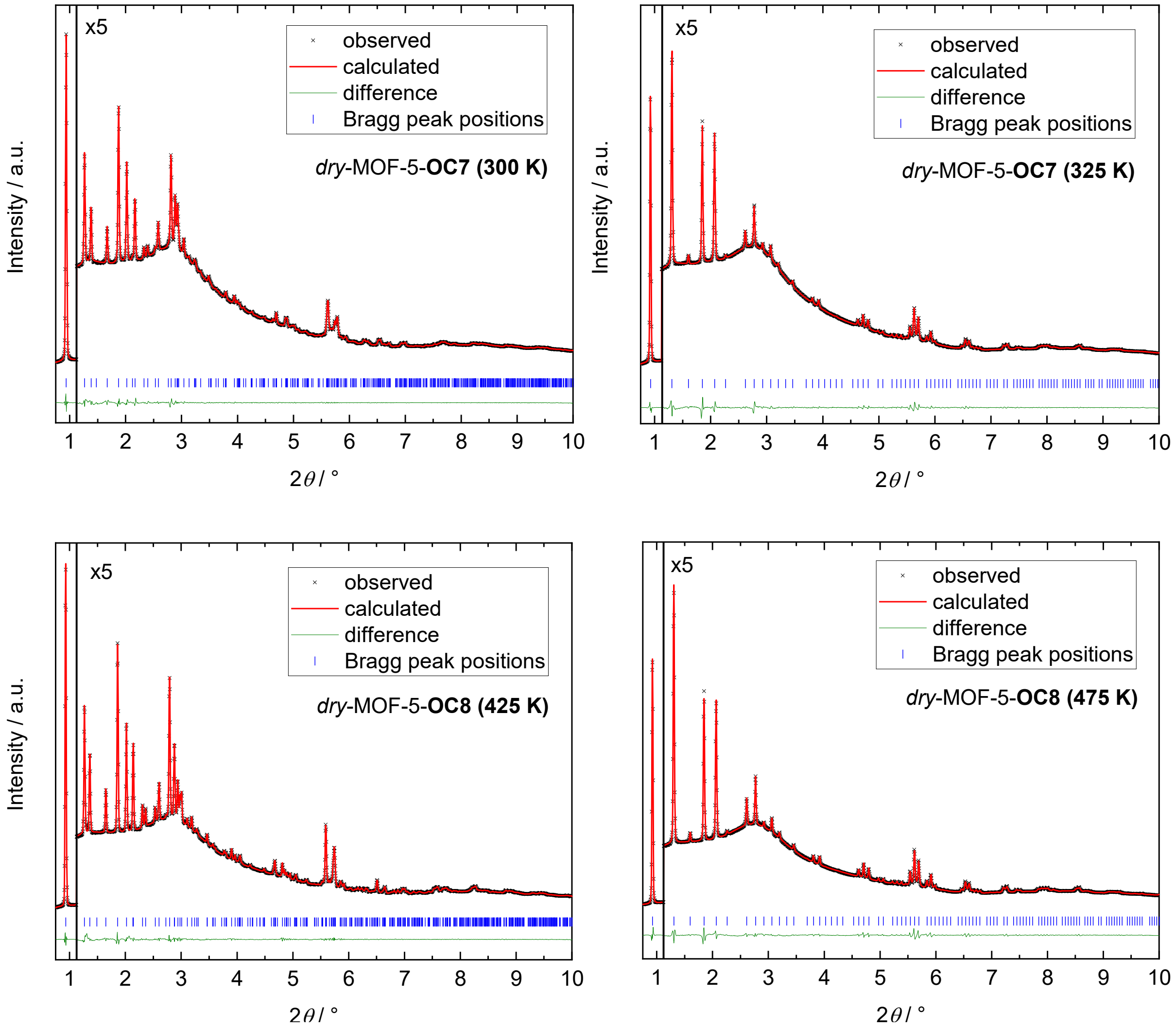

Figure 8.86: Structureless profile fits (Pawley method) of *dry*-MOF-5-**OC7** (at 300 and 325 K, top) and *dry*-MOF-5-**OC8** (at 425 K and 475 K, bottom).

Table 8.32: Structureless profile fit (Pawley method) data of *dry*-MOF-5-**OC7** (at 300 and 325 K) and *dry*-MOF-5-**OC8** (at 425 and 475 K) used to determine the ΔV percentage between the rhombohedral and cubic phases ($\Delta V = 2\%$ (**OC7**) or 1.5% (**OC8**)).

	dry-MOF-5-**OC7**			*dry*-MOF-5-**OC8**		
	300 K		325 K	425 K		475 K
crystal system	trigonal	rhombohedral	cubic	trigonal	rhombohedral	cubic
space group	$R\bar{3}$		$Pm\bar{3}m$	$R\bar{3}$		$Pm\bar{3}m$
a / Å	17.230(1)	12.7765(6)	12.8142(1)	17.4054(5)	12.8237(4)	12.8474(2)
b / Å	17.230(1)	12.7765(6)	12.8142(1)	17.4054(5)	12.8237(4)	12.8474(2)
c / Å	24.053(2)	12.7765(6)	12.8142(1)	23.899(1)	12.8237(4)	12.8474(2)
α / °	90	84.795(4)	90	90	85.475(3)	90
β / °	90	84.795(4)	90	90	85.475(3)	90
γ / °	120	84.795(4)	90	120	85.475(3)	90
V / Å^3	6183.9(7)	2061.3	2104.18(6)	6270.2(5)	2090.1	2120.5(1)
R_{wp}	0.82		0.86	1.00		1.71
R_{exp}	1.51		2.15	1.43		2.03
χ^2	0.54		0.40	0.70		0.85

VT-PXRD Patterns of *dry*-MOF-5-**OC2** and *dry*-MOF-5-**OC3**

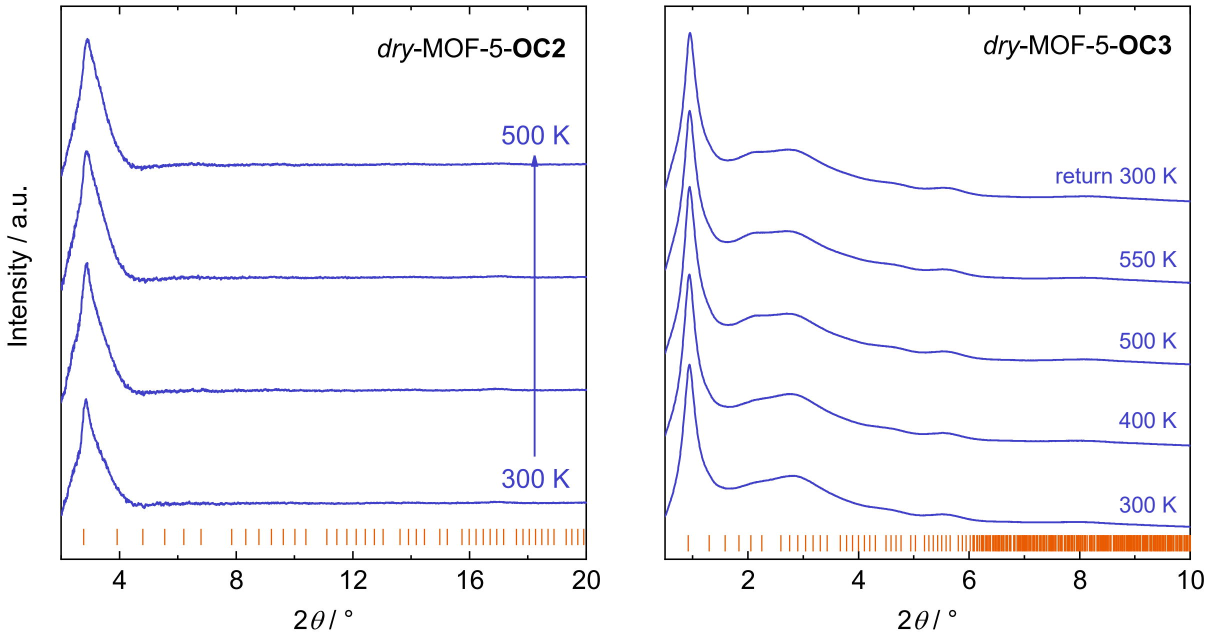

Figure 8.87: VT-PXRD patterns recorded of a dried sample of MOF-5-**OC2** in the range from 300 – 500 K (DELTA, $\lambda = 0.6199$ Å, left). VT-PXRD patterns recorded of a dried sample of MOF-5-**OC3** in the range from 300 – 550 K (P02.1 of DESY, $\lambda = 0.2073$ Å, right). Tick marks correspond to positions of allowed Bragg reflections of the corresponding cubic as-synthesized phase of the MOF.

8.2.8 Isothermal Gas Sorption

CO_2 Sorption Isotherms

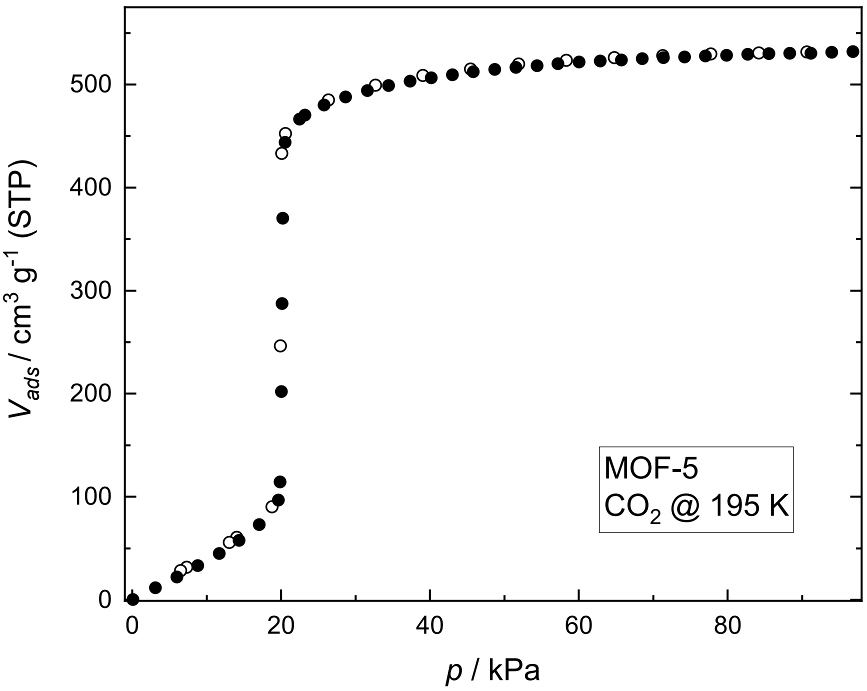

Figure 8.88: CO_2 sorption isotherms of dry MOF-5 recorded at 195 K. Adsorption and desorption branches are shown with closed and open symbols.

8.2.9 *In-situ* Gas Sorption Powder X-ray Diffraction

In-situ CO_2 Sorption PXRD

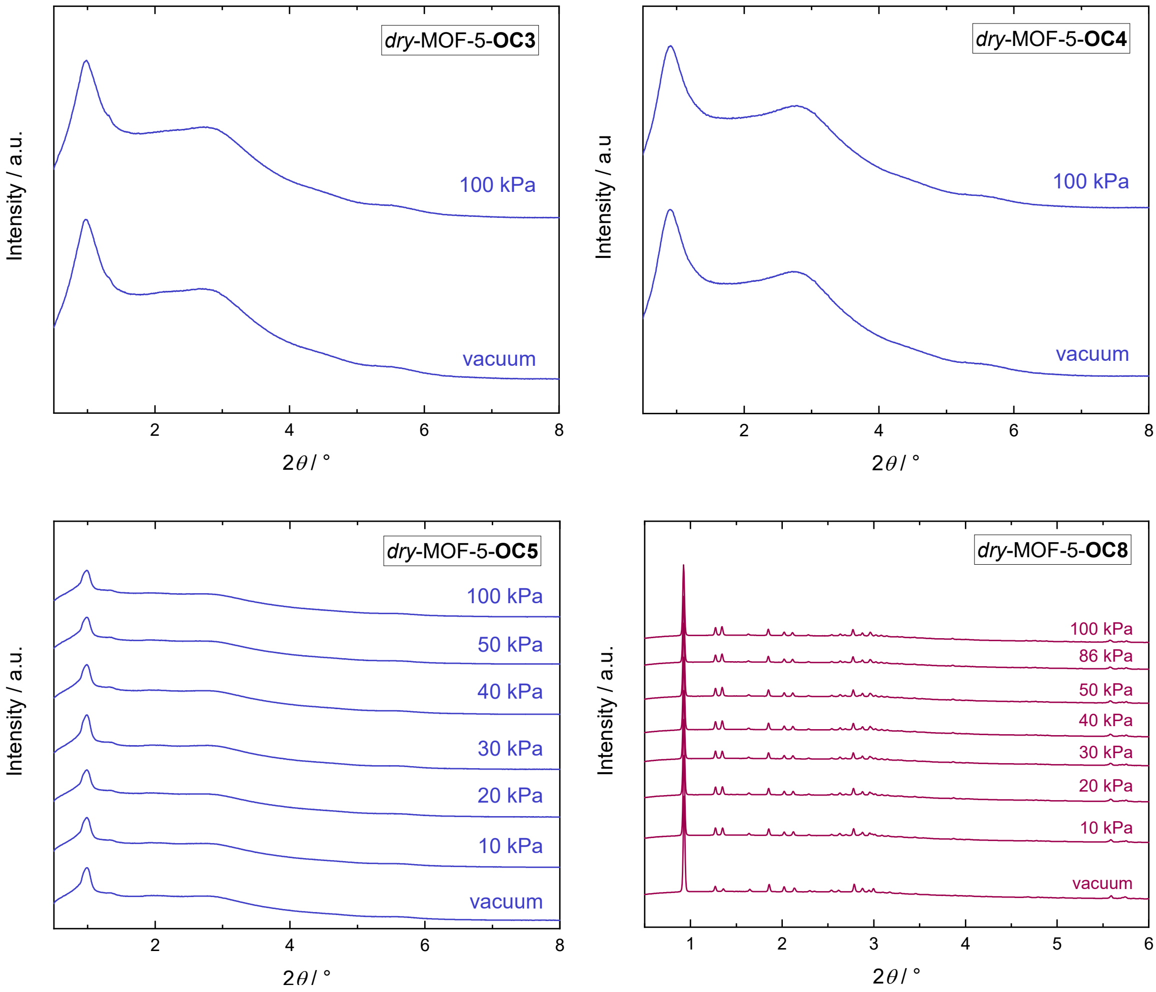

Figure 8.89: *In-situ* CO_2 sorption PXRD patterns of *dry*-MOF-5-**OC3** to *dry*-MOF-5-**OC5** and *dry*-MOF-5-**OC8** recorded at 195 K (DESY).

In-situ n-Butane Sorption PXRD

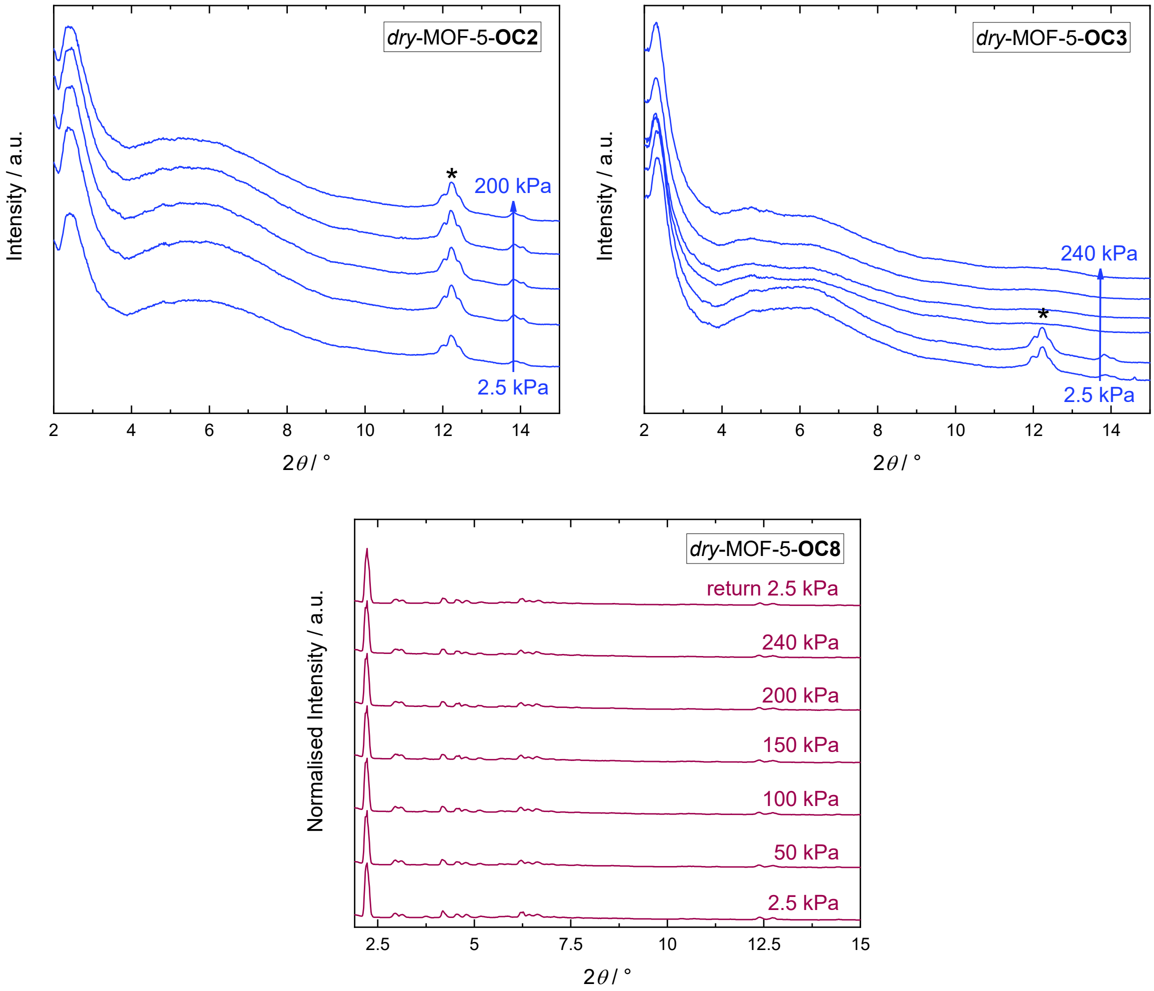

Figure 8.90: *In-situ n*-butane sorption PXRD patterns of *dry*-MOF-5-**OC2**, *dry*-MOF-5-**OC3** and *dry*-MOF-5-**OC8** recorded at 298 K (DELTA, $\lambda = 0.4600$ Å). Marked reflections (*) result from the gas cell being hit by the X-ray beam.

8.2.10 Additional Data on MOF-5-**OC9** and MOF-5-**OC10**

Linker & MOF synthesis

If not otherwise mentioned the experimental data listed herein were collected under the same conditions as stated under Materials & Methods.

2,5-Nonyloxy-1,4-benzenedicarboxylic acid and 2,5-decyloxy-1,4-benzenedicarboxylic acid were prepared using the same procedure as stated under Materials & Methods section 6.1.3 by replacing the alkyl halide with 1-Bromooctanefor H_2(**C9O**-bdc) and 1-Bromodecane for H_2(**C10O**-bdc).

2,5-Nonyloxy-1,4-benzenedicarboxylic acid (H_2(**C9O**-bdc), ^1H NMR (400 MHz, DMSO-d_6): δ 12.89 (s, 2 H, COOH), 7.26 (s, 2 H, Ar–H), 3.97 (t, $J = 6.4$ Hz, 4 H, OCH_2), 1.72-1.62 (m, 4 H, CH_2), 1.45-1.36 (m, 4 H, CH_2), 1.34-1.20 (m, 20 H, CH_2), 0.86 (t, $J = 6.9$ Hz, 6 H, CH_3) ppm; ^{13}C NMR (126 MHz, DMSO-d_6): δ 166.83, 150.43, 125.49, 115.53, 69.13, 31.29, 28.98, 28.71, 28.64, 25.32, 22.10, 13.9 ppm.

2,5-Decyloxy-1,4-benzenedicarboxylic acid (H_2(**C10O**-bdc), ^1H NMR (500 MHz, DMSO-d_6): δ 12.84 (s, 2 H, COOH), 7.24 (s, 2 H, Ar–H), 3.96 (t, $J = 6.4$ Hz, 4 H, OCH_2), 1.69-1.62 (m, 4 H, CH_2), 1.43-1.36 (m, 4 H, CH_2), 1.32-1.19 (m, 24 H, CH_2), 0.84 (t, $J = 6.9$ Hz, 6 H, CH_3) ppm; ^{13}C NMR (101 MHz, DMSO-d_6): δ 167.36, 150.87, 125.98, 115.93, 69.54, 31.78, 29.51, 29.42, 29.20, 29.18, 29.16, 25.79, 22.59, 14.45 ppm.

The corresponding materials MOF-5-**OC9** and MOF-5-**OC10** were synthesized using the linkers H_2(**C9O**-bdc) or H_2(**C10O**-bdc) and the methods described under Materials & Methods section 6.1.3.

Powder X-ray diffraction data

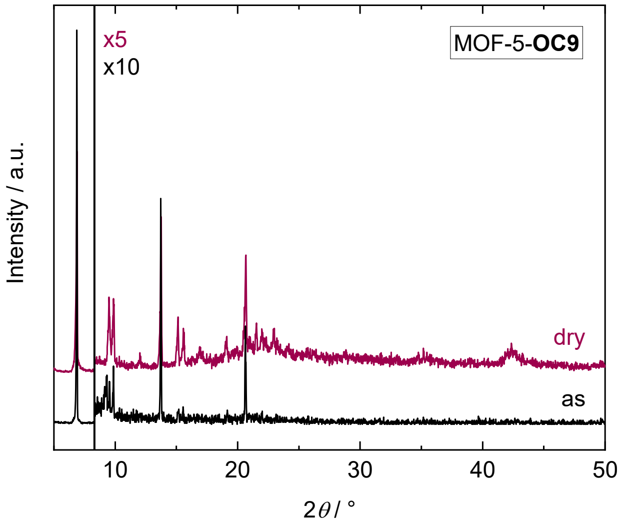

Figure 8.91: PXRD patterns of *as*-MOF-5-**OC9** and *dry*-MOF-5-**OC9**. The data quality of the diffraction pattern of *as*-MOF-5-**OC9** is limited, however, the compound appears to be rhombohedral. *dry*-MOF-5-**OC9** clearly is rhombohedral (see profile fit in Figure 8.93). The rhombohedral distortion of *dry*-MOF-5-**OC9** is a bit smaller compared to *dry*-MOF-5-**OC8** and *dry*-MOF-5-**OC7**, as expected due to the larger bulk of the **-OC9** side chains.

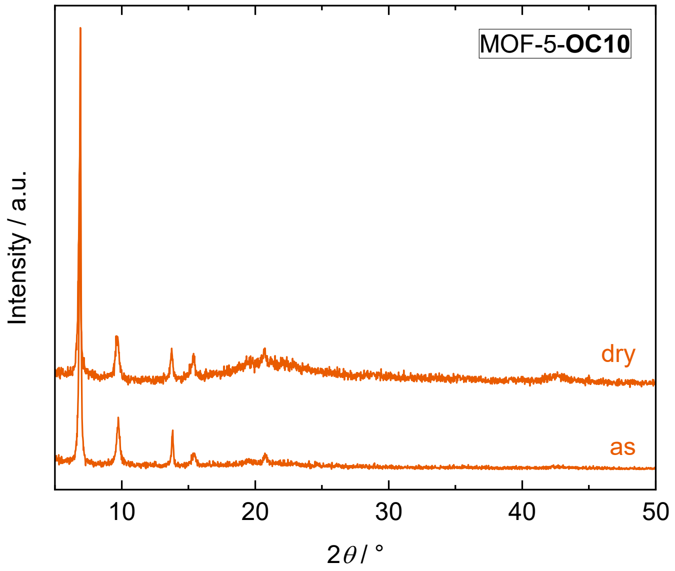

Figure 8.92: PXRD patterns of *as*-MOF-5-**OC10** and *dry*-MOF-5-**OC10**. MOF-5-**OC10** is cubic in the as synthesized state and remains cubic after guest removal (see profile fit in Appendix Figure 8.93). We thus conclude that the **-OC10** side chains fully occupy the pores in the cubic form, so that a rhombohedral distortion is not possible in the guest-free state.

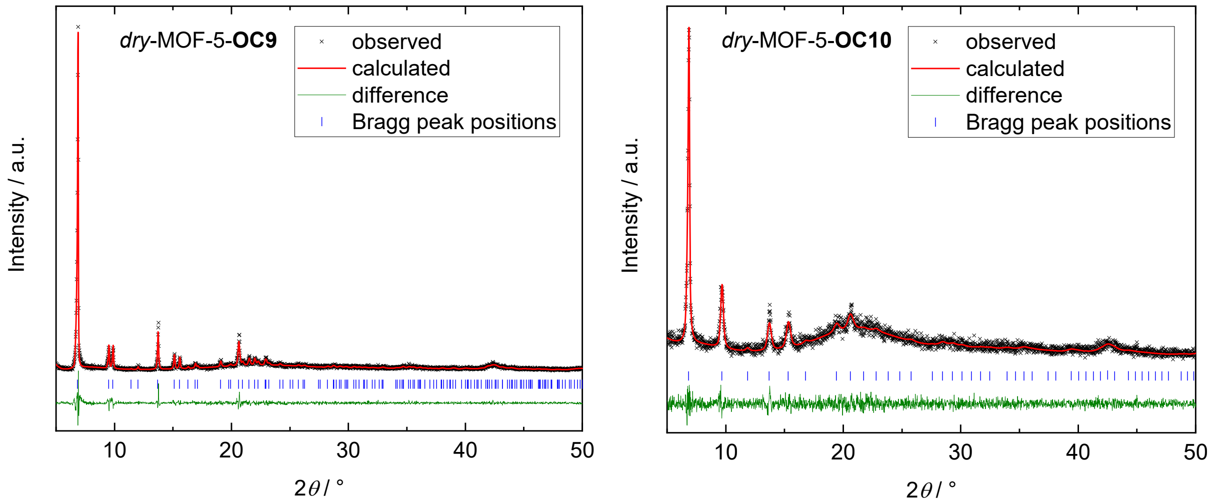

Figure 8.93: PXRD pattern with profile fits (Pawley method) of *dry*-MOF-5-**OC9** and *dry*-MOF-5-**OC10** (see Table 8.33 for crystallographic data).

Table 8.33: Unit cell parameters a, b, c and cell volume V determined by profile fitting (Pawley method) of the PXRD patterns and the corresponding R_{wp}, R_{exp} and χ^2 values for the *dry*-MOF-5-**OC9** and *dry*-MOF-5-**OC10**.

Compound	*dry*-MOF-5-**OC9**		*dry*-MOF-5-**OC10**
crystal system	trigonal	rhombohedral	cubic
space group	$R\bar{3}$		$Pm\bar{3}m$
a / Å	17.957(4)	12.944(3)	12.931(10)
b / Å	17.957(4)	12.944(3)	12.931(10)
c / Å	23.252(7)	12.944(3)	12.931(10)
α / °	90	87.84(2)	90
β / °	90	87.84(2)	90
γ / °	120	87.84(2)	90
V / Å^3	6493(3)	2164(2)	2162(5)
R_{wp}	19.31		17.25
R_{exp}	15.85		16.41
χ^2	1.48		1.11

FT-IR spectroscopy

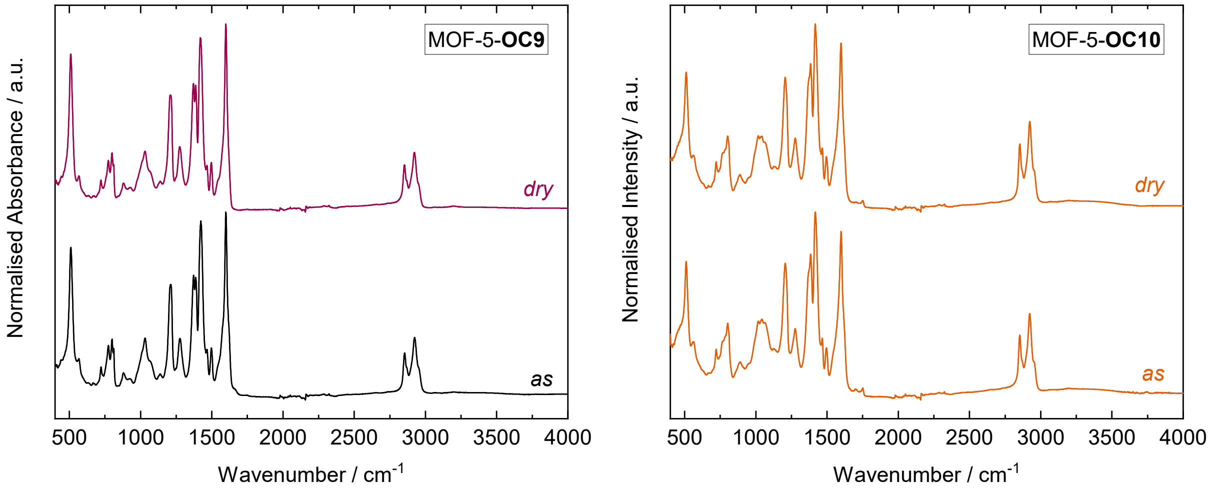

Figure 8.94: FT-IR spectra of MOF-5-**OC9** (left) and MOF-5-**OC10** (right) in *as*- and *dry* states.

TG-DSC

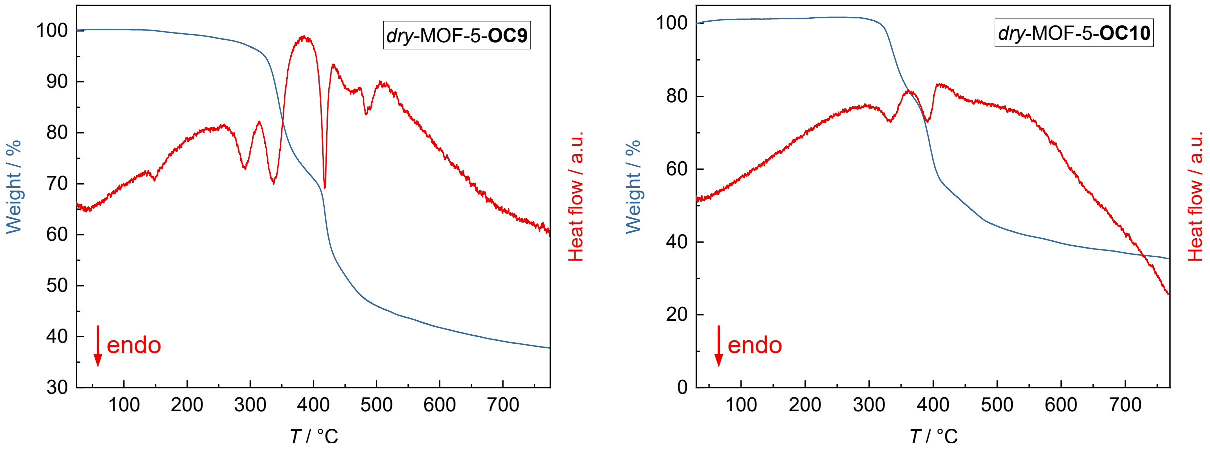

Figure 8.95: TG-DSC data of *dry*-MOF-5-**OC9** (left) and *dry*-MOF-5-**OC10** (right). The endothermic signal of *dry*-MOF-5-**OC9** at approx. 160 °C is ascribed to the phase transition from the rhombohedral to the cubic phase. This is in excellent agreement with variable temperature PXRD data (see Appendix Figure 8.96).

Variable-temperature PXRD

Collection of PXRD data as a function of temperature was conducted at beamline BL9 at DELTA with a monochromatic X-ray beam ($\lambda = 0.6199$ Å) using a MAR345 image plate detector. The samples were finely ground, filled into 1.0 mm diameter quartz capillaries and placed on an Anton Paar DHS1100 hot stage and heated under a polyether ether ketone (PEEK) dome. The temperature calibration of the hot stage was performed by reference XRPD measurements of α-quartz.

A series of additional broad reflections from about 6.9° 2θ originate from the dome's material. Thus, only the reflections between 2° and 6.5° 2θ will be discussed here. Due to the limitations of the setup and the large width of the capillary, the reflections of *dry*-MOF-5-**OC9** are rather broad (see Appendix Figure 8.96). Nevertheless, the rhombohedral crystal structure is clearly visible from the double reflections around 3.9° and 6.2° 2θ. Between 150 °C and 175 °C both double peaks merge into a single peak, which is a clear signature for the rhombohedral-to-cubic phase transition. The transition temperature is in excellent agreement with the TG-DSC data shown in Appendix Figure 8.95.

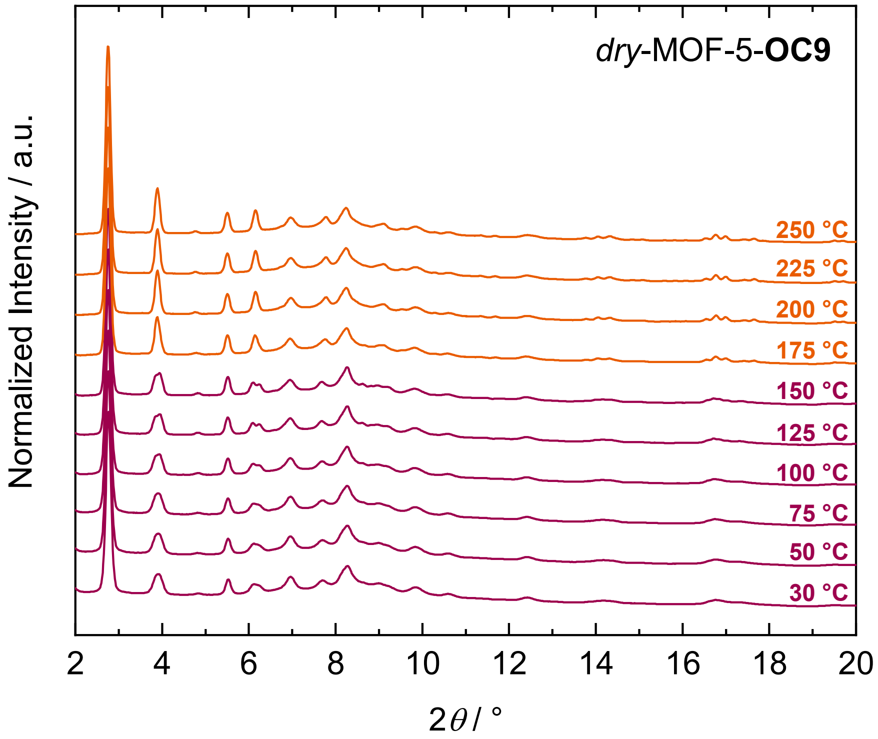

Figure 8.96: Variable temperature PXRD pattern of *dry*-MOF-5-**OC9** recorded in the range from 30 to 250 °C.

8.3 List of Publications

1. R. Pallach, J. Keupp, K. Terlinden, L. Frentzel-Beyme, M. Kloß, A. Machalica, J. Kotschy, S. K. Vasa, P. A. Chater, C. Sternemann, M. T. Wharmby, R. Linser, R. Schmid, S. Henke. Frustrated flexibility in metal-organic frameworks. *Nat. Commun.* **2021**, *12*, 4097.

2. J. Song, R. Pallach, L. Frentzel-Beyme, P. Kolodzeiski, G. Kieslich, P. Vervoorts, C. L. Hobday, S. Henke. Tuning the High-Pressure Phase Behaviour of Highly Compressible Zeolitic Imidazolate Frameworks: From Discontinuous to Continuous Pore Closure by Linker Substitution. *Angew. Chem. Int. Ed.* **2022**, *61*, e202117565.

3. L. Frentzel-Beyme, M. Kloss, P. Kolodzeiski, R. Pallach, S. Henke. Meltable Mixed-Linker Zeolitic Imidazolate Frameworks and Their Microporous Glasses - From Melting Point Engineering to Selective Hydrocarbon Sorption. *J. Am. Chem. Soc.* **2019**, *141*, 12362.

4. L. Frentzel-Beyme, M. Kloß, R. Pallach, S. Salamon, H. Moldenhauer, J. Landers, H. Wende, J. Debus, S. Henke. Porous purple glass - A cobalt imidazolate glass with accessible porosity from a meltable cobalt imidazolate framework. *Mater. Chem. A* **2019**, *7*, 985.

5. H. H.-M. Yeung, A. F. Sapnik, F. Massingberd-Mundy, M. W. Gaultois, Y. Wu, D. X. Fraser, S. Henke, R. Pallach, N. Heidenreich, O. Magdysyuk, N. T. Vo, A. L. Goodwin. Control of Metal-Organic Framework Crystallization by Metastable Intermediate Pre-equilibrium Species. *Angew. Chem. Int. Ed.* **2019**, *58*, 566.

6. D. C. Tymann, L. Benedix, L. Iovkova, R. Pallach, S. Henke, D. Tymann, M. Hiersemann. Photochemical Approach to the Cyclohepta[*b*]indole Scaffold by Annulative Two-Carbon Ring-Expansion. *Chem. Eur. J.* **2020**, *26*, 11974.

7. B. Glowacki, R. Pallach, M. Lutter, F. Roesler, H. Alnasr, C. Thomas, D. Schollmeyer, K. Jurkschat. *Cis* versus *Trans*: The Coordination Environment about the Tin(IV) Atom in Spirocyclic Amino Alcohol Derivatives. *Chem. Eur. J.* **2018**, *24*, 19266.